MICROSTRUCTURAL CHARACTERISATION OF PROTON-IRRADIATED MODEL REACTOR PRESSURE VESSEL STEELS

by

ALEXANDRA C. DICKINSON-LOMAS

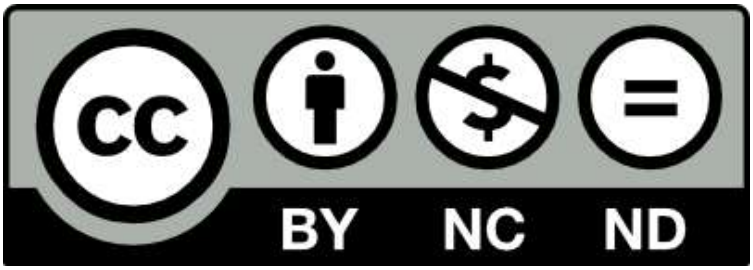
A thesis submitted to the University of Birmingham for the degree of DOCTOR OF PHILOSOPHY

School of Metallurgy and Materials
College of Engineering and Physical Science
School of Metallurgy and Materials

October 2024

UNIVERSITY OF BIRMINGHAM

University of Birmingham Research Archive
e-theses repository



This unpublished thesis/dissertation is under a Creative Commons Attribution-NonCommercial-NoDerivatives 4.0 International (CC BY-NC-ND 4.0) licence.

You are free to:

Share — copy and redistribute the material in any medium or format

The licensor cannot revoke these freedoms as long as you follow the license terms.

Under the following terms:

Attribution — You must give appropriate credit, provide a link to the license, and indicate if changes were made. You may do so in any reasonable manner, but not in any way that suggests the licensor endorses you or your use.

NonCommercial — You may not use the material for commercial purposes.

NoDerivatives — If you remix, transform, or build upon the material, you may not distribute the modified material.

No additional restrictions — You may not apply legal terms or technological measures that legally restrict others from doing anything the license permits.

Notices:

You do not have to comply with the license for elements of the material in the public domain or where your use is permitted by an applicable exception or limitation.

No warranties are given. The license may not give you all of the permissions necessary for your intended use. For example, other rights such as publicity, privacy, or moral rights may limit how you use the material.

Unless otherwise stated, any material in this thesis/dissertation that is cited to a third-party source is not included in the terms of this licence. Please refer to the original source(s) for licencing conditions of any quotes, images or other material cited to a third party.

Abstract

Formation mechanisms of Mn-Ni-Si rich precipitates under irradiation in reactor pressure vessel (RPV) steels are not fully understood. This makes predicting radiation induced embrittlement in RPV steels challenging, leading to uncertainty around lifetime extensions of ageing reactors, and alloy design for new reactors. To understand and predict embrittlement, segregation behaviour of solute elements, and precipitation under irradiation must be understood. Proton irradiation experiments can be used to accelerate understanding of the mechanisms of solute segregation in radiation damage environments. In this work, three ferritic model alloys and an A508-3 reactor pressure vessel steel have been irradiated using a 2.9 MeV proton beam, at approximately 350 °C, to a peak dose of 2 dpa. Microstructural characterisation has been carried out using a range of complementary techniques including: transmission electron microscopy (TEM), atom probe tomography (APT), and small angle neutron scattering (SANS).

Radiation enhanced precipitation led to hardening by enhancing solute segregation, resulting in dense microstructures containing dislocation loops and precipitates. Mn, Ni and Si were observed to segregate to dislocation loops under irradiation in the Fe-Mn-Ni-Si alloy, and then to form precipitates at higher doses. Hardening was greater in the Ni containing alloy, corresponding with higher total number density of precipitates at all doses; close to the Bragg peak it was 2 orders of magnitude higher in the Ni containing alloy at 4.55×10^{22} m^{-3} compared with 1.01×10^{20} m^{-3}. Two new populations of precipitates were identified after irradiation in the Fe-Mn-Ni-Si model alloy, using TEM and APT; Mn-Ni-Si rich precipitates (non-stoichiometric $Mn_6Ni_{16}Si_7$ G phase structures) and Mn-Si nitrogen rich precipitates ($MnSiN_2$). The same cuboidal nitrides were observed in the Fe-Mn-Si alloy after irradiation, and their formation is attributed to nitrogen contamination of the vacuum. These nitrides were only observed close to the Bragg peak in the Fe-Mn-Ni-Si alloy, but were found at all doses in the Ni-free alloy. At higher doses, nitrogen ingress led to precipitation of Mn-Si nitrides inside Mn-Ni-Si precipitates, creating a Mn-Si-N core and Ni-rich shell structure, observed using STEM-EDX. This suggests that there is a lower barrier for radiation assisted nucleation of Mn-Ni-Si precipitates compared with Mn-Si nitrides. The increase in number of precipitates in the Ni containing alloy, compared with the sparsely distributed nitrides in the Ni free alloy, suggests that Ni enhances radiation induced segregation, clustering and precipitation.

Elevated diffusion rates produced by radiation damage led to segregation of Mn, Ni and Si to dislocation loops and the precipitation of Mn-Ni-Si phases. Ni has a significant synergistic effect with Mn and Si, on precipitation of secondary phases in a radiation environment, and is the main constituent element in secondary phases. The precipitation observed in model ferritic alloys is not comparable to neutron-irradiated RPV steel microstructures. However, observations of dislocation loops, segregation and precipitation in these samples contributes to understanding the interaction between Ni, Mn and Si solute elements in a radiation environment and the mechanisms of radiation mediated precipitation.

Acknowledgments

Firstly, I must thank my fantastic supervisory team. Prof. Yu-Lung Chiu for providing excellent support through access to amazing facilities, enthusiasm for interrogating my TEM data, and not least many encouraging analogies over the past 4 years. Scientific research really is a lot like rock climbing! I also have appreciated the involvement of Prof. Martin Freer and Dr. Chris Hardie at various stages of the project.

I acknowledge the financial support provided by the United Kingdom Atomic Energy Authority for part of this project, but more importantly the exceptional supervision I have received. I am extremely grateful to my industrial supervisor, Dr. Luke Hewitt, who has dedicated a huge amount of time to supporting me to write my thesis, and has never failed to be sensible, encouraging, and kind.

I also acknowledge the experimental support and funding received from the National Nuclear User Facility (for access to the Nuclear Materials Atom Probe, at the University of Oxford), and from the Institut Laue Langevin, to access the D33 instrument through the ILL User Access scheme.

I'm very grateful to Dr. Nina Steinke and Dr. Bob Cubitt, (the D33 instrument team) for their experimental support, especially as we were operating the instrument from Birmingham and Switzerland during the extended lock-downs of 2021. I must also thank Dr. Mark Laver for all of his support with planning and carrying out my small angle neutron scattering experiments during my first year, and Dr Helen Swan (National Nuclear Laboratory) for providing feedback and helpful discussion on my small angle neutron scattering analysis.

My visits to Oxford were some of the best days of my PhD, thanks to the lovely people in the Oxford Atom Probe lab, in particular Dr. Christina Hofer and Sophia Von Ungermann. Thank you for the support, everything you have taught me and all our RPV related discussions!

This thesis has been proofread by Thomas Dudley and Anna Dickinson-Lomas, in line with University Regulations on Third Party Editing, thank you both.

I extend my appreciation to my colleagues in the Electron Microscopy Group and the wider School of Metallurgy and Materials at the University of Birmingham; with special thanks to Dr. Minshi Wang, Dr Feng Wang, and Dr. Zhaohe Gao for dedicating time to train me to use the microscopes, and to Dr. Ludwig Schneider for helping with last minute sample preparation. I am very grateful to the teaching staff who I have worked with, who really made the PhD process feel worthwhile, especially Dr Austin Tomlinson, and Prof. Sam Cruchely.

Of course, there is no way to complete a PhD without the support of fellow PhD students. My particular thanks go to Emily Lewis, for her constant friendship and for being an excellent collaborator. Liam and Uthman deserve my thanks (or apologies?), as my go-to friends for jokes about electron microscopy, and I hope that we will continue to work together in future!

I am so grateful to my extremely supportive partner, Tom, thank you for encouraging me with my studies, taking me up mountains and of course reading my thesis. I thank my family for their unfailing support throughout my education. I must acknowledge my grandfather, Brian, for being more consistently invested in my PhD project than anyone over the past 4 years. Enormous credit for this work goes to my mum, Cate, for coping

with two daughters working on full-time PhDs, while another completed her A-levels. I'm so proud of my sisters, Anna and Lottie, and I'm so lucky to have these two mins who never fail to cheer me up and give me much-needed perspective!

Contents

1 Introduction 1

2 Literature Review: Microstructural characteristics of radiation embrittlement in modern RPV steels 7
2.1 Reactor pressure vessel steels . . . 9
2.1.1 RPV compositions . . . 10
2.1.2 Fabrication & heat treatment . . . 12
2.1.3 Degradation of mechanical properties of RPV Steels under irradiation 14
2.2 Radiation damage in RPV steels . . . 18
2.2.1 Accelerated radiation damage techniques . . . 19
2.2.2 Flux & dose rate effects . . . 23
2.2.3 Temperature effects . . . 27
2.3 Radiation damage in RPV steels . . . 29
2.3.1 Radiation induced dislocation loops in bcc Fe . . . 29
2.3.2 Radiation induced segregation in RPV steels . . . 33
2.4 Mn-Ni-Si rich clusters and precipitates in irradiated RPV steels . . . 38
2.4.1 Effect of alloy composition on defect formation in RPV steels. . . . 41
2.4.2 Using model alloys to understand solute segregation and clustering under irradiation . . . 46
2.4.3 Computational modelling of radiation damage mechanisms in RPV steels . . . 50
2.5 Effects of solute rich defects on mechanical properties of RPV steels . . . 55
2.6 Using complementary characterisation techniques for radiation damage analysis . . . 56
2.7 Motivation for further research . . . 60

3 Materials & Methods 63
3.1 Model reactor pressure vessel steels . . . 63
3.1.1 As-received sample microstructures . . . 64
3.1.2 Sample preparation post-irradiation & sample overview . . . 68
3.2 Proton irradiation . . . 71
3.2.1 Modelling ion damage . . . 71
3.2.2 MC40 cyclotron . . . 73
3.2.3 Irradiation conditions and monitoring . . . 76
3.3 Transmission Electron Microscopy & Energy Dispersive X-Ray Spectrometry 80
3.3.1 Sample preparation . . . 80

3.3.2 TEM imaging, diffraction and STEM-EDX . . . 83
3.3.3 STEM imaging and EDX mapping . . . 85
3.3.4 Diffraction in TEM mode, and CBED thickness measurement . . . 85
3.4 EDX Quantification . . . 87
3.5 Atom Probe Tomography . . . 88
3.5.1 Sample preparation . . . 88
3.5.2 Atom probe tomography measurements . . . 92
3.5.3 Data summary . . . 94
3.5.4 Data processing and reconstruction method . . . 95
3.6 APT data analysis methods . . . 99
3.6.1 Composition analysis and peak overlaps . . . 99
3.6.2 Proxigrams & concentration profiles . . . 101
3.6.3 Nearest neighbour distribution analysis . . . 101
3.7 Small Angle Neutron Scattering . . . 101
3.7.1 Small angle scattering . . . 103
3.7.2 Scattering cross-section . . . 103
3.7.3 Coherent scattering . . . 105
3.7.4 Magnetic neutron Scattering . . . 106
3.7.5 Separation of magnetic and nuclear scattering . . . 106
3.7.6 ILL D33 experiment . . . 107
3.7.7 Measurement summary, counting times and background . . . 110
3.8 SANS data analysis . . . 113
3.8.1 Separation of magnetic and nuclear scattering . . . 116
3.8.2 Shape independent fitting . . . 116
3.8.3 Shape factor & scattering contrast fitting using a priori information 118
3.9 Nanoindentation . . . 121
3.10 Summary . . . 124

4 Defect Size Distribution and Composition Analysis using TEM & STEM-EDX 127
4.1 Radiation hardening in Fe-Mn-Ni-Si and Fe-Mn-Si alloys. . . . 127
4.2 TEM Specimen information . . . 131
4.3 Size distribution analysis of radiation induced defects using STEM Imaging & EDX mapping . . . 133
4.3.1 Fe-Mn-Ni-Si . . . 133
4.3.2 Fe-Mn-Si . . . 138
4.4 Composition analysis of defect types using STEM-EDX . . . 144
4.4.1 Fe-Mn-Ni-Si . . . 144
4.4.2 Fe-Mn-Si . . . 165
4.5 Precipitate structure analysis in Fe-Mn-Ni-Si using selected area electron diffraction . . . 169
4.6 Grain boundary segregation in Fe-Mn-Ni-Si . . . 181
4.7 Summary of observations . . . 185
4.7.1 Population characteristics with dose . . . 185
4.7.2 Composition . . . 188
4.7.3 Structure . . . 190
4.7.4 Segregation to defects . . . 190

4.8 Conclusion . . . 190

5 Local Composition Analyses of Proton-Irradiated and unirradiated Model Alloys and RPV Steel Using Atom Probe Tomography 191
5.1 Matrix composition results & depletion analysis . . . 191
5.1.1 Fe-Mn-Ni-Si matrix composition . . . 196
5.1.2 Fe-Mn-Si matrix composition . . . 196
5.1.3 Fe-Mn-Ni matrix composition . . . 197
5.1.4 Summary of matrix composition analysis of model alloys . . . 197
5.2 Fe-Mn-Ni-Si precipitate analysis: Large precipitate . . . 198
5.2.1 1D concentration profiles . . . 199
5.2.2 Proxigram composition analysis . . . 201
5.2.3 Field evaporation effects on ion density . . . 202
5.3 Comparison of measured compositions for whole and partial precipitates. . . 205
5.3.1 Partial precipitate composition . . . 205
5.3.2 Comparison of measured compositions . . . 205
5.4 Fe-Mn-Ni radiation-induced clustering analysis . . . 207
5.4.1 Proxigram & concentration profiles . . . 207
5.4.2 Nearest neighbour distribution analysis . . . 212
5.5 A508-3 RPV steel results . . . 212
5.5.1 A508-3 steel composition analysis . . . 216
5.5.2 Irradiated carbide-matrix interface . . . 218
5.5.3 Irradiated A508-3: Grain boundary segregation . . . 221
5.6 Summary and Conclusion . . . 222

6 Statistical analysis of radiation induced microstructural changes using small angle neutron scattering 225
6.1 Validity of assumptions and experimental limitations . . . 226
6.2 Magnetic and nuclear scattering from radiation induced microstructural changes . . . 227
6.3 A Ratio Analysis . . . 230
6.4 Size distributions, volume fractions and scattering length densities . . . 231
6.4.1 Maximum Entropy Method (MEM) Calculated Size Distributions of Scattering Particles . . . 232
6.4.2 Summary of MEM fitting outputs . . . 237
6.4.3 Log normal fitting . . . 237
6.5 Fe-Mn-Ni-Si & Fe-Mn-Si Model Fitting . . . 242
6.5.1 Morphology fits . . . 242
6.5.2 Composition fits: Fe-Mn-Ni-Si . . . 244
6.5.3 Size and volume fraction fits: Fe-Mn-Si . . . 248
6.6 Summary of fitting outputs . . . 250
6.7 Summary & Conclusion . . . 254

7 Discussion 257
7.1 Summary of results and use of complementary techniques . . . 257
7.1.1 Summary of results . . . 262
7.2 Precipitate phase identification . . . 269

7.2.1 Mn-Ni-Si rich precipitates . . . 269
7.2.2 Mn-Si-N rich precipitates . . . 278
7.3 Discussion on precipitation mechanisms . . . 281
7.3.1 Mn-Ni-Si precipitation mechanisms . . . 281
7.3.2 The effect of nitrogen on radiation induced precipitation . . . 287
7.3.3 Summary . . . 290
7.4 Dose/dose rate & temperature effects on microstructural evolution . . . 293
7.5 Clustering of Mn & Ni at dislocation loops in Fe-Mn-Ni alloy . . . 297
7.6 Hardening effect of proton-irradiation on model alloys . . . 299
7.7 Improving proton-irradiation experiments . . . 304

8 Conclusions and Further Work 307
8.1 Proposed future work . . . 310

A Appendices 345
A.1 SANS Experimental Proposal- D33, ILL . . . 345
A.2 SANS D33 Supplementary Experimental Information . . . 348
A.3 Consideration of Sector Angle in Calculation of Magnetic and Nuclear Scattering . . . 350

List of Acronyms

APT - Atom probe tomography
AKMC - Atomistic kinetic Monte-Carlo
BCA - Binary collision approximation
BCC - Body centred cubic
BF - Bright field
BSE - Back-scattered electron
CBED - Convergent beam electron diffraction
CIF - Crystallographic information file
CRP - Cu rich precipitate
DBTT - Ductile to brittle transition temperature
DF - Dark field
DFT - Density functional theory
dpa - displacements per atom
EDX - Energy dispersive X-ray spectroscopy
FCC - Face centred cubic
HAADF - High angle annular dark field
IAEA - International Atomic Energy Agency
ICSD - Inorganic crystal structures database
ILL - Institut Laue Langevin
LEAP - Local electrode atom probe
MEM - Maximum entropy method
MNSP - Mn, Ni & Si rich precipitate
NRT-dpa - Norgett-Robinson-Torrens displacements per atom
NuMAP - Nuclear Materials Atom Probe facility, University of Oxford
PFIB - Plasma focussed ion beam
PIA- Post-irradiation annealing
PKA - Primary knock-on atom
PWR - Pressurised water reactor
RAFM - Reduced activation ferritic/martensitic
RIS - Radiation induced segregation
RPV - Reactor pressure vessel
SADP - Selected area diffraction pattern
SANS - Small angle neutron scattering
SEM - Scanning electron microscopy/microscope
SRIM - Stopping Range of Ions in Matter
STEM - Scanning transmission electron microscopy
TEM - Transmission electron microscopy
USE - Upper shelf energy
XRD - X-ray diffraction

Chapter 1

Introduction

There is a huge global demand for electricity, which is rising year-on-year, with the electrification of many industries providing a solution to the burning of fossil fuels in areas such as transport and manufacturing [1]. Traditional power generation methods, such as burning fossil fuels, pollute the planet and contribute to global warming, threatening the safety and energy security of people across the world. Although renewable energy sources are becoming more widespread, they are not sufficiently consistent providers of base-load electricity in many nations, and much of the infrastructure and storage solutions required for renewables to replace existing energy sources are still in development. It is essential that other sustainable energy sources, such as nuclear power, are both available and increasing their electricity generation.

Light-water cooled reactors account for the majority of operational nuclear reactors globally, making up 83.6 % of operational reactors in 2024 and providing 90 % of nuclear electricity generated [2]. 90 % of all reactors currently under construction are also light-water cooled designs [2]. The average age of operating nuclear reactors worldwide is 39 years, and with pressurised water reactor (PWR) design lives ranging between 40 and 60 years, this means the decline in the number of operating nuclear reactors since 2018 is likely to continue as the average age increases, fig. 1.1 [3, 4].

There are significant challenges faced by governments inhibiting the rate of new build projects, particularly in Europe: with Germany's nuclear programme being scaled down from 2011 ([5]), and the Hinkley Point C new-build project, in the UK, running over 5 years behind schedule and more than £8 billion over budget [6]. There needs to be a solution to the gap in

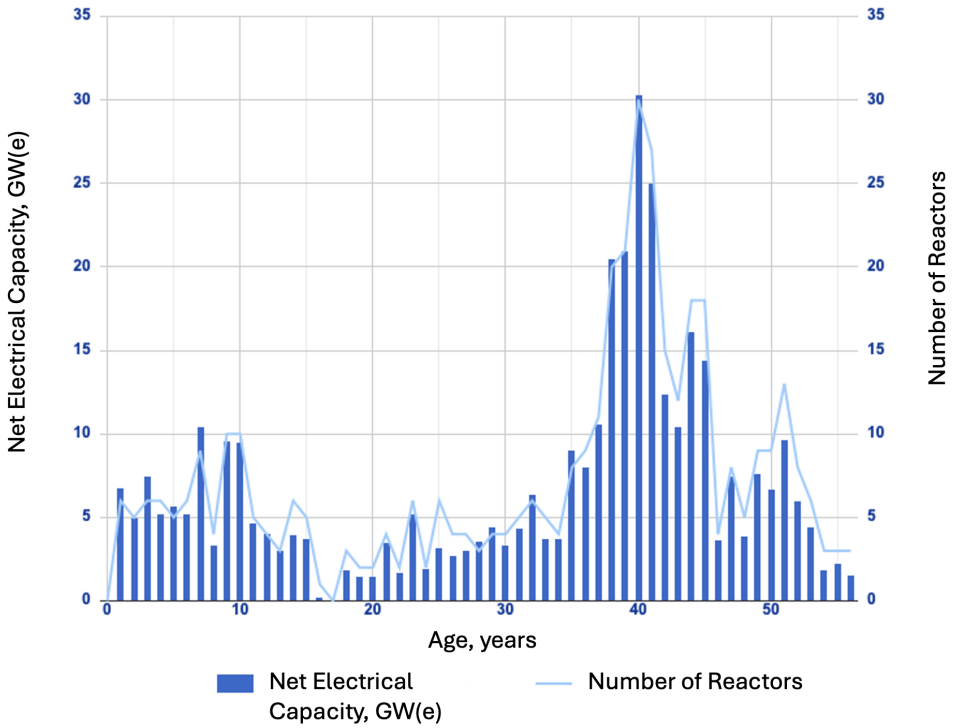


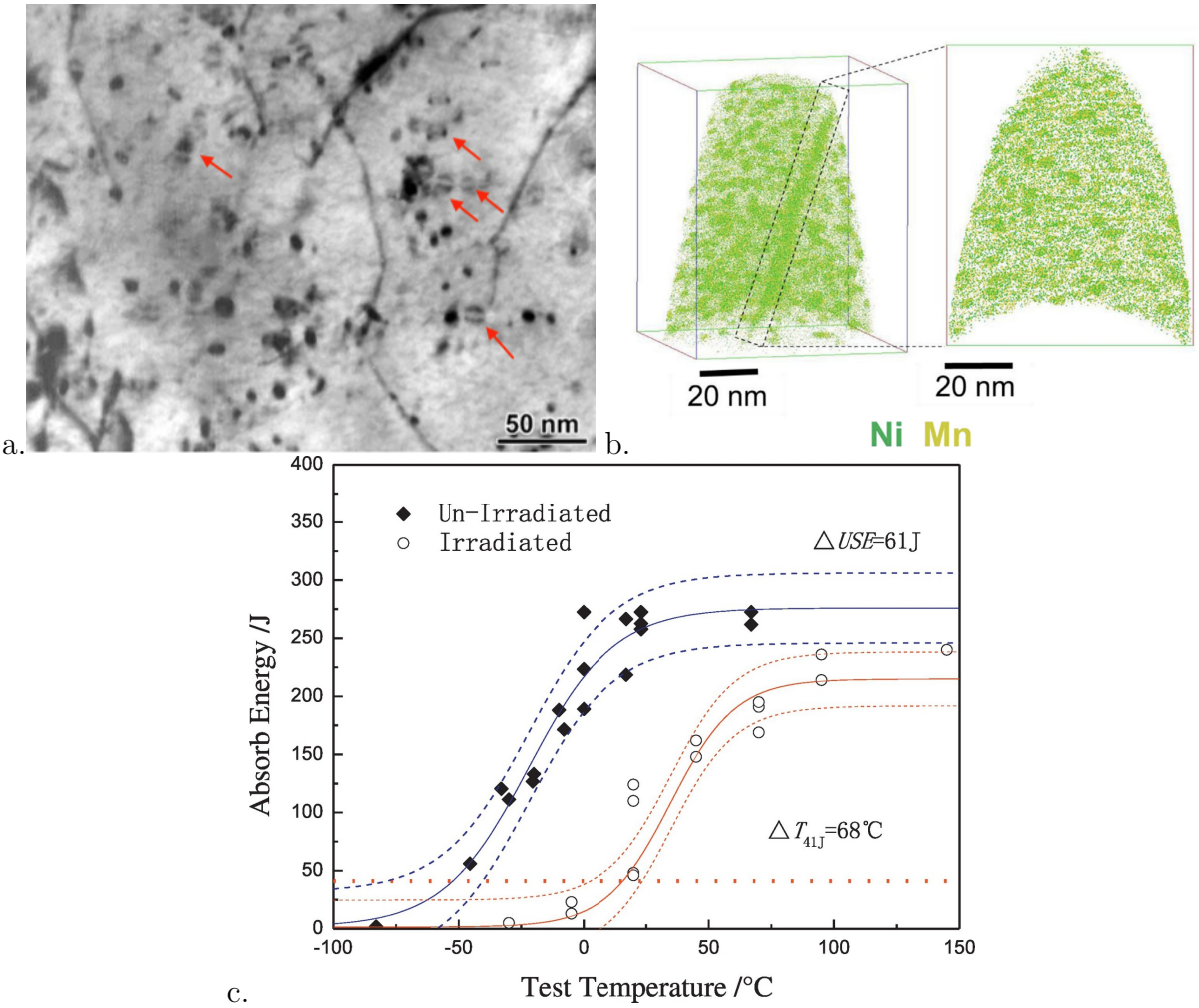
Figure 1.1: Plot showing the total power output, and number of reactors globally in operation as a function of the age of the plant, data accurate as of February 2025 [3]. PRIS - Power Reactor Information System (`www.iaea.org/pris`), 2025© IAEA

supply being faced by many nations. As many generation II reactors approach the end of their design life, there is growing interest in life-extension to provide electricity supply continuity and cost savings [7, 8]. Reactor lifetimes have already been extended from 60 to 80 years in France, and the Palisades reactor, set for shutdown in the US, is currently in recommissioning with a view to extending RPV operating life by an extra 20 years [9, 10]. This approach has the opportunity to provide energy security and economic and environmental benefits by maximising the efficiency of reactor plants. However, there are some key risks to safety involved with extending the lifetime of a nuclear plant.

The reactor pressure vessel (RPV) of a nuclear reactor is the primary containment for radioactive fuel, cladding, and coolant. It has to maintain its structural integrity at elevated temperatures, under high energy (E> 1 MeV) neutron fluxes of around 10^{13} to 10^{16} n.m^{-2}.s^{-1} ([11]), and be resistant to thermal transients. It is economically unrealistic and extremely hazardous to replace the whole RPV vessel during reactor lifetime. Breach of containment could have disastrous consequences for the environment and local communities. The RPV is a life limiting component of a nuclear plant, and mitigating the risk of catastrophic failure is essential for lifetime extension to be a viable solution.

In order to mitigate these risks, it is essential that reactor integrity is monitored closely and that there are accurate regulatory models predicting the degradation of RPV steel fracture toughness. RPV embrittlement leads to an increased probability of brittle fracture, and sudden catastrophic failure of the reactor pressure vessel. Radiation damage leads to embrittlement by producing defects in the material such as dislocation loops, solute clusters and precipitates which act as barriers to dislocation movement. Figure 1.2 shows some examples of microstructural changes observed in neutron irradiation RPV steels leading to deterioration in mechanical properties. This contributes to an increase in yield stress, which at low temperatures can become higher than the stress required to initiate brittle fracture. Therefore, thorough understanding of the mechanisms behind radiation induced defect formation and subsequent embrittlement in radiation environments is essential for safe operation of reactors beyond their original lifetimes.

Current models underpredict embrittlement of low-Cu RPV steels because much of the previous data used to devise them was based on Cu bearing steels and older alloy designs, which did not account for the roles of other solutes in embrittlement [15, 16, 17]. Copper increases



a. b. c.

Figure 1.2: A range of images showing neutron radiation induced defects in RPV steels. a. Radiation induced dislocation loops in a piece of neutron-irradiated surveillance material (Sv-10KhMFT) irradiated up to 26×10^{24} m^{-2}, shown by red arrows [12], b. Mn-Ni-Si clustering in neutron irradiated low-Cu, high-Ni steel with segregation of Mn, Ni and Si to a grain boundary.[13], c. Absorbed energy of Charpy specimens at a rang of temperatures for neutron irradiated and unirradiated A508-3 RPV steel, showing that irradiation led to reduced fracture toughness and increased ductile to brittle transition temperature[14].

a. Reprinted from Journal of Nuclear Materials, 303, Kočík,E Keilová,J Čížek,I Procházka, TEM and PAS study of neutron irradiated VVER-type RPV steels, Pages 52-54, Copyright 2002, with permission from Elsevier.
b. Reprinted from Materialia, 11, Benjamin M. Jenkins, James O. Douglas,Nathan Almirall,Nick Riddle,Paul A.J. Bagot, Jonathan M. Hyde, G. Robert Odette, Michael P. Moody, The effect of composition variations on the response of steels subjected to high fluence neutron irradiation, Page 100717., Copyright 2020, with permission from Elsevier.
c. Reprinted from Engineering Failure Analysis, 82, Yun Lin, Wen Yang, Zhenfeng Tong, Changyi Zhang, Guangsheng Ning, Charpy impact test on A508-3 steel after neutron irradiation, Pages 733-740, Copyright 2017, with permission from Elsevier.

radiation sensitivity by forming high volume fractions of copper rich precipitates (CRPs) under irradiation, leading to hardening and embrittlement [18]. Contemporary alloys have sufficiently low copper content to prevent significant CRP formation, but manganese, nickel, and silicon also cluster under irradiation, leading to embrittlement, fig. 1.2b. The nature of these solute clusters is not fully understood, and the possible phases forming in various alloys under irradiation are not confirmed. Microstructural characterisation of irradiated materials plays a key role in determining the effects of alloy composition on radiation embrittlement.

Lifetime extensions are leading to a reduction in available surveillance material for future monitoring intervals, as the original volume needs to cover a longer period than planned for. This enhances the need for accelerated radiation studies into existing alloys to gain mechanistic understanding to support predictive model development.

Mn-Ni-Si rich defect formation is not yet fully understood, with questions surrounding their thermodynamic stability and precipitation mechanisms. Understanding solute interactions in radiation environments is also relevant to new reactor materials, as many structural materials proposed for Generation IV fission reactors and fusion reactors are steels containing Mn and Si, which will see much higher temperatures and neutron fluxes than those experienced in a Generation II or III fission reactor.

Chapter 2 is a review of the current understanding of radiation embrittlement mechanisms and microstructural evolution in low-Cu RPV steels, relating specifically to Mn-Ni-Si solute segregation and defect formation. This is followed by a description of the methods used in this work and associated analysis methods, chapter 3. The results obtained from proton-irradiated samples are then presented in chapters 4 (TEM & Nanoindentation), 5 (Atom Probe Tomography) and 6 (Small Angle Neutron Scattering). Finally, the discussion, chapter 7, addresses the results in context with literature, suggests possible phases and the microstructural evolution observed in the work are discussed in the context of literature. The conclusions are summarised in chapter 8, along with proposed future studies.

Chapter 2

Literature Review: Microstructural characteristics of radiation embrittlement in modern RPV steels

This review aims to summarise some key characteristics of RPV steels and to then focus on the influences of Mn, Ni and Si on radiation hardening and embrittlement. The role of computational modelling and experimental irradiations are discussed, with consideration of how findings can be transferred to understanding the microstructural and mechanical behaviour evolution of RPV steels in reactor environments. Key arguments surrounding the proposed mechanisms of formation and evolution of Mn, Ni, and Si rich defects under irradiation are presented, focusing on the use of complementary modelling and characterisation techniques.Radiation embrittlement of reactor pressure vessel steels has been widely acknowledged since the 1960s [19]. However, in depth microstructural understanding could not be obtained using characterisation techniques available at that time. With the development of advanced nanoscale characterisation techniques such as APT and high resolution TEM, significant advances in understanding RPV embrittlement have been made [20, 19]. Copper was present in many of these early ingots due to contamination due to the use of scrap materials in fabrication and was present in much higher concentrations in weld regions, as copper was also used as a protective coating for weld wires [21]. As a result, the main radiation embrittlement mechanism is due to the formation of copper-rich

precipitates, first observed using field ion microscopy by Smidt et al. in the 1970s [22]. The first experimental evidence provided for copper-rich precipitates and phosphorus clustering in irradiated RPV steels was found using APT by Miller et al. in 1981 [23]. These precipitates were more thoroughly characterised, through international collaborations run by the IAEA between 1977-1983, leading to a reduction in copper content used in RPV steels due to its correlation with radiation sensitivity [24]. Since the 1970s, RPV steels have been fabricated with < 0.1 wt.% copper content in plate forgings, and phosphorus content < 0.015 wt.%, due to the effects of P content on non-hardening embrittlement [24, 25]. The first physically motivated model for embrittlement, proposed by G.R Odette in 1983, assumed embrittlement was wholly caused by the precipitation of copper-rich precipitates under irradiation, due to radiation enhanced ageing [26].

However, radiation embrittlement continues to be observed in RPV steels, and this has been found to be due to the clustering of other solute elements, primarily Mn, Ni, and Si. The mechanism of formation and nature of these features is different to that of copper-rich precipitates. In RPV steels, Mn Ni and Si are all present in quantities below their solid solubility limits in BCC-Fe at reactor operating temperatures, table 2.1, indicating no thermodynamic driving force for precipitation, and instead there are various proposed mechanisms involved radiation induced segregation and the interaction of point defects stabilising metastable semi-coherest phases that would not form in equilibrium. However, Mn-Ni-Si rich defects have been observed experimentally at higher irradiation fluences.

Table 2.1: Table showing solid solubility limits of solute elements in BCC-Fe from literature, compared with the nominal composition of a Chinese A508-3 RPV steel used in this study.

Solute Atom	Solid solubility limit in BCC-Fe (at. %)	Chinese A508-3 nominal composition (at. %)
Copper	0.076 [27])	0.024
Manganese (at 573K)	3.2 [28]	1.36
Nickel (at 800K)	6.0 [29, 30]	0.7
Silicon	19.3 [31]	0.38

2.1 Reactor pressure vessel steels

Light-water reactor pressure vessels are required to contain nuclear fuel and water at high pressures, around 155 bar (pressurised water reactors) and 70 bar (boiling water reactors), and at operating temperatures between 290-315 °C and 275-288 °C for lifetimes of over 40 years [19, 32]. The RPV is one of the largest components in a nuclear reactor. Sizewell B, the only operating pressurised water reactor in the UK, has an inner diameter of 4.39 m, an inside height of 13.55 m and in the core region the RPV steel is approximately 215 mm thick [33]. Figure 2.1 shows a schematic diagram of the reactor pressure vessel in a PWR. A key region is the beltline, where neutron flux is highest and where structural integrity is most critical.

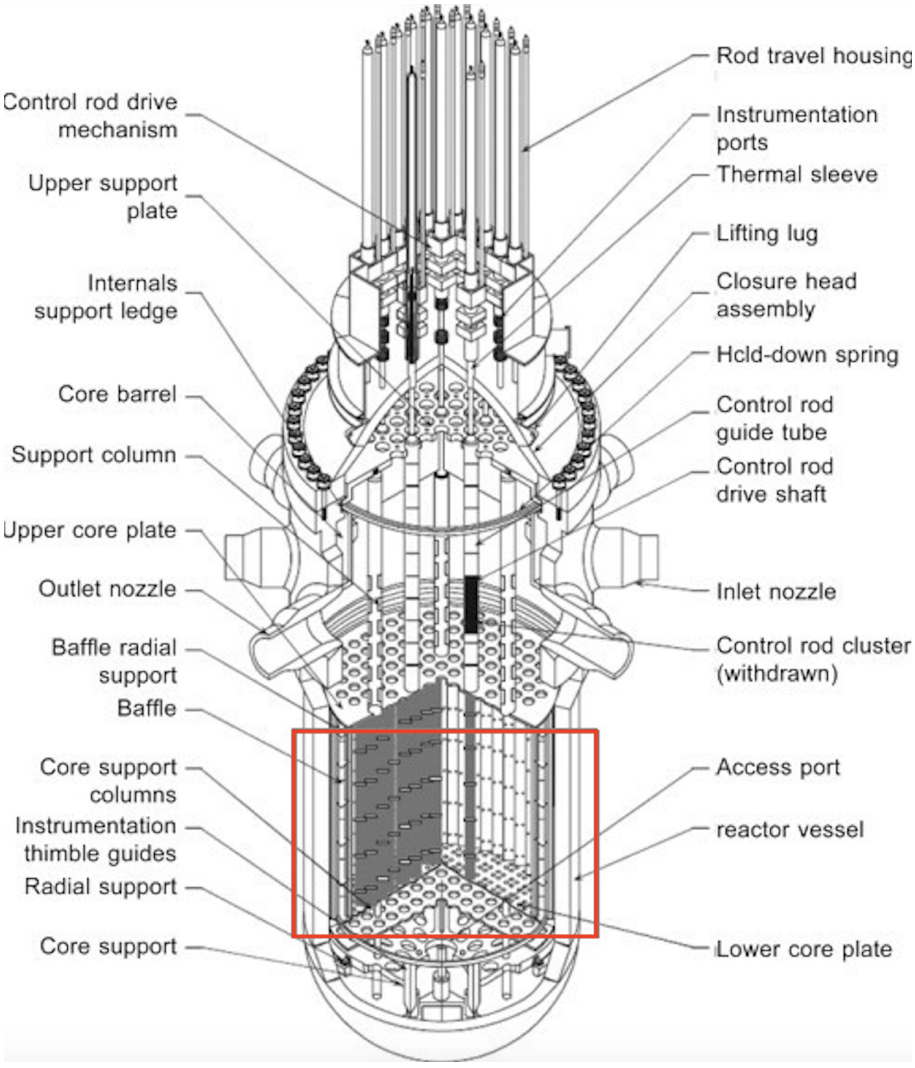


Figure 2.1: Reactor pressure vessel and internals, showing contents of RPV and the region around the beltline (red) with no inlets [34].

2.1.1 RPV compositions

Low alloy bainitic steels are used as pressure vessel materials in light-water cooled reactors. Historically alloys with over 0.1 wt.% copper and 0.012 wt% phosphorus were used, but after observations of significant reductions in fracture toughness and shifts of the DBTT to above room temperature after irradiation, these elements are reduced as much as possible in modern RPV steels [35]. Table 2.2 shows a range of steel compositions used in light-water reactors globally. Mn is added to steels to suppress grain boundary embrittlement by forming stable phosphides and sulphides with P and S impurities that segregate to grain boundaries [18]. As a result, Mn is added in sufficient quantities to ensure S and P are scavenged, and any excess Mn remains in solution. Ni is an austenite stabiliser which is added to low alloy steels to enhance the toughness by promoting grain refinement. However, increased Ni content leads to an increase in radiation sensitivity, so although initial toughness is improved, the ultimate embrittlement is increased [36, 37]. Silicon is added to low alloy steels to increase strength, through solid solution strengthening, and deoxidise the melt, and the role it plays in radiation embrittlement is less clear than Mn and Ni [18, 38].

VVER RPV steels have significantly higher Cr contents than alloys used in western PWRs because earlier designs did not have full internal cladding, so greater corrosion resistance was required [39].

Table 2.2: Table of common low alloy steel compositions, in wt. %, using in forgings for RPVs, from Chapter 10, Structural Alloys for Nuclear Energy Applications [18].

Origin	Alloy	C	Si	Mn	Mo	Ni	Cr	V
France	18MnD5 RCC M2112 (1988)	0.00-0.20	0.10-0.30	1.15-1.55	0.45-0.55	0.50-0.80	0.00-0.24	0.00-0.01
Russia (VVER 440)	15Kh2MFA	0.13-0.18	0.17-0.37	0.30-0.60	0.60-0.80	0.00-0.40	2.50-3.00	0.25-0.35
Russia (VVER 1000)	15Kh2NMFA	0.13-0.18	0.17-0.37	0.30-0.60	0.50-0.70	1.00-1.50	1.80-2.30	0.00-0.10
Germany	22NiMoCr37 (1991)	0.17-0.23	0.15-0.35	0.50-1.00	0.00-0.60	0.50-1.20	0.25-0.50	0.00-0.02
USA	ASME A508 C13 (1989)	0.00-0.25	0.15-0.40	1.20-1.50	0.45-0.60	0.40-1.00	0.00-0.25	0.00-0.05

2.1.2 Fabrication & heat treatment

Reactor pressure vessels in light-water reactors are fabricated from large forged and welded high strength low alloy steels. The steels undergo a heat treatment of austenitisation at $\sim$ 890 °C, followed by quenching (at around 7.5 °C/minute) and tempering at $\sim$ 640 °C [40]. The microstructures of RPV steels vary, but they are generally a mixture of martensite, bainite, and allotriomorphic ferrite depending on the heat treatment and cooling rate, as shown in fig. 2.2[41, 42, 43].

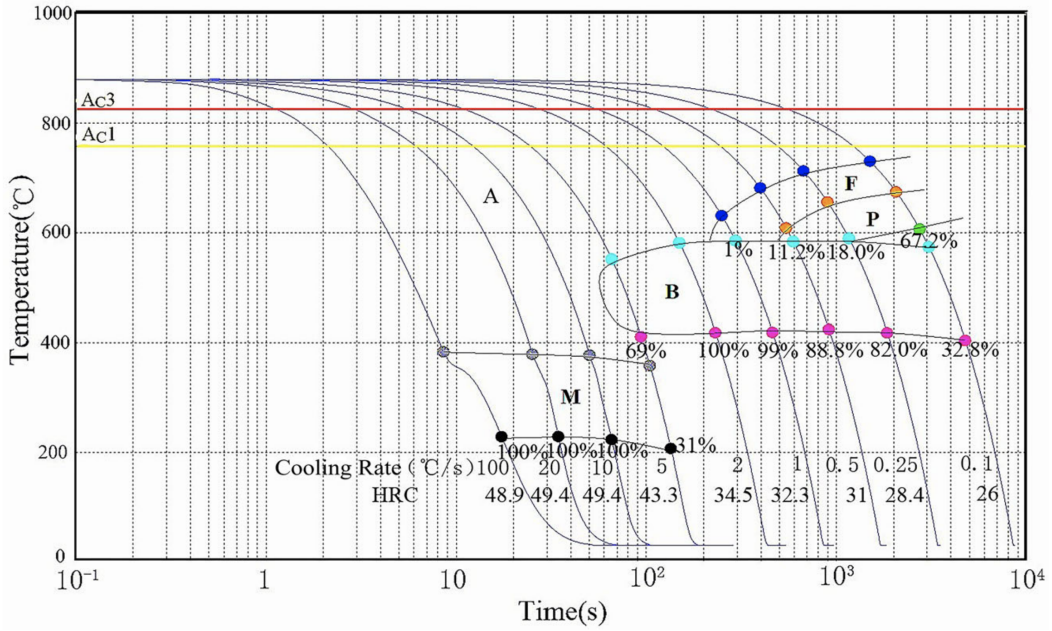


Figure 2.2: Continuous cooling transformation diagram showing the microstructures predicted for a range of cooling rates from austenite, for A508-3 RPV steel, from Figure 9, Liu et al. 2022 [42], reprinted from Heat Treatment and Surface Engineering, 4, Yong Liu, Nan Qu, Jianwei Ren, Yan Zhang & Jingchuan Zhu,Phase transition kinetics and microstructures of A508-3 steel under continuous cooling processes, Pages 12-19, licensed under CC BY, 2022 (`https://creativecommons.org/licenses/by/4.0/`).

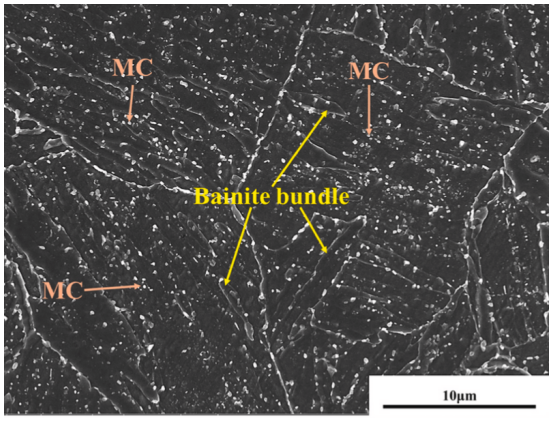
Bainite is formed when austenite starts to decompose during cooling, when the temperature is greater than the martensite start temperature but too low for a fully diffusion dominated transformation into pearlite. Bainite formation is displacive, and leads to a fine microstructure of ferrite plates growing from prior austenite grain boundaries. The plates cannot grow into large grains because as they form, the surrounding austenite cannot accommodate the deformation caused by the growing ferrite and this strain prevents further growth [44]. This results in a fine lath structure. The cooling rate will affect whether upper or lower bainite, or martensite

are formed on quenching. Upper bainite ferrite laths are carbide free, and cementite forms on lath boundaries. With greater undercooling, lower bainite forms, with ferrite laths containing a fine distribution of carbides [45]. Martensite formation is diffusionless and occurs when steel is quenched from austenite, at a sufficiently high cooling rate for a transformation from austenite to a body-centred tetragonal structure to occur. This transformation leads to significant retained carbon in the martensite lattice, which diffuses to form fine carbides on tempering.

Lower bainite can look very similar to tempered martensite, which also contains finely distributed carbides within martensite laths. However, the orientation-relationships between laths in martensite and bainite vary due to the difference in formation mechanisms. The need to temper martensite can result in lower toughness than bainite, as during tempering non-hardening embrittlement can occur, caused by segregation of sulphur and phosphorus[41].

Quenching such large components leads to a wide range of cooling rates through the thickness of the RPV steel, and large castings display macro-segregation of alloying elements, leading to inhomogeneous microstructures, as shown by Pickering and Bhadeshia and Marini et al. in fig. 2.4 [43, 41]. Various micrographs of different types of RPV steel are shown in figs. 2.3 and 2.4, showing mixed microstructures of martensite,ferrite and bainite, with Cr-Mo rich carbides on boundaries and in the matrix after tempering.

a.



b.

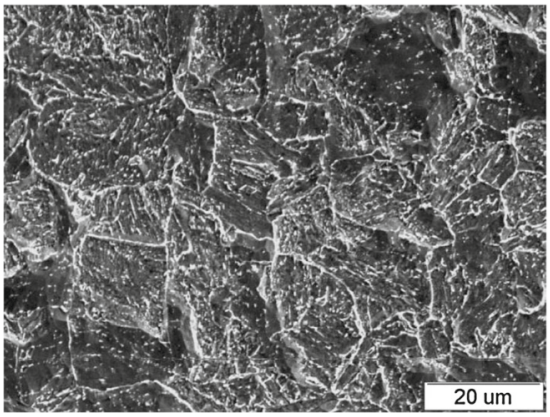
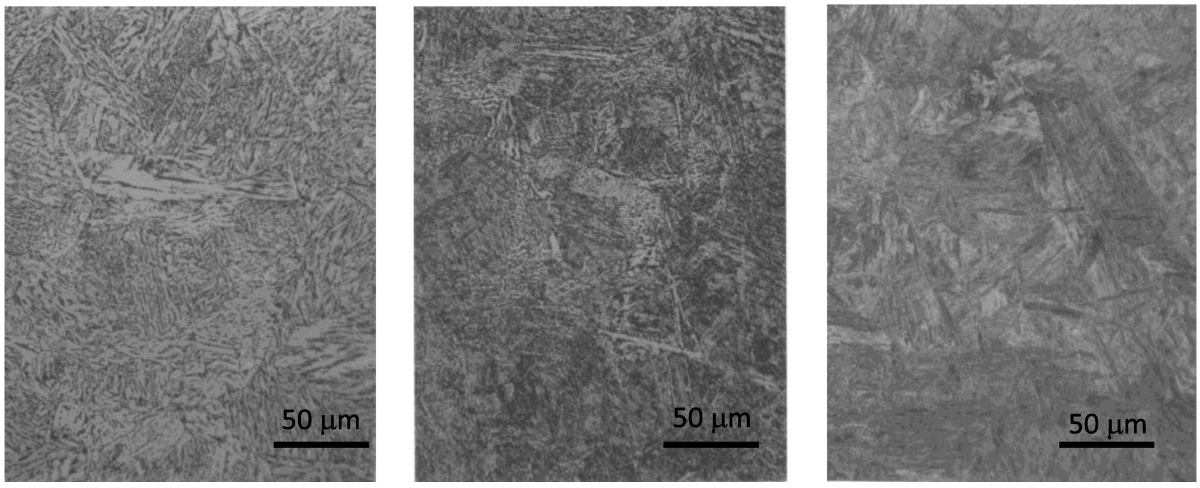


Figure 2.3: Micrographs from literature showing the microstructure of low-alloy RPV steels. a. Secondary electron image of etched 15Kh2NMFA-A (Cr–Ni–Mo–V) steel [46], which is air-cooled and then temperred to produce mixed bainite-ferrite microstructures and b. an A508-3 steel [47], which was quenched and tempered to form a mixture of martensite and bainite.

a. Reprinted from Journal of Materials Research and Technology, 34, Tengfei Wang, Junkang Gao, Shaohong Li, Jun Li, Junwan Li, Hengyong Bu , Huarong Qi, Zhimin Li, Mengnie Li, Microstructure evolution and mechanical properties degradation behavior of nuclear power pressure vessel steel induced by prolonged thermal aging, Pages 2740-2753, licensed under CC-BY-NC 2025 (https://creativecommons.org/licenses/by-nc/4.0/).

b. Figure 1 from International Journal of Fracture, Guangsheng Ning et al, Effect of environmental media on the fatigue property of Chinese A508-3 steel of AP1000, Springer Nature, 2021, reproduced with permission from SNCSC.



a. b. c.

Figure 2.4: Micrographs showing the effect of increasing quenching rates a. $1\,^{\circ}\mathrm{C}$/s, b. $5\,^{\circ}\mathrm{C}$/s, and c. $30\,^{\circ}\mathrm{C}$/s, on the resultant microstructure of a steel with composition similar to that of 16MND5 and A508-3, from figure 2, Marini et al.[41]. Reprinted from Journal of Nuclear Materials, 465, B. Marini, X. Averty, P. Wident, P. Forget, F. Barcelo, Effect of the bainitic and martensitic microstructures on the hardening and embrittlement under neutron irradiation of a reactor pressure vessel steel, Pages 20-27, Copyright 2015, with permission from Elsevier

RPV steels also contain sub-micron molybdenum and chromium carbides. In most contemporary water-cooled reactors, large ring forgings have been used to produce the beltline, to minimise the amount of weld material exposed to high neutron fluence, although current designs are moving towards advanced welding techniques to reduce costs [48].

2.1.3 Degradation of mechanical properties of RPV Steels under irradiation

The most important mechanical properties of an RPV steel are the fracture toughness and the ductile to brittle transition temperature shift (ΔDBTT) after irradiation. Some key mechanical properties of A508-3 steel are shown in table 2.3.

Table 2.3: Measured values of A508-3 RPV steel as manufactures, including DBTT measured as the T_{41J}, yield strength and fracture toughness(critical stress intensity factor K_{IC}) measured in the ductile fracture regime.

Property	Measured value, in unirradiated A508-3 steel
DBTT, T_{41J}	$-40\,^{\circ}\mathrm{C}$-$-50\,^{\circ}\mathrm{C}$ [49, 50]
Yield strength	>450 MPa [49]
K_{IC} (above DBTT)	350 MPa.m$^{\frac{1}{2}}$ [49]

A reduction in fracture toughness and increase in DBTT both increase the probability of catastrophic failure. If fracture toughness drops, the material is less resistant to rapid crack propagation and brittle behaviour, and as DBTT increases, the range of temperatures at which brittle fracture is the dominant failure mode becomes closer to room temperature fig. 2.5.

DBTT is the temperature at which the yield stress and fracture stress of a material are equivalent, i.e. $\sigma_y = \sigma_f$, such that the material displays no ductility before fracture occurs, although in steels there is always some local ductility leading to a curve between the ductile and brittle regime, rather than a vertical step [51]. Under irradiation, as the increased density of defects in the material inhibits the motion of dislocations, causing the yield stress to increase, as a greater applied stress is required to cause plastic deformation. This leads to a higher temperature at which the yield stress and fracture stress are equivalent [51]. The DBTT can also be increased by a reduction in fracture stress, caused by grain boundary segregation. The segregation of solute elements to grain boundaries reduces the cohesion of the boundary, reducing the threshold of applied stress for intergranular fracture, and leading to lower fracture toughness. The upper shelf energy drop observed after irradiation is also caused by this increase in yield stress, leading to a drop in the energy absorbed by plastic deformation [51].

Fracture toughness describes the ability of a material, with a pre-existing crack, to resist fracture. Therefore, materials which have microstructures that can slow down crack propagation, without initiating brittle fracture mechanisms, have higher fracture toughness. This is most commonly measured using a compact tension test, with a pre-cracked, notched specimen, where the critical stress intensity factor, K_{Ic}, is measured by monitoring the load on the specimen, and measuring the crack path [53].

If cracks are able to travel quickly through a material, then brittle fracture can occur. The pile-up of dislocations at interfaces, such as grain boundaries, can lead to inter-granular cracking. The presence of secondary phases, which can precipitate under irradiation in the matrix, can pin dislocations, and lead to hardening embrittlement. Without the ability to plastically deform, the material cannot blunt the crack tip and slow its propagation through the material. Brittle failure can also occur by cleavage fracture, where fracture occurs along low index planes in the material [54].

The results of Charpy impact testing and compact tension testing (measuring fracture tough-

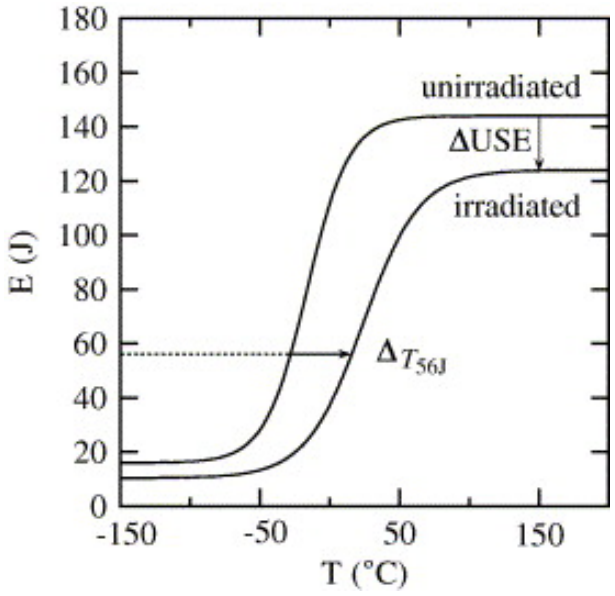
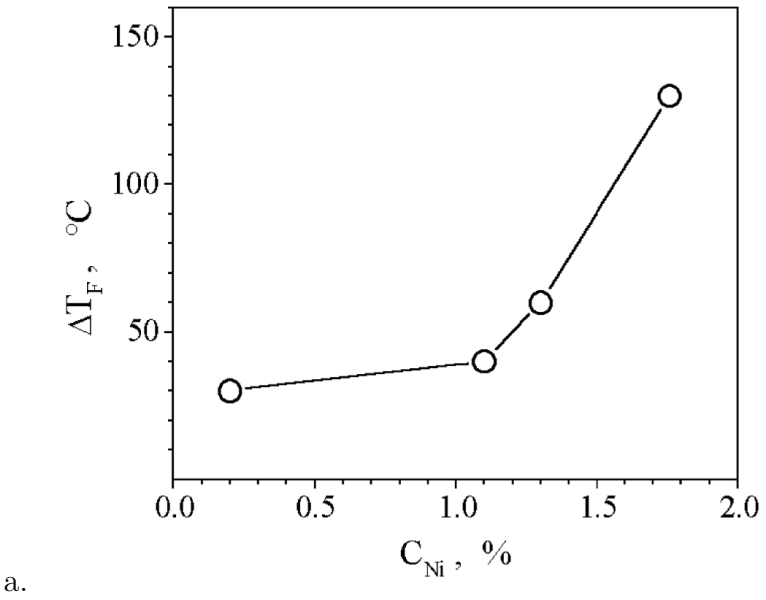
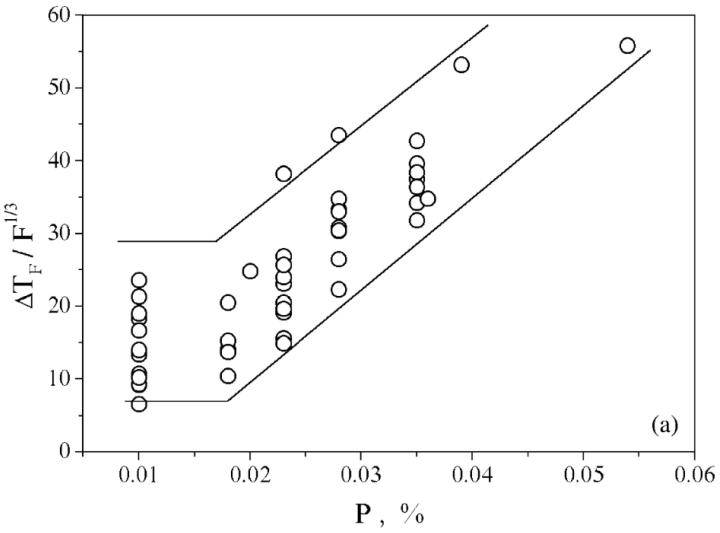


Figure 2.5: Graph of absorbed energy as a function of temperature, showing a neutron-irradiated steel (fluence= 4.65×10^{19} n/cm^2), and an unirradiated A508-3 steel, which has a higher DBTT and lower upper shelf energy, [52]. Reprinted from Computational Materials Science, 32, C. Bouchet, B. Tanguy, J. Besson, S. Bugat, Prediction of the effects of neutron irradiation on the Charpy ductile to brittle transition curve of an A508 pressure vessel steel, Pages 294-300, Copyright 2005, with permission from Elsevier

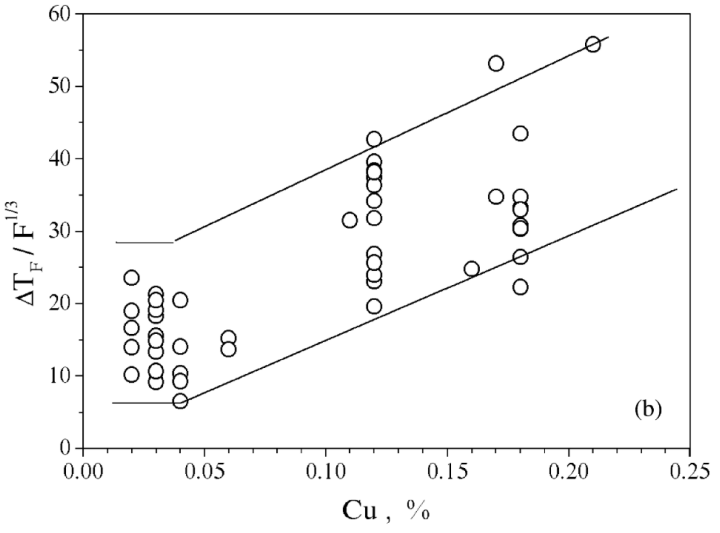
ness using K_{Ic}) can produce a prediction of the ΔDBTT and ΔUSE for a single material, but this requires large volumes of material, to measure across a range of temperatures and produce master curves like those in fig. 2.5. Reactor pressure vessel steel degradation is monitored in reactors using surveillance samples installed in the reactor and removed at various intervals throughout the service life for mechanical and microstructural analysis. Applied studies using in-service materials often focus on shifts in fracture toughness or Charpy impact toughness in irradiated samples to provide data that directly transfers into maintenance and monitoring regimes [55, 56]. For example, Nikolaev et al., observed an increase in DBTT and reduction in upper shelf energy in steels with higher Cu, P and Ni content indicating that these elements enhance embrittlement in RPV steels under irradiation, fig. 2.6 [55]. The key standards relating to the maintenance and monitoring of radiation damage in RPVs are ASTM E706 [57], which details surveillance standards for the prevention of brittle fracture, and ASTM E900-15 [58], for predicting radiation induced DBTT shifts. Almirall et al. [15], in the USA, and Kuleshova et al. [16], in Russia, state that current standards under predict embrittlement in low copper RPV steels due to a dependence of models on Cu, P and Ni content. There is a need for improved



a.



b.



c.

Figure 2.6: Plots of DBTT shift versus Ni (a.) and P (b.) and Cu (c.) content, as observed by Nikolaev et al. in steels irradiated at 270 °C to a neutron fluence of 1.1024 n/m^2[55] Reprinted from International Journal of Pressure Vessels and Piping, 79, Yu.A Nikolaev, A.V Nikolaeva, Ya.I Shtrombakh, Radiation embrittlement of low-alloy steels, Pages 619-636, Copyright 2002, with permission from Elsevier.

models of embrittlement in low Cu steels, with consideration for other solute elements such as Mn and Si.

As reactor lifetimes are extended, the amount of material available for surveillance is diminishing. This has led to numerous collaborative projects such as FRACTESUS, aiming to devise small scale and micromechanical testing methods that yield measurements of bulk fracture toughness to replace the traditional fracture toughness specimens [59]. Advances in mechanical testing have led to the frequent application of mini-compact tension testing, a method that uses 4x4x30 mm notched specimens and enables more test pieces to be measured and irradiated in test reactor cells than would be possible using full size specimens [60, 61]. Kolluri et al. have used another small specimen technique; mini-Charpy testing, to identify a synergistic effect between manganese and nickel when present in wt.% greater than approximately 2.9%. DBTT shift increased proportionally with increasing Ni content, with a significant reduction in upper shelf energy in high Mn containing steels [62]. While these test results show how the material's properties have changed, it is challenging to predict how these will evolve into the future, particularly beyond the design life of the component. Therefore, much research in the field of RPV steel embrittlement focusses on the use of accelerated irradiation experiments and modelling to understand the underlying mechanisms of embrittlement.

2.2 Radiation damage in RPV steels

Nuclear fission produces heat and neutrons, which are emitted in all directions from the fuel inside the reactor core. Some of these neutrons will be moderated by the water in the core and be reflected into the fuel rods to produce more heat, but others are incident on the reactor pressure vessel internals and structural steel. Neutrons can interact in many ways with other nuclei, but the most relevant mechanism leading to microstructural changes, in RPV steels, is via elastic collision. A neutron collides with an atom in the matrix of the RPV steel, transferring kinetic energy to it. This primary knock-on atom (PKA) then moves through the material, having secondary collisions leading to a cascade of vacancies and interstitials being created, as visualised in fig. 2.7. The first part of the radiation damage cascade is the ballistic stage, where the PKA produces a cascade of interstitial-vacancy pairs (point defects) which, in high densities, are analogous to localised melting of the material. In the picoseconds after the cascade, some

vacancies and interstitial atoms will undergo recombination and many atoms return to their lattice sites. Some point defects, vacancies and interstitial atoms, do not recombine and this leads to elevated point defect concentration and enhanced diffusion rates leading to secondary microstructural changes [63].The recombination rate will depend on the shape of the damage cascade, and the incident particle type.

The increase in vacancy concentration leads to higher diffusion rates within the material [64]. Combined with the elevated temperatures at which a nuclear reactor operates; diffusion rates can be sufficiently high for self-interstitial atoms, solutes, and vacancies to move through the material and form larger scale defects by clustering together. Recombination rates depend on the incident particle type, radiation temperature, composition, and microstructure.

The key defects induced by irradiation can comprise matrix effects, such as vacancy and self-interstitial clusters, precipitates, and segregation of solute atoms to grain boundaries and dislocation loops [65]. These defects cause barriers to dislocation movement through the alloy, and thus cause it to become harder. Neutron fluence is the number of neutrons incident over a given area. Through the RPV this is approximately 10^{19} n.cm^{-2} over a 40-60 year reactor lifetime. This corresponds to approximately 0.1 displacements per atom (dpa) in a 900 MW PWR, meaning that 1 in 10 atoms will have moved from its original lattice site to another position in the material over the irradiation period [19].

2.2.1 Accelerated radiation damage techniques

With a dwindling supply of surveillance material in older reactors, and new reactors in construction using steels with more limited datasets on radiation responses, accelerated testing is required to understand radiation damage at higher doses. This relies on the use of test reactors and charged particle irradiation, which can reduce the time required to achieve lifetime doses from 40 years to hours, table 2.4. In many experimental studies into Mn-Ni-Si rich defects, features are too small to be analysed using available techniques and defects aren't always present, so accelerated irradiations enable higher doses to be reached within realistic timescales to investigate high fluence effects. For example, no Mn-Ni rich defects were observed in irradiated RPV steels below 0.1 dpa in one study, suggesting the need for higher doses to produce measurable defects [66].

Table 2.4: Table showing the comparative time to achieve 0.1 dpa and approximate dose rates for each irradiation method.

Irradiation method	Time to end of life fluence (0.1 dpa)	Approximate Dose Rate (dpa/s)
Operational PWR	40-60 years	$\sim 5 \times 10^{-11}$ [19]
Surveillance capsule in PWR	$\sim >$ 13 years (lead factor <3)	$\sim 1 \times 10^{-10}$ [67]
High flux test reactors	$\sim$ days-months	1×10^{-8}-1×10^{-7} [68, 69]
Light ion irradiation	$\sim$ days	1×10^{-7}-1×10^{-5} [70]
Heavy ion irradiation	$\sim$ hours	1×10^{-6}-1×10^{-3} [71, 72]

Surveillance material provides the closest analogues to operational RPV steels at end of life. They experience the same thermal transients and are from the same alloy heat as the pressure vessel, so they are accurate representations of a specific RPV material. However, the volume of material is limited, often already manufactured into mechanical test pieces, and it takes years before testing can be carried out.

Test reactors are a more flexible alternative, with even higher flux than surveillance capsules. However, neutron irradiation campaigns using test reactors are significantly more costly than ion beam irradiation. They have the benefit of space for investigations into new alloys, and model alloys for investigation into the specific effects of different compositions and microstructures on radiation response.

Protons are charged particles, so they have a strong Coulomb scattering interaction with nuclei, transferring kinetic energy to a primary knock-on atom. It is possible to achieve damage levels equivalent to 80 years in a reactor, a dose of around 0.2 dpa, in less than 24 hrs using a proton beam, assuming a dose rate of 2.5×10^{-6} dpa.s^{-1}. This high damage rate is partly due to charged particles having a shorter stopping distance in materials due to their electronic interactions and small mean free path, and also due to the high fluxes that can be achieved using ion accelerators. Low to intermediate energy protons have a high interaction cross-section for elastic collision with atoms in materials, so they can induce high levels of damage over a much shorter time period than neutrons. Ions also have a significantly smaller penetration depth than neutrons; in the region of 30 µm for 3 MeV protons in Fe. This is because they are charged, leading to interactions with electrons in the material leading to local heating and loss of kinetic energy.

Protons produce much smaller cascades, due to lower energy PKAs, and create a lower density of Frenkel pairs, which leads to a much higher defect survival efficiency than neutrons or heavy ions, of around 60-110 % NRT dpa for a PKA energy of around 200 eV [73, 63]. Self-ion irradiation in BCC-Fe leads to larger cascades, with higher PKA energies around 5 keV, and lower survival efficiencies of around 20-40 % [73, 63]. The cascade size of heavy ions is much more similar to that of a neutron damage cascade, particularly in the case where the injected Fe atom has sufficient energy to cause cascade splitting, which is common in neutron induced cascades [74]. Figure 2.7 shows the efficiency of defect production varies for different cascade morphologies caused by different incident particles.

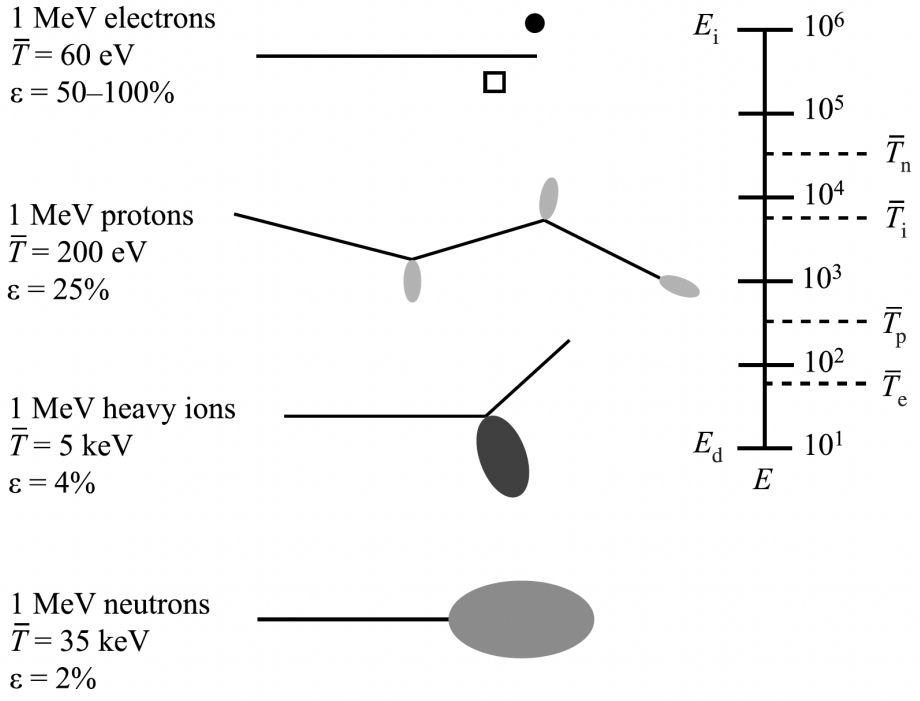


Figure 2.7: Schematic showing damage cascade morphology and size, comparing neutrons with heavy and light ions, from [63, 75]. $\bar{T}$ is the average energy transferred per primary knock-on atom, and ε is the efficiency of production of defects that are free to migrate in the material. Reprinted from Materials Characterization, 32, G.S. Was, T. Allen, Radiation-induced segregation in multicomponent alloys: Effect of particle type, Pages 239-255, Copyright 1994, with permission from Elsevier.

Light ions produce smaller cascades, producing more dpa per incident ion than heavy ions, and leading to a greater concentration of mobile point defects which cause enhanced diffusion and segregation [76]. In general, during light ion irradiations cascades are not overlapping and causing ballistic mixing as occurs in heavy ion irradiation at high dose rates, so segregation and

clustering of solutes is not disrupted during the early stages of formation [76].

There is an argument that proton irradiation, despite its high dose-rate, can provide a more realistic way to simulate accelerated radiation induced microstructural changes, particularly where these are diffusion led processes, due to the cascade size leading to greater survival of point defects. They provide greater penetration depth than heavy ions, leading to larger irradiated volumes which opens up a wider range of small scale testing techniques such as SSJ tensile specimens which are on the order of mm^3, which are commonly used in test reactor campaigns [77]. In a study into the effects of neutron, heavy-ion and proton irradiation on binary Fe-Cr alloys, some interesting comparisons were made between the observed microstructures after irradiation, (fig. 2.8) [78]. Heavy ions led to no precipitation, suggesting that the high dose rate may have led to overlapping cascades, disrupting clustering [78]. The loop morphology observed in the heavy-ion irradiated samples also contrasted with the neutron irradiated microstructure, with only vacancy type dislocation loops. The proton-irradiated sample yielded much more similar dislocation structures and precipitate distributions to the neutron irradiated sample [78].

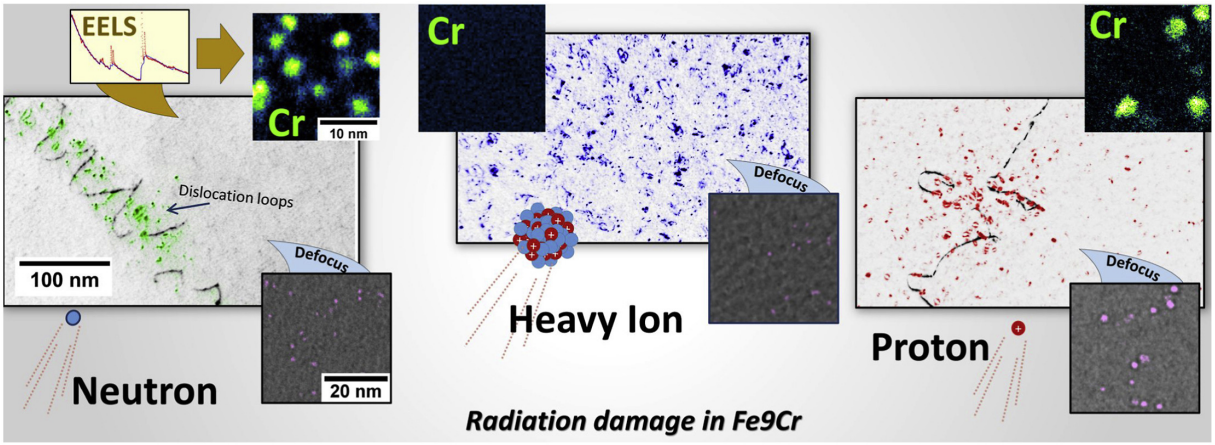


Figure 2.8: Figure showing the differences in solute clustering observed across various studies using neutron, proton and self-ion irradiations, showing the similarity in solute rich features formed under neutron and proton irradiation [78].Reprinted from Journal of Nuclear Materials, 533, J.C. Haley, S. de Moraes Shubeita, P. Wady, A.J. London, G.R. Odette,S. Lozano-Perez, S.G. Roberts, Microstructural examination of neutron, proton and self-ion irradiation damage in a model Fe9Cr alloy, Pages 1, Copyright 2020, with permission from Elsevier

Comparisons of radiation induced precipitation in neutron and heavy-ion irradiated RPV steels has shown that ion-irradiation led to volume fraction and number density increases of

solute rich features by a factor of 1.5-2, for equivalent dpa [79]. The dose rate from heavy ions was between 10^{-6}-10^{-5} dpa/s, and precipitate composition was not significantly different. In a large scale collaborative project aiming to produce matching radiation damage results using protons, with neutron irradiated materials, Was et al. found that the grain boundary segregation and dislocation loop distributions from neutron and proton irradiations were comparable for a stainless steel [80]. However, there were distinct differences in cavity and void formation between neutron and ion irradiations and in dislocation loop densities, which were much lower in neutron irradiated alloys. Almirall et al. observed lower number density and volume fraction of defects and larger average sizes in self-ion irradiated RPV steels, compared with neutron irradiated equivalent steels [15]. Strikingly, the compositions of the Mn-Ni-Si clusters, and their bulk solute content, across the steels in both conditions, were remarkably consistent [15]. A comparison of self-ion and proton irradiation of a binary Fe-Ni alloy showed that nickel precipitation only occurred in self-ion irradiated material, where there were sufficient concentrations of point defect clusters. In the proton irradiated sample, there was significant segregation to existing defects, but no evidence of dislocation loops or point defect clustering, attributed to the small cascade size [71]. In contrast with this work, Laver et al. observed accelerated precipitation of Mn-Ni-Si rich defects in a proton irradiated RPV steel using small angle neutron scattering, and showed that increasing Ni led to increased volume fraction, and that higher dose rates led to delayed precipitation [70]. One benefit of both self-ion and proton irradiation is that the samples produced are not as radioactive as they would be if they were neutron irradiated, and much smaller volumes of radioactive material are produced, but there is large variety in the observations made across difference ion irradiation experiments.

2.2.2 Flux & dose rate effects

The dose rate during irradiation experiments has a large impact on the microstructural evolution of RPV steels under irradiation. A review into neutron flux effects, by Ortner et al., observed that high flux test irradiations generally delayed the microstructural evolution and embrittlement that would be observed at lower fluence in low flux irradiations, but these trends were less conclusive for low-Cu RPV steels [81]. In some cases reviewed in this study, the fluxes were above the threshold for a regime in which solute clustering, precipitation and growth were accelerated,

leading to microstructures with fewer embrittling defects [81]. This poses a significant risk in terms of accuracy of prediction of RPV embrittlement, when flux differences lead to different microstructural evolution.

Ion irradiation leads to significantly higher dose rates than test-reactor neutron irradiation, due to higher displacements per atom (dpa) per ion, high beam fluxes and smaller interaction volumes. This also leads to much smaller radiation damaged volumes, with inhomogeneous dose/ dose rate profiles with a distinctive Bragg peak just before the maximum ion penetration depth [82]. In the case of self-ion irradiation, this means that despite the cascade size being more similar to a neutron cascade, there can be significant differences in the microstructural evolution of materials due to the dose rate [83, 78].

Dose-rate affects the vacancy diffusion rate in the material for a given fluence. At high and low dose-rates, vacancy diffusion is dose-rate dependent, but there is an interim range where dose-rate does not affect vacancy diffusion [84, 85]. It is proposed that this is caused by thermal ageing effects at low dose rates and inter-cascade interaction at high dose-rates. Kinetic Monte-Carlo simulations of point-defect migration and cluster in BCC-Fe have shown that the dose rate independent range is around 10^{-10} to 10^{-6} dpa.s^{-1} [85]. At higher dose rates, point defect concentrations are high, so recombination is more likely to occur, and the number density of solute-rich defect clusters is so large that vacancies no longer migrate rapidly as they stabilise at clusters within very short distances [85]. This is consistent with observations of solute cluster number density in model alloys at high temperature; as the temperature increases and diffusion is accelerated, more solute-rich defects are likely to form [86]. In two binary Fe-Ni and Fe-Mn alloys, higher dose rate self-ion irradiation led to less precipitation, reduced solute segregation to dislocation loops, and a smaller and denser population of dislocation loops, suggesting that the enhanced number density of features may have reduced the mobility of vacancies and suppressed solute segregation, fig. 2.9 [83].

The effect of dose rate is important to consider when using accelerated irradiation methods, as whether the dominant diffusion mechanisms of various solutes are vacancy- or interstitial-mediated depends on the vacancy concentration in the material [87]. Phase-field modelling has been used to investigate the effect of dose-rate on solute segregation, suggesting that higher dose rates increase the incubation dose required for radiation-induced segregation to start by

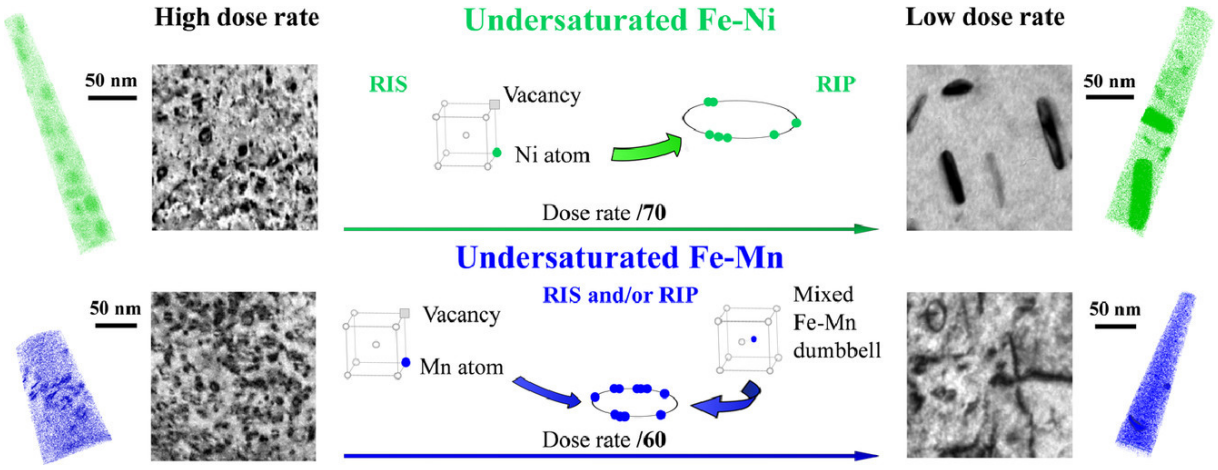


Figure 2.9: Graphical abstract showing the contrasting behaviour of Mn and Ni in binary Fe alloys at two different self-ion irradiation dose rates [83]. Reprinted from Journal of Nuclear Materials, 548, L.T. Belkacemi, E. Meslin, J-P. Crocombette, B. Radiguet, F. Leprêtre, B. Décamps, Striking effect of solute elements (Mn, Ni) on radiation induced segregation/precipitation in iron-based model alloys, Page 1, Copyright 2021, with permission from Elsevier.

increasing the number of vacancy sinks in the material [88]. The incubation dose is the fluence required for matrix defects (dislocation loops) to stabilise and grow in number, producing sinks for solutes to segregate to or from. Kuleshova et al. studied the flux effects on microstructural evolution in high Ni WWER-1000 welds and found at lower fluxes, more diffusion of Ni and P was observed to grain boundaries, but no links were observed for other solute elements, consistent with diffusion models suggesting that other solutes such as Mn and Si diffuse via dumbbell-mediated mechanisms at RPV operating temperatures [56, 87].

Unstable matrix defects, small clusters of vacancies and interstitials, have been suggested as the cause for increase post-irradiation annealing recovery in materials exposed to higher fluxes [20, 89]. However, Chaouadi et al. have investigated the effects of flux on hardening in RPV steels using post-irradiation annealing, and found no recovery and therefore no evidence of unstable matrix damage in high fluxes [90, 91]. Interestingly, for the range of fluxes in these studies, there was no observed flux dependence on the change in yield strength, see fig. 2.10 [90].

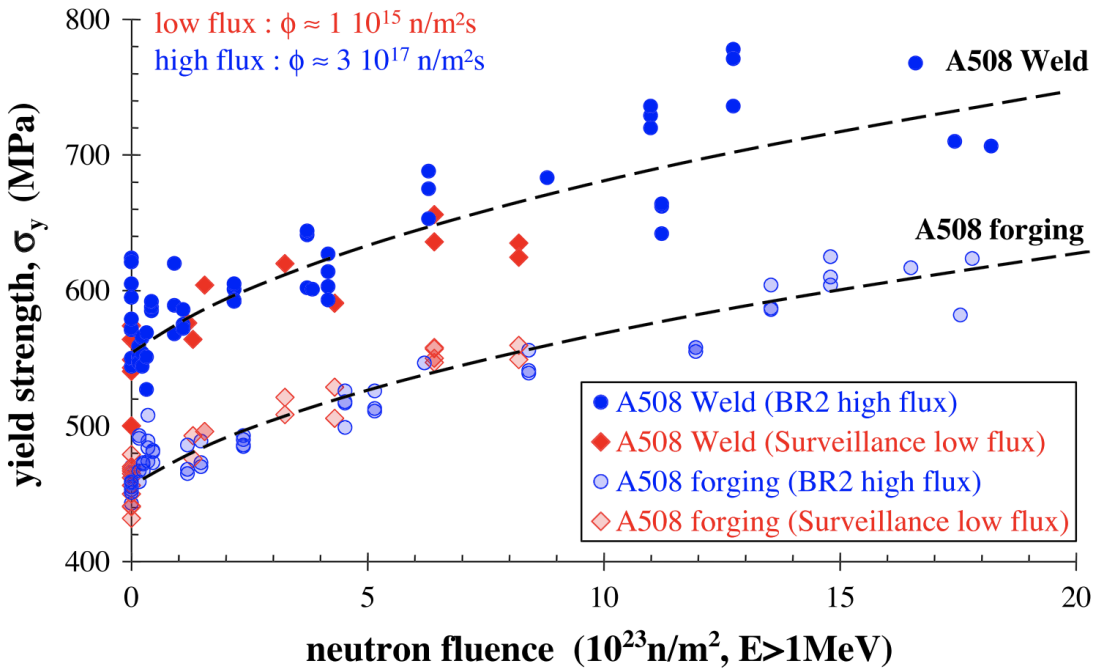


Figure 2.10: Comparison of A508 weld and plate forging materials, irradiated at two different fluxes, showing no flux-dependence on the change in yield strength with dose. From figure 10. [90]. Reprinted from Journal of Nuclear Materials, 418, R. Chaouadi, R. Gérard, Neutron flux and annealing effects on irradiation hardening of RPV materials, Pages 137-142, Copyright 2011, with permission from Elsevier.

2.2.3 Temperature effects

Irradiation temperature will affect all stages of microstructural evolution under irradiation, from cascade recombination rates, to the thermodynamic stability of precipitated secondary phases. Irradiation temperature and particle energy spectrum has been found to affect defect generation rates drastically in BCC-Fe using a range of modelling techniques for each stage of the damage cascade [92]. Novoselov et al. observed that the defect production rate at 600 K was half that calculated at 0 K for both heavy ion and neutron irradiation, due to defect mobility in the annealing stage of the damage cascade [92]. Various temperature shifts have been proposed to compensate for the discrepancy in defect survival rates in order to produce microstructures that have been observed in neutron irradiated materials, using alternative irradiations, but these vary significantly. For example, the shift proposed by Mansur et al., proposes that a higher temperature should be applied to increase defect annihilation and slow down solute segregation, based on emulating the void swelling observed in austenitic steels using heavy ions [93]. However, this has been disputed in the context of nanoscale solute clustering behaviour under irradiation in proton-irradiated Fe-Cr alloys and self-ion irradiated ferritic-martensitic steels [78, 94]. Due to the wide range of nuclear structural alloys, and types of radiation damage defect of interest to the research community, there is unlikely to be a single shift that can be applied to all experiments due to the complex dependencies of defect stability on both composition and temperature. Dislocation loop Burgers vector varies with temperature in irradiated BCC-Fe (fig. 2.11 [95]). The $\frac{1}{2} < 111 >$ loops are mobile, whereas $< 100 >$ type loops are sessile. This study suggests that at higher temperatures, the mobility of the $< 111 >$ loops increases, and they are absorbed into $< 100 >$ loops at such small sizes that they are no longer visible in TEM [95].

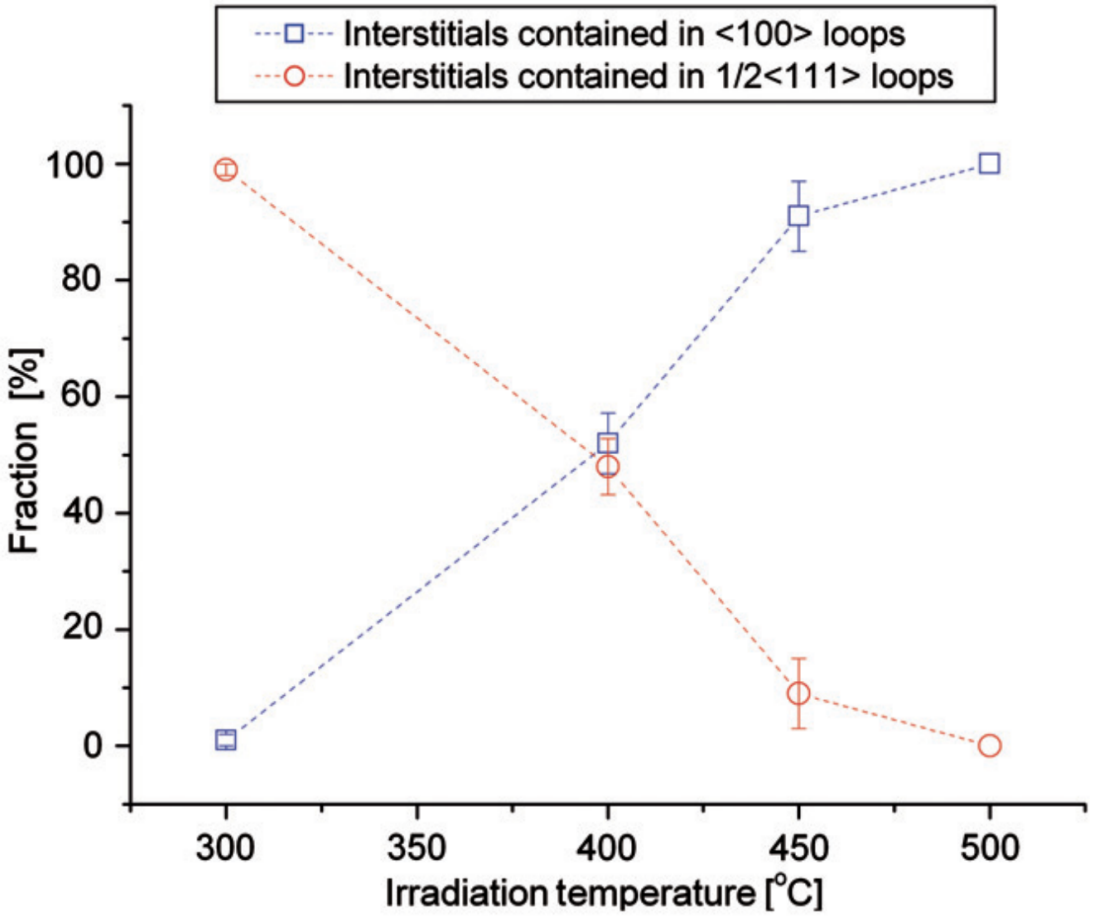


Figure 2.11: Plot showing the fraction of loop types forming under heavy-ion irradiation, in BCC-Fe, at a range of temperatures with the fraction of $\frac{1}{2} < 111 >$ loops showing in red, and the fraction of $< 100 >$ loops shown in blue. From figure 5 of "The temperature dependence of heavy-ion damage in iron: A microstructural transition at elevated temperatures", Z. Yao, M. L. Jenkins, M. Hernandez-Mayoral & M.A. Kirk, Philosophical Magazine, © copyright 2010, reprinted by permission of Informa UK Limited, trading as Taylor & Francis Group, https://www.tandfonline.com [95].

Kuleshova et al. found that irradiation temperatures of 400 °C led to much greater segregation of solute elements to the grain boundaries [96]. Connolly's study in radiation temperature effects between 255 °C and 310 °C found that the increasing temperature reduced Si content in clusters [97]. Both radiation flux and temperature have a significant impact on radiation-induced segregation, as can be seen in fig. 2.12 [98]. At low temperatures, defects have low mobility, even when present in high concentrations, so recombination occurs. At much higher temperatures, the equilibrium concentrations of vacancies is very high, slowing segregation and leading to back-diffusion.

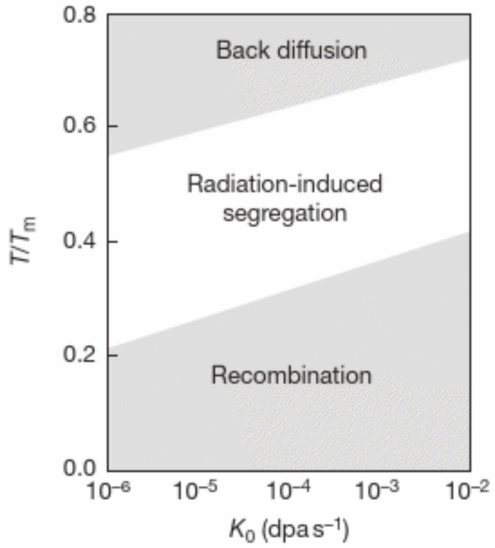


Figure 2.12: Schematic showing the effects of temperature and flux on radiation-induced segregation regime. From figure 3, [98]. Reprinted from Comprehensive Nuclear Materials, M. Nastar, F. Soisson, Chapter 1.18- Radiation-Induced Segregation, Pages 471-496, Copyright 2012, with permission from Elsevier.

2.3 Radiation damage in RPV steels

2.3.1 Radiation induced dislocation loops in bcc Fe

When there are high concentration of vacancies and interstitial atoms in an alloy, these defects start to cluster together and form dislocation loops within the crystal structure. In BCC-Fe, radiation induced dislocation loops form with a Burgers vector of either $\frac{1}{2} < 111 >$ or $< 100 >$, fig. 2.13,[95, 99, 100, 101]. There is a temperature dependence on the fraction of $\frac{1}{2} < 111 >$ and $< 100 >$ type loops in BCC-Fe investigated by Yao et al., with increasing the fraction of

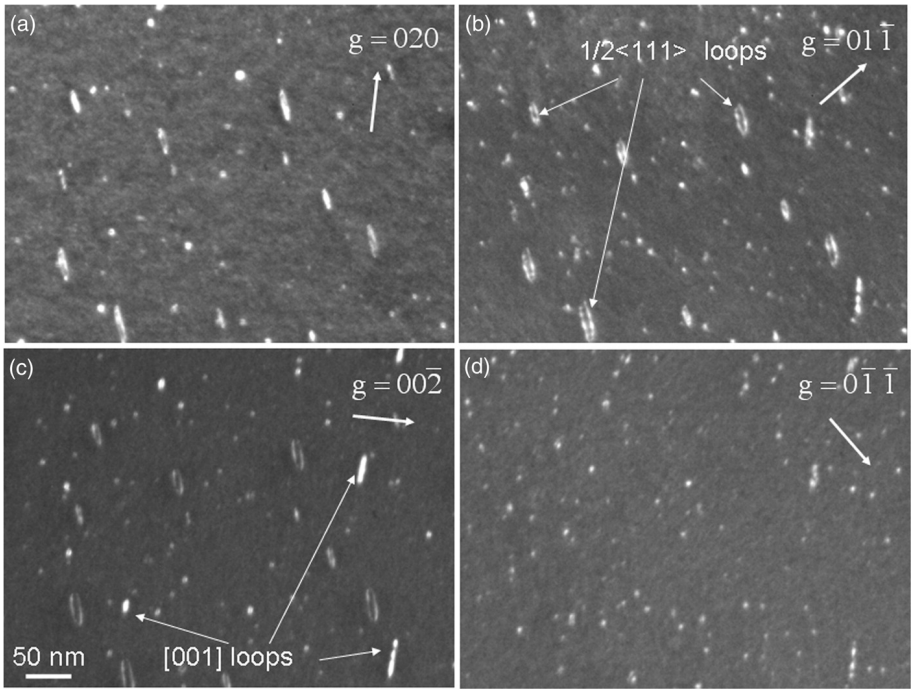


Figure 2.13: TEM micrographs, Yao et al. 2010 [95] showing dislocation loops in self-ion irradiated ultra high purity iron, 400 °C, and a dose of 2×10^{18} ions m^{-2} (1.3 dpa). The g-vector is given in each image, and shows the effect of altering the diffraction vector on the loop contrast. In image (a) $g = 020$, $b = [100]$ loops are invisible; (b) $g = 01\bar{1}$, $b = \frac{1}{2}[\bar{1}11]$ and $b = \frac{1}{2}[11\bar{1}]$ are invisible; (c) $g = 00\bar{2}$, $b = [010]$ loops are invisible; (d) $g = 0\bar{1}\bar{1}$, $b = \frac{1}{2}[1\bar{1}1]$ and $b = \frac{1}{2}[11\bar{1}]$ loops are invisible. Figure 2 from "The temperature dependence of heavy-ion damage in iron: A microstructural transition at elevated temperatures", Z. Yao, M. L. Jenkins, M. Hernandez-Mayoral & M.A. Kirk, Philosophical Magazine, © copyright 2010, reprinted by permission of Informa UK Limited, trading as Taylor & Francis Group, https://www.tandfonline.com

$< 100 >$ increased from 0% at 300 °C, to 100% at 500 °C (see fig. 2.11 in section 2.2.3) [95]. In general, stable loops larger than 2nm in irradiated BCC-Fe are interstitial type loops, although in heavy-ion irradiated Fe-Cr alloys, small voids have been observed, suggesting an influence of alloy composition on loop stability [95].

Shi et al. [102], combined TEM analysis of RPV steel microstructures with nanoindentation tests on alloys proton-irradiated to three doses; 0.05 dpa, 0.1 dpa and 0.2 dpa, corresponding to doses equivalent to 20, 40 and 80 years of reactor operation. It was observed that the number density of dislocation loops increases with dose; between 1.5×10^{21} m^{-3} and 1.1×10^{22} m^{-3}, but the average size is similar; approximately 3 nm at all doses. This increase in number density causes greater hardening, and is consistent with a number of other TEM analyses of dislocation loop number density in ion irradiated RPV steels [101, 100, 95]. Comparing these data with neutron irradiated RPV steels suggests that the elevated dose rates and different interaction of ions with matter in proton and Fe ion irradiated specimens leads to significantly more loops forming for a given dpa, at comparable temperature. In a study of a neutron irradiated low-Cu steel, irradiated up to 0.097 dpa, TEM characterisation of dislocation loops calculated densities of 5.1×10^{20} m^{-3} and an average diameter of 3.9 nm, compared with 6.5×10^{21} m^{-3} in a proton irradiated alloy at 0.1 dpa (micrographs shown in fig. 2.14) [103, 104]. This may be due to the higher defect survival rate in proton induced cascades, combined with the high dose rate, leading to higher vacancy concentrations in the RPV steel. This will accelerate diffusion rates in the material and promote the clustering of defects and immobilisation of loops through radiation induced solute segregation.

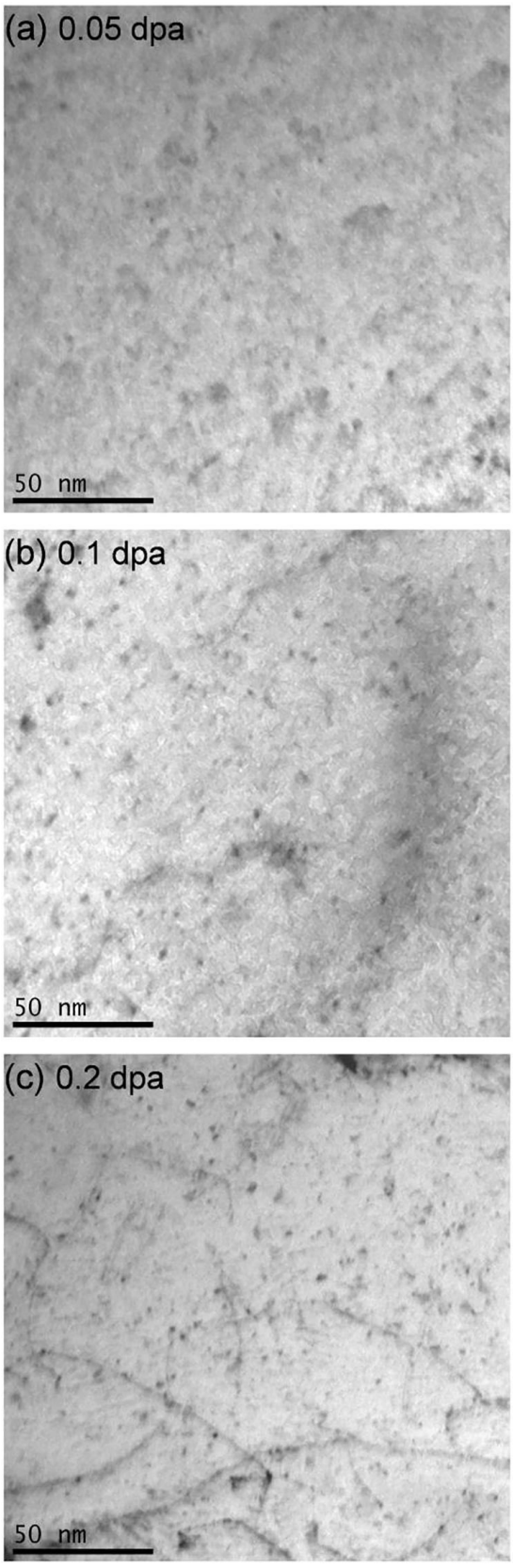


Figure 2.14: TEM micrographs showing dislocation loops, visible as black dots, in 110 keV proton irradiated A508-3 steel, with doses of (a) 0.05 dpa, (b) 0.1 dpa, and (c) 0.2 dpa from Shi et al. [102]. Reprinted from Nuclear Instruments and Methods in Physics Research Section B: Beam Interactions with Materials and Atoms, 443, J.J. Shi, W.Z. Zhao, Y.C. Wu, X.B. Liu, J. Jiang, Characterization of proton-irradiated Chinese A508-3-type reactor pressure vessel steel by slow positron beam, TEM, and nanoindentation, Pages 62-69, Copyright 2019, with permission from Elsevier.

2.3.2 Radiation induced segregation in RPV steels

The constant production of point defects leads to the creation of point defect fluxes towards defect sinks. This leads to radiation enhanced diffusion, as solutes can diffuse much faster when there is a higher vacancy concentration in the material because this increases the rate at which vacancy-solute jumps occur for substitutional solute atoms. Comparing the diffusivity of solute elements without irradiation, to the diffusivity calculated by Messina et al. [87], for solutes in materials where point -defect concentration is elevated, diffusion is significantly faster under irradiation (table 2.5). The dominant diffusion mechanisms of various solutes in under-saturated BCC-Fe have been investigated by Messina et al. [87].

Table 2.5: Diffusion coefficients, D_0, of various solute elements in BCC-Fe, activation energies, Q, (Mn[105], Ni[106], Si[107], P[108], compared with calculated values using values of D_0 and Q from Messina et al., for solute complexes showing much lower activation energies and increased diffusion distances [87].

Element	D_0 ($cm^2.s^{-2}$)	Q ($kJ.mol^{-1}$)	$D_{0,SC}$, ($cm^2.s^{-2}$) [87]	Q_{SC} ($kJ.mol^{-1}$) [87]
Mn	1.49	234	0.0041	-22.3
Ni	1.4	246	0.0134	50.8
Si	0.78	220	0.0087	43.6
P	0.2	23	0.0077	30.9

Ni diffuses primarily via vacancy-mediated mechanisms at lower temperatures, but the dominant diffusion mechanism for Mn atoms is dumbbell-mediated [87]. Fe-Mn dumbbells are stable, so they migrate more readily before dissociating, but the activation energy for diffusion is higher than for vacancy jumping mechanisms. Therefore, Ni diffusion was calculated to diffuse faster than Mn in ferrite at RPV relevant vacancy concentrations [87]. If solutes are diffusing by competing mechanisms, there is also the possibility that back-diffusion will take place, with vacancies dragging some solute toward defect sinks, and interstitial complexes moving in the opposite direction. Radiation-induced segregation of various elements depends on the stability of solute complexes, activation energy for diffusion, and temperature, as shown in fig. 2.15 [87].

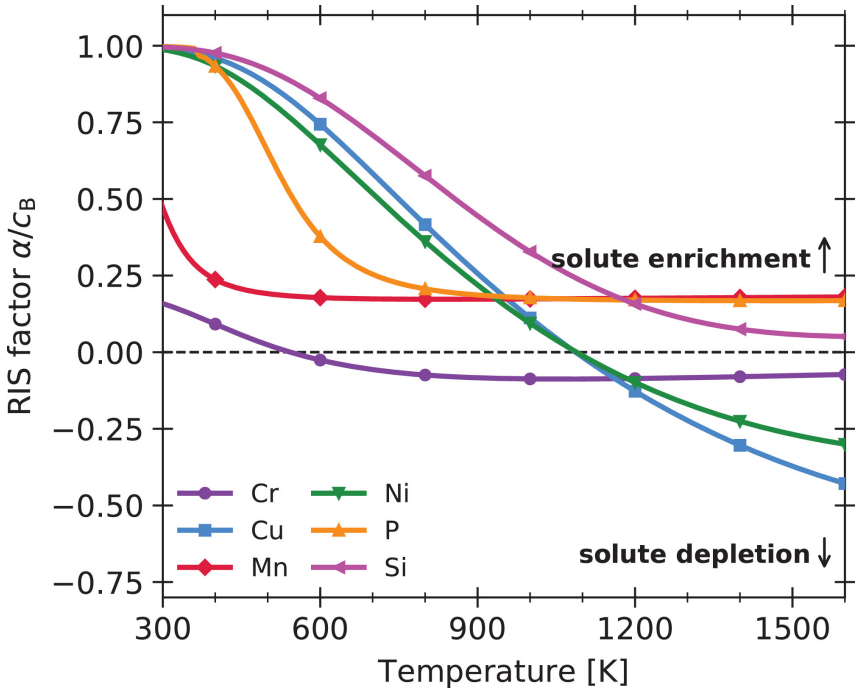


Figure 2.15: Radiation-induced segregation (RIS) factors (describing the tendency of a solute for enrichment at a defect sink), for a range of solutes present in RPV steels, modelled using ab initio calculations and the KineCluE transport code, from figure 10, [87]. Reprinted from Acta Materialia, 191, Luca Messina, Thomas Schuler, Maylise Nastar, Mihai-Cosmin Marinica, Pär Olsson, Solute diffusion by self-interstitial defects and radiation-induced segregation in ferritic Fe–X (X=Cr, Cu, Mn, Ni, P, Si) dilute alloys, Pages 166-185, Copyright 2020, with permission from Elsevier.

Radiation-induced segregation is an essential precursor to the formation of secondary phases in dilute alloys, as it leads to compositional heterogeneity, which can produce regions in the material where local compositions are sufficiently high in solute for new phases to nucleate and grow. Under irradiation, point defects migrate to pre-existing defect sinks in materials such as grain boundaries, carbide interfaces and dislocations [88]. This occurs to reduce the local interfacial free energy associated with interfaces in a material. In an investigation into grain boundary segregation in an Fe-Mn-Si-C model alloy, there was a distinct difference in Mn segregation with and without radiation exposure, but Si segregation was similar in both cases [109]. The same work observed that Mn segregated preferentially to dislocations over grain boundaries, suggesting that dislocations were stronger sinks for Mn atoms than grain boundaries.

Jenkins et al., found that 70 % of the Mn-Ni-Si rich precipitates in an aged RPV steel were located at heterogeneous nucleation sites like grain boundaries or dislocation loops but no general segregation of Mn, Ni or Si to grain boundaries was observed without irradiation[110]. Edmondson et al. used complementary microscopy methods to examine Ni-Mn-Si-precipitates in neutron-irradiated weld surveillance specimens, which showed precipitate denuded zones around carbides and grain boundaries, indicating that RIS is a key driving force in the precipitation of these features, fig. 2.16 [111].

The segregation of solutes to dislocation loops relieves stress in the matrix and lowers the local Gibbs free energy of the system. It has been widely observed that the presence of Ni in BCC-Fe alloys leads to the immobilisation of dislocation loops, and reduced size and increased number density [101, 112, 97, 86]. Oversized substitutional solute elements such as Ni can prevent dislocation loop growth because they create a region of compressive stress around the solute atom, preventing loop growth in the region[113]. The presence of oversized solutes may also provide improved trapping for undersized substitutional solutes such as Mn in these areas, to relieve the local elastic strain, and clustering of Mn and Ni is often observed in irradiated RPV steels. Prak Tom et al. observed that there was a reduction in the fraction of $< 100 >$ loops in alloys containing Mn and Ni, and proposed that solute segregation immobilises $\frac{1}{2} < 111 >$ loops, suppressing the growth of $< 100 >$ loops by preventing coalescence [112]. A follow-up study on the same materials observed that Ni atoms were located on the inside of dislocation

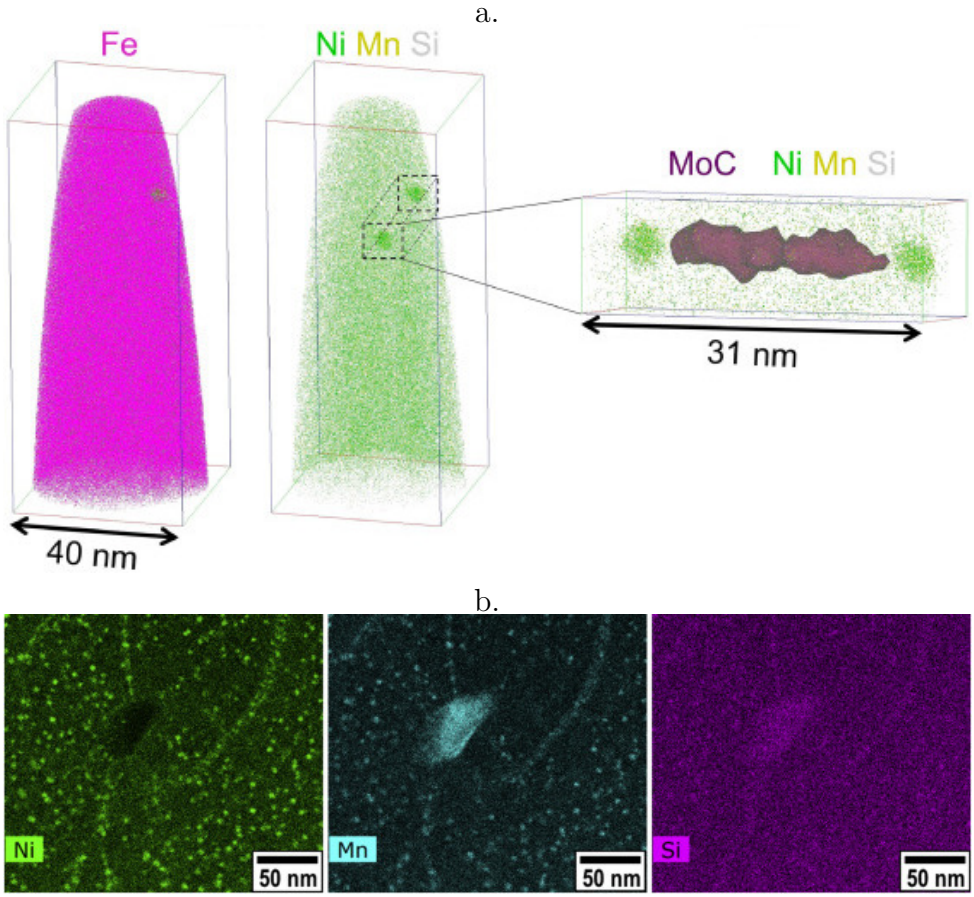


Figure 2.16: Comparison of observations of segregation and clustering at dislocations in a. an unirradiated, thermally aged (**365 °C**, for 2.4 years) RPV steel, using APT [110]) and b. radiation-induced grain boundary segregation in a RPV steel using STEM-EDX, showing precipitate denuded zone around the grain boundary [111].

a. Reprinted from Scripta Materialia, 191, B.M. Jenkins,P.D. Styman, N. Riddle, P.A.J. Bagot, M.P. Moody, G.D.W. Smith, J.M. Hyde, Observation of Mn-Ni-Si-rich features in thermally-aged model reactor pressure vessel steels, Pages 126-130, Copyright 2021, with permission from Elsevier.
b. Reprinted from Acta Materialia, 134, P.D. Edmondson, C.M. Parish, R.K. Nanstad, Using complimentary microscopy methods to examine Ni-Mn-Si-precipitates in highly-irradiated reactor pressure vessel steels, Page 9, Copyright 2017, with permission from Elsevier.

loops, see fig. 2.17, whereas Mn atoms were located on the outside, perhaps due to the lack of Si and vacancies required to nucleate a stable secondary phase [114]. Various atomistic simulations

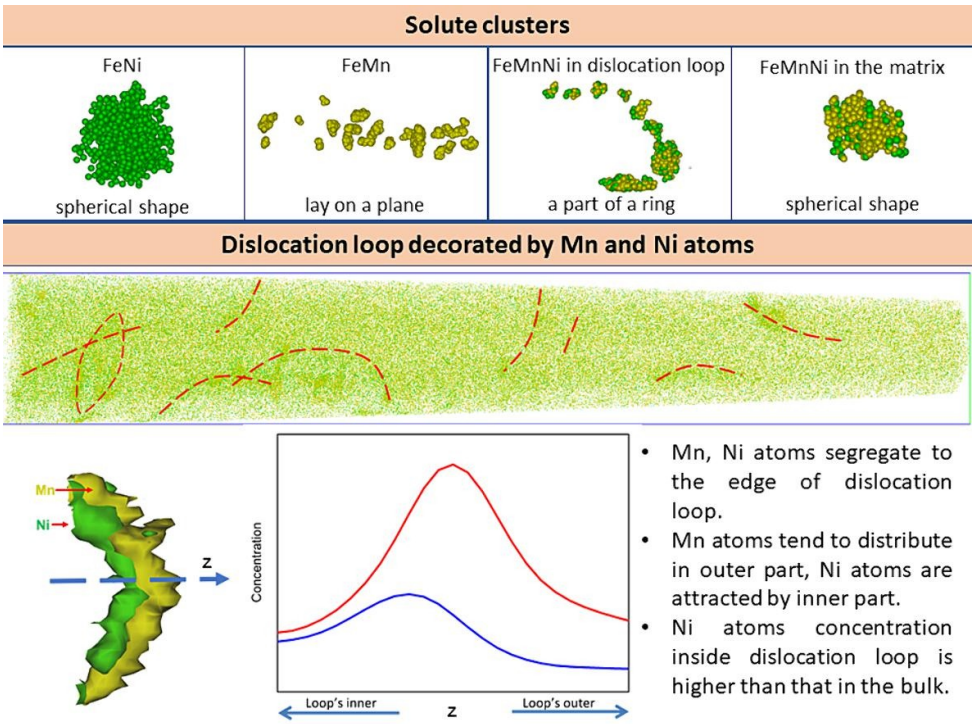


Figure 2.17: Graphical abstract from Nguyen et al. 2024 [114], showing a tendency for Ni atoms to be observed on the inside of dislocation loops and Mn on the outside, in an irradiated model alloy. Reprinted from Nuclear Materials and Energy, 39, Nguyen Ba Vu Chinh, Kenta Murakami, Liang Chen, Phongsakorn Prak Tom, Xinrun Chen, Takashi Hashimoto, Taehyun Hwang, Akinori Furusawa, Tatsuya Suzuki, Interaction of solute manganese and nickel atoms with dislocation loops in iron-based alloys irradiated with 2.8 MeV Fe ions at 400 °C, 101639, licensed under CC BY NC ND license 2024 (`https://creativecommons.org/licenses/by-nc-nd/4.0/`).

have shown that solute atoms and complexes diffusing to dislocation loops can stabilise and immobilise interstitial defects such as dislocation loops [115, 116]. Castin et al. used atomistic simulations to show that the dominant mechanisms for the clustering of solutes was segregation to interstitial type dislocation loops, which are more stable than vacancy type loops [115]. The separation of solutes on loops observed by Nguyen et al. is consistent with modelling work suggesting that complexes containing only Mn and Ni atoms have repulsive interactions, and Si is required to produce stable clusters [117, 118].

It has been widely suggested that solute segregation to radiation induced defects leads to nucleation of semi-coherent precipitates. The change in local composition combined with local

strain relief around dislocation loops caused by an excess of point defects, from radiation damage cascades, results in a lower energy barrier for nucleation of a secondary phase [98, 73].

2.4 Mn-Ni-Si rich clusters and precipitates in irradiated RPV steels

In 1997, the Odette group found that in lower copper-containing steels, Mn-Ni rich precipitates formed under irradiation, indicating that significant hardening should also be expected in irradiated low copper steels [119]. It was suggested that metastable vacancy cluster-solute complexes formed in displacement cascades to create stable nano-void complexes. This provides sites that attract solute atoms and act as precipitate nucleation sites. Odette and team described these Mn-Ni rich clusters as "late blooming phases", referring to the fact that they had only been observed at high fluence and then found to grow rapidly, leading to significant increases in hardening and yield strength in RPV steels [119]. The term has been greatly disputed in recent years, with other researchers suggesting that the solute clusters are not stable phases, and that clusters start to nucleate at very low doses, but are not experimentally observable using available characterisation techniques [120].

However, Mn-Ni-Si rich clusters have been widely observed in neutron irradiated steels. For features of interest with sizes, on the order of nm, APT is the most common method for determining the composition of clusters, although TEM is more suited to identifying their structure and location, providing more information on possible formation mechanisms. In a study investigating neutron irradiated HIPped A508-3 RPV steel, it was observed that there was slightly reduced clustering in bainite compared with ferrite, perhaps due to the sequestration of Mn in carbides, and increase in interfaces for defects to segregate to, see fig. 2.18 [121]. This supports the theory that precipitation of any Mn-Ni-Si phases under irradiation requires heterogenous nucleation sites and radiation-induced segregation in order to occur.

One of the key arguments surrounding Mn-Ni-Si rich features in irradiated RPV steels is whether their formation is radiation enhanced, and that they precipitate into thermodynamically stable phases, or their formation is radiation-induced, and they are metastable features that would not form without radiation exposure [122]. There are contrasting results from various

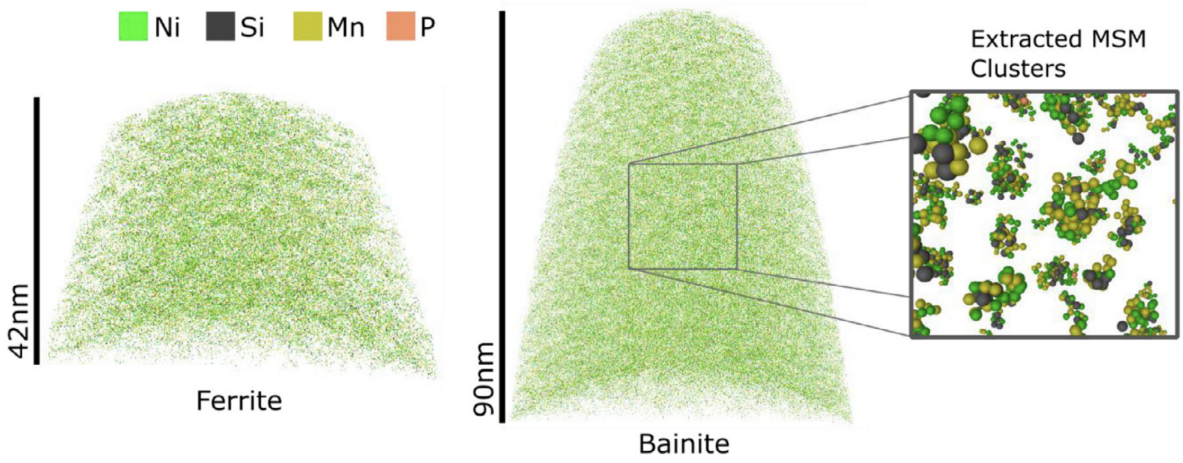


Figure 2.18: Radiation induced solute clusters in SA508 RPV steel ferrite and bainite samples, following neutron irradiation to 100 mdpa at 155°C [121]. Reprinted from Journal of Nuclear Materials, 559, Megan Carter, Claudia Gasparrini, James O. Douglas, Nick Riddle,Lyndon Edwards, Paul A.J. Bagot, Christopher D. Hardie, Mark R. Wenman, Michael P. Moody, On the influence of microstructure on the neutron irradiation response of HIPed SA508 steel for nuclear applications, Page 153435, Copyright 2022, with permission from Elsevier.

studies using post-irradiation annealing (PIA) to establish the stability of features formed under irradiation. Ulbricht et al. found that neutron radiation led to a population of solute rich defects whose composition evolved with dose, and which all dissolved after annealing at 673-748 K [123]. However, Almirall et al., annealed a range of neutron-irradiated RPV steels at 700 K and observed coarsening and growth of Mn-Ni-Si rich precipitates above a critical radius estimated to be around 2.5 nm, suggesting the precipitation of thermodynamically stable phases. fig. 2.19. [15]. Calculations based on the same data led to the conclusion that the features over r_c are thermodynamically stable at 425 °C, so would be even more stable at PWR operating temperatures of around 290 °C, based on calculations of the Ni solvus line for the G and Γ_2 phases, fig. 2.19,[15, 124].

Other in-situ SANS investigations of post-irradiation-annealing of irradiated Fe-Mn-Ni model steels have showed both increases in scattering intensity after annealing [125], and decreases in scattering intensity after annealing [126].Wagner et al. observed that annealing led to no change in scattering particle radius or volume fraction, so proposed that this increase in scattering occurred due to cluster interface changing during annealing. The average size of precipitates calculated in this study was approximately 0.75 nm after 10^{22} n.cm^{-2} fluence [125]. Bergner et

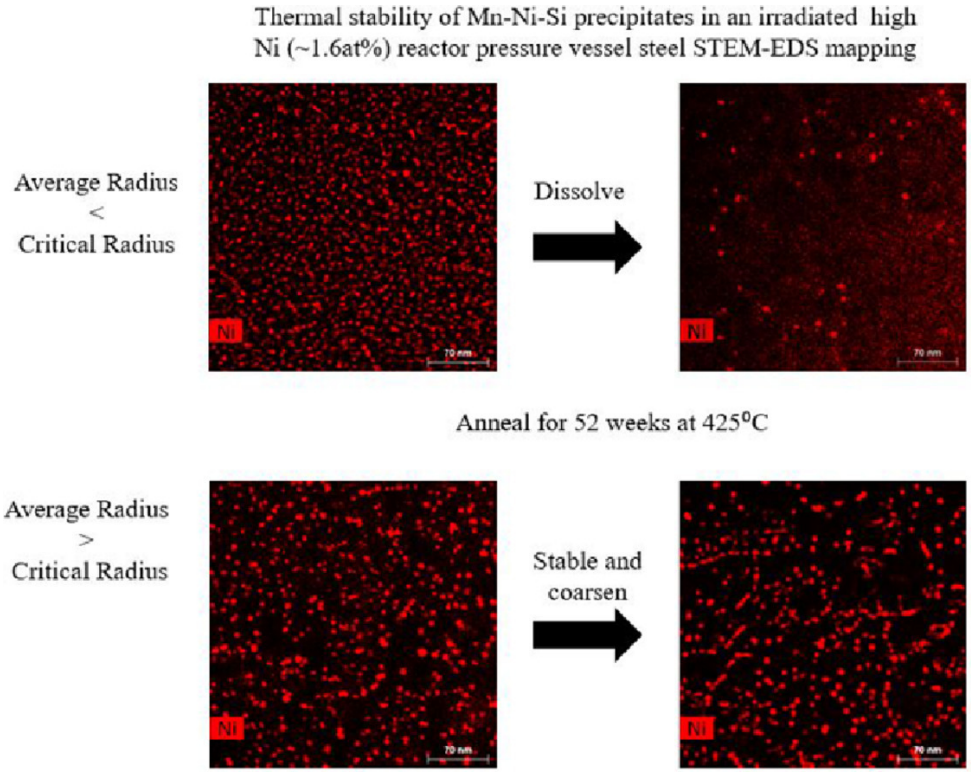


Figure 2.19: Graphical abstract from Almirall et al.2020 showing STEM-EDX maps of Ni rich precipitates in neutron irradiated steels, and the effect of post-irradiation annealing on their size and number density [15]. Reprinted from Scripta Materialia, 181, N. Almirall, P.B. Wells, S. Pal, P.D. Edmondson, T. Yamamoto, K. Murakami, G.R. Odette, The mechanistic implications of the high temperature, long time thermal stability of nanoscale Mn-Ni-Si precipitates in irradiated reactor pressure vessel steels, Pages 134-139, Copyright 2020, with permission from Elsevier.

al. observed a reduction in magnetic scattering intensity as annealing temperature increased, corresponding with a reduction in average cluster radius, suggesting dissolution was occurring above 350 °C and Mn-Ni rich features were not thermodynamically stable [126]. Although a reduction in magnetic scattering may correspond with a reduction in volume fraction of precipitates, scattering intensity is also dependent on precipitate composition, so this reduction could have occurred due to a compositional evolution leading to precipitates with different magnetic scattering contrast with the matrix. In both studies it was assumed that precipitates and clusters are non-magnetic, so the contrast with an Fe matrix does not change [125, 126].

There are strong arguments made that radiation-induced segregation and enhanced vacancy concentrations induce the formation of these secondary phases, and they would not otherwise be stable without the accelerated diffusion and point defect fluxes present under irradiation [83, 86, 111].

The precipitation occurring under irradiation may be a combination of heterogenous and homogenous nucleation, and the features may have different stabilities depending on their nucleation site. This has been observed in the work of Tencé, who has observed G phase precipitates in self-ion irradiated model RPV alloys, forming both at dislocations and in the bulk with different compositions [127]. In this case, post-irradiation annealing led to the dissolution of matrix precipitates but compositional evolution of precipitates towards the Mn-Ni-Si G phase when they were located at defects such as dislocation and loops. An ageing study on RPV steels has observed Mn-Ni-Si rich clusters forming without irradiation, suggesting a thermodynamic driving force for clustering and precipitation, although it was found that over 70% of clusters were observed on existing crystal defects, not in the bulk [110]. Cluster composition varied significantly with bulk alloy composition and features with compositions consistent with the G phase, Γ_2 phase and B2 phase were all observed in different alloys, fig. 1.2 [110].

2.4.1 Effect of alloy composition on defect formation in RPV steels.

Different solute elements behave differently under irradiation in ferritic steels, and contribute to a variety of changes in microstructure via radiation-induced segregation and clustering. Early research focussed on Ni as the primary element leading to radiation embrittlement in low Cu steels, based on the observations of Ni segregation to dislocation loops and high Ni compositions

observed in Mn-Ni-Si rich features [23]. However, a key study, by Burke et al., in 2002 identified the synergistic effect of Mn and Ni on radiation embrittlement in RPV steels, by characterising a range of steels with varying Ni and Mn content using a range of techniques [36]. This was the first clear indication that Mn was playing a key role in radiation embrittlement, as a significantly smaller change in DBTT of 21 °C was observed for a high Ni, low-Mn alloy, compared with 59 °C a lower Ni and higher Mn steel with comparable Cu content (fig. 2.20) [36]. Almirall et

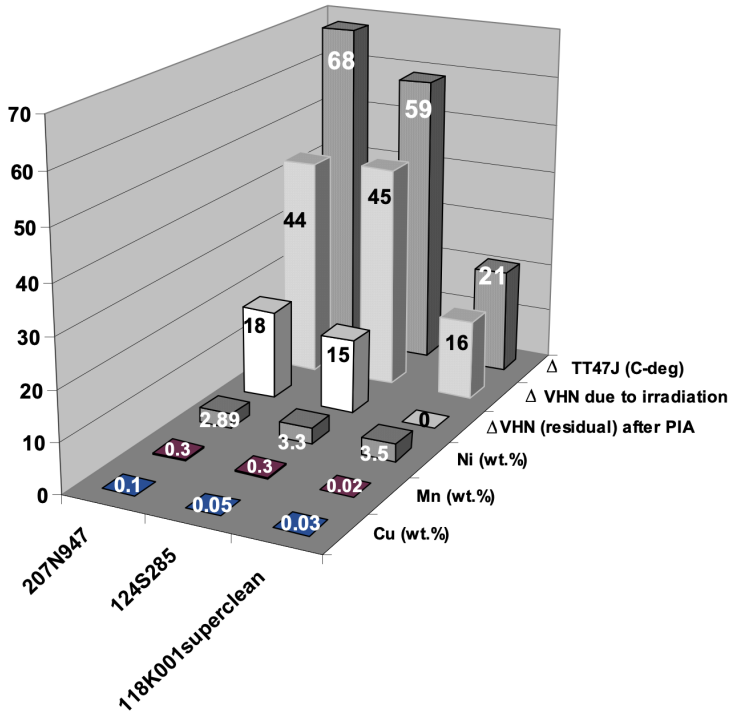


Figure 2.20: Comparison of the hardening and embrittlement in three steels, illustrating the effect on embrittlement of elevated Mn and Ni content (124S285), compared with very low Mn steel (superclean) and a high Cu, low Ni steel (207N947). The plot shows that at very low Cu and Mn content, there is a much smaller ΔDBTT (measured as $\Delta TT47J$) than would previously have been expected from a high Ni alloy, confirming the synergistic effect of Mn and Ni on embrittlement in RPV steels The low Mn and Cu steel shows less hardening than the other two, measured here as Vickers hardness (ΔVHN) and fully recovered after post-irradiation annealing. From fig.6, Burke et al. 2002, [36]. Reprinted from Burke, M, Stofanak, R, Hyde, J, English, C, & Server, W. "Microstructural Aspects of Irradiation Damage in A508 Gr 4N Forging Steel: Composition and Flux Effects." Effects of Radiation on Materials: 21st International Symposium, 2004 with permission from ASTM International.

al. also observed that very low Mn steels experienced very little hardening, suggesting that Mn content has an effect on segregation and stabilising of defect clusters, and on Mn-Ni-Si precipitate formation [37]. In the same study, a relationship between Mn and Ni content and

the overall volume fraction of precipitates was devised, see fig. 2.21, showing that although Ni is the dominant solute in contributing to radiation induced solute rich defects, Mn plays a significant role, particularly when Mn content is very low [37].

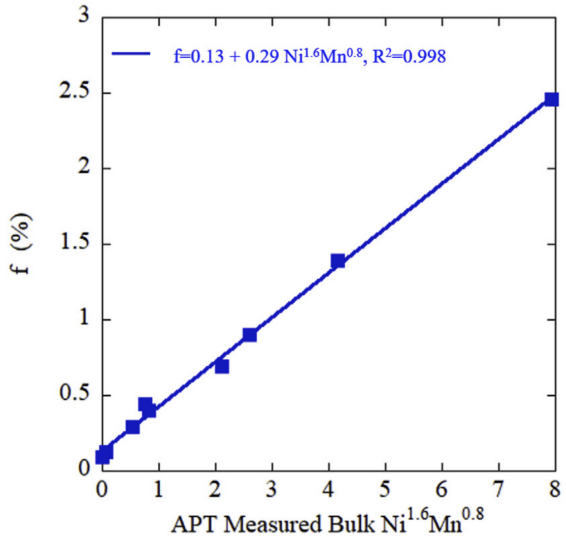


Figure 2.21: Plot of measured volume fraction of Mn-Ni rich clusters formed after irradiation versus bulk Ni & Mn content showing a combined link between solute content and radiation precipitation response, from figure 8 [37]. Reprinted from Acta Materialia, 179, N. Almirall, P.B. Wells, T. Yamamoto, K. Wilford, T. Williams, N. Riddle, G.R. Odette, Precipitation and hardening in irradiated low alloy steels with a wide range of Ni and Mn compositions, Pages 119-128, Copyright 2019, with permission from Elsevier.

A wide range of compositions have been observed in clusters and precipitates in low-Cu RPV steels. In general, they are predominantly rich in Ni, and the Mn and Si content varies depending on bulk compositions. Various Mn-Ni-Si containing phases have been proposed as structures for solute rich defects in RPV steels, and a summary is shown in table 2.6

Table 2.6: Range of phases proposed as structures for Mn-Ni-Si rich clusters and precipitates forming in irradiated RPV steels.

Phase	Chemical Formula	Observed/modelled	Observed Compositions	Coherent in BCC-Fe
G phase	$Mn_6Ni_{16}Si_7$[128]	Neutron irradiated, 1.10×10^{21} n.cm^{-2} at 290 °C, alloy comp: 0.74-1.68 wt.% Ni, 1.37-1.5 wt.% Mn 0.17-0.23 wt.% Si[129]	21-31 at.% Mn, 52-55 at.% Ni, 12-24 at.% Si[129]	-
		Modelled as stable when <18 at/% Fe[130]	-	Yes, at 757 K[131]
		Fe^+ ion irradiation, T=400 °C, alloy comp at.%= A2: 0.8 at.% Ni, 0.4 at.% Si, 1.4 at.% Mn, A3: 1.8 at.% Ni, 0.7 at.% Mn, 0.8 at.% Si [127]	A2:$(Ni,Fe)_{16}(Mn,Fe)_6Si_7$, A3:$Ni_{16}(Mn,Fe)_6Si_7$[127]	Semi-coherent[127]
		Thermal ageing at 330-365 °C[110]	58.4-51.8 at.% Ni, 16.9-22.8 at.% Mn, 22.0-21.6 at.% Si[110]	-
Γ_2 phase	$Mn(Ni_xSi_{1-x})_2$[128]	Modelled as stan;e when <30 at % Fe[132]		-
		Neutron irradiation, INL ATR, 563K, 1.1×10^{21}n.cm^{-2}[128],	46.0-54.0 at.% Ni, 33.3 at.% Mn, 12.7-20.7 at.% Si[128]	-
		Thermal ageing, 3.1 at.% Ni at 405 °C[110]	54.4 at.% Ni, 29.2 at.% Mn, 12.67 at.% Si[110]	-
$Ni_{(2-3)}Si$	$(Ni,Mn)_{(2-3)}Si$[16]	Neutron irradiation, T=290 °C, flux of $6-101\times10^{22}$ n/cm^2, Fe^+ ion irradiation, T=400 °C, excess of SIA[127]	45 at.% Ni, 33 at.% Si, 22 at.% Mn $(Ni_{1.33}Mn_{0.67}Si)$[16]	-
B2	$(Ni,Fe)_3Mn_2(Si,Fe)$	1.6 at.% Ni, 1.4 at.% Mn, 1.1 at.% Si thermally aged at 405 °C[110]	44.5 at.% Ni, 40.2 at.% Mn, 12.3 at.% Si[110],	Yes[131]
		Self-ion irradiated, 623K, alloy comp: 1.33 at.%Mn, 0.72 at.% Ni, 0.41 at.% Si[133]	47.02 at.% Mn, 37.3 at.% Ni, 15.05 at.% Si[133]	-

The composition of Mn-Ni-Si features is variable, and generally depends on the bulk composition of the alloy. Their compositions are not always observed to be close to thermodynamically stable phases [134, 86].

Many studies into cluster compositions in irradiated RPVs show variable results which are often in line with the ratios of Mn, Ni and Si present in the original bulk alloy, rather than pointing to a stoichiometric stable phase such as the $Mn_6Ni_{16}Si_7$ G phase [79, 86, 110]. Courilleau et al. investigated a range of RPV compositions and resulting clustering, and observed that Mn and Si cluster content corresponds approximately to the bulk concentrations, but Ni content is higher in clusters than might be expected in lower Ni containing alloys (fig. 2.22) [86]. This is consistent with the work of Almirall et al. who found that cluster content of Mn and Si varied depending on the nominal composition of the alloy [37].

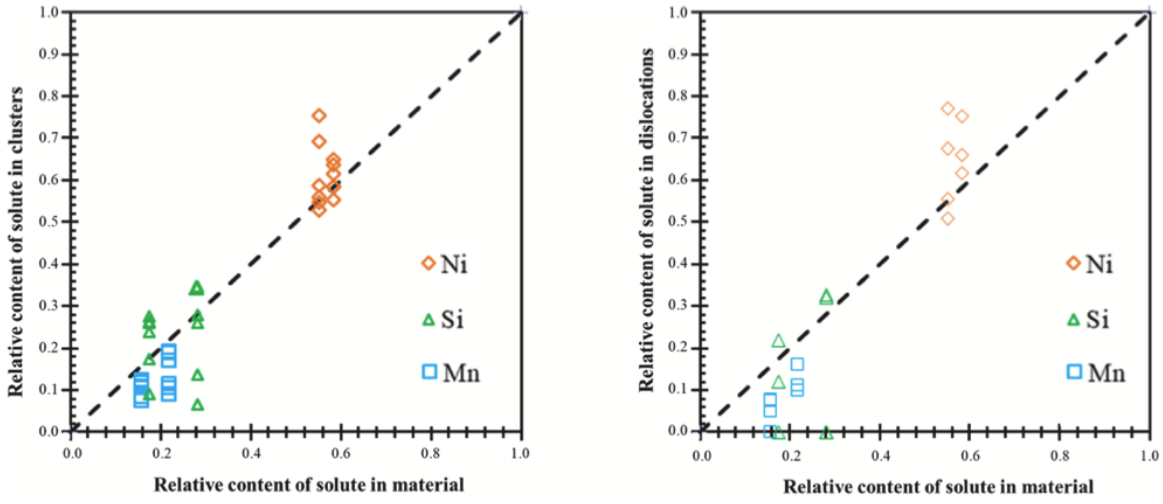


Figure 2.22: Plots from Courilleau et al. 2023, showing the relative content of solute in clusters and dislocations compared with the bulk material (measured using APT), in irradiated VVER steels. This shows that only nickel is proportionally present in much higher quantities at these defect sinks [86]. Reprinted from Journal of Nuclear Materials, 585, C. Courilleau, B. Radiguet,R. Chaouadi, E. Stergar, A. Duplessi, P. Pareige, Contributions of Ni-content and irradiation temperature to the kinetic of solute cluster formation and consequences on the hardening of VVER materials, Page 154616., Copyright 2023, with permission from Elsevier.

2.4.2 Using model alloys to understand solute segregation and clustering under irradiation

Model alloy studies have been applied to investigate the synergistic effects of specific solute elements on radiation embrittlement and to accelerate the solute clustering and growth to identify precipitate structures. The simplified compositions allow clearer conclusions to be drawn about the impact of various solutes on clustering and precipitation under irradiation.

Hernandez-Mayoral et al. carried out TEM analysis of a range of neutron irradiated model binary and ternary alloys [101]. This work analysed pure iron and model RPV steels, irradiated up to 0.19 dpa. In this case, the size of defects increased with dose, but compared with CRPs, Mn-Ni-Si precipitates showed smaller average sizes and narrower size distribution. No change in microstructure was observed in the RPV steel samples at any dose, consistent with the paper's conclusion that defect size decreases with increasing complexity of alloy composition [101]. This observation has been corroborated more recently by Prak Tom et al., fig. 2.23 [112].

Yabuuchi et al. (2011) investigated Fe-Mn binary alloys and found that an increasing Mn content led to an increase in the number density of dislocation loops and hardening under neutron irradiation. This paper proposes a mechanism by which Mn acts as a loop nucleus and traps interstitial atoms and concluded that Mn clusters only reach measurable sizes at high fluence [135]. This study found that both ½ $< 111 >$ and $< 100 >$ loops formed in the model Fe-Mn alloy. The $< 100 >$ loops were determined to be interstitial type and the average size of loop was 9 nm, concurring with the findings of Hernandez-Mayoral et al. [135, 101] Ni increases the number density and volume fraction of defects, both dislocation loops and Mn-Ni-Si clusters or precipitates, in irradiated ferritic alloys [36, 86, 136, 62]. Belkacemi et al. studied the effect of solutes on radiation induced precipitation in two binary Fe alloys at high and low dose rates [83]. In the Fe-3.3Ni alloy, precipitates formed at low dose rates, but not at higher ones, whereas no precipitation occurred in the Fe-2.8Mn alloy. Mn also segregated more significantly to radiation induced dislocation loops, and solute concentration at defect sinks in both alloys reached over 50 at.% [83]. This suggests that Mn diffuses faster than Ni in a binary Fe-Mn system.

There is a much smaller body of research experimentally investigating the effect of Si content on clustering in the Fe-Mn-Ni-Si system [133]. Xue et al. found that comparing ion irradiated

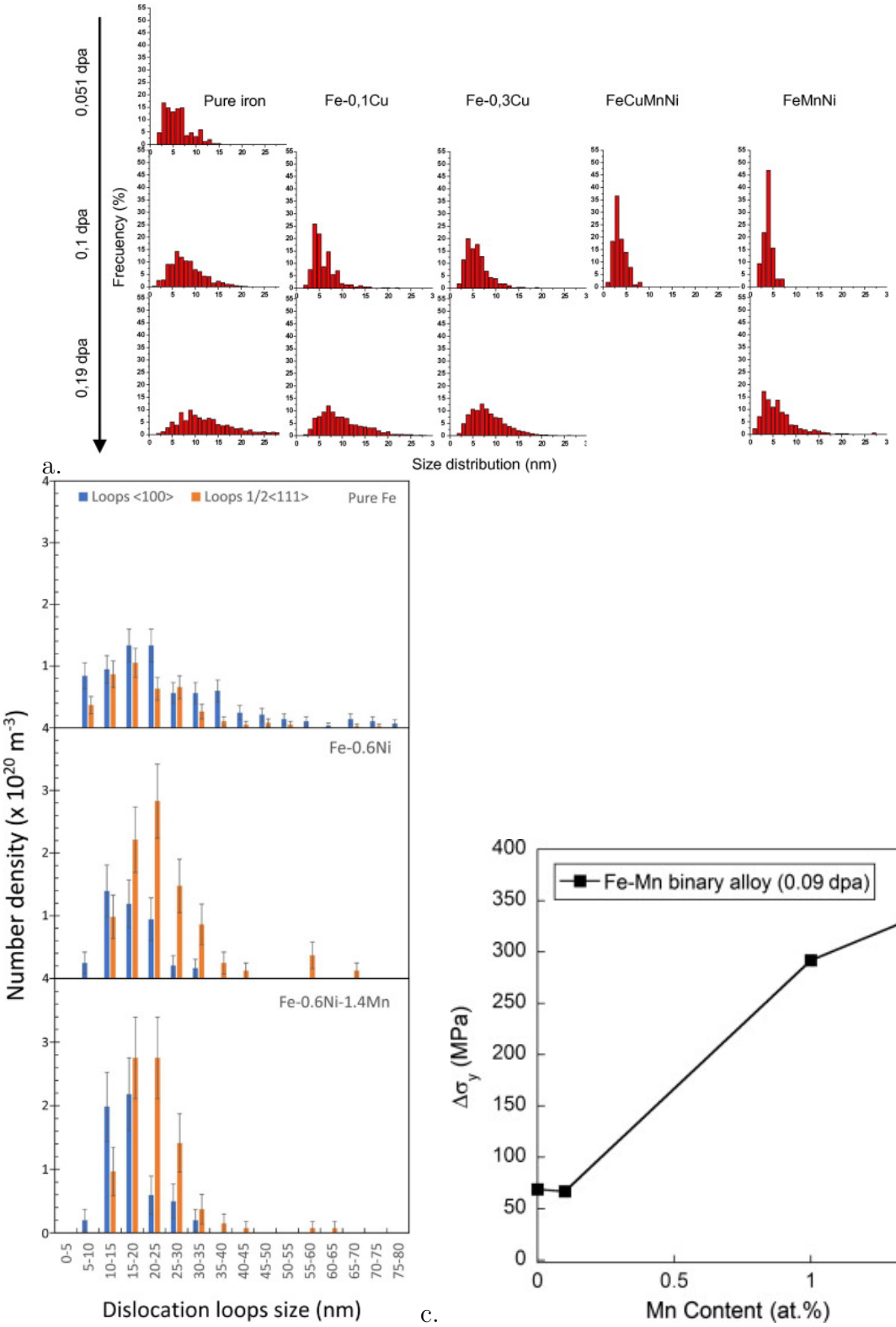


Figure 2.23: Comparison of two TEM observations (a. and b.) in irradiated RPV steels and model Fe-Mn-Ni alloys, where decreasing loop size, and increasing loop number density has been identified with increasing compositional complexity, and the effect of Mn addition on the hardening (c.), measured in terms of change in yield stress, made by a. Hernandez Mayoral et al. [101], b. Prak Tom et al. [112], and c. Yabuuchi et al. [135].

a. Reprinted from Journal of Nuclear Materials, 399, M. Hernández-Mayoral, D. Gómez-Briceño, Transmission electron microscopy study on neutron irradiated pure iron and RPV model alloys, Pages 146-153, Copyright 2010, with permission from Elsevier.
b. Reprinted from Journal of Nuclear Materials, 559, Phongsakorn Prak Tom, Kenta Murakami, Vu Nhut Luu, Ba Vu Chinh Nguyen, Liang Chen, Effect of solute elements (Ni, Mn) in Fe-based alloys on dislocation loop evolution under Fe2+ ion irradiation, Page 153489 , Copyright 2022, with permission from Elsevier.
c. Reprinted from Journal of Nuclear Materials, 414, Kiyohiro Yabuuchi, Masashi Saito, Ryuta Kasada, Akihiko Kimura, Neutron irradiation hardening and microstructure changes in Fe–Mn binary alloys, Pages 498-502, Copyright 2011, with permission from Elsevier.

Fe-Mn-Ni and Fe-Mn-Ni-Si model alloys, it was clear that Si led to a doubling in number density of defects suggesting that Si promotes clustering, perhaps by stabilising clusters at early stages of formation, fig. 2.24 [133]. However, they also observed very slow evolution of cluster composition in the Fe-Mn-Ni-Si alloy, suggesting that Si slows growth at least while the composition is unstable and suggest that the initial structure is that of a B2 BCC phase, which transforms into the G phase or the Γ_2 phase at higher fluences [133]. Earlier work on quaternary

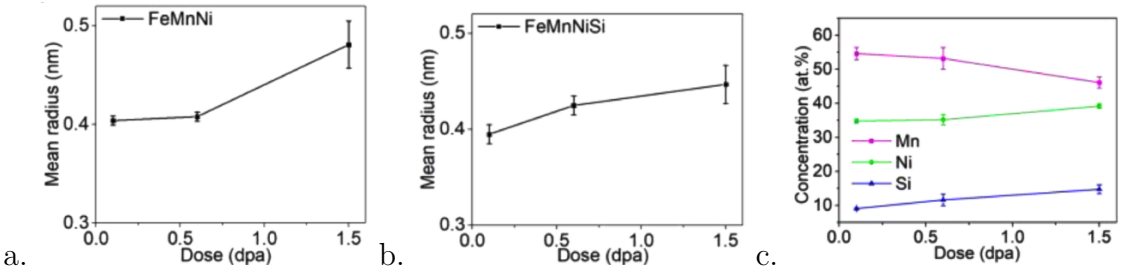
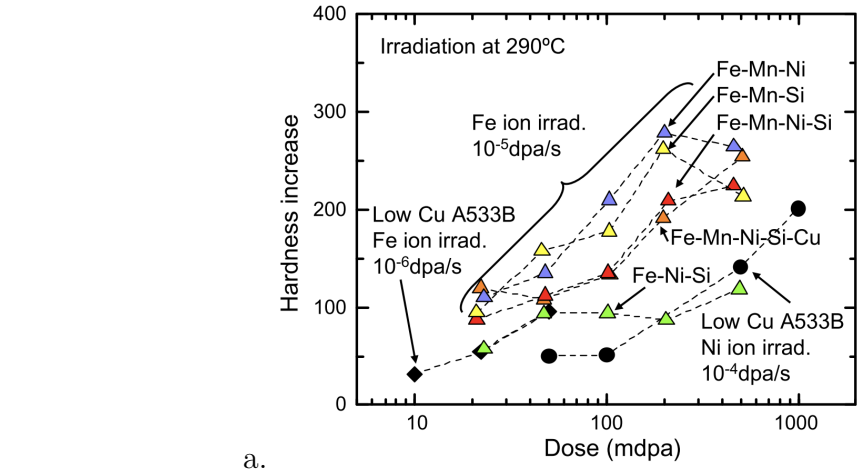


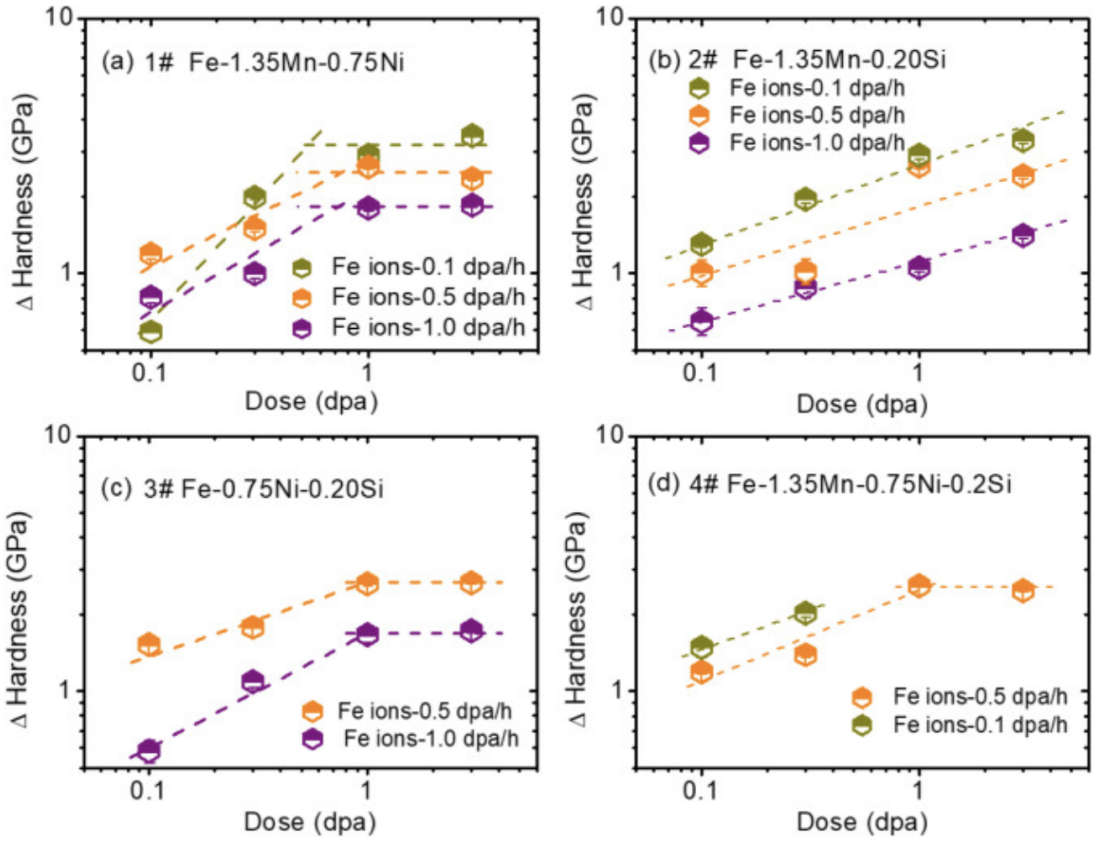
Figure 2.24: APT cluster size measurements from Xue et al. for self-ion irradiated a. Fe-Mn-Ni model alloy and b. Fe-Mn-Ni-Si model alloys, and c. plot showing the evolution in cluster composition with increasing dose in the Fe-Mn-Ni-Si alloy[133]. Reprinted from Journal of Nuclear Materials, 560, Jing Xue, Shenbao Jin, Rong Hu, Fei Xue, Gang Sha, Ion-irradiation-induced clustering in Fe-Mn-Ni-(Si) steels: Nucleation, growth and chemistry evolution, Page 153477, Copyright 2022, with permission from Elsevier.

and ternary alloys of Fe-Mn-Ni-Si, Fe-Ni-Si and Fe-Mn-Ni, found that in self-ion irradiated steels, the addition of silicon reduced radiation hardening, and Mn accelerated hardening [137]. Takamizawa et al. measured the effect of silicon content on cluster composition in a range of Cu bearing and low-Cu RPV steels. They found that Ni and Si cluster content increases more with fluence than Mn content, again suggesting a stabilising interaction occurring in clusters between Ni and Si [38]. Model alloy studies by Yang et al., and Fujii et al. aimed to investigate the synergistic effects of Mn, Ni and Si, by measuring radiation induced hardening of a range of ternary and quaternary alloys (fig. 2.25)[138, 139]. Fujii et al. observed that in alloys with Mn, greater hardening was present after irradiation, and alloys with both Ni and Si present showed comparatively lower hardening, suggesting a synergistic effect of Ni and Si content [138]. This contrasts with the work by Yang et al. which observed that Si and Ni increased cluster nucleation and there was very little difference in radiation hardening between the model alloys [139].

There is of course a disadvantage to using simplified alloys as they cannot be used to directly



a.



b.

Figure 2.25: Change in hardness after irradiation with Fe and Ni ions, for a range of Fe-Mn-Ni-Si model alloys, from Fujii et al. 2011 (Fig. 4, [138]) (a.), and Yang et al. 2024 (Fig. 6 ,[139])(b.).

a. Reprinted from Journal of Nuclear Materials, 417, Katsuhiko Fujii, Tadakatsu Ohkubo, Koji Fukuya, Effects of solute elements on irradiation hardening and microstructural evolution in low alloy steels, Pages 949-952, Copyright 2011, with permission from Elsevier.
b. Reprinted from Journal of Nuclear Materials, 588, Yitao Yang, Chonghong Zhang, Jianyang Li, Jie Gou, Zhaonan Ding, The influence of solute elements on grain size, hardness and irradiation-induced defect clusters in dilute Fe-based alloys, Page 154818, Copyright 2024, with permission from Elsevier.

predict the behaviour of a more complex material, but it does allow the investigation of specific combinations of solutes and radiation particles and their effects on the microstructural and mechanical properties. This is very useful for the creation of empirical models that predict embrittlement based on the interaction between different solute elements.

Although generally only present in atom fractions below 0.015 wt.% ([24]), phosphorus has been shown to play a key role in the stabilisation of radiation induced defect clusters, due to its strong trapping properties [113]. Warren et al. investigated a range of self-ion irradiated binary model Fe alloys with Cr, N and P, and the Fe-P alloy showed significantly higher number density of matrix defect clusters than the other two [113]. In another study investigating solute clustering in a range of very low Cu RPV steels, atom probe tomography was used to identify the role in P in promoting the precipitation of solute rich features and concluded that in Cu free steels, P clustering provides nucleation sites for Mn-Ni-Si precipitates [140]. Sharma et al. also concluded that P stabilised interstitial clusters, which act as heterogeneous nucleation sites in a ferritic matrix, but given its low composition in the alloy, is not likely to contribute to the growth of precipitates [141].These observations are consistent with ab initio modelling of phosphorous substitutions into various proposed Mn-Ni-Si rich phases in RPV steels, which have found that phosphorus can stabilise the Mn-Ni-Si G phase by substituting onto the Si sublattice [142]. In RPV steels, phosphorus segregated significantly to grain boundaries, leading to a large shift of DBTT with increase in number density of precipitates [143].

2.4.3 Computational modelling of radiation damage mechanisms in RPV steels

At the very early stages of clustering, analysis using experimental techniques with the ability to accurately identify chemical composition is very challenging due to the small size of features, and it isn't possible to observe solute segregation in-situ experimentally with atomic scale resolution. Therefore, computational modelling techniques play a key role in understanding the mechanisms behind solute clustering and growth [66]. The stability of solute clusters in a ferritic matrix has been the topic of many Density Functional Theory (DFT) and atomistic modelling investigations [73].

One of the challenges of modelling these mechanisms is that they rely on the accuracy of

inter-atomic potentials between elements in the steels, and the use of different potentials and assumptions on solute-interactions leads to a wide variety of conclusions on solute clustering. For example, a study using atomistic kinetic Monte Carlo (AKMC) and DFT concluded that solute clustering is radiation induced [120], and another study calculated thermodynamically stable structures at 290 °C in BCC-Fe are radiation enhanced [144]. The DFT approach has evolved from considering the stability of pairs of defects to triplet and quartet clusters, to investigate the synergistic effects of solutes on local cluster stability [145, 117]. Modelling larger clusters has enabled better understanding of the role of silicon and vacancies in stabilising Mn and Ni containing defect-solute complexes. Silicon atoms in quartet clusters have been shown to form stable covalent bonds with other solute species, stabilising early stage clusters [145]. However, when silicon atoms are close enough they begin to change the magnetic behaviour of the surrounding cluster, leading to a reduction in stability [145]. As clustering evolves, there are then two key arguments around the nature of Mn-Ni-Si rich features in RPV steels. One proposed theory is that precipitation of Mn-Ni-Si rich features is induced by radiation, through RIS, and the generation of heterogenous nucleation sites in the form of dislocation loops. The defect fluxes maintained under radiation exposure lead to the formation of metastable phases at defect sinks. Nastar et al. suggest that the induced lattice volume mismatch from high concentrations of solute atoms or vacancies lowers the Gibbs free energy of formation for precipitate phases. This results in a widening of the temperature and compositional ranges in which precipitation would be expected to occur as shown in fig. 2.26[146]. The other dominant theory is that the Mn-Ni-Si rich features are thermodynamically stable phases, whose precipitation is being accelerated by the presence of radiation induced defects, and elevated diffusion. Ngayam-Happy et al. strongly disagreed with experimental and computational studies stating that Mn-Ni-Si precipitates are late blooming stable phases, instead arguing that Mn-Ni clusters nucleate but cannot form stable phases[120]. However, they assumed that the presence of other solutes would not alter the stability of solute clusters, which has since been proven not to be the case [120].

The role of vacancies in mediating diffusion and forming parts of precipitate structures will affect the stability of structures under irradiation. Structural vacancies are a key part of the difference between an ordered $L2_1$ (Heusler) phase and the G phase (fig. 2.27) [142, 131]. Therefore, in an environment where vacancy concentration is significantly higher than equilibrium

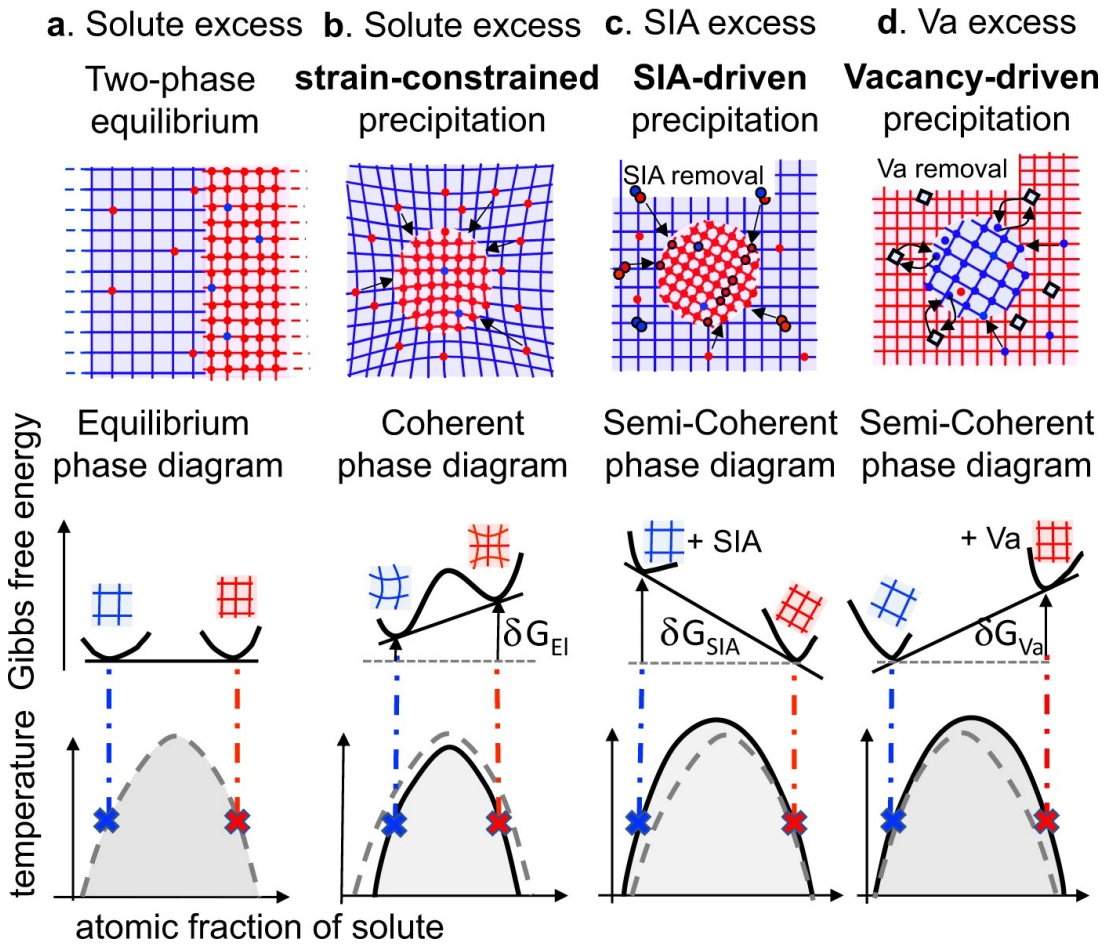


Figure 2.26: Figure 1 from Nastar et al.[146], showing the effects of point defect accumulation on the Gibbs free energy of formation for semi-coherent phases in a variety of scenarios. Reprinted from Communications Materials, 2, M. Nastar, L. T. Belkacemi, E. Meslin, and M. Loyer-Prost, Thermodynamic model for lattice point defect-mediated semi-coherent precipitation in alloys, Page 32, licensed under CC BY 4.0, 2021 (`https://creativecommons.org/licenses/by/4.0/`).

for a given temperature, phases that would not normally be thermodynamically stable, may form. Hosseinzadeh et al. considered the stability of various Fe-Mn-Ni-Si structures in BCC-Fe, and found a range of phases can form with negative formation energies and coherent lattice parameters, including: Fe-Mn-Ni-Si-P G phases structures and ordered B2 and $L2_1$ structures [142].

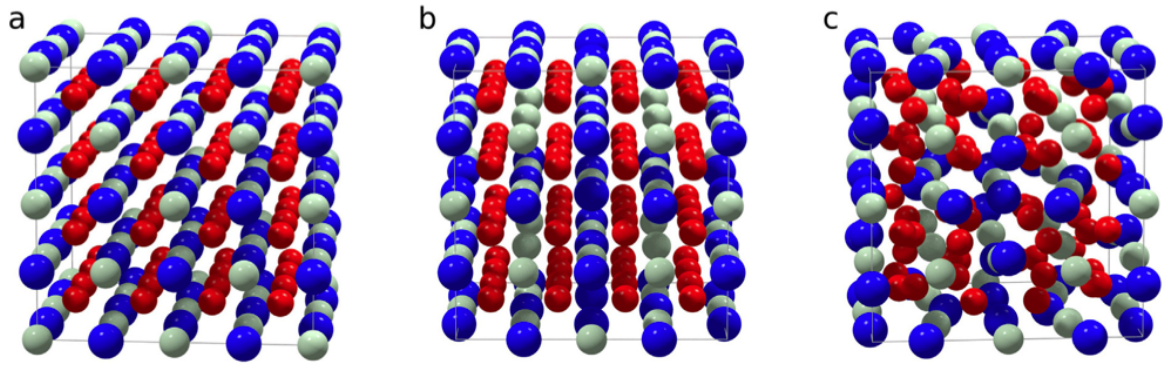


Figure 2.27: Figure 2 from Hosseinzadah et al. [142], showing (a.) an $L2_1$ structure, (b.) an $L2_1$ structure with the same stoichiometry as the MnNiSi G phase, and (c.) $Mn_6Ni_{16}Si_7$ g phase. Nickel shown in red, manganese in blue, and silicon in grey. Reprinted from Journal of Nuclear Materials, 509, A. Hosseinzadeh Delandar, O.I. Gorbatov, M. Selleby, Yu.N. Gornostyrev, P.A. Korzhavyi, Ab-initio based search for late blooming phase compositions in iron alloys, Pages 225-236., Copyright 2018, with permission from Elsevier.

DFT studies are widely used to investigate the stability of various structures proposed to be formed under irradiation. The Mn-Ni-Si G phase has been calculated to have a negative formation energy in BCC-Fe, and is expected to form when local concentrations of Fe drop below 18 at.% [131]. At small radii solute clusters are likely to have semi-coherent interface with the matrix, but above a critical radius a rearrangement of crystal structure may occur whereby it is more energetically favourable for a cluster to have a different crystal structure to that of the matrix. At this point the cluster can be described as a precipitate as it is a separate distinguishable thermodynamically stable phase from the matrix material. Unless the surface energy for formation can be overcome, clusters will be more stable in ordered BCC structures, such as a B2 or $L2_1$ [131, 142]. Hosseinzadeh et al. propose that the G phase has a lower formation energy than other phases in fig. 2.27, due to its internal vacancy concentration [142].

Xiong et al. predicted that Mn-Ni-Si precipitates are thermodynamically stable at reactor operating temperatures using CALPHAD models [128]. In their comparisons with existing APT

data from neutron irradiated steels, they identified the most probable phases modelled to be stable in a reactor environment are: Γ_2-$Mn(Ni_xSi_{1-x})_2$ (T6), and G phase, $Mn_6Ni_{16}Si_7$ (T3), see phase diagram in fig. 2.28, [128]. Subsequent work by Ke et al., used the same CALPHAD databases to predict equilibrium phases in a range of materials, and compare experimental observations of neutron irradiated materials at 300 °C in previous studies [147, 148, 143, 149]. The cluster dynamics model demonstrated the ability to predict the development of Mn-Ni-Si rich precipitates in a range of steels at lower fluxes, whereas at higher fluxes the model seemed to underestimate the impact of Ni content on diffusion and segregation to small dislocation loops. This is in contrast with Almirall et al.'s cluster dynamics model which over predicts the stability of Mn-Ni-Si precipitates over longer time periods, in this case due to predicting a smaller critical radius of precipitate than is generally observed [136].

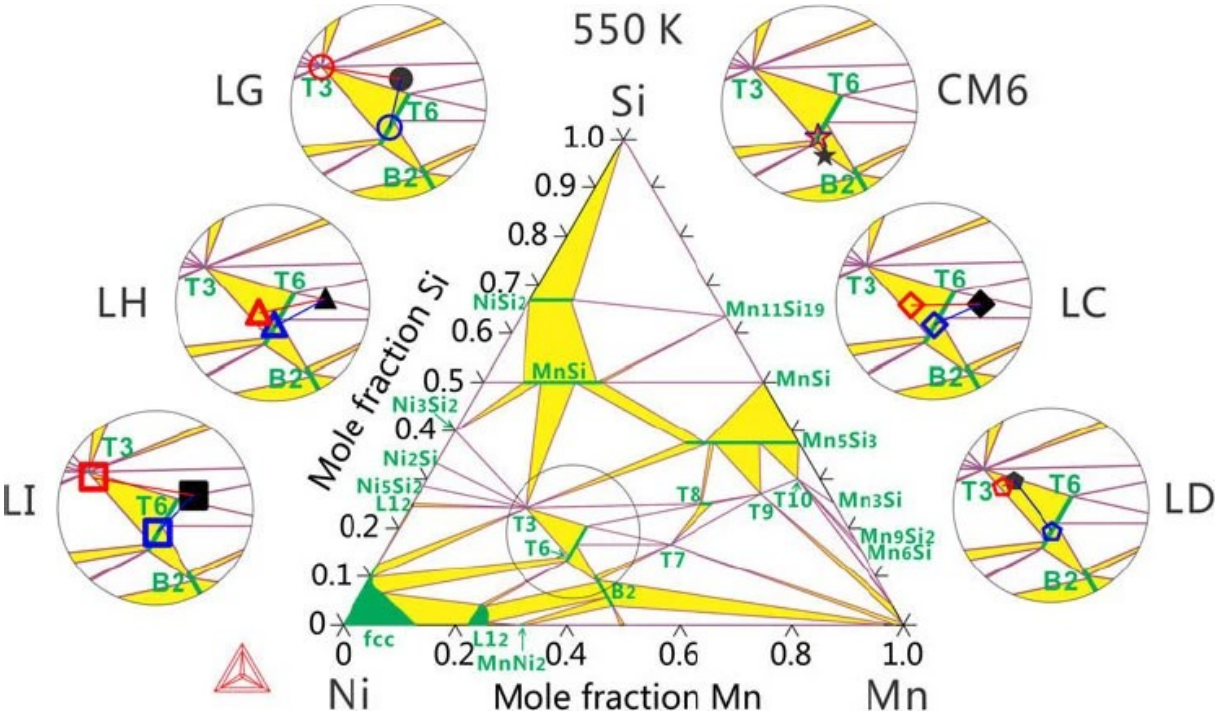


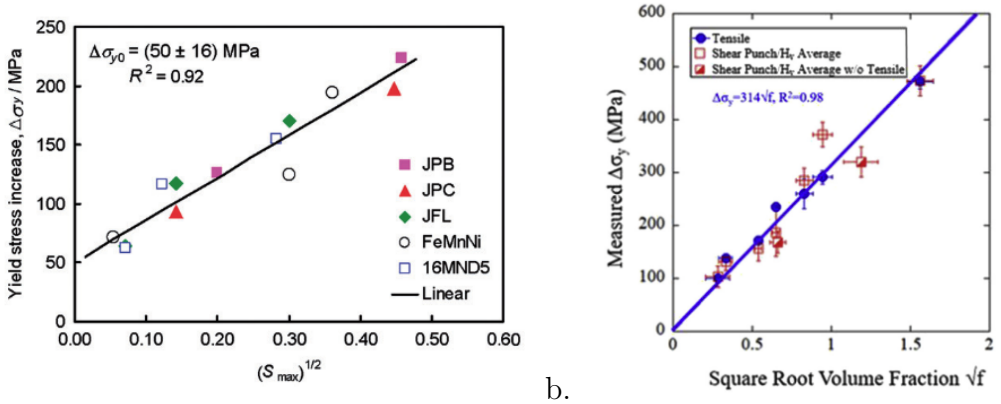
Figure 2.28: Mn-Ni-Si phase diagram at 550 K (276.85 °C) from Xiong et al. [128], showing most probable phases for Mn-Ni-Si precipitates forming in RPV steels under irradiation and ageing, alongside plotted APT cluster compositions in solid black. The open symbols are calculated compositions of precipitates in RPVs calculated using the UW1 database (blue) and the TCAL2 database (red). Thermodynamic models of low-temperature Mn-Ni-Si precipitation in reactor pressure vessel steels, Wei Xiong et al, MRS Communications, Springer Nature, 2014, reproduced with permission from SNCSC.

2.5 Effects of solute rich defects on mechanical properties of RPV steels

In copper-containing steels, a greater increase in $\Delta DBTT$ occurs due to the increased strength of dislocation interaction with copper-rich precipitates compared with Mn-Ni-Si precipitates [143]. However, significant reduction in fracture toughness and increase in DBTT have been observed for low Cu RPV steels, necessitating further research into the mechanisms around Mn-Ni-Si rich features and interactions with dislocations. The two key causes of DBTT shift and loss of fracture toughness are radiation hardening, caused by loops and solute rich defects, and non-hardening embrittlement, caused by segregation of species like P weakening grain boundaries and carbide interfaces [122].

Many studies into the effects of radiation on RPV steels employ micromechanical testing techniques, either due to small available volumes of material from ion irradiations, or to minimise handling of radioactive material. In this case, it is not possible to directly measure fracture toughness or DBTT, and alternative measures are used such as indentation hardness, and yield stress. In this case, hardening of a material or an increase in yield stress correspond to an increase in resistance to plastic deformation, enhanced pinning of dislocations, and an increased likelihood of brittle fracture. There are clear links between microstructural defects and mechanical properties. One well established relationship is between the volume fraction of solute rich defects and the increase in yield stress measured (fig. 2.29) [150, 37]. This is based on the relationship between volume fraction and the number density and defect size, and the dispersed barrier hardening model, which is described in eq. (7.1) [151, 152]. Figure 2.29 shows that additions of Mn, Ni and Si leading to enhanced number density of defects is causing greater hardening under irradiation.

Kolluri et al. have also identified a synergistic effect of Mn and Ni on mechanical properties, observing a drop in upper shelf energy and increase in DBTT after irradiation in alloys containing very high Ni and Mn contents [62].



a. b.

Figure 2.29: Increase in yield stress versus square root of small angle neutron magnetic scattering magnitude (a.), Bergner et al. [150], and increase in yield stress versus square root of volume fraction of Mn-Ni-Si rich clusters formed under irradiation (b.), calculated using APT by Almirall et al. [37].

a. Reprinted from Acceleration of irradiation hardening of low-copper reactor pressure vessel steel observed by means of SANS and tensile testing, A. Ulbricht, F. Bergner, H.-W. Viehrig, et al, Philosophical Magazine: Letters, and © copyright 2009, reprinted by permission of Informa UK Limited, trading as Taylor & Francis Group, https://www.tandfonline.com

b. Reprinted from Acta Materialia, 179, N. Almirall, P.B. Wells, T. Yamamoto, K. Wilford, T. Williams, N. Riddle, G.R. Odette, Precipitation and hardening in irradiated low alloy steels with a wide range of Ni and Mn compositions, Pages 119-128, Copyright 2019, with permission from Elsevier.

2.6 Using complementary characterisation techniques for radiation damage analysis

Analysis of solute rich defects require techniques with chemical sensitivity such as atom probe tomography, and small angle neutron scattering. These techniques are often combined as APT gives accurate measurements of local composition of solute rich defects, which can be integrated into models used to fit SANS data and extract statistical information on size distribution and volume fraction of secondary phases in a well-defined matrix material. The analysis volume of SANS is much larger than TEM and APT, allowing analysis of the bulk material and distribution of defects across a more representative volume. SANS studies have been widely applied to the identification of clusters in irradiated RPV steels, based on the contrast in scattering behaviour between solute elements and Fe. As radiation damage happens over a wide size range and timescale, multi-scale modelling and characterisation is required in order to understand the fundamental mechanisms behind RPV embrittlement, to inform predictive models fig. 2.30. Combining the results from multiple characterisation techniques creates a more comprehensive analysis of radiation induced defects, as shown by many of the previously discussed works [66, 144, 129, 102, 15, 36].

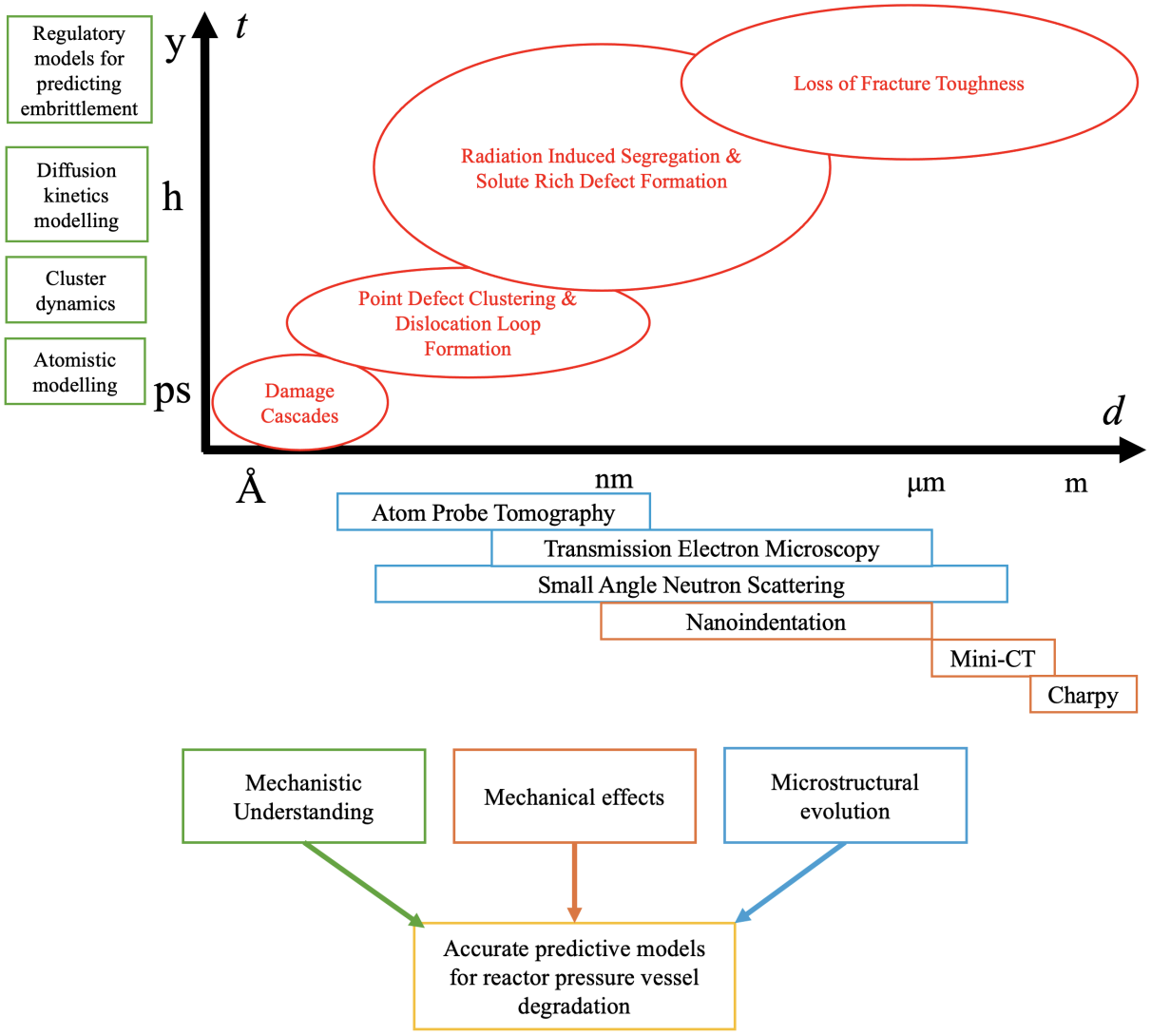


Figure 2.30: Schematic diagram showing the spatial and time range overlap covered by complementary characterisation techniques, and how various techniques can provide information on similar size ranges, contributing to the overall aim of devising predictive models for RPV degradation.

For example, various European projects have been funded by Horizon 2020 to create predictive models relating microstructural evolution of RPV steels under irradiation to the change in mechanical properties using complementary methods, including: FP6 PERFORM60 (2009) [153], FP6 PERFECT (2010) [154], and FP7 LongLife [155]. A key benefit of operating in a large consortium is enhanced access to facilities enabling a variety of characterisation techniques, and the outputs of these projects have used a wide range of complementary characterisation techniques, producing more consistent data on solute rich defect composition, volume fractions and size distributions. For example, Meslin et al. characterised neutron-irradiated ferritic model alloys and an RPV steel using APT, SANS, TEM and positron annihilation spectroscopy, to obtain self-consistent values of precipitate composition, volume fraction and size, as shown in ?? [66]. Atom probe tomography and small angle neutron scattering are often using in a com-

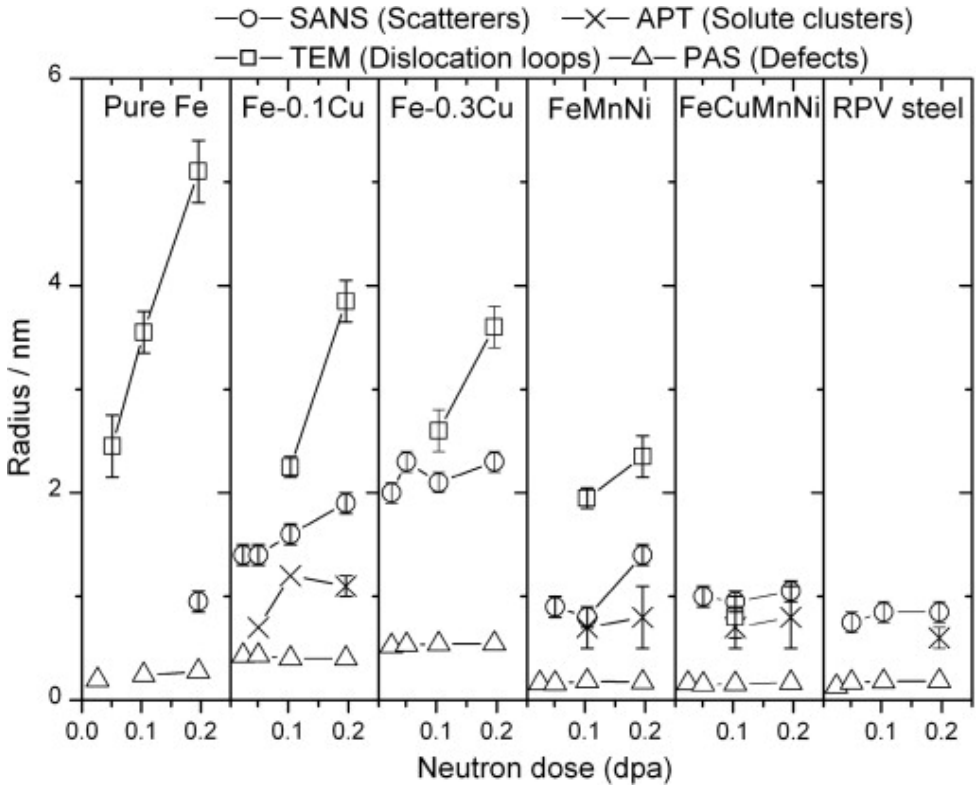


Figure 2.31: Figure showing consistent measurement of solute cluster sizes in a range of Fe alloys investigated by Meslin et al. 2010 [66]. Reprinted from Journal of Nuclear Materials, 406, E. Meslin, M. Lambrecht, M. Hernández-Mayoral, F. Bergner, L. Malerba,P. Pareige, B. Radiguet, A. Barbu, D. Gómez-Briceño, A. Ulbricht, A. Almazouzi, Characterization of neutron-irradiated ferritic model alloys and a RPV steel from combined APT, SANS, TEM and PAS analyses, Pages 73-83, Copyright 2010, with permission from Elsevier.

plementary manner, using APT to obtain essential a priori information such as composition

and estimates of size or number density of scattering features, to enable SANS data analysis to provide values that describe the overall population of radiation induced features [156, 157, 36]. Similarly, APT analyses a very small volume of material, and without accurate reconstruction it is challenging to identify crystal structures and morphology. TEM is the ideal technique for imaging defects, and identifying their relationship to crystallographic directions in the material, but APT has significantly improved chemical sensitivity to elements across the periodic table. Shu et al.'s multi-technique characterisation of neutron irradiated and aged model RPV steels confirmed that the measured Fe present in copper-rich precipitates was an artefact of APT, caused by trajectory aberrations [144]. This would not have been identified had there not been a concurrent study on these materials using SANS, as shown in fig. 2.32. Nano and micro-scale

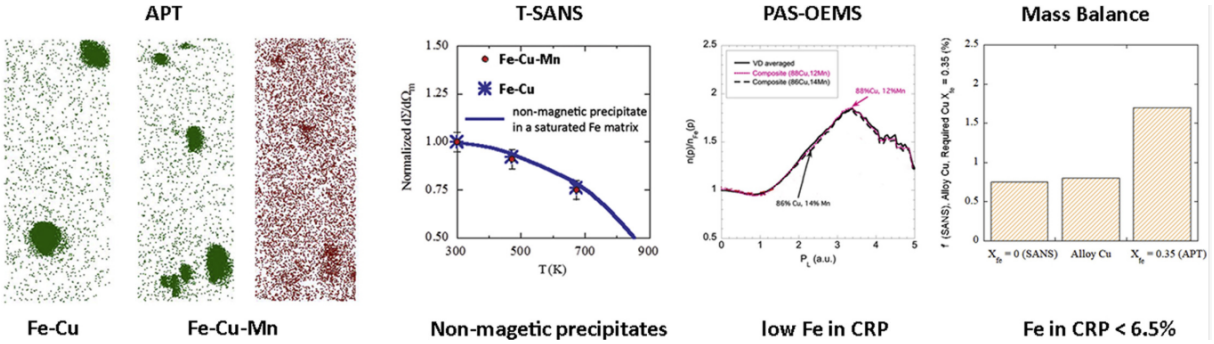


Figure 2.32: Figures from Shu et al. 2018, showing copper rich precipitates in irradiated model Fe-Cu and Fe-Cu-Mn alloys, and comparisons between the measured Fe content in the precipitates using APT, SANS and PAS, indicating an overestimation of Fe content using APT [144]. Reprinted from Acta Materialia, 146, Shipeng Shu, Brian D. Wirth, Peter B. Wells, Dane D. Morgan, G. Robert Odette, Multi-technique characterization of the precipitates in thermally aged and neutron irradiated Fe-Cu and Fe-Cu-Mn model alloys: Atom probe tomography reconstruction implications, Pages 237-252, Copyright 2017, with permission from Elsevier.

mechanical testing can complement these characterisation techniques, by allowing small regions of the material to be testing, and limiting the range of defects that are contributing to the response of the material to deformation. This can help feed into multi-scale modelling of the interactions of dislocations with radiation induced defects. For example, Bergner et al. showed that because neutron scattering intensity is a function of the volume fraction, composition, and structure of scatterers, it is linked to the features' obstacle strength. As a result, there is a relationship between neutron scattering magnitude and the hardening of a material under irradiation,fig. 2.33[150].

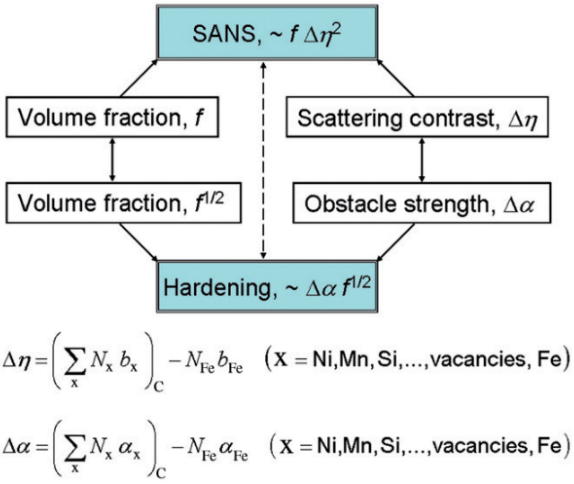


Figure 2.33: Flow chart showing the link between experimentally observed neutron scattering intensities and the change in yield stress caused by the formation of solute clusters under irradiation, from figure 4, Bergner et al. [150]. Reprinted from Acceleration of irradiation hardening of low-copper reactor pressure vessel steel observed by means of SANS and tensile testing, A. Ulbricht, F. Bergner, H.-W. Viehrig, et al , Philosophical Magazine: Letters , and © copyright 2009, reprinted by permission of Informa UK Limited, trading as Taylor & Francis Group, https://www.tandfonline.com

2.7 Motivation for further research

The synergistic effects of Mn, Ni and Si on the formation mechanism of solute rich clusters and precipitates in irradiated RPV steels is not yet fully understood. One key argument is over the thermodynamic stability of Mn-Ni-Si rich defects, with some groups referring to them as precipitates and others maintaining that they are metastable clusters. The Odette group claim they form stable G and Γ_2 Mn-Ni-Si phases after high fluence irradiation [148, 128]. Others claim they are not forming stable phases, and their formation is caused by radiation induced segregation, and the high vacancy concentrations present under irradiation [120, 146, 83]. Solute rich defect clusters are found in irradiated alloys despite solute concentration being below their respective solid solubility limits at irradiation temperatures. At early stages of formation, this suggests that they are not likely to be thermodynamically stable and that any clustering is induced, rather than enhanced, by irradiation [66].

The aim of this work is to investigate the effect of varying solute combinations on radiation induced microstructural changes, to identify synergistic effects between Mn, Ni, and Si and to identify whether proton irradiation can produce comparable microstructures to neutron

irradiated materials in literature.

Despite the evidence that manganese and silicon interact during clustering ([145]), there are limited studies investigating effects of irradiation of nickel free, manganese containing model RPV steels. Existing work on model alloys is predominantly carried out using heavy ion irradiation, which has much more limited irradiated volume, with a constrained region for analysis between the irradiation surface and implanted region. Proton irradiation produces larger damage volumes, and at sufficiently high temperatures, implanted ions diffuse away from the irradiated region quickly, creating a larger volume of material for analysis, and a larger dose range.

Understanding the variation in radiation response depending on composition will help to confirm existing ideas around the interaction of Mn, Ni, and Si in stabilising radiation induced defects, and could lead to insight into chemical tailoring of alloys for future nuclear applications. Identifying the structures of precipitates formed under irradiation will help to establish whether stable phases can be formed under radiation conditions in dilute ferritic steels, or whether the features are likely to be formed via radiation induced mechanisms.

Data collected on microstructural changes in model alloys under proton irradiation will be useful for comparing modelling of radiation induced damage in compositionally simple systems. However, it will not yield representative data for RPV steels due to the significant difference in microstructure and composition. RPV steels have complex microstructures containing fine lath structures, and carbides which create a high density of defect sinks. Therefore, precipitation of solute-rich features will occur more slowly as there is a higher probability for defect annihilation at defect sinks compared with larger grained single phase materials [101, 158].

Chapter 3

Materials & Methods

3.1 Model reactor pressure vessel steels

In this study, three model reactor pressure steels, with compositions shown in table 3.1, are investigated after proton-irradiation to investigate the combined effect of solute additions. These alloys have been chosen to investigate the effect of various combinations of Mn, Ni and Si solute elements in compositions comparable to those in a reactor pressure vessel steel, to see whether there is a difference in interactions between these solutes that results in varying microstructural evolution.

The model alloy samples were produced by Suzhou Nuclear Power Institute. The alloys were melted at 1480°C, poured at 1500°C and forged at 1150°C and 900°C, before air cooling to room temperature [159, 133]. The A508-3 steel is a Chinese reactor steel produced by China Heavy Industries. Unlike the model alloys, these samples were heated to 890°C during forging for 7 hrs, quenched in water and then tempered at 650°C for 10 hrs, before being air-cooled, as described by Jiang and Shi et al. [160, 102]. This heat treatment would be expected to produce a tempered martensitic structure, but has been identified as bainitic by Jiang et al [160]. After tempering, the structures of martensite and lower bainite are similar, with fine carbides inside the laths, but the orientation relationship between the carbides and ferritic matrix differ in martensite and ferrite. In this work, the orientation of carbides and laths within the A508-3 were not investigated so without further information on the size of the original heat, and the cooling rates experienced it is not possible to determine whether the samples are tempered martensite

or lower bainite. 15 x 15 x 1 mm specimens of each of the alloys in table 3.1) were mechanically polished to 0.04 µm finish with colloidal silica before irradiation.

Table 3.1: Nominal compositions (wt.%) of a representative RPV steel (A508-3) and model alloys investigated in this work.

Sample	Fe	C	Mn	Ni	Si	Mo	Cr	V	S	P	Cu
A508-3	96.804	0.167	1.35	0.738	0.193	0.481	0.086	0.007	0.002	0.005	0.167
FMNS	97.7	-	1.35	0.75	0.2	-	-	-	-	-	-
FMN	97.9	-	1.35	0.75	-	-	-	-	-	-	-
FMS	98.45	-	1.35	-	0.2	-	-	-	-	-	-

3.1.1 As-received sample microstructures

All model alloys have a large grained, carbide-free, ferritic microstructure, fig. 3.1. The A508-3 steels has a bainitic microstructure with Cr and Mo rich carbides present on grain boundaries and in the matrix, shown in fig. 3.2.

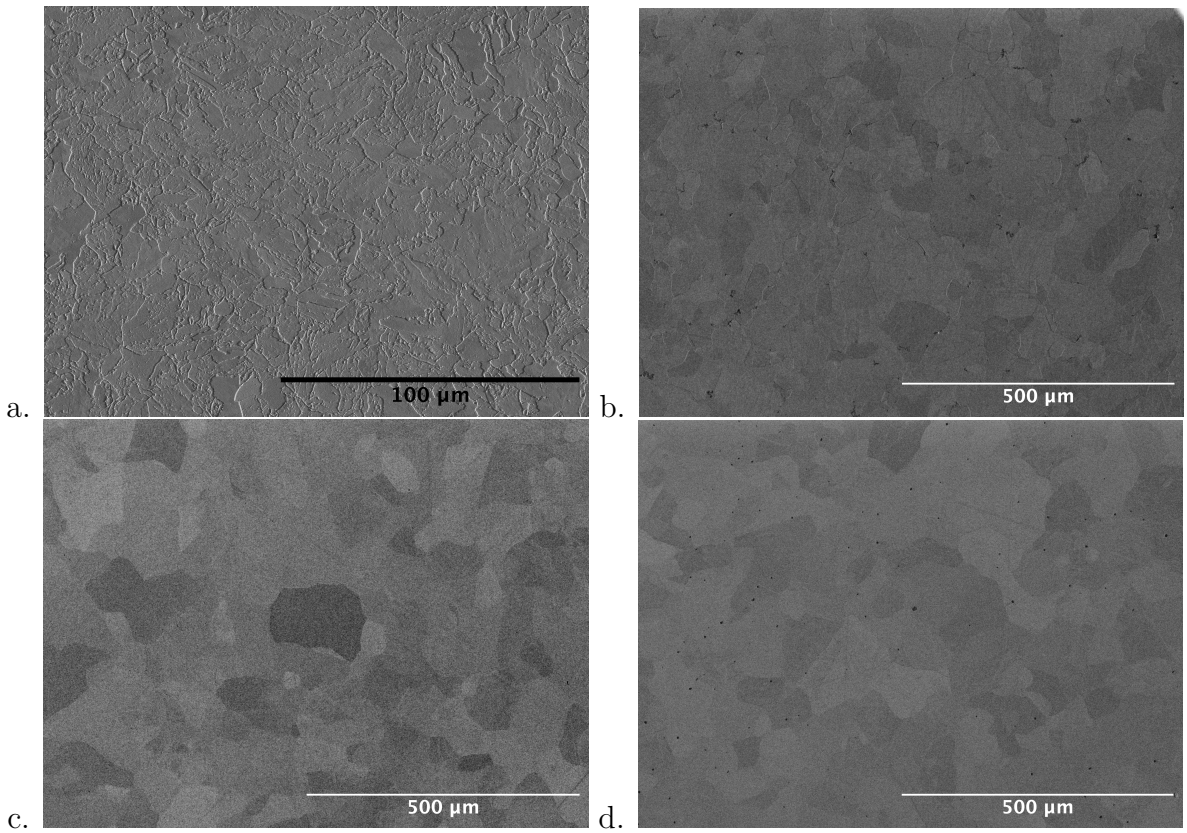
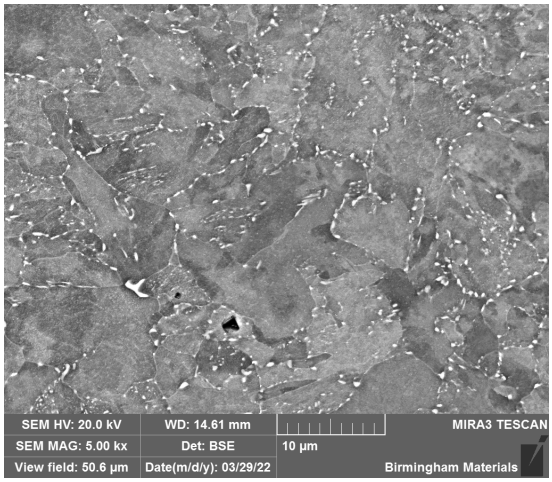


Figure 3.1: Back-scattered electron (BSE) images of etched A508-3 steel (a.), Fe-Mn-Ni-Si (b.), Fe-Mn-Si (c.), and Fe-Mn-Ni (d.). Images taken using PFIB Helios, 10 kV, 0.8 nA beam.

a. 

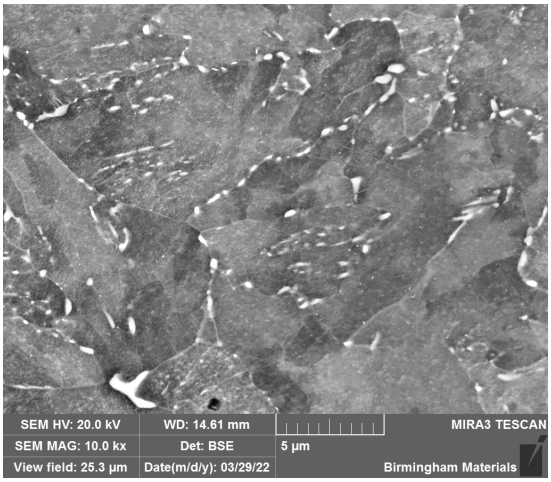
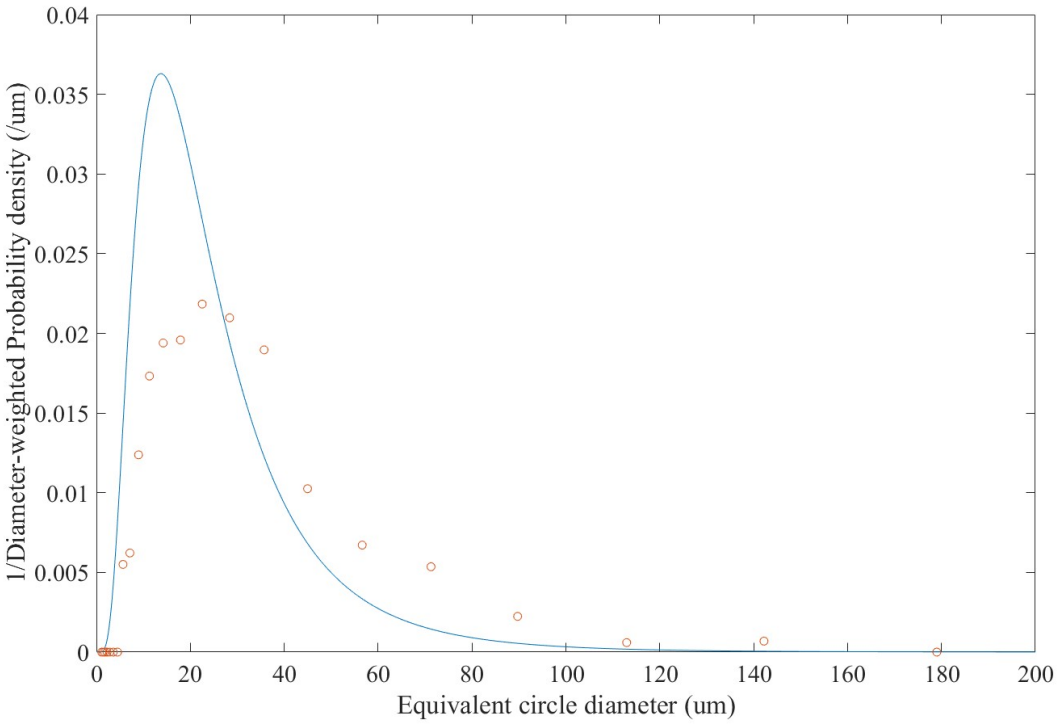
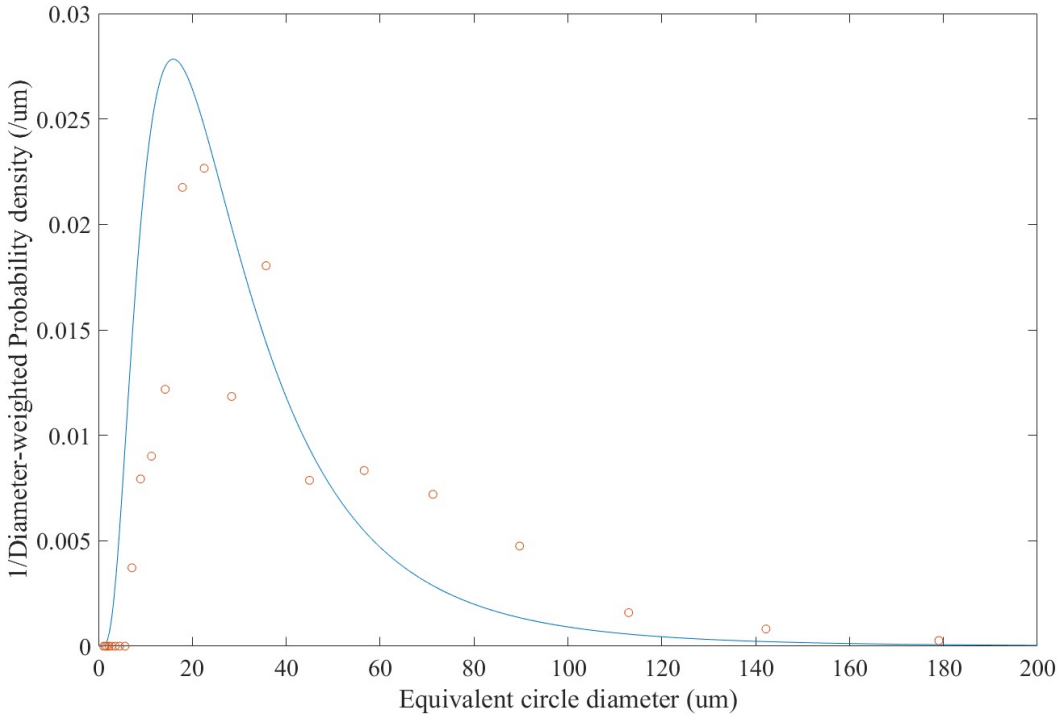
b. 

Figure 3.2: Back-scattered electron (BSE) images of the A508-3 RPV steel at 5 kx (a.) and 10 kx (b.). Images show a complex fine-grained structure with large carbides at grain boundaries and fine carbides in the matrix.

Grain size distributions for Fe-Mn-Si and Fe-Mn-Ni-Si model alloys are shown in fig. 3.3, and fig. 3.4 shows the size distribution of carbides in the A508-3 steel calculated from SEM images in fig. 3.2. The median grain size in the Fe-Mn-Ni-Si and Fe-Mn-Si alloys respectively are 20.9 µm and 24.5 µm.



a.



b.

Figure 3.3: Grain size (measured as the weighted mean equivalent circle diameter) for a. Fe-Mn-Ni-Si as received alloy, and b. Fe-Mn-Si as received alloy, with log normal distributions based on the median size and standard deviation.

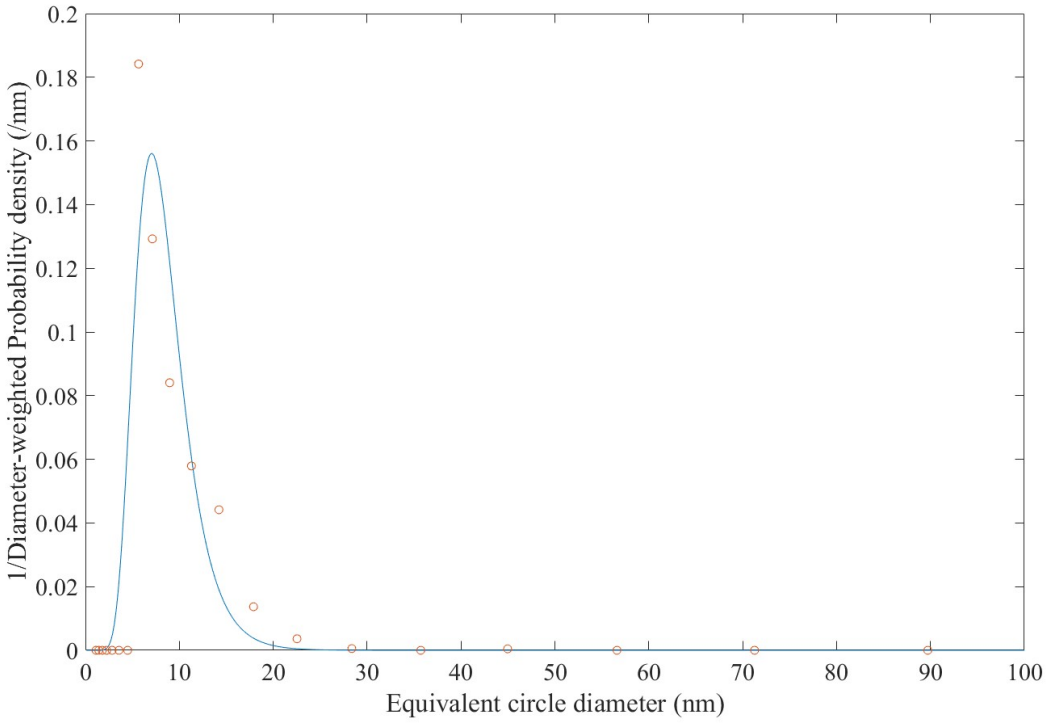


Figure 3.4: Weighted mean equivalent circle diameter of carbides in as received A508-3 steel, as observed in fig. 3.2.

3.1.2 Sample preparation post-irradiation & sample overview

Eight samples were prepared for measurement using SANS, two of each of the compositions detailed in table 3.1. Four were proton-irradiated, and four were heat-treated according to the heating and cooling profile shown in fig. 3.5. The heating and cooling was designed to emulate irradiation runs carried out over three days, assuming a constant temperature after heating, and cooling back to room temperature. The measured temperature profiles of irradiated samples are described in section 3.2, and vary significantly due to proton beam instability.

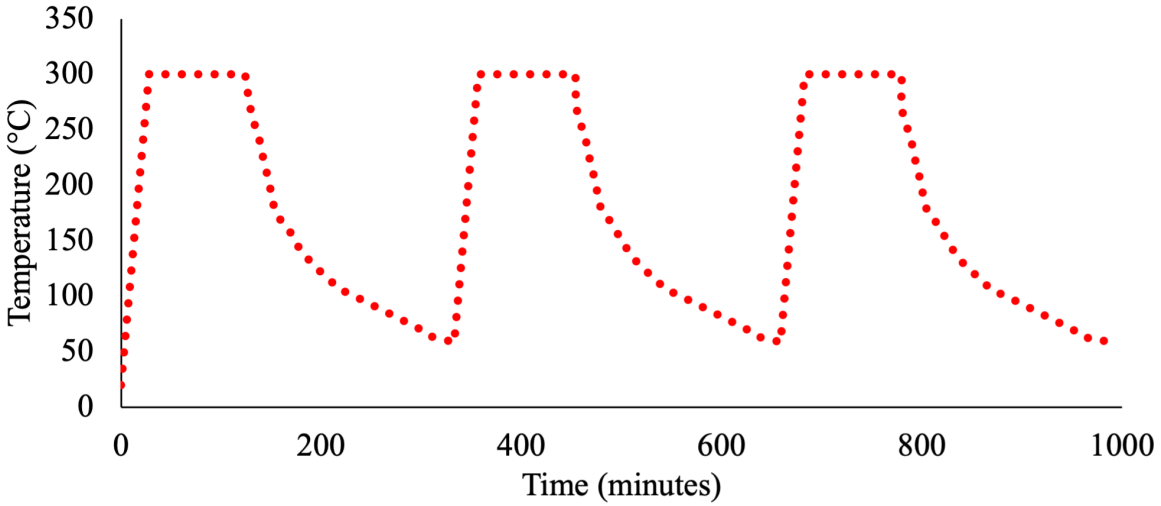


Figure 3.5: Temperature profile for heat-treated samples, mimicking proton-irradiation experiments.

After irradiation and heat treatment, the samples were mechanically thinned, from the back sides, to thicknesses below 300 µm to reduce multiple neutron scattering and self-attenuation during small angle scattering measurements. The irradiated Fe-Mn-Ni sample was only back-thinned to 400 µm as there was a hot-spot causing some localised melting in a small region of the sample. This may have been due to a lack of thermal conductivity between the specimen and the mount, caused by a non-uniform layer of indium behind the sample during proton-irradiation.

A summary of samples can be found in table 3.2. After SANS measurements, the samples were nickel plated to protect the irradiated surface during cross-sectioning and mechanical polishing. Nickel electroplating was carried out using a Watt bath reagent (nickel chloride, nickel sulphate and boric acid electrolyte) and pure solid nickel. Samples were plated for 15 minutes

on the irradiated side facing the electrode, and 5 minutes on the reverse side at 60 °C. The nickel-plated samples were then cold-mounted in resin, before being cross-sectioned using a slow cutting wheel, with a diamond blade at maximum 500 rpm. Then the cross-sections were mechanically polished up to 0.04 µm using colloidal silica. A schematic showing sample geometry can be seen in fig. 3.6.

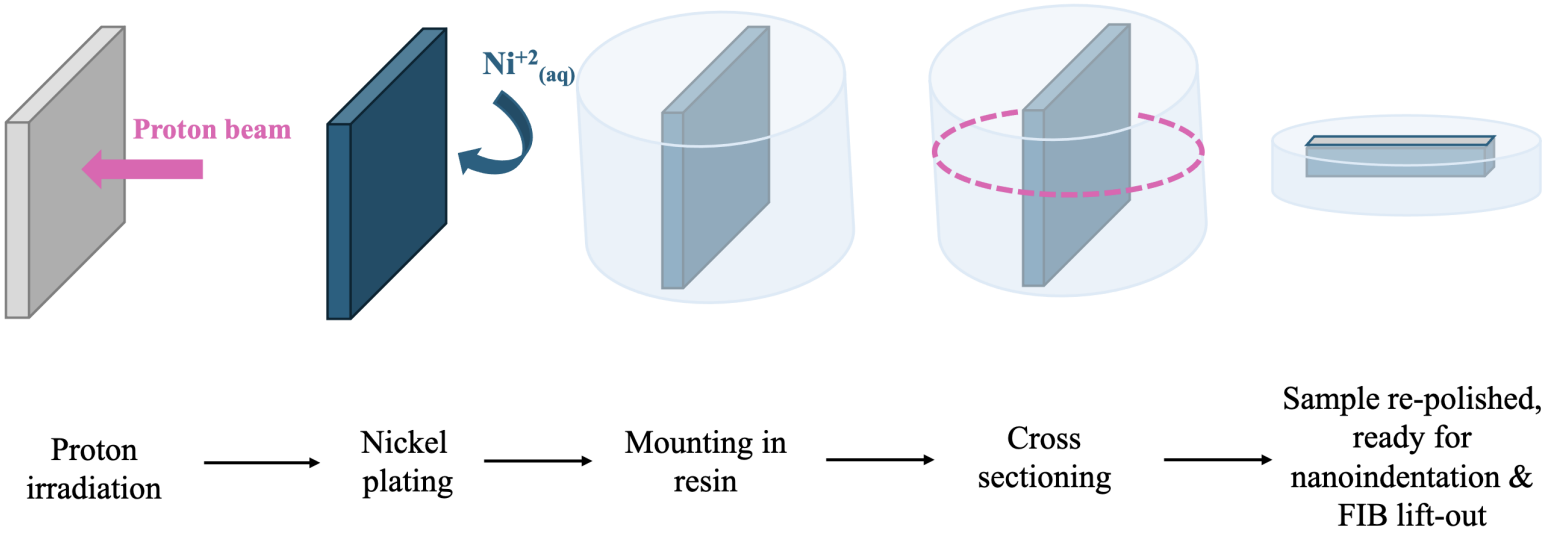


Figure 3.6: Schematic showing sample preparation steps from irradiation to final cross-sections.

Table 3.2: Summary of samples measured during the small angle neutron scattering experiment, along with their thickness and fraction of thickness covered by the proton-irradiated region.

Alloy	Condition	Thickness (µm)	Percentage of thickness in irradiated region
Fe-Mn-Ni-Si	Proton Irradiated	143	20.3 %
	heat-treated	240	-
Fe-Mn-Si	Proton Irradiated	144	19.4 %
	heat-treated	267	-
Fe-Mn-Ni	Proton Irradiated	306	10.1 %
	heat-treated	264	-
	heat-treated	238	-
A508-3	Proton Irradiated	137	17.5 %
	heat-treated	275	-

3.2 Proton irradiation

3.2.1 Modelling ion damage

Protons interact with matter through a mixture of interactions with nuclei and interactions with electrons in the material. This results in a non-uniform damage profile, and finite stopping distance which needs to be modelled in order to calculate the penetration depth of ions, as well as the radiation dose as a function of depth from the irradiation surface. For this, the SRIM-2013 (Stopping Range of Ions in Matter) software has been used to model each of the alloy compositions, irradiated with 2.9 MeV protons, using the quick calculation method [161]. This beam energy was selected to provide a balance between maximising penetration depth, and therefore increasing the volume of damaged material available for analysis, and preventing excessive activation of isotopes due to nuclear interactions of protons with the beam. Generally, higher energy protons are required to produce comparable primary knock on energy spectra with fission neutrons (>1 MeV) [162]. In this work, a mono-energetic 2.9 MeV proton beam was used to irradiate the samples, and compared with an average of around 35 keV average PKA energy from an 1 MeV neutron, the average proton induced PKA energy will be around two orders of magnitude lower [163, 162]. Neutron energy, and subsequent PKA energy also varies throughout the RPV wall so it is impossible to match the cascade energies of an operational reactor neutron spectrum using mono-energetic protons. In general, proton-irradiation provides a way to enhance vacancy concentration and improve understanding of the mechanisms that may be at play in the material under neutron irradiation, rather than to directly mimic it. The cascades produces will be smaller, with greater defect survival efficiency, and as a result mechanisms such as radiation enhanced diffusion are likely to be accelerated. SRIM is based on a binary collision approximation (BCA) and outputs the ion energy, primary knock on energy, number of vacancies and information about ionisations as a function of ion depth into a material.

These outputs can then be used to calculate damage energy, which is a measure of how much kinetic energy is imparted from an ion to a subsequent atom in the lattice leading to a collision cascade.

Damage energy, T_d, can then be used to calculate an estimate of the number of displacements

Table 3.3: SRIM input parameters used for modelling the damage profile in the alloys in this study, for incident 2.9 MeV protons as recommended by [164, 165, 166].

Input parameter	Value
Effective displacement threshold energy (applied to all elements), as recommended by ASTM E521-25 [164]	40 eV
Lattice binding energy, for NRT model [165]	0 eV
Atomic density	$7.85\,\mathrm{g\,cm^{-3}}$

per atom in a material, per incident ion. A modified version of the Kinchin-Pease model to calculate the number of displacements caused by a cascade based on the energy of a primary knock-on ion was devised by Norgett-Robinson-Torrens (NRT) [167]:

$$\nu_{NRT} = \frac{\kappa(E-\hat{Q})}{2E_d} = 0.8\frac{T_d(E_{PKA})}{2E_d} \tag{3.1}$$

Where ν_{NRT} is the total number of stable Frenkel pairs produced in the collision cascade, κ is a constant describing displacement efficiency, assumed to be 0.8, E_d is the threshold displacement energy, and T_d is the damage energy, which is a function of primary knock-on energy, E_{PKA}. $\hat{Q}$ is the total energy lost in the cascade by electron excitation, and E is the incident ion energy.

The damage energy, T_d, can be calculated according to guidance from Stoller et al. [165, 166], detailing the use of SRIM output files, IONIZ.txt and E2RECOIL.txt, to calculate primary knock-on energy and subsequent NRT dpa;

$$T_d = E_{\text{Absorbed by recoil atoms}} - E_{\text{Lost to ionisations by recoil atoms}} \tag{3.2}$$

Where T_d, $E_{\text{Absorbed by recoil atoms}}$ and $E_{\text{Lost to ionisations by recoil atoms}}$ are all in units of $eV\text{Å}^{-1}$ and are extracted from SRIM output files. Experimentally, the charge accumulated on the target was monitored to provide a radiation dose in the plateau of approximately 0.1 dpa, the estimated lifetime dose to the reactor pressure vessel [19]. The dpa, as a function of depth into the sample, was calculated using eq. (3.2) to obtain the number of displacements per atom as a function of depth into the sample, per incident ion, and then multiplying this by the number of incident protons, as measured by accumulated charge on the target, see eq. (3.3) and fig. 3.7.

$$DPA = \frac{\nu_{NRT}}{\rho}.\Phi.t.10^{-8} \tag{3.3}$$

Where v_{NRT} is the NRT displacements produced per ion collision cascade per Å, ρ is the atomic density of the target, in $g.cm^{-3}$, Φ is the proton flux on the sample, in $cm^{-2}s^{-1}$ and t is the irradiation time in s. SRIM outputs are in units of $eV.Å^{-1}$, hence the correction factor of 10^{-8} to convert cm^{-1} into $Å^{-1}$. Figure 3.7 shows the dpa/ion as a function of depth for all the alloys in this work. The average peak radiation region is at 33.5-34 µm.

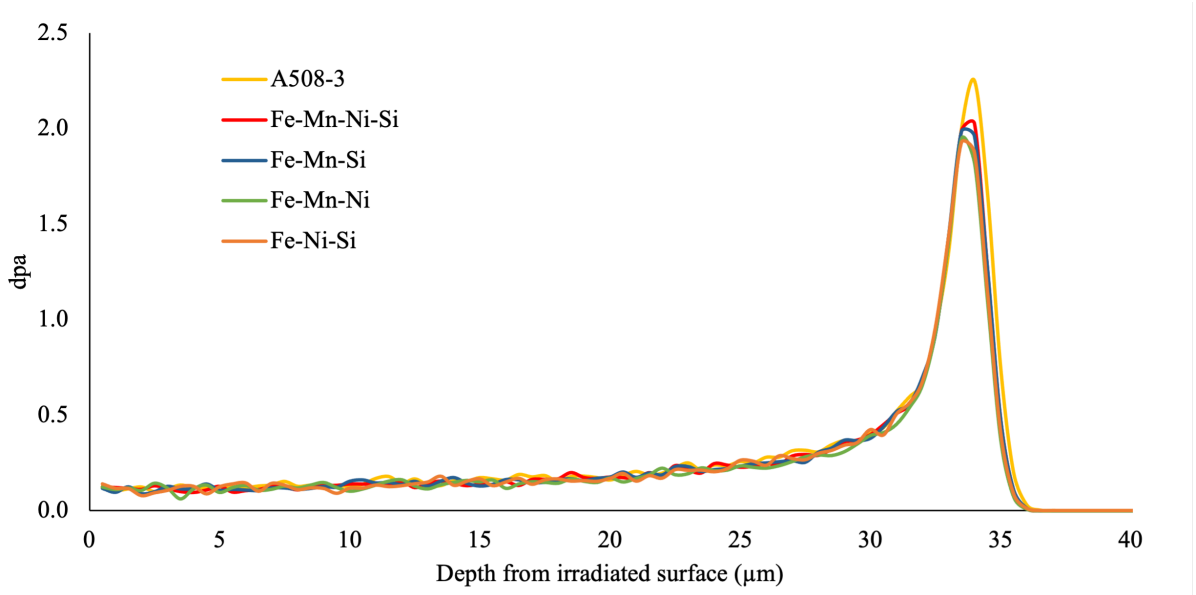


Figure 3.7: Plots of NRT dpa over depth calculated using SRIM for all alloys irradiated in this work.

3.2.2 MC40 cyclotron

Cyclotron ion accelerators are widely used for the production of medical isotopes, tracers and for materials irradiation studies. Figure 3.8 shows a schematic diagram of a cyclotron with the ion source in the centre. Ions are produced by flowing a gas over a filament at high voltage. Atoms in the gas are ionised and accelerated in a circular trajectory, inside a pair of electrodes, the "dees", between two electromagnets, fig. 3.8. The electric field between the dees is alternated using a radio frequency generator so that each time the ions are accelerated across the gap between the dees they gain kinetic energy. The maximum radius of the cyclotron, R, and the applied magnetic field, B, dictate the final energy of the ions, as does their mass, (??)[168]:

$$K.E = \frac{1}{2}mv_{max}^2 = \frac{q^2B^2R^2}{2m} \tag{3.4}$$

Where, m is the particle mass, B is magnetic field strength, q is the charge on the ion, R is the maximum radius of the ion trajectory and v_{max} is the maximum particle velocity reached as the ions leave the vessel via the guide tube, fig. 3.8. Steering magnets are used to direct the beam of ions through collimators to an end station where samples can be irradiated. A schematic and photographs of the end station used for these experiments is shown in fig. 3.9.

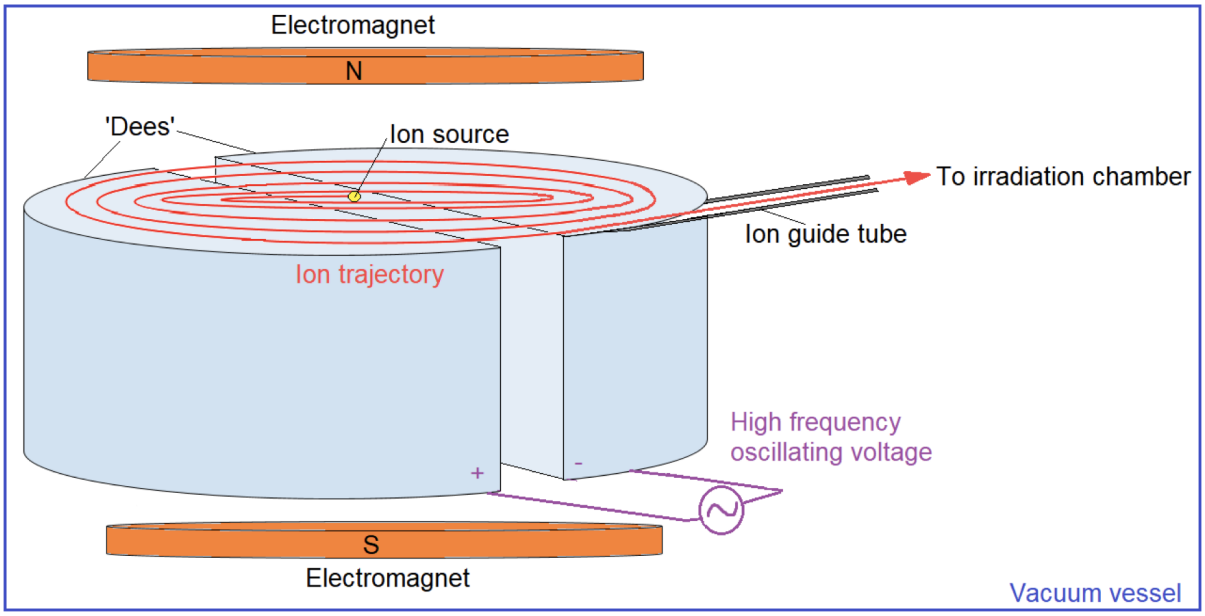
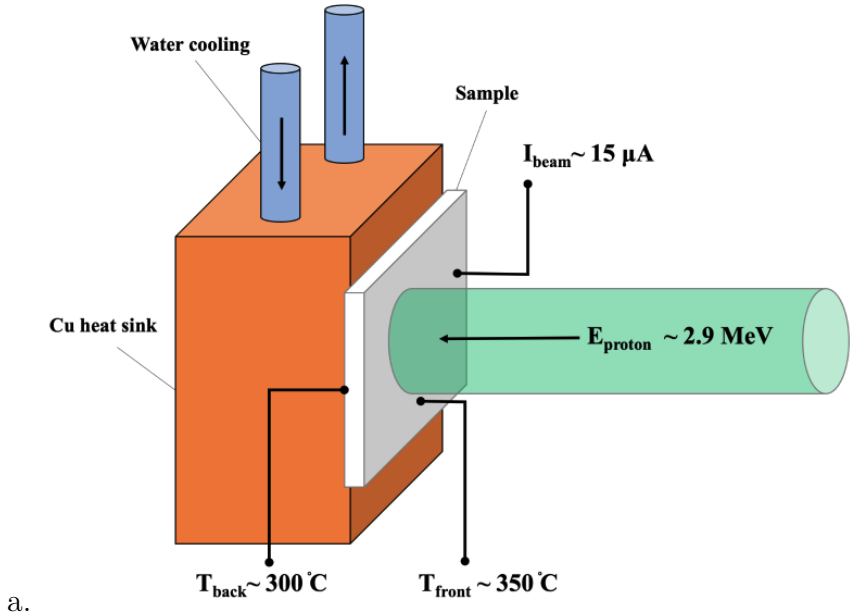
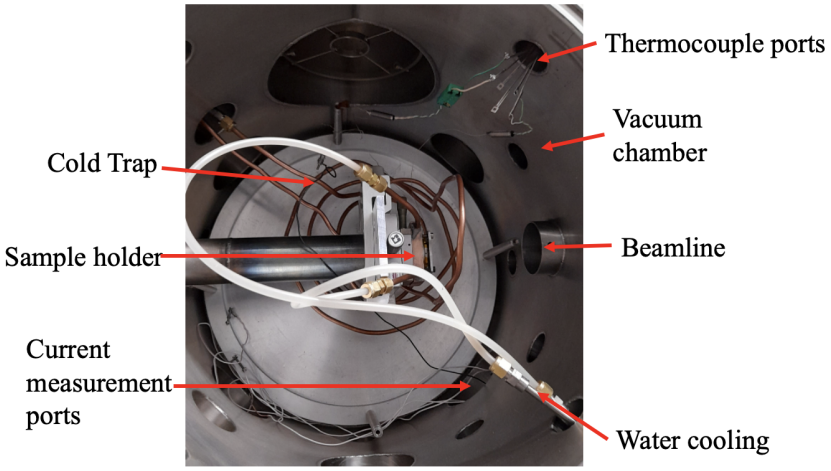


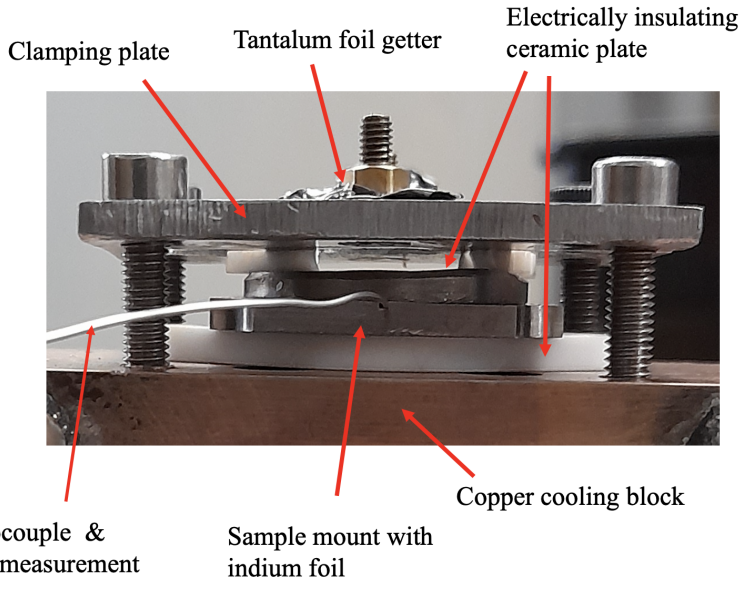
Figure 3.8: Schematic diagram of the accelerating magnets and electrode system in a cyclotron(p209, [169]), reprinted from Advanced scattering techniques for the investigation of radiation-induced damage in nuclear materials, PhD thesis, Ela Young, 2022, licensed under CC BY NC ND (`https://creativecommons.org/licenses/by-nc-nd/4.0/`).



a.



b.



c.

Figure 3.9: Schematic diagram of the material irradiation end station used in this work (a.), photograph of end station with sample holder in situ (b.), and a photograph showing the components of the sample mounting system (c.). Sample thicknesses were 1 mm for irradiation, leading to a thermal gradient between the surface, being heated by incident protons, and the back of the sample, being cooled by the cooling block.

Various measures were implemented in the set-up to improve the vacuum, and prevent target oxidation and contamination. These included;

- Replacement of main seals.
- Venting and purging-pumping cycles before "beam-on" using nitrogen gas.
- Cold trap (copper tubing with flow of liquid nitrogen) to attract volatile species in vacuum.
- Tantalum foil positioned near the sample to act as an oxygen getter, preferentially oxidising over the sample material.
- Baking-out the chamber at approximately 100 °C for a few hours under vacuum to extract any absorbed vapour/gases from internal fittings and chamber walls.

3.2.3 Irradiation conditions and monitoring

Irradiation conditions were selected to mimic the operating conditions of RPV steel in pressurised water reactors, which operate at 290-350 °C and experience a neutron fluence of 10^{19} cm^2 equivalent to 0.1 dpa over their lifetime [19]. The dose rate in the RPV is approximately 1×10^{-11} dpa.s^{-1}. A 2.9 MeV proton beam was used to irradiate the samples, with an average current of 15 µA. The radiation conditions for each sample are shown in table 3.5.

Temperature varied significantly during irradiation exposure for all alloys due to beam instability and multiple drops in beam current caused by electrical faults in the radio frequency generation system.Table 3.5 states the time averaged temperature during irradiation 1 mm behind the irradiated surface, along with the maximum measured temperature during the run, and dose and dose rate modelled in the plateau and peak damage regions. The minimum temperature during runs was approximately room temperature, and profiles of temperature are shown in fig. 3.10. Temperatures were measured using a thermocouple located at the back of the 1 mm thick sample, and using a thermocouple located on the front of the sample just outside of the incident proton beam as shown in fig. 3.9c. No non-contact temperature measurements were made. Dose was controlled by measuring the accumulated charge on the target and converting this into dpa, using SRIM outputs and the NRT model described in section 3.2.1. The diameter of the beam area on the sample was 10 mm. Proton energy has been selected to provide a

balance between radiation damage volume, which increases with proton energy, and the induced radioactivity of iron atoms, which increases for proton energies above 3 MeV due to an increase in the reaction cross section of proton absorption by Fe nuclei leading to the production of ^{56}Co, ^{57}Co and ^{58}Co in $p-\gamma$ reactions [170]. High resolution gamma spectroscopy was carried out after irradiation on each sample to determine the radioactive isotopes present and to calculate sample activity and expected half-life. This data is shown in table 3.4

Table 3.4: Relevant active isotope half lives and sample activities after irradiation, (May 2021) in MBq, measured using HPGe detector system.

Sample	Sample Activity, May 2021 (MBq)			
	^{56}Co ($T_{\frac{1}{2}}$=77.24 days)	^{57}Co ($T_{\frac{1}{2}}$=271.74 days)	^{58}Co ($T_{\frac{1}{2}}$=70.86 days)	Total May 2021 /MBq
A508-3	9.50	5.62	0.07	15.19
FMNS	9.45	9.75	0.12	19.32
FMS	12.95	4.61	0.17	17.73
FMN	6.28	14.56	0.00	20.83
FNS	9.12	10.08	0.07	19.28

Table 3.5: 2.9 MeV proton irradiation temperatures and doses achieved for each alloy. Values in brackets are where temperature just outside the beam, on the front of the sample, was measured. All other temperatures are taken from the back of the sample, approximately 1 mm from the irradiation surface.

Alloy	T_{mean} (°C)	T_{max}(°C)	Time (hrs)	Plateau Region		Peak Region	
				Dose (dpa)	Dose-rate ($dpa.s^{-1}$)	Dose (dpa)	Dose-rate ($dpa.s^{-1}$)
A508-3	275	316	14.66	0.14	2.74E-06	2.33	4.41E-05
Fe-Mn-Ni-Si	266 (290)	336 (402)	20.33	0.13	1.82E-06	2.10	2.87E-05
Fe-Mn-Si	250 (313)	312 (408)	17.5	0.13	2.12E-06	2.04	3.24E-05
Fe-Mn-Ni	209	317	16.28	0.13	2.24E-06	1.95	3.32E-05

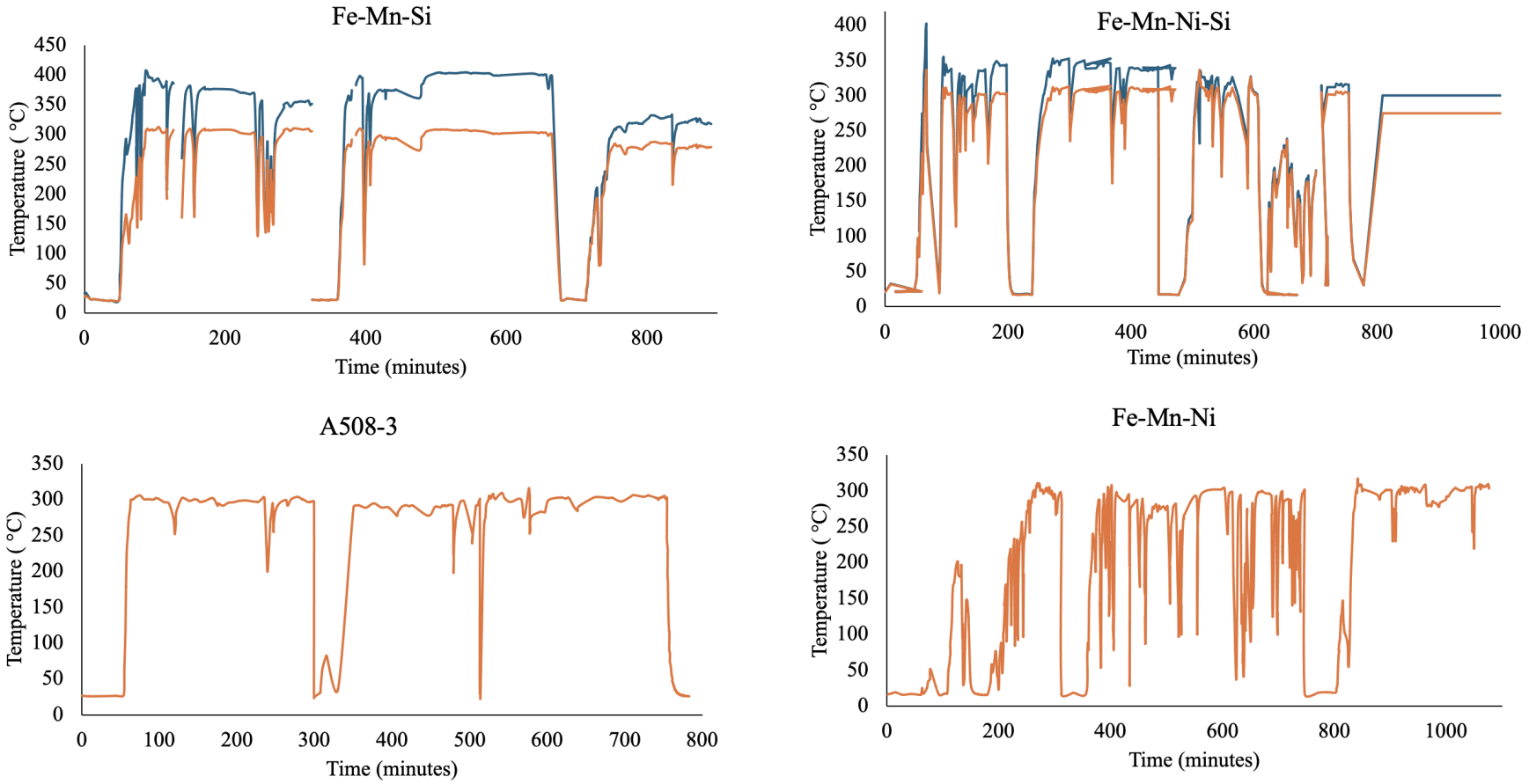


Figure 3.10: Temperatures measured during proton-irradiation for each alloy, showing the monitored temperature 1mm behind the sample surface in orange, and the temperature on the surface measured just outside the beam in blue (only available for the Fe-Mn-Ni-Si and Fe-Mn-Si alloy).

3.3 Transmission Electron Microscopy & Energy Dispersive X-Ray Spectrometry

Transmission electron microscopy (TEM) is a technique used to image thin regions of material in both real and reciprocal space, providing information on phases present, their structure and orientation within a matrix material and chemical distribution. Conventional TEM instruments have an imaging resolution of around 2 Å, although resolution depends on specimen thickness and imaging mode [171].This is of great relevance to RPV steel embrittlement as the size, density, and orientation of dislocation loops will have an effect on hardening and subsequent segregation of solute elements leading to solute-rich defects [134].

3.3.1 Sample preparation

Three TEM samples have been prepared from the irradiated Fe-Mn-Si and Fe-Mn-Ni-Si alloy, to investigate the effect of nickel on radiation response. A Xe ion plasma focussed ion beam scanning electron microscope (PFIB)-SEM (Helios™ G4 PFIB UXe DualBeam™) was used to produce samples following the method shown in fig. 3.12 and table 3.6.

The region of interest in the Fe-Mn-Ni-Si was identifiable in SEM, as there was a line of higher contrast in the back-scattered electron (BSE) images, caused by the increase in dislocation density in the highly damaged region reducing the intensity of BSE signal and leading to contrast in the image. A region behind the peak damage region shows some preferential surface etching, fig. 3.11. This etching is likely to be due to porosity in this region, associated with implanted hydrogen (from protons in the beam) forming bubbles under irradiation.

Samples were lifted out parallel to the incident proton irradiation, so that changes in microstructure could be observed along the damage profile and in the unirradiated region. Thinning was carried out following the steps shown in table 3.6.

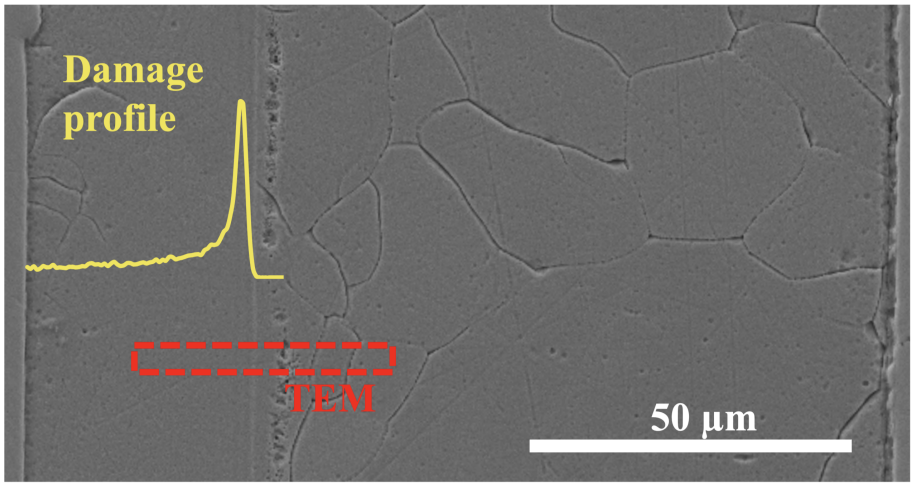


Figure 3.11: SEM micrograph showing the location of TEM lift-out relative to the irradiation surface (LHS) and the Bragg peak. Samples were cross-sectioned and polished before liftout to enable accurate identification of dose region.

Table 3.6: TEM specimen thinning steps, with associated tilting and beam settings, used to produce the samples imaged in this work.

Maximum lamella thickness at end of thinning step (nm)	Tilt, bottom / top side (Ion beam view)	Ion Beam Current and Voltage
1000	56° /48°	4 nA, 30 kV
800	55° /49°	1 nA, 30 kV
500	54° / 49°	1 nA, 30 kV
400	53.5° /50°	0.3 nA, 30 kV
200 (transparent at 5 kV)	53° /51°	30 pA, 30 kV
Low kV cleaning stage 1	55° /49°	30 pA, 5 kV. 1 min milling per window.
Final polishing, low kV	57° /47°	20 pA, 2 kV. 30 seconds milling per thin window.

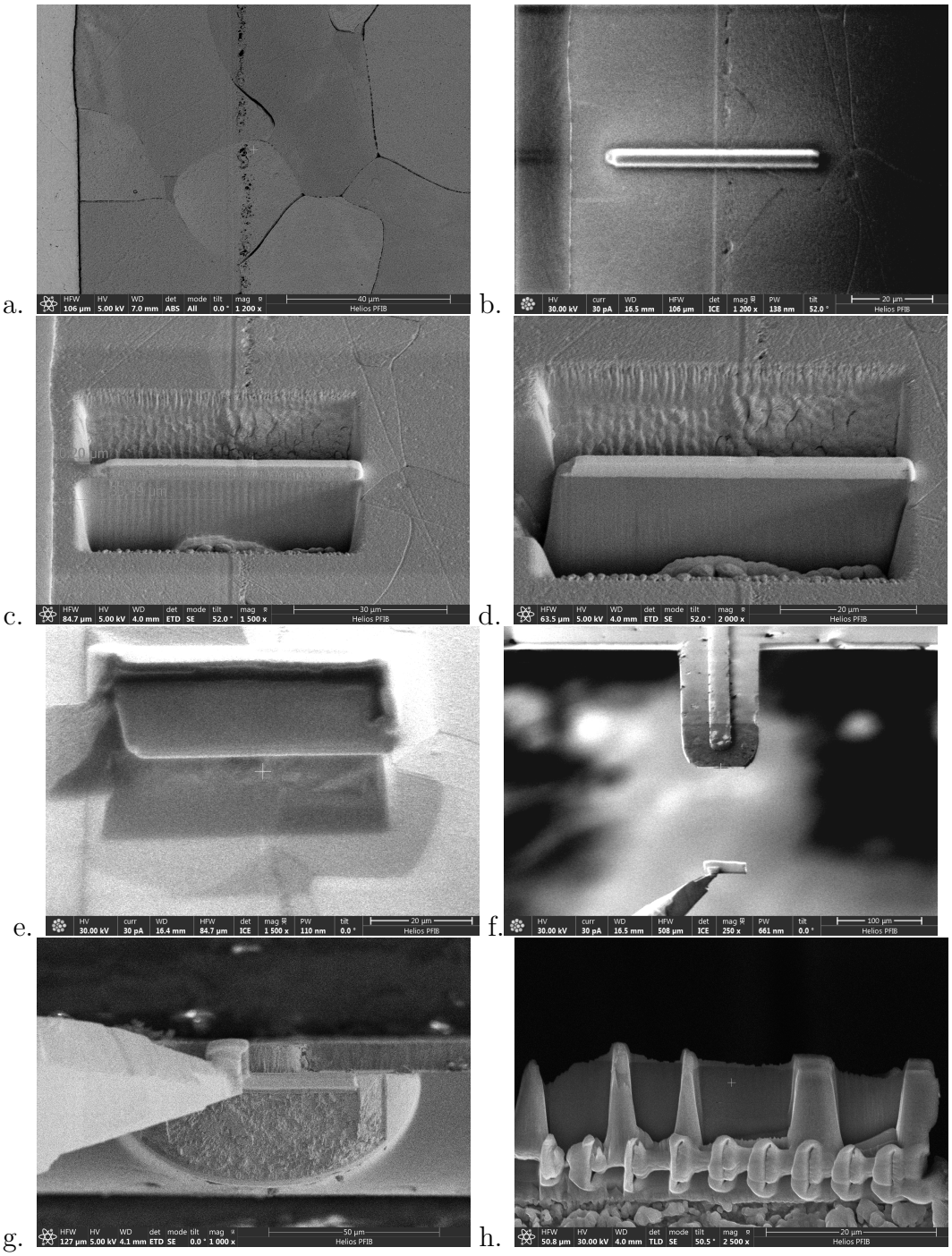


Figure 3.12: Stages of TEM lamella preparation, (a.) BSE image of region of interest, with contrast at Bragg peak, (b.) platinum deposition, (c.) milling of trenches, (d.) cleaning lamella, (e.) undercutting and checking, (f.) reinserting sample to Cu grid, (g.) attaching sample to Cu grid, (h.) post thinning steps, see table 3.6, before final polishing.

3.3.2 TEM imaging, diffraction and STEM-EDX

TEM imaging, selected area diffraction, STEM imaging and energy dispersive X-ray (EDX) mapping have been carried out using a Talos TF200X S/TEM with bright field (BF), annular dark field (DF) and high angle annular dark field (HAADF) detectors covering a solid angle range of 25-200 mrad. The microscope was operated using 200 kV accelerating voltage for all experiments. EDX data processing was carried out using Velox^{TM} software, with thickness corrections applied using convergent beam electron diffraction (CBED) measurements of the foil thickness in specific locations of interest.

Figure 3.13 shows schematics of the configuration of a STEM column for the three types of data collection in this work. In all cases, the beam is produced by a field emission gun, at the top of the column, and the condenser lens shapes and directs the beam down the optic axis of the microscope. Stigmation control of the 2nd condenser lens and adjustment of the 2nd condenser aperture enable the alignment of the beam from the gun to the objective lens, and ensure that the incident beam is aligned with the optic axis. The objective lens alignment dictates the resolution, contrast, and focus of resulting images [172].

In diffraction mode, the intermediate lens bends the incident beams such that the imaging plane and back focal plane align to produce a diffraction pattern on the phosphor screen. In imaging mode, the intermediate lens is weaker and diffracts the beam to project the image of the sample onto the screen.

The selected area aperture is located at the first intermediate imaging plane, so appears to be aligned with the image when viewing the phosphorus screen in imaging mode. It blocks diffraction from outside the aperture area. The objective aperture is much closer to the specimen, and is positioned just below the objective lens, in the back focal plane, so that it filters out diffracted electrons from specific planes in reciprocal space, rather than areas of the sample in real space. This means that the objective aperture is visible in diffraction mode.

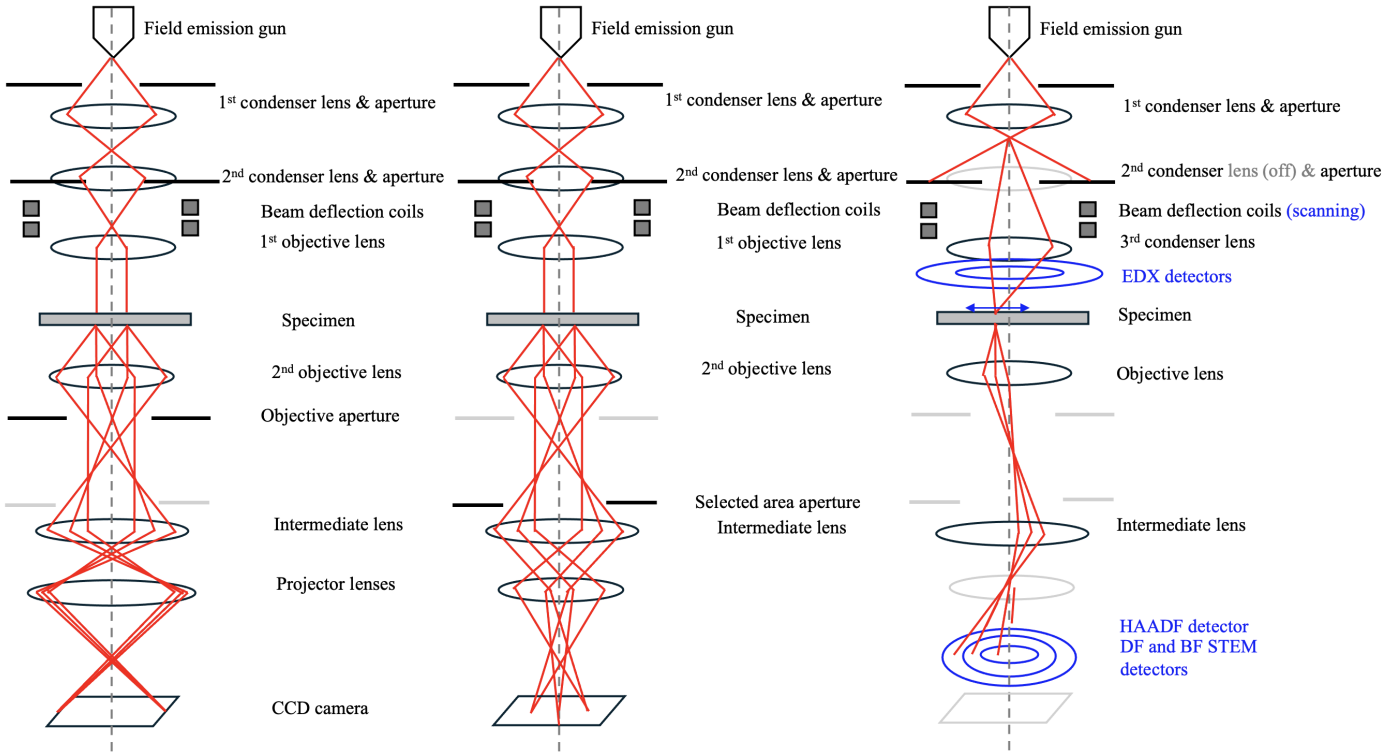


Figure 3.13: Schematic diagrams showing the TEM/STEM lens and beam configuration for TEM bright field imaging (left), selected area electron diffraction (centre) and scanning TEM imaging and EDX mapping (right). Diagrams produced using the Thermo Fisher user guide for Talos TF200x [173, 174]. A single projector lens and deflection coil is visualised here for simplicity; in the TF200x microscope used in this work there are more components in the scanning and projection systems.

3.3.3 STEM imaging and EDX mapping

In STEM imaging mode, the beam is converged onto the specimen, so that the probe is very small when incident on the surface. This converged beam is then rastered across the sample, to produce images where contrast is dependent on the diffracted beam angle, which dictates which annular detector it is incident upon.

In the Talos TF200X S/TEM, there are three detectors positioned below the specimen, and a set of EDX detectors positioned above the specimen, as shown in fig. 3.13. The bright field detector, aligned with the optic axis, produces images similar to that of a bright field TEM image, made up of intensity from the transmitted beam, and low angle diffracted electrons. Then there are two dark field annular detectors, one just outside the bright field region, and the other at high angles. The HAADF detector collects signal from widely scattered electrons, resulting in strong mass contrast in resulting images. Higher Z number atoms cause wider angles of diffraction than lighter elements, as electrons are more likely to scatter when passing through these regions and multiple scattering increases the overall range of probable scattering angles.

Energy dispersive X-ray spectroscopy detectors are positioned in an annulus about the specimen, and record hits from secondary X-rays emitted when electrons in orbit around atoms relax to their original energy states after being excited by electrons from the beam. The energy of the X-rays emitted depends on the electronic configuration of the atom, and the range of energy emitted by a specific element is characteristic to them. X-ray energy spectra are collected and analysed to identify which elements are present, for every pixel scanned with the beam. This data is used to produce intensity maps for elements identified. Elemental quantification is described in section 3.4. To obtain size distribution information from EDX maps, open source software, FIJI ([175]), was used to apply thresholding and particle analysis algorithms to extract sets of data on precipitate size. Histograms were plotted showing the size distribution of solute-rich features at various doses.

3.3.4 Diffraction in TEM mode, and CBED thickness measurement

Conventional selected area diffraction patterns were obtained using a parallel beam from irradiated and unirradiated regions of each specimen at three low order zone axes; [001], [011], [111]. A 40 µm selected area aperture and camera lengths between 1.1 m and 1.35 m were used and

patterns compared with simulated diffraction for possible candidate phases made using Single Crystal 5 [176].

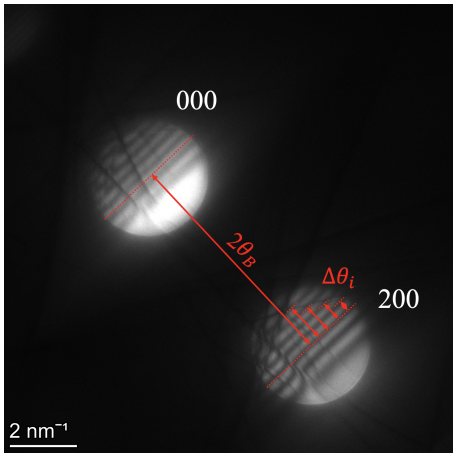
Sample thickness measurements were carried out using convergent beam electron diffraction as described by Hirsch et al. [177] and Williams and Carter [178], using the $g = [200]$ two-beam condition for the Fe-Mn-Si alloy and the $g = [\bar{1}2\bar{1}]$ for the Fe-Mn-Ni-Si alloy. This involved collecting converged beam electron diffraction patterns in two beam conditions, an example of which is shown in fig. 3.14. Then the distance from the centre of the transmitted beam to each fringe was measured to obtain values of $\Delta\theta$ and then these were used to calculate the estimated thickness using the following equations. [177, 178]

$$\frac{s_i^2}{n_i^2} = \frac{1}{\xi_g^2}.\frac{1}{n_i^2} + \frac{1}{t^2} \tag{3.5}$$

Where s_i is the deviation from the Bragg conditions for each fringe minima, n_i is an integer associated with each fringe i, ξ_g is the extinction distance for the g vector of the diffracted spot in the material, and t is the thickness of the specimen in the region where the CBED pattern was collected. The deviation is calculated by measuring the change in Bragg angle for each fringe, [177, 178]

$$s_i = (\frac{\lambda}{d_{hkl}^2})(\frac{\Delta\theta_i}{2\theta_B}) \tag{3.6}$$

Where λ is the wavelength of electrons in the incident beam, d_{hkl} is the interplanar spacing of the diffraction plane, $\Delta\theta_i$ is the fringe spacing for each fringe, and θ_B is the Bragg angle for the diffracting plane. The integer value n has been arbitrarily chosen to produce a plot that has the closest possible fit to a straight line of $\frac{s_i^2}{n_i^2}$ vs $\frac{1}{n_i^2}$ to facilitate the extraction of the y-intercept as $\frac{1}{t^2}$. If n values are selected which produce a function closer to a quadratic function the thickness can be overestimated, for positive second derivatives, and underestimated for negative second derivatives [179]. Selected area diffraction patterns were all taken using a $40\,\mu m$ selected area aperture.

a. 

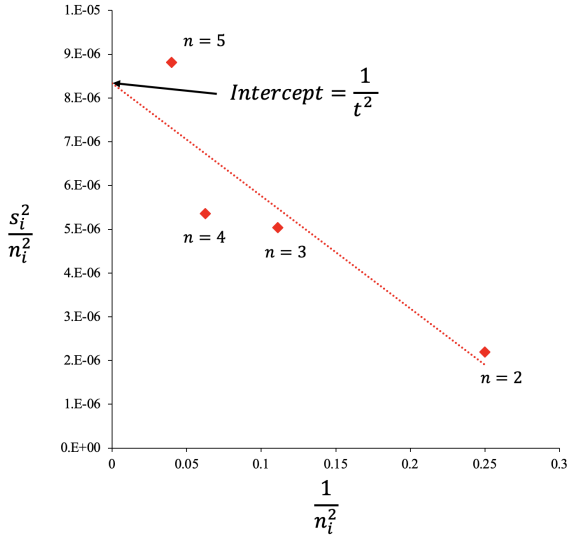
b. 

Figure 3.14: a. Converged beam diffraction pattern obtained from the proton-irradiated Fe-Mn-Si alloy in this work, showing direct beam and 200 diffraction spot, and b. Plot of $\frac{s_i^2}{n_i^2}$ vs $\frac{1}{n_i^2}$, where the y intercept is equal to $\frac{1}{t^2}$, according to eq. (3.5).

3.4 EDX Quantification

Precipitate composition was analysed using STEM-EDX. It must be noted that the most accurate quantification of composition possible using EDX requires the measurement of pure elemental samples and calculations of absorption correction factors for a specific specimen and instrument. These calibrations were not performed for the samples analysed in this work so all quoted atomic fractions are estimates based on the Cliff-Lorimer k-factors calculated in the Velox^{TM} software using the Brown-Powell ionisation model[180, 181]. The Cliff-Lorimer k-factor method calculates the relative concentration of elements in a mapped area, based on the counts under a given peak and the k-factor describing the probability of each element atom emitting an X-ray for a given energy, see eq. (3.7) [181].

$$\frac{I_A}{I_B} = k_{A,B}^{-1}\frac{n_A}{n_B} \tag{3.7}$$

Where $I_{A,B}$ are the peak intensities for peaks corresponding to elements A and B, $k_{A,B}$ is the Cliff-Lorimer sensitivity factor and $n_{A,B}$ are the atomic densities of elements A and B[181]. Velox^{TM} applies a thickness correction to the instrument k-factors, based on user input sample thicknesses which were taken to be the thickness calculated using CBED. The results quoted in at.% in

chapter 4 are therefore quantitative estimates of precipitate compositions, as accuracy using the Cliff-Lorimer method is generally limited by both counting statistics and a lack of accurate factors determine by specimens of accurately known thickness and composition for k-factor calculation and absorption correction.

3.5 Atom Probe Tomography

Atom probe tomography (APT) combines; field emission, mass spectroscopy and position sensitive detection, to produce an analysis technique providing atomic scale spatial and compositional resolution for small volumes of material. APT has been an essential tool in characterising Mn-Ni-Si rich features in irradiated steels since 1967 [23]. Where small, densely-distributed clusters or precipitates are present in a sample, APT is a useful method for analysis of specific defects, especially when features are smaller than can be resolved in conventional TEM, or when the compositional variation is too subtle for analysis using STEM-EDXS. The key advantages of using APT to characterise nanoscale microstructural features are:

- Uniform efficiency and chemical sensitivity across periodic table.
- High accuracy compositional analysis of isotopes across the periodic table.
- Spatial reconstructions with resolution 0.1-0.3 nm in depth and 0.3-0.5 nm in the lateral plane [182].

There are some limitations to APT analysis:

- Volumes of material analysed are very small;$<0.05\,\mu m^3$ and are destroyed during measurements.
- Interpretation of results, particularly of shape and size of microstructural features, is heavily influenced by reconstruction parameters.

3.5.1 Sample preparation

APT specimens were prepared using the same Xe (PFIB)-SEM (Helios™ G4 PFIB UXe DualBeam™) as in section 3.3.1, following the steps illustrated in figs. 3.16 and 3.17 and the beam currents and milling dimensions in table 3.7.

$25 \times 1 \times 5\,\mu m$ sections were lifted out from the 0.1 dpa region, fig. 3.15, and between three and five specimens were produced from each lift-out, resulting in a total of 23 specimens for measurement. This region was chosen to correspond with the region of the SRIM modelled profile with a dose comparable to the end of life neutron dose received by a PWR reactor pressure vessel. Producing multiple specimens perpendicular to the irradiation direction allowed for a greater volume of similarly irradiated material to be analysed, to optimise statistical validity of the results given limited access to atom probe facilities.

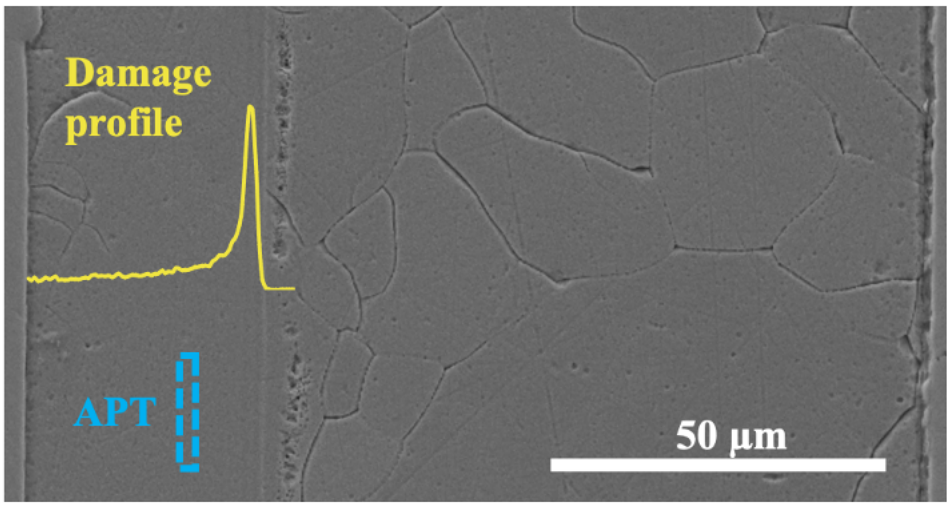
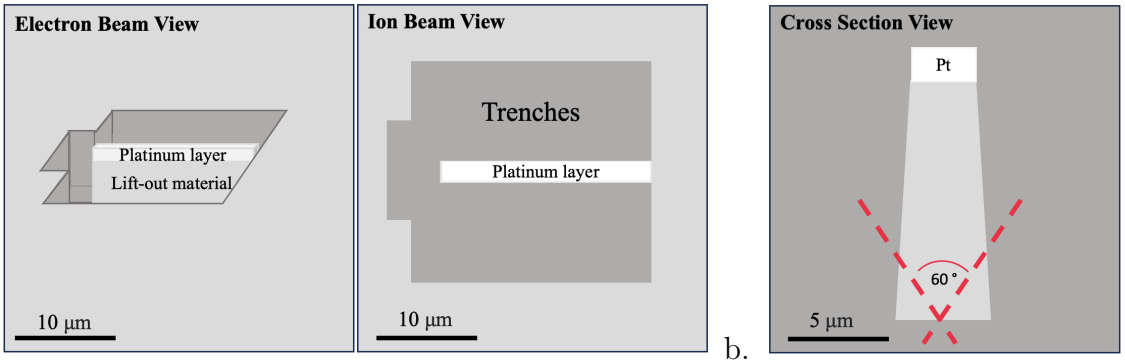


Figure 3.15: SEM micrograph, showing cross-sectioned proton irradiated sample, with radiation damage profile overlaid and region of APT sample extraction shown, inside the plateau region corresponding to approximately 0.1 dpa.

Trenches were milled in the same way as for TEM sample preparation, but the U cut was performed at 22°, on both sides of the sample, to produce a 60° triangular apex at the bottom of the sample, as shown in figure 3.16. Samples were welded onto a silicon coupon before the final shaping into sharp tips. Samples were stored and transported under vacuum (~-0.1 MPa) to prevent oxidation of sample surface before measurement.

a. 

b.

Figure 3.16: (a.) Deposit a protective layer of platinum over the sample region of interest and mill trenches around the sample. (b.) U cut at 22°, to create tapered bottom of lift-out.

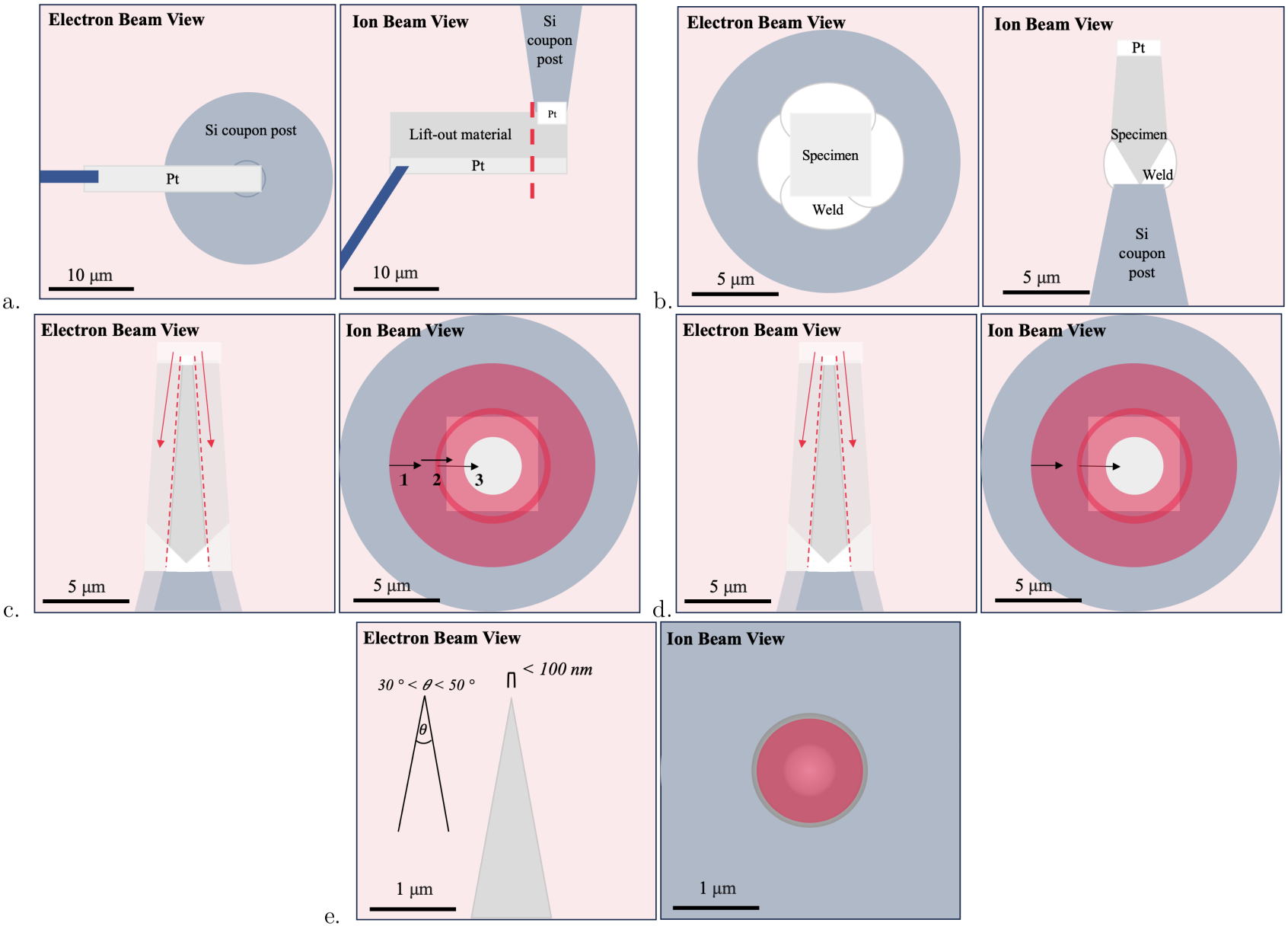


Figure 3.17: Schematics showing the sample preparation steps detailed in table 3.7.

Table 3.7: APT specimen shaping and sharpening steps, shown in figs. 3.16 and 3.17

Step	Settings	Notes
(a.) Lift-out and attach to coupon, (b.) cut off, and Pt weld on each side.	0° tilt	
(c.) Create square pillars.	Tilt to 52°, rectangular milling patterns, Si milling, 30 kV, or 4 nA	Square pillar should be <5 x 5 µm
(d.) Create round pillars — 1	1 nA, outer diameter 8 reducing to 5, inner diameter 4 reducing to 3.5	Concentric milling pattern, inner to outer.
(d.) Create round pillars — 2	1 nA	Outer 5 µm to 3 µm Inner 3.5 µm to as small as possible.
(d.) Create round pillars — 3	0.3/0.1 nA	Outer approx. 3 to 2, inner reduce down to 1 µm or less.
(e.) Final sharpening	5 kV, 50pA, circular milling all over tip.	Final shaping of needle with tip < 100 nm and taper angle 30-50° [183].

3.5.2 Atom probe tomography measurements

Specimens were measured using a LEAP (local electrode atom probe) 5000 XR, at the Nuclear Materials Atom Probe (NuMAP) facility at the University of Oxford. All specimens were measured using voltage mode, to obtain improved spatial distribution resolution for lighter elements, compared with laser pulsed samples.

The LEAP combines a time of flight mass spectroscopy system with a position sensitive detector. A needle specimen is cooled, and a high standing voltage is applied between the specimen and the local electrode. This creates an electric field at the specimen tip that is below the critical value for evaporation to occur. Then a pulsed voltage is applied above the standing voltage, causing atoms to evaporate from the tip and become ionised. These ions accelerate through a channel in the centre of the local electrode towards the position sensitive detector. This controlled evaporation enables reconstruction of ion position through the depth of the sample. Reflectron instruments produce data with sharper m/Z peaks by reducing the effect of energy spread of ions emitted with the same m/Z values on the measured time of flight. Ions with higher kinetic energy will travel further into the reflectron than lower energy ions, so

although they are moving faster, they are travelling over a longer flight path so arrive at the detector at the same time as lower energy ions, as shown in fig. 3.18.

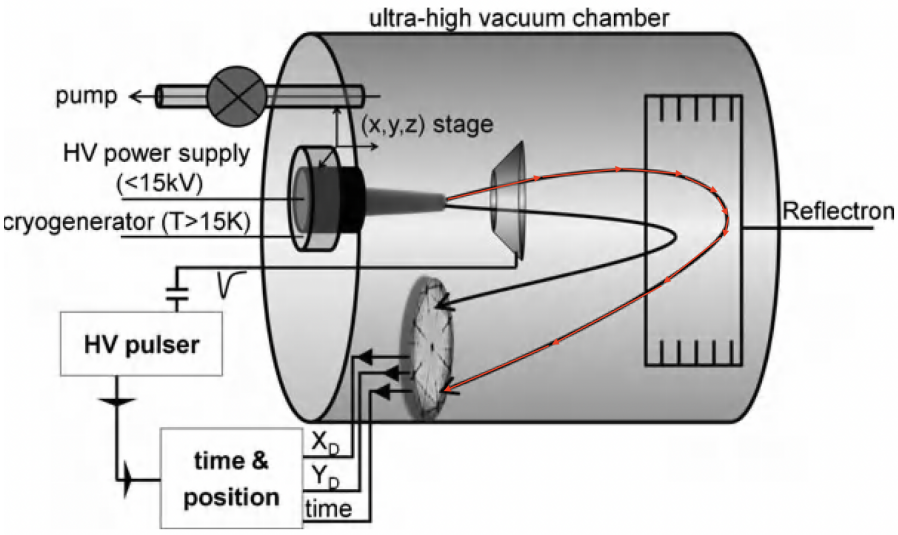


Figure 3.18: Schematic diagram showing a local electrode atom probe with a reflectron. The top red line shows the higher energy ion travelling a greater distance before reaching the detector, compared with the black line or the lower energy ion. Fig 3.25, p62 [184], Baptiste Gault, Michael P. Moody, Julie M. Cairney et al, From Field Desorption Microscopy to Atom Probe Tomography, Atom Probe Microscopy, Springer Nature, 2012, reproduced with permission from SNCSC.

The detector in a LEAP has two layers, the first is a microchannel plate which amplifies the charge of the incident ion, creating a cascade of electrons which then hits a position sensitive detector. This records the (x,y) coordinate on the detector, and the time of flight from the voltage pulse. At the start of each run, specimens were aligned with the detector at low voltages. The running parameters are detailed in table 3.8.

Table 3.8: Running parameters used to measure samples on LEAP 5000 XR.

Parameter	Setting
Acquisition Mode	Voltage
Temperature (K)	55
Detection Rate (%)	0.2-0.5
Pulse Fraction (%)	20
Pulse Rate (kHz)	200

APT measurements are carried out at low temperatures (20-55 K) to minimise atomic movement and surface diffusion across the specimen, which can cause a deterioration of spatial res-

olution. To increase evaporation probability, the temperature selected here is slightly higher than conventionally used [184]. Pulse rate determines the mass to charge ratio (m/Z) range of ions that can be detected during an acquisition. The m/Z dictates the time it takes for ions to travel from the specimen to the detector, so lower pulse rates allow measurement of longer times of flight. Pulse fraction must be sufficiently high to ensure that in between pulses the standing voltage is not causing ion evaporation of the specimen, as this will lead to noisy datasets with standing voltage evaporated ions having incorrectly assigned time of flight values. A low detection rate was selected to maximise the sample yield. A rate of 0.2-0.5 % means that 0.2-0.5 ions are detected every 100 pulses, and ensures that a high fraction of single ion events are recorded to produce a good quality dataset. High fractions of multiple hit events, where more than one ion hits the detector within a given timestamp, make it harder to resolve time of flight, and m/Z ratio, leading to increased noise.

During the measurement, the standing voltage was increased to keep the detection rate constant, and the background detections were monitored to identify any spurious emitters or fracture events. As ions from the tip evaporate, it blunts and its radius increases, meaning that a higher standing voltage is required to evaporate ions. The output data is a set of ion positions on a 2D detector, measured per pulse, with the time of flight from start of pulse to detection event. This measured time of flight, t_{flight}, is then converted into mass to charge ratio, $\frac{m}{Z}$, using the following expression [184].

$$\frac{m}{Z} = 2eV(\frac{t_{flight} - t_0}{L})^2 \tag{3.8}$$

V is the total voltage, e is the charge of the electron, L is the flight distance from specimen to detector and t_0 is the time shift.

3.5.3 Data summary

Table 3.9 shows the range of compositions and conditions measured. Some datasets have been omitted from further analysis due to their small size, leading to overestimation of bulk content of contaminant elements like carbon and oxygen, or due to multiple fractures at sites with high Xe content, suggesting implantation during sample preparation, despite the low energy polishing steps described in table 3.7.

Table 3.9: Summary of collected APT data by alloy composition.

Alloy	Condition	No. APT Specimens	Total No. Ions Measured	Observed Microstructure
Fe-Mn-Ni-Si	Proton Irradiated	4	92,409,862	Mn-Ni-Si rich precipitates, ferritic matrix.
	Unirradiated	3	3,272,065	Ferritic Matrix
Fe-Mn-Si	Proton Irradiated	2	2,933,040	Ferritic Matrix
	Unirradiated	1	20,056,505	Ferritic Matrix
Fe-Mn-Ni	Proton Irradiated	2	25,625,667	Ferritic Matrix
	Unirradiated	1	15,820,126	Ferritic Matrix
A508-3 Steel	Proton Irradiated	3	31,330,132	Ferritic matrix and Mo, Cr, Mn rich carbide.
	Unirradiated	2	58,768,325	Ferritic Matrix

3.5.4 Data processing and reconstruction method

Datasets have been reconstructed using the APSuite (v6.3.1) software, following the steps below:

1. Range of ions for reconstruction are selected using the voltage curve.

In general, the first 100,000-1,000,000 ions (depending on sample size) have been omitted to prevent inclusion of surface contamination such as an oxide layer or hydrocarbon contaminants. Figure 3.19 shows an example of a voltage curve where voltage increases rapidly early in the run and levels off for a large fraction of the run, with no spikes indicative of fracture events.

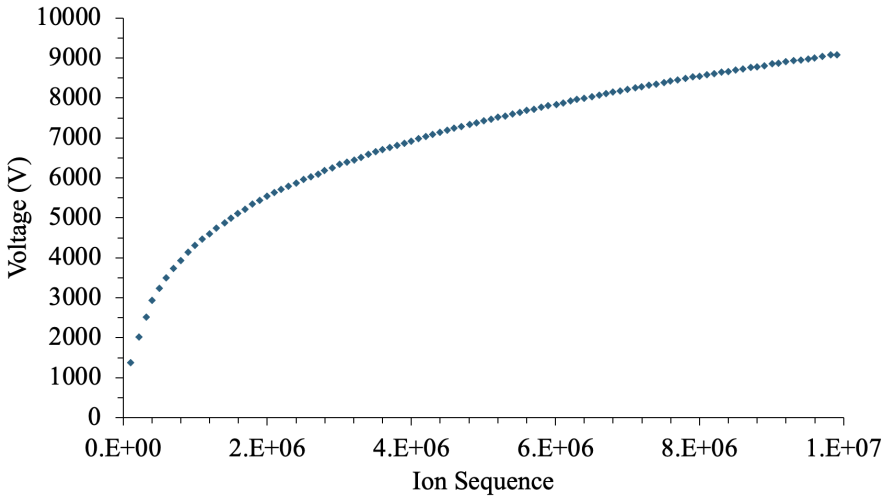


Figure 3.19: Voltage curve for irradiated Fe-Mn-Ni-Si (41381) dataset, showing smooth increase to maximum voltage set at 9,500 V.

2. Time of flight calibration

The raw mass spectrum data measured requires correction for the following factors:

- Not all ions will evaporate with the maximum energy to achieve the minimum time of flight, energy deficits create a tail after the minimum m/Z peak.

- Time of flight measured will vary based on the trajectory of the ion, with ions hitting the outer region of the detector taking longer than those in the centre, as they travel further.

A 'bowl' correction is applied to the data, modelling the detector surface as a bowl shape and then fitting the flight distance, L, of each ion, with a given m/Z ratio, to this surface, to adjust the travelled distance and thus the time of flight. At this stage a voltage correction is also applied to account for the change in voltage over the measurements, to obtain V in eq. (3.8).

3. Mass calibration and ion ranging

The mass spectrum is calibrated by assigning m/Z values to known peaks. Using eq. (3.8), and the measured values of voltage and time of flight the time shift, t_0 can be calculated and applied to the mass spectrum so that the m/Z values of unknown peaks will accurately correspond to their mass to charge ratios and the ions in these peaks can be identified. In this work peaks for Fe^{2+}, Ni^{2+}, Si^{2+}, Mn^{2+} H^{+}, O^{+} and C^{+} were used for calibration. Ranging of peaks was carried out separately for each dataset, accounting for variation in peak widths and intensities. Where no visible peak was present at expected m/Z positions, no peak was ranged for that ion. Ranges were selected to cover the peak, where values were <2x local background counts. Figure 3.20 shows an example of a ranged mass spectrum with range width adjusted based on local peak height.

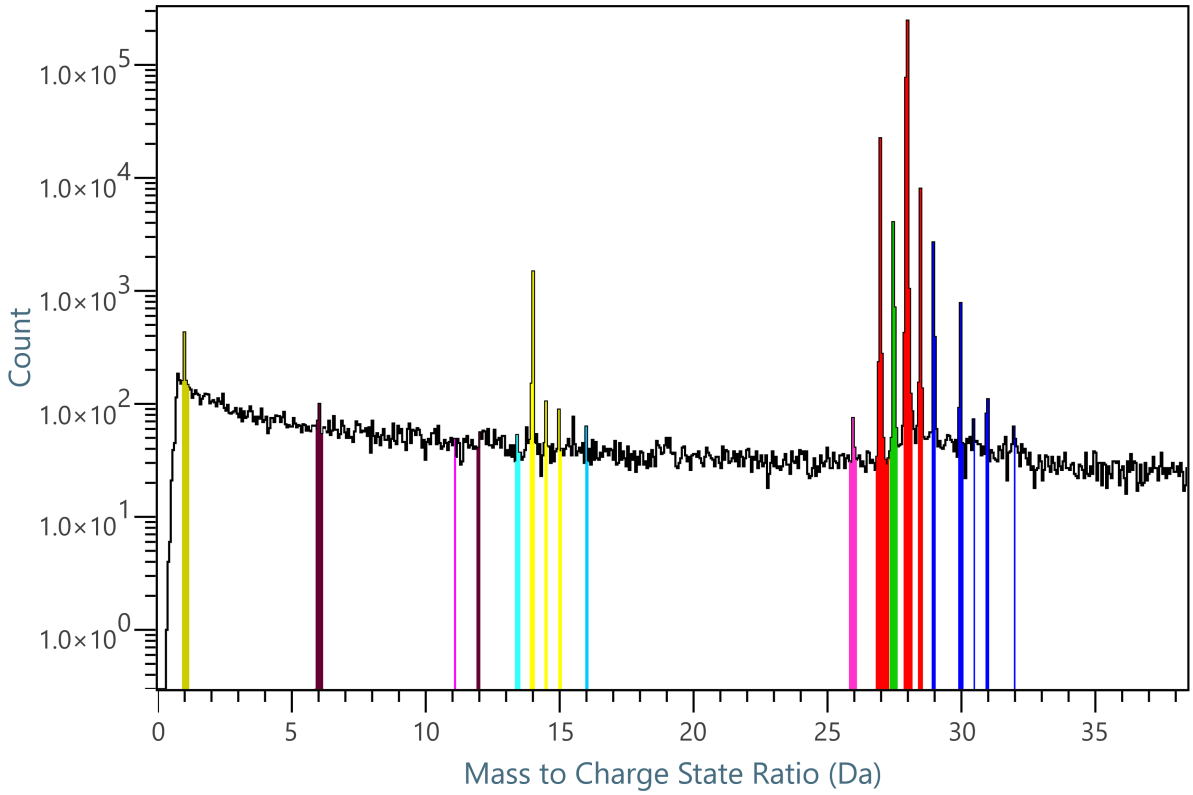


Figure 3.20: Ranged mass spectrum for dataset 41382, proton-irradiated Fe-Mn-Ni-Si alloy.

4. Spatial reconstruction

Once ions have been assigned an ion type using the mass spectrum, they are given 3D coordinates based on spatial reconstruction parameters. The voltage curve was used for the spatial reconstruction in this work. The voltage required for evaporation is linked to the tip radius by eq. (3.9), where R is the radius of curvature, F_e is the evaporation field of the material, in this case assumed to be that of pure iron, with a value of 33 Vnm^{-1} and k_f is a value which is governed by the tip geometry as well as the distance between the specimen and the local electrode [185].

$$R = \frac{V}{k_f F_e} \tag{3.9}$$

V is the total applied voltage, i.e. the sum of the standing voltage and pulse voltage. This equation can be used to model the radius of the sample over the experiment to assign the z coordinate of each ion, and can then be combined with a point projection model to assign x and

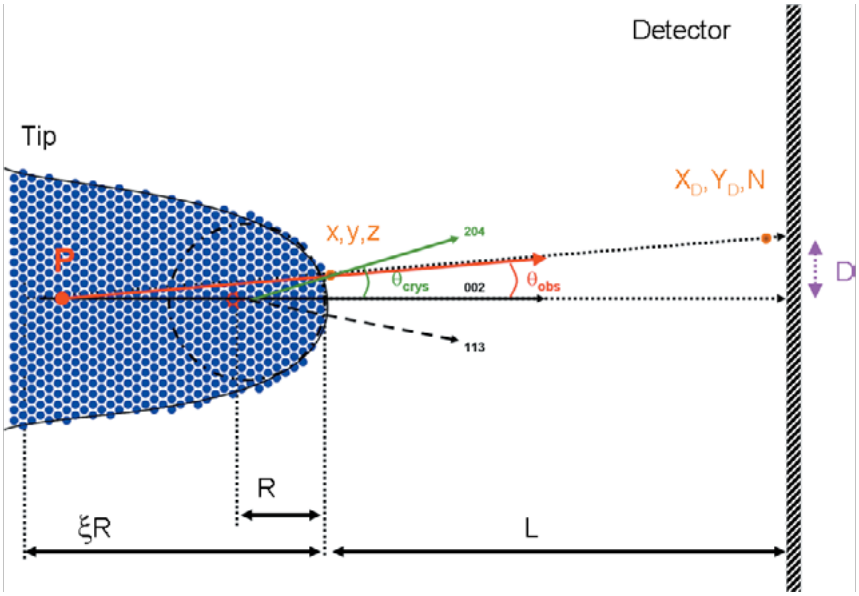


Figure 3.21: Schematic of the point projection model, showing the difference between the angle between crystal planes in the material and the observed (projected) angle, from Figure 4, Gault et al., 2008 [186]. Reprinted from Gault, Baptiste; de Geuser, Frederic, Estimation of the Reconstruction Parameters for Atom Probe Tomography, Microscopy and Microanalysis , 2008, 14, 4, Pages 296-305, by permission of Oxford University Press.

y coordinates for each ion (fig. 3.21).

The purpose of this model is to convert (x,y) detector coordinates into specimen coordinates where the xy plane is perpendicular to the specimen measurement axis.

A correction must be made to account for the fact that ion trajectories do not travel radially from the specimen tip as if it were spherical. The shank of the specimens leads to trajectories that are focused inwards, leading to a compressed image on the detector. Image magnification, M, depend on R, L, and the image compression factor, ξ eq. (3.10) [186].

$$M = \frac{L}{\xi R} \tag{3.10}$$

Values of ξ are between 1 and 2, modelling a scenario between a radial and stereographic projection. The reconstruction x and y values are then calculated as the detector coordinates divided by the image magnification.

The depth dimension, z, is deduced by combining the radial evolution and magnification with the evaporation sequence of the ions measured to obtain an expression for dz [186];

$$dz = \frac{\Omega L^2 {k_f}^2 {F_e}^2}{\eta S_d \xi^2 V^2} \tag{3.11}$$

S_d is the detector surface area and η is the detector efficiency. Ω is the average atomic volume.

For most specimens, the default values for image compression factor, ξ, and K_f of 1.65 and 3.3, were applied and z spacing corrected to achieve an average ion density of 0.01177 ions/nm, as calculated for pure BCC Fe.

Voltage reconstruction was selected as the most appropriate method for these data, based on advice from collaborators at the Oxford Atom Probe laboratory, due to the limited spatial accuracy of using SEM images as tip shape projections. However, using image tracing may have been more appropriate for the single A508-3 specimen in which there was a significant change in evaporation field (72401), which contained both Fe matrix and a carbide precipitate. In this case the shape of the specimen is not reflected by the shape of the dataset. This has no significant effect on bulk phase composition measurements.

Table 3.10: Reconstruction settings applied to datasets in this work

Reconstruction Parameters	
Detector efficiency	0.52
Image Compression Factor, ξ	1.65
k_f	3.3
Primary element	Fe
Evaporation field	33 33 $\mathrm{Vnm^{-1}}$
Average atomic volume	0.011 774 $\mathrm{nm^3 ion^{-1}}$
Radial evolution & z spacing model approach	Voltage (bulk compositions)

3.6 APT data analysis methods

3.6.1 Composition analysis and peak overlaps

All matrix samples have been used to calculate bulk composition using both APSuite (v6.3.1) and AtomProbeLab (v0.2.3) [187]. AtomProbeLab uses a user specified range file to calculate the composition, accounting for mass/charge peak overlaps and decomposing the contributions of different ions to the measured peaks. When calculating composition, it is important to consider

the effect of ranging peaks where multiple ions detected have very similar m/Z ratios. In this case, a single peak will be made up of contributions from detector hits from different types of ion. Ranging can only assign a single ion to each peak, so decomposition analysis is required to calculate the fraction of the overlaps to assign to each ion type. Some key peak overlaps relevant to the alloys in this study are shown in table 3.11. Peaks are considered to be directly overlapping where their m/Z ratio is separated by < 0.1 Da [188]. Isotopes with similar atomic mass will contribute to overlapping peaks, for example Fe 58^{2+} and Ni 58^{2+} both have a m/Z ratio of 29 Da. The Si^{+} peaks also overlap with three of the Fe^{2+} peaks but this is less likely to have an impact during peak overlap solving as there is a significantly lower concentration of silicon in the alloy and it is more likely to evaporate in the 2+ state with evaporation fields above 20 V/nm [189]. These will be in the m/Z range of 14.0 to 15.0 Da, and the most abundance Si^{2+} peak at 14 Da overlaps with the most abundant N^{+} peak, making the separation of nitrogen and silicon challenging using atom probe tomography.

Table 3.11: Table showing the isotopic abundance for each m/Z ratio for elements of interest. m/Z values, where peaks from multiple elements will be overlapped, are shown in the same horizontal line. Added to and adapted from Table 1, London et al. 2019, [188], using abundance data from [190].

m/Z	Fe	Ni	Mn	Si	Cr	V	C2	N
14.0				0.923				0.996
14.5				0.046				
15.0				0.031				0.003
24.0							0.978	
25.0					0.043	0.002	0.022	
25.5						0.997		
26.0					0.838			
26.5					0.095			
27.0	0.058				0.024			
27.5			1.000					
28.0	0.917			0.923				
28.5	0.021							
29.0	0.002	0.683		0.046				
30.0		0.262		0.031				
30.5		0.011						
31.0		0.036						

3.6.2 Proxigrams & concentration profiles

Plotting the concentration of ions through regions of interest can allow characterisation of regions of enrichment and the interfaces of secondary phases.

1 dimensional concentration profiles are formed by creating a region of interest, for example a cylinder intersecting an enriched feature, and then plotting the average concentration of ions in bins through the thickness of this region. Proxigrams (proximity histograms) provide a way of measuring composition analysis, which uses iso-concentration surfaces to define the region of interest [191]. They are calculated by measuring the concentration of ions in bins a set distance away from a defined iso-concentration surface. This means that all ions around the interface can be included in the measurement, regardless of the shape of the feature. However, for non-spherical features, the proxigram is limited in range that can be measured by the minimum dimension of the isosurface. Beyond this distance, the proxigram will start measuring matrix ions as part of the histogram.

3.6.3 Nearest neighbour distribution analysis

Nearest neighbour analysis measures the separation of ions from their n-th nearest neighbour and produces a plot of frequency against the distance between two ions [192]. This provides a measure of the most frequent distances between ions of a specific type and can be used to analyse clustering of solute atoms. At first order, only the first nearest neighbour distances are measured and plotted. Higher order analysis is useful when investigating diffuse clustering where there is a low level of enriched solute, as lower order or first nearest neighbour analysis may not be sensitive enough.

3.7 Small Angle Neutron Scattering

Small angle scattering techniques were first applied by A. Guinier, who discovered that it was possible to produce high intensity x-ray diffraction patterns at very small angles which corresponded to the structures of the materials being probed [193]. X-ray scattering depends on the atomic mass, i.e. Z number, of a material. Therefore, mixtures of transition metals, with similar masses, can be challenging to analyse due to overlapping X-ray peaks. Neutrons have varied

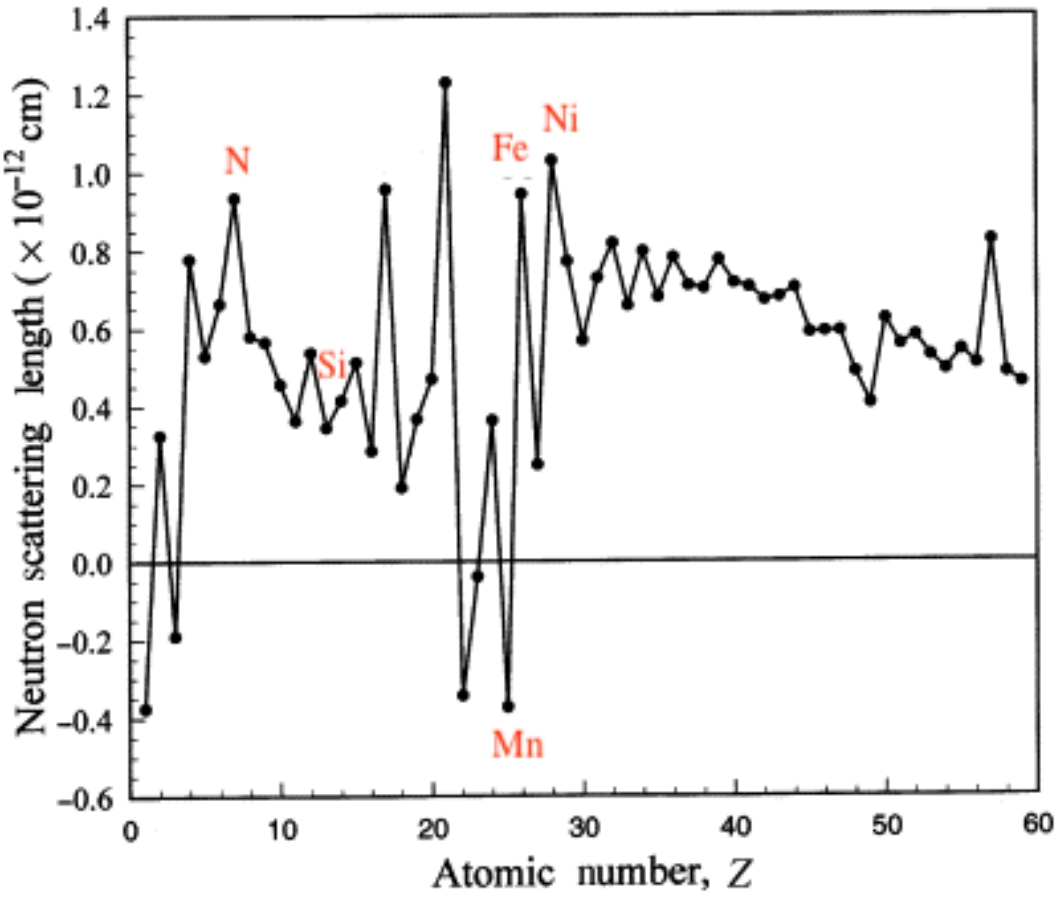


Figure 3.22: Plot (from figure 1, chapter 2, ([195]), showing variation of neutron scattering length with atomic mass. The key elements of interest in this study are labelled in red. Reprinted from Comprehensive Coordination Chemistry, Volume II, G.J. Long, Chapter 2.6 Neutron Diffractions, Pages 83-90., Copyright 2003, with permission from Elsevier.

scattering length densities for different elements and these values are not linear with mass, making neutron scattering an ideal technique for resolving small microstructural changes in complex alloys containing multiple similar mass isotopes. Figure 3.22 shows the variation of neutron scattering length with atomic number. Mn has a negative neutron scattering length, indicating that the interaction of a neutron with a Mn nucleus is attractive, rather than repulsive [194]. The overall neutron scattering intensity is related to the difference in scattering length per unit volume, see eq. (3.15), leading to strong scattering from Mn rich phases in an Fe matrix.

3.7.1 Small angle scattering

At small angles, the scattering is not derived from Bragg scattering through crystal planes, as the scattering vectors of neutrons interacting with nuclei adjacent to one another are approximately equivalent. The differences in scattering come from larger scale average deviations in composition and structure. In small angle scattering, the scattering angle is expressed as the q-vector, fig. 3.23 and eq. (3.12), which is measured on a 2D detector.

$$q = \frac{4\pi}{\lambda} \sin \frac{\theta}{2} \tag{3.12}$$

Neutrons interact with nuclei in a material, as point scatterers, and the short range nuclear interactions lead to a momentum transfer causing a change in neutron direction. This leads to the diffraction pattern on the detector where intensity varies with q, depending on the structures through which neutrons are scattered.

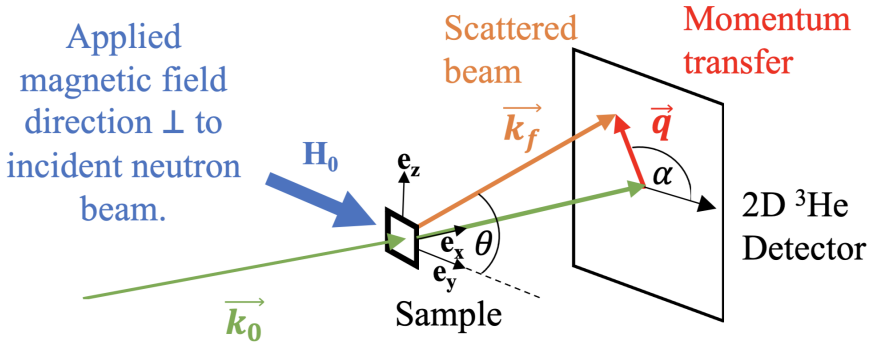


Figure 3.23: Schematic showing the neutron beam direction, sample geometry and applied magnetic field for a magnetic SANS experiment, along with incident, $\vec{k}_0$, and scattered beam, $\vec{k}_f$, vectors and q-vector on a 2D detector. $e_{x,y,z}$ are unit vectors, and H_0 is the applied magnetic field.

3.7.2 Scattering cross-section

The measured scattered neutron intensity $I(q)$ is proportional to the differential scattering cross-section, $\frac{d\Sigma}{d\Omega}$ of a dilute set of scatterers and can be expressed using the general formula for scattering cross-section [196, 197], as shown in eq. (3.13).

$$\frac{d\Sigma}{d\Omega}(q) = \Delta\rho^2 \int N(R) V_p^2(R) P(q,R)\ dR \tag{3.13}$$

Where:

- $\frac{d\Sigma}{d\Omega}(q)$ $(cm^{-1}.sr^{-1})$ is the differential coherent scattering cross-section and is proportional to the corrected scattering intensity.
- $\Delta\rho^2$ is the square of the difference of the scattering cross-section between matrix and particle.
- $N(R)\ dR$ is the number of particles, per unit volume, that have a radius between R and $R+dR$.
- $V_p^2(R)$ is the volume of a single scattering particle.
- $P(q,R)$ is the form factor of the particles which describes their shape, composition and structure.

For a non-dilute system, a structure factor, $S(q)$, is introduced to model inter-particle interactions. The scattering contrast factor, $\Delta\rho^2$ (Å^{-4}) can be expressed as a function of the scattering cross-sections of specific nuclei or atoms and their atomic volume and therefore provides information on the composition of the scatterers [198], eq. (3.14).

$$\Delta\rho^2 = (\rho^p - \rho^m)^2 = \left(\frac{b^p}{v_{at}^p} - \frac{b^m}{v_{at}^m}\right)^2 \tag{3.14}$$

Where:

- $\rho^{p/m}$ is the scattering length density of the particle or matrix.
- b^p is the mean nuclear scattering length of the particles (fm).
- b^m is the nuclear scattering length of the matrix.
- $v_{at}^{p,m}$ (Å^3) are the mean atomic volumes of the particles and the matrix.

Form and structure factors are modelled using the expected particle shapes, correlation functions describing inter-particle interaction and size distributions where a priori information on the

features is available. The form factor models applied to analysis in this study are described in section 3.8.3. The correction of data from intensity to absolute scattering cross-section is essential for obtaining quantitative results about a population of scatterers.

3.7.3 Coherent scattering

Coherent neutron scattering arises from the structure and arrangement of atoms in the sample. It is analogous to Bragg scattering in X-ray diffraction or electron diffraction, but at smaller angles, the structures probed are larger than 10 nm in size. The coherent nuclear scattering length density, ρ_n, is an average of the scattering lengths in a given atomic volume and can be expressed as;

$$\rho_n = \frac{b_n}{V} = \frac{\sum x_i b_{n,i}}{V} \tag{3.15}$$

Where $b_{n,i}$ is the nuclear scattering length of an element i, V is the molecular volume of the phase, and x_i is the atomic fraction of element i in the phase. Molecular volume, atoms.m^{-3}, can be expressed as follows [199]:

$$V = \frac{m}{N_{Av} d} = \frac{Volume\ Unit\ Cell}{No.\ Atoms\ in\ Unit\ Cell} \tag{3.16}$$

Where m is the molecular mass (g), d is macroscopic density (g.cm^{-3}), and N_{Av} is Avogadro's number (atoms).

Some key nuclear coherent scattering lengths are shown in table 3.12.

Table 3.12: Coherent neutron scattering lengths for key elements of interest in this study [200].

Element	Coherent Nuclear Scattering Length (fm)
Fe	9.45
Mn	-3.73
Ni	10.3
Si	4.1491
N	9.36

Incoherent nuclear neutron scattering is caused by scattering from the same atoms, moving around in the material and having multiple interactions with neutrons. The scattered waves do not interact with one another coherently, so the resulting scattering intensity is constant with q and does not yield any structural information about the sample.

3.7.4 Magnetic neutron Scattering

Magnetic neutron scattering is determined by crystal structure and the magnetic domain sizes created by these structures combined with the unpaired magnetic spins from unpaired electrons. Neutrons have magnetic spin and will therefore interact with unpaired spins in atoms, i.e. unpaired electrons. This means that when a neutron beam interacts with a ferromagnetic sample, the resulting scattering will be a combination of nuclear scattering and magnetic scattering [196]. The magnetic moment of a neutron is -1.913 μ_N [196].

Magnetic scattering is dependent on the local environment of atoms in a scattering feature and can be expressed as [201]:

$$\rho_m = \pm \sum_i^n N_i b_{m,i} = \pm C \frac{\sum_i^n x_i \mu_i}{V} = \pm Cm \tag{3.17}$$

Where μ_i is the magnetic moment per formula unit, in Bohr magnetons, μ_B, m is the magnetic moment, C is a constant equivalent to $2.645 \times 10^{-5} \text{Å} \mu_B^{-1}$, and x_i and V as for eq. (3.15)

Calculation of magnetic scattering length density relies on availability of experimentally determined values of magnetic moment per formula unit for the scattering particle phase.

3.7.5 Separation of magnetic and nuclear scattering

Applying a saturating magnetic field to soft-magnetic samples enables the separation of magnetic and nuclear scattering components. It is assumed that all scattering parallel to the applied field is due to nuclear scattering and scattering perpendicular to the applied field can be attributed to the total sum of nuclear and magnetic components of scattering [202]. To determine the values of scattering cross-sections and details of the structure and form factors, the separation of magnetic and nuclear scattering is required. With an applied saturating magnetic field, the scattering cross-section at a given value of α (angle of q axis measured, relative to the magnetic field direction) follows the relationship:

$$\frac{d\Sigma}{d\Omega}(q,\alpha) = \frac{d\Sigma_{nuc}}{d\Omega}(q) + \frac{d\Sigma_{mag}}{d\Omega}(q)\ sin^2(\alpha) \tag{3.18}$$

Where the total differential scattering cross-section over the solid angle is $\frac{d\Sigma}{d\Omega}(q,\alpha)$, and is a sum of the nuclear component ($\frac{d\Sigma_{nuc}}{d\Omega}(q)$)and the product of the absolute magnetic scattering cross-section ($\frac{d\Sigma_{mag}}{d\Omega}(q)$)with $sin^2(\alpha)$ such that it is at a maximum value when measured perpendicular to the magnetic field direction and is zero when parallel [202, 197]. The A ratio, the ratio of total to nuclear scattering, can be used to infer information about the composition of a population of scatterers using the following equation [197, 126, 25],

$$A = \frac{\left(\frac{d\Sigma}{d\Omega}\right)_{\perp H}}{\left(\frac{d\Sigma}{d\Omega}\right)_{\parallel H}} = 1 + \frac{\Delta\rho^2_{mag}}{\Delta\rho^2_{nuc}} \tag{3.19}$$

Where $\Delta\rho^2$ is the scattering contrast factor, which can be compared with fitted values and with theoretically calculated values for given particle compositions. This expression is valid if the magnetic and nuclear scattering data are describing the same set of identical particles with the same volume fraction and size distribution [198].

As scattering contrast factor and volume fraction are both directly proportional to scattering intensity, the A ratio can also be expressed in terms of relative volume fraction;

$$A = 1 + \frac{V_{f\,mag}}{V_{f\,nuc}} \tag{3.20}$$

This is useful when applying analyses such as the maximum entropy method to datasets, where there is no way to output scattering contrast, and it must be fixed during analysis.

3.7.6 ILL D33 experiment

The SANS experiment was carried out using the D33 instrument, a massive dynamic q-range small angle diffractometer at the Institut Laue Langevin (fig. 3.24)[203]. The experiment was No.1-01-184, awarded based on the proposal in appendix A.1. Samples were mounted in clamps made from aluminium and cadmium. Aluminium has a very low incoherent scattering cross-section, and cadmium is a strong neutron absorber, so does not contribute to the incoherent background scattering. The 10 mm irradiated region was marked on each sample and aligned with the neutron beam of 8 mm diameter, to ensure that scattering through irradiated samples was fully through the proton-irradiated region. The irradiated side of the samples was positioned downstream, to reduce attenuation of the scattering signal from radiation damage.

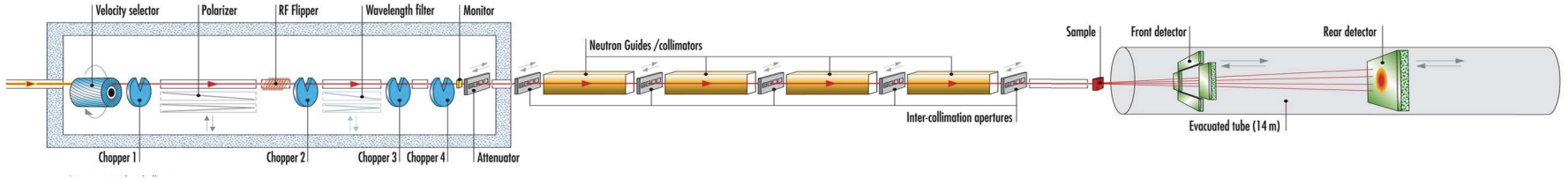


Figure 3.24: D33 diffractometer schematic, showing the velocity selection choppers, collimators, sample position and detector tank. Reprinted with permission from ILL: `https://www.ill.eu/for-ill-users/instruments/instruments-list/d33/description/instrument-layout` [204]

Table 3.13: Summary of SANS measurements carried out and the counting time for each set of data, PI: Proton-irradiated samples, HT: heat-treated samples, Cd: cadmium sample for background correction.

Measurements	λ (Å^{-1})	Aperture Diameter (mm)	Counting Time (mins)	Samples			
				PI	HT	Empty	Cd
Transmission measurements, LQ, MQ, HQ.	6	8	5	x	x	x	
Sample measurements, LQ	6	8	30	x	x	x	x
Sample measurements, MQ	6	8	30	x	x	x	x
Sample measurements. HQ	6	8	60	x	x	x	x

A 0.75 T magnetic field was applied horizontally to the sample and perpendicular to the incident neutron beam, fig. 3.23, to allow separation of magnetic and nuclear components. In this study, the variation of scattering with magnetic field was not measured. It was observed that at very low Q, the Fe-Mn-Ni-Si proton-irradiated alloy showed less scattering when the magnetic field was applied and, at this q range, showed no anisotropy. This indicates that the magnetic domain walls have been fully removed from the sample using the applied magnetic field and the model alloy sample is saturated. If magnetic anisotropy was observed at low q, it would indicate the presence of magnetic domains in the material. It is expected that magnetic scattering from irradiated and unirradiated samples at very low q should overlap, as if the sample is saturated there should be a single large magnetic domain. Figure 3.25 shows the effect of applying a magnetic field on the scattering pattern. In fig. 3.26, it can be seen that while the model alloy, Fe-Mn-Ni-Si (a. and b.) shows a circular scattering pattern at very low q, the RPV steel (c. and d.) does not. The unirradiated model alloy pattern shows a circular pattern at all q, indicating a single phase specimen with no features providing magnetic scattering contrast with the matrix present before irradiation. Even in the unirradiated condition, the RPV steel contains many carbides in the microstructure which are non-magnetic features and contribute to magnetic scattering contrast leading to the 'figure-of-eight' scattering intensity.

As the magnetic field strength required to saturate a material increases with decreasing grain size, in general similar studies on RPV steels use much higher field strengths of between 1.4 T and 1.8 T [150, 125, 157]. The field applied in this work was the highest possible value the instrument could provide, but it may not have fully saturated the A508-3 RPV steel, which has a significantly smaller grain size and finer microstructure than the model alloys.

Small angle neutron scattering background intensity varies with q. There is a constant flat background scattering contribution arising from incoherent nuclear scattering. This is caused by disordered atomic spin in sample atoms and the nuclear spin interactions of incident neutrons. This value has been set to zero for magnetic scattering data analysis, as there cannot be incoherent magnetic scattering.

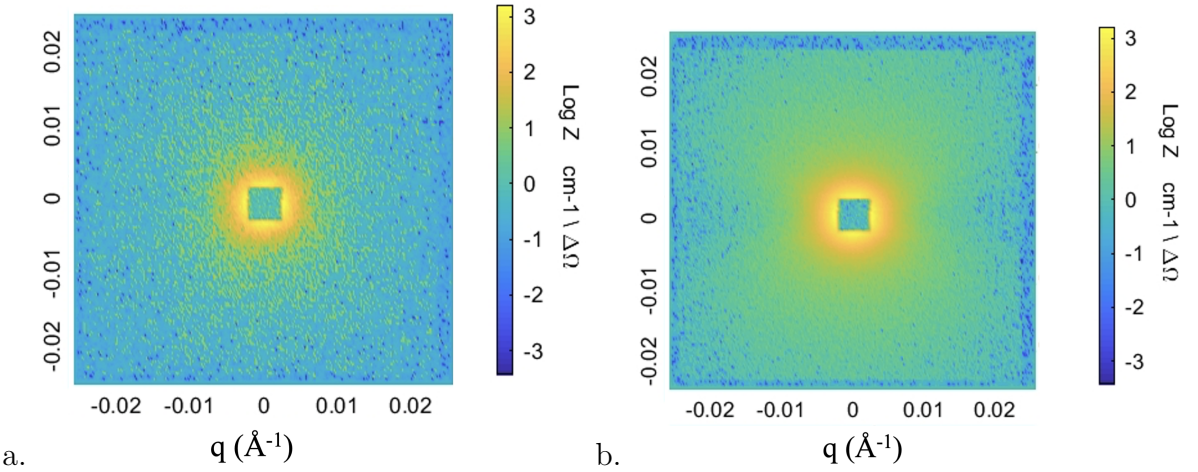


Figure 3.25: Detector images showing scattering from Fe-Mn-Ni-Si proton irradiated sample (a.) under no magnetic field, and with (b.) 0.75T horizontally applied magnetic field.

3.7.7 Measurement summary, counting times and background

The instrument was set up in each q range, starting with the highest (shortest detector distance) to ensure that the beam was aligned with the sample, the beam stop was correctly positioned, and that exterior detectors were not shadowing the main detector. The source aperture used was a 30 x 30 mm square. Each sample was measured over three q-ranges, obtained by measuring at three detector distances, and the datasets were overlapped for analysis.

Detector distances, beam stop settings and collimator positions for each q range can be found in Appendix A. The measured q ranges and counting times for each sample condition are summarised in table 3.13. Counting times were varied to improve statistics in regions where scattering intensity was lower, mostly in the high q range.

Sample transmission was measured, to allow for a correction of self-attenuation for each sample, and to produce thickness independent measurements of scattering intensity. Despite the variation in sample thicknesses, shown in table 3.2, the transmission values were all comparable with values above 0.99. These measurements were carried out at all three q ranges, and overlaps checked to ensure that the sample centre remained consistent. None of the samples were strongly absorbing, and transmission values can be found in appendix A.2.

A cadmium sample was used to measure background incoherent scattering from the beam line and environment. Natural cadmium has a high neutron absorption cross-section for cold neutrons, of over 1000 b [170]. The incoherent background counts were measured at different q

ranges, as the impact of background air scattering is significantly higher at high q, where the length scales probed are similar to that of gaseous species in air.

In the high q configuration, the measured sample signal was very similar to the empty cell background measurements, suggesting that the incoherent background scattering from samples was low and most of the signal was caused by structural features in the material. A neutron wavelength of 6 Å was selected to maximise neutron flux onto the sample and subsequent scattering intensity. In the medium q range, air scattering is lower and there was a significant difference between count rates from samples compared with the empty cell measurement. This increased again at low q, where incoherent background contributions are equivalent to less than 1 % of the overall scattering intensity.

Unirradiated, heated samples have been measured as control datasets so that the resulting datasets (unirradiated scattering subtracted from irradiated scattering) represent the neutron scattering contribution from radiation induced microstructural changes. An example of the difference in observed scattering between heat-treated and proton-irradiated model alloy and RPV samples is shown in fig. 3.26. There is no observable magnetic scattering in the heat-treated model alloy scattering pattern, leading to a circular pattern, rather than a figure of 8, seen in the irradiated sample, indicating the presence of features leading to magnetic scattering contrast. In the A508-3 RPV steel, there is clearly anisotropy in both the unirradiated and irradiated condition, due to the wide distribution of carbides present in the alloys.

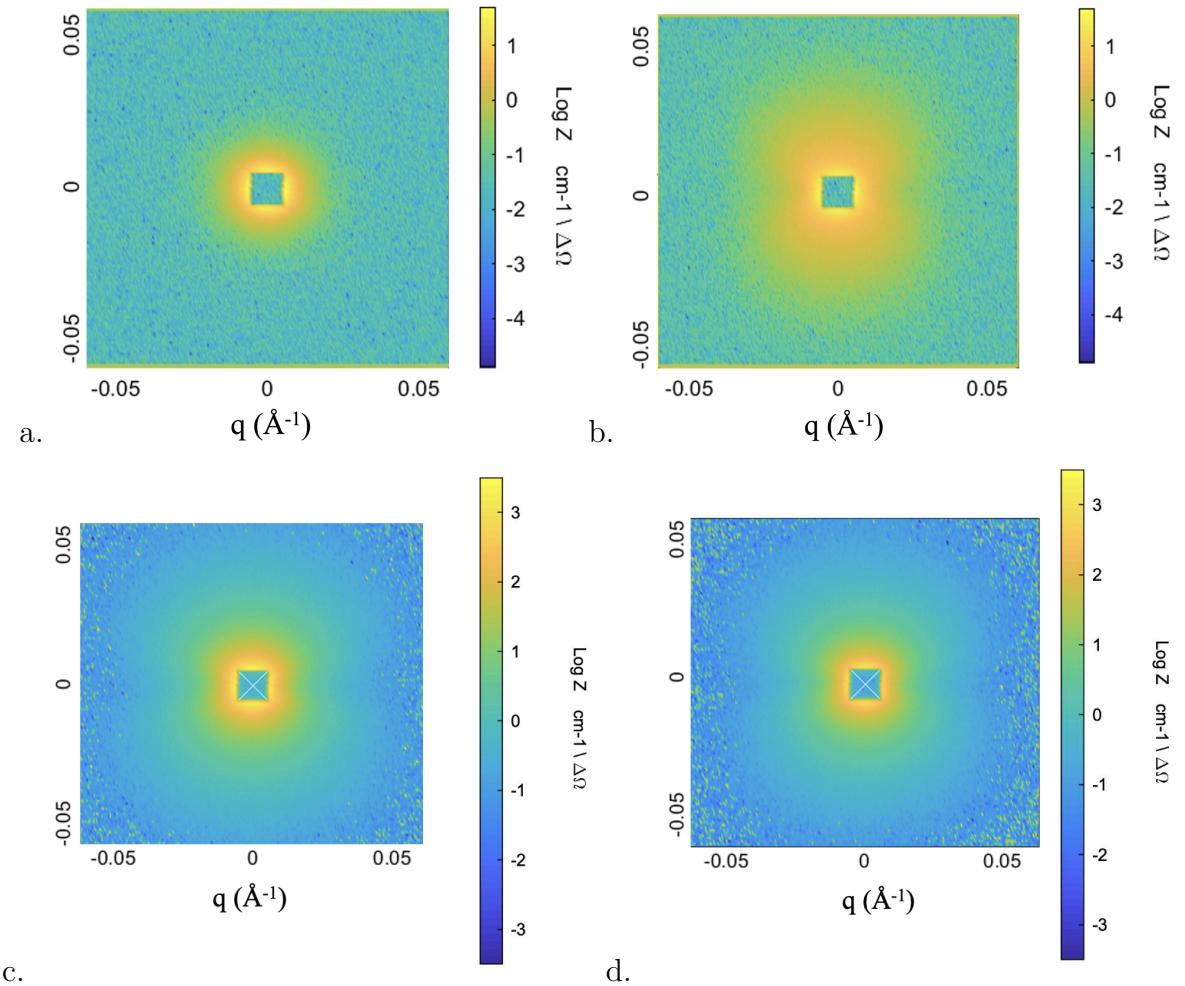


Figure 3.26: Images of the detector intensity data for the heat-treated (a.) and proton-irradiated (RHS) Fe-Mn-Ni-Si alloy, (b.) and heat-treated (c.) and proton-irradiated (RHS) A508-3 RPV steel, in the medium q measurement range.

3.8 SANS data analysis

The following process has been followed to analyse SANS data:

1. The 2D data is normalised to counting time and reduced to 1D plots of I vs q.
2. Difference in scattering is observed, and unirradiated data subtracted from irradiated datasets to provide datasets describing the radiation induced microstructural changes.
3. Magnetic and nuclear scattering datasets are separated, and A ratio calculated to inform analysis of solute-rich feature composition.
4. Shape independent model fitting using Guinier-Porod function is applied to full q-range to observe whether this is an appropriate comparison and range of data to fit.
5. Shape specific model fitting applied to a reduced q-range, using a priori information available from APT and TEM analysis (where data were collected), to obtain quantitative information about the population of radiation induced solute-rich features.

Each of these sections are described below.

Data reduction

Data was reduced using GRASansP ([205]). For each sample and q range, the measured data was averaged, and the empty cell and cadmium measurements subtracted. These two background measurements are required to account for the background neutrons from chamber scattering and from attenuated scattering through the sample from the chamber. The measured intensities are combined with sample measurements to produce a background corrected dataset:

$$\begin{aligned} I_{\text{Corrected}} &= I_{\text{Sample}} - I_{\text{Attenuated background}} - I_{\text{Unattenuated background}} \\ &= I_{\text{Sample}} - I_{Cd} - \frac{I_{\text{Empty Cell}} - I_{Cd}}{T} \end{aligned} \tag{3.21}$$

Where T is the transmission measurement through the sample, for which measured values can be seen in appendix A.2. A correction was carried out to account for the counting time and solid angle, to provide $I(q)$ in absolute units of cm^{-1}. As the neutron source at ILL has a constant flux, the measured counts were divided by the counting time, and corrected for

detector efficiency using a standard instrument calibration. To obtain data representing the total scattering contribution form irradiation induced scattering features, the unirradiated (heat-treated) data sets have been subtracted from the proton-irradiated datasets. Figure 3.27 shows the increased scattering intensity in irradiated samples for most alloys.

Comparison of total scattering with and without proton irradiation

Figure 3.27 shows the total scattering averaged over q for each sample. Irradiated and unirradiated results for each alloyed are compared, and show that in general, samples exposed to radiation have an increase of scattering intensity in specific q ranges.

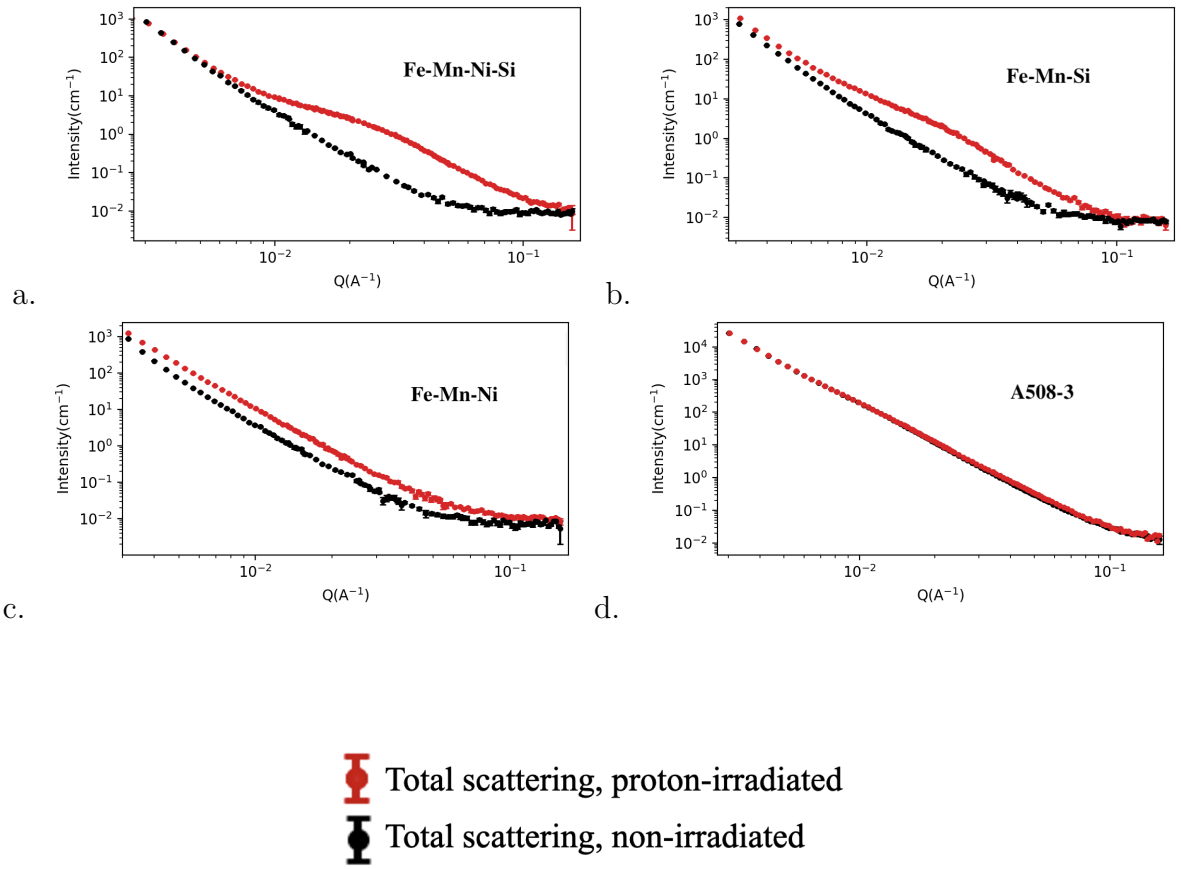


Figure 3.27: Total neutron scattering, averaged over q-range over sector, perpendicular to applied magnetic field, for proton-irradiated (red) and heat-treated (black) (a.) Fe-Mn-Ni-Si, (b.) Fe-Mn-Si, (c.) Fe-Mn-Ni, and (d.) A508-3 RPV steel.

Overlap at low q around $0.004\,\text{Å}^{-1}$, corresponding to a feature size of around $15\,\mu\text{m}$, shows

there are no macroscopic structural changes after irradiation in any of the alloys. Three of the alloys show clear increase in scattering in the irradiated condition, with the Fe-Mn-Ni-Si and Fe-Mn-Si showing a distinct region of increased scattering intensity between 0.007 and 0.1 $Å^{-1}$. The Ni containing alloy's increased scattering is shifted to higher q than the Ni free alloy, suggesting a smaller average size (fig. 3.27). The Fe-Mn-Ni shows an increase across the entire measured low q range up to approximately 0.1 $Å^{-1}$. It would be expected that these data would overlap at low q if there were no new larger microstructural features after irradiation.

The irradiated Fe-Mn-Ni sample showed a melt pool and surface contamination, likely due to carbon contamination and oxidation during irradiation. There particles are likely to be much larger than fine scale matrix radiation damage so further analyses of this data focus on the q range greater than 0.01 $Å^{-1}$, to omit any of the contributions from larger scattering features not investigated in this work.

All heat-treated alloys show a scattering intensity trend close to a power law function of q, corresponding to background scattering from larger features such as grain boundary networks, as shown in fig. 3.27.

Radial averages over sector areas perpendicular and parallel to the applied magnetic field were extracted to produce 1D datasets of $I(q)$. Sector angles have been selected for each sample to balance reducing statistical counting errors and increasing signal-to-noise ratio. The angles have been selected for each alloy based on balancing these factors and are shown in table 3.14. Subtraction of heat-treated alloy datasets from irradiated datasets then provides a measurement of scattering resulting only from differences in microstructures between the two conditions. It is assumed that the resultant scattering intensity corresponds to radiation induced microstructural changes.

Table 3.14: Table of selected sector angles used for each alloy dataset.

Alloy	Sector Angle Selected (°)
Fe-Mn-Ni-Si	30
Fe-Mn-Si	20
Fe-Mn-Ni	20
A508-3 RPV Steel	35

3.8.1 Separation of magnetic and nuclear scattering

Separating magnetic and nuclear scattering contributions is useful when fitting models to the data as it allows more parameters to be fixed or constrained, to make the results more physically meaningful.

Separation of magnetic and nuclear scattering relies on a $\sin^2\alpha$ dependence of magnetic scattering as a function of α, the angle on the detector measured from the line parallel to the applied magnetic field. Therefore, a correction has been made to account for the underestimation of magnetic scattering magnitude due to integration, ([205]), over a finite sector perpendicular to the magnetic field, and an overestimation of nuclear scattering magnitude parallel to the magnetic field.

The derivation of this correction is shown in Appendix A, and the overall correction factor, as a function of the measured A ratio, A_m and the sector angle, ϕ, is shown below:

$$A_{corrected} = \frac{2B(A_m - 1)}{2 - (A_m - 1)(B - 1)} + 1 \tag{3.22}$$

Where,

$$B = \frac{\phi}{\sin\phi} \tag{3.23}$$

Coupled with the assumption that scattering features are non-magnetic, it is expected that lower A ratios indicate greater quantities of manganese in the features. Mn has a negative scattering length, so will reduce the overall scattering length density of a phase significantly if present in large quantities. This will lead to an increase in nuclear scattering contrast and decrease in the magnitude of the ratio of magnetic to nuclear scattering intensity, M/N.

3.8.2 Shape independent fitting

The Guinier-Porod function is an empirical model that can be fitted to SANS data from a population of scatterers to estimate their radius of gyration, R_g. It gives qualitative information about the approximate size of scattering features but cannot account for effects of inter-particle interactions or polydispersity. This can lead to underestimates of radius of gyration. The Guinier function is applied at low q (generally where $qR_g < \sqrt{3} \simeq 1.3$), and the Porod function at high q,

and provides values of dimensionality, s, which vary depending on the shape of scatterers, [206];

$$I(q) = \begin{cases} \frac{G}{Q_s} \exp\left[\frac{-Q^2 R_g^2}{3-s}\right] & Q \leq Q_1 \\ \frac{D}{Q^m} & Q \geq Q_1 \end{cases} \tag{3.24}$$

Where, D and G are functions ofR_g, Q and s. For more detail on these expressions, see Hammouda's "A new Guinier-Porod model" [207]. The ranges can be internally calculated for each fit, based on forcing continuity of the two functions, eq. (3.24), across the fitted q range.

Guinier plots are shown in fig. 3.28, for the resultant nuclear scattering from each alloy, caused by radiation. Based on TEM observations, it has been assumed that the features have smooth interfaces with the matrix and therefore the Porod exponent has been fixed to -4 [199]. The fitting outputs are shown in table 3.15, and show very small radii for the Fe-Mn-Ni-Si, Fe-Mn-Si and A508-3. The Fe-Mn-Ni alloy showed fits with much higher volume fractions than physically possible, based on the assumption that the features are mostly solute containing. These alloys also had a larger R_g. This suggests there may be some contamination, or large scale features with compositional variation in the Fe-Mn-Ni after irradiation. There could also be more significant scattering coming from grain boundary segregation or the formation of iron-rich features, leading to a Guinier-Porod fit with a greater χ^2 value. The dimensionality parameter, s, ranges between 0.99, close to that of a rod-like feature, and 1.97 which is close to the expected value for platelets or lamellae [207]. This suggests that the models applied to the scattering here are covering a wide q-range that is likely to be incorporating contributions from grain boundary segregation and precipitation, rather than contributions from only matrix features, and in this case no q-dependent background was modelled.

Table 3.15: Guinier-Porod output parameters for nuclear scattering data fits shown in fig. 3.28

Alloy	Scale	Incoherent Background(cm^{-1})	R_g (Å)	S	χ^2
Fe-Mn-Ni-Si	2.50E-03	4.00E-04	32.71	1.5548	1.39
Fe-Mn-Si	6.56E-04	1.47E-03	39.97	1.9762	0.96
Fe-Mn-Ni	1.26E-01	6.00E-04	277.25	1.4088	6.71
A508-3	5.36E-03	5.94E-05	39.72	0.98619	2.20

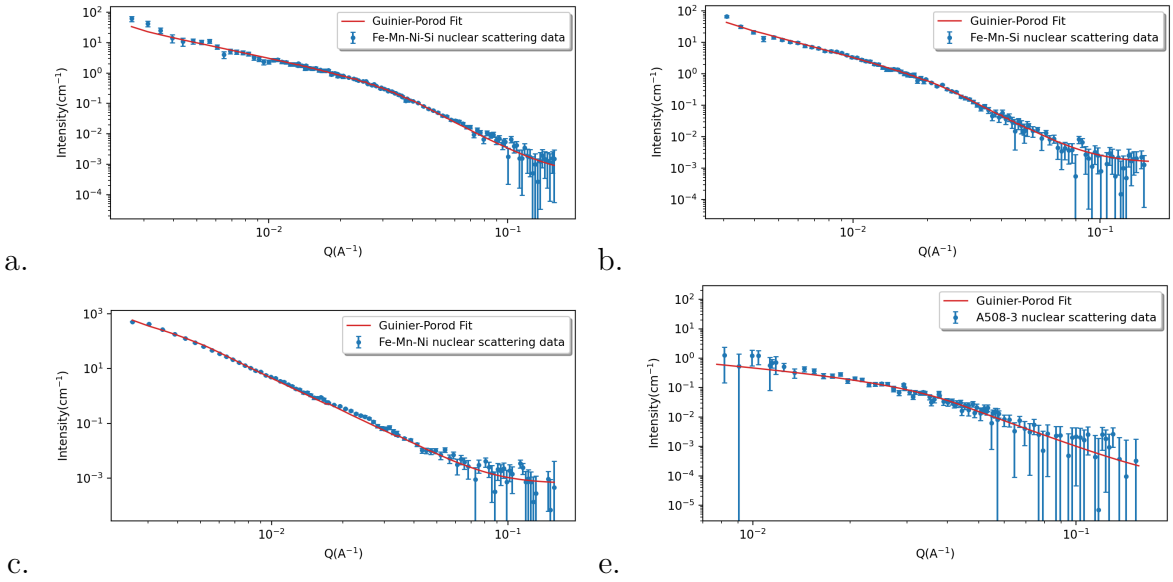


Figure 3.28: Guinier-Porod fits to nuclear datasets for all alloys, to obtain estimates of R_g for (a.) Fe-Mn-Ni-Si, (b.) Fe-Mn-Si, (c.) Fe-Mn-Ni and (d.) A508-3 RPV steel.

3.8.3 Shape factor & scattering contrast fitting using a priori information

The size distribution of R cannot be directly determined from SANS data due to the discrete measurements of intensity over a limited q range. Fitting models to the available data is required to obtain measurements of particle size distribution. Fitting models to data requires a number of assumptions to be made about the system to simplify eq. (3.13), and limit the number of free parameters describing the population of scatterers in order to obtain a physical set of values. The following assumptions have been applied to enable numerical fitting of datasets to obtain quantitative results;

1. The system is dilute (there are no inter-particle interactions affecting the local magnetisation or nuclear scattering) and the structure factor, $S(q)$, is set to 1. In a dilute system, it is assumed that volume fraction is sufficiently small that $V_f(1-V_f) \simeq V_f$. For non-dilute systems, a structure factor $\neq 1$ is required.

2. Particles are randomly dispersed in a homogeneous matrix.

3. The system has a population of particles which all have the same shape (assumed to be spherical, ellipsoidal or cubic depending on the sample) and chemical composition, contributing to magnetic and nuclear scattering.

4. Particles are polydisperse and their sizes follow a log-normal distribution.

To further constrain numerical fitting, it was generally assumed that the scattering population is non-magnetic. The magnetic scattering contrast can be calculated and fixed using a theoretical value of magnetic scattering length density for pure BCC Fe. Substituting literature values of scattering length ([208]) and lattice parameter ([209]) for BCC Fe into eqs. (3.15) and (3.16) gives;

$$\rho_{Mag,BCC\ Fe} = \frac{5.87\times10^{-5}\text{Å}}{\frac{(2.87\text{Å})^3}{2}} = \frac{5.87\times10^{-5}\text{Å}.2}{23.29\text{Å}^3} = 4.98\times10^{-6}\text{Å}^{-2} \tag{3.25}$$

It is then possible to determine absolute values of nuclear scattering contrast, volume fraction and average size. Otherwise, the obtained volume fraction and scattering contrasts will be relative values as they are both directly proportional to $I(q)$. The assumption that particles are dilute allows for the impact of interaction between particles on neutron scattering to be ignored, and for this to hold $V_F < 20\%$ [210].

a. Form factor modelling using numerical fitting

The following models have been used to extract quantitative data from neutron scattering profiles for each alloy. More detailed model documentation can be found at: sasview.org [206]. The models take the general form of :

$$\begin{aligned}\text{Intensity}(cm^{-1}) =& Ae^{-P} + V_f.\Delta\rho^2.V.P(q) + B \\ =& Ae^{-P} + V_f.\Delta\rho^2.\int F(r,q,\theta)drB\end{aligned} \tag{3.26}$$

Where B is the incoherent background (cm^{-1}), Ae^{-P} accounts for coherent background scattering at low q , V_f is the volume fraction of scatterers, $\Delta\rho^2$ is the scattering contrast factor, and $P(q)$ is the form factor function representing the volume and shape of particles. In general, this is a function of q, and r or a (radius or length). These are all parameters that can be constrained or fixed by the user, or left free to be varied during the fitting to obtain the values giving a χ^2/n as close to 1 as achievable within the model function constraints. At low q there can be contributions from structures at larger size scales such as grain boundary networks. Alloys investigated using TEM showed distinctive precipitate morphology, including cubic Mn-Si rich features in both the Fe-Mn-Si and Fe-Mn-Ni-Si and ellipsoidal Ni-Mn-Si features in the Fe-Mn-

Ni-Si alloys. Therefore, for the Fe-Mn-Si alloy, a cubic form factor has been applied to fitting. A range of morphologies were observed in the Fe-Mn-Ni-Si alloy, but an ellipsoidal fit has been carried out as an approximation to the average shape of solute-rich features. All other alloys have been fitted to a spherical model of scatterers. Form factors, $P(q)$, have been taken from documentation in SASView ([206]) and NIST([211]) for spherical particles (A508-3 steel and Fe-Mn-Ni), ellipsoids (Fe-Mn-Ni-Si) and cubic particles (Fe-Mn-Si). This analysis package was also used to impose a log-normal size distribution on the scattering populations to investigate polydispersity.

b. Maximum Entropy Method fitting for size distribution analysis

SASView and other form factor fitting software are limited to mathematically defined size distribution functions. Therefore, alternative methods are required to investigate the most appropriate size distribution fit to the data.

This method employs an algorithm that does not require any empirical model fitting and therefore produces results that are not biased by assumptions around particle shape and size [212]. It generates trial fits to the data by changing the size distribution probability function to achieve the closest fit to eq. (3.13). $N_p(r)$ is a histogram of size distribution which is varied to minimise χ^2 of the trial fit. The solution obtained aims to maximise a parameter corresponding to entropy in the system, which leads to the resulting distribution always being positive. The maximum entropy algorithm works by assigning a flat probability distribution to the variable being fitted, in this case particle size, and then calculating the 'entropy' of the system, S, where this value describes how much information is represented by the probability distribution P_i [213] as follows:

$$S = -\sum_{i=1}^{N} p_i \log p_i \tag{3.27}$$

Maximising the entropy of the distribution, S, leads to a best fit because, within the constraints of the provided data, the uncertainty is maximised, giving the least biased fit to the data, rather than forcing a biased distribution. The fitting process works by processing the data using an algorithm that takes a starting distribution to calculate the initial difference between the data and the scattering intensity calculated using the modelled distribution, by calculating the χ^2

value [214]

$$\chi^2 = \sum_{i=1}^{N} (\frac{I_i - y_i}{\sigma_i})^2 \tag{3.28}$$

Where i describes the number of each data point in the dataset, I_i is the measured intensity corresponding to i and y_i is the calculated intensity based on the modelled size distribution $p_i(r)$. Therefore, the modelled distribution, $p_i(r)$ should produce a result of differential scattering cross-section that matches the measured data when the mean value of χ^2 is equal to the number of data, with a converged fit yielding a $\frac{\chi^2}{N}$ of one. The IRENA package, designed by Jan Ilavsky, has been used for maximum entropy method (MEM) analysis in this work [210, 214]. This code takes user inputs of scatterer size range, histogram binning information and model background functions and produces a fitted I(q) function, median and mean radii of the scatterers, as well as a size distribution and volume fraction of scattering features. The output of this algorithm is a particle size distribution that does not have to follow any predetermined function. This is the key difference between this method and fitting models using form factor expressions.

3.9 Nanoindentation

Nanoindentation measurements were carried out on two of the irradiated alloy cross-sections; the Fe-Mn-Ni-Si and Fe-Mn-Si model alloys. Arrays of 250, and 300 indents were carried out on cross-sections of the samples at angles of between 10 and 30°degrees to the irradiation surface as shown in fig. 3.29. A Hysitron TI950 indenter was used, with a Berkovitch tip, to obtain hardness measurements. All indents were carried out up to a maximum load of 10 N. Indents were spaced 10 µm apart, corresponding to over 20x the indentation depth (max depth for indents was around 500 nm). This should be sufficient to avoid overlapping plastic zones. Despite the standard recommending a spacing of 20 x the indentation depth, Phani and Pharr have shown this is conservative and recommend a spacing of 10x for a Berkovitch tip[215]. Tip area calibration was carried out before each indentation array, as advised in the TI950 manual, [216]. Hardness values were extracted from the indentation curves using Hysitron Triboscan 9 software, based on the method described by Oliver & Pharr, 1992 [217], using the following expressions:

$$H = \frac{P_{max}}{A} \tag{3.29}$$

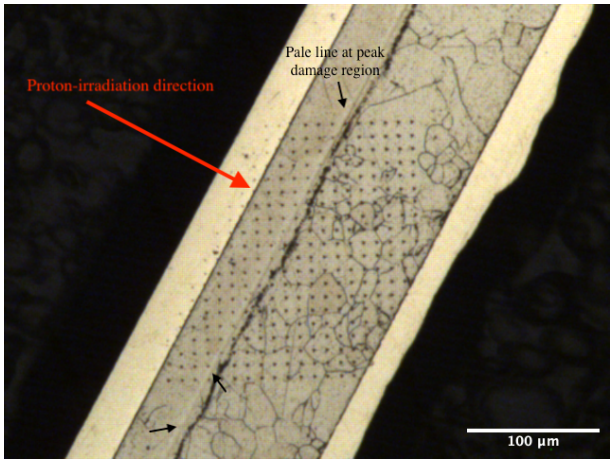


Figure 3.29: Optical microscope image showing the indentation array on the Fe-Mn-Ni-Si alloy. The bright white line close to the dark line parallel to the irradiation surface is the location of the Bragg peak, marked with black arrows in the image. The darker line was caused by preferential etching beyond the Bragg peak in this sample during polishing.

Where H is the hardness, P_{max} is the maximum applied force and A is the projected contact area of the indenter. If the tip area is calibrated, then the contact area can be calculated based on the true contact depth, h_c, which is, [216];

$$h_c = h_{max} - \varepsilon \frac{P_{max}}{S} \tag{3.30}$$

Where, h_{max} is the maximum depth, S is the stiffness of the unloading curve (the initial gradient of the unloading curve) and ε is a geometric factor that varies with indenter tip shape. For a Berkovitch tip is set to 0.75, to account for deflection at the edges of indents [216].

All load-displacement curves were reviewed to identify anomalous readings. Data points with bowed loading curves (usually observed near interfaces with Nickel or by grain boundaries) were omitted, as they yielded anomalous values of hardness. Curves with sharp jumps in displacement (see fig. 3.30, were also omitted as they are likely to have been pop-in events where new dislocations have nucleated under the indenter tip [218]. These phenomena were observed in indents across the irradiated and unirradiated regions. Some curves, where the zero point of the indent could not be accurately identified due to dirt on the surface causing a rapid displacement at low loads, were also omitted from the presented data. The indentation hardness values were plotted as a function of distance from the irradiated surface to investigate the effect of the radiation induced microstructural changes on the mechanical response of the alloy as a function

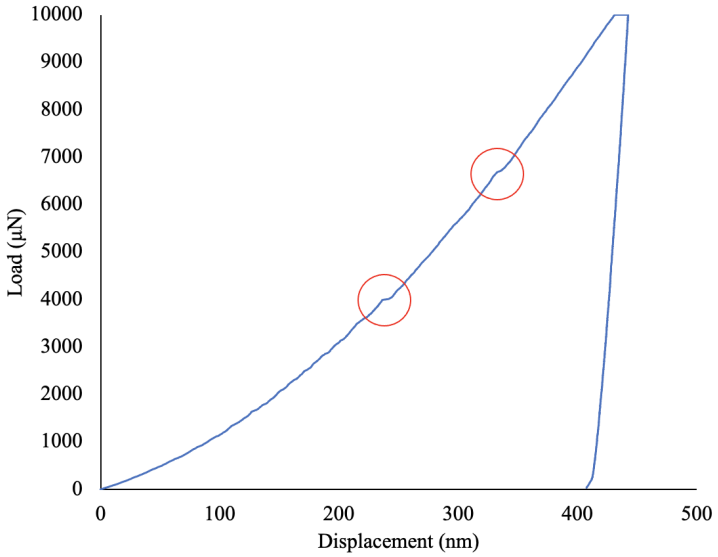


Figure 3.30: Example load-displacement curve from one of the Fe-Mn-Si indents showing two pop-in events, where the displacement suddenly increases with no increase in load.

of dose/ dose rate.

3.10 Summary

The results obtained are presented in the following chapters, with fig. 3.31 showing how data collected using each technique have been combined in order to investigate the interaction between solute elements and their precipitation behaviour under irradiation. After initial characterisation results, the TEM and nanoindentation results are presented for two key alloys which showed contrasting precipitation behaviour after irradiation (chapter 4). Then atom probe tomography (chapter 5) and small angle neutron scattering(chapter 6) results obtained for all irradiated and as received alloys are presented. It should be noted that the order in which data has been collected was dependent on sample sizes and preparation methods. Therefore, in practice, the SANS experiment was carried out first, on the largest possible sample size, and subsequently APT, TEM and nanoindentation testing was carried out on specimens extracted from the SANS specimens. The discussion, chapter 7, combines the techniques and considers the impact of these findings as a whole so that conclusions can be drawn on the effects of proton radiation on the solute behaviour in model RPV steels.

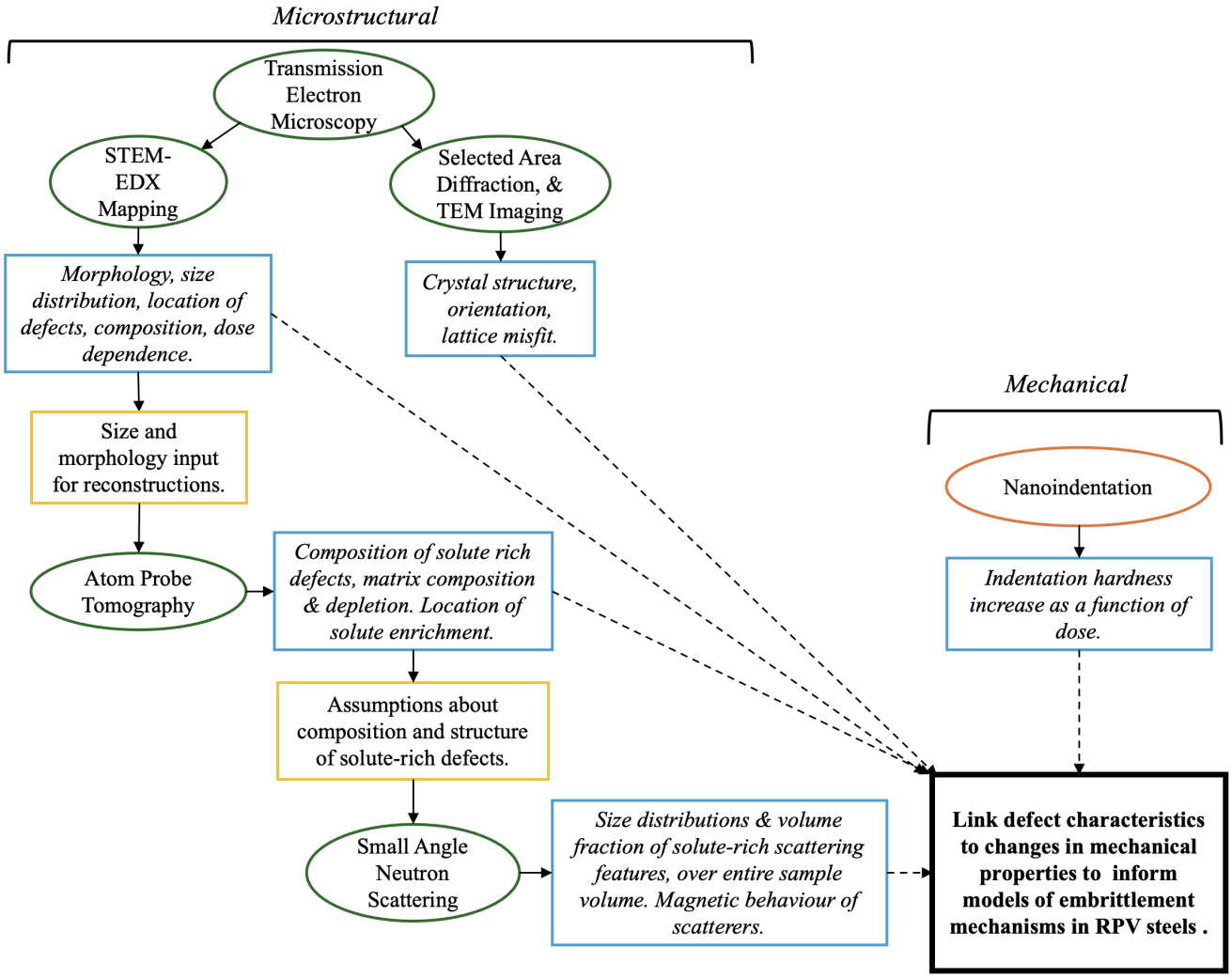


Figure 3.31: Diagram showing the links between various characterisation techniques, with the outputs used in subsequent methods.

Chapter 4

Defect Size Distribution and Composition Analysis using TEM & STEM-EDX

Two alloys have been studied using TEM and STEM-EDX to characterise radiation induced defects and precipitation. The Fe-Mn-Ni-Si and Fe-Mn-Si model alloys were selected as they showed the most significant increase in scattering after irradiation during the SANS experiment. TEM/STEM-EDX results are split into quantification of size distribution of precipitates, composition analysis, and structure determination. For each section, images and data are presented for the Fe-Mn-Ni-Si alloy and then the Ni free Fe-Mn-Si alloy. Initial nanoindentation data is shown for these alloys first, showing the effect of these microstructural changes on hardening.

4.1 Radiation hardening in Fe-Mn-Ni-Si and Fe-Mn-Si alloys.

Due to the small size of samples, and the irregular dose profile produced by proton irradiation, nanoindentation was chosen to attempt to correlate microstructural evolution observed as a function of dose/dose rate, with the response of the materials to plastic deformation. Although this approach does not yield bulk mechanical properties, it does indicate the effect of radiation induced defects such as dislocation loops and precipitates on the ability for dislocations to move through the material. In turn, this can inform the expected effect of these microstructural changes on the toughness of the alloys and provides an indication of where there are likely to be key microstructural changes worth investigating using local characterisation techniques.

Nanoindentation hardness is plotted against distance from the irradiated surface for the Fe-Mn-Ni-Si and Fe-Mn-Si alloy in fig. 4.1. The dose profiles from fig. 3.7 are plotted on the same axes and show that the higher dose regions have greater hardening. A sharp peak in hardening can be seen at the Bragg peak, where protons stop in the material, indicating a significant increase in hardening features in this region in both alloys.

The average indentation hardness of the unirradiated region of the Fe-Mn-Ni-Si alloy has been measured to be 1.90 ± 0.02, and 1.82 ± 0.01 GPa for the Fe-Mn-Si alloy. These values have been subtracted from the measured hardness values, and the hardening, ΔH, has been plotted against dose, dpa, in fig. 4.2. Indentation was carried out to constant load, rather than to a constant indentation depth, making it difficult to determine the hardening accurately without contribution from the indentation size effect. The range of indentation depths were between 195 nm and 518 nm, for the Fe-Mn-Ni-Si alloy, larger than the indentation depth range in the Fe-Mn-Si alloy of 251 nm to 458 nm. This is due to the quality of surface finishing, leading to a rougher surface and more variable data collected from the Fe-Mn-Ni-Si alloy. As a result, the data collected be influenced by the indentation size effect, leading to a general overestimate in hardness compared with the bulk hardness of the material, and a variation in measured hardness across the data. However, there is still a clear difference in hardening behaviour between the Fe-Mn-Ni-Si and Fe-Mn-Si alloys, with more significant hardening in the Ni containing alloy.

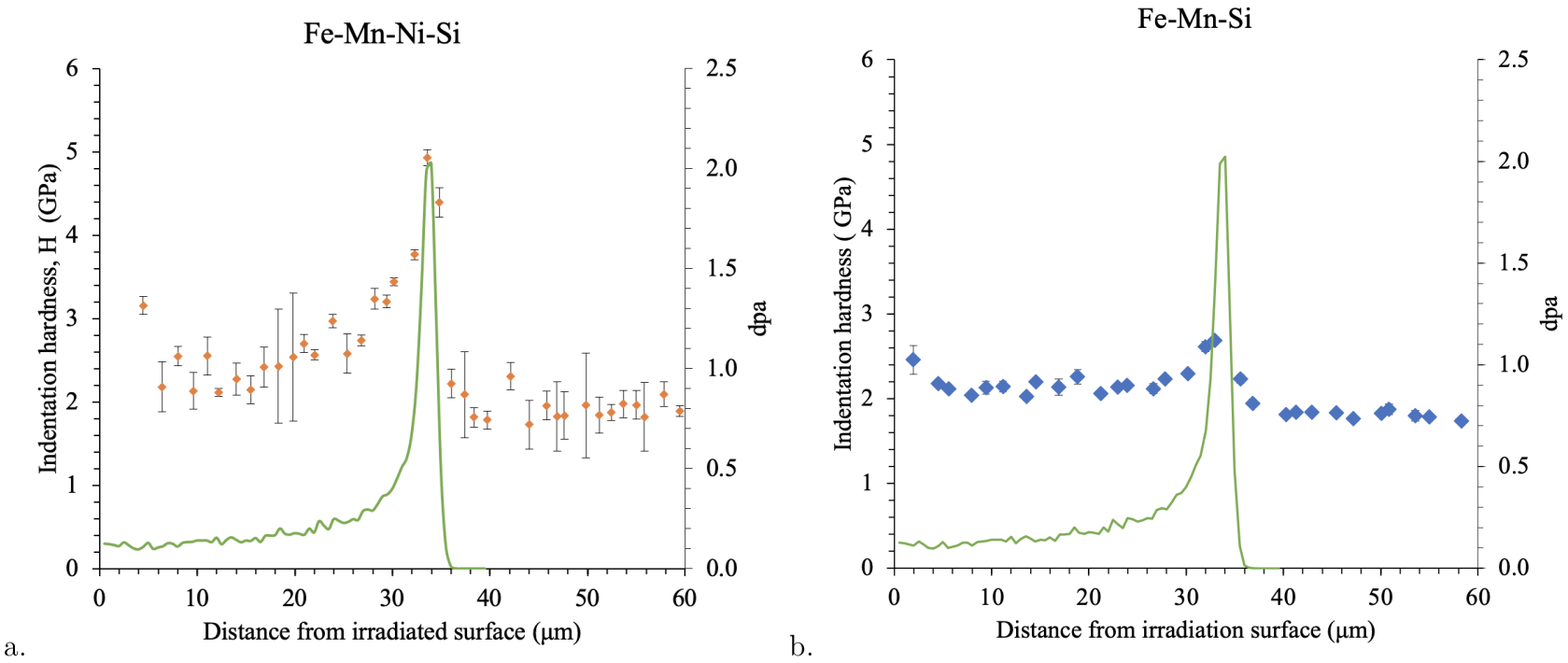


Figure 4.1: Nanoindentation hardness measured as a function of depth from the irradiated surface of the Fe-Mn-Ni-Si alloy (a.) and the Fe-Mn-Si alloy (b.). Error bars correspond to the standard error on the mean of three measurements .The high hardness measurements at negative depth correspond to Ni plating used to protect edges during polishing.

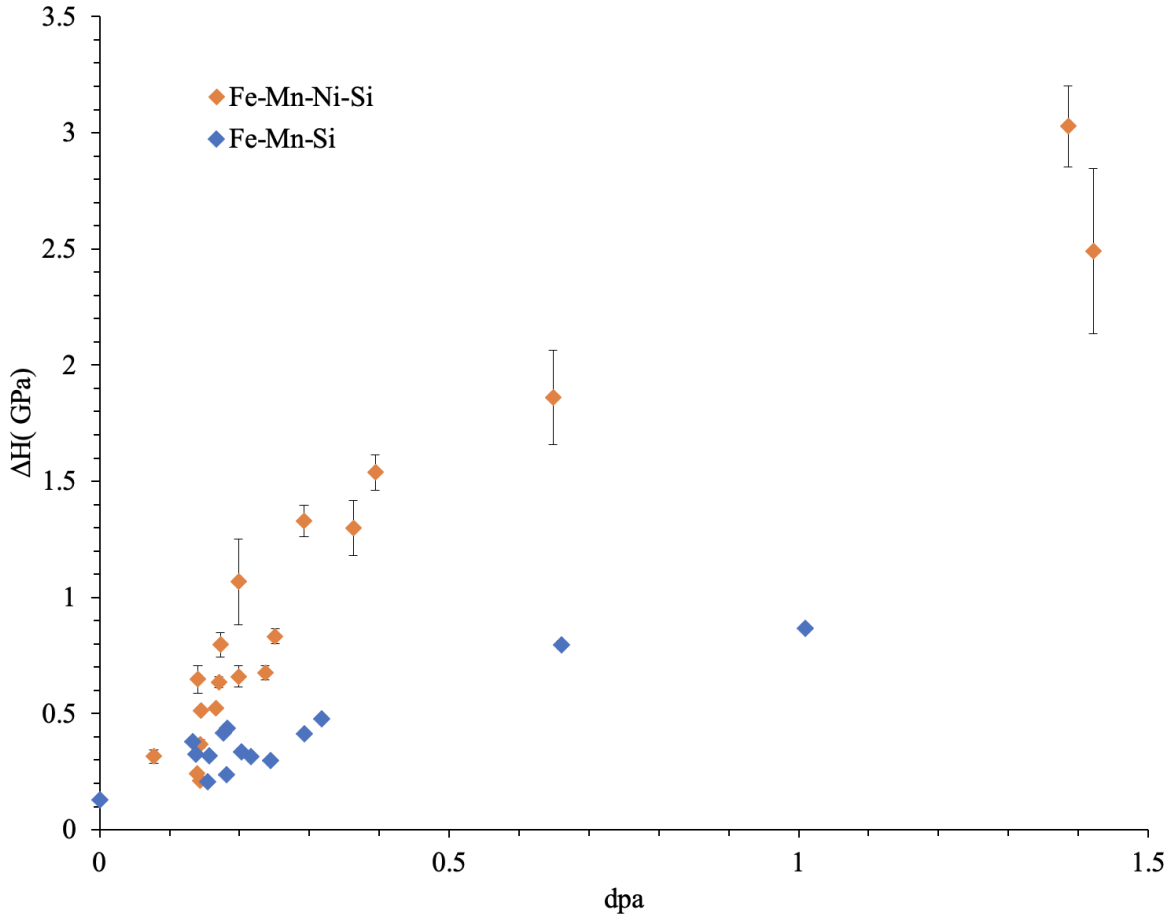


Figure 4.2: Change in hardness versus dpa, for both Fe-Mn-Ni-Si (orange) and Fe-Mn-Si (blue). These measurements were carried out to the same load, and therefore have varying indentation depths between approximately 200 nm and 500 nm.

4.2 TEM Specimen information

Each TEM sample has multiple thin areas, with at least one in the plateau region, 0.1 dpa, one covering the peak radiation region, 2 dpa, and one window in the unirradiated region, 0 dpa. Figures 4.3 and 4.4 show low magnification images of the specimens with labelled irradiation directions and dose regions. With increasing dose, there is an increasing number density of dislocation loops and precipitates observed in both alloys, with cubic precipitates and large loops observed in the Fe-Mn-Si alloy and smaller loops and precipitates with higher number density observed in the Fe-Mn-Ni-Si alloy. Precipitate quantification has been carried out by averaging number density, size and volume fraction over images approximately 500 nm wide, leading to much greater uncertainty in regions close to the damage peak as damage increases over smaller depths. The regions analysed for precipitate distribution and composition are all located in the ferritic matrix, away from grain boundaries. Variation in precipitate composition as a function of distance from a grain boundary was not quantified.

Microstructures very close to the Bragg peak are likely to be affected by high concentrations of implanted hydrogen during irradiation, which can lead to nanoscale porosity, although this was not observed using STEM imaging. SRIM modelling (fig. 3.7) shows that the hydrogen implantation concentration rapidly increases above 32 µm depth, which may result in changes to the mechanisms of radiation induced microstructural changes.

CBED analysis of the thickness of the samples in the regions of interest shown in the following results is shown in tables 4.1 and 4.2.

Table 4.1: Thickness measurements for regions of interest on the Fe-Mn-Ni-Si specimen, as labelled in fig. 4.3, in order of increase dose, measured using the CBED method.

Specimen location	Dose range in measured range	Thickness (nm)
a.	0.1 dpa	170±10
b.	0.1 dpa	133±27
c.	0.2-0.5 dpa	119±9
		112±8
		148±9
		121±2
d.	0.5-1 dpa	87±28
e.	2 dpa	57±13

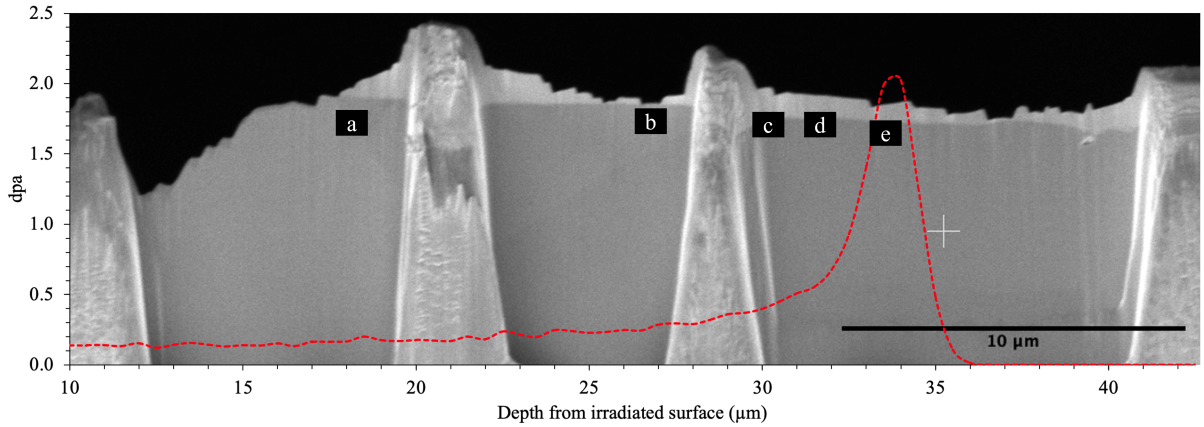
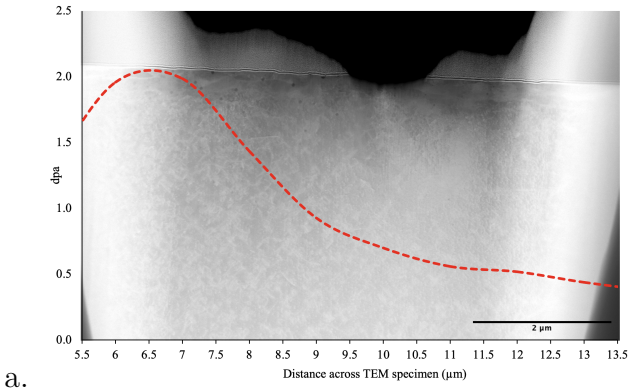


Figure 4.3: SEM image (before final thinning) showing proton-irradiated Fe-Mn-Ni-Si alloy TEM specimen with 3 thin areas covering a range of doses across the proton-irradiation dose profile . The red dotted line shows the dpa across the specimen.



a.

b.

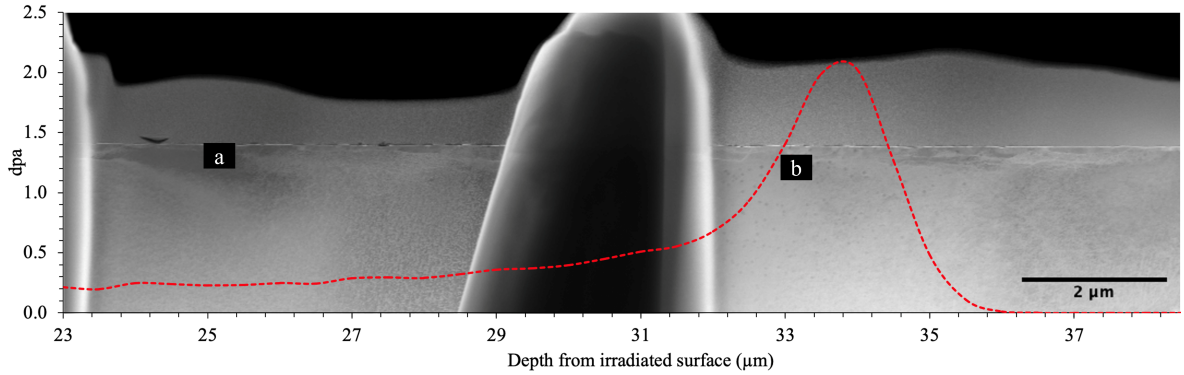


Figure 4.4: HAADF STEM images showing thin window regions of Fe-Mn-Si proton-irradiated samples used for analysis in this work. The first specimen (a.) shows a thin area covering a dose region of approximately 0.3-2.1 dpa and the second (b.) contains two thin areas, the left-hand side covering 0.1 dpa plateau region, and the right-hand side covering the peak (up to 2.1 dpa) damage region. The red dotted line shows the dpa across the specimens.

Table 4.2: Thickness measurements for regions of interest on the Fe-Mn-Si specimen (, as labelled in (b.)fig. 4.4, measured using the CBED method.

Specimen location	Dose region	Thickness (nm)
a. 2-4 µm from surface	0.1 dpa	212±27
b. 2-0.05 µm from specimen surface.	1-2 dpa	240±13

4.3 Size distribution analysis of radiation induced defects using STEM Imaging & EDX mapping

4.3.1 Fe-Mn-Ni-Si

A range of solute-rich defects, including Mn-Ni-Si enriched dislocation loops, and Mn-Ni-Si/Mn-Si-N rich precipitates can be observed across the different dose regions in the Fe-Mn-Ni-Si alloy. Figure 4.5 shows the increase in number density of solute-rich defects at 1-2 dpa, compared with 0.1 dpa in the plateau region and a unirradiated region (0 dpa). These EDX maps (fig. 4.5) have been used to calculate size distribution and number density of precipitates, and compared across datasets in fig. 4.7. These values were calculated first by thresholding EDX maps for each element (Mn, Ni and Si) using the Renyi Entropy thresholding method in FIJI (ImageJ)([175]), from fig. 4.5. For the overall values the Ni EDX map was used to acquire the largest number of features as most features were enriched in Ni. The ImageJ 'Analyze particles' function was applied to extract a list of equivalent circle diameters which have been taken as size measurements for the precipitates. CBED thickness measurements were carried out as described in chapter 3, and the total volume of precipitates in the region imaged was calculated assuming they are all spherical and that the thickness of the sample is constant across the entire area imaged. Number density was calculated as the total number of precipitates observed in the field of view divided by the observed volume.

At lower doses, there are Ni-Mn-Si enriched dislocation loops ((g.) fig. 4.15) and Ni-Mn-Si enriched defects ((a., b., c., d., e., f. in fig. 4.15). Some of these are smaller, ellipsoidal and located in the matrix, while larger ones have less uniform shape and are located on larger dislocation loops. As the dose increases, the number density of dislocation loops increases significantly, as does the number density of solute-rich defects. Above 0.1 dpa there is an increasing number

and size of nitrogen-rich precipitates, fig. 4.5. The lack of any observable solute segregation in the 0 dpa region confirms that the formation mechanism of these defects is related to radiation exposure.

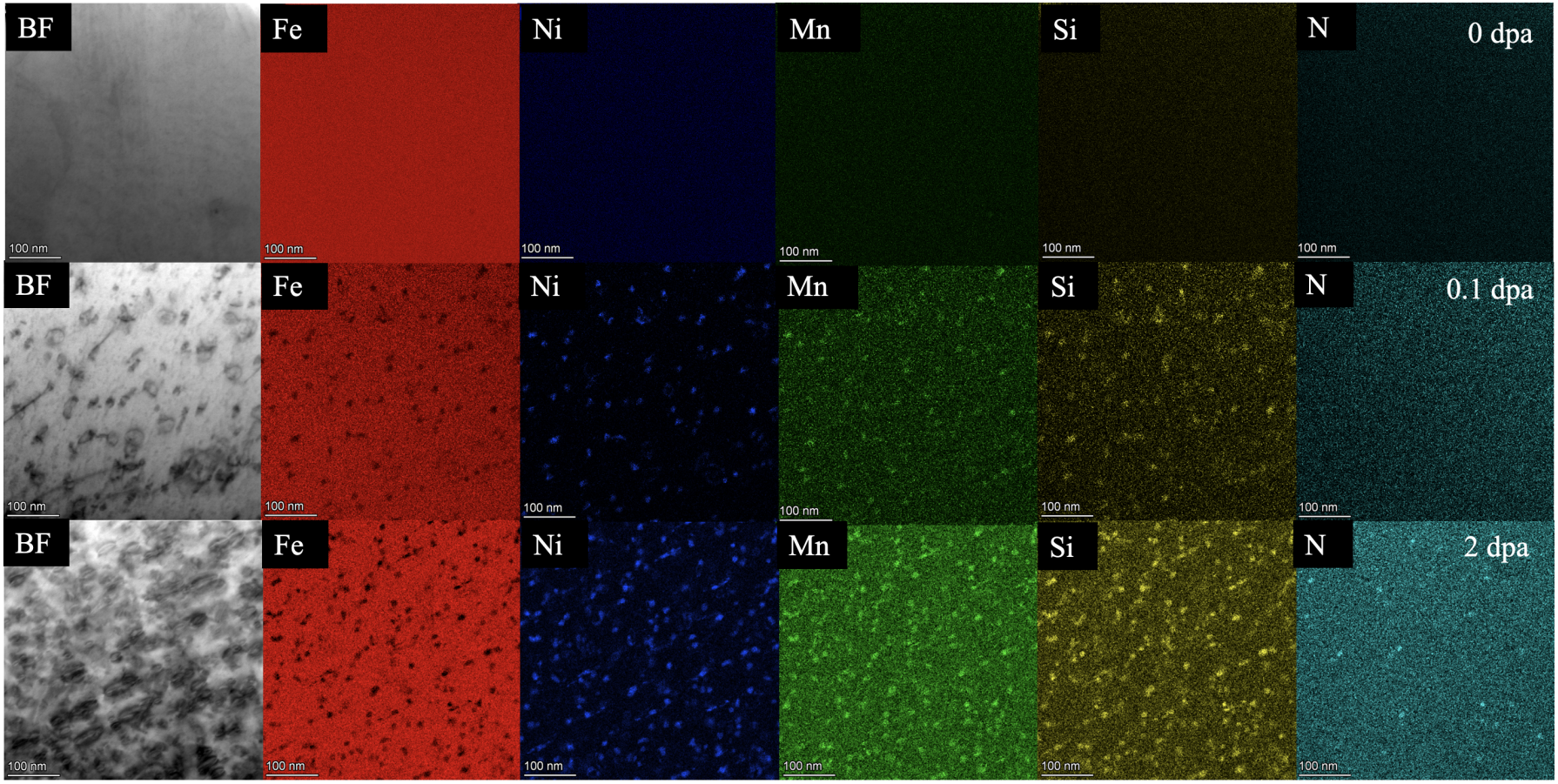


Figure 4.5: Bright field STEM images and corresponding Fe (red), Ni (blue), Mn (green), Si (yellow) and N (turquoise) EDX at. % maps showing the change in Mn-Ni-Si enriched precipitates, dislocation loop density and formation of nitrogen-rich regions with increasing dose. Extracted from Velox

Table 4.3: Quantitative data obtained from STEM imaging and Ni EDX maps, showing the change in number density, average size and volume fraction of solute-rich defects with dose. Values have been calculated using the thickness as measured in table 4.1.

Dose	N_d (m^{-3})	Average Diameter (nm)	V_f
0.15	2.64E+21	8.56 ± 0.32	0.0009 ± 0.0001
0.475	7.10E+21	9.30 ± 0.25	0.0030 ± 0.0002
0.554	8.55E+21	7.29 ± 0.89	0.0023 ± 0.0008
2.1	2.19E+22	7.87 ± 0.62	0.0116 ± 0.0027

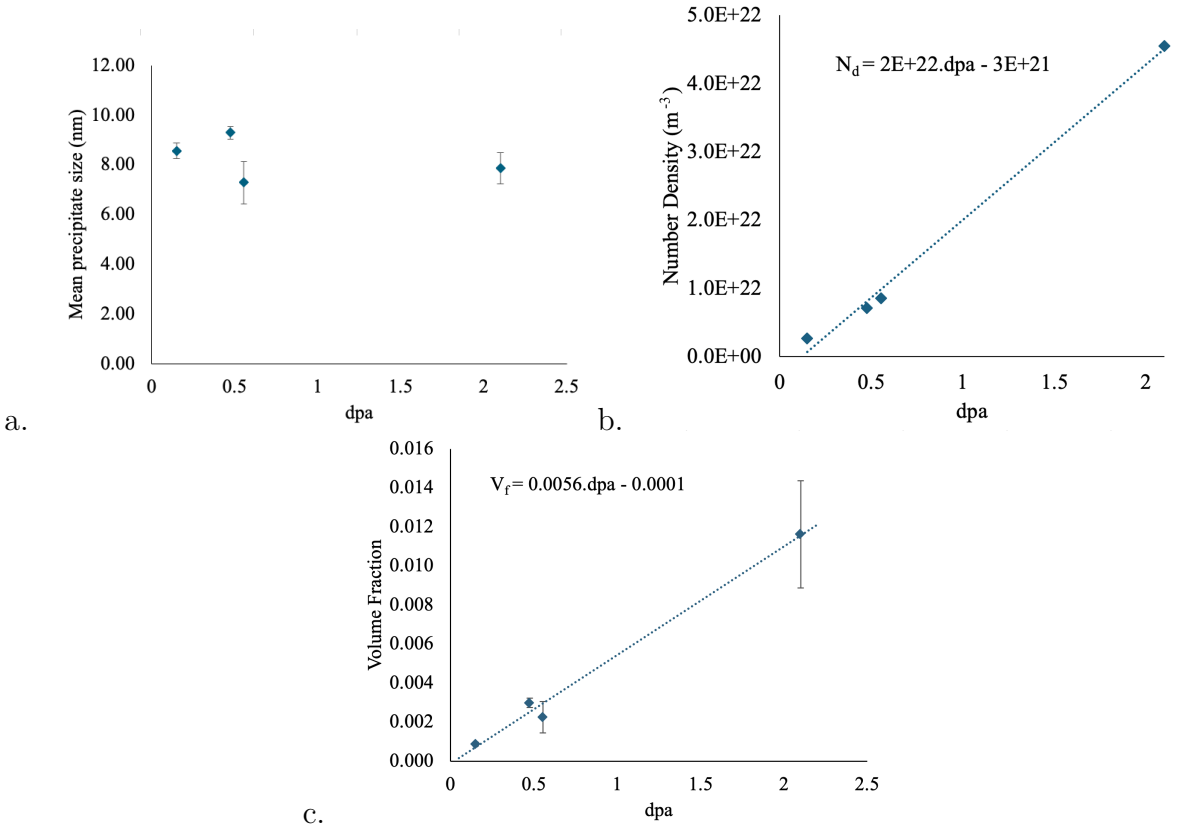


Figure 4.6: Plots of (a.) mean precipitate size vs dose, (b.) number density of precipitates vs dose, and (c.) volume fraction of precipitates vs dose for Mn-Ni-Si precipitates observed in the irradiation Fe-Mn-Ni-Si alloy.

Table 4.3 and fig. 4.6 summarises the measured number density, average precipitate size and calculated volume fractions for a range of dose regions in the Fe-Mn-Ni-Si alloy. The Ni map was used to quantify the Ni rich precipitates, as these are the most significant new microstructural features observed after irradiation. The number density and volume fraction increase linearly with the dose, with an order of magnitude increase in number density from 0.1 dpa to 2 dpa

(fig. 4.6).

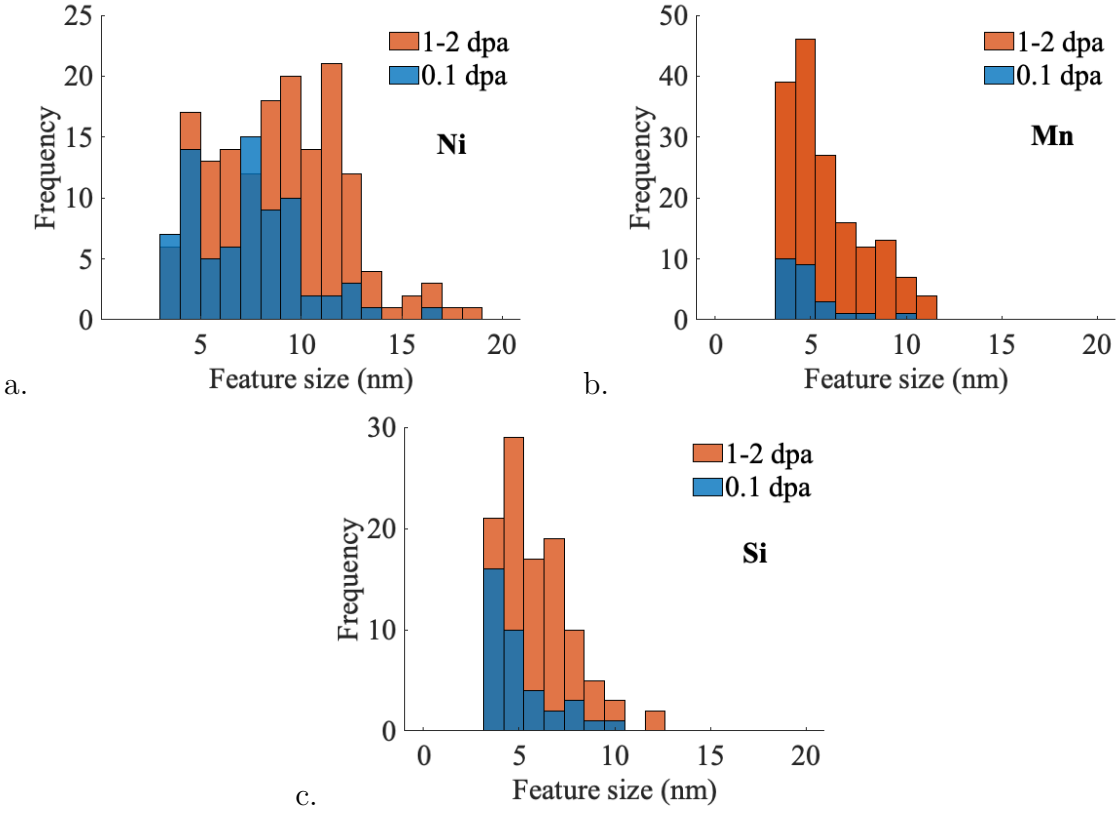


Figure 4.7: Histograms showing the size distributions calculated using FIJI ([175]) software and EDX maps of the Fe-Mn-Ni-Si alloy shown in fig. 4.5 A Renyi entropy thresholding algorithm was applied to each of the EDX maps to identify enriched (Mn,Ni & Si) regions corresponding to solute-rich defects and data presented above shows the 0.1 dpa and 1-2 dpa results for each data set, for all precipitates with a greater area than $10\,\mathrm{nm}^2$. (a.) Ni, (b.) Mn, (c.) Si. Frequency is the number of precipitates measured in each size bin.

All precipitates grow and increase in number, in a comparable volume, with increasing dose, fig. 4.7. The Mn and Si plots show a narrower distribution of precipitate sizes than the Ni plot (fig. 4.8).

The size distributions of precipitates varies depending on the EDX element map used for analysis, suggesting there are multiple populations of precipitates with different compositions. Figure 4.8 shows that Mn and Si are always found in the same regions, producing very similar size distributions, but Ni rich precipitates have a much wider size range, and have a larger average size compared with the average size of Mn and Si containing features. This is consistent with the features identified in fig. 4.5. Smaller precipitates seem to be more enriched in Mn than

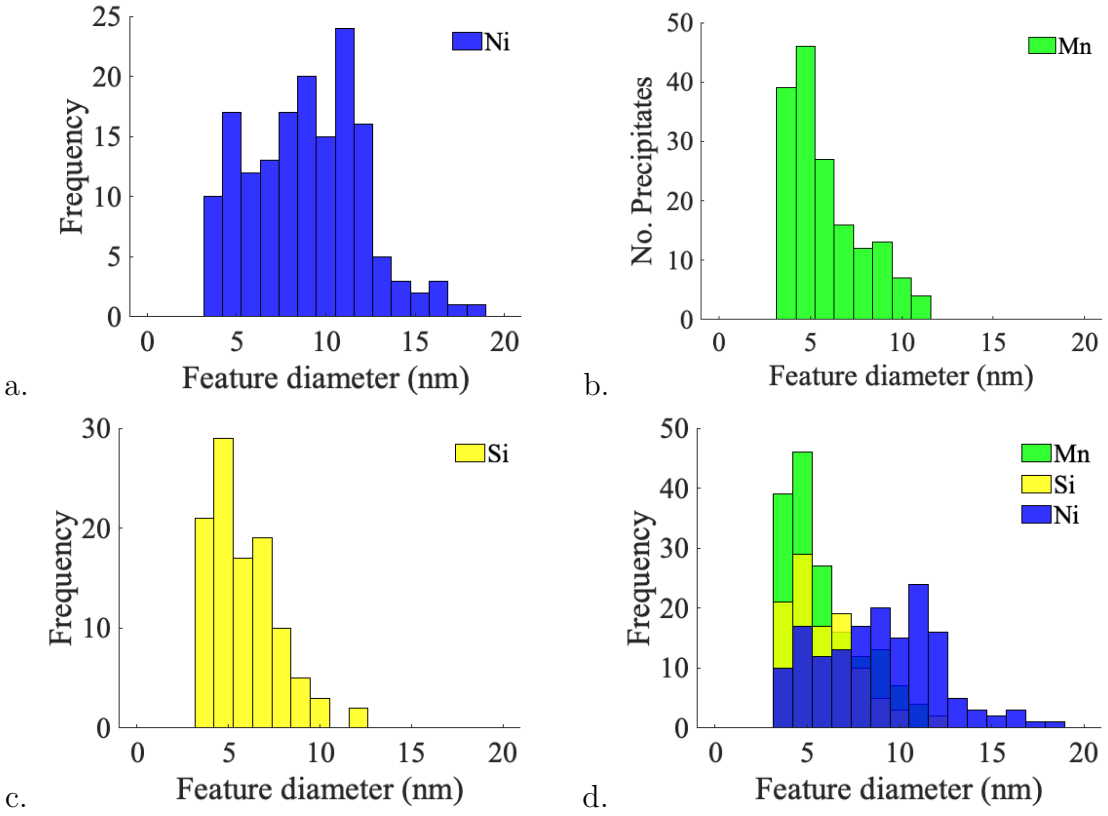


Figure 4.8: Histogram showing the size distribution of precipitates in the 2 dpa region of the Fe-Mn-Ni-Si sample, for each elemental EDX map shown on the bottom row of fig. 4.5, with (a.) Ni showing a different pattern in size to (b.) Mn and (c.) Si.

Ni and Si, whereas at larger precipitate size, they become lower in Mn and Si than Ni, fig. 4.8. Further analysis of individual precipitate composition in the following section shows that there are two populations of precipitates, some rich in Ni, Mn and Si and others containing N, Mn and Si.

4.3.2 Fe-Mn-Si

A population of Mn-Si-N rich precipitates were observed in the Fe-Mn-Si alloy after irradiation. The number density and average size of precipitates increase between 0.1 and 2.0 dpa, as shown in figs. 4.9 and 4.10, and calculated as for the Fe-Mn-Ni-Si datasets, this time using the HAADF images for thresholding and precipitate analysis. The precipitates have a cubical morphology at higher doses of 2 dpa. 170 Mn-Si-N rich precipitates have been measured across a field of view of $5.25 \times 1.5\,\mu m$, corresponding to a dose range of 0.35-1.98 dpa, using the HAADF and Mn EDX maps to ensure features are Mn rich. Mean size, number density and volume fraction

of precipitates is plotted against dose, this time assuming a cubical shape, fig. 4.10. Volume fraction increases linearly with dose, and number density appears to begin to level off at higher doses. There is a general increase in the average precipitate size with dose.

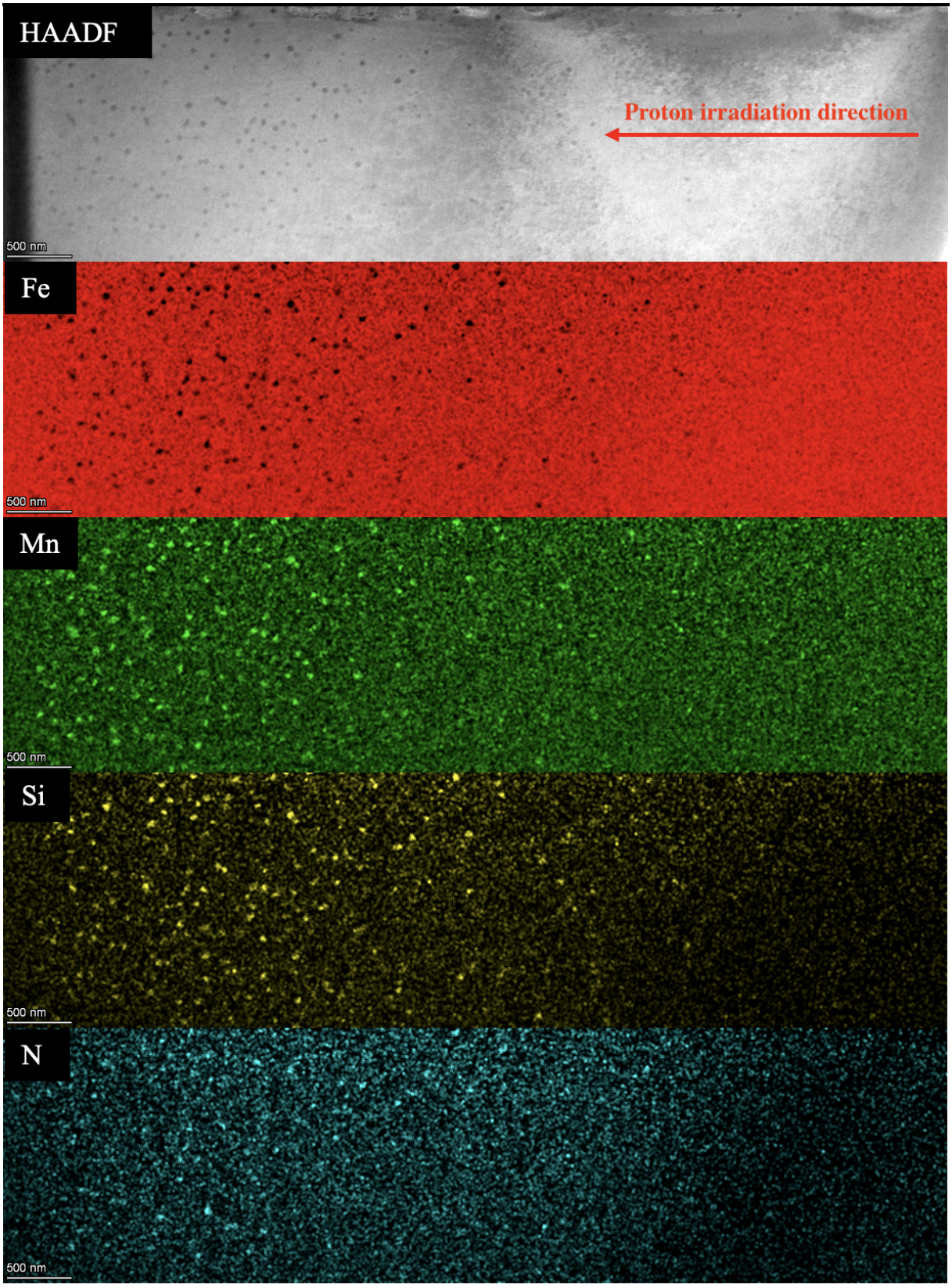


Figure 4.9: STEM HAADF image and corresponding EDX elemental maps for Fe (red), Mn (green) and Si (yellow), and N (turquoise), showing an increase in size and number density of precipitates with increasing dose from 0.38 dpa on the far right-hand side, to 1.97 dpa on the far left, as shown in fig. 4.10.

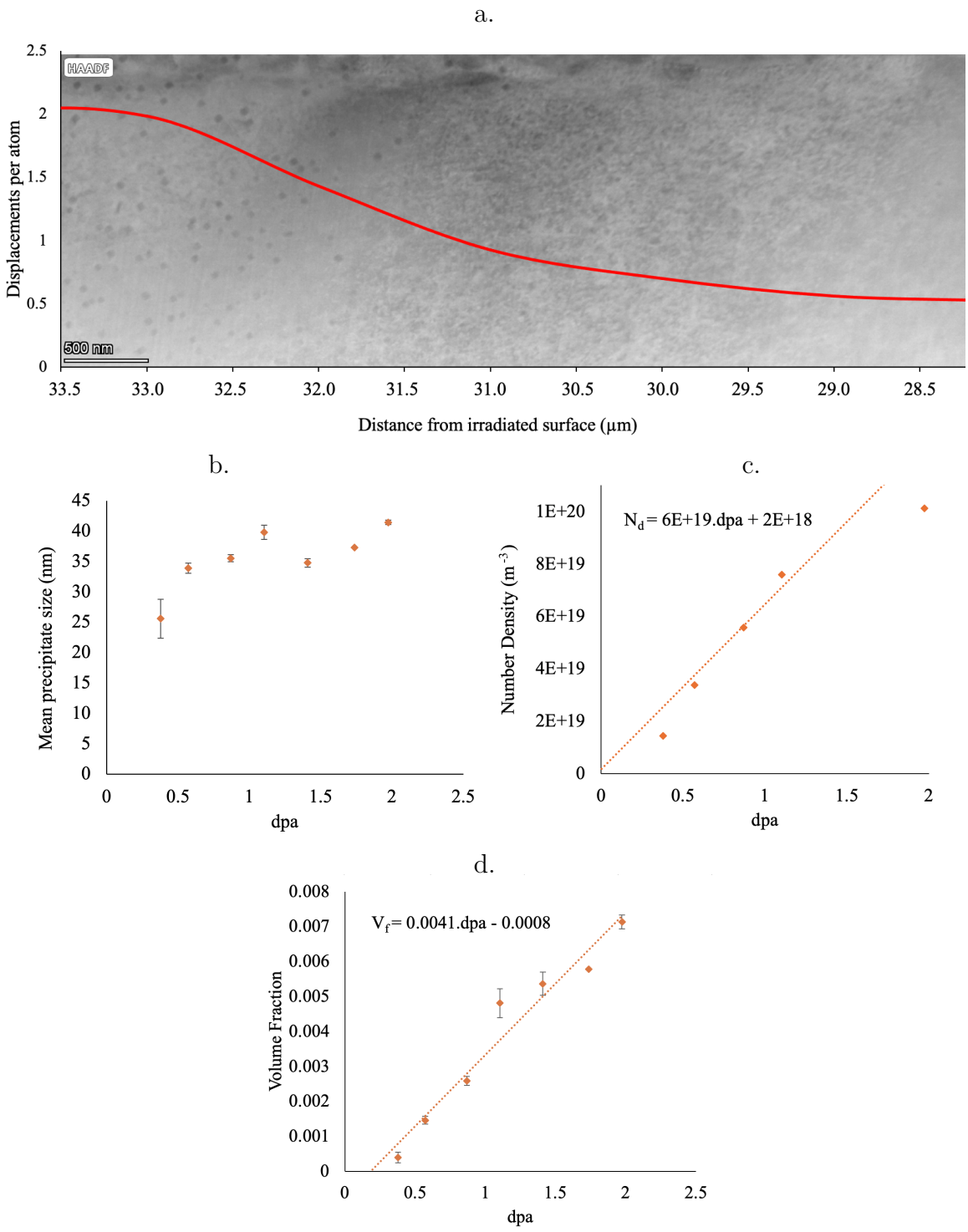


Figure 4.10: (a.) STEM HAADF image with overlaid radiation dose profile as a function of proton depth for Fe-Mn-Si alloy, (b.) plot of mean precipitate size vs dose, (c.) Number density of precipitates vs dose, (d.) Volume fraction of precipitates vs dose.

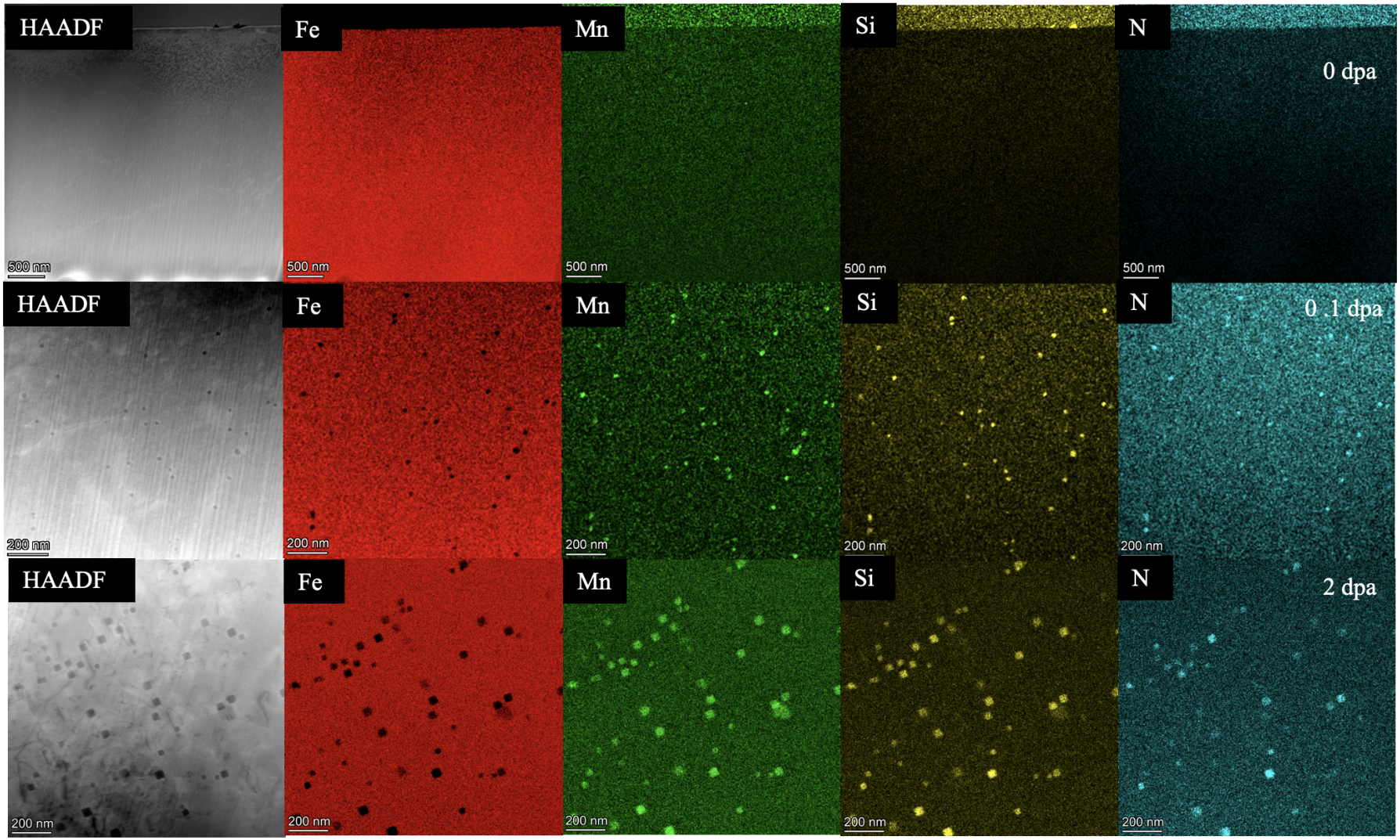


Figure 4.11: STEM HAADF image and corresponding EDX elemental maps for Fe (red), Mn (green) and Si (yellow), and N (turquoise), showing regions of the Fe-Mn-Si sample at 0 dpa, 0.1 dpa and 2 dpa.

Table 4.4: Quantitative data obtained from HAADF STEM images of the Fe-Mn-Si alloy, showing the change in number density, average size and volume fraction of solute-rich defects with dose. Values have been calculated using the thickness of each region imaged, shown in table 4.2.

Dose Region	Number Density (m^{-3})	Mean precipitate size (nm)	Volume Fraction	Mean aspect ratio
2.0 dpa	$1.21 \pm 0.09 \times 10^{20}$	33.7 ± 1.1	0.0054 ± 0.0004	1.01 ± 0.01
0.1 dpa	$4.02 \pm 0.97 \times 10^{19}$	21.2 ± 0.7	0.0004 ± 0.0001	0.98 ± 0.03

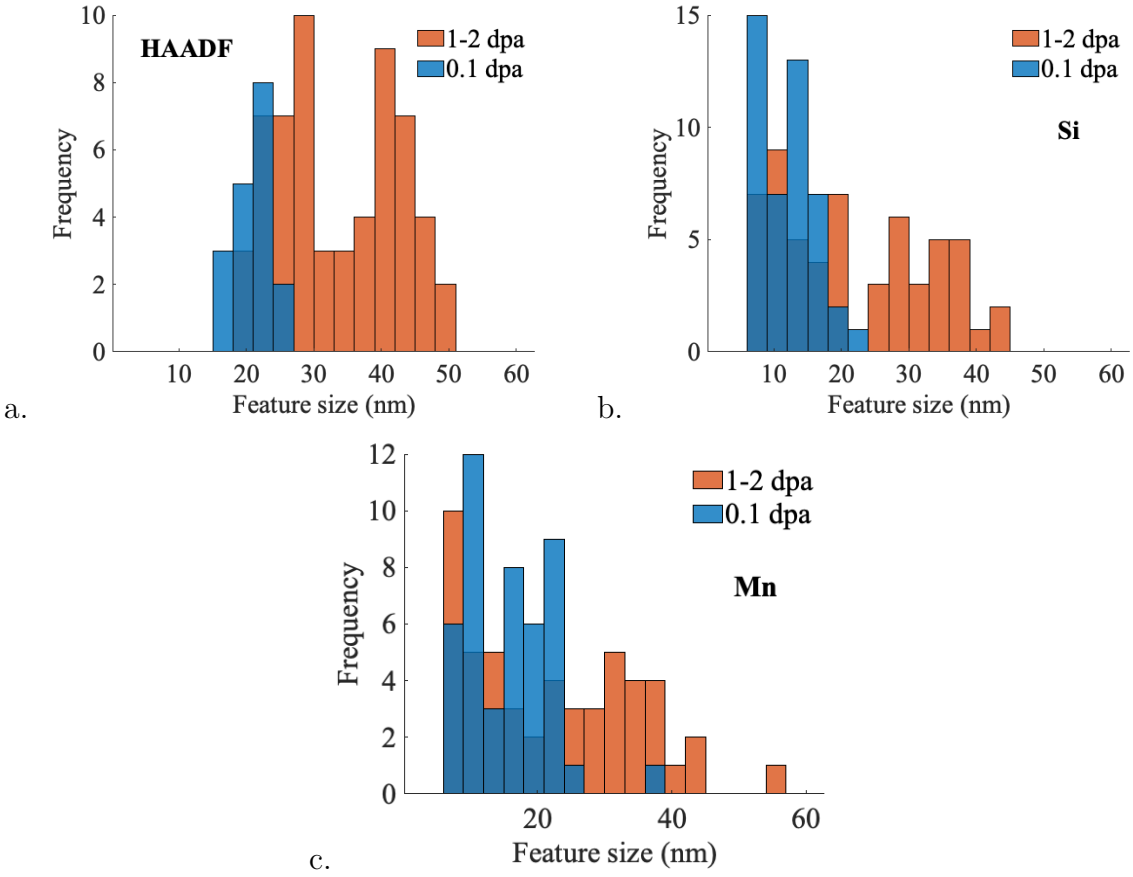


Figure 4.12: Size distribution histograms obtained using (a.) HAADF images, and Renyi entropy thresholding of (b.) Si and (c.) Mn EDX maps (fig. 4.11), showing an increase in average size of solute-rich precipitate with dose.

All the plots show a similar trend of increasing average size with dose, with a maximum size in the 0.1 dpa region of around 20-25 nm, and a maximum size in the 2 dpa region of 45-55 nm, fig. 4.12. There is a difference in the measured size between the HAADF datasets and the EDX maps, with the EDX data having a smaller average size. As the precipitates have smaller thicknesses than the overall specimen, there will be scattering from the matrix contributing to

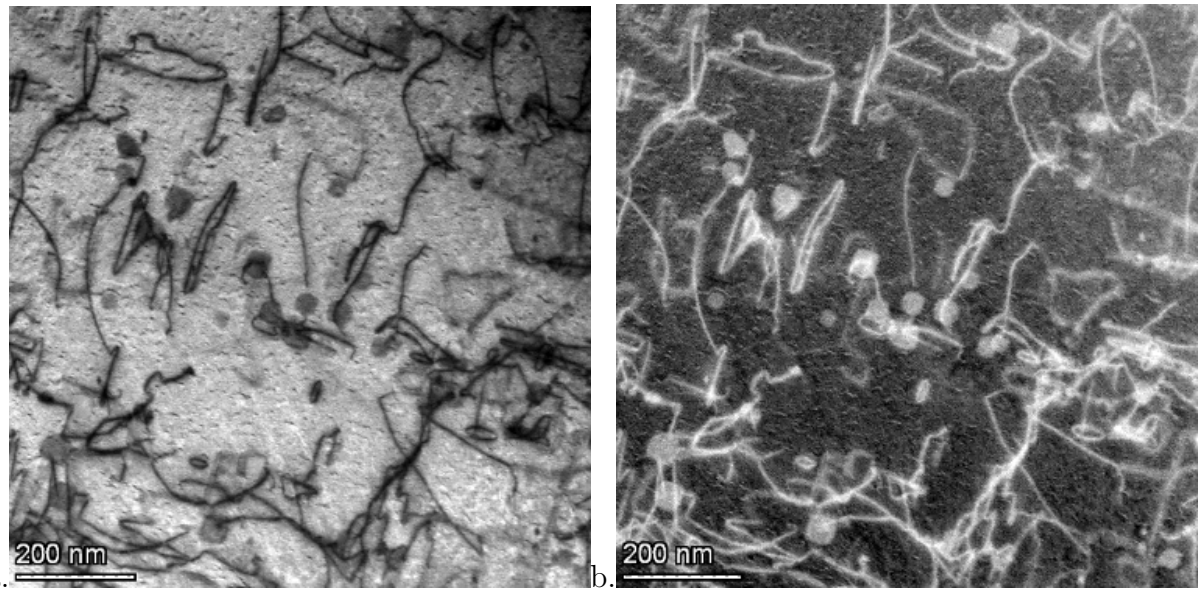


Figure 4.13: On-axis STEM images, taken on the [$3\bar{1}1$] zone axis (a.) BF & (b.) ADF images of 2 dpa proton irradiated Fe-Mn-Si showing Mn-Si rich precipitates and dislocation loops.

noisier interfaces in EDX maps than are observed in STEM imaging, making the precipitates look smaller. Only the centre of the precipitates will give the strongest EDX signals, so thresholding the intensity will cut off the precipitate interface regions. This observation suggests that the sizes of precipitates observed in the Fe-Mn-Ni-Si alloy (fig. 4.5) using EDX map data are also likely to be underestimates. In this case the precipitates have much poorer mass contrast so could not be measured using HAADF image analysis. Figure 4.13 shows an on-axis STEM image showing the 2 dpa region with distinctly cubical precipitates and a mixture of large rectilinear dislocation loops and smaller circular loops, that are not clearly associated with the precipitates.

4.4 Composition analysis of defect types using STEM-EDX

4.4.1 Fe-Mn-Ni-Si

Higher magnification STEM-EDX data shows that multiple types of solute-rich defect are present in the irradiated regions, and that composition varies with dose. At 0.1 dpa there are small ellipsoidal Ni-rich precipitates with no obvious association to radiation induced defects such as dislocation loops. There are also precipitates enriched in Ni which are larger, with less uniform

morphology, located at, or on, dislocation loops, and dislocation loops have been observed with significant Ni, Mn, and Si enrichment figs. 4.14, 4.15 and 4.17. The EDX spectrum in fig. 4.16 shows the increase in characteristic X-ray emissions from Ni, Mn, and Si relative to the Fe matrix. EDX line scans show that all solute-rich features observed in the 0.1 dpa condition are Ni-Mn-Si rich, with the highest enrichment of Ni, followed by Mn and Si, fig. 4.17. There are three general categories of feature observed in fig. 4.15; those with high Ni content at an approximate Ni:Mn:Si ratio of 4:2:1, lower Ni content with the Ni:Mn:Si ratio around 2:2:1 and a Ni-Mn-Si enriched dislocation loop, fig. 4.17.

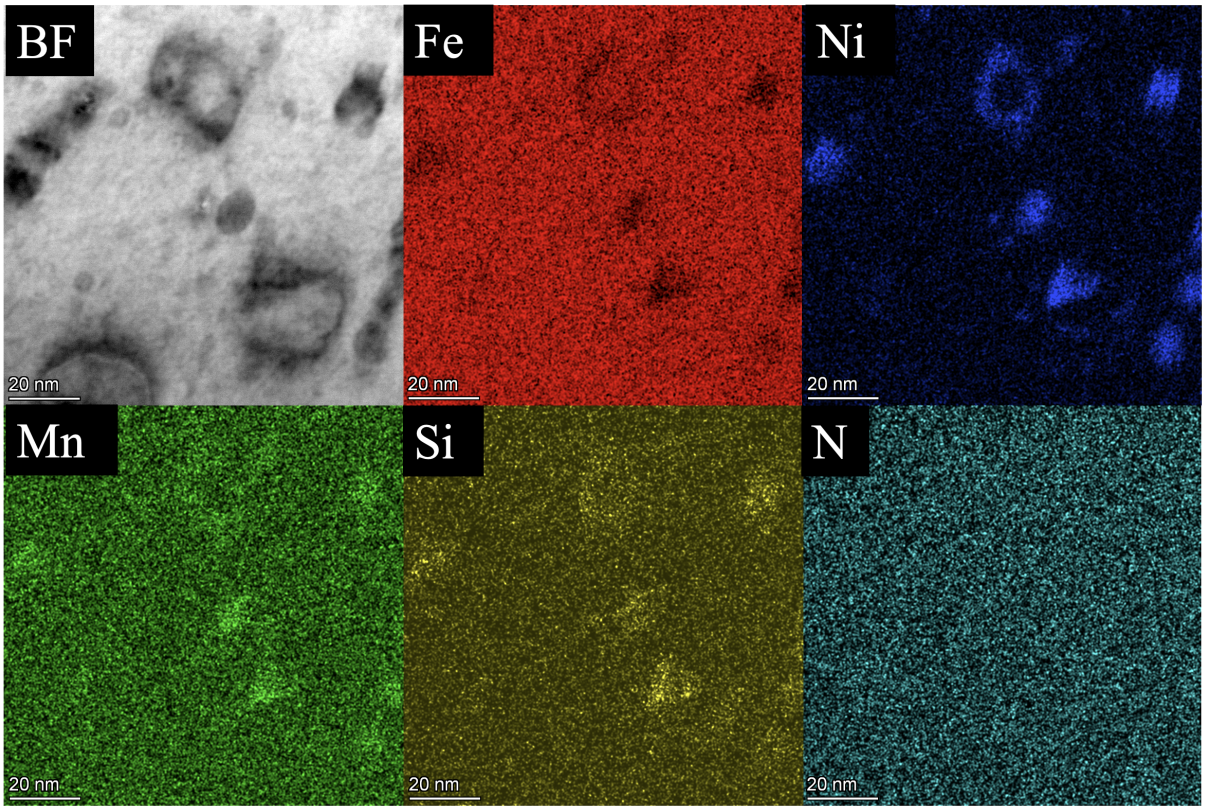


Figure 4.14: High magnification BF STEM image and at.% EDX maps of 0.1 dpa proton irradiated Fe-Mn-Ni-Si alloy. Fe (red), Ni (blue), Mn (green), Si (yellow), N (turquoise).

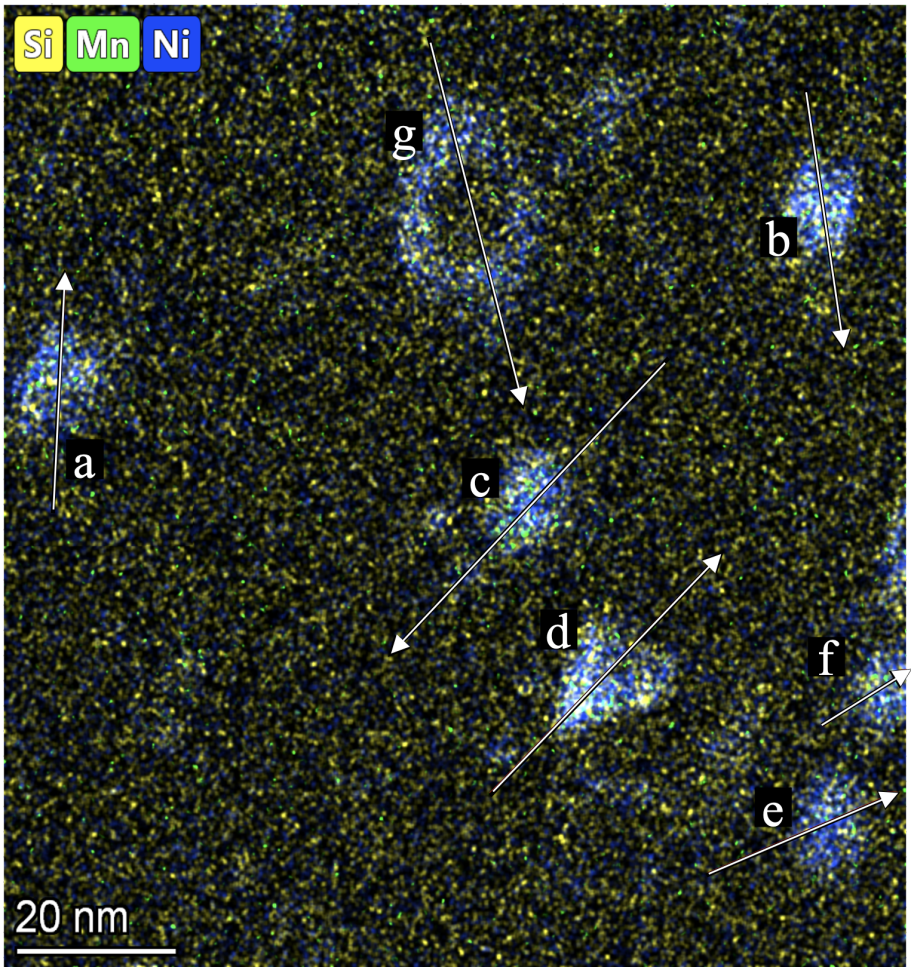


Figure 4.15: Mn, Si, and Ni overlaid EDX map of 0.1 dpa proton irradiated Fe-Mn-Ni-Si, showing 7 solute enriched defects. Labels correspond to line scan plots shown in fig. 4.17.

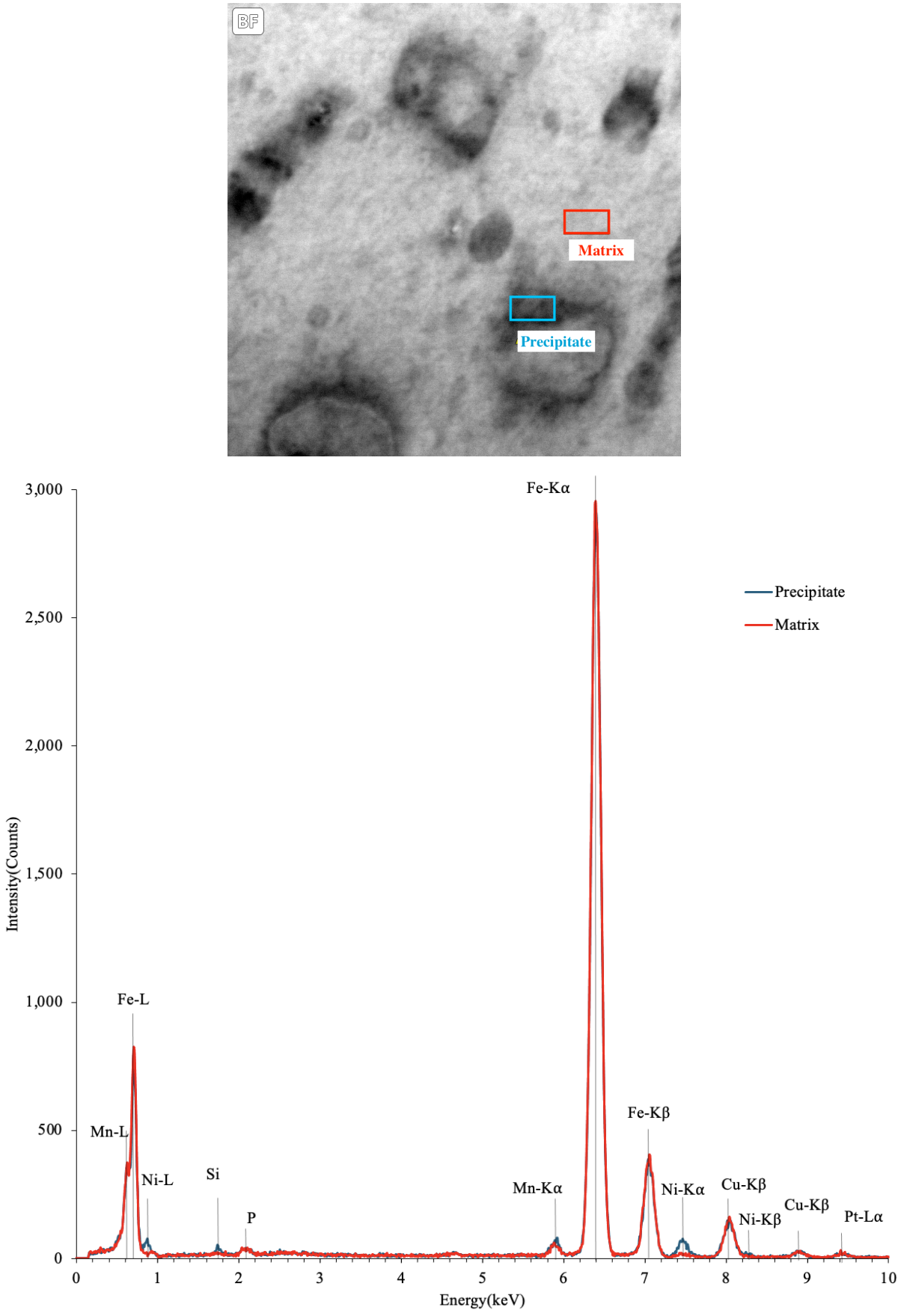


Figure 4.16: EDX area spectrum taken from Ni-Mn-Si precipitate (labelled as region d in fig. 4.15) shown in the BF STEM image above the spectrum, and a matrix region with equivalent area, with characteristic X-ray peaks labelled by emission type. Cu peaks are present due to scattering from the copper grid on which the sample was mounted. The precipitate shows increase in Ni, Mn, and Si emissions relative to the matrix.



Figure 4.17: Line scans corresponding to precipitates and an enriched dislocation loop in 0.1 dpa proton-irradiated Fe-Mn-Ni-Si, labelled in fig. 4.15 covering a range of precipitate types and a dislocation loop (g). Atomic fraction has been calculated using a thickness correction applied in Velox, and underestimates precipitate composition due to matrix Fe scattering.

At 0.5 dpa, there are two types of precipitate. There are Ni rich precipitates and Mn-Si-N rich precipitates with a cubical shape and Ni shells, fig. 4.18. There is a clear split in precipitate type based on composition which can be seen in ternary diagrams of precipitate composition measured as a function of dpa (see fig. 4.28). Figures 4.19 and 4.20 (a), (b) and (e), clearly show Mn, Si and nitrogen-rich precipitates with an approximate stoichiometry of $MnSiN_2$. These precipitates contain higher levels of Ni than the matrix, particularly at the boundaries, suggesting a Mn-Si-N rich core and Ni shell structure. The other 4 precipitates are enriched in Ni, but unlike the 0.1 dpa precipitates, the ratio of Si to Mn is much closer to 1:1, with more Si than Mn in the larger precipitates (c & d) suggesting a compositional evolution with size. In general, the atomic fraction of solutes measured in this region of the sample is higher than in the 0.1 dpa region due to the sample being thinner. Fe content cannot be determined conclusively as precipitates are not through thickness. Figures 4.19 and 4.20 shows the cubical precipitates have a core-shell structure with Mn-Si-N centre and a Ni enriched shell at the edges of the feature.

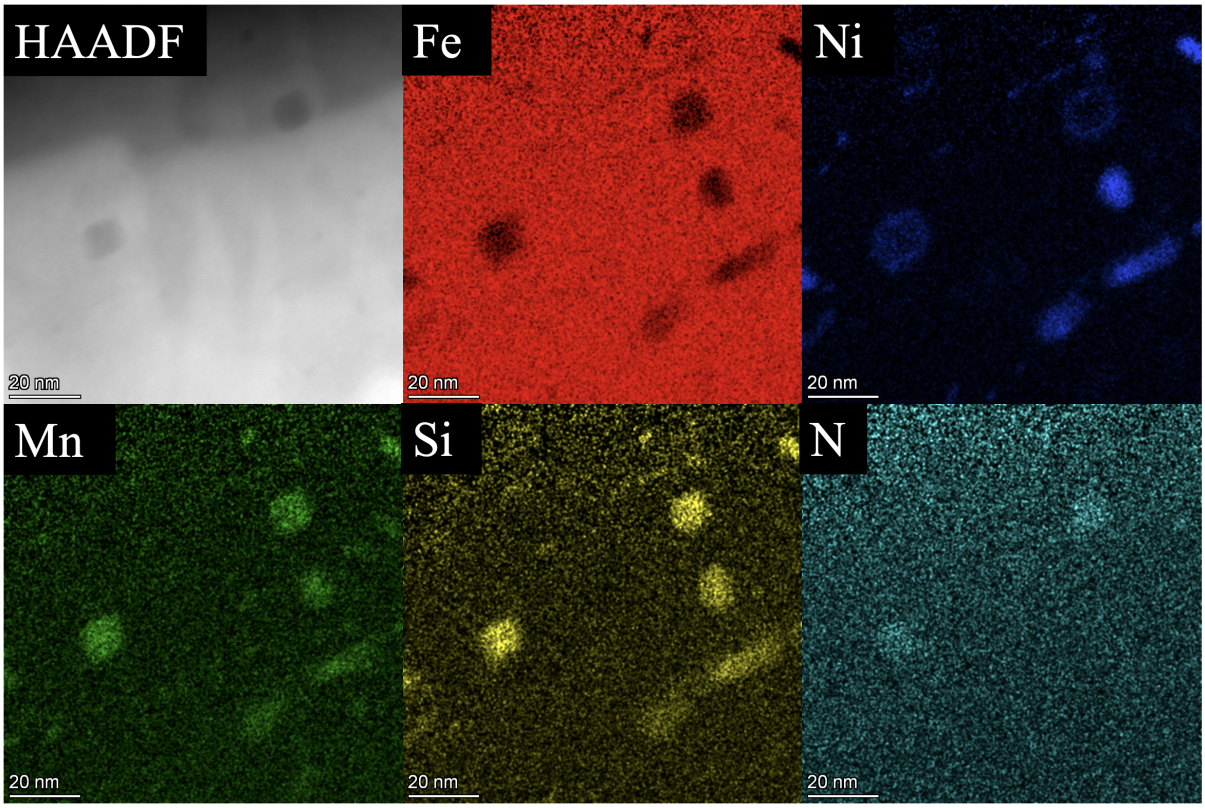


Figure 4.18: High magnification HAADF STEM images and at.% EDX maps of 0.5 dpa proton irradiated Fe-Mn-Ni-Si alloy. Fe (red), Ni (blue), Mn (green), Si (yellow), and N (turquoise).

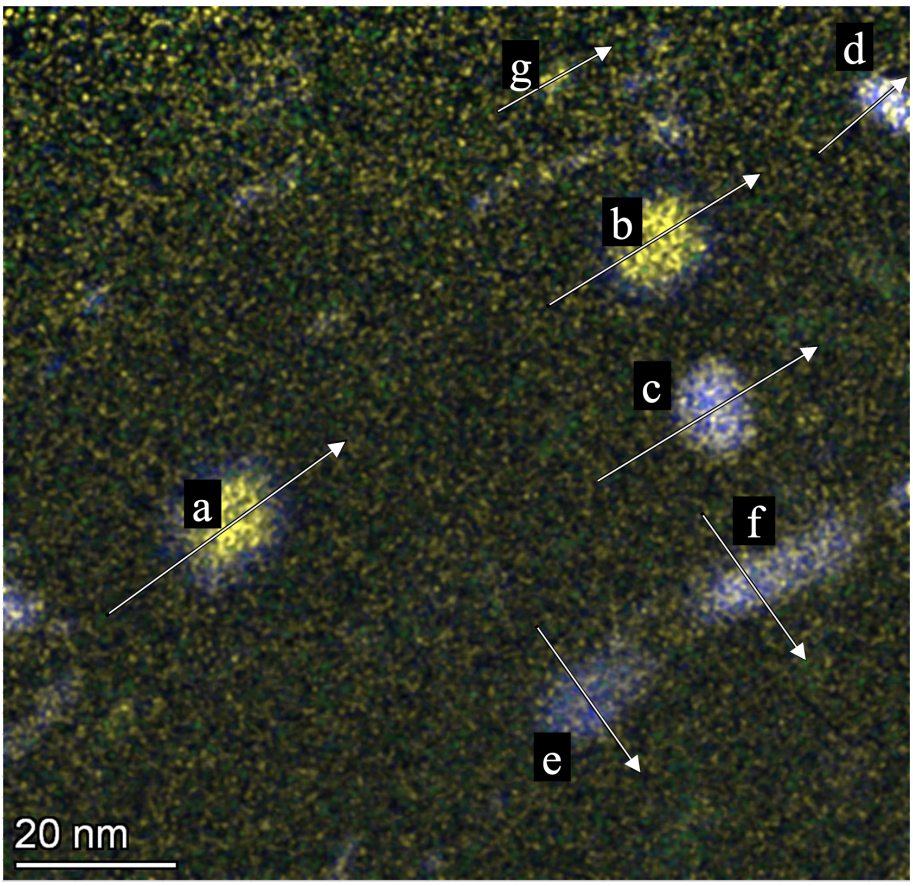


Figure 4.19: Mn (green), Si (yellow) and Ni (blue) overlaid EDX map of 0.5 dpa proton irradiated Fe-Mn-Ni-Si, showing 7 solute enriched defects. Labels correspond to line scan plots shown in fig. 4.20

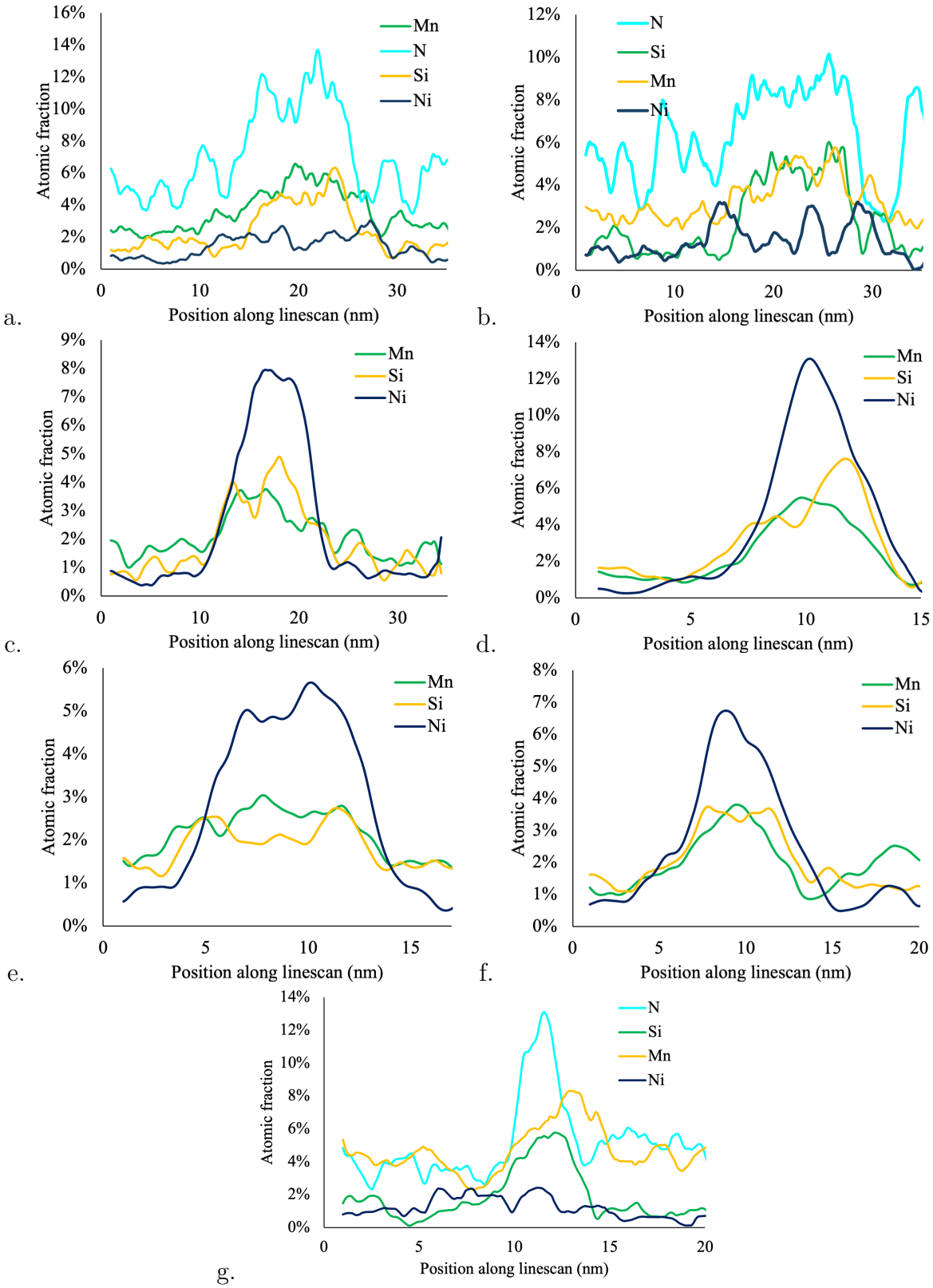


Figure 4.20: Line scans corresponding to solute enriched precipitates in 0.5 dpa proton irradiated Fe-Mn-Ni-Si, labelled in fig. 4.19 covering a range of precipitate types. Atomic fraction has been calculated using a thickness correction applied in Velox, and underestimates precipitate composition due to matrix Fe contributing to the signal in each region. Nitrogen content has been omitted for Ni rich precipitates, which showed no N peak in the EDX spectrum.

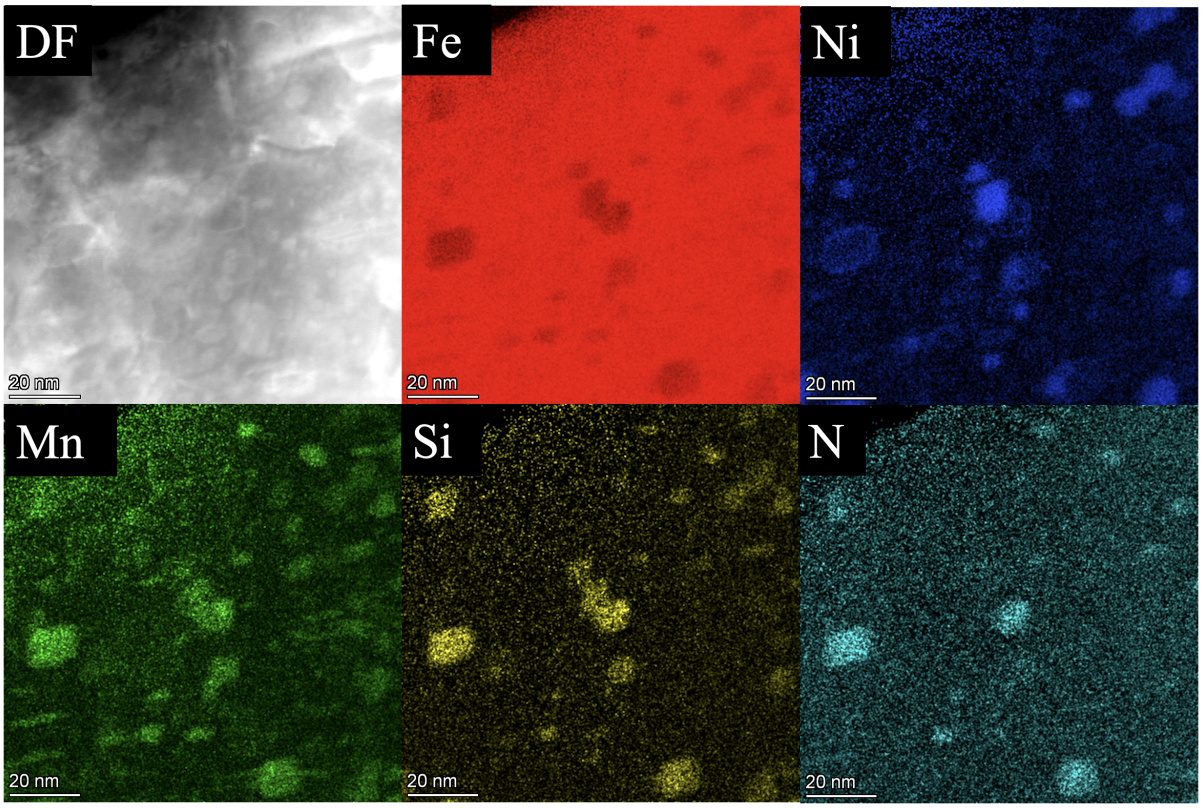


Figure 4.21: High magnification DF STEM image and at.% EDX maps of approximately 2 dpa proton irradiated Fe-Mn-Ni-Si alloy (approaching peak region). Fe (red), Ni (blue), Mn (green), Si (yellow), and N (turquoise).

In the peak radiation damage region, at 2 dpa, 27 solute-rich defects have been measured using EDX line scans to examine their composition. These are split into two categories: Ni rich precipitates, fig. 4.22, and Ni lean, nitrogen-rich precipitates, fig. 4.25.

A comparison of EDX spectra taken from the matrix and nitrogen-rich precipitate (j, fig. 4.25) shows an increase in N, Mn and Si in the region, with no increase in nickel content compared with the matrix, fig. 4.23.

Similarly to the 0.5 dpa region, there are two key types of precipitate: Ni rich precipitates, and Mn-Si rich precipitates. These Mn-Si precipitates have a Ni enriched shell around them, as can be seen in scans g, c, and i in fig. 4.22 and m, a and d in fig. 4.25. These plots show peaks in Ni concentration at the edges of the Mn and Si peaks, and then a depletion of Ni content in the centre. There is large variation in the Ni shell centre composition in similar shaped profiles, for example (c.), (g.) and (l.) in fig. 4.22 and (a.) in fig. 4.25. This suggests that the composition in the centre of the precipitates is different to the outer regions. This could be due to the diffusion

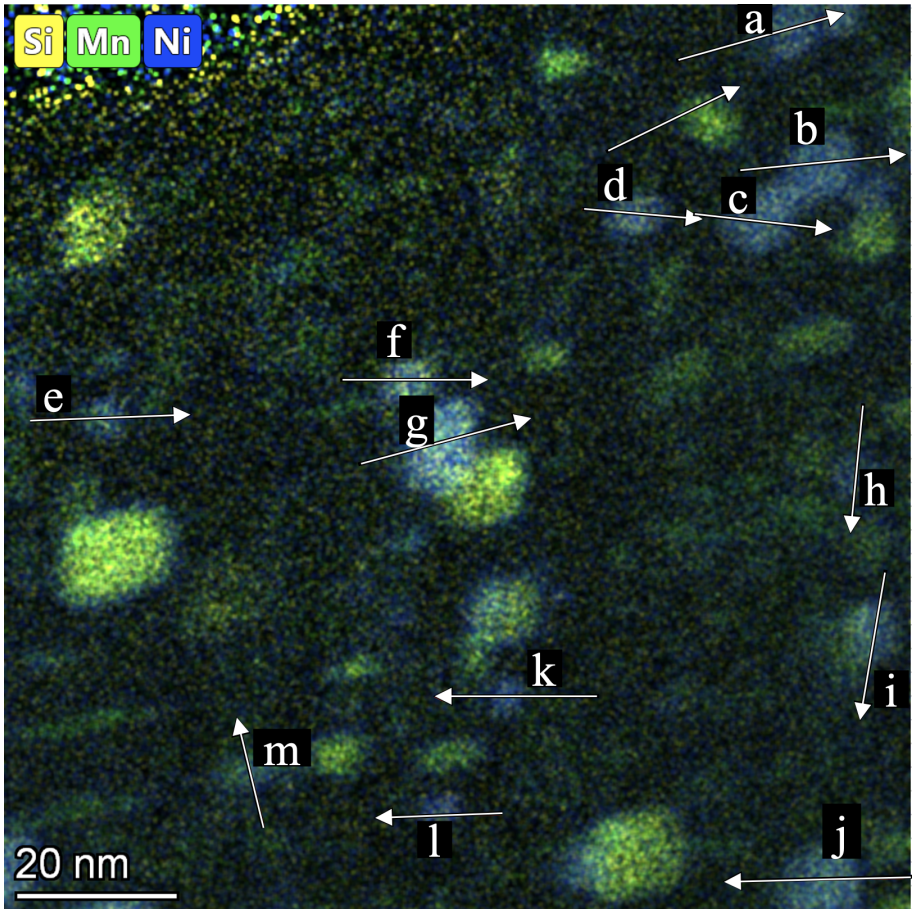
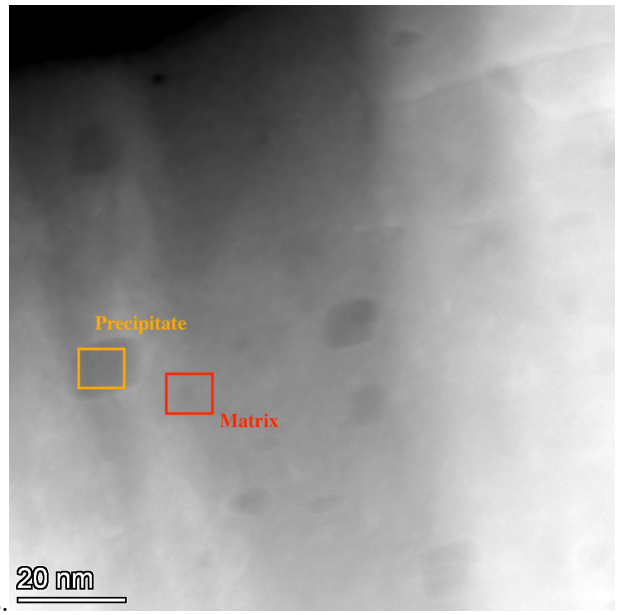
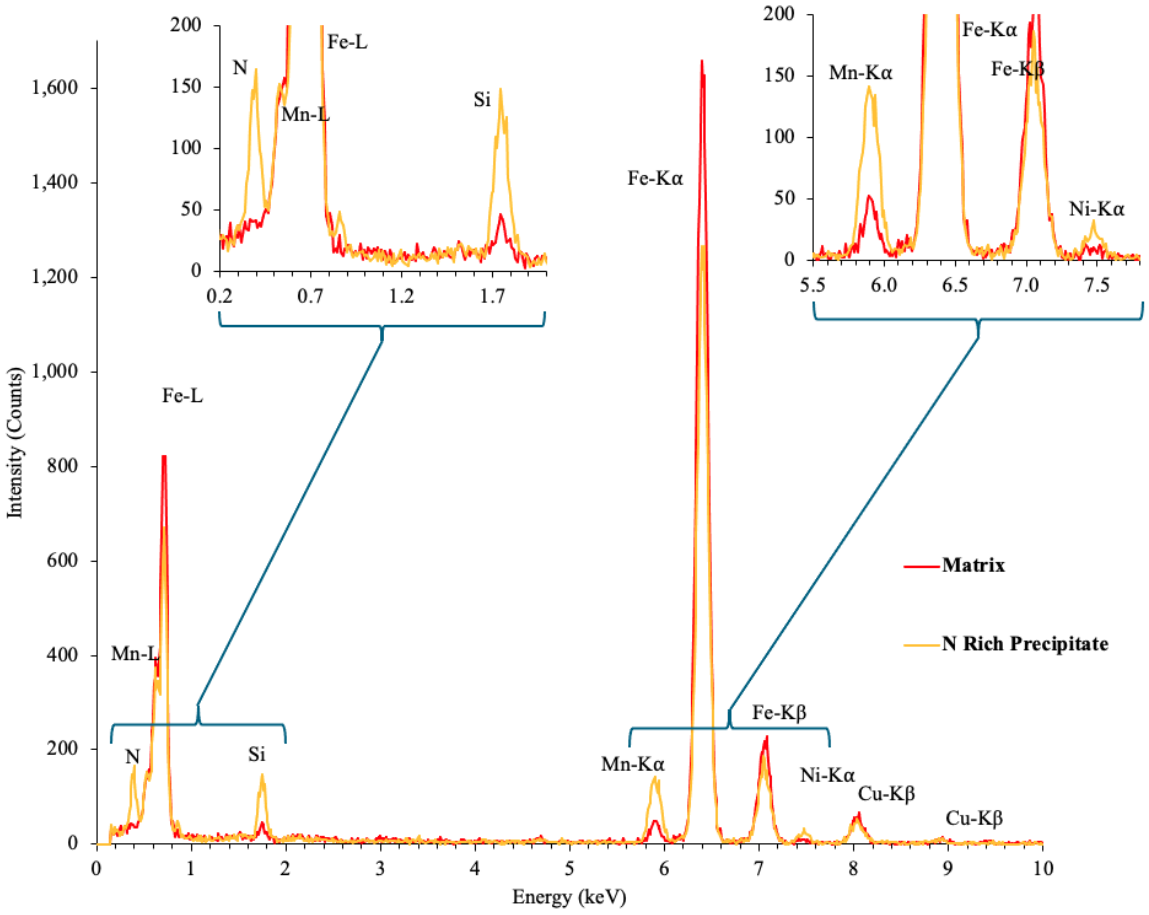


Figure 4.22: Mn, Si and Ni overlaid EDX map of 2 dpa proton irradiated Fe-Mn-Ni-Si. Labels correspond to line scan plots shown in fig. 4.24, and include all Ni rich precipitates observed in this region.



a.



b.

Figure 4.23: (a.) BF STEM image of 2 dpa irradiated region in the Fe-Mn-Ni-Si alloy, showing regions of nitride and matrix used for comparison in the EDX spectrum (uncorrected) (b.), showing spectra from equivalent areas of the matrix and a nitrogen-rich precipitate (corresponding to (j.), fig. 4.25).

of Ni, under irradiation, to the interface between Mn-Si rich precipitates or it could be that there is some diffusion of Ni out of Mn-Ni-Si rich precipitates, where nitrogen concentrations have increased sufficiently to stabilise Mn-Si nitride precipitates. Some precipitates are very low in Ni, whereas others are still highly enriched compared with the matrix, despite showing a Ni rich shell. This may be due to the effect of size on calculated composition, as smaller precipitates show lower quantities of Fe, due to the matrix not being omitted from these plots.

In general, the Ni rich precipitates in this region are slightly smaller than the Mn Si rich precipitates, suggesting they are forming first, and Mn-Si nitrogen features are nucleating inside these precipitates and ejecting the Ni as they grow.

The ratio of Mn:Si in the nitrogen-rich precipitates varies significantly across the precipitates measured in this region. At the greatest, the ratio of Mn:Si is approximately 3:1 (l, fig. 4.25) and the lowest is around 1:1 (d, e, fig. 4.25). This contrasts with observations in the 0.5 dpa sample, where the Ni lean precipitates have higher Si content than Mn.

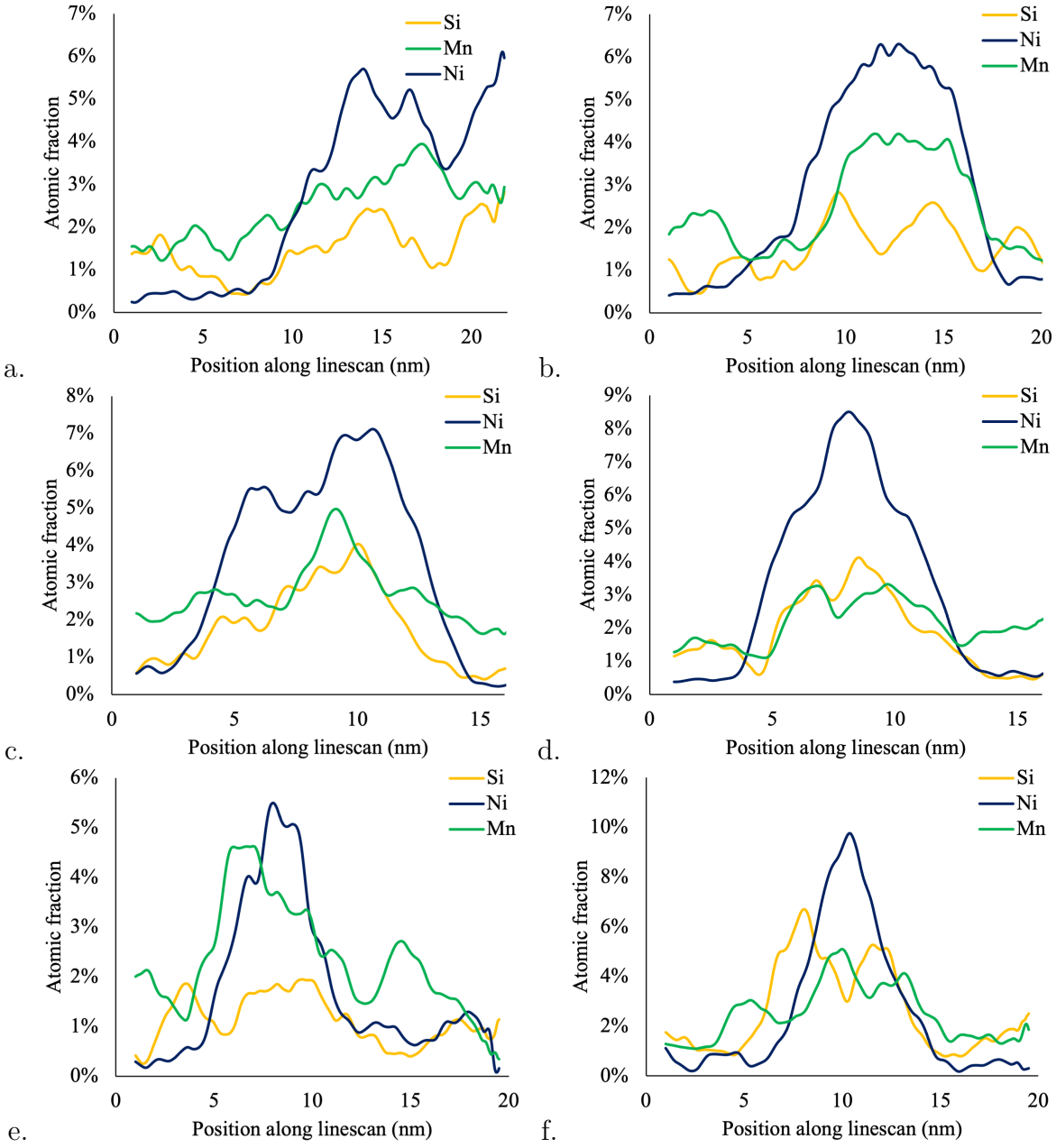


Figure 4.24: Linescans corresponding to Ni rich precipitates labelled in fig. 4.22. Atomic fraction has been calculated using a thickness correction applied in Velox, and underestimates precipitate composition due to matrix Fe scattering.

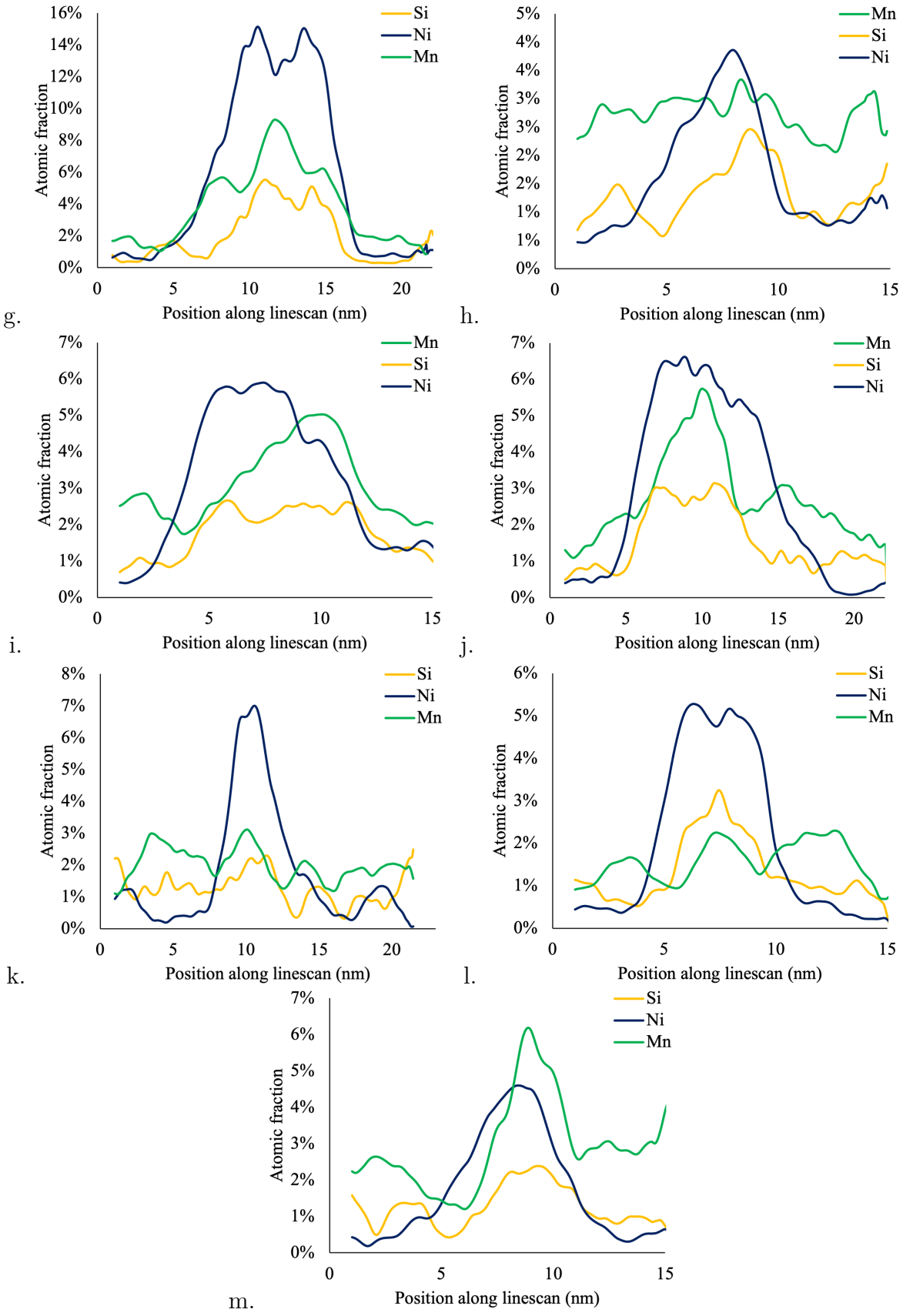


Figure 4.24: Linescans corresponding to Ni enriched precipitates, in 2 dpa proton-irradiated Fe-Mn-Ni-Si, labelled in fig. 4.22. Atomic fraction has been calculated using a thickness correction applied in Velox, and underestimates precipitate composition due to matrix Fe scattering.

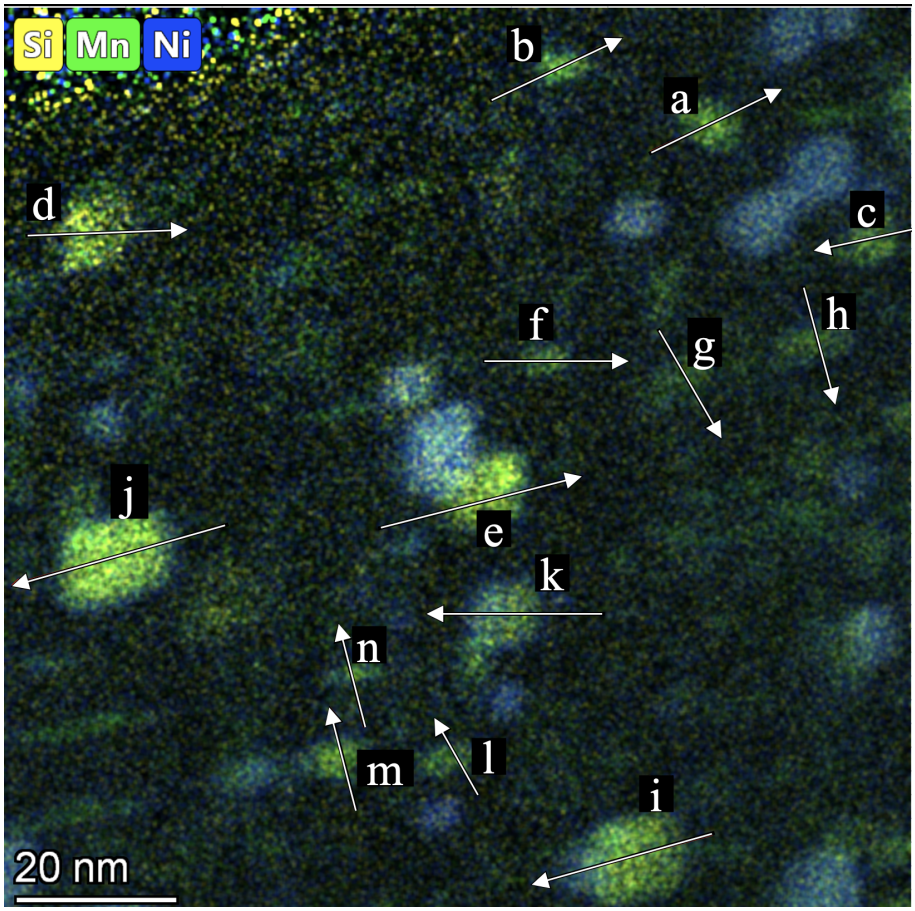


Figure 4.25: Mn, Si and Ni overlaid EDX map of 2 dpa proton irradiated Fe-Mn-Ni-Si. Labels correspond to line scan plots shown in fig. 4.26, and include all Ni lean precipitates observed in this region.

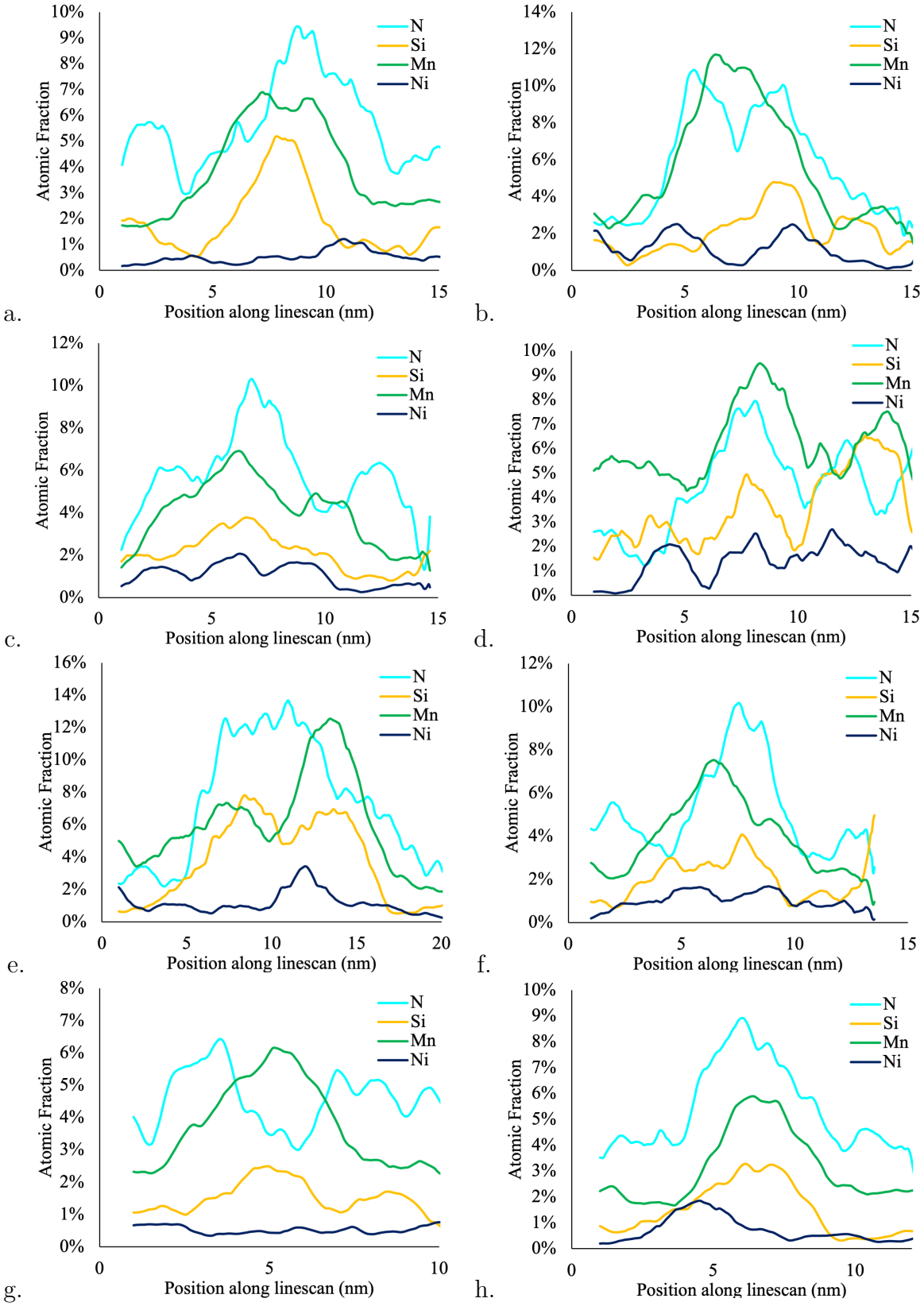


Figure 4.26: Line scans corresponding to solute enriched precipitates, in 2 dpa proton-irradiated Fe-Mn-Ni-Si, lean in Ni, enriched in N and labelled in fig. 4.25. Atomic fraction has been calculated using a thickness correction applied in Velox, and underestimates precipitate composition due to matrix Fe scattering.

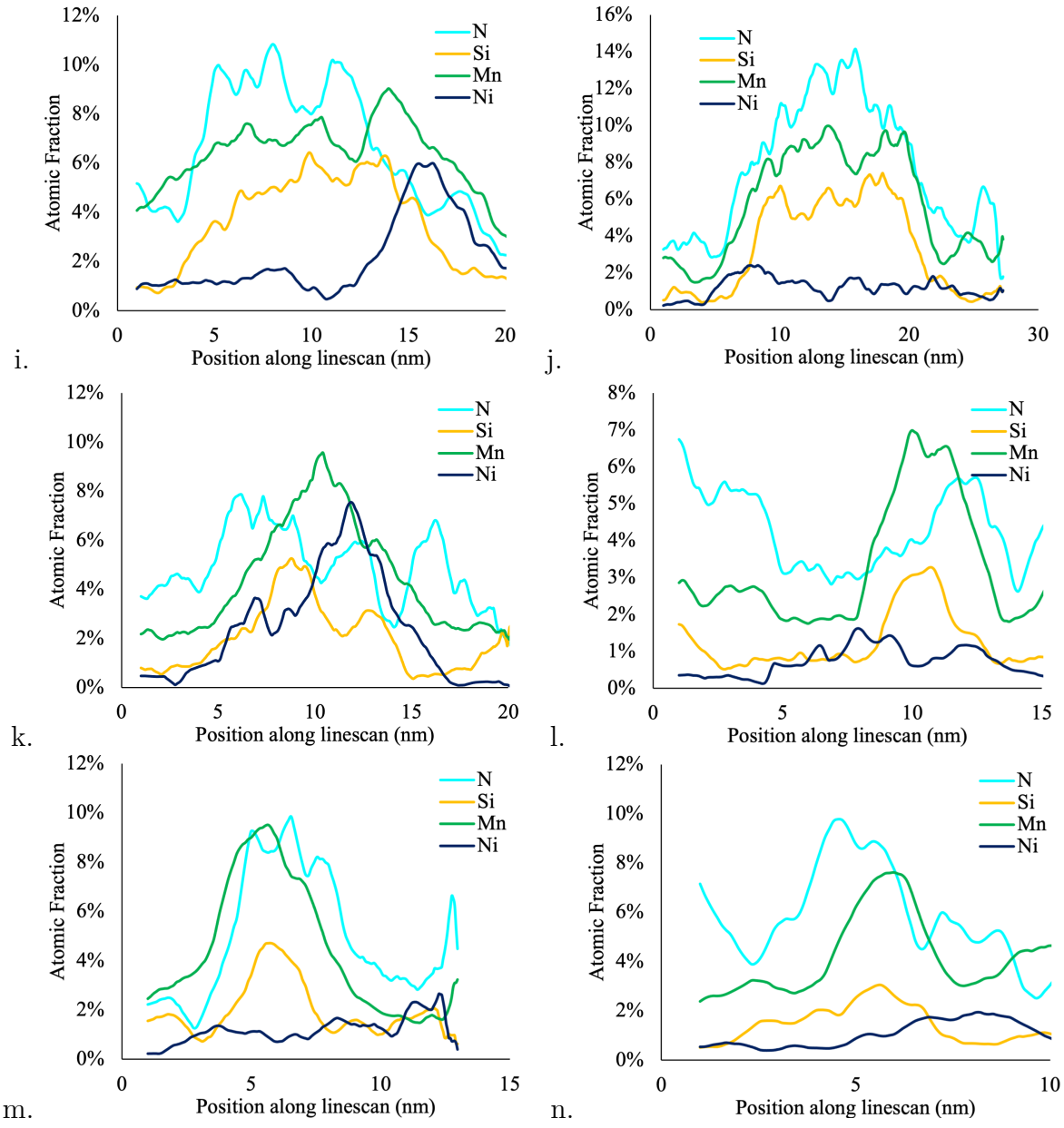


Figure 4.26: Line scans corresponding to solute enriched precipitates, in 2 dpa proton-irradiated Fe-Mn-Ni-Si, lean in Ni, enriched in N, labelled in fig. 4.25. Atomic fraction has been calculated using a thickness correction applied in Velox, and underestimates precipitate composition due to matrix Fe scattering.

Maps from the datasets in figs. 4.14, 4.18 and 4.21 were analysed using Velox software ([180], with a thickness correction applied (table 4.1), to compare the compositions of different areas of solute enrichment. Compositions were calculated using spectrum images of small areas in the centre of each feature. Mn-Ni-Si ternary plots, fig. 4.27, show an evolution in solute-rich precipitate composition with dose, when considering only Ni, Mn and Si. As the dose increases, two distinct compositional populations appear, with the Ni rich precipitates still present at around 50-60 at.% Ni, and a Ni lean population of Mn-Si-N rich precipitates increasing in number. The compositions shown in fig. 4.27 are not absolute, as the real fraction of Fe is difficult to determine due to the sample thickness. Fe content has therefore been omitted and the ratios of solute elements have been calculated to deduce possible phases of precipitates. The ternary diagrams show a clear effect of dose/dose rate on the composition of structures forming in the Fe-Mn-Ni-Si alloy. At low doses, 0.1 dpa, a single composition of defect is observed, with approximately 40-50 % Ni, 35-45 % Mn and 15-22 % Si. As the dose increases, compositions increase in Si and Mn content, and Ni drops to below 10 %. In these low Ni precipitates, the approximate composition is $MnSiN_2$. Figure 4.28 shows some overlap in Mn:Si ratio across doses and precipitate population.

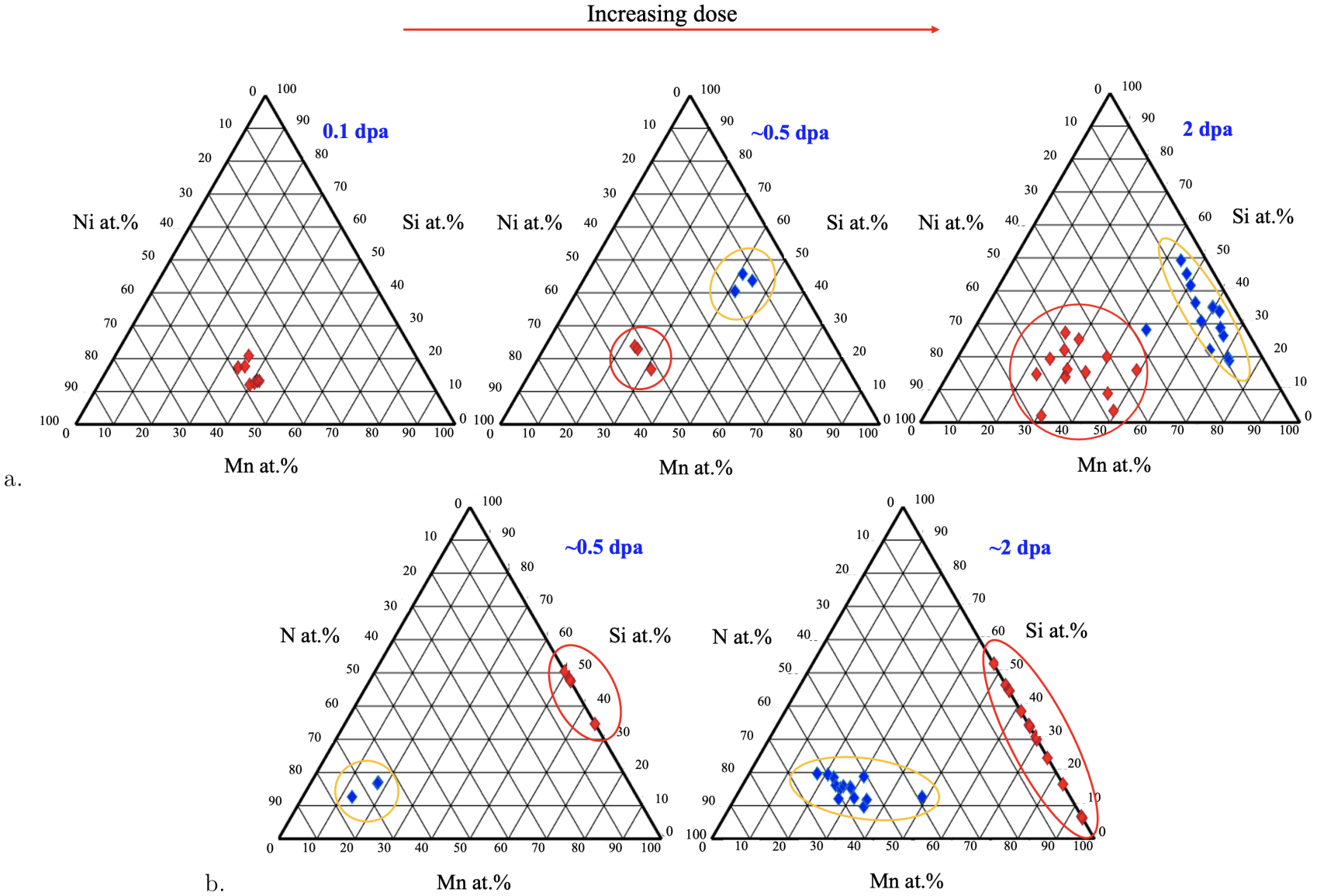


Figure 4.27: Ternary at.% composition plots using data obtained from EDX maps of solute enriched precipitates from regions of the proton irradiated Fe-Mn-Ni-Si alloy from 0.1 dpa to 2 dpa.(a.) Ni, Mn and Si, omitting Fe and N content and (b.) N, Mn and Si omitting Ni and Fe content. As dose increased, two populations of composition emerge; Ni-Mn-Si rich precipitates (red) MnSi nitrides (blue).

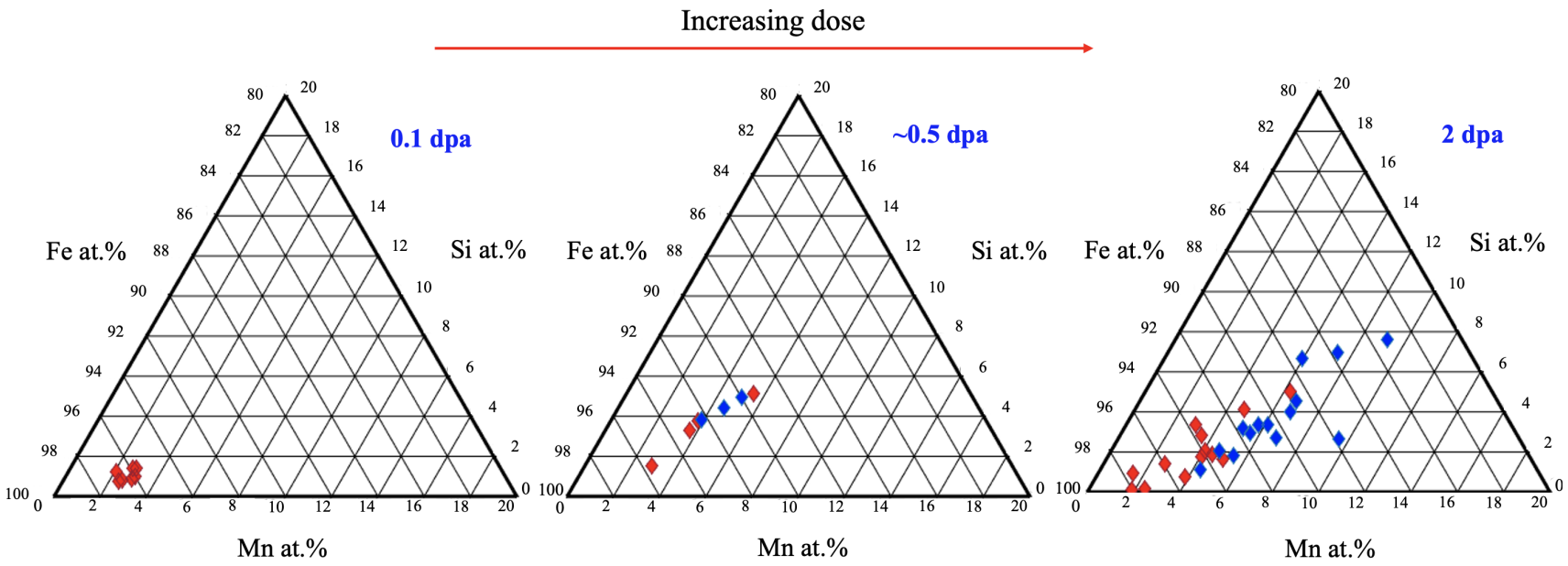


Figure 4.28: Ternary Fe, Mn and Si at.% composition plots showing data obtained from EDX maps of solute enriched precipitates from regions of increasing dose in the proton irradiated Fe-Mn-Ni-Si alloy from 0.1 dpa to 2 dpa. Red = Ni-Mn-Si rich precipitates and blue = MnSi nitrides.

4.4.2 Fe-Mn-Si

High magnification STEM-EDX images and corresponding line scans, fig. 4.29, show some variation in the ratio of Mn:Si in the precipitates, which is not correlated with size. Figure 4.30 shows a clear enrichment of nitrogen, manganese, and silicon in the precipitate region, compared with the matrix.

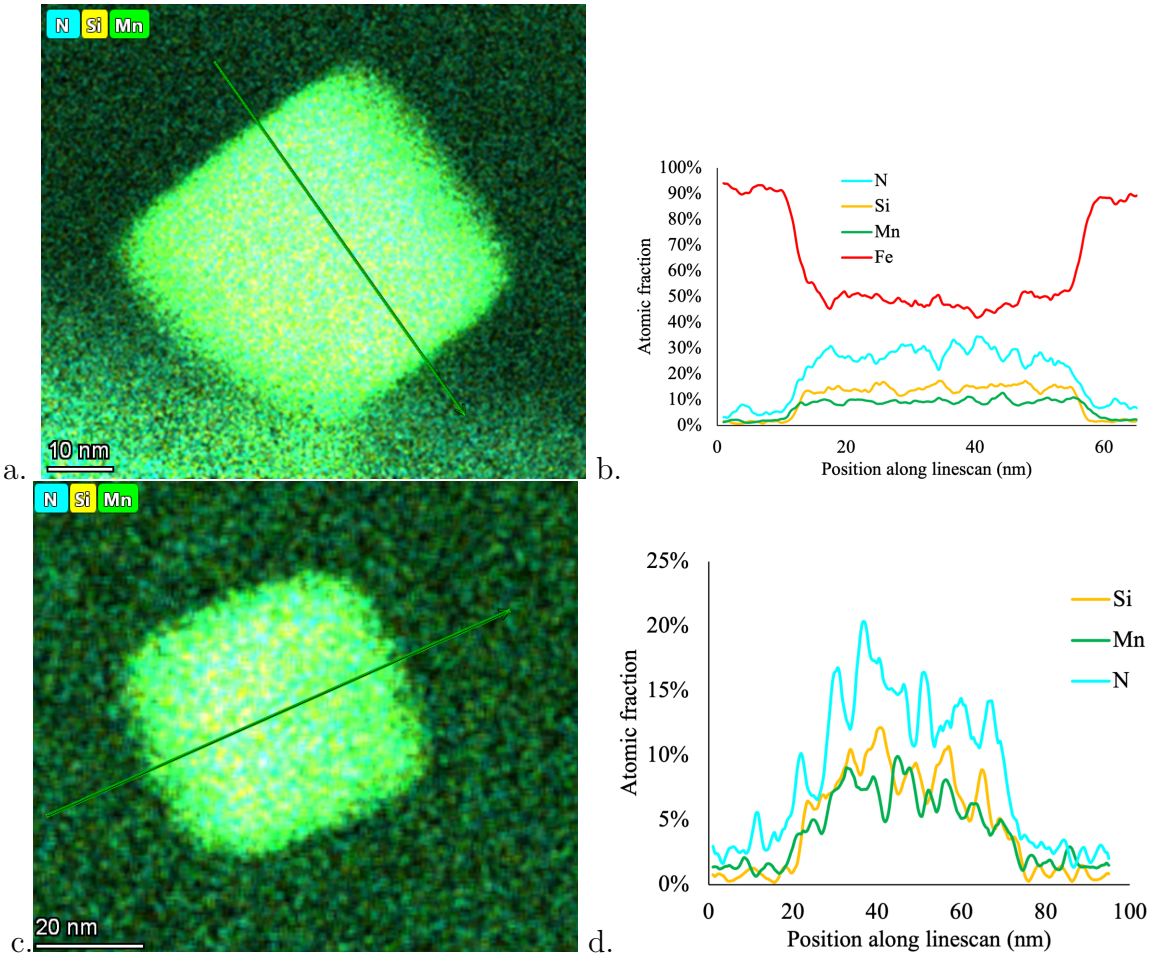


Figure 4.29: STEM EDX at. % maps and associated line scans, showing fraction of Mn (green), Si (yellow) and N(turquoise) measured in precipitates in irradiated Fe-Mn-Si alloy.

In general, the ratio of (Mn, Si):N is approximately 1.2 in the 0.1 dpa region, and 0.6 at 2 dpa, fig. 4.31. It can be seen that the Mn:Si ratio also varies with dose, with a lower ratio of Mn:Si at lower doses. This trend does not seem to be due to the increase in average size of precipitates, as small precipitates in the 2 dpa region are also lower in N than in the 0.1 dpa region, fig. 4.32.

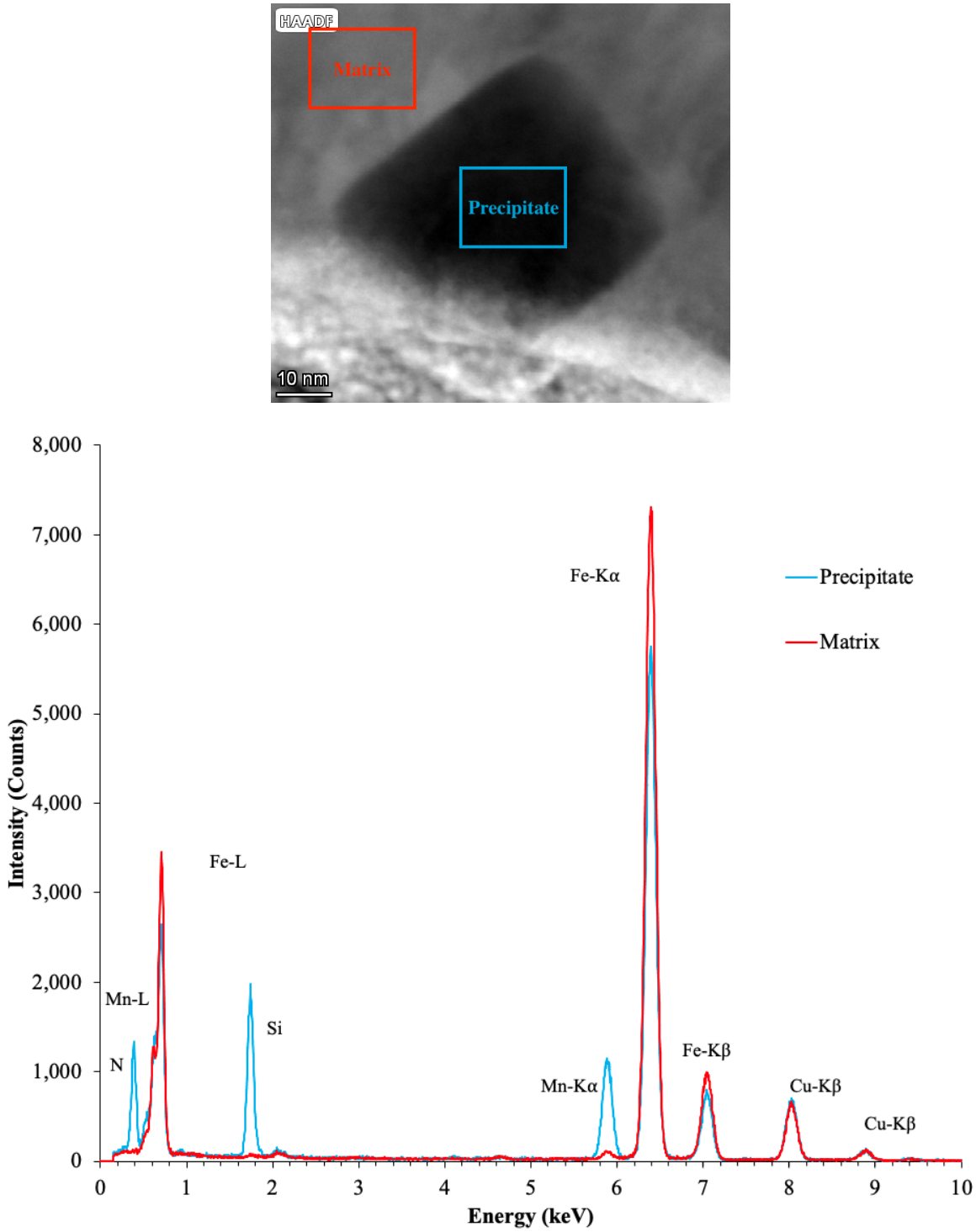


Figure 4.30: Comparison of EDX measured spectra obtained from equivalent areas of matrix and precipitate in the 2 dpa irradiated region of the Fe-Mn-Si alloy, normalised using the 8 keV and 8.9 keV background Cu peaks.

Table 4.5: STEM-EDX composition of precipitate shown in fig. 4.30 (a.), calculated using Velox automated quantification function, assuming through thickness precipitates. Fe is likely to be due to matrix contribution.

Element	Atomic Fraction (%)
N	24.64 ± 3.83
Si	14.71 ± 3.64
Mn	9.17 ± 1.88
Fe	51.49 ± 10.51

Table 4.6: STEM-EDX composition of precipitate shown in fig. 4.30 c., calculated using Velox automated quantification function, assuming through thickness precipitates. Fe is likely to be due to matrix contribution.

Element	Atomic Fraction (%)
N	14.56 ± 2.72
Si	8.06 ± 2.16
Mn	5.89 ± 1.35
Fe	71.49 ± 16.37

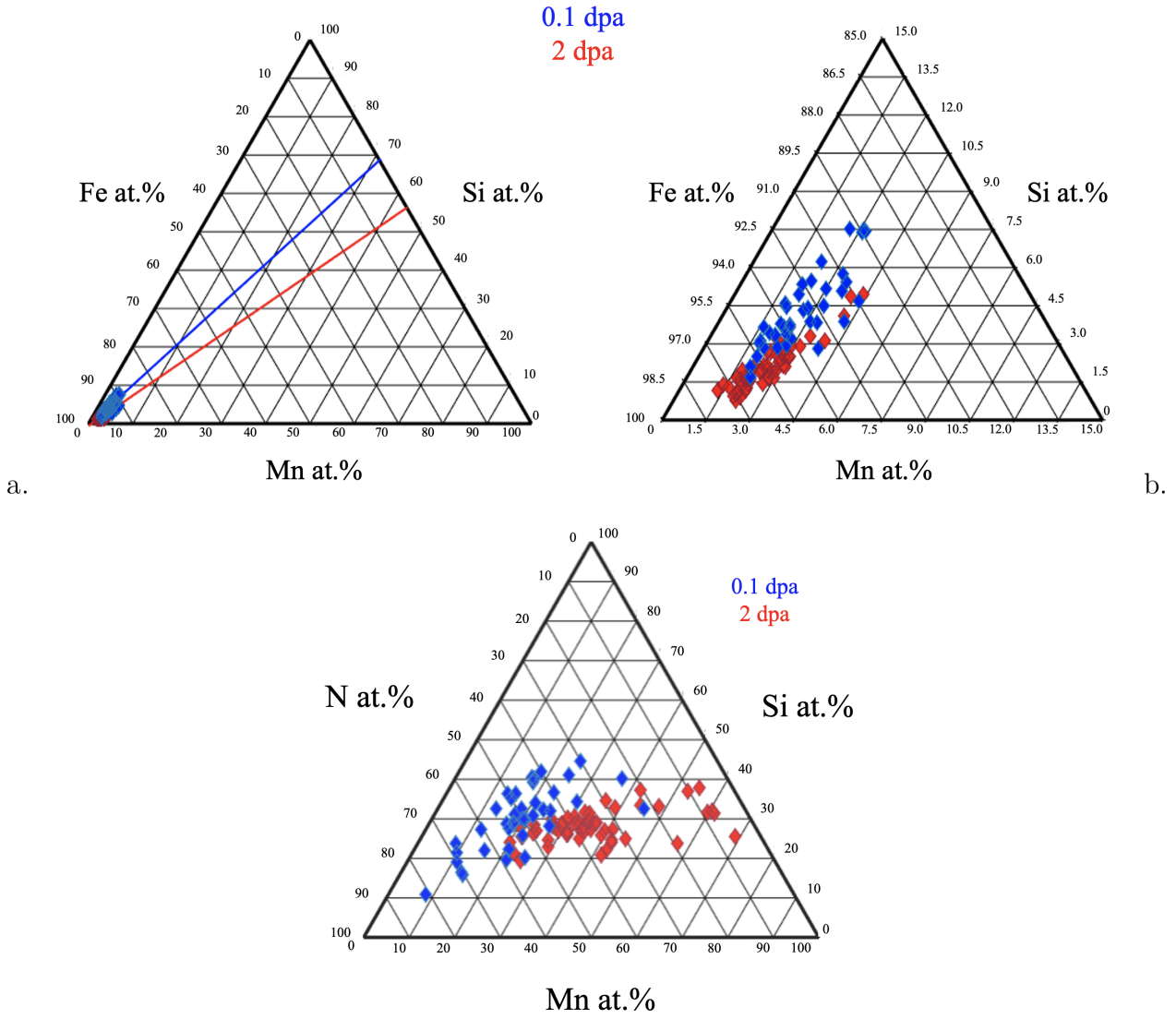


Figure 4.31: Ternary plots showing the composition of precipitates measured using EDX maps, with precipitates in the 2 dpa proton-irradiated region in red, and 0.1 dpa region in blue. (a.) Fe-Mn-Si, excluding nitrogen, a condensed and full plot with lines projecting ratio of Mn:Si as 8:17 in the 0.1 dpa region and 9:11 in the 2 dpa region. (b.) N-Mn-Si ternary diagram, excluding Fe, showing very wide range of compositions, with decreasing nitrogen content in some higher dose precipitates.

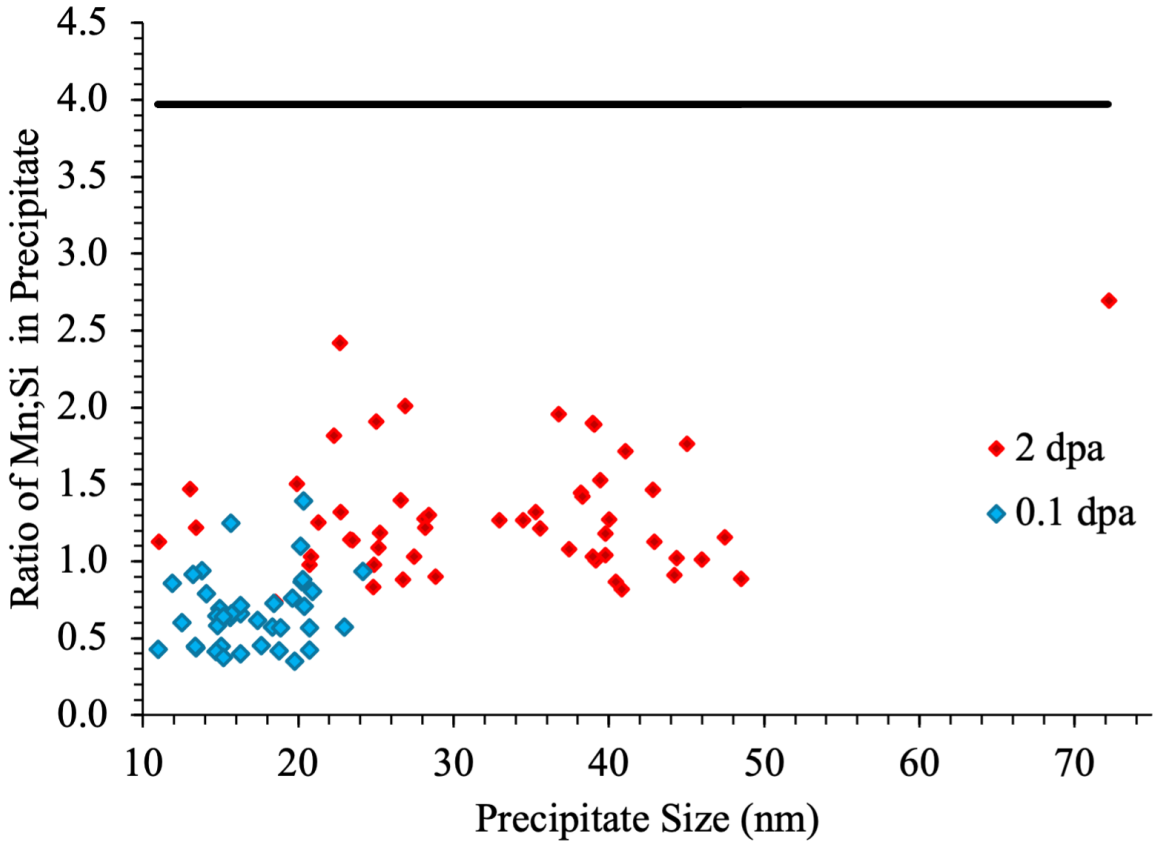


Figure 4.32: Plot showing variation of the precipitate Mn:Si ratio with size, for 0.1 and 2 dpa regions in the Fe-Mn-Si alloy. Mn:Si ratio slightly increases at higher doses and larger sizes. The solid horizontal line shows the matrix ratio of Mn:Si before irradiation.

4.5 Precipitate structure analysis in Fe-Mn-Ni-Si using selected area electron diffraction

Selected area diffraction patterns have been collected from the 0 dpa and 2 dpa regions of the Fe-Mn-Ni-Si alloy, over areas containing a range of precipitates, along three zone axes, to enable the identification of possible secondary phases and calculation of their lattice parameters (fig. 4.33).

For each zone axis, the inverted selected area diffraction patterns (SADPs) are shown alongside simulated indexed bcc iron diffraction patterns and possible structures at the same zone axis, assuming a cube-on-cube orientation relationship: figs. 4.34, 4.35 and 4.38. A cube-on-cube orientation relationship with bcc ferrite has been assumed for most of the phases, given that

they are cubical and have low theoretical misfit with a bcc matrix in this orientation. Also the G phase has been observed in ferritic stainless steels to form with a cube-on-cube orientation relationship [219, 220]. Some proposed phases, such as the Γ_2, assume an FCC structure and may be more likely to form a Kurdjumov-Sachs orientation relationship (where $\{111\}_{fcc}//\{110\}_{bcc}$ and $<111>_{bcc}//<110>_{fcc}$ [221]) to reduce lattice strain. A simulated Γ_2 phase pattern on the [111] zone axis shows no overlapping spots with the [011] bcc Fe pattern. The CIFs (crystallographic information files) have been obtained using the ICSD (inorganic crystal structures database), [222], for the $Mn_6Ni_16Si_7$ [223] (using a lattice parameter of 11.09 Åfrom King et al., [131]), Fe_2MnSi Heusler phase, [224], Mn_3Si, [225], Γ_2 $Mn(Ni, Si)_2$, [226], $MnSiN_2$ [227], and Fe_3O_4, [228].

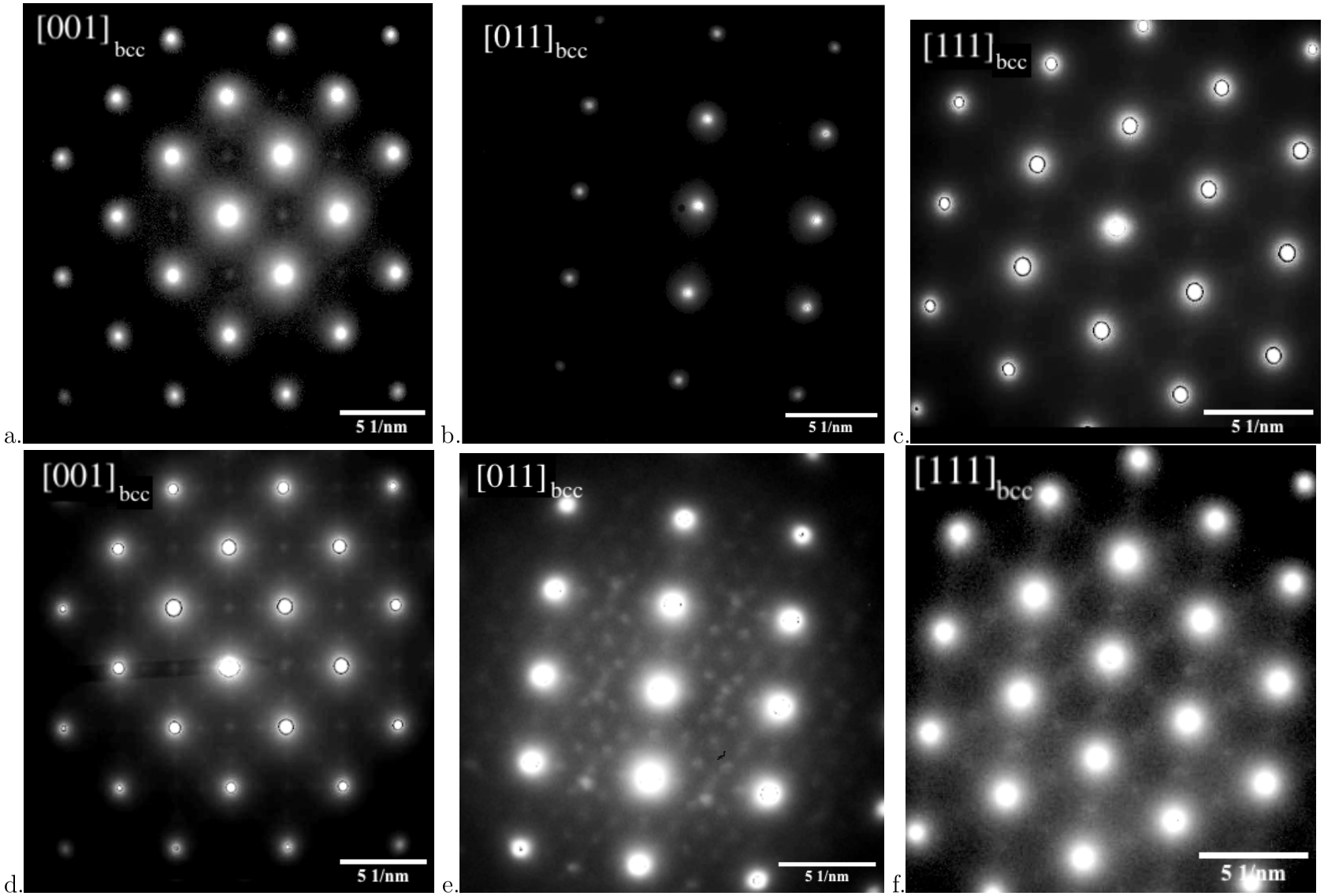


Figure 4.33: Selected area diffraction patterns on the (a. & d.) [001], (b. & e.) [011] and (c. & f.) [111] zone axes, using 40 µm aperture at camera lengths of 1.1 m (001, 011) and 1.35 m [111], on the (a., b. & c.) peak irradiated region of the Fe-Mn-Ni-Si alloy and in a (d., e. & f) unirradiated region beyond the maximum proton penetration depth, on the same TEM specimen.

The set of nine spots arranged in a square between each set of four bcc Fe spots is consistent with the G phase [001] diffraction pattern, fig. 4.34 a, c. However, the highest intensity secondary spots are directly between the bcc Fe diffraction spots, and could correspond to an ordered $L2_1$ structure such as the $(Fe, Mn)_3Si$ structure, or (200) type spots in the $MnSiN_2$ structure, which also has some overlapping reflections with the G phase pattern, fig. 4.34; a, e, f. The relative intensity of these spots does not match the G phase simulated pattern, suggesting the presence of more than one secondary phase. The Γ_2 phase diffraction pattern at the [001] zone axis overlaps with that of bcc iron, so its presence cannot be determined at this orientation.

The secondary diffraction spots on the [011] zone axis are complex and suggest the possible presence of various phases, fig. 4.35. The G phase diffraction pattern simulated shows a similar diamond shaped pattern with a good fit to the observed pattern using a modelled lattice parameter of 11.09 Å([131]. The Γ_2 simulated pattern does not overlap closely with the observed patterns despite the range of lattice parameters modelled for the phase, between 0.663 and 0.668 nm [132]. There are some high intensity diffraction spots that are not consistent with the G phase reflections modelled. The $(Fe,Mn)_3Si$ pattern approximately overlaps with the G phase pattern. $MnSiN_2$ has some first order overlapping reflections of the (011) and (111) planes that may explain the diffuse spots observed horizontally between the bcc Fe spots, as they would be expected to be slightly misaligned with G phase reflections based on the simulated patterns, fig. 4.35.

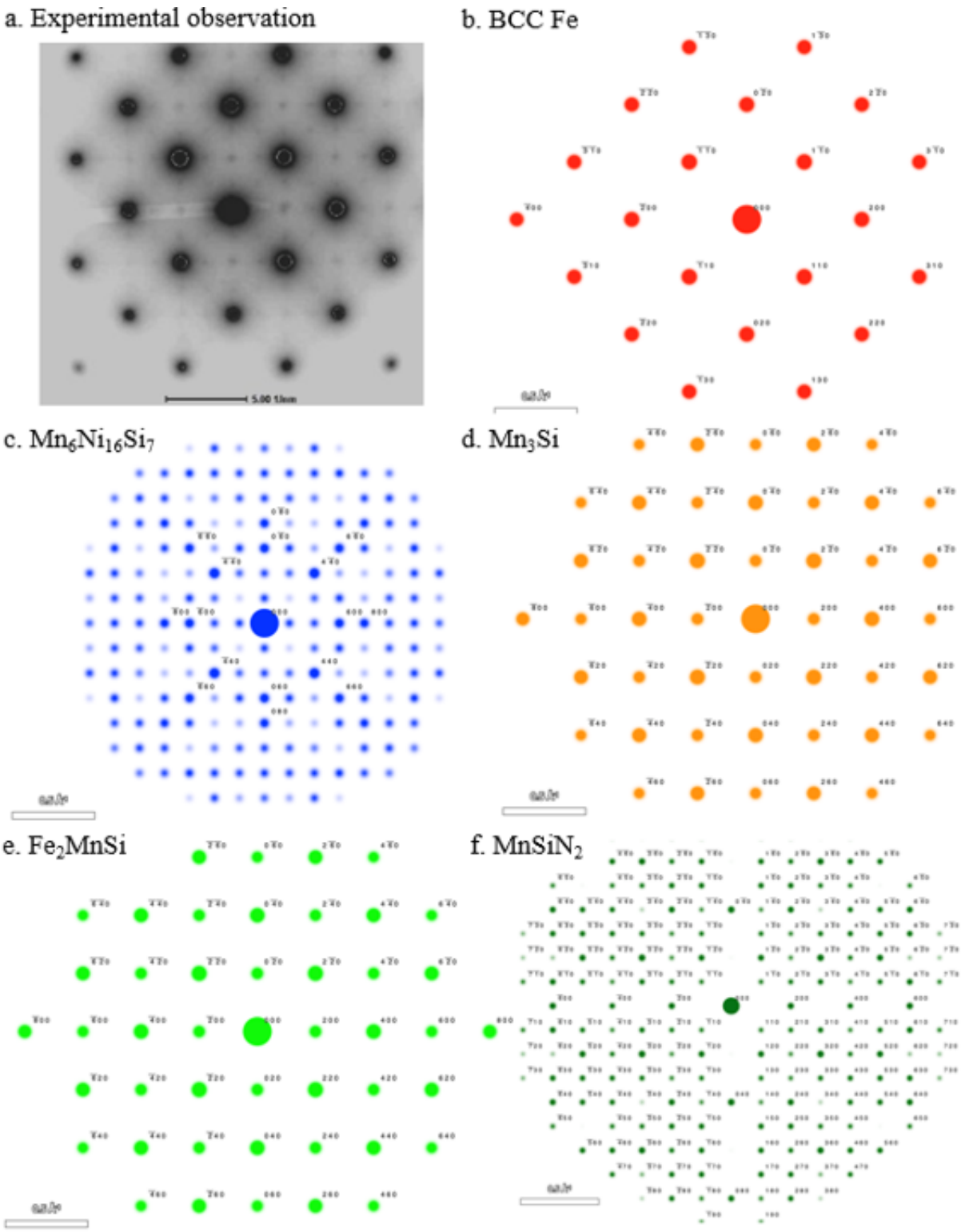


Figure 4.34: inverted selected area diffraction pattern obtained from irradiated Fe-Mn-Ni-Si alloy on the [001] zone axis (a.), bcc Fe [001] diffraction pattern (b.) and simulated [001] patterns for proposed phases: (c.) $Mn_6Ni_{16}Si_7$ G phase, (d.) Mn_3Si, (e.) Fe_2MnSi, (f.) $MnSiN_2$.

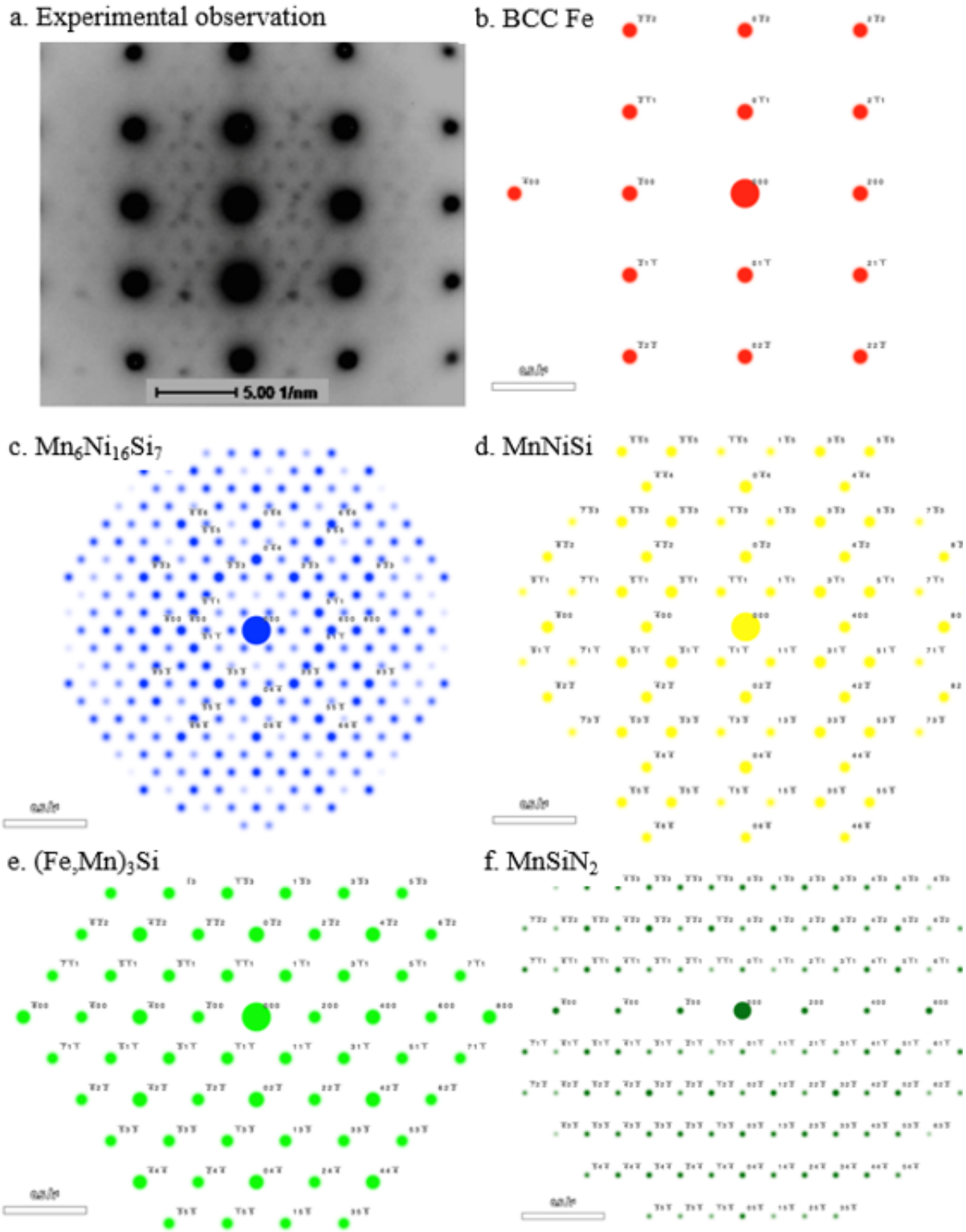


Figure 4.35: inverted selected area diffraction pattern obtained from irradiated Fe-Mn-Ni-Si alloy on the [011] zone axis (a.), bcc Fe [011] diffraction pattern (b.) and simulated [011] patterns for proposed phases; (c.) $Mn_6Ni_{16}Si_7$ G phase, (d.) Γ_2 MnNiSi, (e.) $(Fe,Mn)_3Si$, f.$MnSiN_2$.

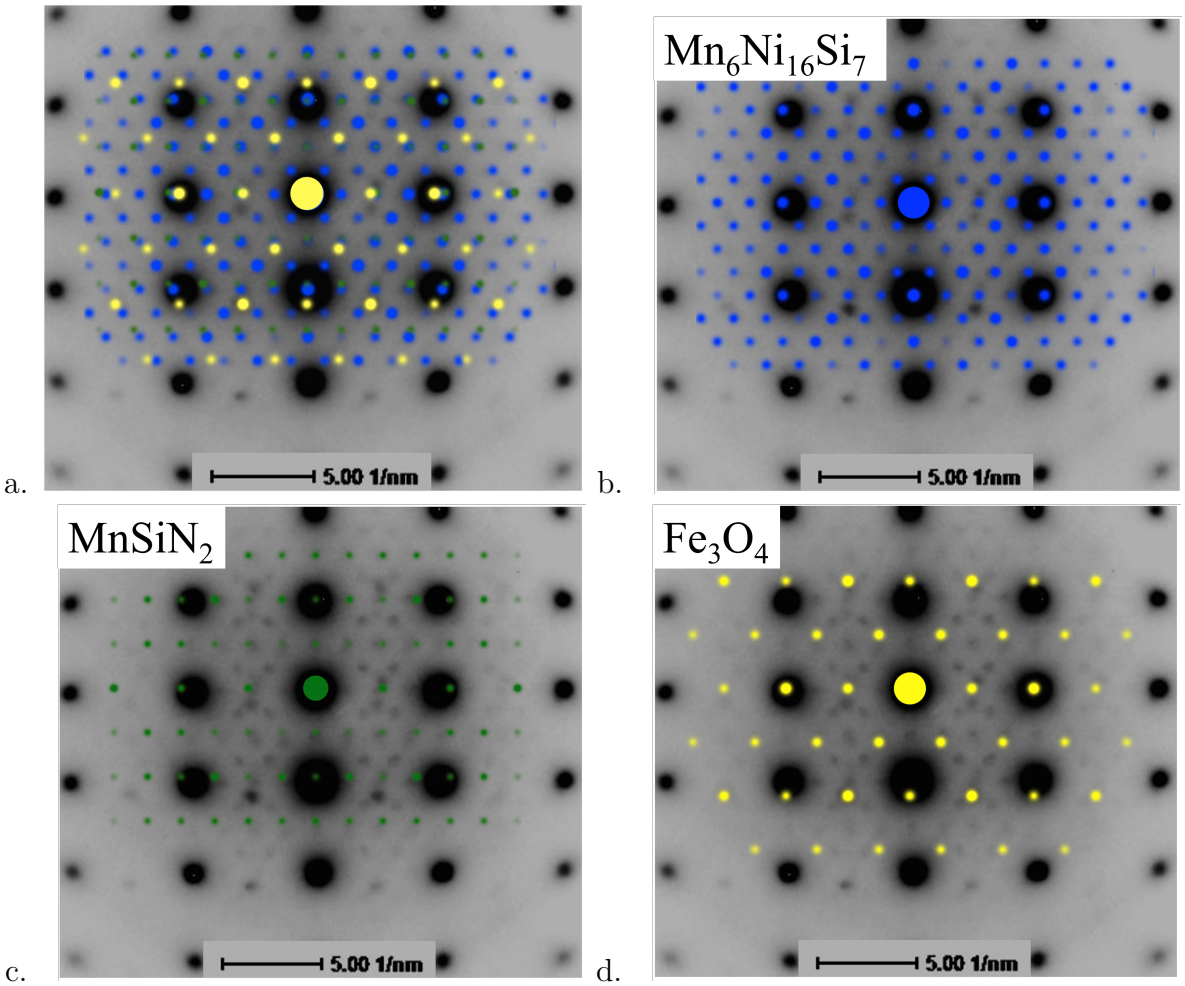


Figure 4.36: Inverted [011] zone axis diffraction pattern with overlaid simulated patterns (a.), for (b.) G phase (blue), (c.) $MnSiN_2$ (green) and (d.) Fe_3O_4 (yellow).

The six most intense secondary spots do not overlap with the expected diffraction patterns for any of the discussed phases. These spots may be coming from electrons diffracted by epitaxial surface oxide, Fe_3O_4, that has grown on the sample after preparation. Fe_3O_4 grows with a K-S orientation relationship such that $\{111\}_{fcc}//\{110\}_{bcc}$ and $<111>_{bcc}//<110>_{fcc}$ [221].

If the [111] zone axis diffraction pattern simulated for Fe_3O_4 is overlaid with the [011] pattern for bcc Fe, and rotated by 30°, as can be seen in fig. 4.36, the high intensity spots observed are likely to be from this thin layer of oxide forming on the sample surface. This figure also clearly shows that this oxide contaminant cannot be responsible for all the secondary diffraction spots. On-axis dark field imaging was carried out on the Fe-Mn-Ni-Si alloy to determine whether secondary patterns were coming from precipitate phases, and to rule out the possibility that all secondary pattern intensity was due to epitaxial growth of Fe_3O_4 on the surface of the specimen, as has been observed by Carter et al. in irradiated RPV steel FIB prepared specimens [121]. The objective aperture location is shown in each image, fig. 4.37. These images show clear precipitates with high intensity in the size range of 10-40 nm which is consistent with STEM images of solute-rich precipitates. An oxide layer would produce intensity across the sample surface, and therefore it is assumed that most of the secondary scattering is due to secondary phases formed from solutes.

At the [111] zone axis, there is clearly three-fold symmetry matching with the bcc lattice, suggesting a cubical precipitate with approximately twice or four times the lattice parameter of pure bcc iron. This is consistent with all reflections in the simulated G phase [111] diffraction pattern, and some spots from the $MnSiN_2$ pattern fig. 4.38.

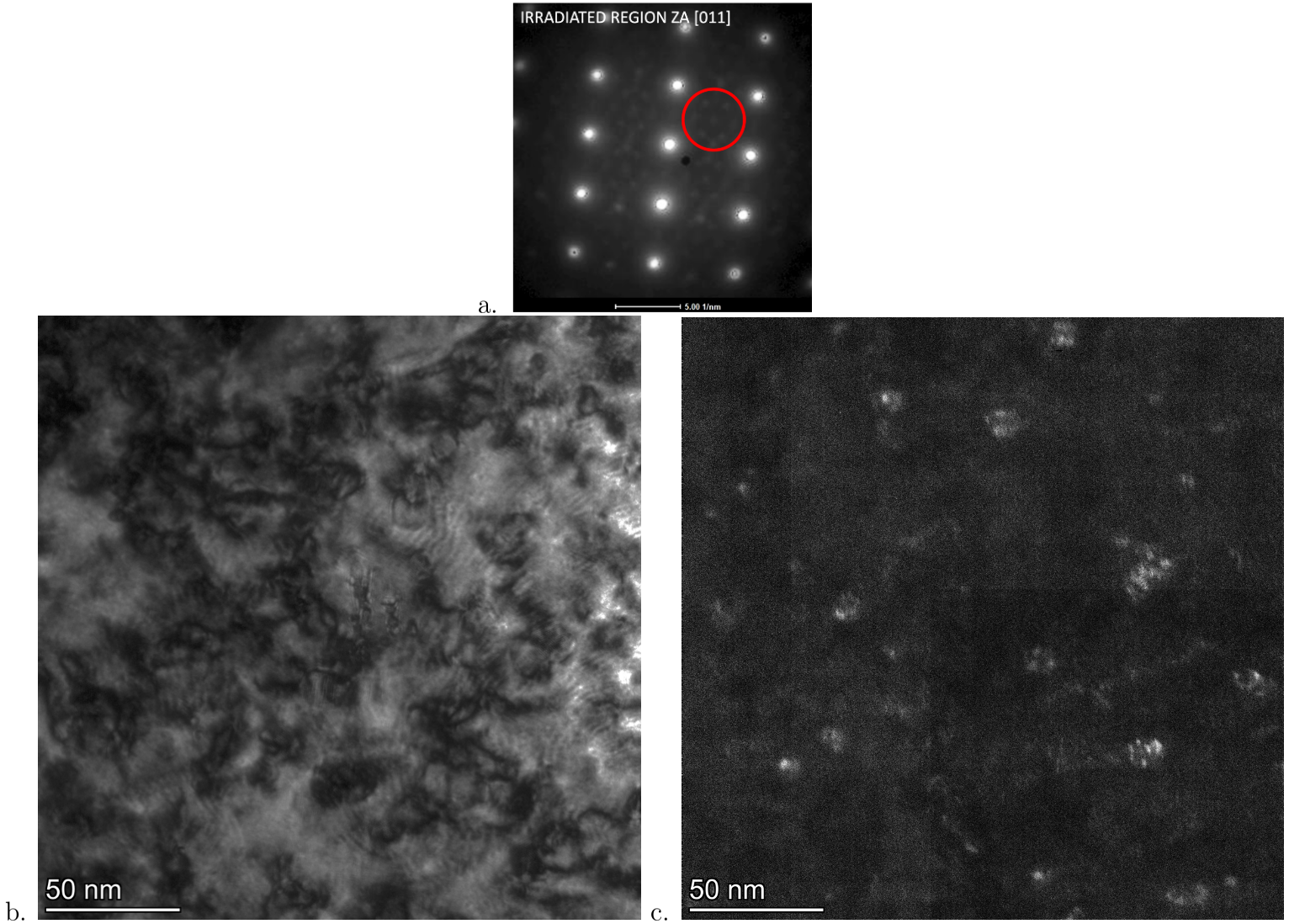


Figure 4.37: On zone axis [011] (b.)bright field and (c.) dark field images on the 2 dpa irradiated Fe-Mn-Ni-Si, with the dark field image taken with the objective aperture located as shown in (a.).

To quantitatively determine the likely phases, distances between the [000] spot and secondary spots have been measured, and the angles between sets of diffraction spots. Then the measured values have been compared with theoretical spacings and angles as well as calculating lattice parameters based on the spot *hkl* values for each proposed structure. The average value of lattice parameter using all indexed spots observed (excluding the BCC-Fe matrix spots) is shown for each zone axis pattern in table 4.7. Errors on these values have been calculated using the statistical error on the mean lattice parameter calculated for each of the spots. Calculated lattice parameters, assuming spots are caused by planes in the proposed structures, have been compared with literature values. The calculated lattice parameters shown are all within one standard error of values obtained from literature.

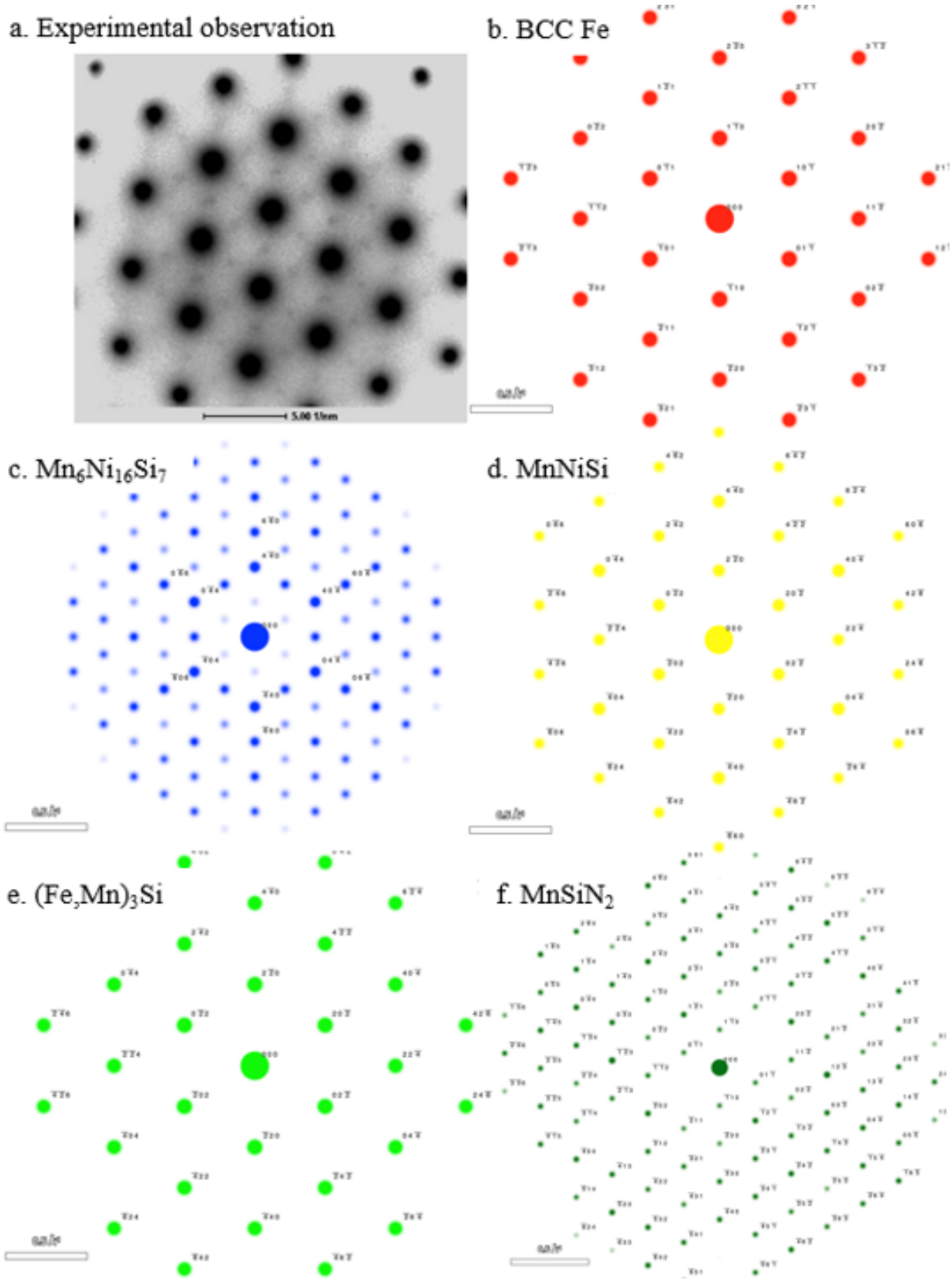


Figure 4.38: inverted selected area diffraction pattern obtained from irradiated Fe-Mn-Ni-Si alloy on the [111] zone axis (a.), bcc Fe [111] diffraction pattern (b.) and simulated [111] patterns for proposed phases: (c.) $Mn_6Ni_{16}Si_7$ G phase, (d.) Γ_2 MnNiSi, (e.) $(Fe,Mn)_3Si$, (f.) $MnSiN_2$.

Table 4.7: Table of measured lattice parameters using selected area diffraction patterns, compared with literature values of lattice parameter and lattice misfit, ε. For each zone axis ✓= relevant reflections observed, ×= no matching reflections observed.

Phase	Zone Axis of Pattern [001]	[011]	[111]	Lattice Parameter (nm)	Lattice misfit, ε^*	Literature Lattice Parameter (nm)	Literature Misfit, ε
$Mn_6Ni_{16}Si_7$[223]	✓	✓	✓	$a = 1.136 \pm 0.006$	-0.71±0.01 %	1.15[226], 1.17[229]	-1.33%[131]
Fe_2MnSi[224]						0.559	-2.6%
Mn_3Si[225]	✓	✓	×	$a = 0.575 \pm 0.010$	+0.4%	0.572	-0.3%
$(Fe,Mn)_3Si$						0.567	-1.1%
				$a = 0.525 \pm 0.011$	$-9.1 \pm 0.41\%$	0.527	-8.6%
$MnSiN_2$[227]	✓	✓	✓	$b = 0.649 \pm 0.014$	$11.5 \pm 0.5\%$	0.651	12.1%
				$c = 0.596 \pm 0.011$	$-13.6 \pm 0.6\%$	0.507	-12.8

4.6 Grain boundary segregation in Fe-Mn-Ni-Si

Grain boundary segregation was also observed in the plateau region, with clear enrichment of Mn and Ni at the grain boundary and a solute-rich precipitate depleted zone of approximately 23±2 nm from the boundary, in which there are no solute-rich defects observed. The grain boundary is likely to be affecting the absorption of defects which would later act as nucleation sites under irradiation fig. 4.39. Linescans across the boundary show Ni and Mn enrichment at the boundary and a small depleted region of Mn, fig. 4.41. A Mn-Si-N rich precipitate can be seen at the boundary, fig. 4.39. Assuming it contains no Fe or Ni, the stoichiometry is approximately $MnSiN_{1.4}$, table 4.8, which is lower in nitrogen than the nitrogen-rich precipitates observed in the matrix, shown in figs. 4.19 and 4.25.

Table 4.8: Table showing EDX measured atomic fractions in area corresponding to the Mn-Si-N rich precipitates shown in fig. 4.39, using Velox software for quantification, accounting for the thickness of the precipitates and only considering Mn, Ni, N, Si and Fe emissions. K lines have been used for quantification

Element	Atomic Fraction (%)
N	10.17 ± 1.87
Si	7.35 ± 1.96
Mn	7.34 ± 1.67
Ni	2.40 ± 0.55
Fe	72.74 ± 16.51

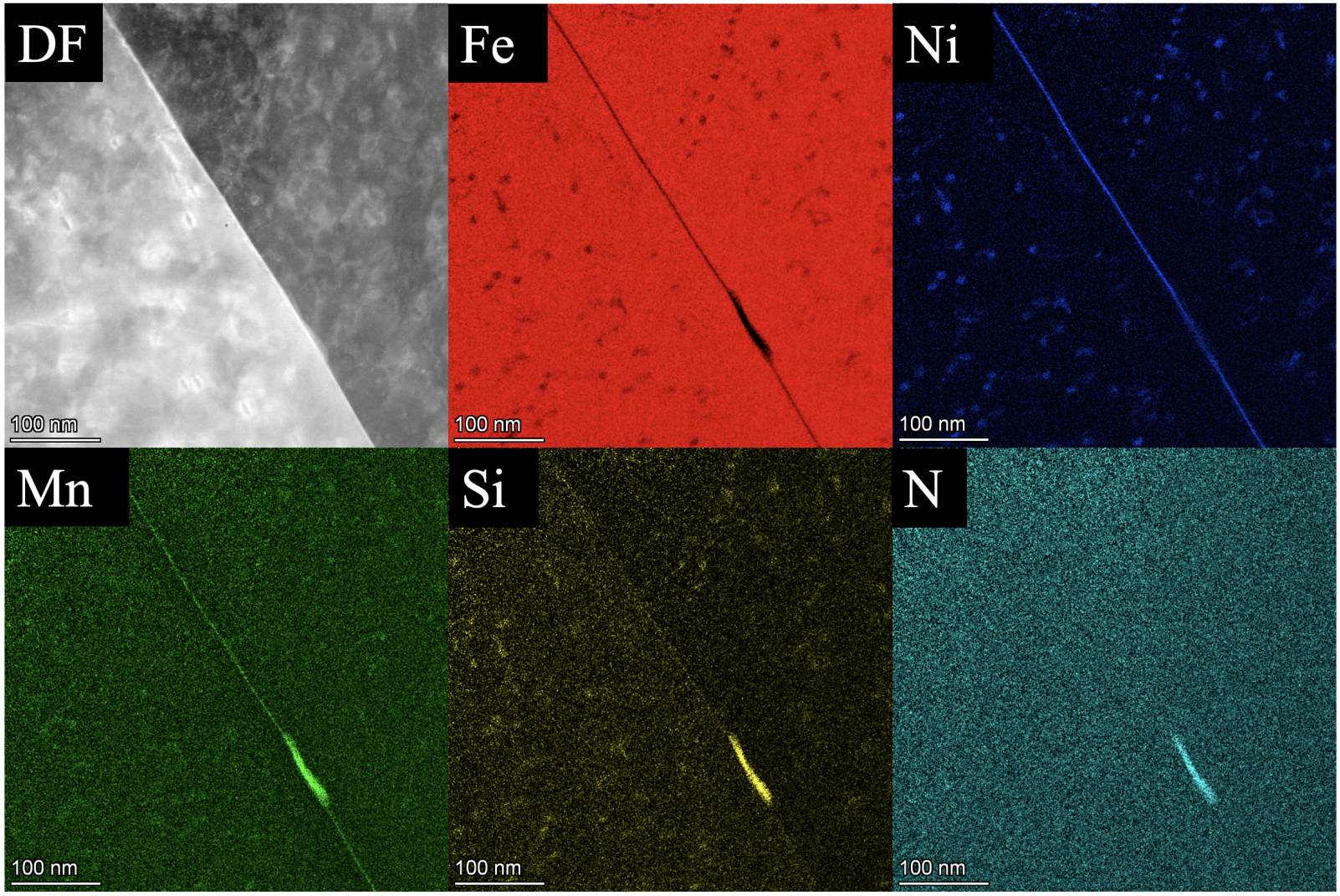
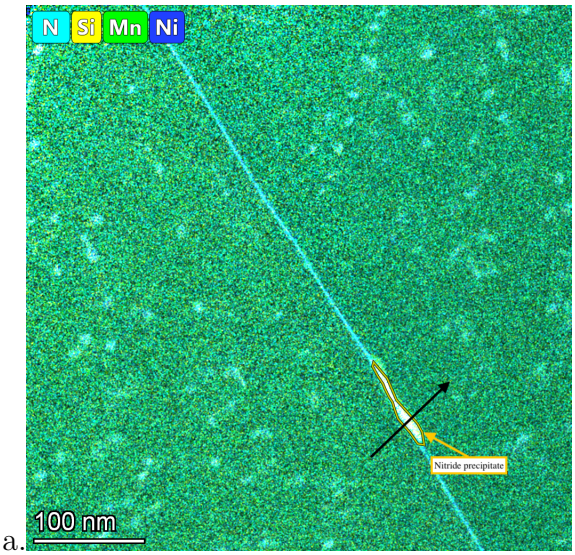
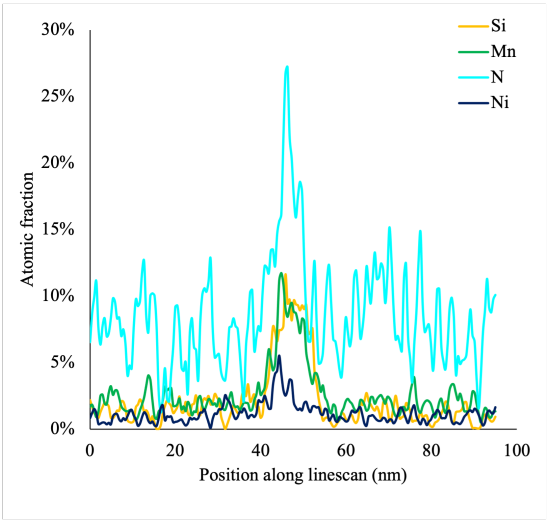


Figure 4.39: Dark field STEM image and EDX (atomic fraction) maps of a grain boundary in 0.1 dpa irradiated region of the Fe-Mn-Ni-Si alloy. , Fe (red), Ni (blue), Mn (green), Si (yellow), N (turquoise) maps showing solute enrichment at the grain boundary and a large Mn-Si-N rich precipitate.

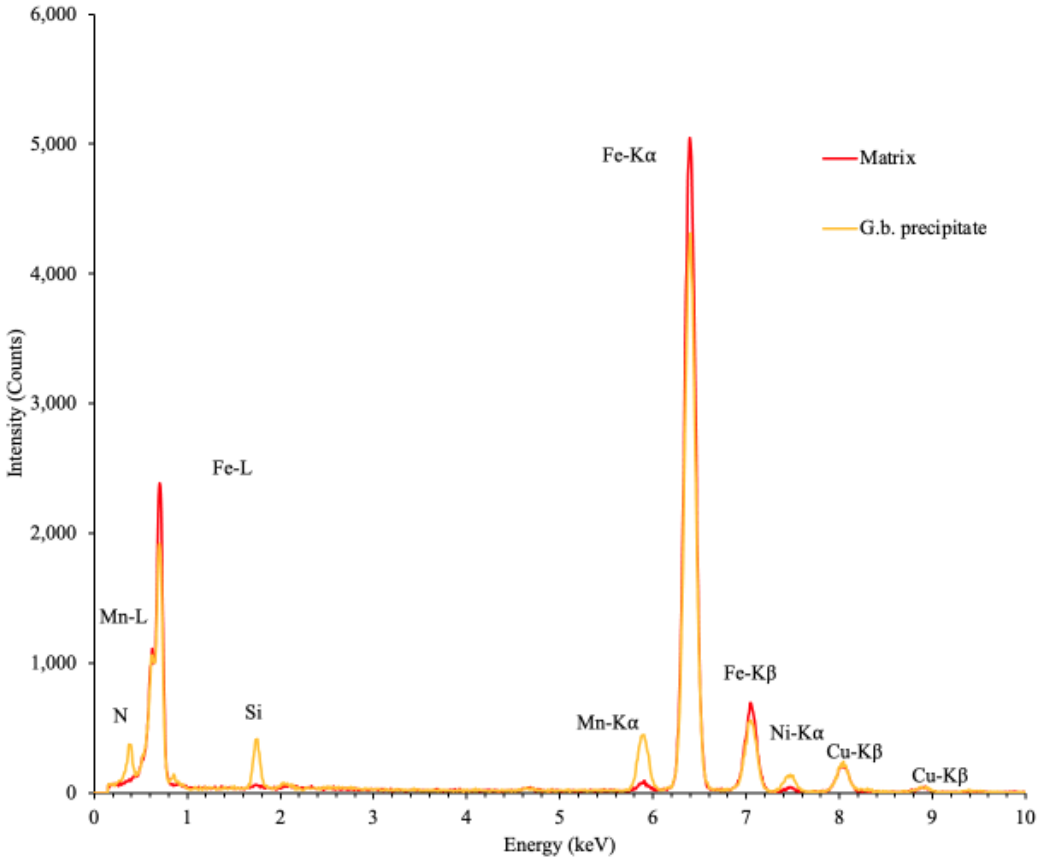
The EDX line profile over the grain boundary shows enrichment in all solute elements at the grain boundary, though most significantly for Mn and Ni. Ni content does not vary either side of the boundary, but there is a small depleted Mn region, fig. 4.41. The Si drop on one side of the grain boundary may be due to X-ray absorption due to orientation of the grain, or an increase in sample thickness in the right-hand grain. The misorientation angle of this grain boundary was not measured, and as a single boundary was observed in these samples, no mechanistic understanding of grain boundary segregation and precipitation can be proposed based on this data. The radiation induced grain boundary segregation of solutes will depend on local geometry, and conclusions on this behaviour would require significantly more data on a variety of grain boundaries [109].



a.



b.



c.

Figure 4.40: EDX at. % overlaid maps for N, Mn, Ni and Si (a.), showing the spectrum area plotted in (c.), comparing X-ray emissions from the matrix and grain boundary precipitate, which is clearly enriched in N, Mn and Si. The line shown was used to produce the linescan of composition across the precipitate(b.)

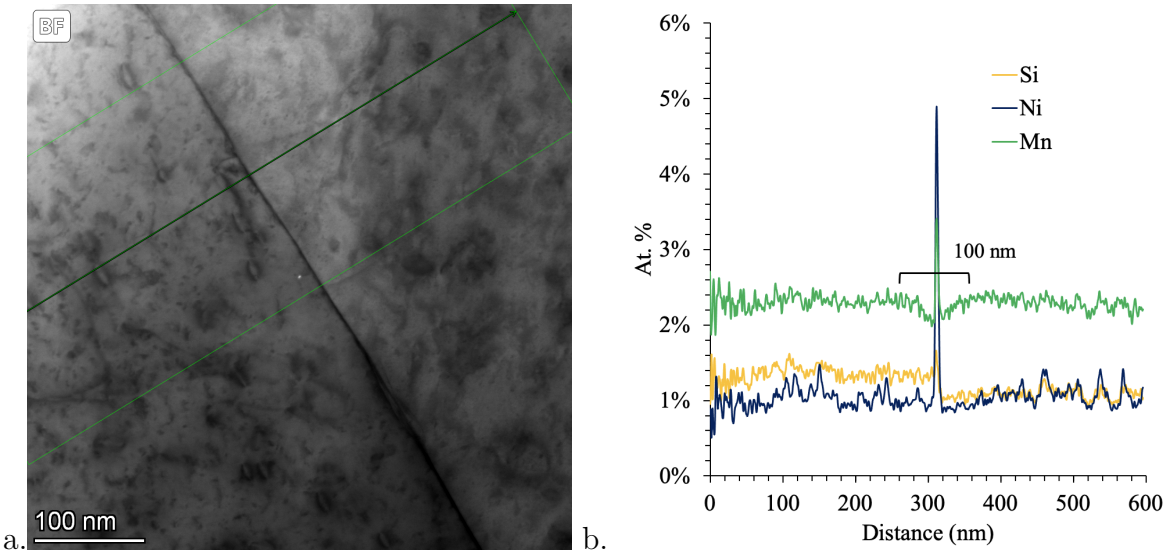


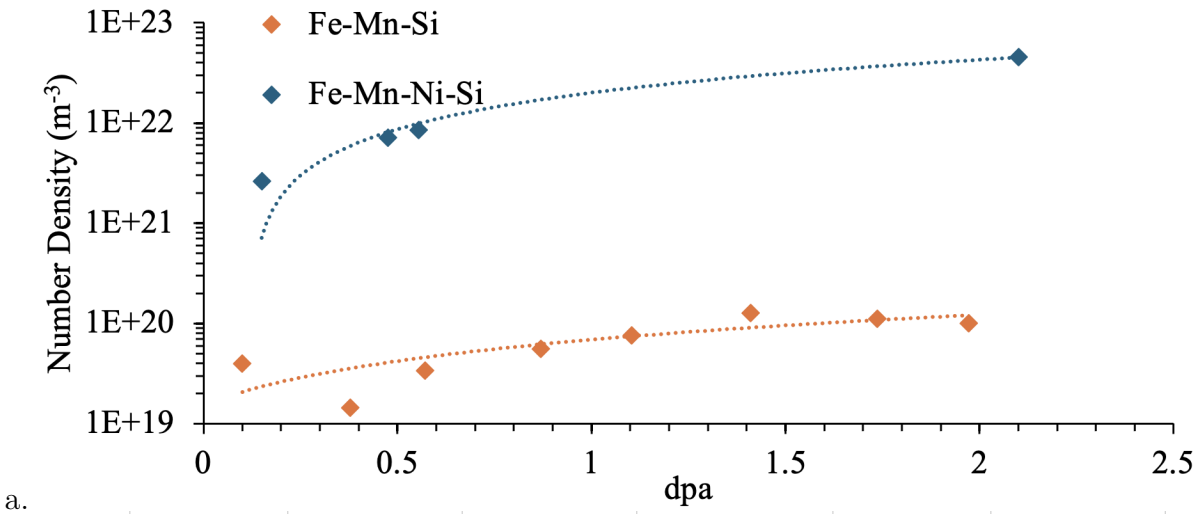
Figure 4.41: (a.) BF STEM image of a grain boundary, and (b.) linescan across the boundary, which shows the enrichment of Ni and Mn, with a small Si peak and a 100 nm Mn depleted region.

4.7 Summary of observations

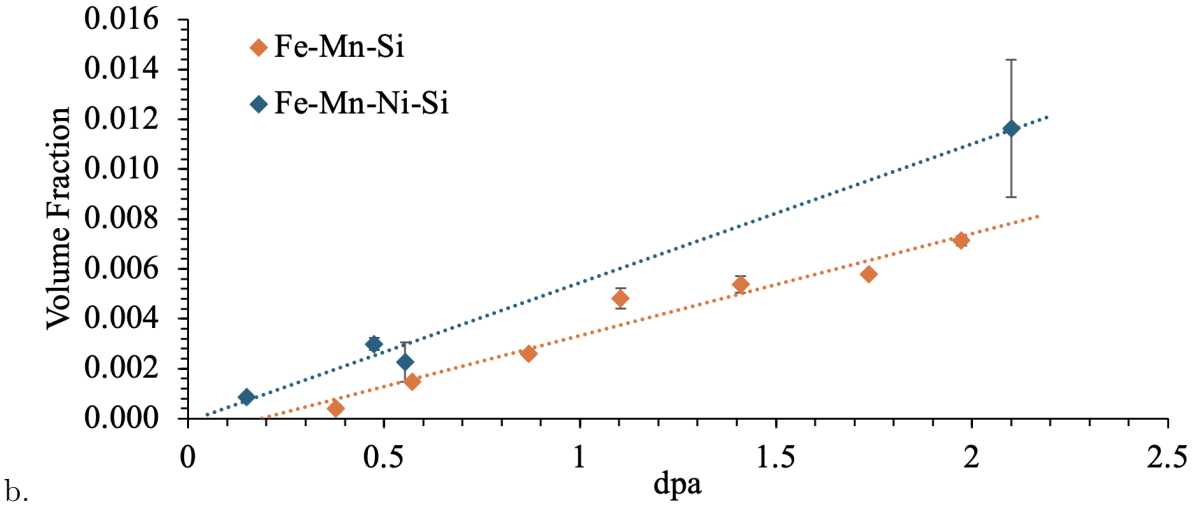
4.7.1 Population characteristics with dose

Figure 4.42 shows the calculated values describing precipitates observed at a range of doses in Fe-Mn-Ni-Si and Fe-Mn-Si. Both alloys have a similar linear behaviour of increasing number density with dose, but the gradient of the line is much steeper in the Ni containing alloy at 2×10^{22} m^{-3}/dpa compared to 6×10^{19} m^{-3}/dpa (fig. 4.42). The size of precipitates is fairly constant with dose in both alloys, although the average size of precipitates was higher in both at higher doses, figs. 4.7 and 4.12. Based on the linear trend-lines added to plots in (a.) and (b.) in fig. 4.42 there is a threshold dose for volume fraction, below which there are no precipitates. If this is the case, the threshold dose for the Fe-Mn-Ni-Si alloy is much lower than the Fe-Mn-Si alloy. Volume fraction is greater in the Fe-Mn-Ni-Si alloy compared with the Fe-Mn-Si, and the Ni containing alloy has a larger gradient, suggesting that the nickel content is increasing the rate of precipitate nucleation and growth with radiation dose (fig. 4.42). In the Fe-Mn-Ni-Si alloy the size distribution of Mn/Si rich precipitates is narrow, and at 0.1 dpa seems to have a log-normal shape with a positive tail, fig. 4.7. In the peak damage region the size distribution is broader. The number density of solute-rich precipitates in the Fe-Mn-Ni-Si alloy at 2 dpa is

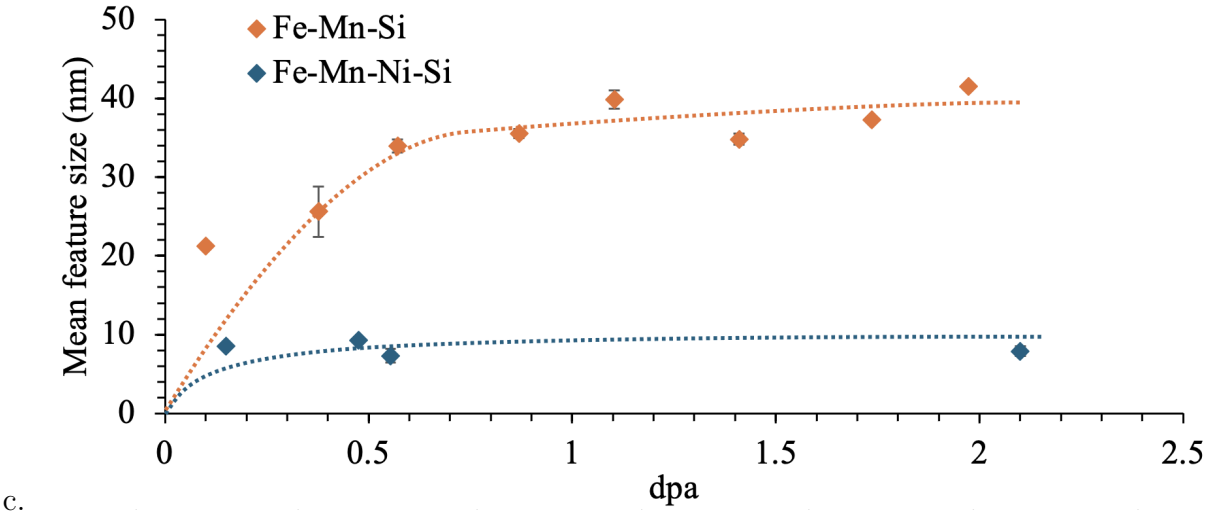
significantly higher than in the lower dose regions observed, at 4.56×10^{22} m^{-3} compared with 2.6×10^{21} m^{-3} (fig. 4.42). The increase of precipitate number density in the Fe-Mn-Si is smaller, from 1.4×10^{19} to 1.3×10^{20}.



a.



b.



c.

Figure 4.42: Plots showing the evolution of (a.) precipitate number density, (b.) volume fraction and (c.) size with dpa, for the Fe-Mn-Ni-Si and Fe-Mn-Si alloys, based on figs. 4.5 and 4.11. Dotted lines added to show observed trends with dose, with linear trend in number density and volume fraction plots, and an increase and stabilisation of mean size of solute-rich feature..

4.7.2 Composition

In the Fe-Mn-Si alloy, the Mn-N-Si precipitate compositions varied with dose. The ratio of Mn:Si was higher, and the fraction of N was lower at 2 dpa, compared with 0.1 dpa, table 4.11. The Mn:Si ratio is not correlated with precipitate size.

In the Fe-Mn-Ni-Si alloy, two clearly contrasting precipitate compositions emerge at higher doses; one with Ni content around 50 at.% and one with very low Ni content, in a shell around a Mn-Si-N rich core, fig. 4.27.

At low doses, only one population of precipitates was observed with approximate stoichiometry of $Mn_{2.5}Ni_{3.0}Si_{1.0}$. At higher doses, the composition fluctuates but maintains an average of approximately 50 at.% Ni, with a reduction of Mn relative to Si, table 4.9. The Ni lean precipitates have less Ni present at higher doses, and a higher Mn:Si ratio, increasing from 0.89 to 1.84 from 0.5 to 2 dpa, table 4.10.

Table 4.9: Average atomic fraction Mn, Ni and Si, in Ni rich precipitates plotted in fig. 4.27 with corresponding Mn-Ni-Si stoichiometry, omitting Fe & N.

Dose (dpa)	Mn	Ni	Si	Stoichiometry
0.1	38.37±1.08	46.29±0.40	15.34±1.26	$Mn_{2.5}Ni_{3.0}Si_{1.0}$
0.5-1.0	26.72±8.38	51.24±11.4	22.05±6.90	$Mn_{1.2}Ni_{2.3}Si_{1.0}$
2.0	31.19±4.60	49.01±5.83	17.95±3.56	$Mn_{1.7}Ni_{2.7}Si_1$

Table 4.10: Average atomic fraction Mn, Ni and Si, in Ni lean precipitates plotted in fig. 4.27 with corresponding N-Mn-Ni-Si stoichiometry, omitting Fe.

Dose (dpa)	N	Mn	Si	Ni	Stoichiometry
0.1	-	-	-	-	-
0.5-1.0	65.21 ± 3.54	15.02 ± 1.31	14.60 ± 1.24	5.17 ± 1.08	$N_{12.6}Mn_{2.9}Si_{2.8}Ni$
2.0	53.68 ± 1.77	27.36 ± 1.86	14.53 ± 0.81	4.43 ± 0.88	$N_{12.1}Mn_{6.2}Si_{3.3}Ni$

Table 4.11: Average atomic fraction Mn and Si, in precipitates plotted in fig. 4.31 in the Fe-Mn-Si alloy, with corresponding N-Mn-Si stoichiometry, omitting Fe.

Dose (dpa)	N	Mn	Si	Stoichiometry
0.1	50.52 ± 2.06	19.45 ± 1.18	30.04 ± 1.30	$N_{2.6}MnSi_{1.5}$
2.0	36.39 ± 1.74	35.64 ± 1.44	28.07 ± 0.55	$N_{1.3}Mn_{1.3}Si$

Figure 4.43 shows a comparison of composition profiles across the main types of precipitate observed in the irradiated alloys. It suggests that the phase forming in the Fe-Mn-Si alloy, is

similar to the phase with the Ni shells observed in the Fe-Mn-Ni-Si alloy and that the low nickel content is likely to be due to the outer shell, rather than Ni dispersed inside the precipitate.

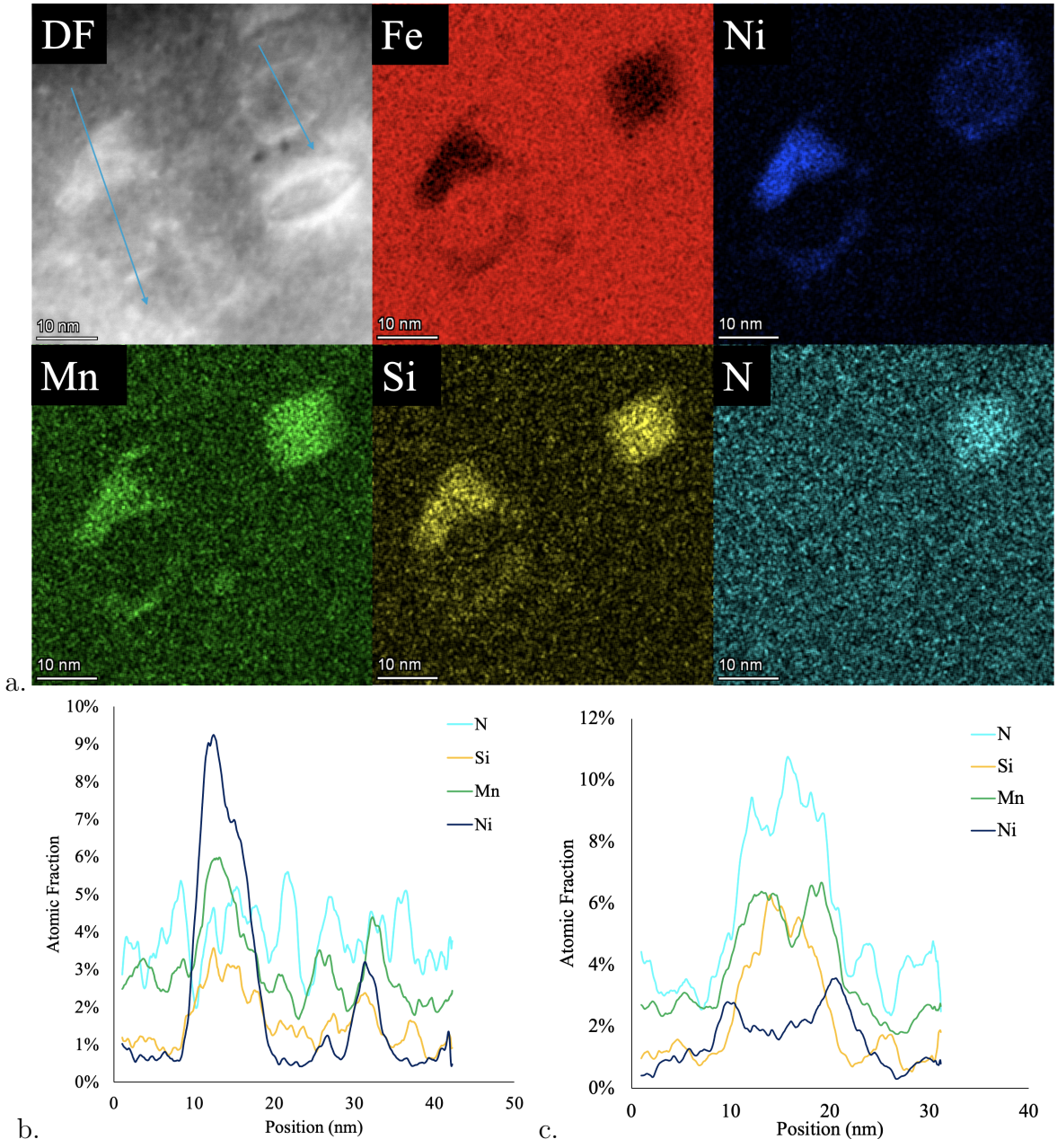


Figure 4.43: (a.) DF STEM image and Fe (red), Ni (blue), Mn (green), Si (yellow) and N (turquoise) EDX at.% maps, (b.) line scan of atomic concentration profile across Ni rich precipitate on an enriched dislocation loop, and (c.) Line scan atomic concentration profile across Ni lean nitrogen rich precipitate with Ni enrichment at the interface.

4.7.3 Structure

SADPs suggested the presence of at least two secondary cubic phases, with some spots suggesting a coherent structure with approximately 2-4 x the lattice paraemter of bcc Fe. The closest matching patterns were the G phase ($Fm\bar{3}m$), with a calculated lattice parameter of 1.13 ± 0.02 nm and $MnSiN_2$, ($Pna2_1$) with calculated lattice parameters of a = 0.525 ± 0.011 nm, b= 0.649 ± 0.014 nm and c= 0.596 ± 0.011 nm, table 4.7.

4.7.4 Segregation to defects

Ni segregation was observed both to grain boundaries and to dislocation loops. Mn segregation to grain boundary was observed, but there is no significant grain boundary segregation of Si. This may be due to its very low concentration in the matrix and measurement times being insufficiently long. Mn and Si were observed qualitatively to segregate to dislocation loops, (figs. 4.14 and 4.15), to a smaller extent than Ni.

4.8 Conclusion

Two distinct types of precipitates have been identified, using TEM, in the irradiated Fe alloys; Mn-Ni-Si rich features, with high Ni and Mn, and Mn-Si nitrides. Observation of fewer Mn-Si nitrides than Mn-Ni-Si precipitates in the Fe-Mn-Ni-Si alloy suggests that the Mn-Si nitrides have slower formation kinetics than Mn-Ni-Si precipitates, and require higher levels of radiation enhanced diffusion to form. However, they may be more thermodynamically stable, given that they seem to nucleate inside Mn-Ni-Si precipitates leading to the displacement of Ni from these phases into a shell. No nitrides were observed at lower doses/ dose rates.

Hardening has been observed in the plateau region of both alloys, where the majority of damage is made up of Mn-Ni-Si or Mn-N-Si precipitates and dislocation loops, and Ni addition has led to greater number densities of dislocation loops and precipitates and greater subsequent hardening.

Chapter 5

Local Composition Analyses of Proton-Irradiated and unirradiated Model Alloys and RPV Steel Using Atom Probe Tomography

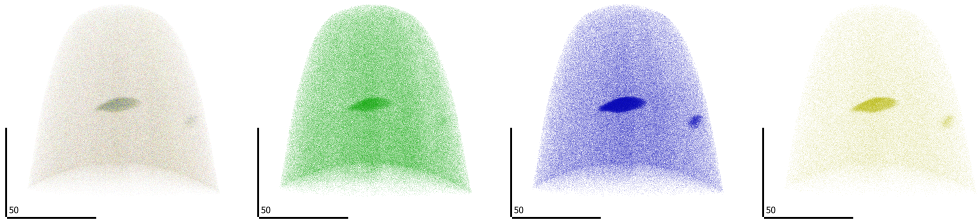
In this chapter APT has been used to characterise the composition of the matrix and precipitates, where identified, in both proton-irradiated and unirradiated Fe-Mn-Ni-Si, Fe-Mn-Si, Fe-Mn-Ni and A508-3 samples, as described in chapter 3. Atom probe tomography enables the identification of elements across the periodic table as well as three-dimensional location information for those elements, making it an ideal way to assess radiation induced segregation and the presence of precipitates less than 100 nm in size. In this chapter, APT results have been used to measure the composition of Mn-Ni-Si precipitates observed in the irradiated Fe-Mn-Ni-Si alloy, and to compare matrix solute content in specimens where no segregation was observed.

5.1 Matrix composition results & depletion analysis

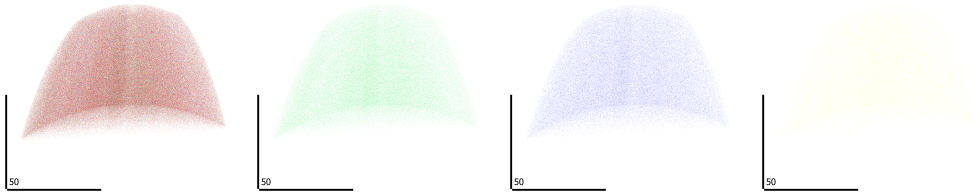
The results of composition calculations for each alloy are presented below. The average composition is the at.% calculated for each alloy in each condition, weighted by the size (no. ions reconstructed) of the measured dataset. Where multiple datasets have been acquired, the error

is the standard error on the mean value of at.%. Otherwise, the errors were calculated by finding the confidence interval obtained from peak decomposition. As this is a statistical error based on the number of ions in a dataset it is not representative of the uncertainty on composition of the material so where these values are smaller than 0.01 at.%, they have been rounded up. Ion maps for all model alloy collected data sets are shown in figs. 5.1 to 5.3, showing homogenous distributions of solute in the matrix of all as-received specimens, and in irradiated Fe-Mn-Si.

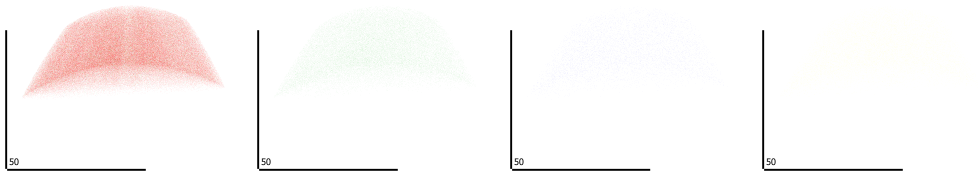
a. Fe-Mn-Ni-Si, proton-irradiated (41382), all ions, Mn, Ni, Si.



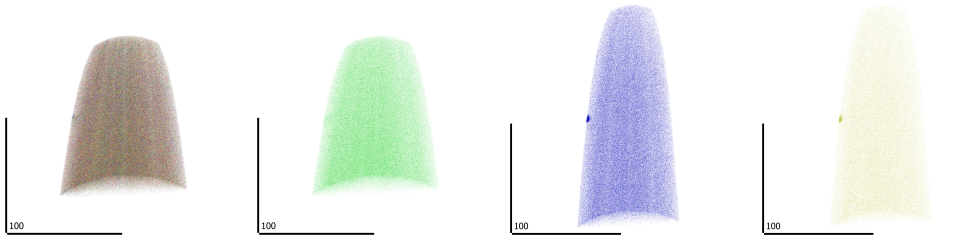
b. Fe-Mn-Ni-Si, proton-irradiated (41383), all ions, Mn, Ni, Si.



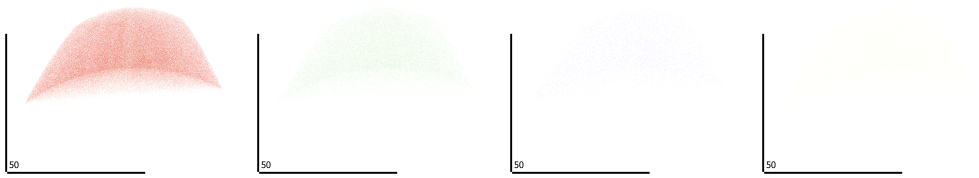
c. Fe-Mn-Ni-Si, proton-irradiated (62216), all ions, Mn, Ni, Si.



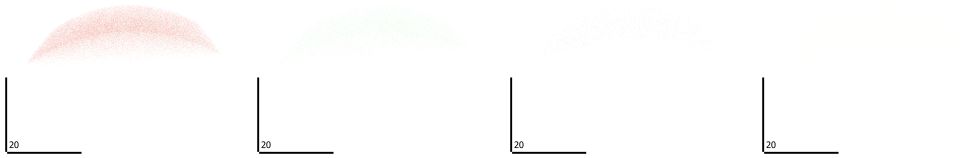
d. Fe-Mn-Ni-Si, proton-irradiated (62217), all ions, Mn, Ni, Si.



e. Fe-Mn-Ni-Si (62209), all ions, Mn, Ni, Si.



f. Fe-Mn-Ni-Si (62210), all ions, Mn, Ni, Si.



g. Fe-Mn-Ni-Si (62213), all ions, Mn, Ni, Si.

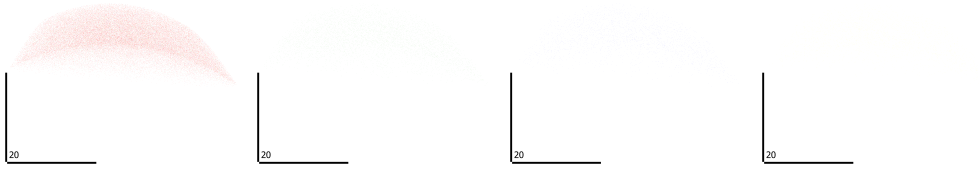
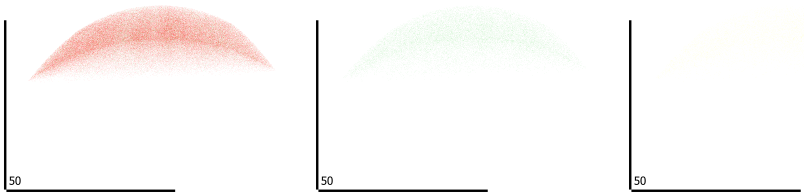


Figure 5.1: Ion maps for Fe-Mn-Ni-Si model alloy APT specimens.

a. Fe-Mn-Si, (41390), all ions, Mn, Si.



b. Fe-Mn-Si, proton-irradiated (41391), all ions, Mn, Si.

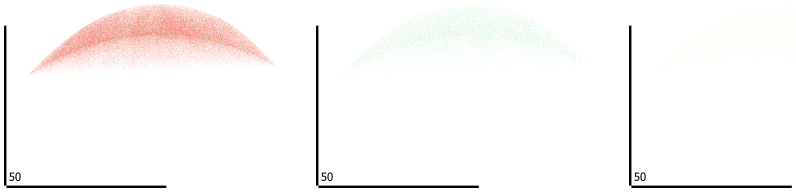
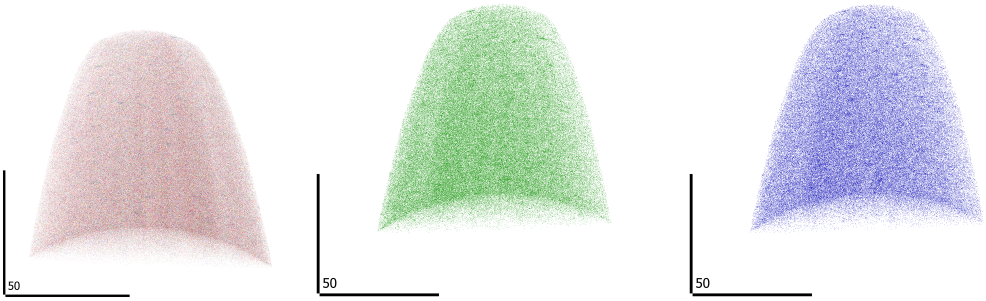
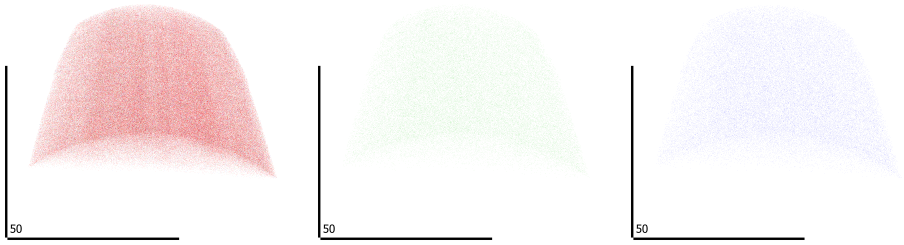


Figure 5.2: Ion maps for Fe-Mn-Si model alloy APT specimens.

a. Fe-Mn-Ni, proton-irradiated (72447), all ions, Mn, Ni.



b. Fe-Mn-Ni, proton-irradiated (72310), all ions, Mn, Ni.



c. Fe-Mn-Ni, (132780), all ions, Mn, Ni.

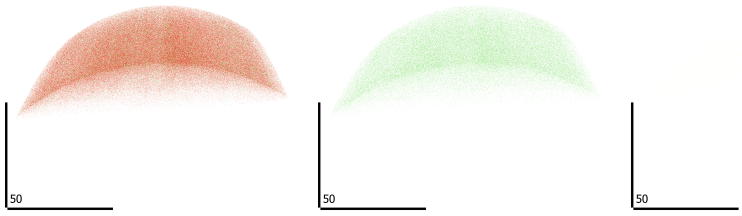


Figure 5.3: Ion maps for Fe-Mn-Ni model alloy APT specimens.

5.1.1 Fe-Mn-Ni-Si matrix composition

The bulk matrix compositions of proton-irradiated and unirradiated Fe-Mn-Ni-Si is shown in table 5.1, and shows some depletion of solute content after irradiation. Peak overlaps were calculated for Fe and Ni peaks and Si and N peaks using AtomProbeLab ([187]). Nitrogen content was calculated to be below 1×10^{-5} in all specimens except one small matrix specimen from the irradiation region, 62216, which had a calculated nitrogen content of 0.02 ± 0.02, suggesting any measured nitrogen is present in quantities too low to accurately measure. Therefore, N has been omitted from further analysis of composition in these specimens as no N rich features were present in the samples.

Table 5.1: Averaged matrix composition, in at. %, of Fe-Mn-Ni-Si alloy, in original and proton-irradiated conditions.

Element	Fe	Mn	Ni	Si
unirradiated	97.20 ± 0.03	1.43 ± 0.01	0.88 ± 0.01	0.49 ± 0.02
Irradiated	97.94 ± 0.01	1.18 ± 0.01	0.55 ± 0.01	0.33 ± 0.01

Where calculated errors are below 0.01 at.% they have been rounded up to 0.01 at.%. The change in composition is shown in table 5.2. It shows a significant depletion in Mn, Ni and Si content in the matrix, with a reduction of between 17.8 and 37.4 % of the original matrix content, corresponding to a drop in 0.16-0.33 at.%.

Table 5.2: Change in at.% composition between irradiated and unirradiated material, showing depletion of Mn, Ni and Si after irradiation.

Element	Fe	Mn	Ni	Si
Irr-Unirr	0.74	-0.25	-0.33	-0.16
% change	0.8%	-17.8%	-37.4%	-32.5%

This depletion suggests radiation enhanced diffusion and segregation of solute out of the ferritic matrix to other microstructural features.

5.1.2 Fe-Mn-Si matrix composition

Compositions of Fe-Mn-Si (table 5.3 before and after irradiation showed no significant difference, with all values within standard error of one another. Only 3 samples were measured in total, with 2 irradiated and 1 unirradiated. Peak overlaps were calculated for Si and N peaks using

AtomProbeLab ([187]). Nitrogen content was calculated to be below 8×10^{-5} in all specimens so has not been included in matrix composition analysis using APT.

Table 5.3: Averaged matrix composition, in at. %, of Fe-Mn-Si alloy, in original and proton-irradiated conditions.

Element	Fe	Mn	Si
unirradiated	98.14 ± 0.01	1.37 ± 0.01	0.49 ± 0.01
Irradiated	98.21 ± 0.02	1.36 ± 0.01	0.43 ± 0.04

5.1.3 Fe-Mn-Ni matrix composition

There was no significant difference observed across the unirradiated and irradiated Fe-Mn-Ni samples, and, only 3 specimens were measured, one unirradiated and two irradiated. It is unlikely that this number of ions is sufficiently large enough to provide a reliable assessment of the overall microstructure. The nitrogen content in the matrix was measured in this alloy to investigate whether the nitriding effects seen in chapter 4 were likely to be occurring in other samples, but there is no statistically significant difference in N content between the samples measured here.

Table 5.4: Averaged matrix composition, in at. %, of Fe-Mn-Ni alloy, in original and proton-irradiated conditions, including nitrogen content, based on results in chapter 4.

	Fe	Mn	Ni	N
unirradiated	98.13 ± 0.01	1.13 ± 0.01	0.72 ± 0.01	0.01 ± 0.01
Irradiated	98.06 ± 0.07	1.19 ± 0.04	0.74 ± 0.03	0.01 ±0.01

5.1.4 Summary of matrix composition analysis of model alloys

Only one alloy showed statistically significant evidence of solute depletion after irradiation; Fe-Mn-Ni-Si. This was the sample with the largest datasets and highest solute content. All alloys containing silicon had lower measured solute matrix content after irradiation. The Fe-Mn-Ni alloy seemed to have an increase in solute in the matrix after irradiation. However, due to the small volume of material analysed, this cannot be used to draw conclusions about radiation induced segregation and precipitation.

5.2 Fe-Mn-Ni-Si precipitate analysis: Large precipitate

In total, one full precipitate and 2 partial precipitates were observed in two specimens of irradiated Fe-Mn-Ni-Si, which were produced from the same region of material. Figure 5.4 shows a Mn-Ni-Si rich feature with an ellipsoidal shape in a ferritic matrix, along with a similar region of enrichment that is cut off by the side of the specimen. It has an approximate size of 30 x 25 x 10 nm.

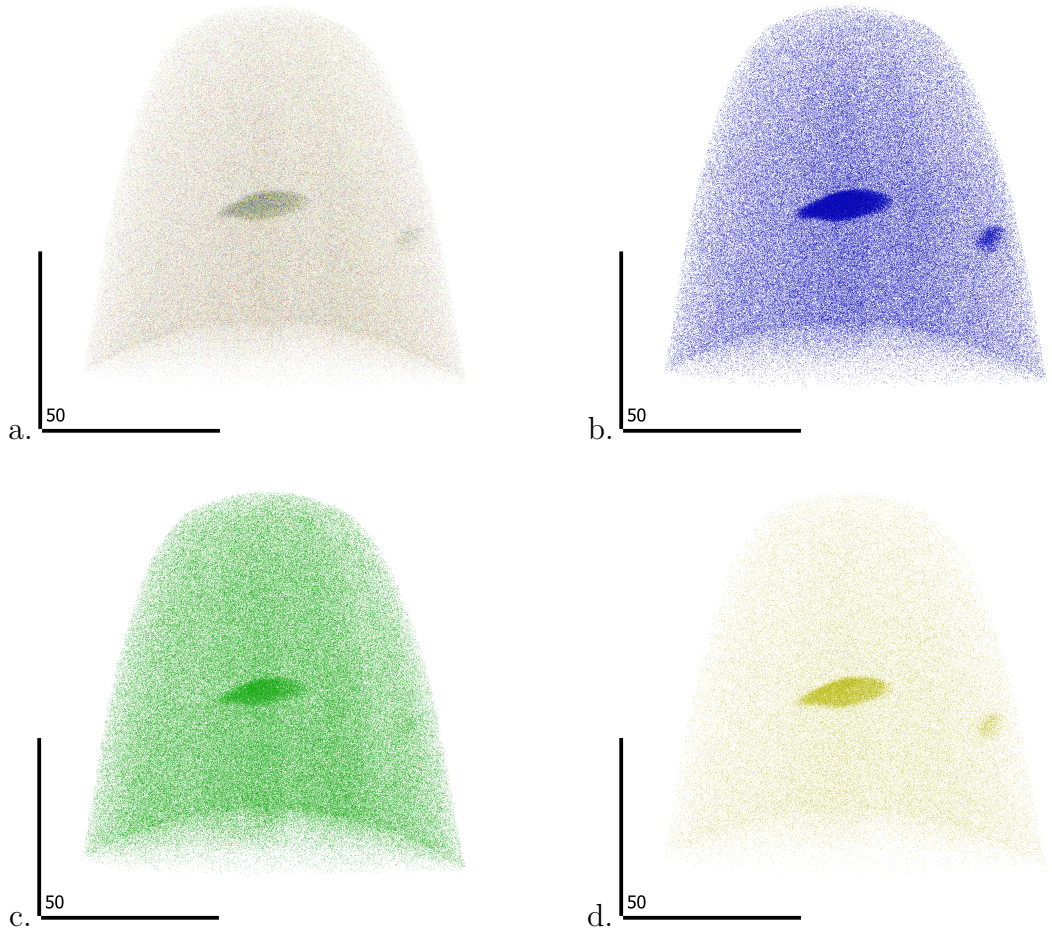


Figure 5.4: APT reconstructed irradiated Fe-Mn-Ni-Si alloy dataset showing (a.)10% Fe (red) ions and 100 % Mn (green), Ni (blue) and Si (yellow) ions visualised, (b.) Ni ions, (c.) Mn ions and (d.) Si ions.

Composition of the Mn-Ni-Si rich precipitate has been analysed as a 1D concentration profile along a cylinder ROI positioned perpendicular to x, y and z measurement axes and using a proxigram around a 50% Mn-Ni-Si atomic concentration iso-surface.

5.2.1 1D concentration profiles

The largest precipitate, shown in figure 5.4, was analysed using concentration profiles and proxigrams to calculate composition. Figure 5.6 shows the reconstruction with only Mn Ni and Si ions visible and isoconcentration surfaces at 50 at.% Mn+Ni+Si, used for proxigram analysis and positioning of analysis regions.

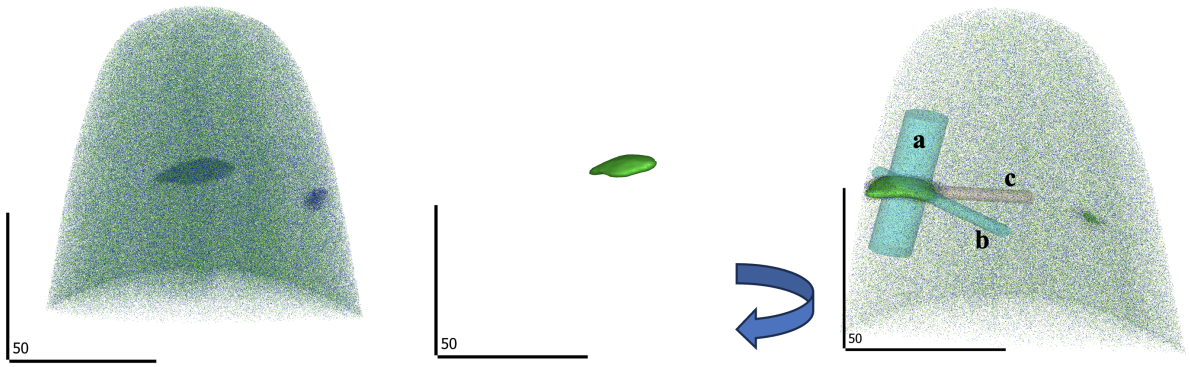


Figure 5.5: Reconstruction showing one whole Mn-Ni-Si rich feature (centre) and one partial feature (RHS), a 50 at.% isoconcentration surface, and 3 analysis cylinders; a, b & c, used for z profile concentration plots in figure fig. 5.6

Ionic concentration profiles were plotted with a bin size of 0.1 nm, and values averaged over 1 nm sections (fig. 5.6). They show a stabilisation of solute content towards the lowest region of Fe content, corresponding with the centre of the feature. Table 5.5 shows the average precipitate compositions calculated using the z profiles in each direction, using the region where the composition of Mn, Ni and Si, exceeds that of Fe to calculate the average composition.

The central average composition of Mn, Ni and Si is consistent across analysis direction, considering the variation due to the curvature of the interface at difference orientations.

Table 5.5: Average atomic concentration of Fe, Mn, Ni and Si, in given range with corresponding MnNiSi stoichiometry, omitting Fe.

Cylinder Range (nm)	Fe	Mn	Ni	Si	Stoichiometry
1 : 21.7-26.2 nm	24.3±1.8	14.2±0.5	42.8±1.1	17.7±0.3	$Mn_{5.3}Ni_{16}Si_{6.6}$
2 : 33.5-47.7 nm	22.3±1.0	15.1±0.4	43.7±0.7	17.9±0.4	$Mn_{5.5}Ni_{16}Si_{6.6}$
3 : 0-16.2 nm	20.6±0.8	14.8±0.4	45.5±0.6	18.1±0.3	$Mn_{5.2}Ni_{16}Si_{6.4}$

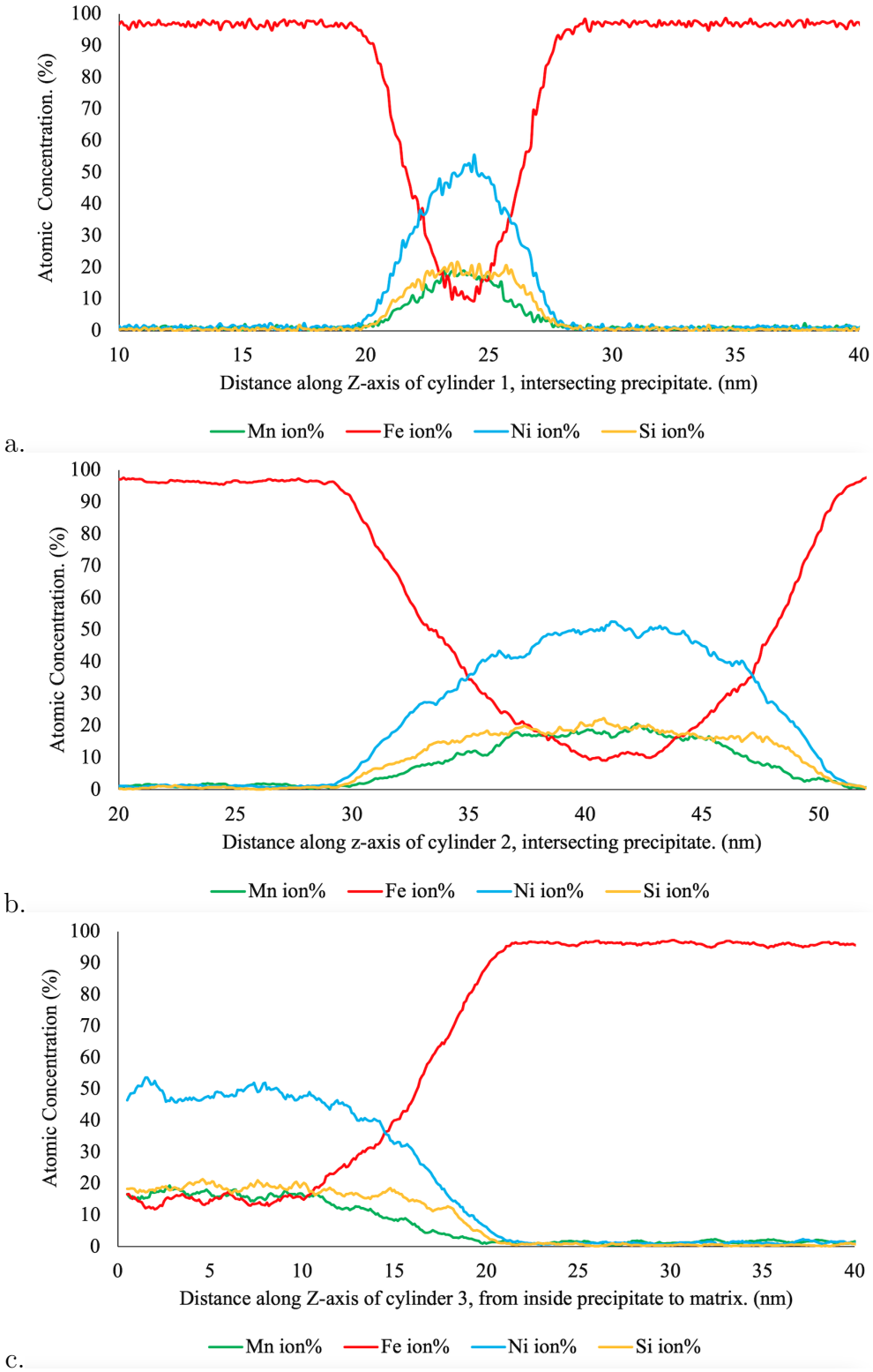


Figure 5.6: Atomic concentration profile, showing the average atomic concentration through Mn-Ni-Si rich feature along z axis of cylinders a, b and c as labelled in figure 5.5.

5.2.2 Proxigram composition analysis

Composition of the precipitate has also been calculated using a proxigram calculated using an isoconcentration surface at a 50 at.% Mn+Ni+Si threshold. This method takes the average concentration along lines intersecting the 50% threshold isoconcentration surface shown in figure 5.5 and plots atomic fraction as a function of distance from this interface, as shown in fig. 5.7.

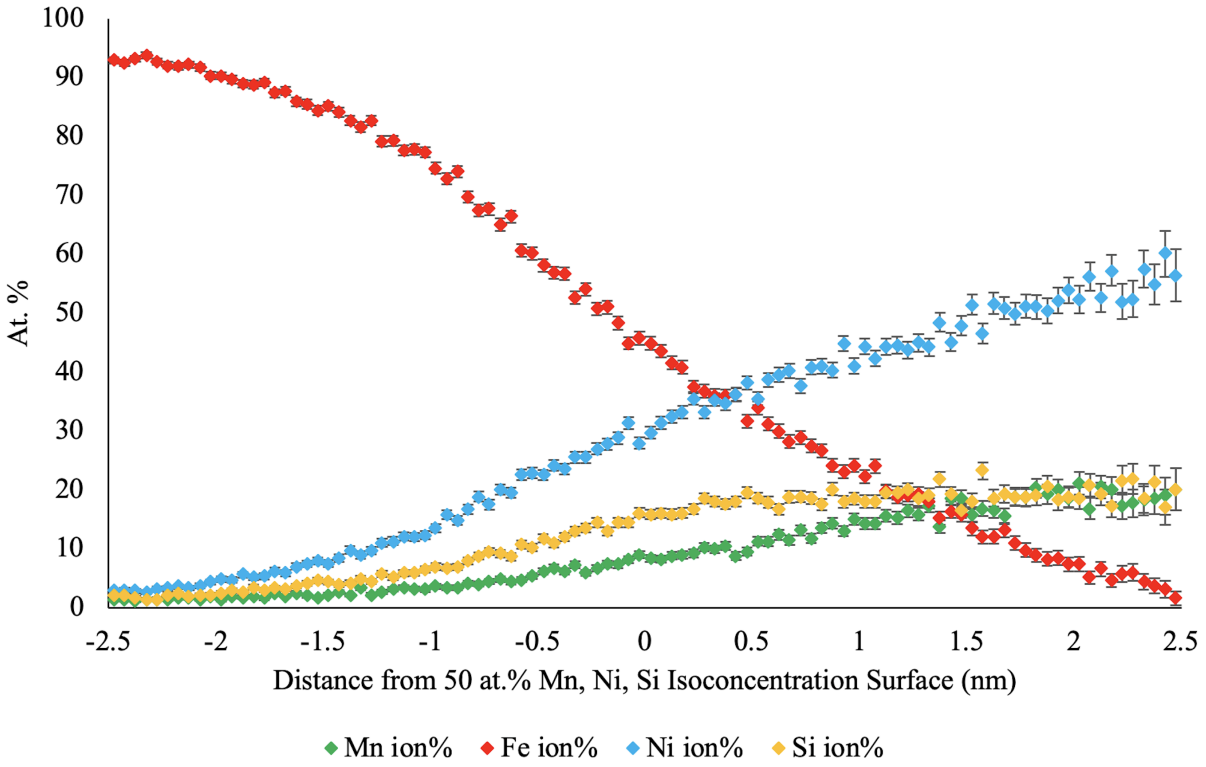


Figure 5.7: Proxigram for large whole precipitate, 0 nm is the 50 at.% Fe threshold, showing at. % of Fe, Mn, Ni and Si. Bin size= 0.05 nm.

The proxigram and concentration profiles show that the composition of manganese and silicon stabilises inside the precipitate, with measured compositions of approximately 17 at.% Mn and 19 at.% Si. This indicates that the precipitate has a stable composition across the feature, and is a distinctly separate phase from the matrix (fig. 5.7). The proxigram plot only measures the concentration over a short distance from the centre of the precipitate so at the furthest distance measured from the 50 at.% threshold there is still significantly more solute measured than the nominal matrix compositions stated in table 5.1. Measurements of matrix composition cannot be taken from this proxigram analysis.

Average compositions calculated at various iron thresholds are shown in table 5.6. They are

consistent with the compositions in table 5.5. At the centre of the precipitate in the proxigram however, the concentration of iron drops to 1.61±1.13 at.%. The ratio of Mn:Ni:Si is consistent with the 1D concentration profiles and does not change significantly with changing Fe threshold. Silicon concentration does not decrease significantly as more iron is included in the calculation.

Table 5.6: Large precipitate proxigram calculated feature compositions measured using lowest values of Fe content, values at <20 at. % and <40 at. %.

Fe threshold	Fe at.%	Mn at.%	Ni at.%	Si at.%	Stoichiometry, omitting Fe
Minimum Fe content.	1.61±1.13	20.16±3.60	56.45±4.45	20.16±3.60	$Mn_{5.7}Ni_{16}Si_{5.7}$ ($Ni_{16}(Mn,Si)_{11.4}$)
Fe <20 at. %	10.58±1.06	17.95±0.32	50.89±0.74	19.47±0.39	$Mn_{5.6}$ $Ni_{16}Si_{6.1}$ ($Ni_{16}(Mn,Si)_{11.8}$)
Fe <40 at. %	18.15±1.62	15.59±0.52	49.19±1.06	19.00±0.21	$Mn_{5.4}Ni_{16}Si_{6.6}$ ($Ni_4(Mn,Si)_3$)

The proxigram cannot measure the whole region of interest from the matrix into the centre of the precipitate and averages over all directions, removing any dependence of composition on measurement direction or feature orientation. This may account for the smoothing of the interface, compared with the sharper increase in solute observed in the 1D concentration profiles.

In the concentration profiles, fig. 5.6, manganese content increases more gradually than silicon and nickel, but silicon levels off near the interface. Nickel content peaks in most profiles, at 52 at.%, near the centre of the feature. This is consistent with the proxigram compositional gradients. The proxigram shows a ratio of approximately 1:1 , Mn:Si, concentration at the centre of the precipitate, but both this and the concentration profiles suggest there is slightly more silicon than manganese in the precipitates outside of the centre.

The ratio of Ni:(Mn+Si) remains approximately constant across the range of the proxigram, but the ratio of Si:Mn fluctuates, increasing up to 1.93, when iron is around 60 at.% and then decreasing into the centre of the precipitate, stabilising at 1.06.

5.2.3 Field evaporation effects on ion density

Plotting the total ion counts as a function of z direction along the data collection axis, shows a significant increase in the region of Mn-Ni-Si enrichment. Ion density decreases back to the

previous constant when the evaporation surface passes through the precipitate. This is shown in fig. 5.8, where it can be seen that this effect is more significant in the z direction (almost parallel to the measurement axis) than in the lateral plane.

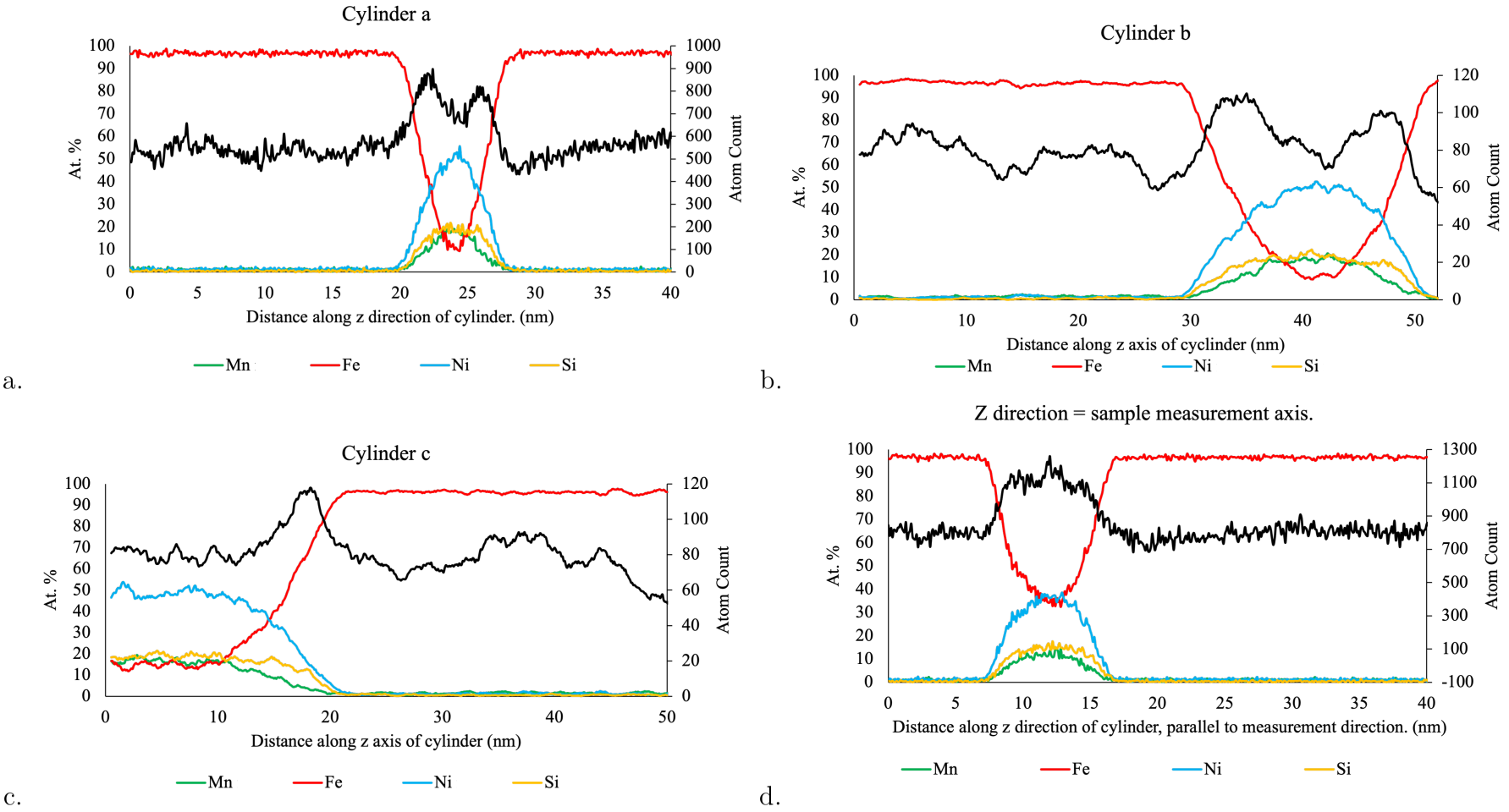


Figure 5.8: 1D concentration profiles with atom count recorded on right hand axis, showing an increase in ion measurement density in the region enriched in Mn, Ni and Si in (a.) cylinder a, (b.) cylinder b, (c.) cylinder c and (d.) along the sample measurement axis (z), all from fig. 5.5.

The density of the precipitate is approximately 1.5x the matrix, which implies it is low field, and there is a focusing of ions from the matrix into the feature so the iron content in the precipitate is likely to be lower than measured using the proxigram in fig. 5.7.

There is a smaller difference in ion density inside the precipitate and outside when measuring along the lateral plane fig. 5.8.

All interfaces show an increase in ion density, corresponding to a low field evaporation threshold. This is due to ions at interfaces requiring less energy to be evaporated from the specimen than those in a stable matrix.

5.3 Comparison of measured compositions for whole and partial precipitates.

5.3.1 Partial precipitate composition

One other dataset contained a Mn-Ni-Si enriched feature and is shown in fig. 5.9. The feature is cut-off by the edge of the specimen but it can be seen from a concentration profile that there is increasing Mn, Ni and Si content.

Proxigrams for partial precipitates observed in the data set in fig. 5.9, and in the datasets containing a whole precipitate (fig. 5.4) are shown in fig. 5.10. A similar trend of increasing Ni, Mn, and Si in the specimens and a levelling off of composition of Mn and Si are observed, as in fig. 5.7.

5.3.2 Comparison of measured compositions

The compositions of all the observed precipitates, averaged below 40 at.% Fe are shown in table 5.7, along with estimated stoichiometry.

Both smaller precipitates have higher silicon content than the larger feature, and higher composition of iron measured as being 'inside' the feature. This may be due to the calculated composition being based on an edge section of the precipitate, as complete features weren't observed. The trend observed in fig. 5.10 (a.), matches that of the increasing silicon with slower manganese increase. The shapes of the partial precipitates are difficult to determine; they may be ellipsoidal or spherical.

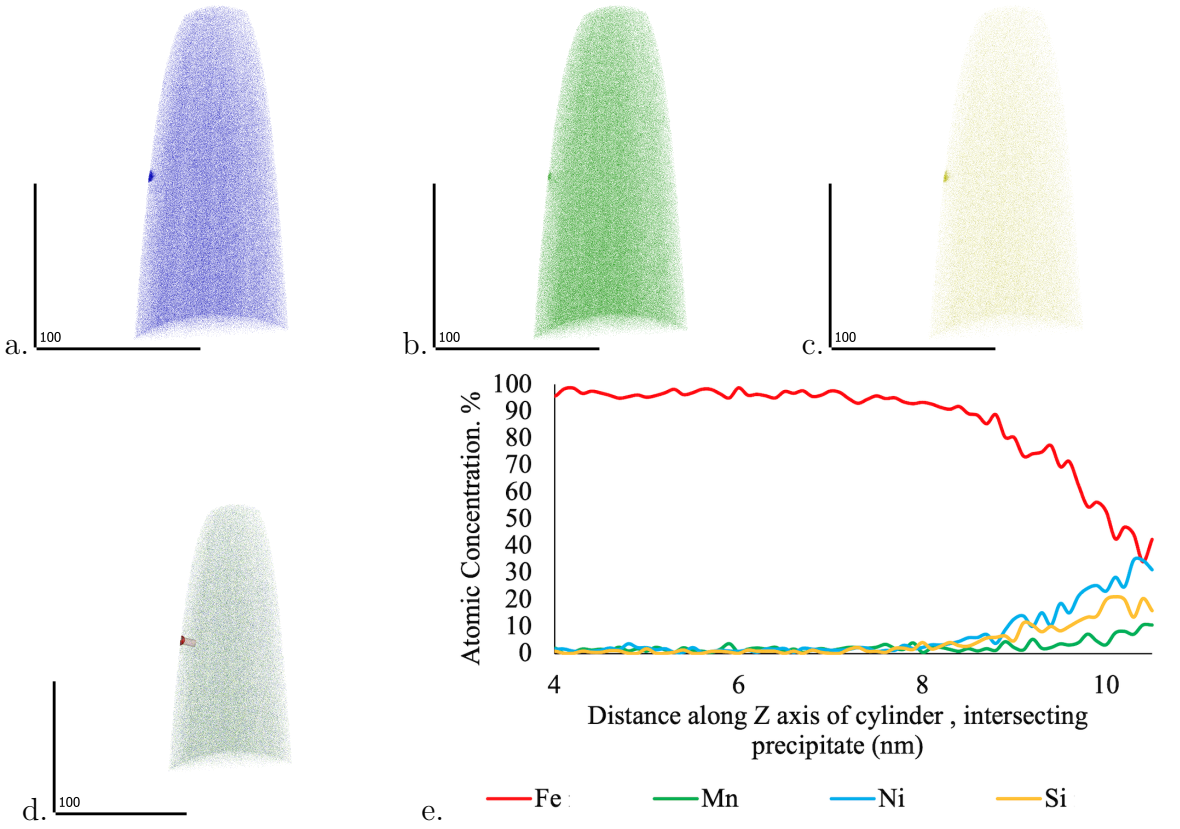


Figure 5.9: Proton-irradiated Fe-Mn-Ni-Si alloy dataset containing part of a Mn-Ni-Si rich precipitate. Visualisations of ion reconstructions showing (a.) Ni, (b.) Mn, (c.) Si. A 1D concentration profile (e.), across a cylinder oriented perpendicularly to a 20% Mn-Ni-Si concentration iso-surface (d.), shows enrichment of Mn, Ni, and Si inside a partial precipitate on the edge of the data set.

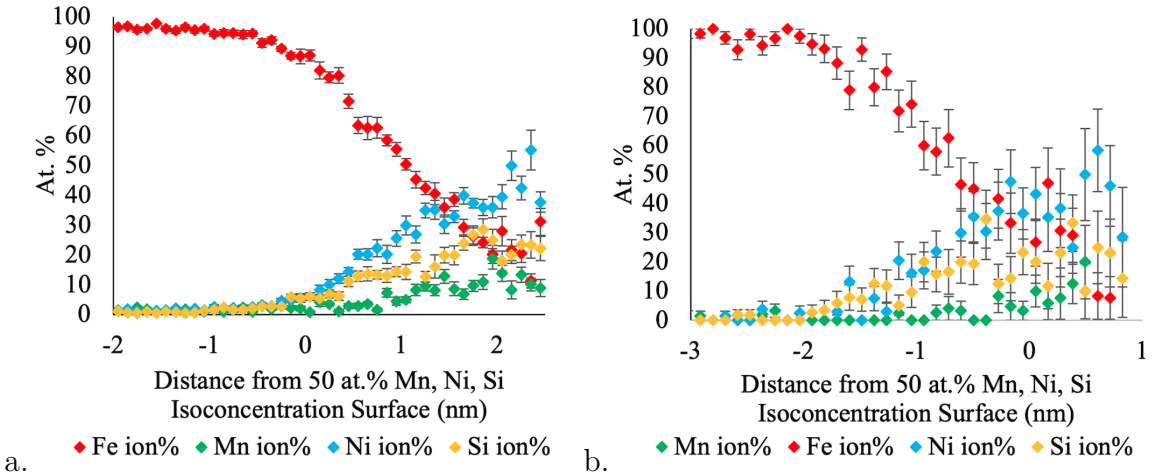


Figure 5.10: Proxigrams showing variation in Fe, Mn, Ni, and Si concentration around the 50 at.% concentration threshold for (a.) the partial precipitate observed in dataset shown in 5.9 and (b.) the partial precipitate observed in dataset from 5.4, with the large precipitate.

Table 5.7: Comparison of average precipitate compositions for <40 at.% Fe content.

Composition	Fe	Mn	Ni	Si	Approximate stoichiometry, omitting Fe.
Large precipitate	18.15±1.62	15.59±0.52	49.19±1.06	19.00±0.21	$Mn_{5.4}Ni_{16}Si_{6.6}$ $(Ni_{16}(Mn,Si)_{12})$
Partial precipitate, 62217	23.74±0.96	11.28±0.83	41.23±1.28	23.55±1.03	$Mn_{4.4}Ni_{16}Si_{9.1}$ $(Ni_{16}(Mn,Si)_{13.5}$
Partial precipitate 41382	24.60±3.60	11.83±2.92	40.46±3.34	22.12±2.52	$Ni_{16}Mn_{4.6}Si_{8.7}$ $(Ni_{16}(MnSi)_{13.4}$

5.4 Fe-Mn-Ni radiation-induced clustering analysis

One irradiated Fe-Mn-Ni specimen showed some possible clustering of Mn and Ni when visualising iso-concentration surfaces for Mn and Ni, figs. 5.11 and 5.12. However, the fluctuations in composition observed are very small, and features are very diffuse, as indicated by the lack of clustering identified between low order nearest neighbours, fig. 5.15. These fluctuations could be due to random compositional variation present in the alloy, and further investigation is required to confirm the presence of Mn-Ni clustering in this proton-irradiated alloy.

5.4.1 Proxigram & concentration profiles

1D concentration profiles have been plotted vertically through the two of the enriched regions, fig. 5.13. These show an increase of Mn content up to 25 at.% and Ni content up to 19 at.%, with clear depletion of iron in these regions. Both profiles show the peaks of Mn and Ni slightly offset, suggesting the clustering of solute on different sides of the feature, with the average solute content over the enriched region approximately remaining constant.

A proxigram was plotted using the 5% Mn-Ni iso-surface (fig. 5.12), and the results of this are shown in fig. 5.14. Mn and Ni content increase in line to around 15 at.%, consistent with

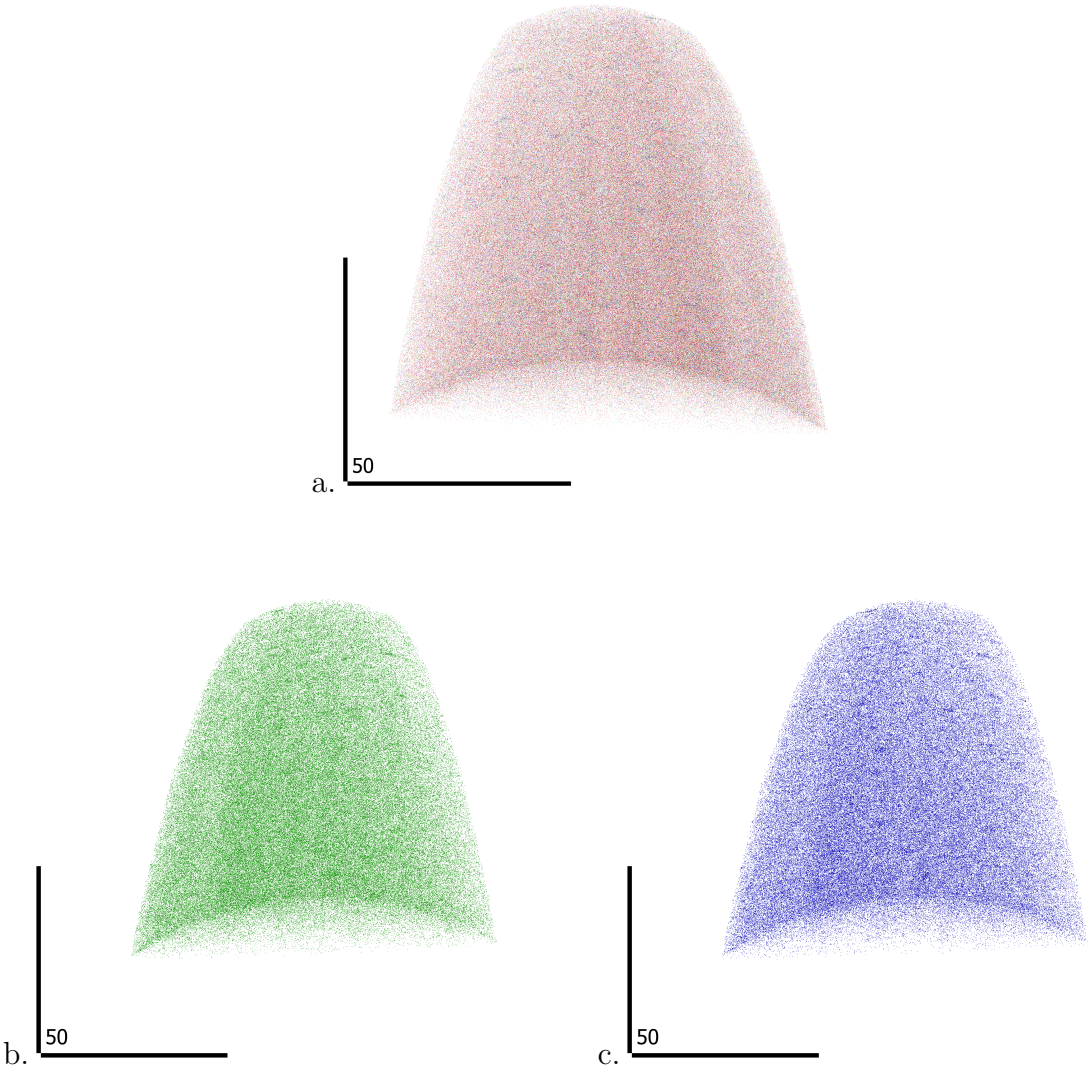


Figure 5.11: Irradiated Fe-Mn-Ni alloy specimen ion maps, showing (a.) 10% Fe, 100% Mn and Ni, (b.) Mn only and, (c.) Ni only, showing very small clusters of Mn and Ni.

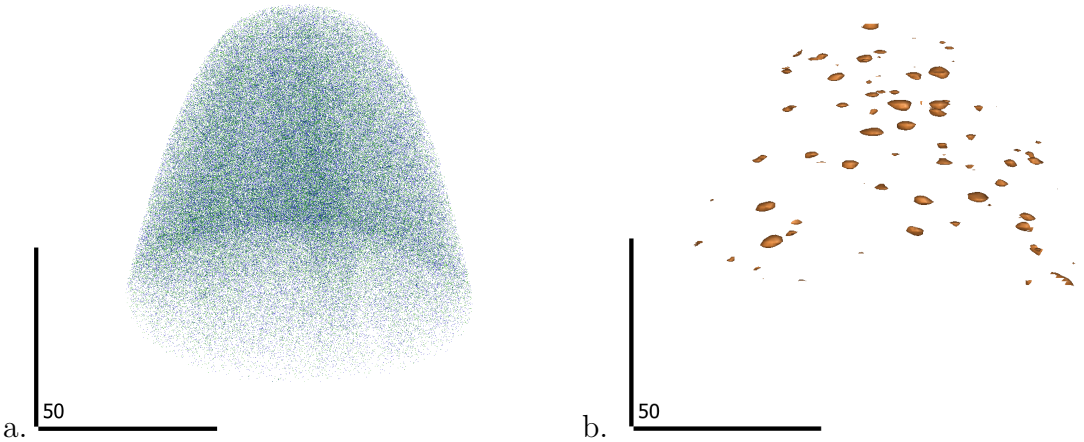


Figure 5.12: Mn and Ni ion map (a.) and corresponding 5% isoconcentration surface for Mn and Ni (b.), showing very small clusters enriched in Mn and Ni.

the enrichment observed in 1D concentration profile.

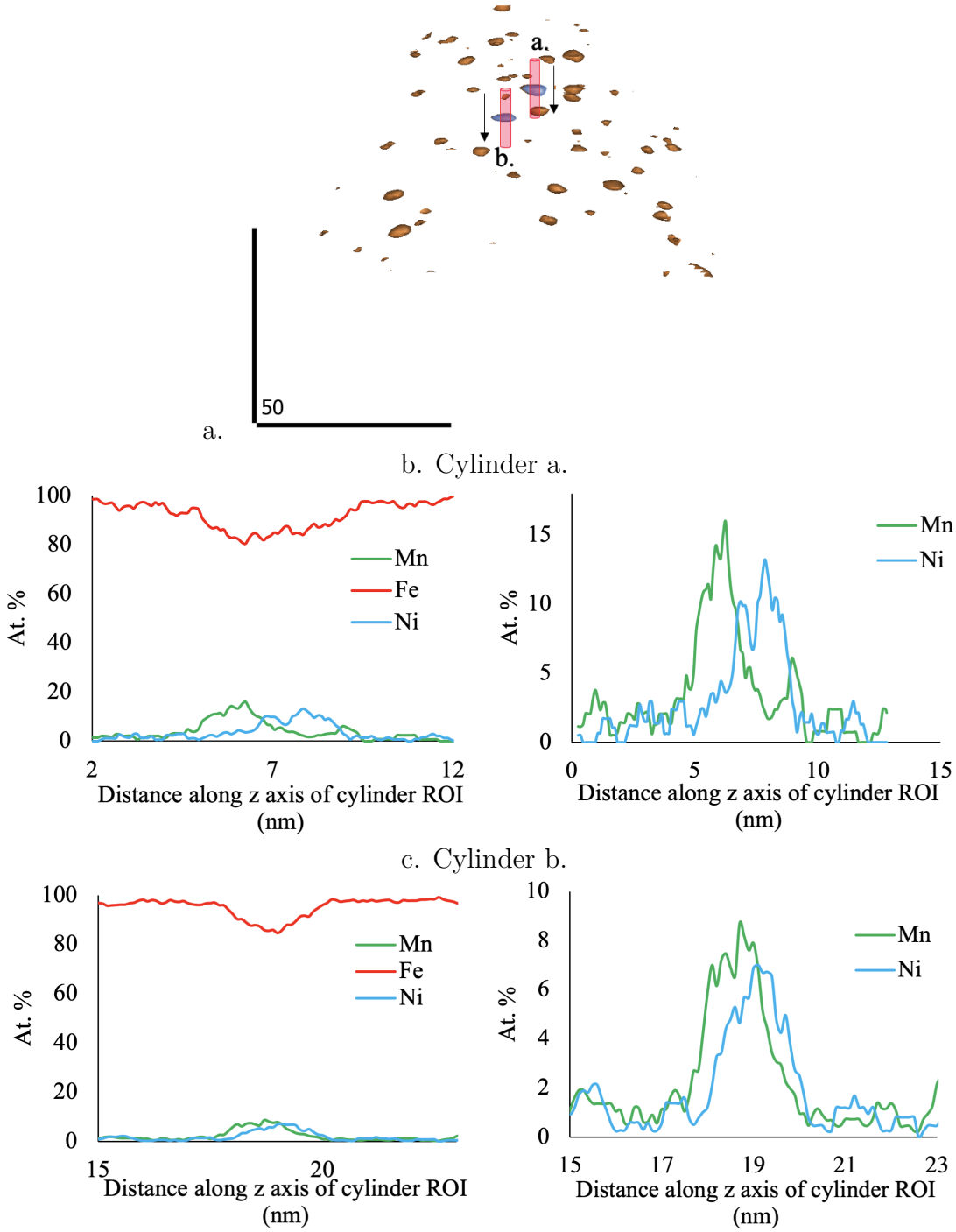


Figure 5.13: 1D concentration profiles (b. & c.) through cylinders(a.) , showing increasing Mn and Ni concentration in offset peaks.

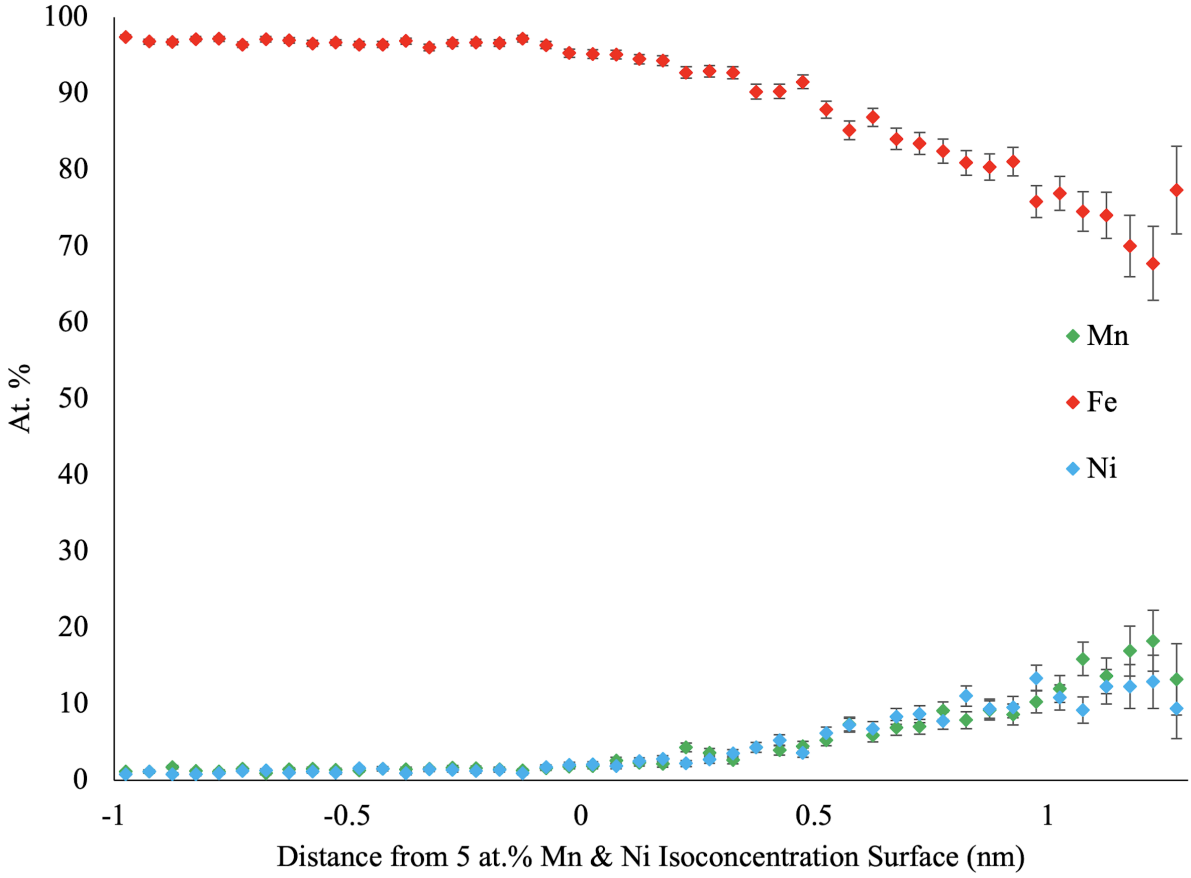
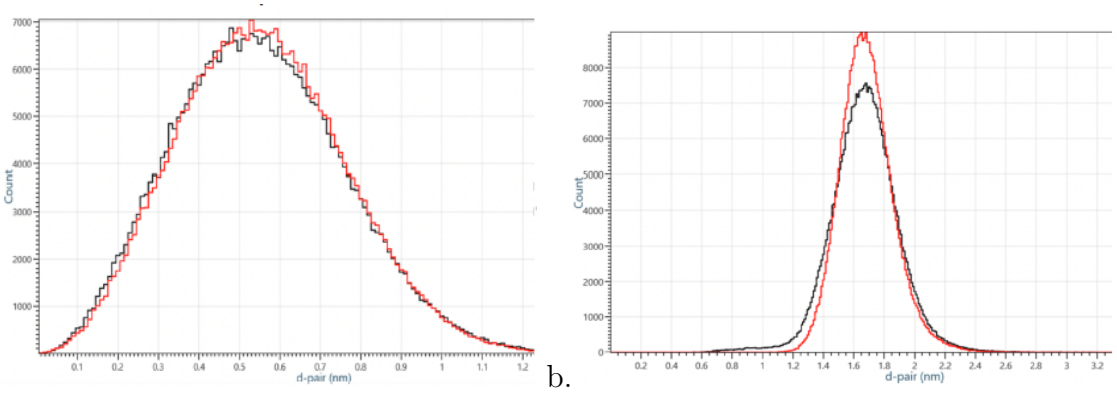


Figure 5.14: Proxigram showing concentration of Fe, Mn and Ni inside and outside 5 at.% Mn & Ni isoconcentration surface shown in fig. 5.12.

5.4.2 Nearest neighbour distribution analysis

First order nearest neighbour analysis shows no difference between the distribution of first nearest neighbours for Mn and Ni and a randomised distribution. However, at higher order, k=20, there is some deviation from the random distribution. A very small shift, of approximately 0.1 nm in the peak to slightly lower than random separation distance, could suggest very early stage clustering is taking place. However, the overall peak shape is narrower and the lower tail is shifted to larger spacing, which is not a clear indicator of clustering, fig. 5.15. These data do not provide confidence that solute clustering is taking place, and more data is required to draw conclusions on solute behaviour in this specimen.



a. b.

Figure 5.15: Nearest neighbour distributions for Mn and Ni ions, showing measured data from proton-irradiated Fe-Mn-Ni alloy in red, and a randomised distribution of ions in black for (a.) $k = 1$, and (b.) $k = 20$

5.5 A508-3 RPV steel results

Five APT specimens of A508-3 reactor pressure vessel steel were measured; three irradiated and two unirradiated. Both unirradiated samples only contained matrix material. The proton-irradiated material measured includes a grain boundary, a carbide and a matrix sample. The variation in observed microstructures from a single lift-out demonstrates the inhomogeneity of this steel.

Reconstructed ion maps for elements identified in these samples are shown in figs. 5.16 to 5.20.

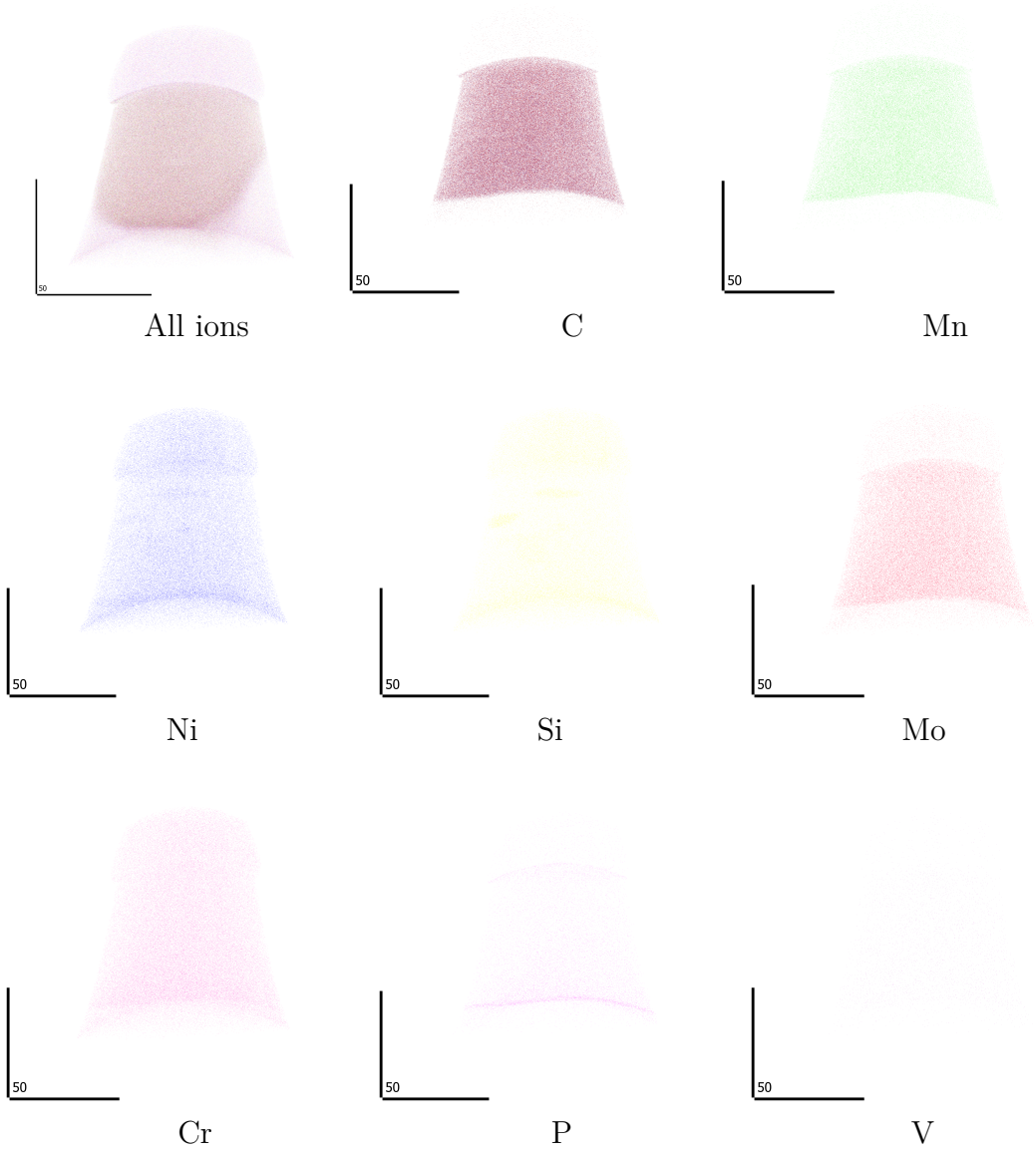


Figure 5.16: A508-3, proton-irradiated (72401) RPV steel ion maps, showing carbide in the centre with ferritic matrix above and below it.

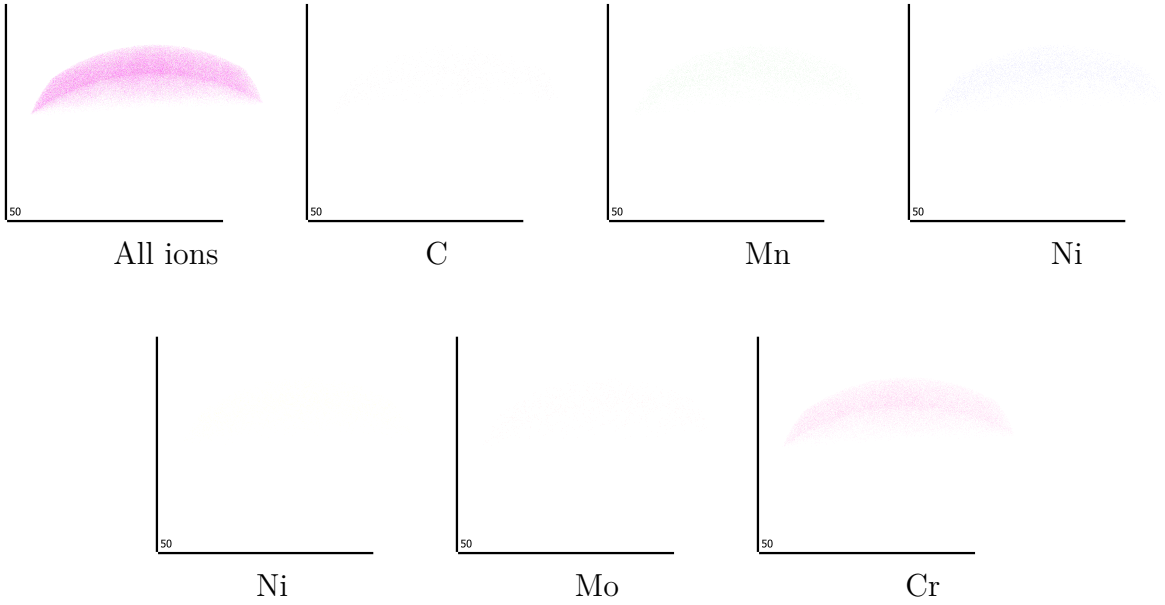


Figure 5.17: A508-3, proton-irradiated (72402) RPV steel reconstructed ion maps.

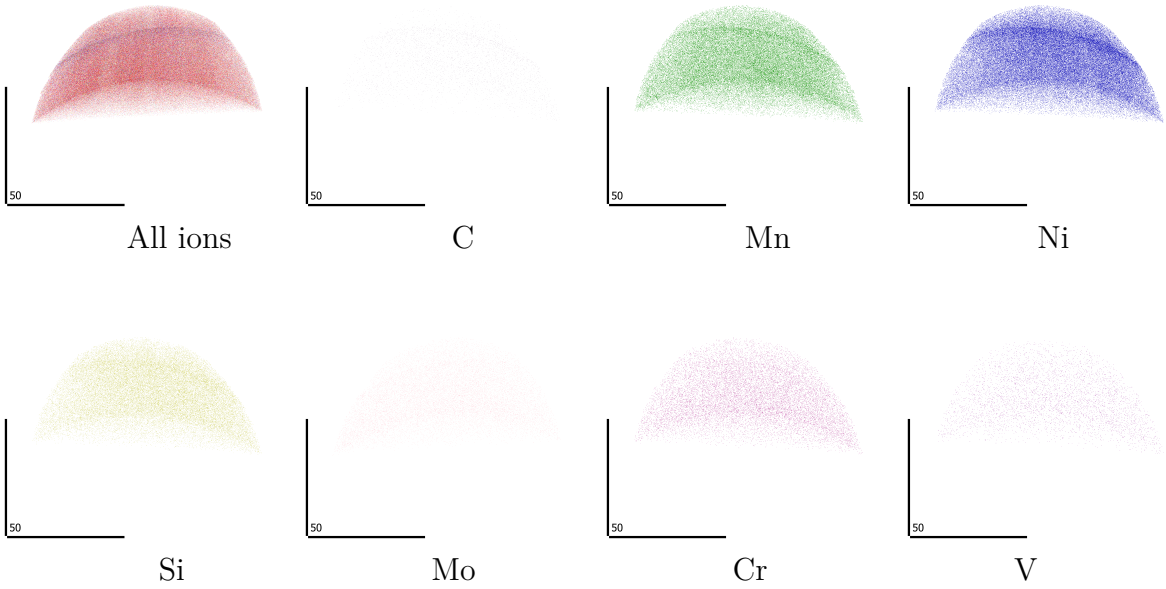


Figure 5.18: A508-3, proton-irradiated (72312) RPV steel reconstructed ion maps.

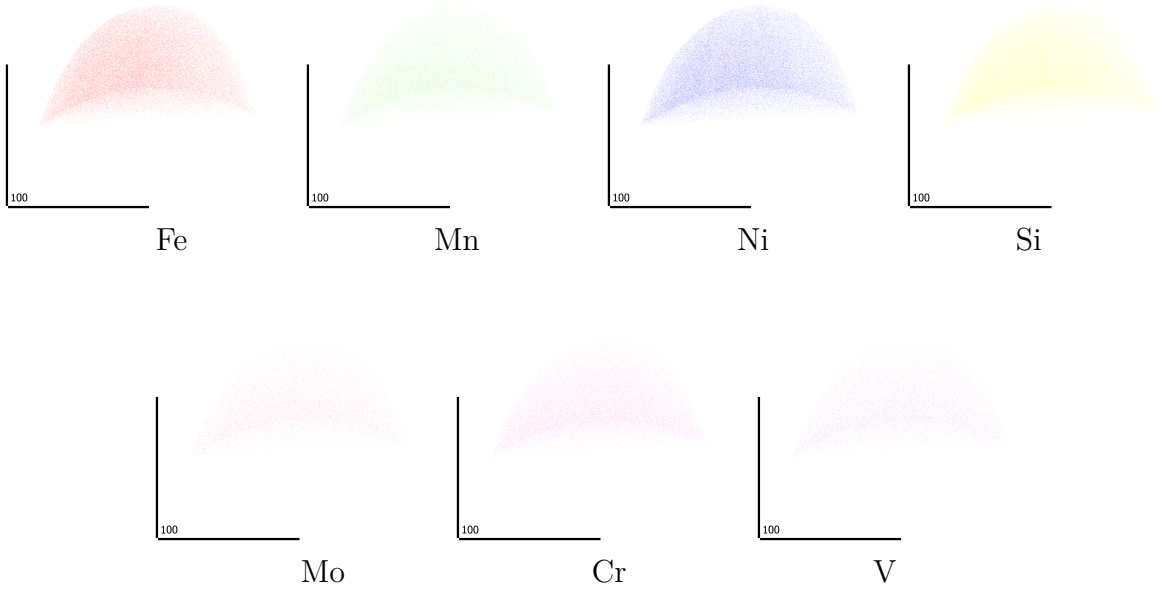


Figure 5.19: A508-3 (72406) RPV steel reconstructed ion maps.

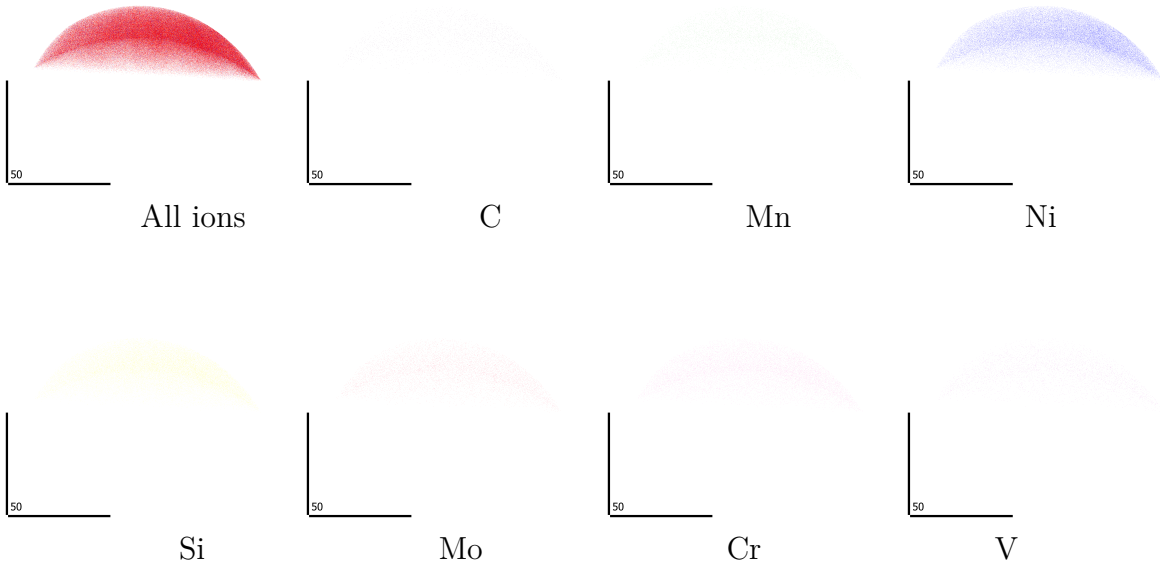


Figure 5.20: A508-3 (82439) RPV steel reconstructed ion maps.

5.5.1 A508-3 steel composition analysis

Average matrix compositions for the unirradiated and irradiated specimens are shown in table 5.8. The irradiated matrix calculation omits the grain boundary and carbide-matrix interface regions and is weighted based on the total number of ions used to calculate each composition. Trace impurities have been excluded from composition calculations including oxygen and hydrogen. Sulphur and phosphorus are often found in steels as impurities and contribute to the radiation sensitivity so have been included in composition analysis. Where peaks were not ranged for an element, the values have not been included in the average as zero, this may lead to a small overestimate of trace element composition. Standard errors on the weighted mean have been calculated as an estimate for the uncertainty but have been rounded up to 0.01 where below this. A summary of all measured compositions and comparison with the nominal alloy composition is shown in table 5.9. The variation in solute content across A508-3 specimens and sample conditions is expected due to the inhomogeneity of microstructure generally observed in bainitic low alloy steels.

Table 5.8: Averaged APT measured RPV matrix compositions for unirradiated and irradiated conditions.

Element	unirradiated	Irradiated
Fe	98.79±0.17	97.94±0.1
Mn	0.05± 0.016	0.84±0.05
Ni	0.7±0.016	0.666±0.02
Si	0.3±0.008	0.353±0.01
C	0.016±0.003	0.022±0.02
Cr	0.018±0.006	0.076±0.002
Mo	0.001±0.003	0.08±0.02
V	0.001±0.002	0.000±0
Cu	0.000±0.001	0.003±0.001

Table 5.9: APT matrix (& carbide) bulk compositions, after peak overlap solving in AtomProbeLab [187], with nominal composition of A508-3 steel provided for comparison.

			unirradiated (at.%)		Irradiated (at.%)			
Element	Nominal Wt%	Nominal At%	Matrix (82439)	Matrix (72406)	G.B in matrix (72312)	Matrix (72402)	Matrix (72401)	Carbide (72401)
Fe	96.94	96.34	98.50±0.01	98.83±0.01	97.58±0.01	97.56±0.03	97.93±0.02	56.81±0.06
Mn	1.35	1.36	0.05±0.01	0.05±0.01	0.88±0.01	1.02±0.01	0.74±0.01	11.89±0.02
Ni	0.738	0.698	0.80±0.01	0.77±0.01	0.93±0.01	0.74±0.01	0.70±0.01	0.21±0.01
Si	0.193	0.381	0.35±0.01	0.33±0.01	0.44±0.01	0.36±0.01	0.39±0.01	0.08±0.01
Cr	0.086	0.092	0.03±0.01	0.02±0.01	0.07±0.01	0.08±0.01	0.08±0.01	1.66±0.01
Mo	0.481	0.278	0.006±0.003	0.0008±0.0007	0.06±0.01	0.11±0.01	0.11±0.01	1.12±0.01
C	0.167	0.772	0.02±0.01	-	0.04±0.01	0.10±0.02	0.04±0.02	28.11±0.06
V	0.007	0.008	0.004±0.002	0.0010±0.0005	-	-	0.0000004± 0.000001	0.01±0.01
P	0.005	0.009	-	-	-	-	0.004±0.002	0.003±0.002
S	0.002	0.003	-	-	-	0.02±0.01	0.007±0.002	0.098±0.01
Cu	0.027	0.024	0.0002±0.001	-	0.004±0.001	0.003±0.002	0.0009±0.0021	-

All matrix compositions measured consistent atomic fractions of carbon. Ni content was measured to be lower in the irradiated matrix samples than in the unirradiated matrix with a composition averaging 0.72 ± 0.01 at.% , compared with an unirradiated average matrix Ni content of 0.79 ± 0.01 at.%. There was a higher at.% Ni measured in the irradiated specimen containing a grain boundary. Significantly more Mn was observed in the irradiated matrix samples. There is no statistically significant difference in silicon content across the sample conditions. Both Cr and Mo were present in higher quantities in the irradiated matrix. P and S content was very low in most specimens, and no peaks for these ions were observed in the mass spectra for the unirradiated sample. Phosphorus was only measured in the carbide containing specimen, and was enriched at the carbide-matrix interface.

5.5.2 Irradiated carbide-matrix interface

Reconstructed dataset in fig. 5.22 shows a carbide, with high concentrations of Mn, Cr and Mo, compared with the matrix.

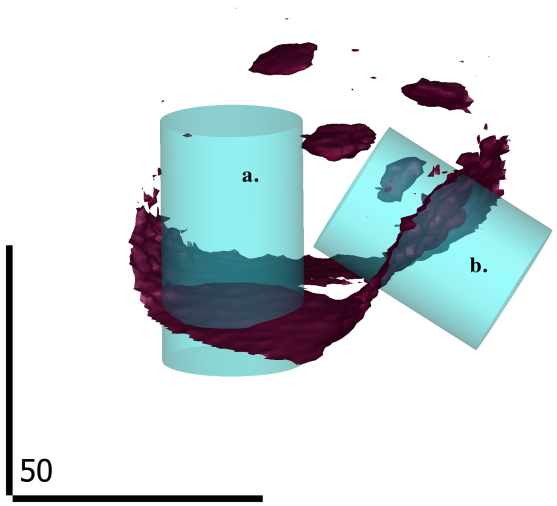


Figure 5.21: 20% carbon iso-surface concentration surfaces with cylinders through which 1D concentration profiles have been measured.

1D concentration profiles have been plotted across a 20% carbon concentration iso-surface (fig. 5.21).

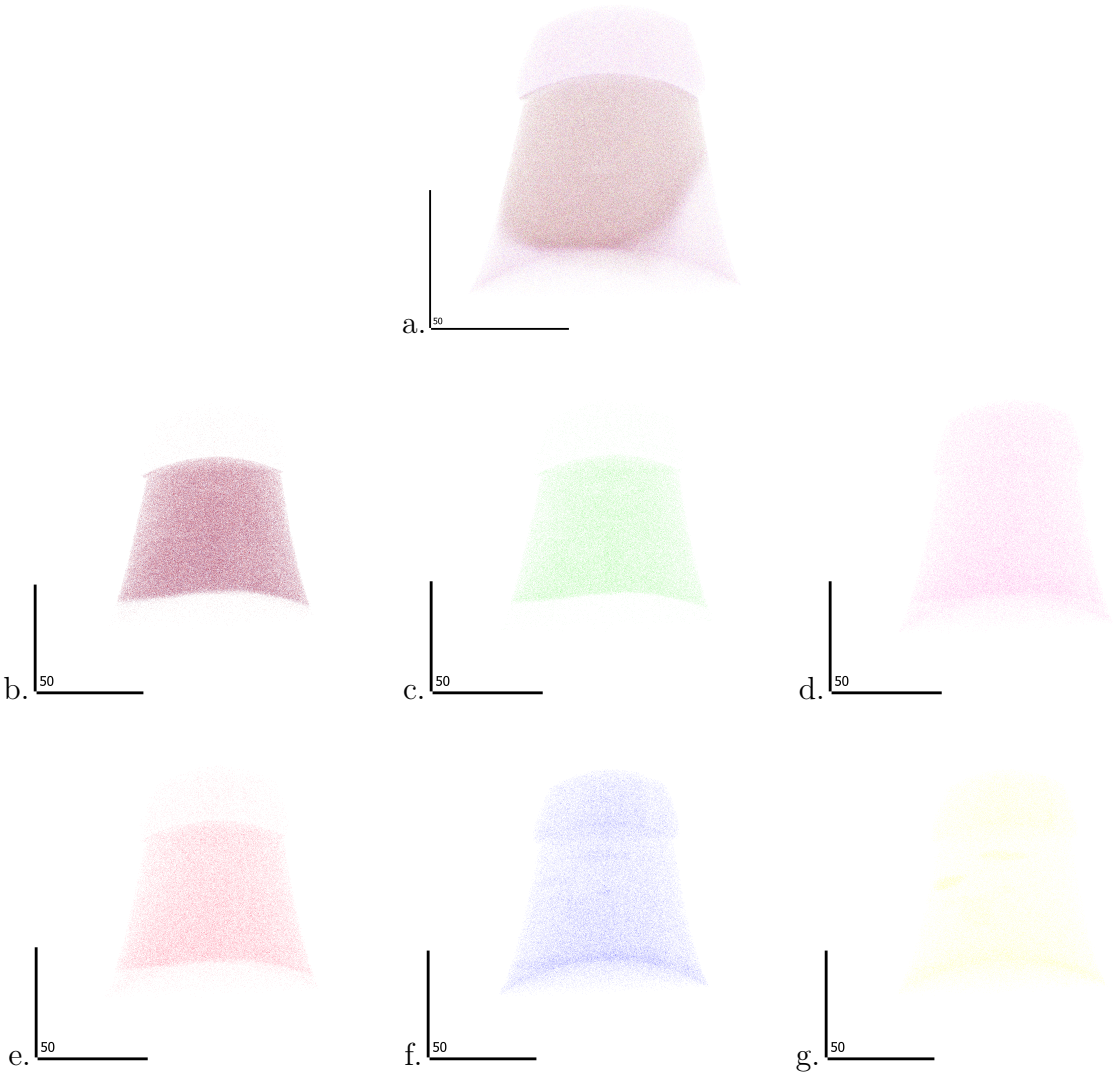


Figure 5.22: Ion reconstructions showing dataset containing carbide in the centre, and Fe (pink) matrix above and below, with (a.) all ions measured visualised, Fe at 10%, solute at 100%, (b.) carbon, (c.) manganese, (d.) chromium, (e.) molybdenum, (f.) nickel and (g.) silicon.

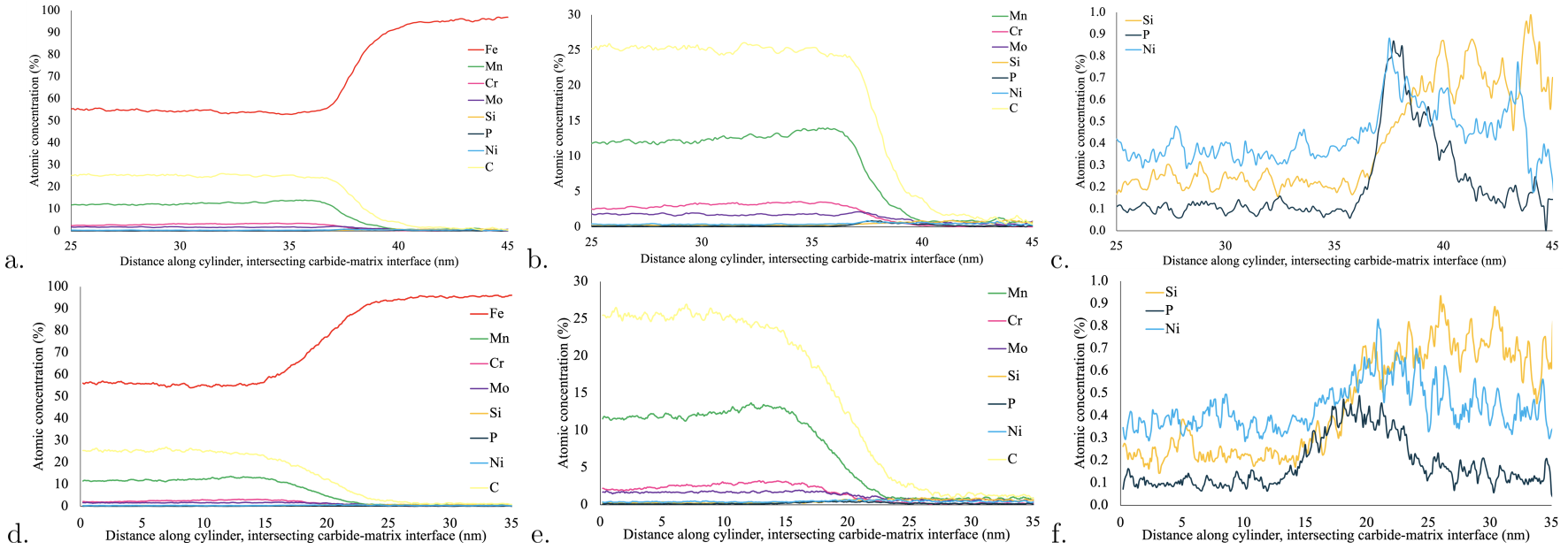


Figure 5.23: 1D concentration profiles through the carbide matrix interface, showing enrichment of carbon, manganese, chromium and molybdenum inside the carbide and depletion of nickel and silicon, with enrichment of phosphorus at the interface for (a., b., & c.) cylinder 1 (fig. 5.21) and (d., e. & f.) cylinder 2 (fig. 5.21).

The profiles in fig. 5.23 show a mixed M_xC_y composition, where the majority carbide forming metal is iron, followed by manganese, chromium, and molybdenum. The approximate stoichiometry of the carbide, using the composition shown in table 5.9, is $M_{2.54}C$, close to cementite (Fe_3C). As expected, the measured composition of these carbide formers in the unirradiated matrix is lower than the nominal compositions.

Nickel and silicon are ferrite stabilisers, and as expected, are present in the carbide in concentrations lower than nominal composition and measured matrix compositions, table 5.9 and fig. 5.23.

5.5.3 Irradiated A508-3: Grain boundary segregation

Although no direct comparison can be made in this study with an unirradiated grain boundary, enrichment of Ni and Mn to a grain boundary has been observed. Two different pole figures were obtained from the top and bottom of this dataset, suggesting a different crystal orientation in the bottom section compared with the top. Reconstructions also show a clear segregation of solute elements indicating the location of a grain boundary, figure 5.24.

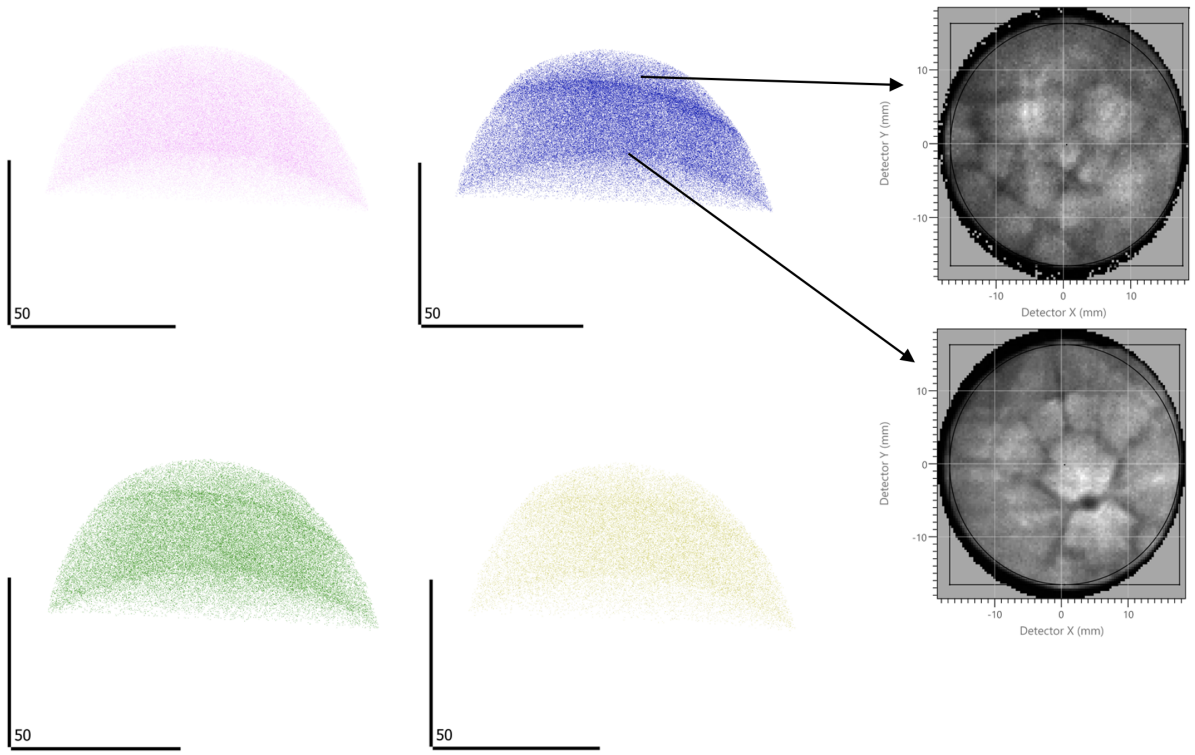


Figure 5.24: Irradiated A508-3 steel APT reconstructions showing Fe, Mn, Ni and Si ions and pole figures corresponding to top and bottom locations in dataset. (72312)

Figure 5.25 shows a 5% Mn Ni Si isoconcentration surface which corresponds to the location of the grain boundary. The average atomic concentration is plotted along the z axis of the cylinder and shows clear enrichment of Ni and Mn at the grain boundary, with a small increase in carbon. The silicon profile does not show variation across the grain boundary and nor did any other solute elements.

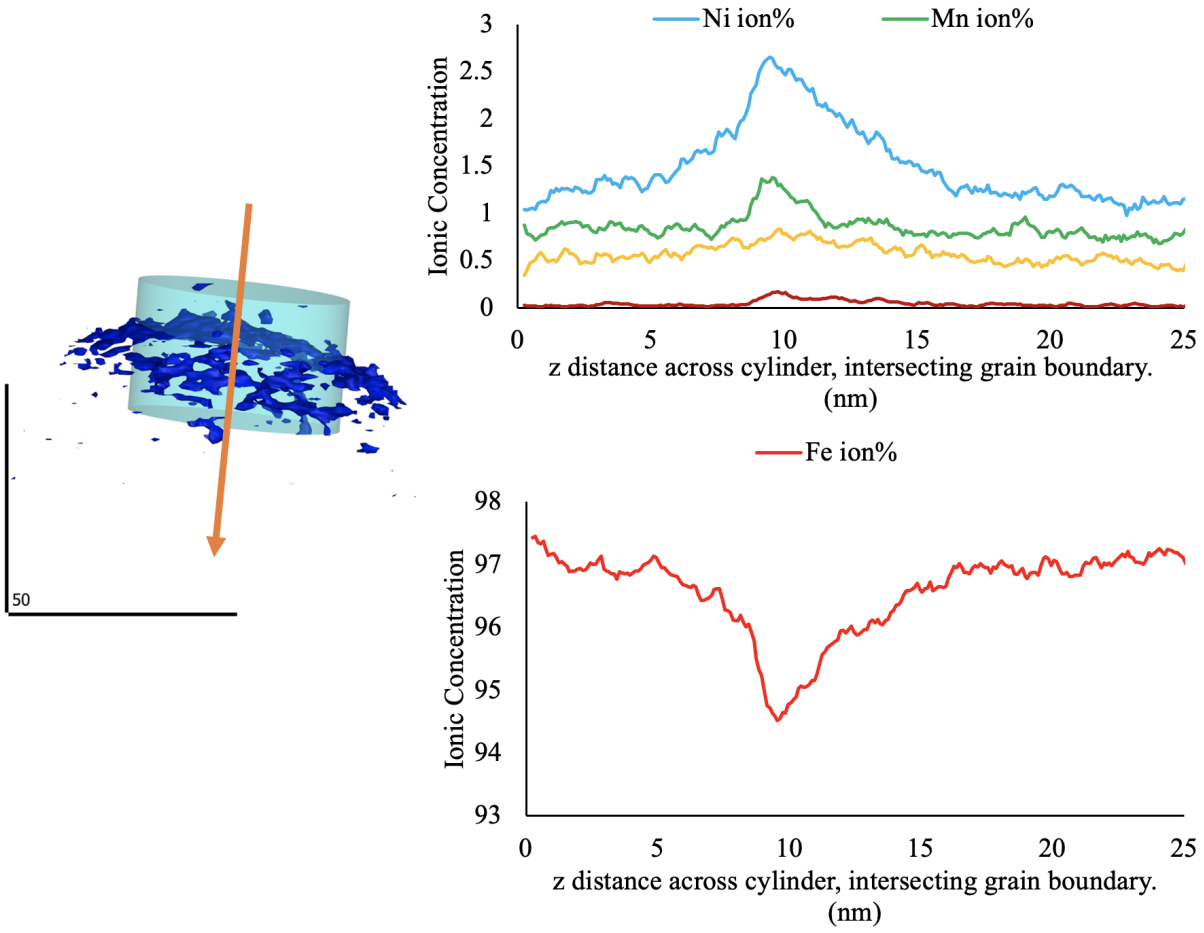


Figure 5.25: Isoconcentration surface for 5% Mn-Ni-Si concentration (a.) showing enrichment over the surface of the grain boundary, (b.) 1-D concentration profile showing enrichment of Mn and Ni at the grain boundary and (c.) 1-D concentration profile showing depletion in Fe content at grain boundary.

5.6 Summary and Conclusion

APT has facilitated the measurement of the composition of a large precipitate formed after proton-irradiation in the Fe-Mn-Ni-Si. These features are much larger than precipitates commonly identified in RPV steels and dilute model alloys, and it can be concluded that there is no

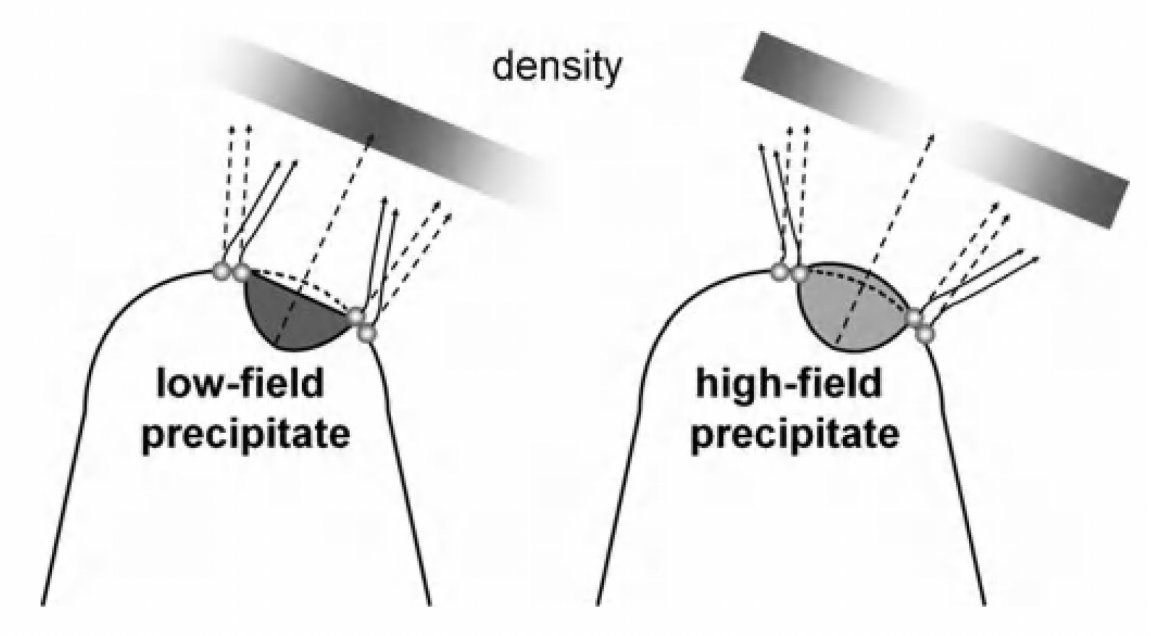


Figure 5.26: Schematic showing the effects of low and high field precipitates on the sample curvature, trajectory aberrations and subsequent density on the detector. Figure 7.19, [185]. Reprinted with permission from Springer Nature, Baptiste Gault, Michael P. Moody, Julie M. Cairney et al, Tomographic Reconstruction, Atom Probe Microscopy, Page 186, 2012.

iron present in the precipitate. This suggests that the phases previously identified as clusters in irradiated RPV steels using APT may also be iron free. One key limitation in APT analysis is the effect of field evaporation and trajectory aberrations on characterisation of the size of secondary phase precipitates. The significant changes in measured ion density observed across the matrix-precipitate interface (fig. 5.8) are due to field evaporation effects. Low field precipitates evaporate preferentially and create a flattening on the specimen surface, leading to inward projection of ions from the matrix into the feature and a higher hit density on the detector, fig. 5.26 [185].

The compositions measured at the centre of the large precipitate are consistent with that of the G phase nickel silicide, $Mn_6Ni_{16}Si_7$, which has an atomic density of approximately 83.23 atoms.nm^{-1}, compared with 84.60 atoms.nm^{-1} for BCC iron [229, 209]. The density ratio of these phases is approximately 1:1, so the measurement of a higher density of ions in the Mn-Ni-Si enriched regions of irradiated Fe-Mn-Ni-Si alloy specimens suggests that the features have a phase with a lower evaporation field than the matrix.

There was no statistically significant solute segregation observed in the APT matrix mea-

surements of the ternary alloys, indicating that all three solutes are required for significant solute segregation to occur in this radiation condition (tables 5.3 and 5.4). All three solutes must play a synergistic role in the formation of secondary phases under irradiation.

Chapter 6

Statistical analysis of radiation induced microstructural changes using small angle neutron scattering

The aim of these experiments was to characterise the size distribution of clusters or precipitates formed under irradiation and, using complementary data from APT and TEM (Chapters 4 & 5) , to compare likely compositional values of scattering contrast with possible structures.

This section covers observations and qualitative analyses of the resultant scattering in each alloy, followed by quantification of the A ratio from measurements and comparative values of A ratios using both form factor model fitting, and the maximum entropy method (MEM). Nuclear scattering length densities of scatterers and size distributions of scatterers are presented for each alloy, using both the MEM method and by modelling a log-normal size distribution. Finally, values of $|\Delta\rho^2|$ (scattering length density contrast) and A ratio have been calculated for a range of possible phases using literature values. These are compared with the measured values, to establish likely phases for the observed solute rich features.

This work is based on data collected as part of experiment 1-04-140.
DOI: (https://doi.org/10.5291/ILL-DATA.1-04-140).

6.1 Validity of assumptions and experimental limitations

Various assumptions have been made in the analysis of data obtained using SANS. A description and discussion of key assumptions is below.

- Assumption 1: Samples are fully saturated in 0.75 T magnetic field The assumption that the applied field is saturating can be assumed to be valid for the model alloys in this study. However, the applied field of 0.75 T is lower than many other investigations into RPV steels which have used applied fields of between 0.7 T and 1.8 T [70, 198, 125]. Landgraf et al. and Loffler et al. have both shown that the coercive field, H_c, required to saturate a material is inversely proportional to the grain size [230, 231]. The coercive field required to saturate a material with large grains, such as the model alloys used in this study, would be expected to be lower than for bainitic steels with finer grains. This is likely to explain why the data were more easily separable for the Fe-Mn-Ni-Si and Fe-Mn-Si alloy in this work, compared with the A508-3 steel which yielded data with large statistical errors, and minimal observable differences between the unirradiated and irradiated specimens.

  Some SANS studies into magnetic behaviour of various defects, have observed an effect on magnetic scattering from dislocation loops, even without solute segregation to these defects [232]. The strain field around dislocations can cause spin disorder which contributes to magnetic scattering contrast. However, in RPV steels there will be limited contrast from dislocation loops without solute segregation, and nuclear scattering length contrasts would be much smaller [150].

- Assumption 2: Scattering particles are dilute and randomly dispersed. In this context, "dilute" means that there is no correlation between the orientation of particles or their location and they are homogeneously distributed and sufficiently far from one another that there are no inter-particle effects. At low q values inter-particle effects have a much stronger impact on intensity [233]. The only alloy showing some low q deviation from the control measurements is the Fe-Mn-Ni alloy. With the surface contamination formed on this sample, there may be inter-particle effects on scattering leading to a structure factor that has not been accounted for in analysis. All other data sets showed overlap at low q.

- Assumption 3: Measured volume fractions can be corrected to the proton-irradiated region thickness to give an average value over the damage profile. The thickness of the irradiated region in the samples is a fraction of the total thickness measured in the study. Much of the SANS analysis of irradiated reactor pressure vessel steels is on neutron irradiated samples, or samples that have been ion irradiated through thickness, so there is no requirement for a correction of volume fraction for the thickness of the sample. In this work the volume fraction measured is assumed to be the average over the entire sample thickness and the corrected value is the average over the whole irradiated region based on SRIM modelling of ion penetration depth. There has not been a correction to account for the proton damage profile as the relationship between volume fraction and dose cannot be determined using a bulk technique like SANS. In general multiple scattering is not considered when transmission on samples are >90 % [234]. All transmission values for samples in this work were > 98 % suggesting sample thicknesses were sufficiently small to minimise any multiple scattering and that multiple scattering is likely to be less than 2 % of the measured scattering intensity [235].

6.2 Magnetic and nuclear scattering from radiation induced microstructural changes

The plots in fig. 6.2 show the magnetic and nuclear scattering components for each alloy produced by changes in microstructure after irradiation. The datasets come from subtracting the heat-treated data from the proton-irradiated data (an example is shown in fig. 6.1), and extracting magnetic and nuclear scattering components as described in section 3.8. All irradiated samples showed clear magnetic anisotropy, in the medium to high q range of scattering under the applied magnetic field, indicating the presence of microstructural features with contrasting magnetic scattering behaviour compared to the bcc Fe matrix. If anisotropy was not observed, there would be no bumps in magnetic scattering such as that at 0.01-0.05 $Å^{-1}$ in the Fe-Mn-Ni-Si plot (a.,fig. 6.2). The model alloys all showed no anisotropy in the unirradiated condition, indicating a lack of secondary microstructural features leading to magnetic contrast. Based on the observation of lower intensity scattering after irradiation in the A508-3 steel, and strong

magnetic scattering in both conditions, it is much harder to draw conclusions on the response of this sample to irradiation. Given the smaller grain size and presence of a bainitic structure, it is likely that these samples were not saturated by the applied magnetic field and the assumption of a saturating field is invalid for the A508-3 steel.

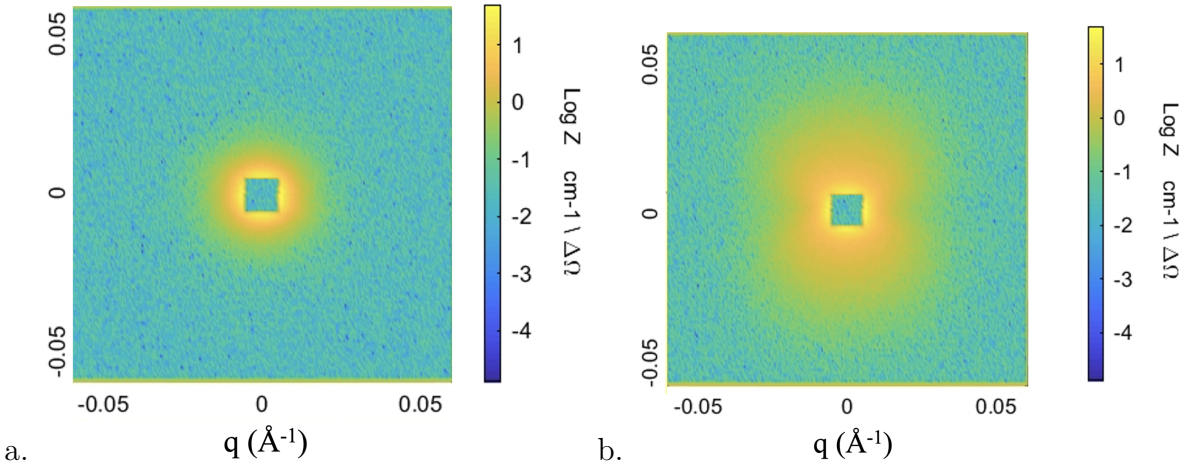


Figure 6.1: Images of the detector intensity data for the heat-treated (a.) and proton-irradiated (RHS) Fe-Mn-Ni-Si alloy, in the medium q measurement range (b.).

The magnetic and nuclear scattering intensities for the Fe-Mn-Ni alloy shows a much less pronounced increase in scattering intensity in the measured range, with scattering intensity following a power law. The lack of bump in the scattering curve could indicate that there is not a population of precipitates or clusters formed after irradiation, or it could be due to elevated background scattering from other microstructural features such as oxide formation, contributing to the signal. At low q, both magnetic and nuclear scattering follow a power law, corresponding to scattering from large microstructural features such as grain boundary networks. In the Fe-Mn-Ni-Si, the low q intensity is dominated by nuclear scattering, caused by background contributions of microstructural features in the size range >100 nm ($0.02\,\text{Å}^{-1}$, q range), which are not contributing to significant magnetic scattering. Then as q increases, the magnetic scattering intensity is greater than nuclear. This suggests there may be multiple populations contributing to scattering, giving different contrast factors in different q ranges. In the A508-3 steel and the Fe-Mn-Si alloy, the magnetic scattering intensity is high at low q values, suggesting that there are magnetic and nuclear scattering features in the size ranges >100 nm, and that there are larger features contributing to scattering than in the other two alloys.

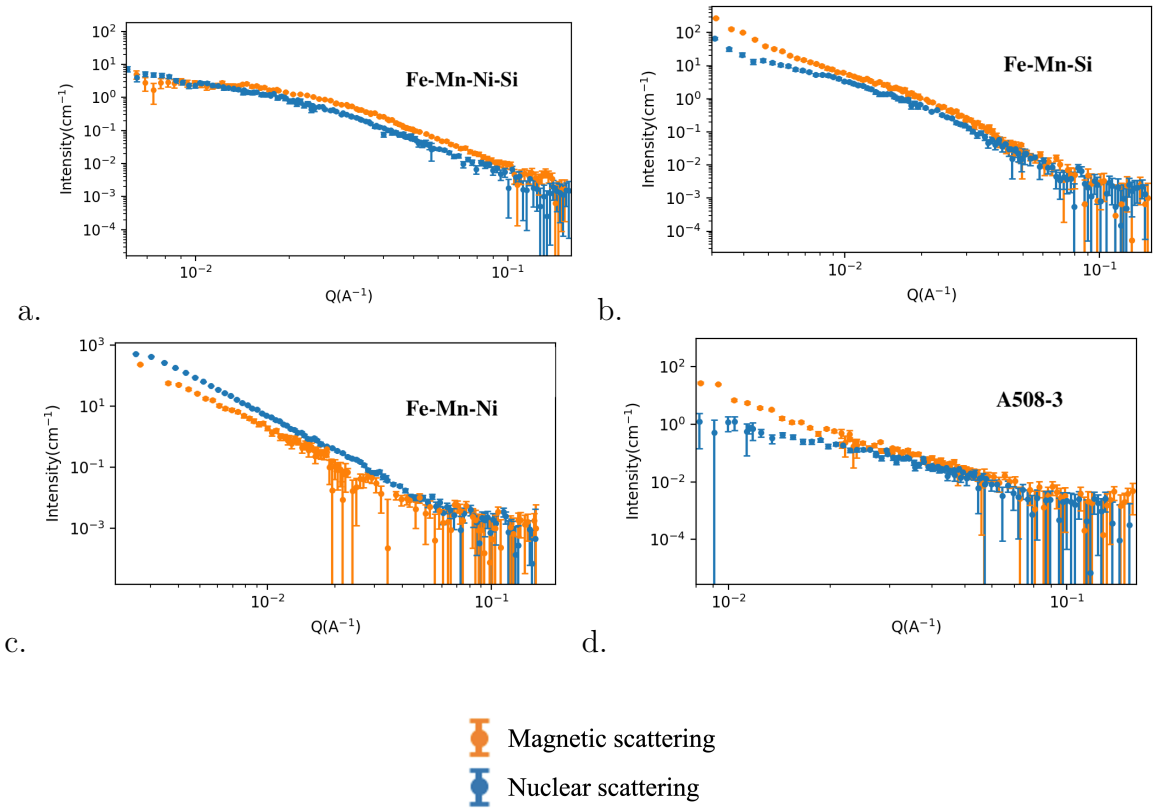


Figure 6.2: Magnetic and nuclear scattering from radiation induced features in the (a.) Fe-Mn-Ni-Si, (b.) Fe-Mn-Si and (c.) Fe-Mn-Ni model alloys and (d.) A508-3 RPV steel.

6.3 A Ratio Analysis

A ratio as a function of q value has been plotted for each data set, using data shown in fig. 6.2. Variation in A ratio over q corresponds to compositional evolution or variation as a function of particle size, and may indicate a change in precipitate composition with growth.

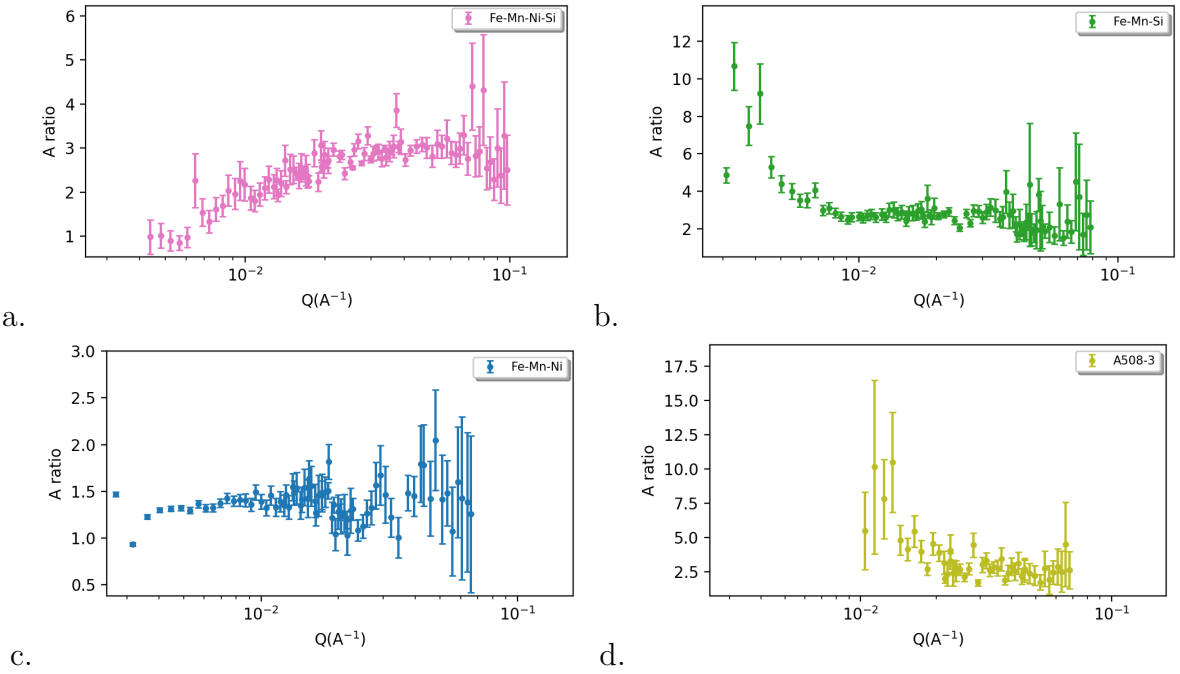


Figure 6.3: Plot of total:nuclear scattering ratio, A, versus Q, showing a variation in A ratio with q value for radiation induced scattering features in (a.) Fe-Mn-Ni-Si, (b.) Fe-Mn-Si, (c.) Fe-Mn-Ni and (d.) A508-3.

Figure 6.3 (a.) shows an increasing A ratio from around 1 to 3.3, with increasing q for Fe-Mn-Ni-Si. The change in A ratio as a function of q, suggests that smaller scattering features have a different composition or magnetic structure compared with larger features in the material. It has been assumed that all expected secondary phases are non-magnetic, based on their expected compositions, acquired inchapters 4 and 5, and specific proposed phases are discussed in detail in chapter 7. Based on this assumption and eq. (3.19), the magnetic scattering contrast between non-magnetic precipitates and the Fe matrix will be constant for all secondary phases. This then suggests that for the Fe-Mn-Ni-Si alloy, larger features have greater nuclear scattering contrast with the matrix. For Fe-Mn-Si, the A ratio is approximately constant with Q, suggesting the precipitation of a single population of features with fixed composition.

The A ratio of the A508-3 steel is approximately constant at high q values suggesting that

radiation induced features are forming with stable compositions. The Fe-Mn-Ni alloy shows fairly constant A ratio at low q. However, in the region greater than 0.1 $Å^{-1}$, there is large uncertainty in the value of A, with no constant value of A across the measured q range. The average values of A ratio measured in the regions of interest for each alloy, and the corrected values accounting for the sector averaging, are shown in table 6.1. At high q, corresponding with smaller features, the A ratios for the Fe-Mn-Ni-Si alloy are close to the A ratio observed in the A508-3 steel, suggesting that perhaps the features forming in the RPV steel under irradiation may eventually experience a similar evolution to those identified in the Fe-Mn-Ni-Si alloy. However, due to the identification of two distinct types of precipitate in this alloy using TEM, conclusions using A ratios cannot be drawn without further analysis and fitting of precipitate scattering functions to the data.

Table 6.1: A ratios, averaged over q-ranges of interest as stated for each alloy. Fe-Mn-Ni-Si values averaged over three regions of the A ratio plot, LQ= close to 1, Medium q averaged over slope and higher q averages over stable A ratio between 0.02-0.06 $Å^{-1}$.

Alloy	$A_{measured}$	$A_{corrected}$	q-range
Fe-Mn-Ni-Si, average	2.13 ± 0.05	2.21 ± 0.05	0.004-0.06
Fe-Mn-Ni-Si, LQ	0.90 ± 0.05	0.90 ± 0.05	0.004-0.006
Fe-Mn-Ni-Si, MQ	2.35 ± 0.07	2.47 ± 0.07	0.006-0.02
Fe-Mn-Ni-Si, HQ	3.13 ± 0.05	3.34 ± 0.05	0.02-0.06
Fe-Mn-Si	2.81 ± 0.04	2.88 ± 0.04	0.008-0.03
Fe-Mn-Ni	1.41 ± 0.02	1.42 ± 0.02	0.004-0.02
A508-3	2.91 ± 0.13	3.17 ± 0.14	0.015-0.06

6.4 Size distributions, volume fractions and scattering length densities

The following results show outputs from using the MEM to fit magnetic and nuclear scattering data to obtain a size distribution function for each sample as well as a measure of $V_f.\Delta\rho^2$, to use in a calculation of A ratio.

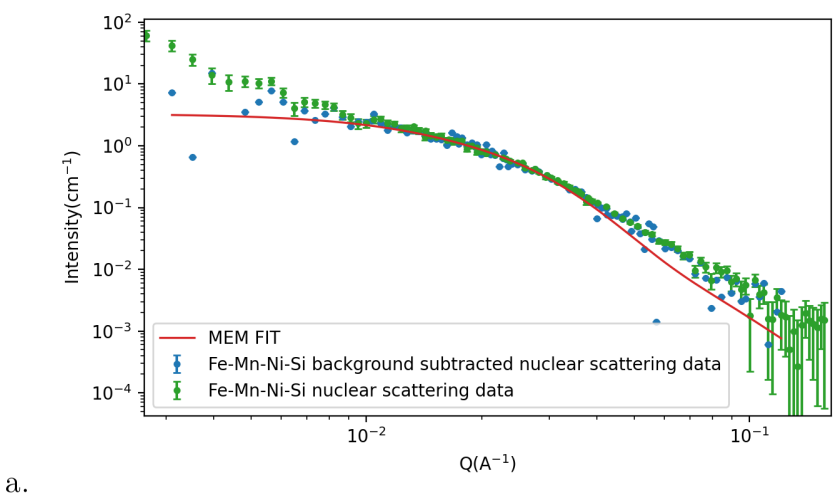
6.4.1 Maximum Entropy Method (MEM) Calculated Size Distributions of Scattering Particles

The fitted MEM functions are shown in figs. 6.4 to 6.7, along with the original datasets and the background subtracted data, for four of the alloys. The MEM was used to fit functions to background subtracted data sets, not raw data.

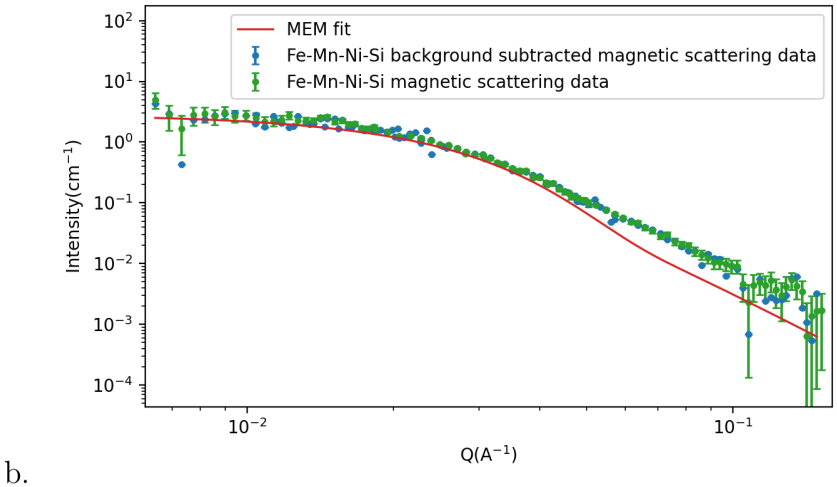
The resulting size distributions obtained for MEM fits to Fe-Mn-Ni-Si data, are both consistent with a log-normal distribution, despite this method allowing the shape of the distributions to be a free parameter(fig. 6.4). The magnetic scattering data distribution is narrower than the one obtained from nuclear scattering, but both have similar median particle diameter. Similarly to the Fe-Mn-Ni-Si sample, the size distribution of particles obtained from magnetic data for the Fe-Mn-Si alloy is narrower, with a smaller median diameter (fig. 6.5).

The Fe-Mn-Ni alloy shows distinct and contradictory bimodal size distributions when analysing the magnetic and nuclear scattering(fig. 6.6). There is an increased scattering intensity from very low q, leading to the second peak, and it is possible that the two peaks are separate populations of secondary structures, for example enriched dislocation loops, secondary phases or segregation to grain boundaries.

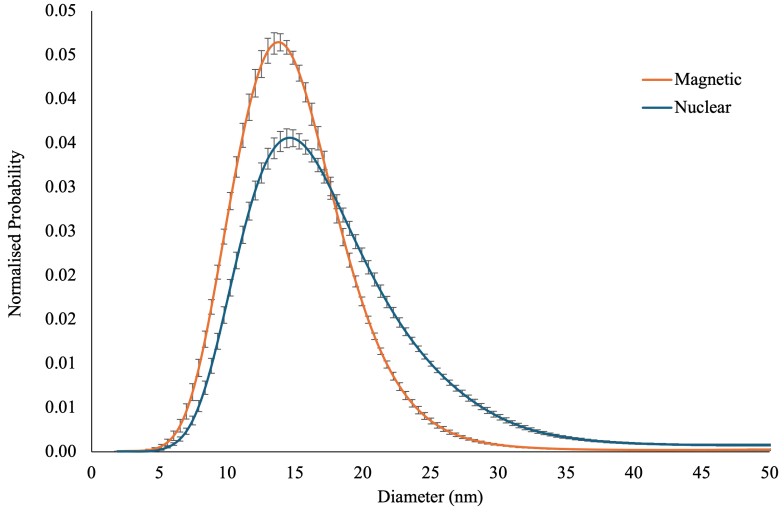
The size distribution of scatterers in the A508-3 steel is log-normal in shape, although there is a shift to higher median size for the nuclear scattering data, suggesting that there may be multiple populations of features with contrasting scattering behaviour. The shifted magnetic data size distribution could suggest that the interfaces of secondary phases are diffuse and therefore, the effect of the change of composition on local magnetic behaviour in the interface region means that they 'appear' smaller in terms of magnetic interactions. The median size of features in the A508-3 steel is approximately half of those in the Fe-Mn-Ni-Si and Fe-Mn-Si alloy.



a.



b.



c.

Figure 6.4: Plots showing nuclear (a.) and magnetic (b.) scattering data (green), power law background subtracted data (blue), and maximum entropy method curve fitted to the background subtracted data (red) for Fe-Mn-Ni-Si, with (c.) size distributions calculated from each fit in.

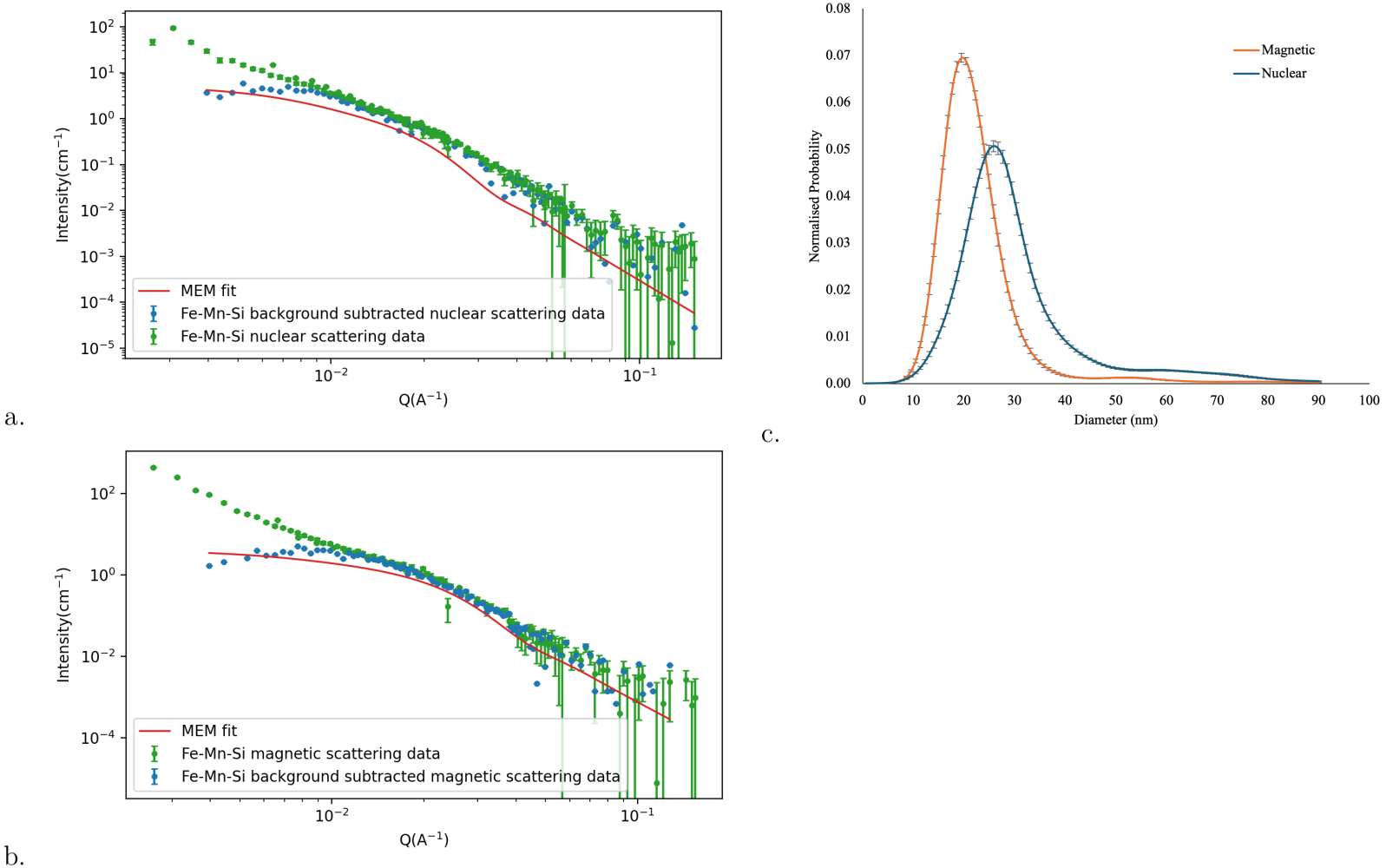


Figure 6.5: Plots showing nuclear (a.) and magnetic (b.) scattering data (green), power law background subtracted data (blue), and maximum entropy method curve fitted to the background subtracted data (red) for Fe-Mn-Si, with (c.) size distributions calculated from each fit.

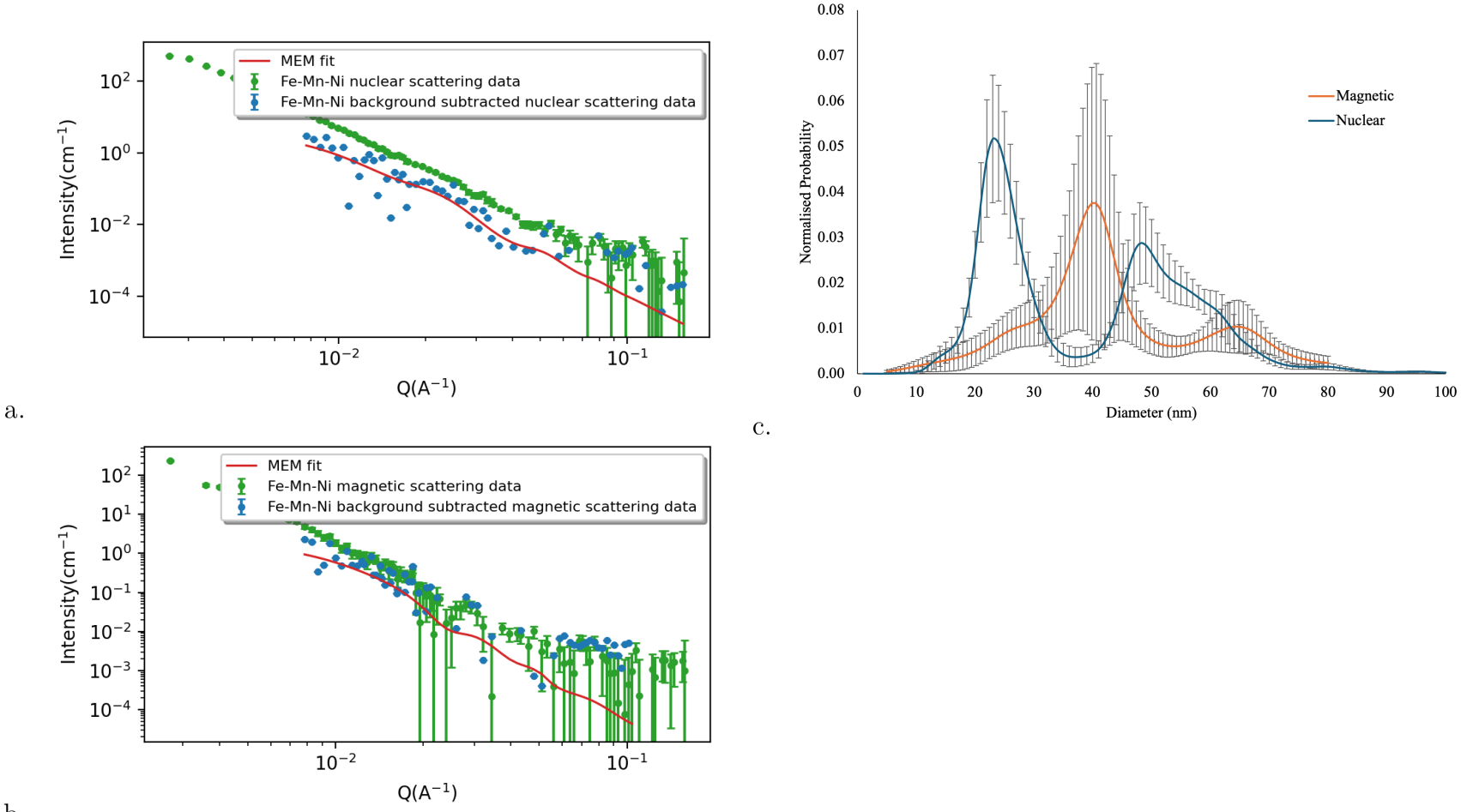
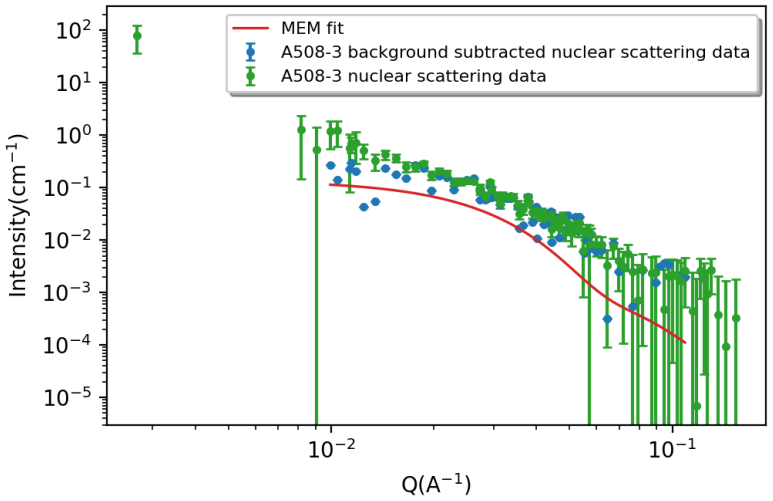
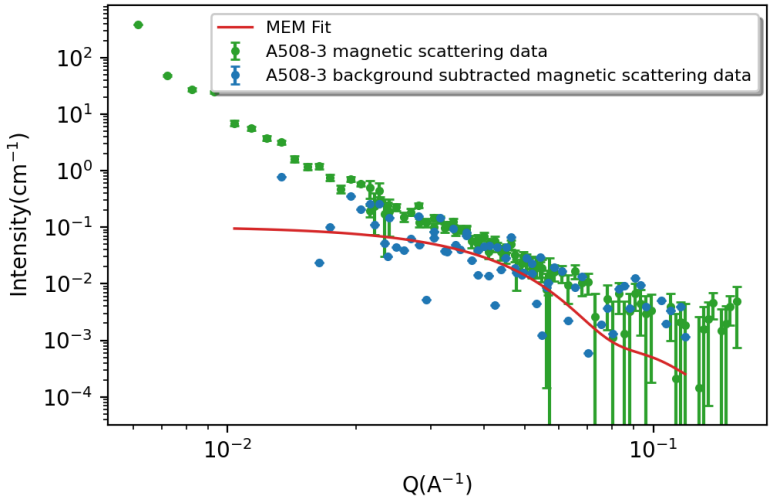


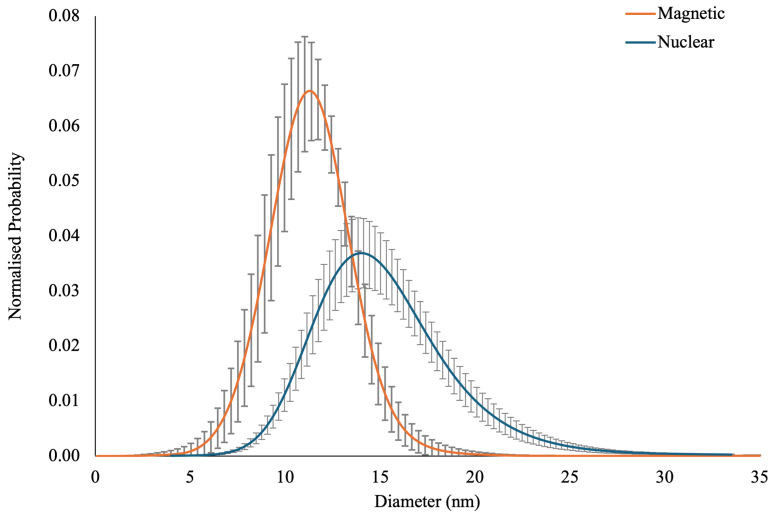
Figure 6.6: Plots showing nuclear (a.) and magnetic (b.) scattering data (green), power law background subtracted data (blue), and maximum entropy method curve fitted to the background subtracted data (red) for Fe-Mn-Ni, with (c.) size distributions calculated from each fig.



a.



b.



c.

Figure 6.7: Plots showing nuclear (a.) and magnetic (b.) scattering data (green), power law background subtracted data (blue), and maximum entropy method curve fitted to the background subtracted data (red) for A508-3 RPV steel, with (c.) size distributions calculated from each fit.

6.4.2 Summary of MEM fitting outputs

Table 6.2: Summary of results obtained using the maximum entropy method.

Alloy	Data	$V_f.\|\Delta\rho\|^2$ ($\times 10^{-3}$)	R_g (Å)	Mean diameter (Å)	Median diameter (Å)	$\frac{\chi^2}{n}$
Fe-Mn-Ni	Nuc	1.02 ± 0.29	214.63	394.73	375.29	1.00
	Mag	0.42 ± 0.25	227.88	431.39	408.04	1.00
Fe-Mn-Ni-Si	Nuc	6.88 ± 0.28	96.45	180.06	166.08	1.00
	Mag	11.3 ± 0.47	79.57	151.61	145.45	1.00
Fe-Mn-Si	Nuc	2.11 ± 0.08	165.73	304.53	273.57	1.00
	Mag	4.02 ± 0.14	121.91	226.77	209.74	1.00
A508-3	Nuc	0.44 ± 0.09	78.39	152.33	147.62	0.96
	Mag	1.36 ± 0.35	57.86	13.43	112.96	1.01

The results of MEM fitting clearly show that the RPV steel has the smallest average and median size of feature, as would be expected based on it's fine grain structure. The Fe-Mn-Ni alloy has very large particle sizes, suggesting that the features causing scattering may not be matrix radiation damage and could be caused by the contamination layer on the surface of the sample. The Fe-Mn-Ni-Si alloy has the second-smallest particle size, but much larger relative volume fraction compared with the other alloys.

6.4.3 Log normal fitting

Results for the A508-3 steel and Fe-Mn-Ni alloys were fitted, assuming a spherical form factor and background structures contributing to a power law scattering. The primary fits were carried out with fixed magnetic scattering contrast, assuming radiation induced features are non-magnetic, and using a spherical form factor, with no consideration of polydispersity. Then the volume fractions calculated using both datasets were fixed and fits carried out allowing for a variable particle diameter, following a log-normal size distribution. The plots of constrained and polydisperse fits are shown in figs. 6.8 and 6.9.

For the RPV steel, a log-normal distribution was indicated by the shape of the distribution shown in fig. 6.7. It can be seen that adding a log-normal polydispersity to the model leads to an improvement in fit to the data. Fitting models to the Fe-Mn-Ni dataset yielded poor fits, with larger values of chi squared and feature sizes on the order of 1 µm. The maximum

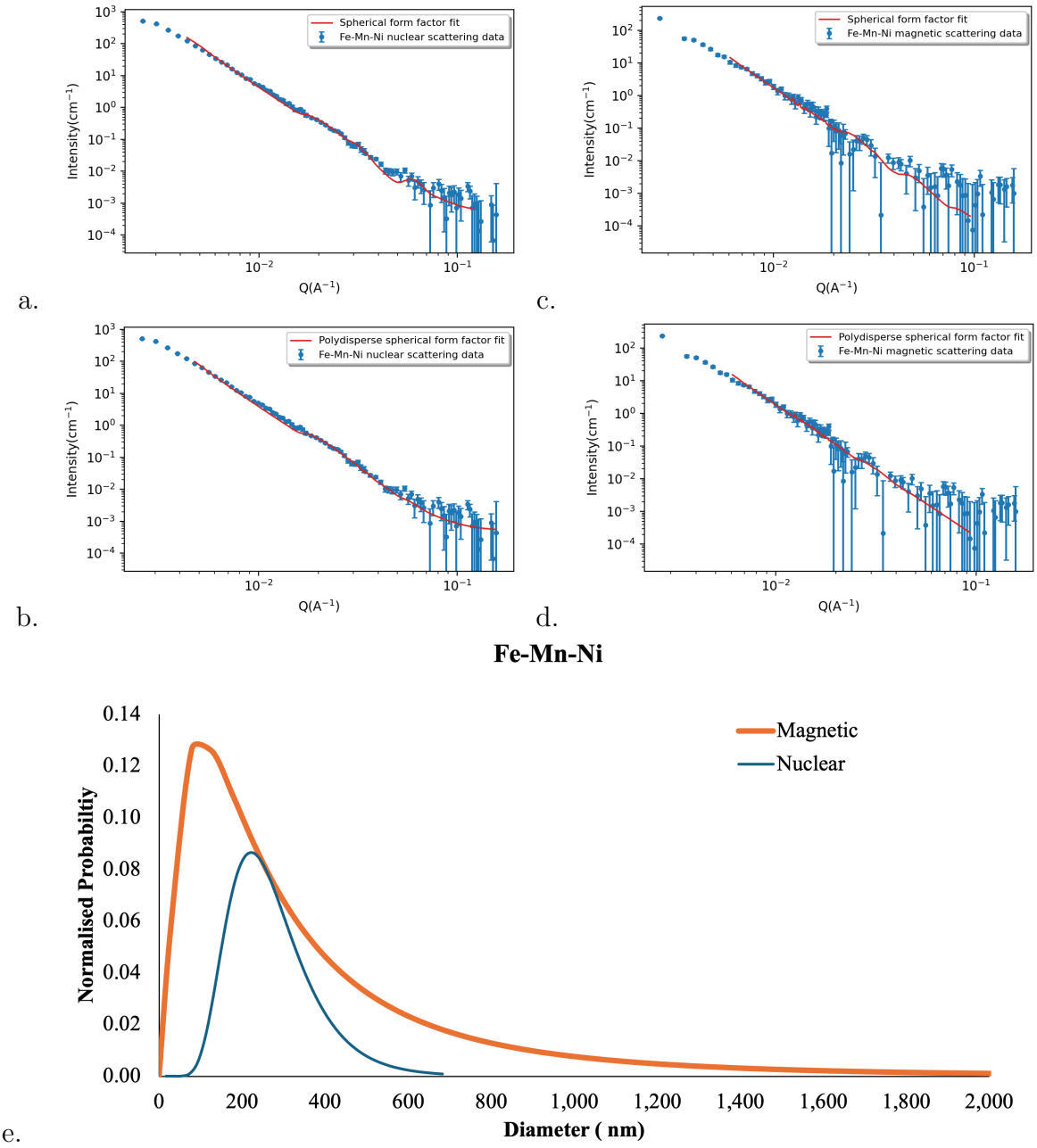


Figure 6.8: Spherical form factor fits, constrained across nuclear and magnetic scattering datasets obtained for Fe-Mn-Ni scattering features, (a. & b.) then showing an improvement in fit when scatterers are allowed to have some polydispersity (c. & d.). The size distribution of scatterers is modelled using the constrained fits, where the magnetic value shows the mean size (e.).

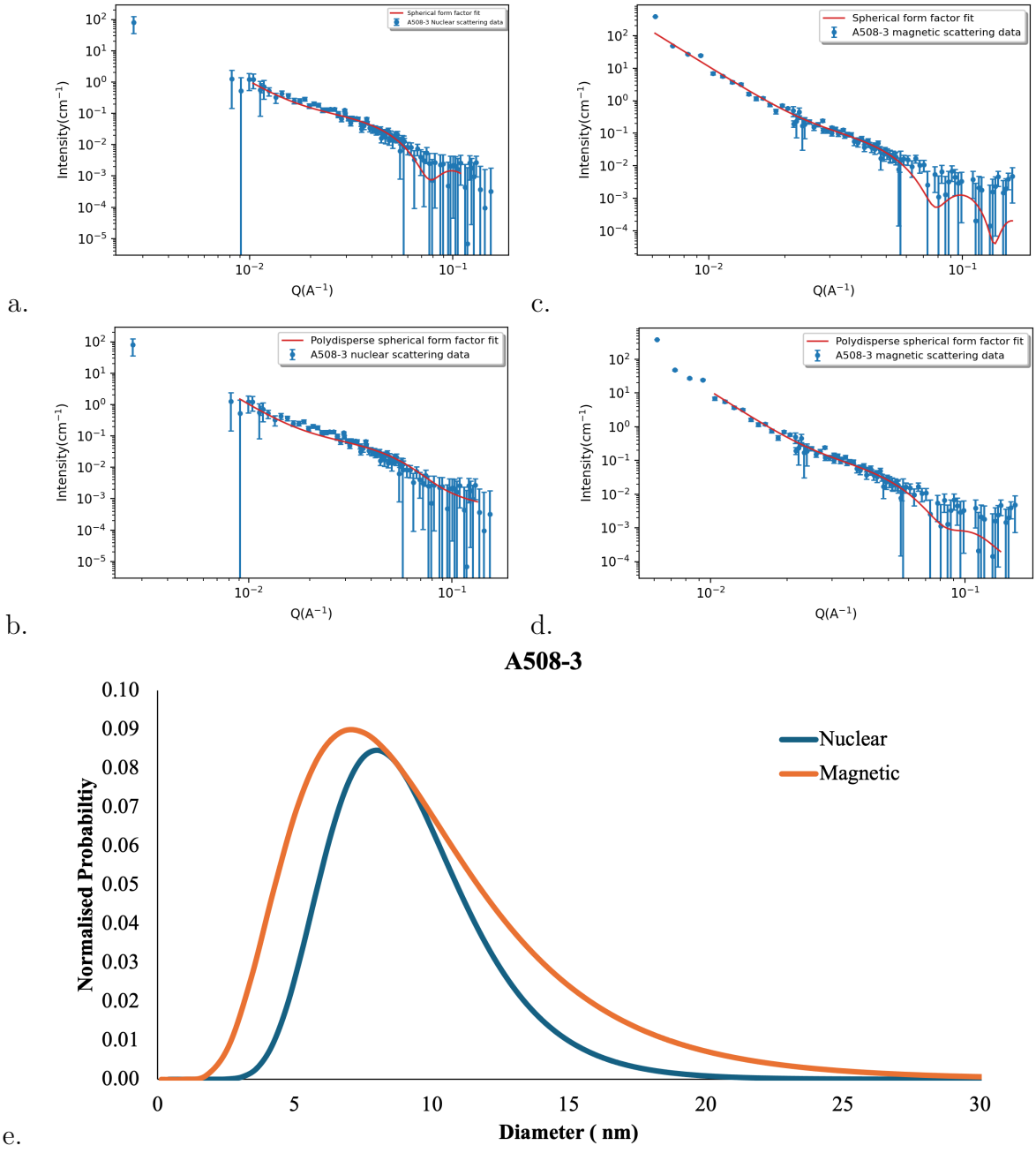


Figure 6.9: Spherical form factor fits, constrained across nuclear and magnetic scattering datasets obtained for A508-3 scattering features, (a. & b). then showing an improvement in fit when scatterers are allowed to have some polydispersity (c. & d.) The size distribution of scatterers is modelled using the constrained fits, where the magnetic value shows the mean size (e.).

entropy method size distribution yielded similar sizes of scatterer but with a complex multi-modal distribution. This may explain the poor fit quality when applying an overly simplified size distribution model. The fitted outputs for spherical particles in the A508-3 and Fe-Mn-Ni alloys are shown in table 6.3 and figs. 6.8 and 6.9.

Table 6.3: Final output parameters from model fitting using a form factor for polydisperse spheres following a log-normal size distribution with power law background function to SANS data for the Fe-Mn-Ni, Fe-Ni Si and A508-3 steel.

Alloy	Dataset	Modelled Volume Fraction	ρ (10^{-6}/Å^2)	A Ratio	Median Diameter (nm)	σ Value	$\frac{\chi^2}{n}$
Fe-Mn-Ni	Nuclear	0.0097 ± 0.0013	3.84 ± 0.38	2.43 ± 0.34	1270 ± 54	0.37 ± 0.02	1049
	Magnetic		0.00			0.97 ± 0.08	62.78
	Magnetic		0.00 ± 0.49			0.45	7.47
A508-3	Nuclear	$7.27 \pm 0.34 \times 10^{-5}$	2.91 ± 0.16	2.96 ± 0.11	8.76 ± 0.51	0.30	1.8
	Magnetic		0.00			0.46	1.72

6.5 Fe-Mn-Ni-Si & Fe-Mn-Si Model Fitting

A priori information has been collected for Fe-Mn-Ni-Si and Fe-Mn-Si on the morphology and composition of precipitates using TEM and APT (chapters 4 and 5. STEM images showed ellipsoidal and cuboidal precipitates in the Fe-Mn-Ni-Si and Fe-Mn-Si alloys (figs. 4.13 and 4.16). Therefore, form factors for ellipsoids and cuboidal particles have been fitted to these data.

6.5.1 Morphology fits

Plots, fig. 6.10, show the constrained fits to an ellipsoidal form factor, for Fe-Mn-Ni-Si data, and constrained fits using a cuboidal particle form factor for Fe-Mn-Si data.

The parameters obtained using the fits in fig. 6.10 were used as a starting point to then fit particle sizes with a log-normal size distribution, to obtain a measure of polydispersity. A summary of the output data is presented in tables 6.4 and 6.5.

Good agreement between magnetic and nuclear distributions can be seen for both fits, with much higher volume fraction calculated in the Fe-Mn-Ni-Si alloy compared with the Fe-Mn-Si alloy. Combined with the smaller average diameter of feature identified, this indicates a larger number density of scattering features in the Ni containing alloy, consistent with TEM data.

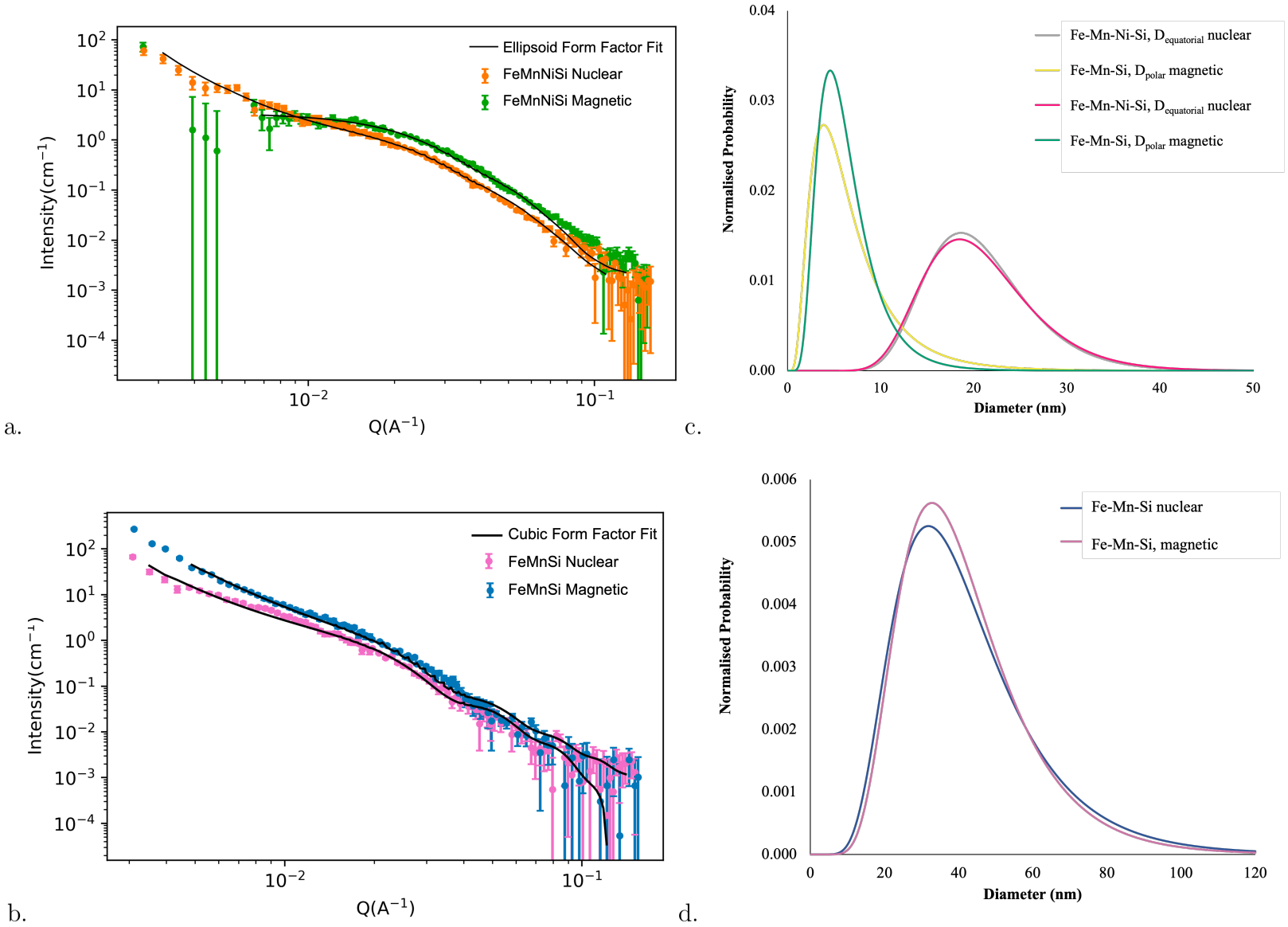


Figure 6.10: Constrained fits to nuclear and magnetic scattering data for (a.) Fe-Mn-Ni-Si using an ellipsoidal form factor, and (b.) Fe-Mn-Si using a cuboidal particle form factor. Log normal size distributions for both ellipsoidal radii modelled to Fe-Mn-Ni-Si data (c.) and cuboidal length of particles in Fe-Mn-Si (d.).

Table 6.4: Output parameters from model fitting cuboidal form factor and power law background function to SANS data for the Fe-Mn-Ni-Si alloy.

	Corrected Volume Fraction	$\Delta\rho^2$ $(10^{-6}/\text{Å}^2)^2$	ρ $(10^{-6}/\text{Å}^2)$	$R_{equatorial}$ (nm)	R_{polar} (nm)	$\frac{\chi^2}{n}$
Nuc	0.00234±0.00005	10.31 ± 0.06	4.91 ± 0.04	12.54 ± 0.15	3.713 ± 0.004	2.51
Mag		24.82				2.64

Table 6.5: Output parameters from model fitting cuboidal form factor and power law background function to SANS data for the Fe-Mn-Si alloy.

	Corrected Volume Fraction	$\Delta\rho^2$ $(10^{-6}/\text{Å}^2)^2$	ρ $(10^{-6}/\text{Å}^2)$	A length (nm)	$\frac{\chi^2}{n}$
Nuc	0.00043 ± 0.00001	20.22 ± 0.16	3.52 ± 0.13	19.25 ± 0.24	3.64
Mag		24.82			1.91

6.5.2 Composition fits: Fe-Mn-Ni-Si

A second model was applied with a mixture of cuboidal and ellipsoidal scattering feature form factors and fitted to the background subtracted data set produced for MEM fitting. The aim was to attempt to separate contributions of scattering from two different populations observed in TEM data.

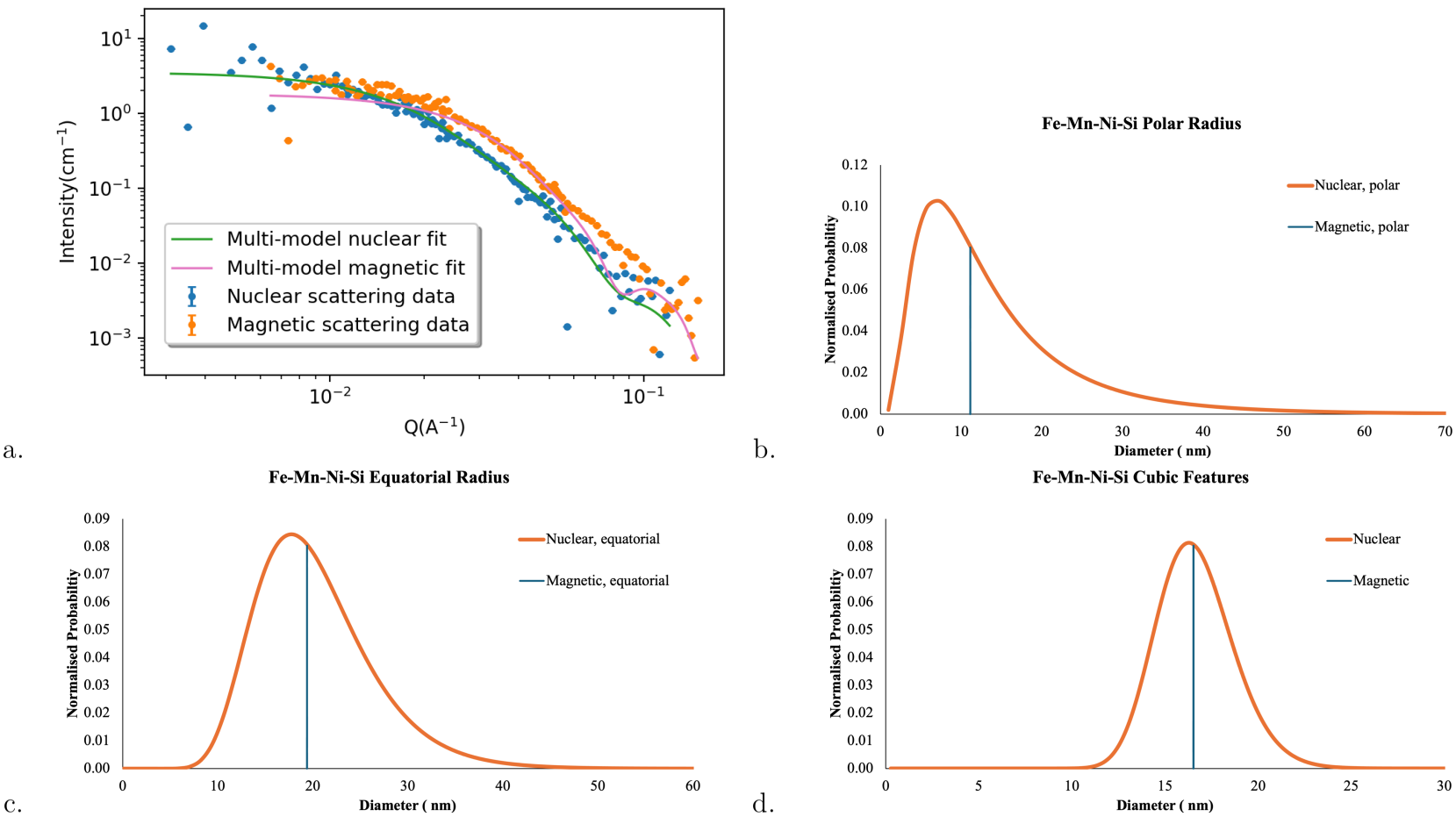


Figure 6.11: Constrained fit to background subtracted Fe-Mn-Ni-Si data (a.), using a summed ellipsoidal and cuboidal population of scatterers model, and corresponding size distribution plot. Normalised probability distributions showing the spread in sizes for the ellipsoidal features (b. & c.) and the cuboidal features (d).

As this model introduces more parameters, there is greater uncertainty on the output values. Therefore, TEM data has been used to constrain parameters, to yield more realistic results. The values in tables 6.6 and 6.7 were calculated by fitting a sum of a model for ellipsoidal scatterers, with median polar and equatorial radii of no more than 40 nm, and cuboidal structures with median size less than 15 nm. The volume fraction was constrained to being less than 0.0003, based on the measured volume fractions for the irradiated region observed in TEM, being corrected to account for the sample not being irradiated through its thickness. The ellipsoidal scattering length density was calculated using the composition of the Ni rich feature observed using atom probe tomography, with a stoichiometry of $Mn_{5.7}Ni_{16}Si_{5.7}$, giving a scattering length density of $\rho = 4.48 \times 10^{-6}\text{Å}^{-2}$.

Table 6.6: Table showing results from fitting a form factor model of the sum of an ellipsoidal and a cuboidal population of scatterers to datasets for Fe-Mn-Ni-Si. This table shows data describing the distribution of ellipsoidal features.

	V_f of ellipsoidal features	$\rho_{Ellipsoids}$ (10^{-6}Å^{-2})	$\Delta\rho^2_{Ellipsoids}$ (10^{-12}Å^{-4})	$A_{Ellipsoids}$	Median polar diameter (nm)	Median equatorial diameter (nm)	σ_{Polar}	$\sigma_{Equatorial}$
Nuc	$2.74E-04 \pm 0.40E-04$	3.74 ± 0.33	18.32 ± 2.29	2.35 ± 0.29	11.11 ± 1.87	19.39 ± 1.86	0.69 ± 0.10	0.30 ± 0.04
Mag		0.00	24.80				$5.04 \pm 6.65E-7$	$5.81 \pm 3.57E-7$

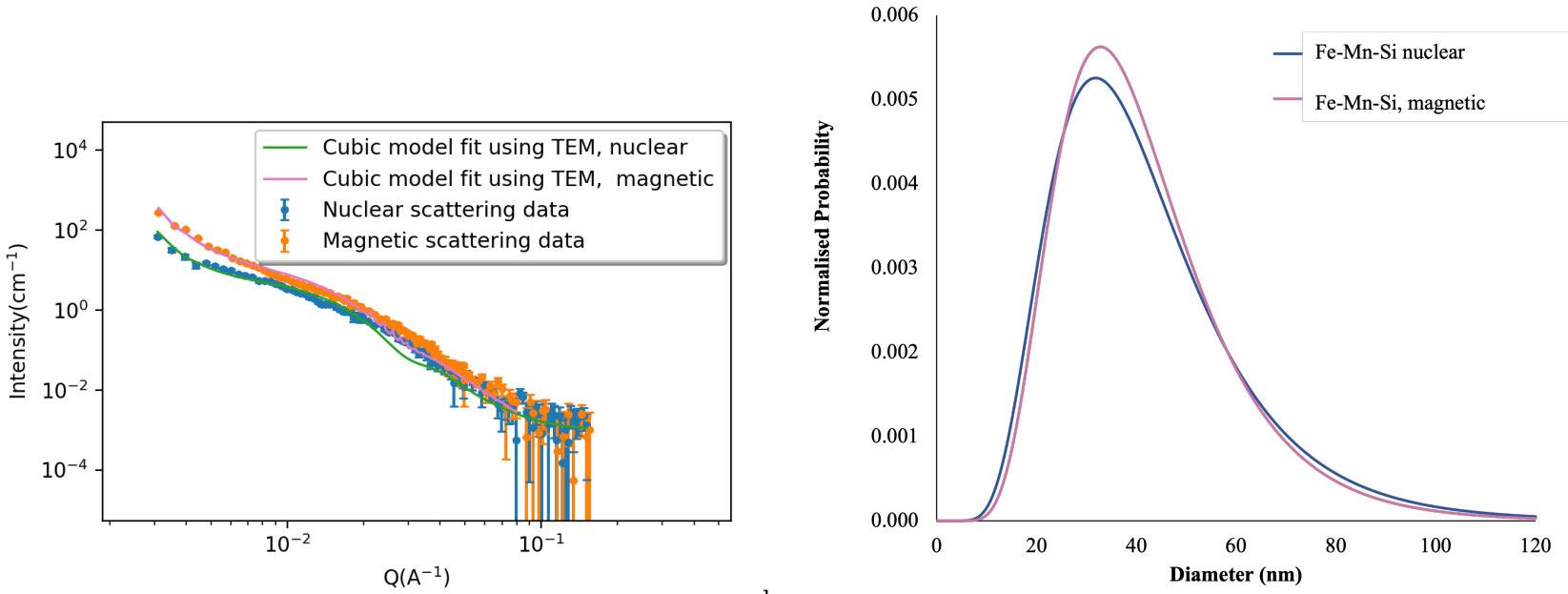
Table 6.7: Table showing results from fitting a form factor model of the sum of an ellipsoidal and a cuboidal population of scatterers to datasets for Fe-Mn-Ni-Si. This table shows data describing the distribution of cuboidal features.

	V_f of cuboidal features	ρ_{Cubes} (10^{-6}Å^{-2})	$\Delta\rho^2_{Cube}$ (10^{-12}Å^{-4})	A_{Cubes}	Median cube length (nm)	$\sigma_{Cubelength}$	$\frac{\chi^2}{n}$
Nuc	$2.36E-04 \pm 1.61E-04$	4.17 ± 1.32	14.83 ± 6.62	2.67 ± 1.19	8.26 ± 2.13	$1.23E-01 \pm 2.17E-01$	1.65
Mag		0.00	24.80			$4.82E-07 \pm 5.32E-07$	0.41

Size distributions are shown in fig. 6.11, with the magnetic data corresponding closely to the mean diameter. With the constrained non-magnetic assumption for magnetic scattering contrast, there was insufficient flexibility in parameters to produce size distributions fitted to magnetic data, hence the very low polydispersity values modelled. The ellipsoidal radii both follow log-normal distributions, with a sharp increase in probability between 2 nm for polar and 10 nm for equatorial diameters. The cuboidal feature size distribution looks more Gaussian and has a lower mean size, but narrower distribution of sizes, with the minimum being around 12 nm and the maximum around 22 nm. These differences in shape suggest there may be different formation mechanisms for the ellipsoidal and cuboidal features, and different drivers for their nucleation and growth. The nuclear scattering contrast calculated for the cuboidal features is smaller than that calculated for the ellipsoidal features. This suggests there may be significant Fe content, giving reduced contrast with the matrix. However, Ni content would be more effective at reducing the scattering contrast in the presence of Mn, due to its higher nuclear scattering length. The reason for this discrepancy may be that there are too many unconstrained parameters in the model and the scattering length densities have been assigned to the wrong population in fitting, due to their similar size distributions. The modelled A ratios for the ellipsoidal and cuboidal features are 2.35 ± 0.29 and 2.67 ± 1.20 respectively.

6.5.3 Size and volume fraction fits: Fe-Mn-Si

The size distribution of Mn-Si rich features in the irradiated Fe-Mn-Si alloy has been analysed using TEM. In the model fitted below, a corrected volume fraction has been calculated and a log-normal distribution of particle sizes is assumed. The median size has been fixed to the value observed via TEM analysis; 22.6 nm. Then a constrained fit has been carried out to identify the nuclear scattering length density, first assuming the features are non-magnetic, secondly allowing the magnetic scattering length density to be unfixed.



a. b.

Figure 6.12: Plot showing cuboidal form factor model (a.) fitted to magnetic and nuclear scattering data from Fe-Mn-Si alloy, using fixed values for median radius and volume fraction based on TEM results. The log normal size distribution of cuboidal features in Fe-Mn-Si (b.) is also shown, obtained from fits to nuclear and magnetic datasets.

Table 6.8: Output data from cuboidal form factor fitting to the Fe-Mn-Si scattering data, using fixed values obtained via TEM analysis for volume fraction and median size.

	Data V_f	ρ	$\Delta\rho^2$	Size (Å)	σ	A ratio	$\frac{\chi^2}{n}$
	Nuc 0.00016	3.16 ± 0.03	23.62 ± 0.23	226.16	0.18	2.05	5.87
$\rho_m = 0$	Mag	0	24.80		1.6×10^{-7}	2.05	38.7
$\rho_m \neq 0$	Mag	-1.51 ± 0.03	42.09 ± 0.87		0.21	2.78	16.7

cuboidal fits of Fe-Mn-Si data have been carried out to assess the possible magnetic scattering contrast of the secondary phase, in order to identify whether it may be magnetic. This analysis method only allows distributions defined in the SASView code to be applied to datasets, so a log-normal has been selected as the closest to the distribution observed in the MEM fitting. Results below show the fitting output values for magnetic scattering length density. A ratios measured assuming non-magnetic features are 2.05, but allowing the magnetic scattering length density of the cuboidal features to be non-zero, led to a calculated A ratio of 2.78. This is much closer to the measured value of 2.88 ± 0.04, within $3\frac{\sigma}{\sqrt{n}}$, suggesting the features may be magnetic at room temperature.

6.6 Summary of fitting outputs

The following figures summarise the data presented in the preceding section. Volume fractions and number densities have been adjusted to provide an average value in the irradiated region. For the model alloys, the maximum entropy method yielded closer values of A ratio to the measured values, as no assumptions were made regarding the shape of the particle size distributions. The A ratios calculated for the Fe-Mn-Si alloy are very consistent across methods, suggesting that the form factor modelling of the scatterers as a population of cuboidal features with some magnetic behaviour is describing this system accurately. The Fe-Mn-Ni-Si fitted values are not as consistent with the measured values as the Ni free alloy. This is expected for the MEM fit as this method assumes a constant composition of scatterer and multiple compositions have been observed in this sample. The form factor model does not have sufficient a priori inputs to provide an accurate set of characteristics of the system, and the 3 phase model applied may still

be too simple to accurately describe the system.

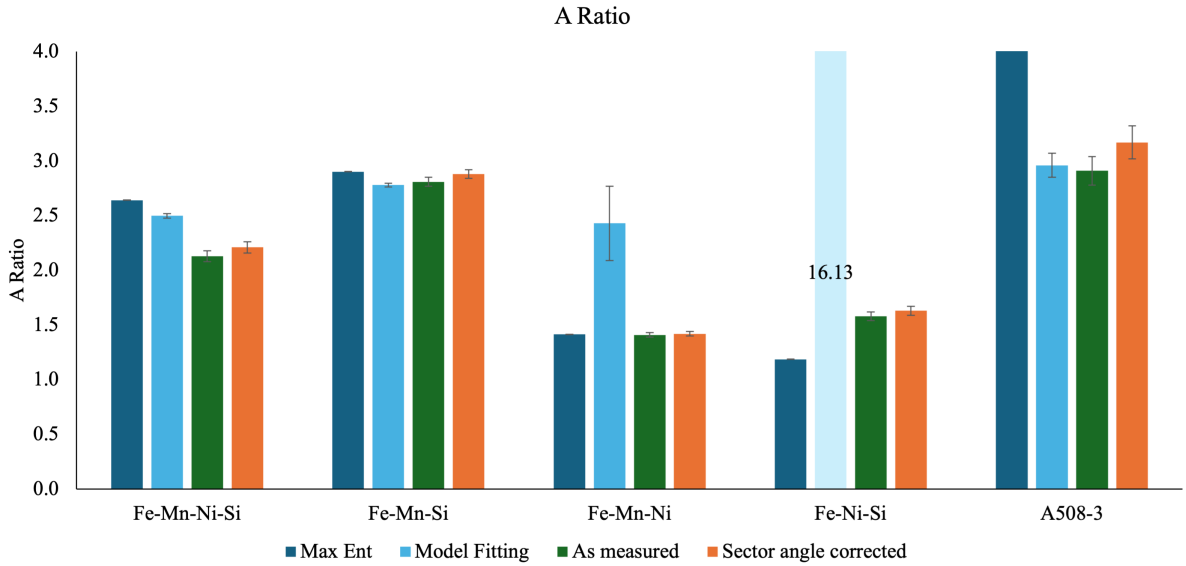


Figure 6.13: Bar chart comparing all A ratios measured and calculated in this study for each alloy.

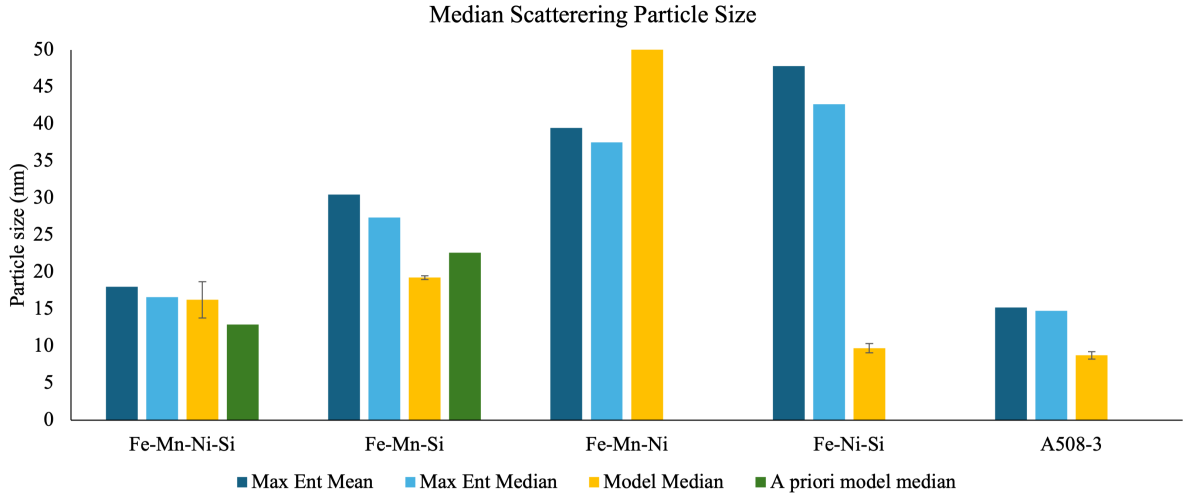


Figure 6.14: Bar chart comparing all median and mean particle sizes obtained from fitting for each alloy using the maximum entropy method and form factor modelling.

In most cases, the maximum entropy method has calculated larger median particle sizes than model fitting, fig. 6.14. These values are more likely to be realistic, as the maximum entropy method allows for the particle size to be fitted without any constraints on the shape of the size distribution. The Fe-Mn-Ni-Si data is the most consistent across analysis methods, as the size distribution of precipitates seemed to follow a log-normal distribution. This was not the case for

the Fe-Mn-Ni sample, hence the large differences in the values of median radius calculated using the MEM and a log-normal distribution shape factor model. There is relatively good agreement in A ratio and median scattering particle size between methods for the Fe-Mn-Ni-Si alloy, with the a priori model giving a lower median size than the other methods. The Fe-Mn-Si a priori result gives a larger median size, which is in between the maximum entropy method and the morphology model fit.

It can be seen clearly here that most of the results for the Fe-Mn-Ni alloy are anomalous when compared with the other datasets, suggesting the surface contamination has had a significant impact on data quality. Volume fractions for the A508-3 steel and Fe-Mn-Si are very similar, with a much larger volume fraction of scattering features measured in the quaternary alloy. Overall, the maximum entropy method is most useful for understanding the size distribution of scattering features, whereas the shape factor fitting enables the extraction of absolute values of scattering contrast and volume fraction, given some a priori information on composition and approximate size. Ideally, the two methods would be integrated such that the MEM size distribution function could be implemented into the SasView models as the polydispersity function, allowing for more physically accurate outputs.

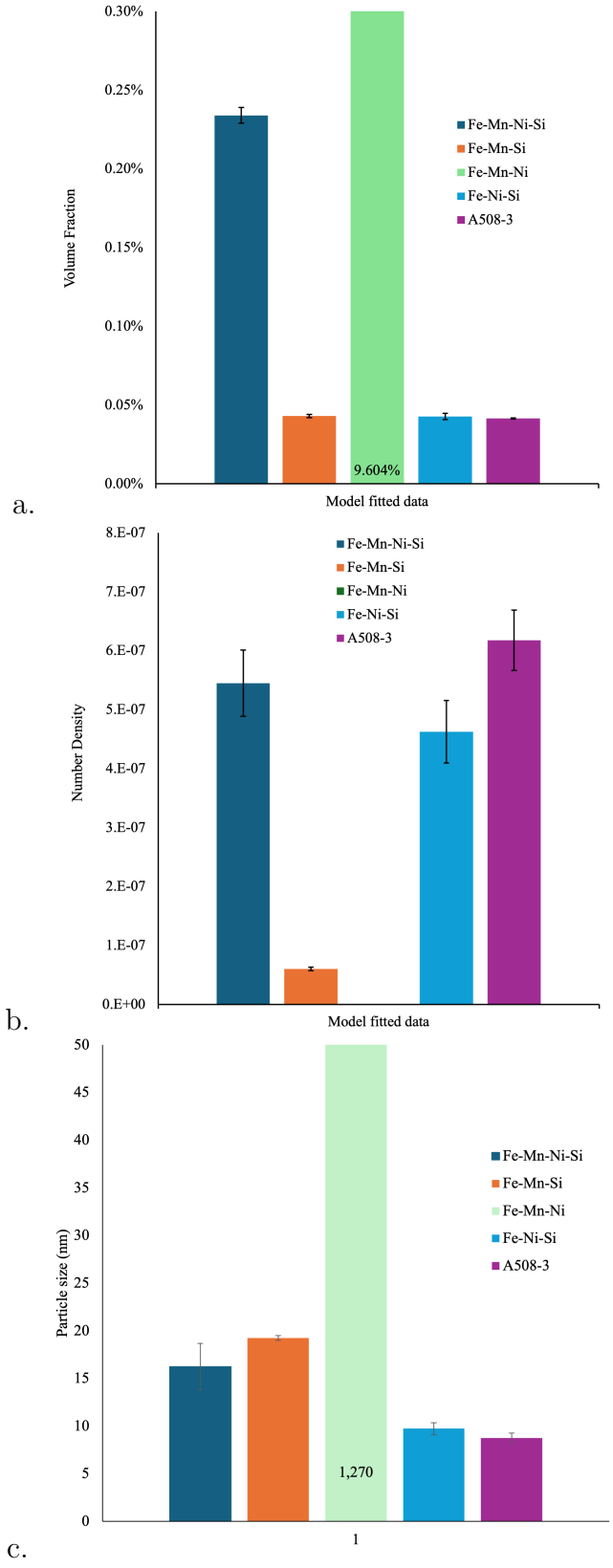


Figure 6.15: Model fitting summary showing (a.) volume fractions, (b.) number densities and (c.) median sizes, for each alloy.

6.7 Summary & Conclusion

Overall, only two alloys showed clear trends in increases in scattering intensity after irradiation; Fe-Mn-Ni-Si and Fe-Mn-Si. The lower quality of data obtained from the A508-3 steel is likely to be because the applied magnetic field was not sufficient to saturate the magnetic domains. Combined with the prescence of carbides in the materials, leading to an as received dataset with significant magnetic scattering (caused by magnetic contrast between the matrix and non-magnetic carbides) this data was too noisy to clearly identify any of the effects of radiation induced precipitation or clustering. The Fe-Mn-Ni specimen clearly showed a melted region on the sample surface, and it's irregular thickness and contamination of oxide on the sample led to significant scattering that could not be subtracted off as background.

The measured A ratios for the Fe-Mn-Ni-Si, Fe-Mn-Ni, Fe-Mn-Si and A508-3 steel are shown in fig. 6.16. The Fe-Mn-Ni value is similar to the A ratios observed at lower doses in a ternary Fe-Mn-Ni neutron irradiated sample, despite the higher dose [66]. The other values are all comparatively higher than the values obtained in neutron radiation studies. The A ratio measured for the A508-3 proton-irradiated steel in this work is higher than most of the A ratios observed in literature for irradiated reactor pressure vessel steels irradiated to similar doses of 0.1 dpa. However, accounting for the increase in average dose, the value is consistent with the linear trend observed in Bergner et al.'s increasing A ratio with dose [150].

In most of the studies referenced in fig. 6.16, A ratio increases with increasing fluence, suggesting either a decreasing Fe content in clusters, caused by an increase in magnetic scattering contrast factor, or increasing Ni content caused by decreasing nuclear scattering contrast [150, 66]. Meslin et al. observed that the increase in A ratio with dose seems to slow down for the model Fe-Mn-Ni-Si and Fe-Mn-Ni alloys, [66], with a smaller increase in A ratio between 0.1 and 2 dpa compared with between 0.2 and 1 dpa. This suggests that while composition is still evolving in the features, perhaps their composition is beginning to stabilise at higher doses. This supports the observation in this work of changing composition with dose, and higher Ni content at 0.5-2 dpa, than 0.1 dpa, table 4.9. Contrasting values of A ratio were obtained by Laver et al., at low doses, with an A ratio of 3.7 for a proton irradiated steel at 0.006 mdpa, at 400 °C[70]. This is consistent with the theoretical A ratio that would be obtained for the G

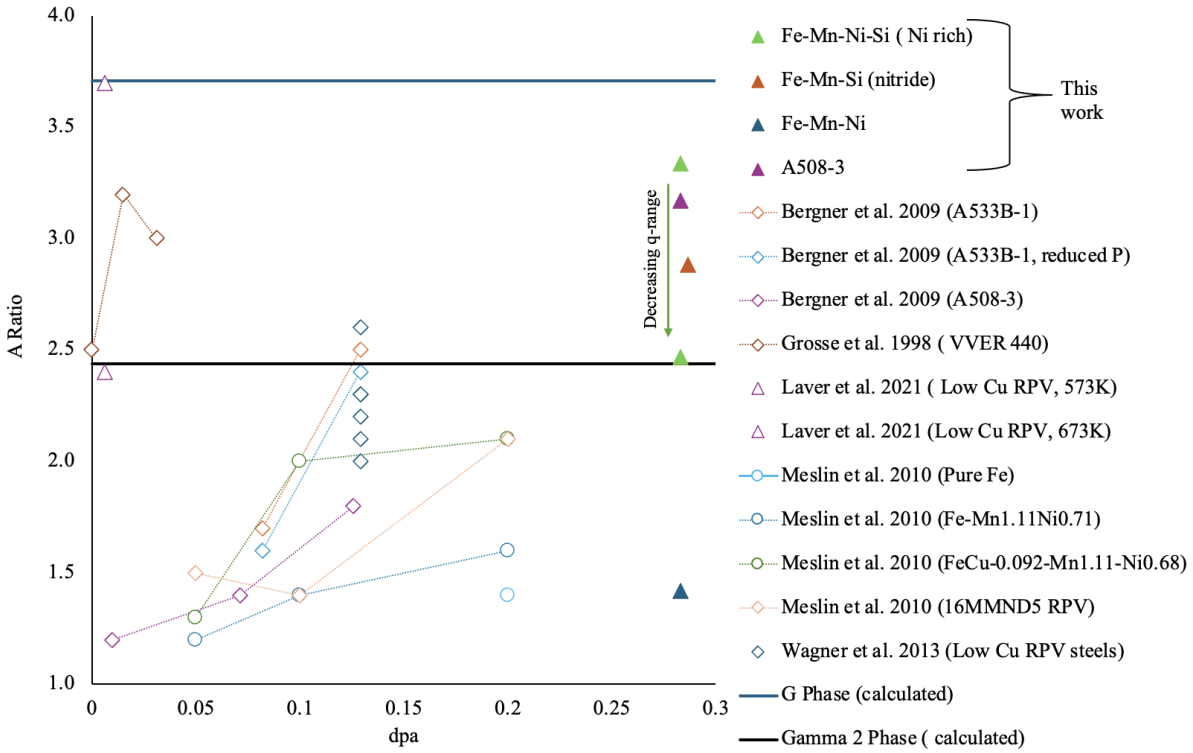


Figure 6.16: Plots of measured A ratio, and values in this study, versus dose (dpa). Dose averaged over the proton damage profile as 0.28 dpa. Solid markers are data from this work, circles are neutron irradiated model alloys, triangles are proton irradiated material and diamonds are neutron irradiated RPV alloys. Horizontal lines correspond to the calculated values of A ratio for the G phase and the Γ_2 phase.

phase. This suggests a contribution of temperature and radiation particle type(i.e. cascade size and dose rate) to the composition of radiation induced defects.

Chapter 7

Discussion

7.1 Summary of results and use of complementary techniques

The combination of results from complementary techniques has enabled the identification of features in this work more comprehensively than would have been possible using only a single technique. A summary of the advantages and limitations of each technique is shown in table 7.1 and for both the Fe-Mn-Si and Fe-Mn-Ni-Si alloy a summary of results is presented visually, showing the connection between each result.

Without atom probe tomography, the compositional STEM-EDX analysis would not have led to the identification of a probable G phase precipitate, or confirmed the lack of Fe present in the Ni rich precipitates, facilitating the assumption of non-magnetic particles in SANS analysis. STEM-EDX analysis was the only technique used that could identify the presence of nitrogen in the Ni lean precipitates in both the alloys investigated. APT and SANS alone could not conclusively detect nitrides clearly present in TEM observations of the Fe-Mn-Ni-Si and Fe-Mn-Si alloy due to key overlaps in both datasets. In the SANS analysis, compositional information is inferred from the scattering length density modelled on experimental data. Nitrogen and iron have very similar values of nuclear scattering length of 9.36 and 9.45 fm respectively [200], so it is challenging to separate contributions as being from Fe or N using SANS. In APT, the mass/charge peaks from N^{+}, are at 14 and 15 Da (corresponding to ^{14}N and ^{15}N), both of which overlap with the first and third most abundant Si^{2+} peaks at 13.99 Da and 14.99 Da (corresponding to ^{28}Si and ^{29}Si) [236]. Decomposition of peaks was attempted, to measure

N content in the matrix of the irradiated alloys, but no statistically significant quantity was measured in any of the specimens in section 5.1. In the Fe-Mn-Ni alloy samples, the 14 Da peak was ranged as nitrogen, but no statistically significant difference was observed between the irradiated and unirradiated sample nitrogen content (table 5.4).

Preferential evaporation of the precipitate leads to a smearing of the interface when measuring 1D concentration and proxigrams. STEM-EDX maps can only avoid interface smearing when the precipitates are through thickness, and the interface is images edge-on, which was not possible in most cases in this alloy, due to their very small size. However, the interfaces observed in figs. 4.17, 4.20, 4.24 and 4.26 are sufficiently sharp to assume that the measured APT interface width is due to instrumental smearing. These effects are of interest to the RPV Mn-Ni-Si clustering research community, as there is disagreement on whether iron atoms should be omitted from analyses of radiation induced cluster composition, and there is wide variation in reporting of Fe content contributing to confusion in the field [237]. In this case, matrix Fe atoms are likely to be focused into the precipitate, meaning that much of the measured Fe content is due to evaporation effects, and is not representative of the stoichiometry of the precipitate. Where clusters have a stable solute composition across their profile, but varying Fe content, it may make sense to omit iron atoms from calculations of composition, and in this work, one large Mn-Ni-Si precipitate was observed in the atom probe, where the Fe content in the centre was very low, < 5 at.% , indicating this assumption is likely to be valid.

Table 7.1: Summary of capabilities and limitations of various complementary techniques used to characterise radiation damage effects in RPV steels.

Method	Feature Size	Morphology	N_d, V_f	Size Distribution	Composition	Feature Location	Effect on mechanical properties	Crystal Structure	Limitations
TEM (STEM EDX, & diffraction)	✓	✓	✓	✓	✓ (Less sensitive to low Z elements, due to overlapping X-ray emission lines.)	✓	-	✓	Quantitative EDXS analysis challenging without use of extraction replica, for precipitates in Fe matrix.
APT	✓	✓ (With accurate reconstruction, and a priori information.)	✓ (If sufficiently high.)	✓	✓	✓	-	-	Morphology of features challenging to reconstruct due to evaporation field effects due to trajectory aberrations. Small specimen volumes make calculation of number density challenging when features are larger than few nm, or sparsely distributed.
SANS	-	-	✓	✓	✓ (Average values, providing a range of possible compositions.)	-	-	-	No information can be obtained on specific defects, and modelling data requires a priori information.
Nanoindentation	-	-	-	-	-	-	✓	-	Not easily scalable to bulk properties, particularly for irradiated materials.

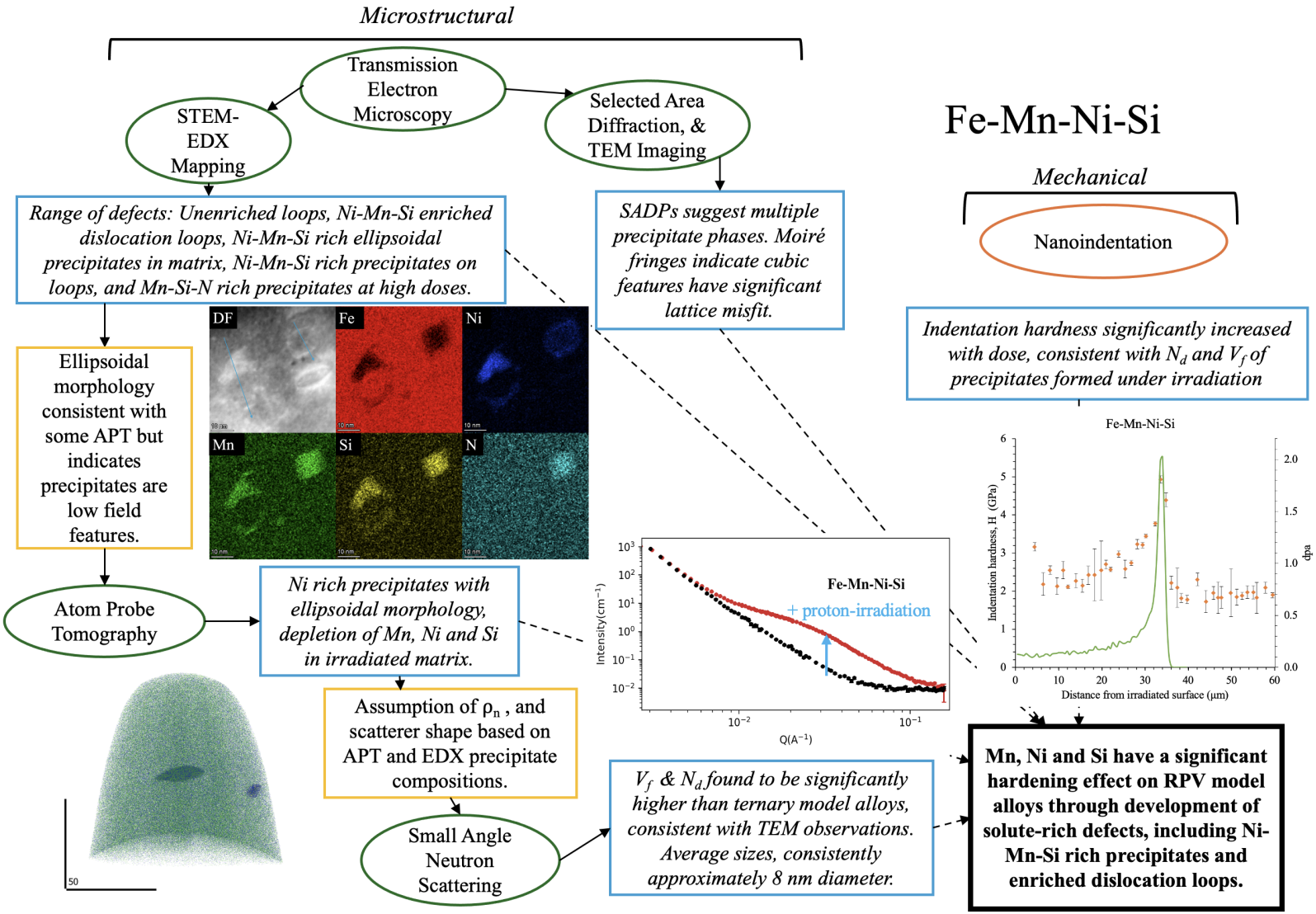


Figure 7.1: Graphical summary of results obtained using complementary techniques for the Fe-Mn-Ni-Si alloy. Various radiation induced defect types have been observed. SANS data showed increased scattering intensity for $0.007\text{Å}^{-1}<q<0.1\text{Å}^{-1}$, indicating precipitates in the size range ~$5<R<90$ nm, consistent with TEM observations.

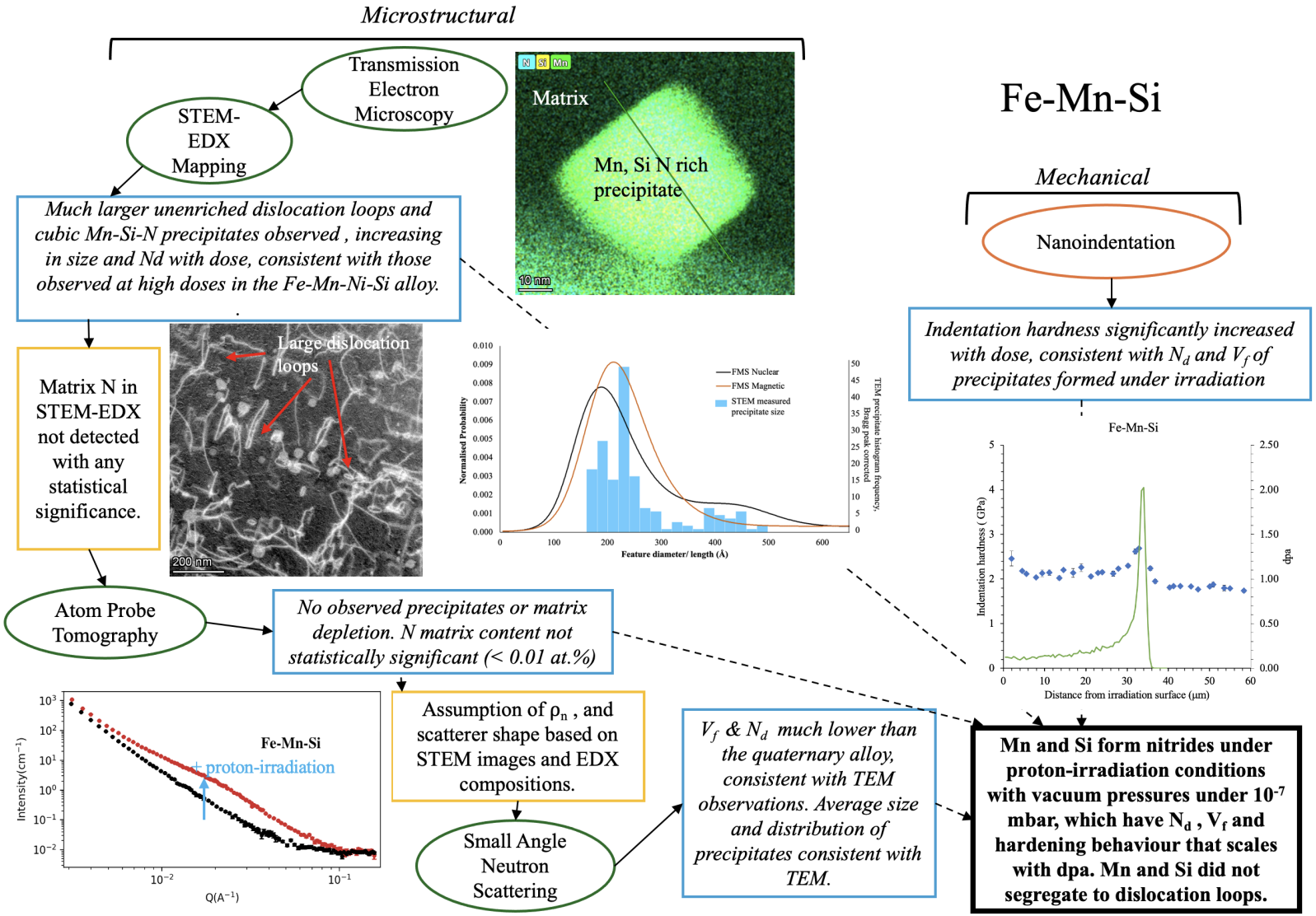


Figure 7.2: Graphical summary of results obtained using complementary techniques for the Fe-Mn-Si alloy. Key observations are that after proton-irradiation the microstructure contained cubical Mn-Si-N enriched precipitates, not obviously associated with dislocation loops. The majority of large dislocation loops have rectilinear morphology, but there are numerous smaller rounded dislocation loops. As for Fe-Mn-Ni-Si, SANS data showed increased scattering intensity for $0.007\text{Å}^{-1}<q<0.1\text{Å}^{-1}$, indicating precipitates in the size range ~$5<R<90$ nm, consistent with TEM observations.

SANS analysis confirmed the observations of precipitates in TEM, yielding very consistent size distributions describing the precipitate populations. For example, the Fe-Mn-Si alloy has a positively skewed log-normal distribution with an increased frequency of precipitates in the size range 50-70 nm for both the SANS data and TEM data averaged over the whole dose region, shown in fig. 7.3. This is consistent with the overlap of two distinctly different dose regions being averaged in SANS measurements, with the high dose region containing a greater number of larger features, but also contributing to the peak at smaller sizes.

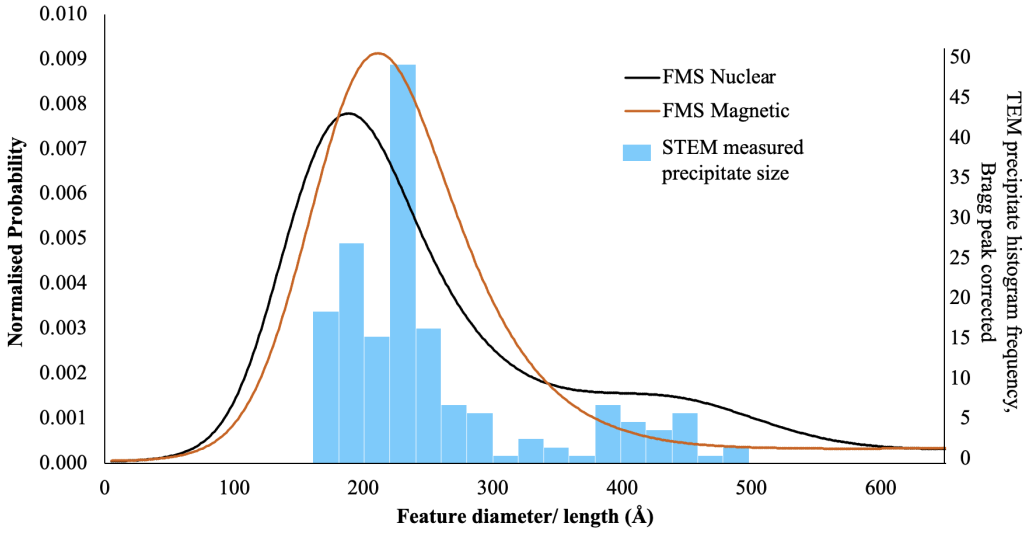


Figure 7.3: Comparison of size distribution data obtained using maximum entropy method fitting of SANS data and TEM precipitate measurements averaged over the dose region, showing consistent size ranges for both analysis methods, for the Fe-Mn-Si N rich precipitates.

7.1.1 Summary of results

Results obtained for characterisation of the Fe-Mn-Ni-Si and Fe-Mn-Si alloys are shown in figs. 7.1 and 7.2 and show the links between characterisation methods, and what data fed into subsequent analyses.

Precipitate Composition

Figure 7.4 and table 7.2 show the compositional information obtained about precipitates in the Fe-Mn-Ni-Si and Fe-Mn-Si alloys, using APT and STEM-EDX. TEM-EDX measurements of precipitates in the Fe-Mn-Ni-Si alloy suggest the presence of two main groups of precipitates;

Ni rich features, with an average stoichiometry of $Mn_{1.74}Ni_{2.66}Si$ (over all dose regions), and a nitrogen rich, Ni lean phase with a Mn:Si ratio increasing with dose. This is not consistent with the APT observations of a $Mn_{5.6}$ $Ni_{16}Si_{6.1}$ composition feature in the 0.1 dpa region of irradiated Fe-Mn-Ni-Si, suggesting there is significant variation in the compositions of individual features. APT matrix depletion measurements found almost twice as much Mn is depleted from the matrix as would be expected had all the precipitating features been pure G phase, suggesting there are other phases present (table 5.2). If depletion of solutes corresponded to a single phase population of precipitates, the stoichiometry, based on absolute depletion values for Mn, Ni and Si, would be approximately $Mn_3Ni_4Si_2$.

Grain boundary segregation may be part of the cause of this significant decrease, and segregation of Ni and Mn has been observed in the 0.1 dpa region of the Fe-Mn-Ni-Si alloy and at a grain boundary in the 0.1 dpa region of the A508-3 steel in one atom probe specimen. As Ni and Mn segregated to grain boundaries under radiation, these depletion values suggest there is even more of an excess of Si depleted from solution than can be accounted for by G phase precipitation. This supports the observations made in TEM of a Mn-Si rich phase, not containing Ni. Comparing the average compositions across the dose profiles in the Fe-Mn-Ni-Si and Fe-Mn-Si alloys, it is clear that increasing depth into the material leads to a reduced quantity of nitrogen in the N rich features (fig. 7.4).

SANS results suggest microstructural evolution caused by irradiation occurred in all alloy compositions. Plots of A ratio vs q showed that there is a population of scatterers with a single stable composition formed after irradiation in the Fe-Mn-Si alloy, confirming TEM observations of the Mn-N-Si precipitate, but that scatterer composition varies with size in the Fe-Mn-Ni-Si alloy (fig. 6.3). This is also consistent with the TEM observations of a wide variety of solute enriched features and the variation between the measured TEM and APT solute-rich feature compositions(fig. 4.5, table 7.2, and ??.

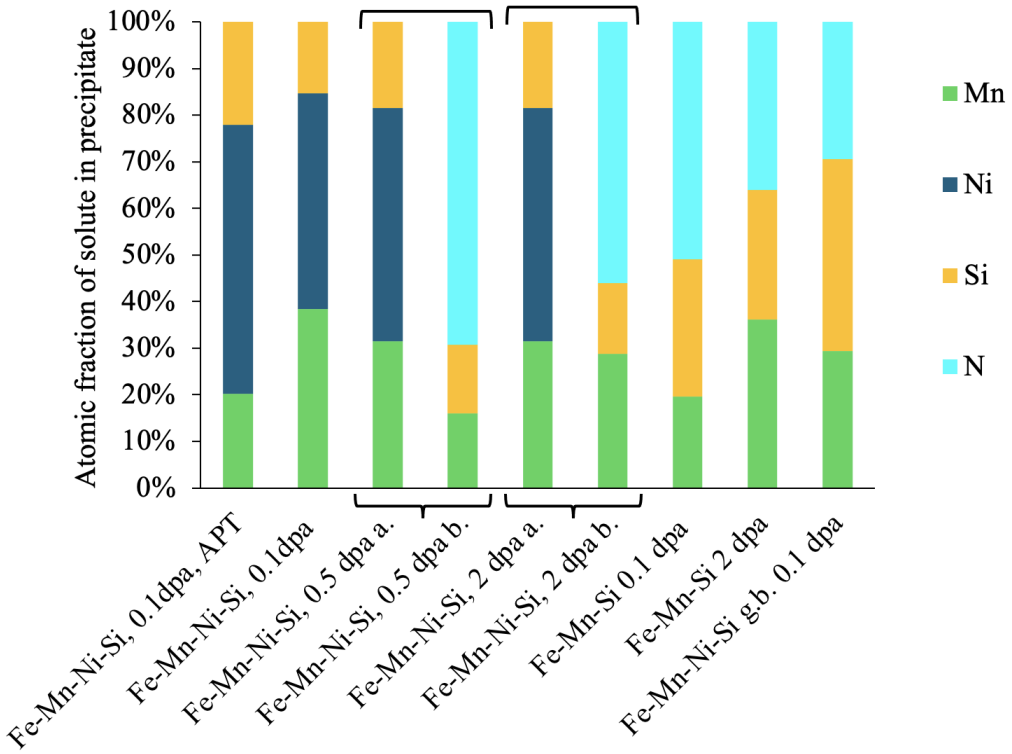


Figure 7.4: Atomic fraction compositions of precipitates observed using APT and STEM-EDX, at a range of doses in the Fe-Mn-Ni-Si and Fe-Mn-Si alloy, based on data from tables 4.9, 4.11 and 5.6, assuming there is no Fe present in the precipitates.

Table 7.2: Compositional information on precipitates observed in Fe-Mn-Ni-Si and Fe-Mn-Si alloy collected using STEM-EDX, APT and SANS, all omitting Fe. The SANS nuclear scattering length densities are taken from figs. 6.11 and 6.12. A ratios are measured values for the Fe-Mn-Si alloy and for Fe-Mn-Ni-Si, are modelled values from table 6.4.

Solute-rich feature	APT	TEM		SANS modelled ρ (10^{-6}/Å^{-2})	SANS A ratio
		0.1 dpa	2 dpa		
Ni-Mn-Si	$Mn_{5.6}Ni_{16}Si_{6.1}$	$Mn_{2.5}Ni_{3.0}Si_{1.0}$	$Mn_{1.7}Ni_{2.7}Si$	3.74 ± 0.33	2.35 ± 0.29
Mn-Si-N-Ni	-	-	$N_{12.1}Mn_{6.2}Si_{3.3}Ni$	4.17 ± 1.32	2.67 ± 1.19
Mn-Si-N, at grain boundary	-	$Mn_3Si_3NiN_{4.2}$	-	-	-
Mn-Si-N	-	$N_{2.6}MnSi_{1.5}$	$N_{1.3}Mn_{1.3}Si$	3.16 ± 0.03	2.88 ± 0.04

Precipitate Distributions

The Fe-Mn-Ni-Si showed significantly higher number density of features compared with all other alloys, suggesting Mn, Ni and Si have a combined effect on solute-rich feature nucleation (table 6.4). This increase in number density was consistent with TEM measurements, and with hardening observed in the Fe-Mn-Si and Fe-Mn-Ni-Si alloys (figs. 4.1 and 4.6). These two alloys, for which TEM and APT precipitate composition data was available, showed populations of scatterers in the region of 5-50 nm in size. Size measurements across TEM and SANS are consistent, with the large precipitate observed in APT being at the higher end of the size distribution measured using TEM & SANS, as shown in table 7.4.

Table 7.3: Table summarising the observations of microstructural changes after proton-irradiation in Fe-Mn-Ni and A508-3 RPV steel, using APT and SANS.

Alloy	APT	SANS, using $d = \frac{2\pi}{\vert\vec{q}\vert}$
Fe-Mn-Ni	Clustering of up to 20 % concentration Mn and Ni, with disc-like morphology.	Increase in scattering after irradiation for $0.004\text{Å}^{-1}<q<0.1\text{Å}^{-1}$, ~5<D<200 nm.
A508-3 RPV steel	Enrichment of Ni and Mn at grain boundary.	Small increase in scattering after irradiation for $0.02\text{Å}^{-1}<q<0.1\text{Å}^{-1}$, ~5<D<30 nm.

Table 7.4: Measured sizes of solute-rich features observed after proton-irradiation using TEM and SANS. The SANS values are taken as the mean sizes of the modelled distributions in table 6.4 (Fe-Mn-Ni-Si), table 6.5 (Fe-Mn-Si), table 6.2 (Fe-Mn-Ni), table 6.3 (A508-3 steel).

Alloy	TEM Size at 0.1 dpa (nm)	TEM Size at 0.5 dpa (nm)	TEM Size at 2 dpa (nm)	Weighted mean TEM Size (nm)	Mean SANS Size (nm)
Fe-Mn-Ni-Si	8.56 ± 0.32	8.30 ± 0.92	7.87 ± 0.62	8.51 ± 0.03	8.13 ± 4.41
Fe-Mn-Si	21.2 ± 0.7	31.69 ± 3.37	33.1 ± 1.1	22.06 ± 0.59	19.25 ± 0.24
Fe-Mn-Ni	-	-	-	-	39.17 ± 1.64
A508-3 RPV steel	-	-	-	-	8.76 ± 0.51

Table 7.5: Comparison of average volume fraction and number densities measured using weighted means of TEM data (over the Bragg peak) and thickness corrected average values calculated using SANS models. *- The Fe-Mn-Ni fit produced very high volume fractions and average sizes of feature, possibly due to sample surface contamination.

Alloy	TEM Weighted mean V_f	SANS V_f	TEM Weighted mean N_d (m^{-3})	SANS N_d (m^{-3}
Fe-Mn-Ni-Si	0.0015 ± 0.0003	0.00234 ± 0.00005	$3.79 \pm 0.60 \times 10^{21}$	$1.04 \pm 0.11 \times 10^{21}$
Fe-Mn-Si	0.0006 ± 0.0002	0.00043 ± 0.00001	$4.34 \pm 0.24 \times 10^{19}$	$6.03 \pm 0.29 \times 10^{19}$
Fe-Mn-Ni	-	0.096 ± 0.001*	-	$8.95 \pm 0.22 \times 10^{16}$
A508-3 RPV steel	-	0.00029 ± 0.00001	-	$1.18 \pm 0.10 \times 10^{21}$

7.2 Precipitate phase identification

Using TEM and APT (chapters 4 & 5) proved challenging in terms of characterising radiation induced precipitation and segregation across all alloy compositions due to the sparsely distributed features, and complex specimen preparation requirements. As a result, only a limited number of discrete feature compositions could be measured in the Fe-Mn-Si and Fe-Mn-Ni-Si alloys. SANS data is interrogated here to assess the most probable phases present in these materials. A range of possible phases have been selected based on literature, and their theoretical nuclear scattering length densities have been calculated using crystal structure information from the Inorganic Crystal Structures Database (ICSD) [222] and eqs. (3.14) and (3.15). Values are shown in tables 7.6 and 7.7. None of the phases proposed have been observed to have ferromagnetic behaviour at room temperature, and those that have been investigated in literature have been found to be paramagnetic. This validates the assumption made during data analysis that all precipitate phases are non-magnetic and have a fixed magnetic scattering contrast factor.

7.2.1 Mn-Ni-Si rich precipitates

Although an almost iron free feature was observed using APT close to the composition of the G phase $Mn_6Ni_{16}Si_7$ silicide, the ratios of Mn and Si to Ni in most of the features measured using EDX do not correspond to this stoichiometry. At 0.1 dpa, solute-rich features are more consistent with the general formula of the previously observed Γ_2 $Mn(Ni, Si)_2$ structure. However, they still have much higher Mn content than might be expected from this phase with a ratio of Mn: Ni & Si of 1.25:2 (table 7.2)[147]. Unlike the G phase where Fe substitutes most stably into Mn, Ni then Si sites [238, 131], in the Γ_2 phase, it is more stable for Fe to substitute first into the Si, Ni then Mn sites [132]. Therefore, the excess of Mn in these phases may be balanced by some Fe present in the precipitate in Ni or Si sites. Whiting et al. calculated that the formation enthalpy of the Γ_2 phase in BCC iron can be below zero with an Fe content up to 30 at.%[132], whereas the G phase is stable when Fe concentration drops below 18 at.% [238]. However, there is no evidence from selected area diffraction patterns that this phase is present in the higher dose regions. The SADPs, which can be found in fig. 4.33, observed in this work, were not consistent with a Γ_2 phase structure when considering either a cube-on-cube or

Kurdjumov-Sachs orientation relationship. Vacancies are highly stable in G phase structures, especially on the Si lattice sites [131]. A high fraction of vacancies or Fe substitutions may explain the lower measured Si values in precipitates compared with stoichiometric phases. In previous studies on aged and neutron irradiated steels, G phase structures have been identified with reduced Si content compared with the stoichiometric composition [239, 129]. In work by Sprouster et al., various neutron-irradiated low alloy steels were analysed using APT, and X-ray diffraction to determine the phase fractions and structures of Mn-Ni-Si rich precipitates [129]. They observed that for all the alloys, the most reliable fit was using a G phase structure, and fitting of the Γ_2 phase structures yielded non-physical parameters. They concluded that the G phase was the dominant structure present, but the measured compositions of features were much lower in Si and higher in Mn than a stoichiometric G phase, with an average composition of 33.3% Mn, 47% Ni, and 19.6% Si [129]. This is very similar to the compositions obtained in this work using STEM-EDX, shown in table 7.2. Ab initio calculations of phase stability of variations of the G phase have found that phosphorus content can stabilise the structure, and that a mixed structure of $Mn_6Ni_{16}SiP_6$ has a lower formation energy than the Mn-Ni-Si G phase, indicating that there are thermodynamically stable alternatives including interstitial solute atoms as well as substitutional [142]. In all observed Ni rich features in TEM, the Si content is lower, and Mn higher than would be expected if the features were a stoichiometric G phase. With increasing dose, the Mn content reduces, and Si content increases, relative to the Ni content, suggesting that the composition is evolving towards an Fe-free Mn-Ni-Si G phase. In early stages of growth, a mixed $(Fe\text{-}Ni)_{16}(Mn,Fe))_6Si_7$ G phase structure, with some sites of the Ni and Mn sublattice occupied by Fe atoms, may be present, as has been suggested by both computational and experimental studies [127, 131]. Tencé identified self-ion radiation induced precipitation of G phase in a model Fe-Mn-Ni-Si alloy at 400 °C to 6 dpa, with a stoichiometry of $(Ni,Fe)_{16}(Mn,Fe)_6Si_7$ in a Fe-Ni0.8-Si0.4-Mn1.4 alloy and $Ni_{16}(Mn,Fe)_6Si_7$ in a Fe-Ni1.8-Si0.8-Mn0.7 alloy [127]. In these cases, the composition of Ni in the precipitates is dependent on the overall alloy composition, but it seems that the Si content remained constant. The composition of G phase formed under irradiation is likely to be dependent on the bulk alloy composition. Predicted phases in models by Xiong et al. suggested that the precipitate composition is likely to be close to the Mn:Ni:Si ratio present in the bulk material [128]. Although the Ni is the

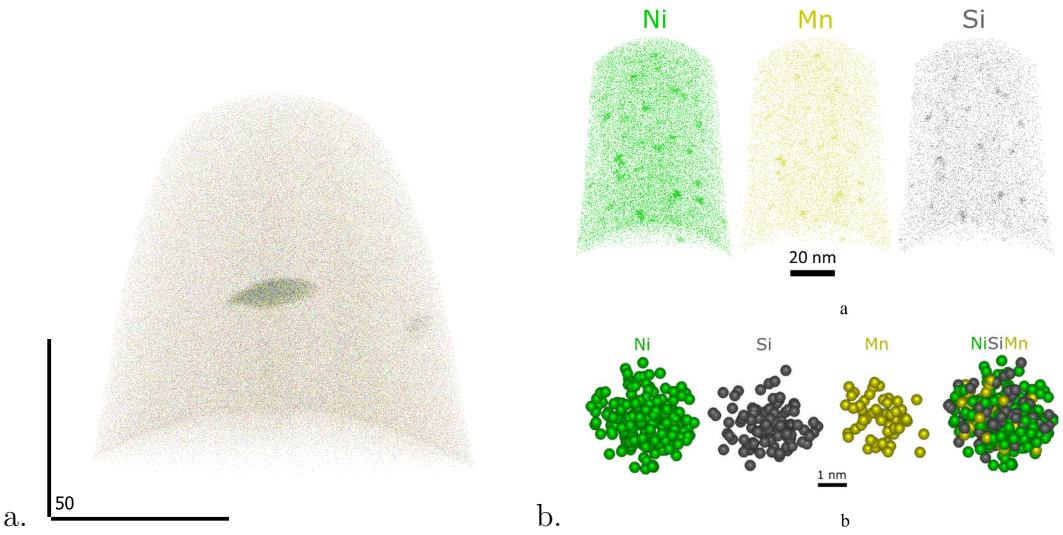


Figure 7.5: Comparison of precipitate observed in the irradiated Fe-Mn-Ni-Si alloy in this work (a.) with Mn-Ni-Si clusters in a neutron irradiated VVER 1000 RPV steel from Kuleshova et al.[16]. Reprinted from Journal of Nuclear Materials, 553, E.A. Kuleshova, G.M. Zhuchkov, S.V. Fedotova, D.A. Maltsev, A.S. Frolov, I.V. Fedotov, Precipitation kinetics of radiation-induced Ni-Mn-Si phases in VVER-1000 reactor pressure vessel steels under low and high flux irradiation, Page 153091, Copyright 2021, with permission from Elsevier.

highest concentration of solute, at lower doses the Mn content is much higher than Si, consistent with the matrix composition, and this ratio starts to tend towards increasing Si with increasing dose (table 7.2).

In lower Mn containing steels, Kuleshova et al. found that for a range of Ni content (1.1-1.94 at.%) RPV steels, the precipitates formed under irradiation have a composition corresponding to a $(Ni,Mn)_2Si$ compound, with 45 at.% Ni, 33 at.% Si, and 22 at.% Mn [16]. The compositions observed here are again consistent with the assertion that initial cluster compositions correspond to bulk alloy compositions. The observations of precipitates up to 15 nm in size, by Kuleshova et al, suggests that the composition does not evolve quickly, despite growth beyond the size of many of the clusters analysed in literature [16]. Compared with this work, high flux neutron irradiation led to much smaller, higher number density Mn-Ni-Si precipitates, shown in fig. 7.5.

In this work, assuming that some Ni and Mn sites are populated with iron atoms in the precipitates, the TEM compositions measured could give a range of G phase or Γ_2 stoichiometries.These differ from the self-ion irradiation experiments carried out by Tencé, as the Mn content of precipitates is significantly higher [127].

The diffraction patterns suggest cubic precipitates with 2 and 4 times the lattice parameter of the ferritic matrix (fig. 4.35). Of the possible structures simulated in chapter 4, the closest matching pattern at all three zone axes is the $Mn_6Ni_{16}Si_7$ G phase. In ferritic stainless steels, cold-rolled and aged at 500 °C, cuboidal $Mn_6Ni_{16}Si_7$ precipitates have been observed with a cube-on-cube orientation relationship [240]. Cold rolling induced dislocations into the microstructure and led to enhanced precipitation, which could be analogous to the production of dislocation loops under irradiation leading to enhanced segregation and precipitation. The diffraction patterns, showing G phase precipitation, are consistent with the patterns observed in this work and are compared in fig. 7.6 [240].

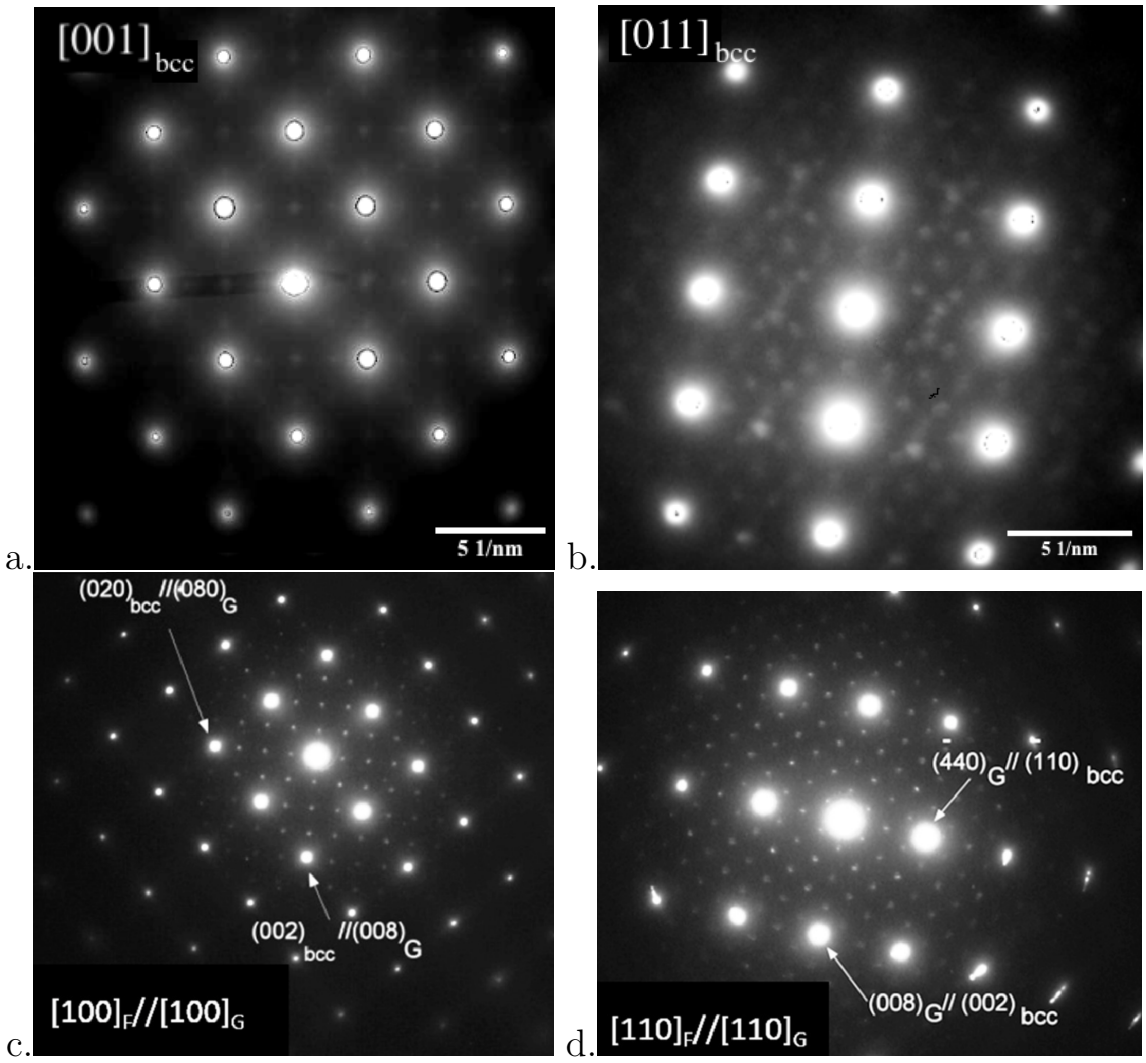
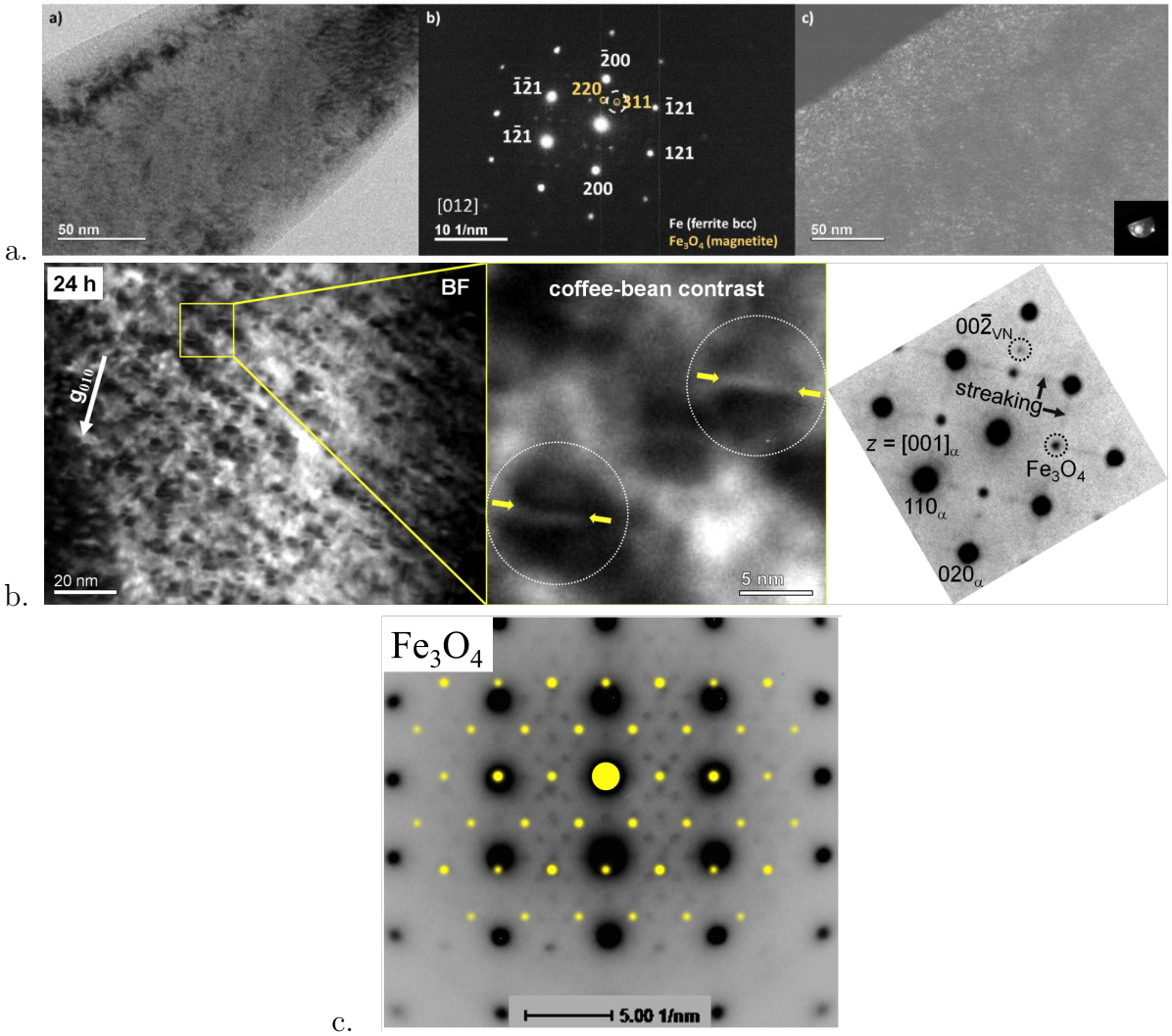


Figure 7.6: Comparison of diffraction patterns observed in this work (a. & b.) and those observed by Yang et al. 2021 (c. & d.), from $Mn_6Ni_{16}Si_7$ in cold-rolled and aged FeCr-20Ni-3Si-3Mn-2 ferritic alloy [240]. Reprinted from Acta Materialia, 205, Mujin Yang, Daniel J.M. King, Ivan Povstugar, Yuren Wen, Junhua Luan, Bernd Kuhn, Zengbao Jiao, Cuiping Wang, M.R. Wenman, Xingjun Liu, Precipitation behavior in G-phase strengthened ferritic stainless steels, Page 116542, Copyright 2021, with permission from Elsevier.

Diffraction patterns on the [001] zone axis showed higher intensity spots in the centre of the matrix patterns, {100}-α, than would be expected purely for the G phase reflections (see fig. 4.34). These brighter spots may be reflections from the cuboidal features, e.g. (200) type spots from $MnSiN_2$, but it is more likely that they are $(220)_{Fe_3O_4}$ reflections from surface oxide, as observed in other TEM studies on low alloy ferritic steels, examples of which are shown in fig. 7.7 [121, 241].



a.

b.

c.

Figure 7.7: Comparison of diffraction patterns attributed to Fe_2O_3 iron oxides obtained from a. A neutron irradiated A508-3 steels from Carter et al.[121] b. nitrided BCC Fe-V-Si alloy from Schwarz et al.[241] and c. diffraction pattern from the irradiated Fe-Mn-Ni-Si alloy this work with overlaid Fe_2O_3.

a. Reprinted from Journal of Nuclear Materials, 559, Megan Carter, Claudia Gasparrini, James O. Douglas, Nick Riddle,Lyndon Edwards, Paul A.J. Bagot, Christopher D. Hardie, Mark R. Wenman, Michael P. Moody, On the influence of microstructure on the neutron irradiation response of HIPed SA508 steel for nuclear applications, Page 153435, Copyright 2022, with permission from Elsevier.

b. Reprinted from Acta Materialia, 76, B. Schwarz, S.R. Meka, R.E. Schacherl, E. Bischoff, E.J. Mittemeijer, Nitriding of iron-based ternary Fe–V–Si alloy: The precipitation process of separate nitrides, Pages 394-403, Copyright 2014, with permission from Elsevier

King et al. investigated the stability of various Mn-Ni-Si rich G phase structures using DFT and calculated that the Mn-Ni-Si G phase would have zero misfit at 757 K [131]. Given that the measured temperatures of approximately 300-400 °C are likely to underestimate the temperature inside the irradiation region of the material, it is possible that this temperature was achieved and stabilised the nucleation and growth of the G phase, by reducing lattice misfit. The ellipsoidal morphology observed in TEM is consistent with a coherent precipitate. The phases with scattering length densities and A ratio closest to the measured values for Fe-Mn-Ni-Si, vary with scatterer size. The smallest features have a higher A ratio of 3.34 ± 0.05 (table 6.1) which is closest to the Mn-Ni-Si G phase value of 3.58 (table 7.6), consistent with APT observations. As the size of features increases, the A ratio decreases, giving a range of possible structures with reducing Ni content. An A ratio of 2.35-2.61 is most consistent with the calculated A ratios corresponding to the Γ_2 phase, which are consistent with the TEM compositional measurements, but not with diffraction information. Then at larger size ranges (low q) the A ratio dropped to around 1, corresponding to features with no magnetic scattering contrast with the matrix. It is possible that these features may be enriched dislocation loops, which would have similar scattering length densities to the matrix, and have been observed at larger sizes than the precipitates in TEM fig. 4.15. The fact that the A ratio dramatically decreases with growing feature size suggests there may be a stage of compositional evolution after nucleation, before growth can occur, as proposed by Xue et al., in a heavy ion irradiation of the same Fe-Mn-Ni-Si and Fe-Mn-Ni model alloys [133].

If it is assumed that all scatterers are non-magnetic in the Fe-Mn-Ni-Si alloy then this means that the nuclear scattering contrast is increasing with size and the composition of the larger features has greater contrast with the Fe matrix. This could be caused by the formation of Mn-Ni-Si rich phases, with some Fe atoms in their structure, gradually evolving in composition to contain more Mn, Ni and Si. If the scatterers contain some iron, they may have a magnetic moment, leading to a decreased magnetic scattering contrast, which will also lead to a reduction in A ratio [156].

Table 7.6: Candidate phases for precipitates observed in the Fe-Mn-Ni-Si alloy, A ratios calculated assuming particles are non-magnetic at room temperature. For some structures, no magnetic information could be found and their magnetic behaviour at room temperature is unknown.

Candidate Phase	Space Group	Composition	Lattice Parameter (nm)	Theoretical ρ_n (10^{-6}Å^{-2})	Theoretical $\Delta\rho^2$ (α-Fe) (10^{-12}Å^{-4})	Paramagnetic at Room Temperature?	Theoretical A Ratio
G Phase	$Fm\bar{3}m$ [219, 131, 147]	$Mn_6Ni_{16}Si_7$ [219, 131, 147]	1.117[219] 1.11[131] 1.108[147]	4.92 5.02 5.04	9.60 9.03 8.87	Yes[223]	3.58 3.75 3.80
Γ_2 Phase	$Fd\bar{3}m$[147, 132]	$Mn\ (Ni,Si)_2$[147] $Mn_8Ni_{13}Si_3$[132] $Mn_8Ni_{12}Si_4$[132] $Mn_8Ni_{11}Si_5$[132]	0.668[147] 0.663[132] 0.662[132] 0.666[132]	4.053 4.00 3.80 3.53	15.74 16.13 17.79 20.18	?	2.58 2.54 2.40 2.23
Ω Phase	$Fd\bar{3}m$[242, 243]	Mn_3Ni_2Si[242]	1.076[243]	1.74	39.40	Yes[243]	1.63
Manganese Nickel Silicide	$P6_3/mm$	$Mn_aNi_bSi_3$ a=4.8−4.95, b=0.2−0.05	0.690-0.691 0.690-0.691 0.481	−0.17−−0.18	66.91-67.25	Yes[244]	1.37
Manganese Nickel Silicide [245]	$P2_13$	$Mn_{0.66}Ni_{0.20}Si_{0.14}$	0.629	2.49	64.84	?	1.38
Mixed Monosilicide,	$P2_13$	$(Mn_{0.5}Ni_{0.5})Si$	0.451	0.14	62.05	?	1.40

7.2.2 Mn-Si-N rich precipitates

The Fe-Mn-Si alloy was observed to have a single population of precipitates in TEM, so the A ratio should represent the composition of the precipitates without needing to be corrected for scatterer size [246]. The measured A ratio of the nitride precipitates in the Fe-Mn-Si alloy is 2.88 ± 0.04 which is within statistical error of the calculated A ratio of $MnSiN_2$, of 2.89 (tables 6.1 and 7.7) and compositions are also consistent, fig. 7.8. This suggests validity of the assumption that nitrides will behave as paramagnets at room temperature, as they have previously been shown to be antiferromagnetic at room temperature [247]. However, the average TEM measured compositions of the cuboidal precipitates in the Fe-Mn-Si alloy showed a decrease in nitrogen content in the higher dose region. This may be due to the larger thickness of the 2 dpa specimen, leading to greater absorption of lower energy X-rays emitted from nitrogen atoms, or there could be some features with lower nitrogen content.

In the Fe-Mn-Ni-Si at higher doses, the specimen thickness at higher dose is lower but measured relative nitrogen content to Mn and Si in the precipitates decreases , suggesting there is some real variation in nitrogen composition as a function of depth from the surface. Therefore, a range of other phases containing Fe, Mn and Si are included for comparison. The largest feature was observed in the Fe-Mn-Ni-Si alloy at a grain boundary in the 0.1 dpa region and had a lower nitrogen content than the average values from any other dose regions, with a stoichiometry of around $Mn_3Si_3N_{4.3}$. Only the measured compositions in the nearer surface region of the Fe-Mn-Si alloy are close to the composition of the only reported stable ternary nitride in ferrite; $MnSiN_2$ [248, 249].

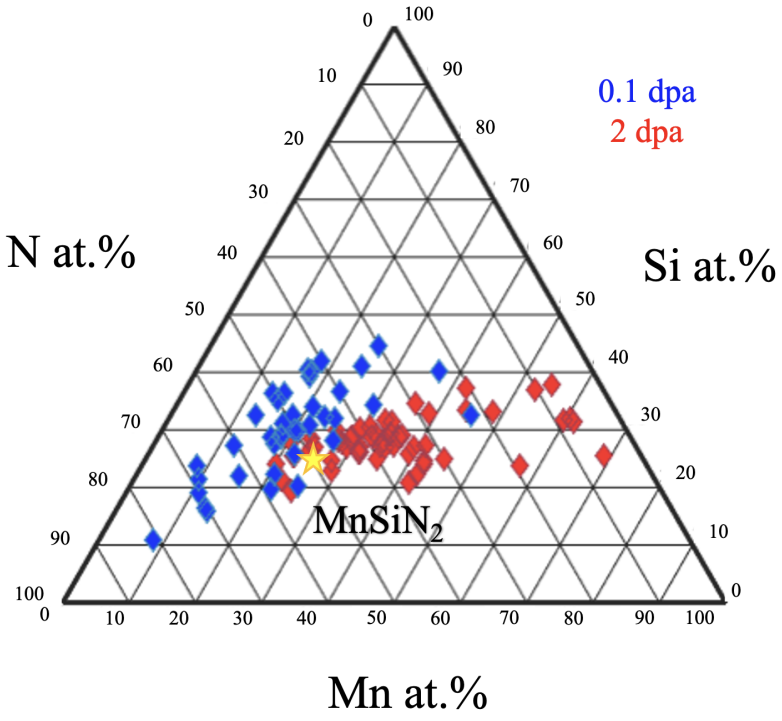


Figure 7.8: Ternary plot from fig. 4.31 with a star indicating the position of the $MnSiN_2$ phase.

Table 7.7: Comparison between calculated neutron scattering values for measured compositions, and candidate phases in literature. As only one ternary nitride phase has been recorded in literature, a range of other (Fe)-Mn-Si are considered for comparison.

Candidate Phase	Space Group	Chemical Composition	Lattice Parameter (nm)	Theoretical ρ_n (10^{-6}Å^{-2})	Theoretical $\Delta\rho^2$ in α-Fe	Paramagnetic at Room Temperature?	Calculated A Ratio, non-magnetic particles
$MnSiN_2$	$Pna2_1$	$MnSiN_2$[247]	a=0.5527 b=0.651 c=0.507	4.39	13.2	AFM*[247]	2.89
Fe,Mn Silicide	$P2_1\bar{3}$[250]	$FeMnSi_2$[250]	0.452[250]	1.24	46.02	?	1.54
Manganese silicides	$P4_11_21_2$	Mn_5Si_2	0.891,0.891, 0.872	-2.16	103.56	Yes[251]	1.25
	$P\bar{4}c2$	Mn_4Si_7	0.553, 0.553, 1.746	-1.12	83.53	Yes[252]	1.30
	$P2_13$	MnSi	4.5559	-1.58	92.12	Yes[251]	1.27
	$P\bar{4}n2$	$Mn_{11}Si_{19}$	0.552, 0.552, 4.820	-1.12	83.50	Yes[253]	1.30
	$R\bar{3}mH$	Mn_6Si_7	0.470, 0.470, 2.561	-1.37	88.18		
$(Fe,Mn)_5Si_3$	$P6_3/mcm$	$Mn_{2-5}Fe_{3-0}Si_3$	a,b=0.683-0.692, c=0.474-0.482	-1.87-2.18	34.08-97.76	Yes[254, 255] if Mn>/= 1. No for Mn_5Si_3 [256]	1.34-1.73
$(Fe,Mn)_3Si$	$Fm\bar{3}m$	$Fe_{0-2.5}Mn_{3-0.5}Si$	0.559-0.572[257, 225]	-1.12-5.10	8.55-108.54	Yes, Fe<2.2[258, 259, 224] No, Fe>2.2, Tc>342K [258]	1.23-4.19

The nuclear scattering length density of the cuboidal features modelled in the Fe-Mn-Ni-Si alloy was $4.17 \times 10^{-6}/\text{Å}^2$, compared with $3.16 \times 10^{-6}/\text{Å}^2$ in the Ni free alloy. This value is much closer to the theoretical value calculated for a $MnSiN_2$, which has a nuclear scattering length density of $4.39 \times 10^{-6}/\text{Å}^2$.

Precipitates with high misfit with the matrix are more likely to form faceted precipitates in a BCC-Fe matrix, in order to minimise elastic strain. The $MnSiN_2$ is the only stoichiometry of ternary Mn-Si nitride observed in a ferritic matrix in the literature. Roberts et al., used X-ray diffraction to determine the crystal structure of ternary MnSi nitride in a range of nitrided Fe-Mn-Si alloys and found that below 670 °C the phase is triclinic, where the Mn:Si ratio is around 1:1 [248]. At higher Mn:Si ratios, of 3:1, below 670 °C it is hexagonal. At higher temperatures, they observed an orthorhombic (Mn,Si)N phase, which had variable Mn:Si ratio between 1:1 and 3:1 [248]. Although the latter has been observed only at high temperatures, it seems to be the most likely fit with diffraction spots based on data obtained in chapter 4.

7.3 Discussion on precipitation mechanisms

In the alloys in this work, Mn, Ni and Si are globally below their solid solubility limits in BCC-Fe and so thermodynamically these precipitates would not be expected to form, table 2.1. Observations of microstructures in the Fe-Mn-Ni-Si alloy suggest that dislocation loops act as nucleation sites for Mn-Ni-Si precipitates. In the 0.1 dpa STEM-EDX data Mn, Ni and Si are observed to segregate to dislocation loops, and to precipitate there, suggesting a radiation induced mechanism. In the higher dose regions nitrogen rich precipitates were observed inside Ni shells, suggesting that they are nucleating inside Mn-Ni-Si precipitates and growing there, ejecting Ni atoms as they grow. In the Ni free alloy, the dislocation loop density and precipitate number density are both much lower, and both increase in the high dose region approaching the Bragg peak, suggesting the nitride precipitates are also forming via nucleation at dislocation loops.

7.3.1 Mn-Ni-Si precipitation mechanisms

The greater number density of precipitates, and clear segregation of solutes to dislocation loops in the Fe-Mn-Ni-Si alloy shows there is much faster solute segregation occurring in this alloy. This

may be due to the higher binding energy of Ni to Si, than Mn to Si, 0.03 eV, compared with 0.01 eV [260]. This means that Si will bind more stably with Ni atoms at the early stages of clustering, and suggests that without Ni, Mn-Si clustering is less stable at early stages. Although Mn-N-Si precipitates have been observed in the N-free alloy, no clustering or segregation of Mn and Si to dislocation loops was identified (fig. 4.11), suggesting that Ni is required to stabilise solute clusters at dislocation loops. However, this is in opposition to many literature observations of Mn segregating to dislocation loops and stabilising point defect clusters in model Fe-Mn binary alloys [83, 135, 112]. This may be evidence that Si is making clustering less stable in the absence of Ni. Similar observations of weaker Mn-Si interactions in a heavy-ion irradiated Fe-Mn-Si alloy were made by Chen et al., when compared with clustering in a Fe-Ni-Si alloy[109]. Mn and Si were observed to cluster and a binary silicide, Mn_9Si_2 was proposed due to the high Mn:Si ratio, but the clusters were very small, all under 1.6 nm at all temperatures up to 1.5 dpa and this ratio of Mn:Si is very close to the ratio of Mn:Si in the nominal alloy composition [109]. Without Ni, no segregation to dislocation loops was observed, suggesting that there is a much stronger effect of radiation on segregation when both Mn and Ni are present. This has also been observed by Phongsakorn et al. [112], who found that Mn and Ni stabilised point defect clusters and dislocation loops more effectively when both present in alloys. This could be explained by the results of DFT calculations by Whiting et al., which show enhanced stability for triplet clusters of Mn and Ni with a vacancy or Si atom, compared with pure Mn-Ni containing complexes. This means that when all three solutes are present more stable clusters are likely to be produced [117]. The observation of much lower SANS scattering intensity after irradiation in the Si free alloy also aligns with computational and experimental studies indicating that Mn and Ni clusters are not stable without the presence of Si or vacancies which stabilise the structure at small sizes, leading to enhanced nucleation when present with Mn and Ni [117, 38]. Interestingly, Whiting et al. also calculated that for Ni-Ni-defect triplets, Si is the most stable third defect in a triplet complex, whereas for Mn-Mn-defect triplets, a vacancy is much more stable in the triplet than Si, see fig. 7.9 [117]. This is consistent with the lack of any co-segregation of Mn and Si to dislocation loops in the Ni-free alloy in this work, and the observations in this work suggest that early stage clustering of Mn and Si is much less stable that Mn, Ni and Si. The number density and volume fraction of features after irradiation in the Fe-Mn-Ni-Si alloy are much greater than in the Fe-

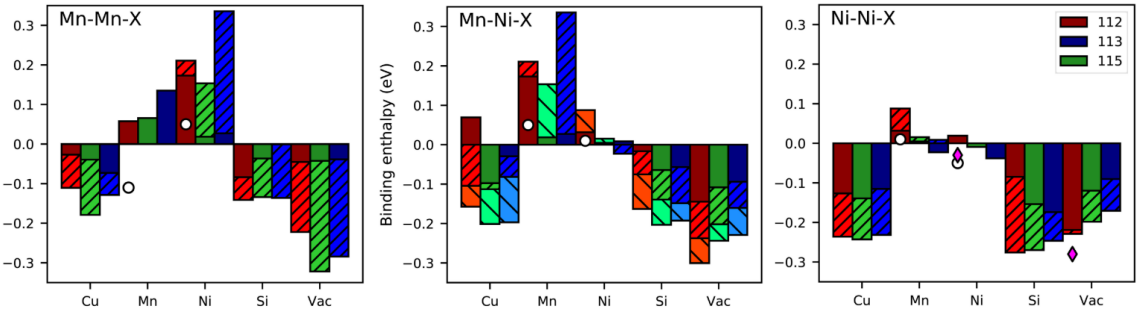


Figure 7.9: Binding enthalpies for a range of triplet clusters modelled using DFT by Whiting et al. ([117]), who showed that the most stable triplet binding species in Mn-Mn clusters are vacancies, but when Ni is present, Silicon atoms produce the most stable triplet clusters. Each line represents a different atomic arrangement of atoms in the cluster, and results from Bonny et al. [261, 262], are shown for comparison in white circles and purple diamonds respectively. Reprinted from T. M. Whiting, P. A. Burr, D. J. M. King, and M. R. Wenman, Understanding the importance of the energetics of Mn, Ni, Cu, Si and vacancy triplet clusters in bcc Fe, J.Appl. Phys, vol. 126, p. 115901, 2019., with the permission of AIP Publishing.

Mn-Si free alloy corroborating previous studies indicating that Ni content in RPV steels leads to increased nucleation of solute-rich defects (tables 6.4 and 6.5 and figs. 4.42 and 6.15)[144, 86]. Kuleshova et al. observed that the number density of precipitates produced in RPV steels under neutron irradiation was around 4 times greater in alloys containing 1.94 at.% Ni compared with those containing 1.2 at.%, see fig. 7.10[16]. In this case the lower Ni alloys in this case also contained lower Mn in the matrix.

There is also a significant difference in volume fraction of scatterers observed in the quaternary alloy, almost 5 times the volume fraction observed in the Fe-Mn-Si alloy despite similar median particle sizes, fig. 6.15. This suggests there is a synergistic effect of Ni combined with Mn and Si leading to enhanced solute clustering and precipitation. This is backed up by the A508-3 steel and Fe-Mn-Ni-Si both containing all three solutes, and both having the highest number density of scatterers measured using SANS in chapter 6.

The range of defect types in the Fe-Mn-Ni-Si alloy is larger, suggesting that the presence of Ni facilitates the nucleation of a wider variety of phases under irradiation conditions. At lower doses, the EDX measured precipitate compositions are still much higher in Ni than Mn, which is significant given the higher fraction of Mn present in the matrix fig. 4.27. Along with observations of Ni enriched dislocation loops, and Ni segregation to grain boundaries, this shows that Ni is the dominant feature in the nucleation of precipitation under irradiation, and promotes

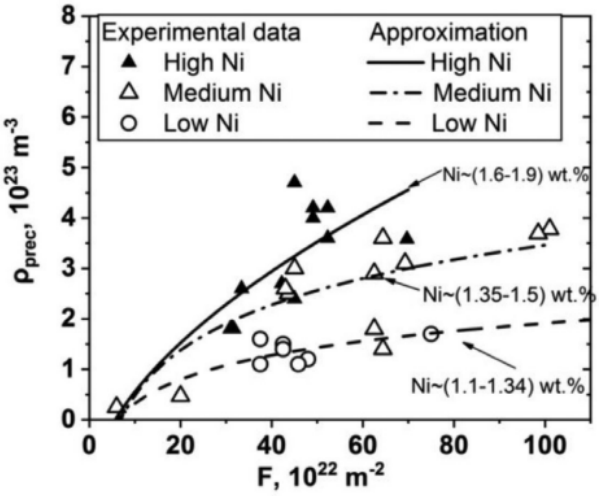


Figure 7.10: Plot from Kuleshova et al., showing the relationship between Mn-Ni-Si precipitate density and radiation dose, in surveillance specimens of various VVER 1000 RPV steels with varying Ni contents [16]. Reprinted from Journal of Nuclear Materials, 553, E.A. Kuleshova, G.M. Zhuchkov, S.V. Fedotova, D.A. Maltsev, A.S. Frolov, I.V. Fedotov, Precipitation kinetics of radiation-induced Ni-Mn-Si phases in VVER-1000 reactor pressure vessel steels under low and high flux irradiation, Page 153091, Copyright 2021, with permission from Elsevier.

formation of secondary phases by diffusing rapidly to defects, stabilising them.

In this work, the Ni rich features have either a small ellipsoidal morphology and are in the matrix, or have no consistent morphology, are larger and are located on dislocation loops in the material, fig. 4.5. These observations suggest that there are multiple nucleation mechanisms leading to the formation of Ni rich features. The small ellipsoidal features are observed in the matrix with no clear attachment to dislocation loops or lines but, based on the lack of these precipitates forming in unirradiated regions, it is likely that they nucleated at radiation induced defects. Similarly, G phase precipitates have recently been observed both on dislocations and in the matrix of a heavy-ion irradiated ferritic model alloy containing Mn, Ni, and Si in ratios matching that of the G phase [127]. Those which had precipitated on dislocations were found to be stable after thermal ageing at 400 °C. Those which precipitated in the bulk dissolved after ageing. This suggests a difference in stability of features formed in different locations indicating variable nucleation and compositional evolution based on whether precipitates are forming on existing dislocations and grain boundaries. In ageing studies the majority of precipitates are observed at heterogeneous nucleation sites, not in the matrix [110].

The observation of larger features forming at dislocation loops suggests that the radiation

induced loops are acting as defect sinks for solute segregation, and providing heterogeneous nucleation sites. There must be a link between the loop sink strength, and its orientation or size, as some dislocation loops were observed with no measurable segregation, while others clearly showed segregation around the loop (??). Further evidence that the precipitation of Ni rich features is driven by nucleation at radiation induced defects is the precipitate denuded zone surrounding the grain boundary observed in the 0.1 dpa region of the Fe-Mn-Ni-Si alloy. There were no observed Ni-Mn-Si rich features in a region around the grain boundary, as there were no stable dislocation loops present to act as nucleation sites (fig. 4.39). Similar observations have been made in surveillance RPV weld materials, where MNSP denuded zones around grain boundaries and carbides suggest that formation is strongly connected to precipitation at radiation induced defects and segregation [111]. A comparison of observations from this work and the work of Edmondson et al. is shown in fig. 7.11, and shows similar defect structures in the proton-irradiation model alloy in this work and neutron-irradiated RPV steel, with the precipitates having a much smaller size distribution in the neutron irradiated alloy[111].

Existing models predict the existence of a Mn-Ni-Si rich B2 phase which is predicted to transform info the Mn-Ni-Si G phase when the Fe content drops below 18 at.%, with sufficient vacancy concentration [144, 238]. This suggests that perhaps some of the features observed in TEM are already G phase, and sufficiently rich in solute, but others may be evolving from a Γ_2 or B2 structure, and are likely to be smaller.

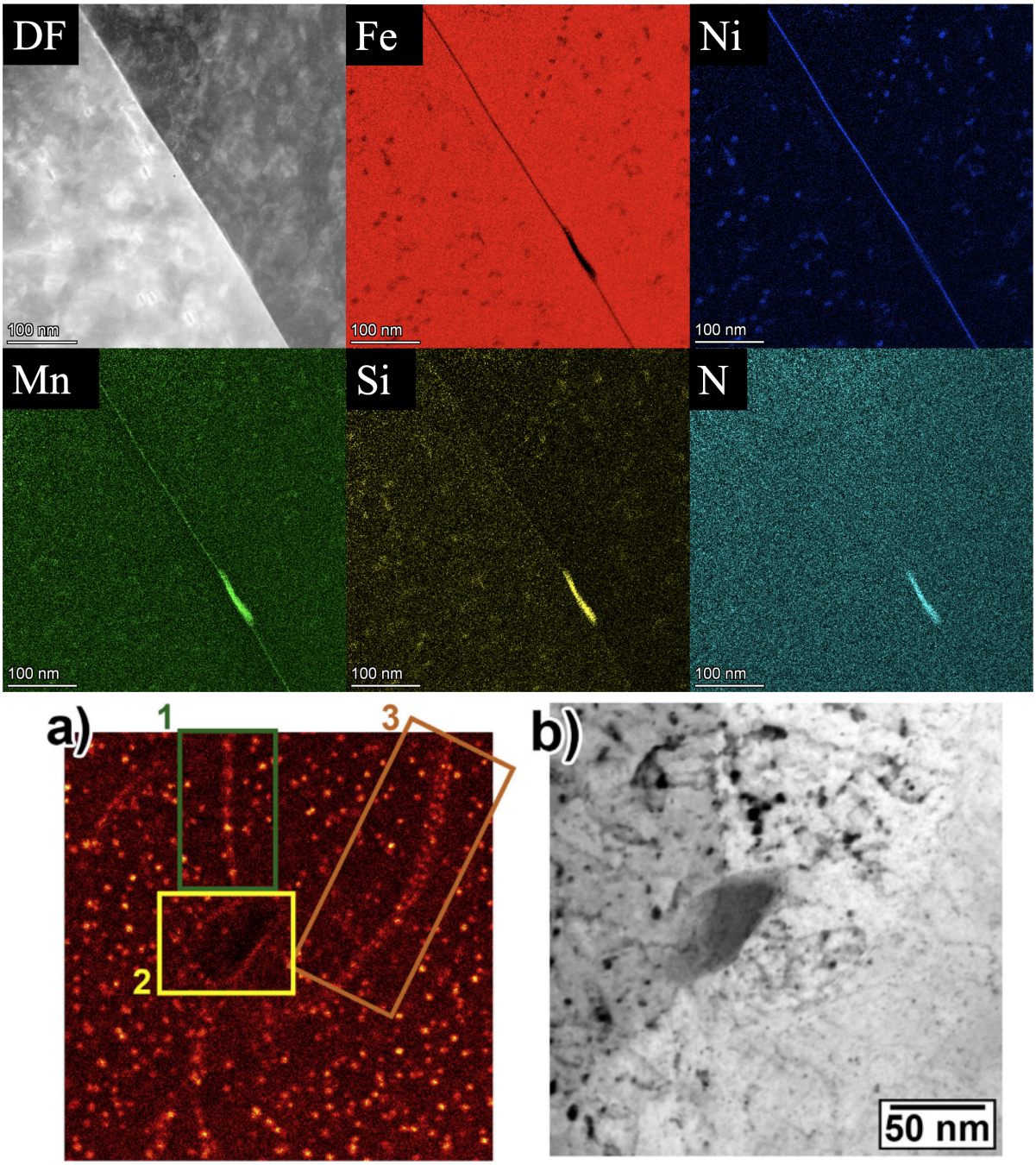


Figure 7.11: Comparison of observations of precipitate denuded zones observed in this work and EDX-MVSA map and BF STEM images from Edmondson et al. in a neutron irradiated RPV steel irradiated to 6.39×10^{23} n.m^{-2} (13.8 full power years), at 284 °C, with 1 showing a denuded zones, 2 showing segregation of Mn-Ni-Si and Cu at a carbide, and 3, a precipitate forming on a grain boundary [111]. Reprinted from Acta Materialia, 134, P.D. Edmondson, C.M. Parish, R.K. Nanstad, Using complimentary microscopy methods to examine Ni-Mn-Si-precipitates in highly-irradiated reactor pressure vessel steels, Page 9, Copyright 2017, with permission from Elsevier.

7.3.2 The effect of nitrogen on radiation induced precipitation

Despite unmeasurable matrix nitrogen content before irradiation, nitrogen rich precipitates have been observed in the model allows after irradiation. The most likely explanation for this is the introduction of nitrogen from the vacuum into the samples via the adsorption of $N_{2(g)}$ to the surface and subsequent diffusion into the ferrite matrix. Combined with the enhanced diffusion rates of solutes in the materials caused by heating from the proton beam, and the creation of high concentrations of mobile point defects, this has resulted in the precipitation of nitrides with number density and size increasing with dose. The observed nitrogen composition in the Fe-Mn-Ni APT matrix was measured to be 0.01 ± 0.01 at.% in both irradiated and unirradiated conditions, table 5.4, which is significantly below the solid solubility of nitrogen in ferrite which is around 0.4 at.% [263]. There was no nitrogen peak observed in matrix EDX spectra from the Fe-Mn-Ni-Si or Fe-Mn-Si alloy, again suggesting nitrogen content in the alloys is still very low, and that almost all nitrogen is located in precipitates, figs. 4.16, 4.23 and 4.30. Therefore, the excess nitrogen observed in precipitates in the Fe-Mn-Ni-Si and Fe-Mn-Si alloys does not seem to have been present in the original alloy.

There is a wide range of N, Mn and Si content measured for precipitates in the irradiated Fe-Mn-Si alloy, with measured compositions from 10 at. % N in the high dose region to 90 at. % in the 0.1 dpa region. This suggests that the features are not precipitating with a fixed composition, and that they may be metastable phases induced by radiation. Further evidence for this is that as the dose increases the ratio of Mn:Si in the precipitates also increases, corresponding to the bulk availability of solutes in the alloy, unlike the Ni rich features which showed increasing Si:Mn ratio with dose, and the number density and size of features increased in the high dose-dose rate region of the sample, see fig. 4.11.

Given this finding, radiation induced segregation must have played a part in creating local regions of sufficiently high nitrogen concentration for precipitation of nitrides to occur. If adsorbed nitrogen were diffusing from the sample surface into the steel without irradiation, the expected concentration with depth would follow an error function according to the solution of Fick's second law [264]. Assuming that the matrix concentration in the irradiated material is around 0.01 at.% (based on APT concentrations measured in Fe-Mn-Ni, table 5.4) and the

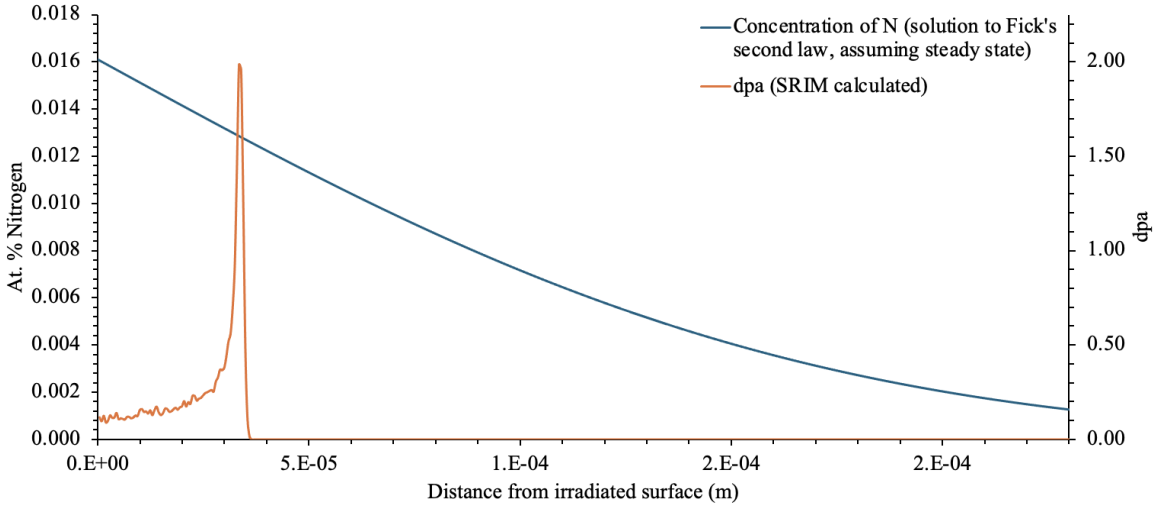


Figure 7.12: Plot showing the theoretical nitrogen concentration in the irradiated region of the Fe-Mn-Si alloy, based on the assumption that nitrogen is present in the matrix at 0.01 at.%, and in precipitates with volume fraction of 0.0054 at 35 µm depth and stoichiometry of $MnSiN_2$. In this case T was taken to be 673 K, and t was 18 hrs.

precipitates are $MnSiN_2$, then the approximate atomic concentration of nitrogen in the peak region is around 0.013 at.%. Figure 7.12 shows the theoretical function of nitrogen concentration extrapolated back to the surface of the material with the dpa profile overlaid. The calculated change in nitrogen concentrations across such a small depth are too small to detect with the techniques applied in this work.

The sources of the nitrogen is likely to be from trapped air outgassing from components within the system and air present in the vacuum system, given that the pressure measured was 10^{-7} mbar. This pressure means that in any given 1 cm^3 volume of the vacuum there is likely to be at least 10^9 molecules of nitrogen gas, close to the sample with a temperature of 600 K, considering the ideal gas law. Nitrogen adsorption onto ferritic steels depends on the local pressure and temperature of the system. The measured sample temperatures overlap with gas and plasma nitriding temperatures, which generally range from 340 °C to 530 °C [265]. However, the pressure in these experiments is still orders of magnitudes lower than the 1-100 kPa of used in low pressure gas nitriding[266].

Although the nitrogen precipitation is a result of contamination, the observations of the distribution and location of precipitates can provide insight into the effect of radiation on these model RPV microstructures. The size and number density are proportional to dose in the Fe-

Mn-Si alloy, but the overall number density of nitrides is significantly lower than the Mn-Ni-Si precipitates in the Fe-Mn-Ni-Si alloy. This suggests that the barrier for nucleation of these Mn-Ni-Si precipitates at dislocation loops is significantly lower than the Mn-Si nitrides.

Radiation dose and dose rate had a significant effect on the precipitation of these phases, and on the rate of diffusion of nitrogen into the material. Observations by Warren et al., in binary Fe-2.3N alloys, found that under self-ion irradiation, nitrogen was found to reduce the number density of defects and lead to larger sizes of dislocation loops, consistent with observations of dislocation loops around 100-200 nm in length, and the much lower number density of precipitates observed in the Fe-Mn-Si alloy [113]. It has been suggested that this reduction in number density is caused by the presence of N in the matrix distorting the lattice and preventing the nucleation of interstitial defect clusters. Therefore, fewer clusters nucleate, and those that do can grow to into large dislocation loops [113]. Other work looking at the effect of nitrogen on the microstructure of irradiated ferritic-martensitic steels has also observed that nitrogen addition leads to larger dislocation loop sizes and lower number densities [236, 267].

Nitrogen has high diffusivity, with a lower activation energy for diffusion than other solutes in these alloys (table 2.5), and low solubility in ferrite, so will readily form nitride precipitates in the presence of metals with a strong affinity for bonding with nitrogen [268]. Nitrogen diffusion coefficients vary with concentration in BCC-Fe [268]. Various transition metals readily form nitrides in ferritic steels, but of these, Si and Mn have a much lower affinity for nitrogen than common alloying elements such as Ti, Cr and V [269]. Ni does not react with nitrogen easily, and will only form nitrides if the chemical potential is very high, which in a ferritic steel, would result in a large volume fraction of Fe based nitride forming first [269]. This could be the reason for the observation of Ni shells around the nitride features in the Fe-Mn-Ni-Si alloy, as the interface has provided a stable sink for diffusing Ni atoms, but they do not react with the precipitate or substitute into the phase.

Only one stoichiometry of a ternary Mn-Si nitride forming in ferrite has been reported, $MnSiN_2$, and it has three crystal structures observed in different temperature and Mn:Si ratio environments [248]. In fact, in the Mn-Si-N system, the $MnSiN_2$ is the only ternary phase, and in bulk Mn-Si-N alloys, will form alongside Mn_3Si when Mn and Si ratios are similar to those in the alloys in this study [270]. In a radiation environment with elevated diffusion and damage

cascades leading to high temperatures, the radiation enhanced diffusion fluxes and higher bulk Mn:Si ratio may have stabilised the orthorhombic phase based on the observations of a cuboidal faceted morphology and consistent diffraction data.

The precipitation of this incoherent phase suggests that there is a strong thermodynamic driving force for nucleation, as precipitates have formed despite the large strain energy and misfit. In binary Fe-Si alloys, nitriding can lead to the precipitation of amorphous cuboidal structures with a stoichiometry of Si_3N_4, with cubic facets aligned with the $[001]_\alpha$ directions. The interface energy of the amorphous precipitate in ferrite is lower than that of the crystalline form due to the large lattice misfit [271]. The $MnSiN_2$ has a large misfit in BCC-Fe, meaning that in order to minimise the Gibbs free energy for homogeneous nucleation, the elastic strain must be minimised. The elastic modulus of the BCC matrix varies with crystallographic direction in Fe, being more flexible in the <100> directions, and stiffer in the <111> directions. This anisotropy can affect the shape of precipitates forming with large lattice misfit and difference in molar volume to the matrix [272]. Many of the measured precipitate compositions had much lower N content than would be expected for the $MnSiN_2$ phase. Binary Mn silicides are not commonly observed in ferritic steels, and given the iron rich matrix, it could be the case that a ternary Fe-Mn-Si phase might be more stable as nitrogen content decreases. The larger features in the high dose region of Fe-Mn-Si have compositions of approximately $N_{1.3}Mn_{1.3}Si$ and the largest observed Mn-Si-N feature on the grain boundary in the Fe-Mn-Ni-Si alloy had a stoichiometry of approximately $N_{10.2}Mn_{7.3}Si_{7.4}$. These are both much lower in N than the $MnSiN_2$ phase, indicating some variability in stoichiometry. No previous observations of this phase in un-nitrided ferritic alloys have been found, and this work seems to be the first observation of $MnSiN_2$ forming in BCC-Fe with this morphology, under proton-irradiation.

7.3.3 Summary

Across the radiation damage profile, the average size of precipitates remains constant, but the composition clearly evolves. There is likely to be some competition between the precipitation of the Ni and N rich features, but the Ni rich features have a higher number density and similar size to the N rich features, so are comparatively stable under the conditions of the proton-irradiation. The nitrogen content in the Mn-Si-N rich features is much higher in the Fe-Mn-Ni-Si alloy than

in the Ni free alloy, likely due to the depletion of Mn and Si in the matrix, as a result of high levels of Mn-Ni-Si precipitation and segregation. Overall, the observations made from the results of this work have led to enhanced understanding of the behaviour of solutes under irradiation in dilute alloys and suggest that the precipitate formation mechanism occurs in the following order, fig. 7.13;

1. Dislocation loops form from clusters of point defects created by damage cascades.

2. Mn, Ni and Si segregate and cluster at dislocation loops, and Ni leads to more stable clustering than Mn and Si alone.

3. When the local concentration of solute becomes sufficiently high, Mn-Ni-Si precipitates nucleate and grow.

4. Nitrogen diffusing through the BCC Fe matrix segregates to precipitates and as its concentration increases in precipitate, MnSi nitrides nucleate inside Mn-Ni-Si precipitates, ejecting Ni into a shell around the cubical nitrides.

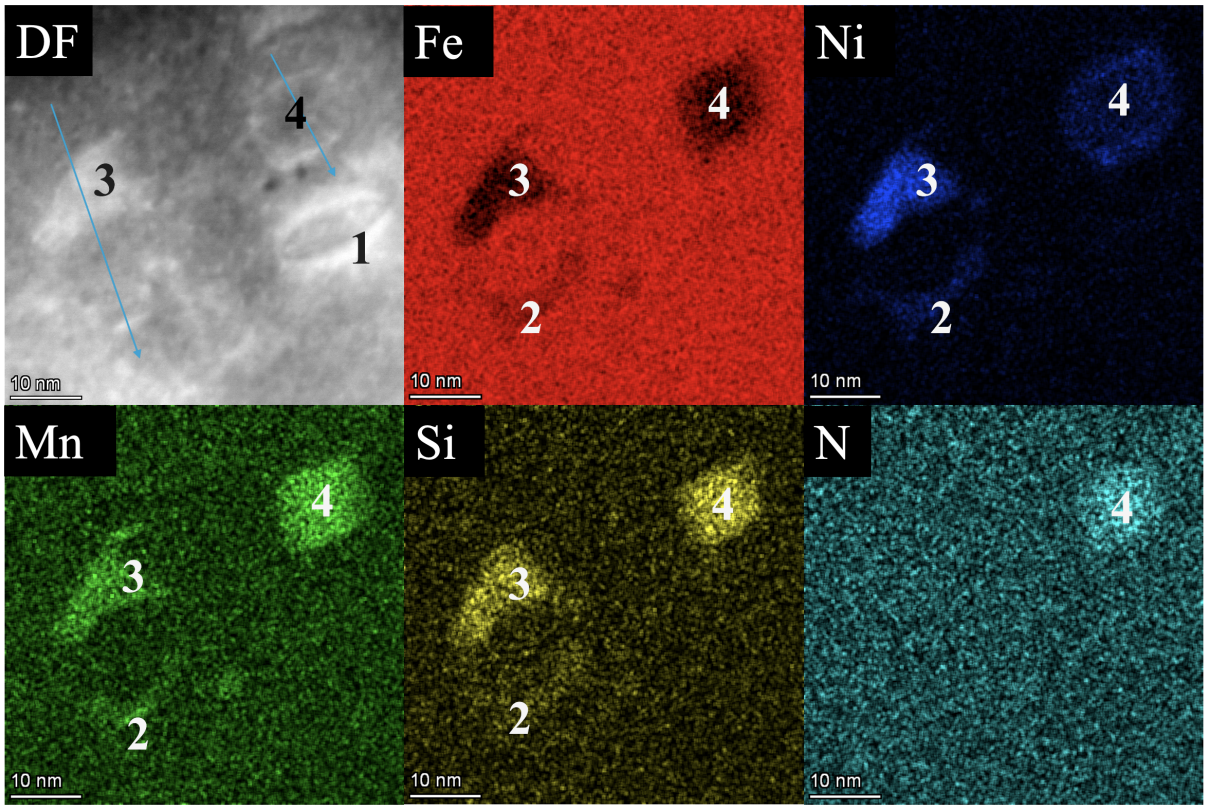
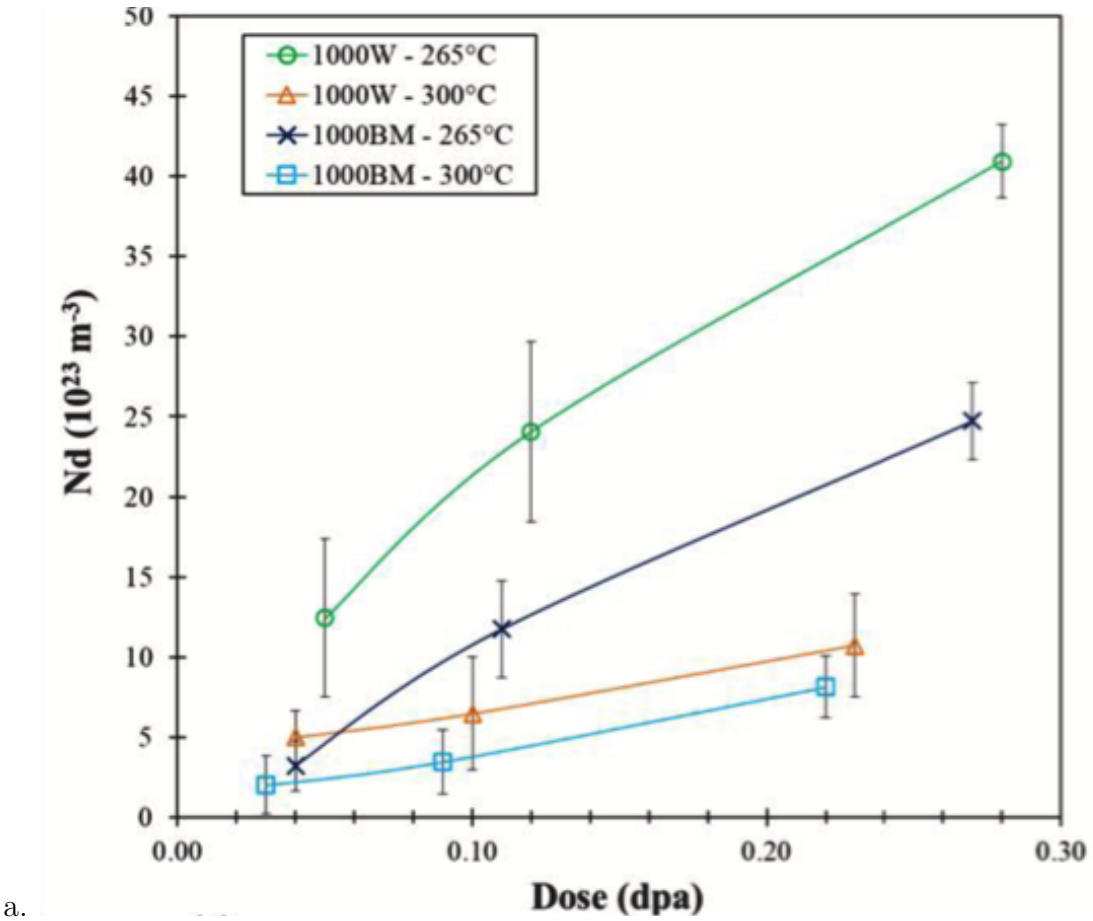


Figure 7.13: STEM BF image and EDX maps of region of high dose proton-irradiated Fe-Mn-Ni-Si alloy with numbers corresponding to features indicated by each step of the proposed mechanism.

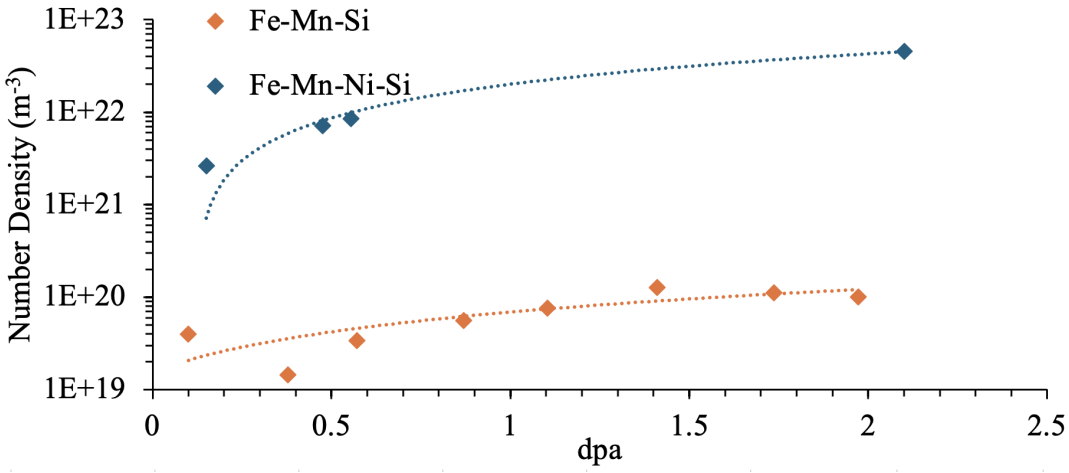
7.4 Dose/dose rate & temperature effects on microstructural evolution

Comparing proton irradiation to neutron irradiation, smaller cascades will lead to higher defect survival rates and higher vacancy concentrations, at lower temperatures ($< 300\,^{\circ}\mathrm{C}$) [63, 273]. The higher temperatures in this work would be expected to lead to higher recombination of defects, but this is likely to have also led to the dominant migration mechanism of Si atoms switching from vacancy to dumbbell mediated [87]. The dose rate experienced by a proton irradiated experimental sample with a $15\,\mu\mathrm{A}$ beam is around 105 times higher than that received by RPV steel in a reactor. The potential interaction of damage cascades will cause a different effect on microstructure due to the changes in diffusion of species through the material during irradiation. Most neutron and self-ion irradiation studies to doses of 0.1-2 dpa observe much smaller solute-rich defects than are observed in this study, in both RPV steels and model alloys [133, 274, 160, 138, 86, 66]. This suggests that the diffusion rates are significantly higher in this work due to the combination of elevated temperature and enhanced defect survival. The linear trend of increasing number density of solute-rich defects with dose is consistent with the $300\,^{\circ}\mathrm{C}$ trend observed by Courilleau et al. [86] (fig. 7.14). This study found that at lower temperatures, Ni composition had a stronger influence on the density of matrix defects [86].

It is likely that the sample temperature was higher than $350\,^{\circ}\mathrm{C}$, causing an increase in mobility of vacancies and solute atoms, leading to larger clustering features. Kuleshova et al. found that irradiation temperatures of $400\,^{\circ}\mathrm{C}$ led to much greater segregation of solute elements to the grain boundaries [96]. Although loop orientation was not quantitatively measured, the morphology of loops in the Fe-Mn-Si and Fe-Mn-Ni-Si are very different. The large rectilinear loops in the Ni free alloy are very similar to the <001> type loops observed at temperatures above $400\,^{\circ}\mathrm{C}$ in heavy ion-irradiated BCC-Fe by Yao et al., see fig. 7.15, suggesting that solute segregation has not reduced loop mobility or coalescence of the mobile $\frac{1}{2} < 111 >$ loops in this alloy [95]. The loops observed in the Fe-Mn-Ni-Si alloy are much smaller, on the order of 10-50 nm, compared with > 100 nm. This may be due to solute segregation inhibiting the mobility of loops and preventing coalescence, consistent with the observations of Connolly et



a.



b.

Figure 7.14: Plot of N_d versus dose, showing 4 high nickel VVER 1000 RPV alloys (a.), irradiated at two temperatures, the green and black alloys (1.2 at.%, weld) have higher Ni content than blue and yellow (1.7 at.% Ni, base metal), [86] and (b.) a plot showing N_d of solute-rich defects in the model Fe-Mn-Ni-Si alloy and Fe-Mn-Si alloy in this study, also showing an increase with added Ni.

a. Reprinted from Journal of Nuclear Materials, 585, C. Courilleau, B. Radiguet,R. Chaouadi, E. Stergar, A. Duplessi, P. Pareige, Contributions of Ni-content and irradiation temperature to the kinetic of solute cluster formation and consequences on the hardening of VVER materials, Page 154616., Copyright 2023, with permission from Elsevier.

al.[97]. In a study into radiation temperature effects between 255 °C and 310 °C, they found that the increasing temperature reduced Si content in clusters and that Ni led to smaller radii [97], consistent with the lower Si content observed in the precipitates in the Fe-Mn-Ni-Si alloy, compared with existing studies (see table 2.6). However, there is the chance that the difference in morphologies are due to temperature variation during irradiation of the samples, as the average temperature of the Fe-Mn-Ni-Si alloy during proton irradiation was measured to be around 23 °C lower than in the Fe-Mn-Si alloy irradiation, with maximum temperatures on the surface measured at 402 °C compared with 408 °C(table 3.5). Although these temperatures are fairly similar, the homogeneity of sample temperature across the irradiated region was not recorded. In the Fe-Mn-Si alloy many of the loops are much larger[95].A comparison of loop morphology in the samples in this work and from literature are shown in fig. 7.15, and indicates that it is likely the temperature was well below 500 °C because there are multiple types of loop present in both alloys, based on the mixture of orientations and morphologies observed .

During irradiation, the temperature of the specimens varied significantly, see fig. 3.10, and these transients may have affected the precipitation observed, by changing the rate of ingress of nitrogen into the sample. Nitrogen gas adsorption and absorption into a steel surface is a strongly temperature dependent process. Gas nitriding of steels generally takes place in the temperature range of 400 °C to 650 °C well within the irradiation temperature range of these experiments [275]. The diffusion of N into the steel, in quantities proportional to the proton induced displacement damage, suggests that nitrogen gas is adsorbing physically, and dissociating, and then atomic nitrogen is diffusing into the steel, assisted by the enhanced vacancy concentration created by proton irradiation.

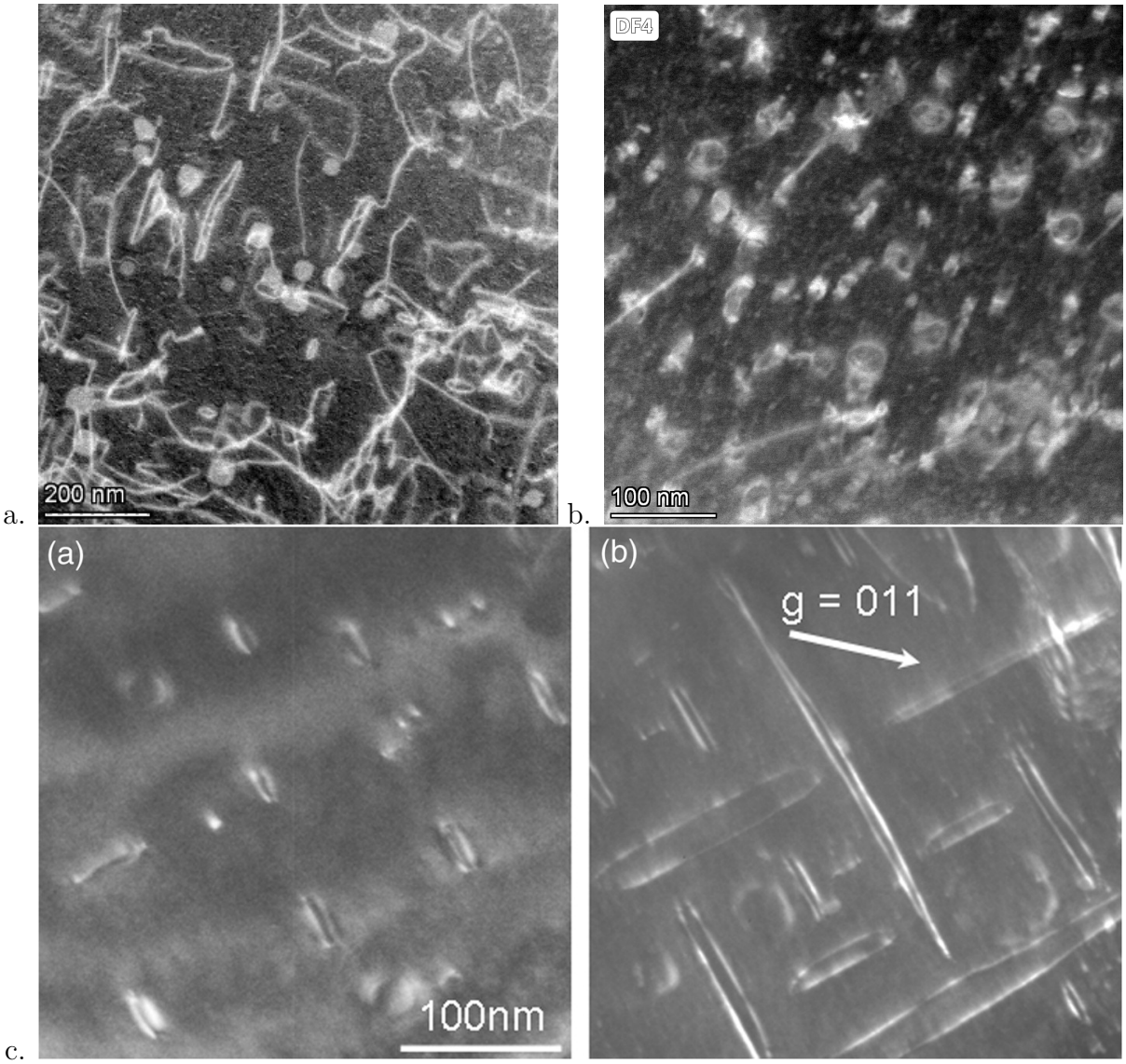


Figure 7.15: Examples of radiation induced dislocation loop morphologies observed in this work (a. Fe-Mn-Si and b. Fe-Mn-Ni-Si), comparing with irradiated pure Fe at c.500 °C, showing only 100 loops, growing with increasing dose from 310^{18} ions.m^{-2} (left) to dose of 110^{19} ions.m^{-2} from Yao et al.[95].

Compositional evolution with dose has been suggested by Xue et al., as an explanation for the slow growth of Mn-Ni-Si rich features under irradiation, and in their study on an Fe-Mn-Ni-Si model alloy with the same composition as this work, the Si content increased up to 1.5 dpa, the Mn content increased and Ni decreased [133]. In these clusters the Mn content is higher than the Ni and Si content, and is close to the Mn_3Ni_2Si B2 phase, which is coherent in BCC-Fe. These compositions are even higher in Mn than those observed in this work, but the features are 1-2 orders of magnitude smaller, with an average size of 0.4 nm [133]. Xue et al. suggest that this is a preliminary structure in the process of precipitating the G phase in RPV steels under irradiation [133]. It could be that as the features grow, their Mn content decreases, towards the compositions as observed in this work, and ultimately the composition is still evolving towards a stable phase.

7.5 Clustering of Mn & Ni at dislocation loops in Fe-Mn-Ni alloy

Some possible Mn and Ni clustering was observed in one of the irradiated APT Fe-Mn-Ni datasets. Solute composition in these enriched regions was up to 20 at.% , with a ratio of Mn:Ni of approximately 1:1 and sizes less than 4 nm (fig. 5.14). Similar features have been observed in a Fe-1.1Mn-0.7Ni ternary alloy, neutron-irradiated at 300 °C to 0.1 dpa, with 10% Mn and 8% Ni enriched clusters forming [276, 66]. These dissolved during post irradiation annealing between 400 °C and 600 °C [276]. This suggested that these features are produced by radiation induced segregation and are not forming stable phases. Ion density measured inside the features is around 20% higher than in the matrix (fig. 5.13), suggesting a lower field structure, also meaning that the features are probably planar defects, as their z dimension will have been stretched by this field variation. This may be caused by the solute segregation alone, or also by local variation in crystal structure, such as the presences of a dislocation loop. Previous work on binary Fe-Ni and Fe-Mn suggests that Mn and Ni do not precipitate into Fe free phases but strongly segregate to dislocation loops and grain boundaries, which could explain the low SANS A ratio, corresponding to Fe rich clusters around grain boundaries and loops [71, 83]. The observations in this work are not conclusive and the clustering observed is very subtle compared with other work on irradiated Fe-Mn-Ni alloys, as can be seen in fig. 7.16.

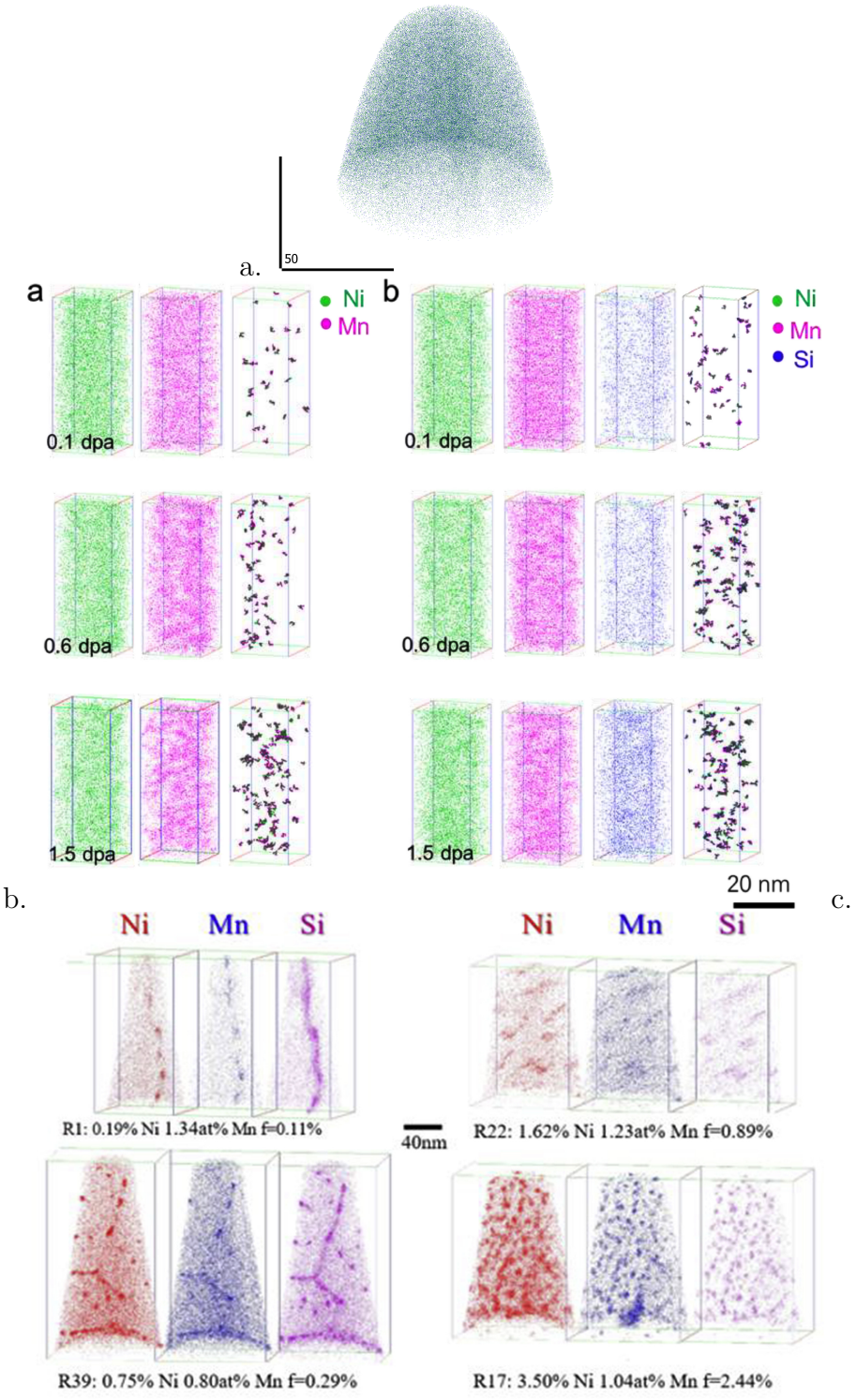


Figure 7.16: Comparison of APT observations of Mn-Ni clustering in proton irradiated Fe-Mn-Ni(a.) with other observations of clustering of Mn and NI in dilute model alloys, b. Fe-Mn-Ni alloy, irradiated with heavy ions at 623 K [133] and c. Mn-Ni clustering observed in neutron irradiated RPV steels by Almirall et al., showing solute maps for alloys with Ni content between 0.19 and 3.3 at.%, and 0.03–0.06 at .% Cu, 0.80–1.34 at.% Mn and 0.39–0.49 at.% Si [37].

b. Reprinted from Journal of Nuclear Materials, 560, Jing Xue, Shenbao Jin, Rong Hu, Fei Xue, Gang Sha, Ion-irradiation-induced clustering in Fe-Mn-Ni-(Si) steels: Nucleation, growth and chemistry evolution, Page 153477, Copyright 2022, with permission from Elsevier.
c. Reprinted from Acta Materialia, 179, N. Almirall, P.B. Wells, T. Yamamoto, K. Wilford, T. Williams, N. Riddle, G.R. Odette, Precipitation and hardening in irradiated low alloy steels with a wide range of Ni and Mn compositions, Pages 119-128, Copyright 2019, with permission from Elsevier.

7.6 Hardening effect of proton-irradiation on model alloys

Nanoindentation results for the Fe-Mn-Ni-Si and Fe-Mn-Si alloys show an increase in radiation hardening with dose, consistent with the observed increase in number density of solute rich defects, suggesting that these features are pinning dislocations and increasing resistance to plastic deformation. The peak in hardening observed around the Bragg peak is likely to include the contribution to hardening from defects caused by the implantation of hydrogen, such as nano-voids, and therefore this region's hardening is not likely to be dominated by the solute rich precipitates and dislocation loops investigated in this work.

Defects lead to hardening of crystalline materials, and this hardening contributes to embrittlement and an increase in the likelihood of brittle failure. The results obtained in this work suggest a strong link between nickel content and radiation hardening, particularly at higher doses, fig. 4.2.

Radiation induced defects contribute to hardening via source hardening and friction hardening. If defects nucleate and grow at existing dislocations in the material, they can pin them, increasing the applied stress required to initiate dislocation glide, and thus leading to a higher yield stress and hardness [152]. Friction hardening due to radiation induced defects occurs when precipitates or dislocations are located in the glide plane or nearby, and they interact with a moving dislocation, acting as an obstacle to glide. Dislocations can interact through bowing around precipitates, cutting through them or climbing around. The change in yield stress caused by a population of barriers present in a material can be described by the dispersed-barrier hardening model [151, 152]:

$$\Delta\sigma_y = \alpha M \mu b \sqrt{Nd} \tag{7.1}$$

Where $\Delta\sigma_y$ is the yield stress in Pa, α is the unknown obstacle strength, M is the Taylor factor $= 3.06$ ([277]), μ is the shear modulus (approximately 93.39 GPa, for pure Fe as measured by [278]), b is the magnitude of the burgers vector of dislocations in BCC-Fe ($b = 0.248$ nm, for a [111] dislocation), N is the number density of obstacles and d is the average size of obstacles.

Therefore, the change in yield stress, which is often considered analogous to the radiation hardening, ΔH, is directly proportional to $\sqrt{N.d}$, assuming that the obstacles have the same size and are homogenously distributed [152]. Various correlations have been identified to link

$\Delta\sigma_y$ with ΔH, and have been summarised for a range of ferritic steels by Busby et al. [279]. Using the correlation for RPV steels stated in this work, $\Delta\sigma_y = 0.306\Delta H$([279]), and plotting $\Delta\sigma_y$ against $\sqrt{N.d}$, a linear trend is observed for both the Fe-Mn-Ni-Si and Fe-Mn-Si alloys in fig. 7.17, although these lines do not pass through the origin. The discrepancies in the fit are likely to be due to the fact that this method has not taken into account the variety of other obstacles to dislocation movement in the microstructure and has assumed that features are all the same size. Taking the gradients of these lines to be equivalent the $M\alpha\mu b$ in eq. (7.1), and using the values stated above, $\alpha_{Fe-Mn-Ni-Si} = 0.99 \pm 0.08$ and $\alpha_{Fe-Mn-Si} = 0.94 \pm 0.16$. Both of these values suggest that the average radiation induced precipitate is acting as an almost perfectly hard barrier, with an obstacle strength of 1.

Without quantitative data on the nature and number density of dislocation loops and their hardening contributions, it is not possible to separate out the effects of hardening from each type of defect using superposition expressions [152]. Enriched loops are likely to have stronger pinning strength for dislocations than unenriched loops as they are immobilised by solute clusters, as found in atomistic simulations carried out by Terentyev et al. who found Mn increases the unpinning stress, contributing to source hardening [280]. Experimentally, it has been observed that dislocation loops have similar or higher obstacle strengths than solute clusters in low and high-Cu RPV steels [103, 281, 282].

Comparing the irradiation hardening results in this work to the findings of Fujii et al. and Yang et al. (fig. 2.25), they show a similar trend to the observations of Yang et al. who used heavy ion-irradiation on very similar alloy compositions, see fig. 7.19. The hardening values obtained by Fujii et al. are about one order of magnitude lower than those measured in this work, and in their study they did not observe any evidence of clusters, precipitates, or dislocation loops using APT and TEM. They attributed the observed hardening to very fine scale clustering or loops that were smaller than could be resolved in TEM or APT. The only obvious differences between this work and the work of Yang et al. was the radiation dose rate which was 1×10^{-5} dpa/s, compared with $>2.5 \times 10^{-5}$ and a lower Ni content in the model alloys of 0.53 wt.% compared with 0.75 wt.% [138, 139]. This supports the finding that increasing Ni content promotes the formation of clusters under irradiation

Figures 7.18 and 7.19 show the hardening data obtained in this work, compared with the

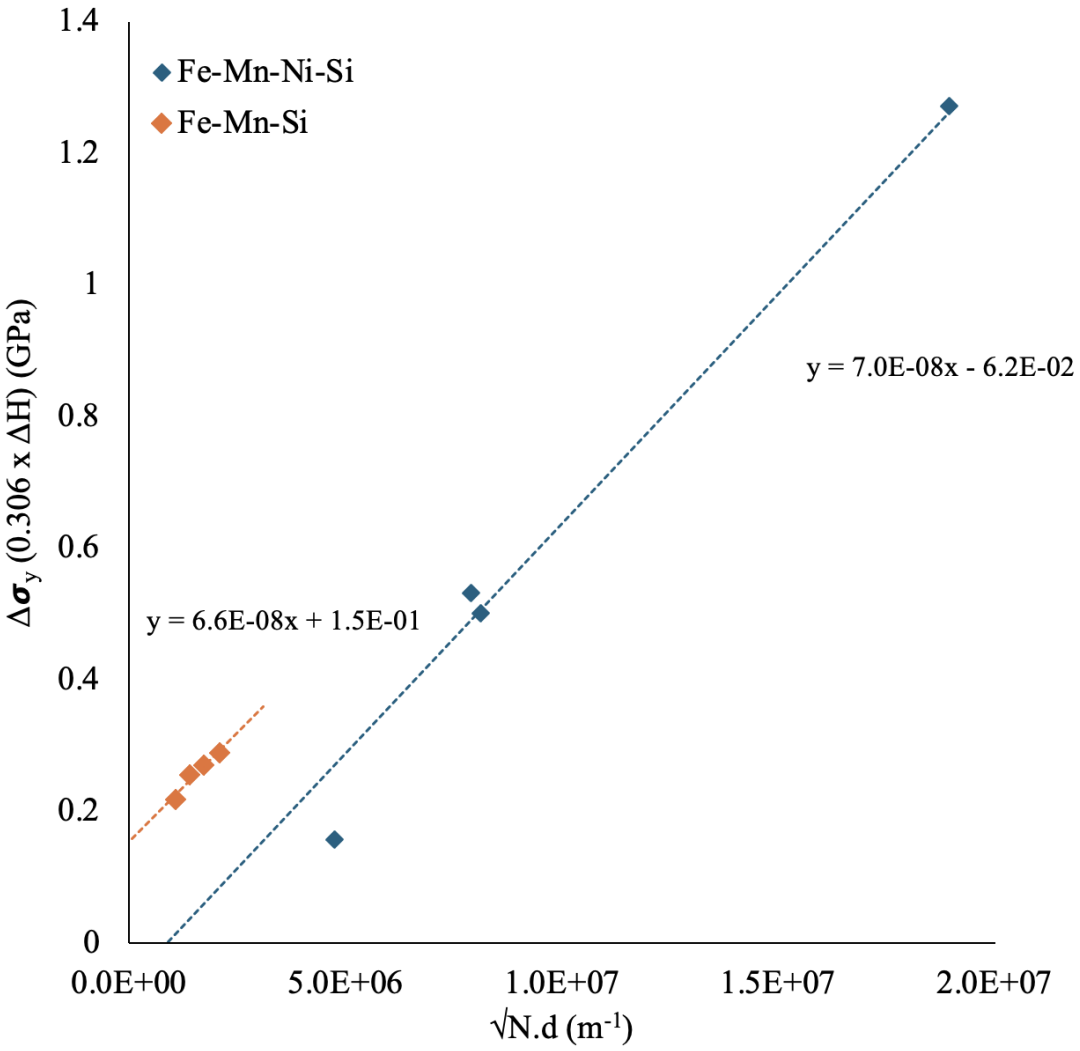


Figure 7.17: Plot of change in yield stress (converted from hardening using factor of 0.306 from Busby et al. [279], against $\sqrt{N_d d}$. The gradient of the straight lines correspond to $M\alpha\mu b$ in eq. (7.1).

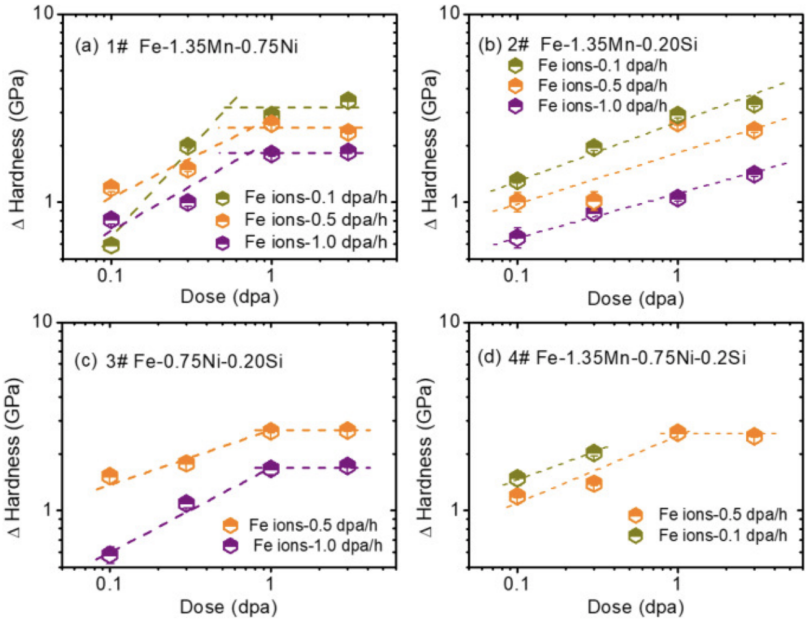


Figure 7.18: Plot of hardening as a function of dose for the heavy-ion irradiated model alloys investigated by Yang et al.[139]. Reprinted from Journal of Nuclear Materials, 588, Yitao Yang, Chonghong Zhang, Jianyang Li, Jie Gou, Zhaonan Ding, The influence of solute elements on grain size, hardness and irradiation-induced defect clusters in dilute Fe-based alloys, Page 154818, Copyright 2024, with permission from Elsevier.

results of Yang et al. [139]. The Ni containing alloys all show an increase in hardening at low doses, followed by a levelling off at higher dose, suggesting a saturation of defects and a slowing down of nucleation. This supports the observation in this work that Ni accelerates solute clustering and precipitation by stabilising solute clusters and providing stable nucleation sites. However, Yang et al. observed significant hardening in their Ni-free alloy, and solute clusters rich in Mn and Si, suggesting that Mn and Si do segregate and lead to radiation induced defects in the absence of Ni. Unfortunately, the microstructural evolution observed in this work is dominated by the presence of N-rich precipitates and no comparable solute clustering to dislocation loops was observed in APT measurements. The radiation hardening observed in these alloys shows that Ni addition leads to a higher number density of defects, contributing to greater hardening.

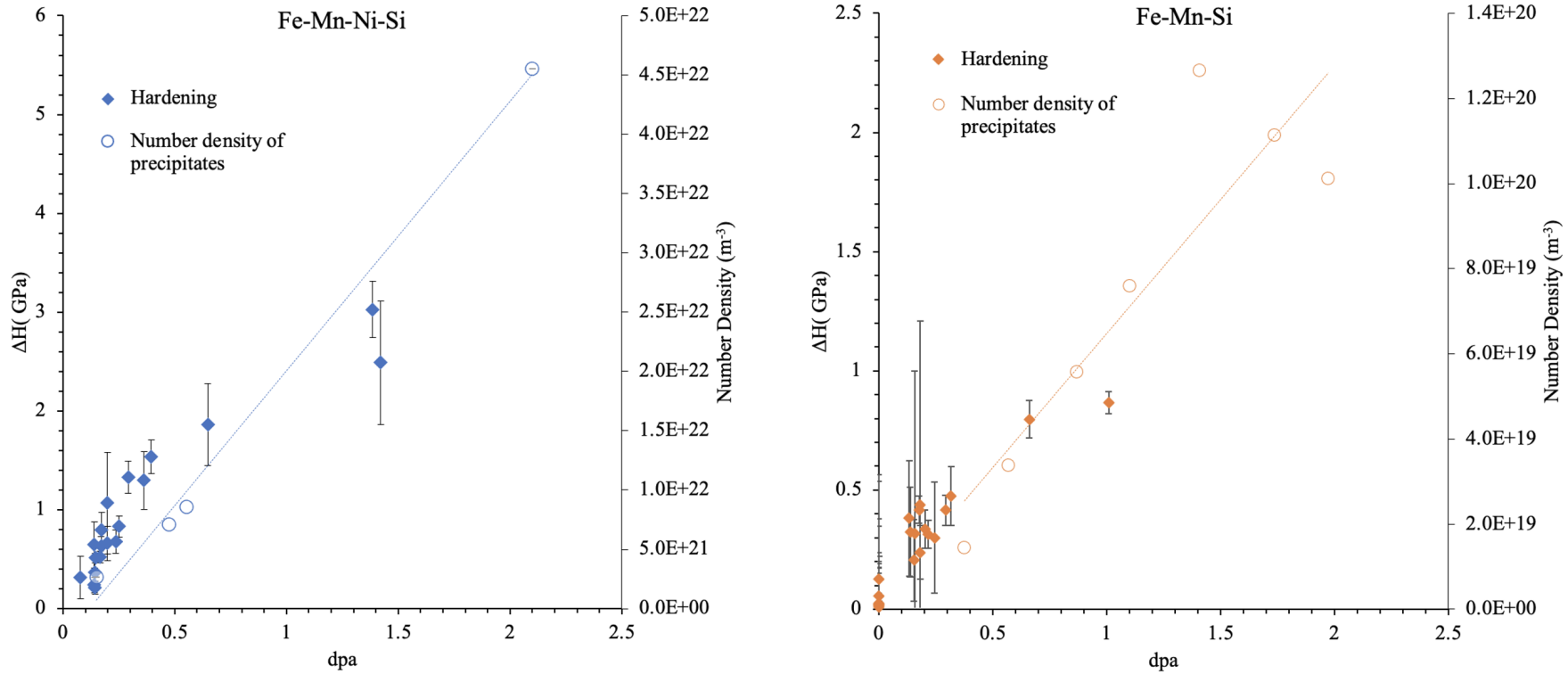


Figure 7.19: Plot showing the observed trends in hardening and number density of solute-rich features with dpa, in the Fe-Mn-Ni-Si (blue) and Fe-Mn-Si alloy (orange).

7.7 Improving proton-irradiation experiments

Although N ingress led to novel precipitation of Mn-Si nitrides under irradiation, the presence of this gas contaminating the vacuum led to results that are not applicable to understanding defects in RPV steels. The microstructural evolution observed is even less representative of those produced by an in service steel than would be expected using ion-irradiated model alloys, had the temperature of the irradiation been constant and the vacuum been cleaner.

Elevated nitrogen content and clustering with Cr has been observed in other ion-irradiation studies in binary Fe-Cr alloys, and attributed to ion-beam contamination [283, 284]. Possible sources of nitrogen contamination are the off-gassing of plastics inside the chamber, such as charge measurement and thermocouple wires. The trapping of air and purge gases, in screw threads, drilled holes in the heating plate and the large surface area of the end station chamber will all have contributed to outgassing during the course of irradiation resulting in contamination species present during irradiation [285]. Added to this, the pump outlet was located in the bottom of the chamber, meaning that any gases released near the sample may be trapped in the region, and are then unlikely to be extracted from the chamber before diffusing into the surface of the sample. Given that nitrogen was used as a purge gas and air is predominantly nitrogen, this is likely to be the source of nitrogen ingress into the alloys.

To improve the radiation experiments, the following suggestions are made, to mitigate the contamination and fluctuating temperatures experienced by the alloys in this work.

- Flush chamber with inert gas e.g. Ar, not N when pumping system down.
- Pump down to a higher vacuum, to pressures less than 1×10^{-5} Pa (or 1×10^{-7} Torr), as recommended by the Michigan Ion Beam Laboratory Annual Report[286], and separate beam line vacuum from sample environment to prevent ingress of hydrocarbons from diffusion pump oil from contaminating the end station.
- Use a heater, positioned behind the sample to maintain constant sample temperature throughout irradiation to avoid condensation of adsorbents onto the surface during time where the beam is off, and to ensure temperature inside the sample is consistent throughout the irradiation.

- Improve temperature measurement by incorporating non-contact measurement using IR (Infra-Red) emissions and camera, to obtain surface temperature measurements, enabling the identification of hot-spots and variation in temperature during irradiation.
- Minimise internal end station surface area, and remove materials that are likely to off-gas when heated such as aluminium components and plastic tubing or wire sheaths.
- Bake out the chamber before every irradiation test, with the sample in place, to ensure that any contamination is minimised.
- To prevent opening the end station chamber during irradiation to realign the sample, another improvement would be arrange continuous beam line access, and a system for beam alignment that does not require opening the vacuum chamber to prevent contaminants from being introduced into the system throughout the experiment when replacing the sample, and to allow for pumping down time before switching the beam on.

Even when implementing all of these improvements, it is still necessary to check for contaminants such as carbon, nitrogen and oxide layers during post irradiation analysis, to ensure that they have been effective and to avoid inaccurate conclusions being drawn around the nature of radiation induced microstructural evolution.

Chapter 8

Conclusions and Further Work

Proton-irradiation of a range of model RPV alloys has led to observations of a range of Ni-Mn-Si and Mn-Si-N precipitates. In the Fe-Mn-Ni-Si alloy, precipitates were observed with compositions close to that of the G phase $Mn_6Ni_{16}Si_7$ using atom probe tomography and with consistent diffraction patterns using selected area electron diffraction. STEM-EDX results suggest a range of Ni rich precipitates, with higher Mn composition than the G phase, with compositions close to the Γ_2 phase or a non-stoichiometric G phase. The large size of these features allowed for the conclusive determination that these precipitates are iron free, and have a consistent chemical composition across their structures. Some of these features were observed with ellipsoidal morphology, suggesting they have a crystal structure that is coherent with the BCC matrix. The number density of precipitates is directly proportional to the dose/ dose rate, suggesting that the formation of point defects is leading to precipitate nucleation by creating nucleation sites. The use of proton irradiation and model alloys has enabled the clear observation of Mn-Ni-Si precipitates forming on radiation induced dislocation loops.

Contamination of the end-station vacuum has led to the formation of $MnSiN_2$ precipitates in at least two of the alloys, confirmed using STEM-EDX spectra, forming with a cubical morphology aligned with the <001> directions in the ferritic matrix. These precipitates nucleated inside existing Mn-Ni-Si precipitates in the Fe-Mn-Ni-Si alloy only at high doses, suggesting the kinetics for their formation were very slow, likely due to their incoherent orthorhombic crystal structure. The observation of formation inside radiation induced Mn-Ni-Si precipitates, combined with the ejection of Ni from the centre of these features has led to the conclusion that,

compared with Mn-Si nitrides, the Mn-Ni-Si are less thermodynamically stable despite their faster precipitation kinetics.

Dislocation loop density and morphology varied significantly between the alloys observed using STEM imaging, with the Ni containing alloy containing a higher number density of smaller loops than the Fe-Mn-Si alloy.

Results across APT, TEM and SANS were consistent with precipitation of multiple precipitate phases and significant solute segregation in the Fe-Mn-Ni-Si alloy. There is indication of clustering at small sizes in the RPV steel, $R_{med} = 10 - 15$ nm, and the A ratio matches that of the high q A ratio in Fe-Mn-Ni-Si suggesting the early stage clustering and precipitation is occurring to produce features with similar composition.

Nanoindentation of the Fe-Mn-Ni-Si and Fe-Mn-Si cross sectioned surfaces showed a clear effect of precipitation and dislocation loop formation on hardening, with a more significant increase in hardening observed in the Fe-Mn-Ni-Si alloy, corresponding to the increase in number density of radiation induced solute-rich defects.

Concerning the application of proton-irradiation, a key pitfall in this work was the contamination of the vacuum by nitrogen gas. Clearly, Mn and Si in ferrite are sensitive to radiation enhanced precipitation in the presence of small quantities of nitrogen. This is a concern for the field, as there is significant interest in the investigation of clustering in Ni free steels containing small quantities of Mn and Si, for fusion applications.

Although using model alloys theoretically enables the decoupling of compositional effects on precipitation under irradiation, by focussing on simple combinations of solute elements, the nature of these compositions leads to microstructural evolution that could never occur in a true reactor pressure vessel steel. In this work, the Mn-Si nitrides observed are likely to be unique to alloys containing extremely low quantities of other elements with high affinity with nitrogen, leading to comparatively unstable nitrides. Reactor pressure vessel steels contain Cr, Mo and V which all form significantly more thermodynamically stable nitride precipitates in the presence of nitrogen than Si and Mn. Observing Mn-Si nitrides with such morphology and crystal structure is relatively novel, but there are limited applications of this observation in the field of nuclear structural steels. The effect of nitrogen addition and clustering has been found to have an effect on reduced-activation ferritic/martensitic (RAFM) structural steels proposed for use in fusion

environments, but this is due to the evolution of existing nitride precipitates in the steel made from elements such as Ti, Cr, and V.

The use of complementary techniques in this study has increased confidence in the identification of the phases identified in proton-irradiated model alloys. However, more intensive TEM characterisation would have been a more efficient method to employ in the earlier stages of the project, to identify the priorities of APT analysis based on volume fraction and number density of solute-rich precipitates.

The application of proton-irradiation to a minimum dose of 0.1 dpa obscured any early stage segregation and clustering but the formation of almost Fe free features, in APT, suggests that the clustering observed in RPV steels under irradiation is the beginning of a precipitation process resulting in phases with low Fe content. Even at 0.1 dpa, the composition of some precipitates observed in this work seem to be evolving towards that of the $Mn_6Ni_{16}Si_7$ G phase, and the diffraction patterns observed in this work are consistent with this structure.

The observations made in the Fe-Mn-Ni-Si alloy suggest that there are multiple mechanisms of defect formation leading to a diverse population of precipitates. Smaller features in the matrix and larger features located on dislocation loops suggest that the dominant mechanism is heterogeneous precipitation caused by the formation of radiation induced dislocation loops. The thermodynamic stability of precipitates has not been confirmed using post-irradiation annealing in this work but, in a radiation environment, with elevated vacancy concentrations, the Ni rich precipitates are comparatively stable to the nitrides formed rich in Mn and Si.

Based on the magnitude of segregation and precipitation observed in the Fe-Mn-Ni-Si alloy the well documented dominance of Ni in stabilising radiation induced defects such as dislocation loops, and segregating in irradiated steels is confirmed. This enhanced segregation and stabilisation of loops led to increase number densities of precipitates and subsequent radiation hardening.

The synergistic effect of Mn and Si was challenging to observe due to the formation of nitride precipitates due to vacuum contamination. However, the huge difference in microstructural evolution observed between the Fe-Mn-Ni-Si and Fe-Mn-Si alloy suggest that Ni has a strong influence on stabilising Mn and Si at dislocation loops, implying there is a synergistic effect of all three solute elements on stabilising solute clusters in RPV model steels. The lack of

observed precipitation in the Fe-Mn-Ni alloy, and some evidence of high density, fine-scale Mn-Ni clustering suggests that Si plays a role in stabilising and growing clusters to allow them to reach a critical radius for growth. Therefore, these results suggest that there is a combined effect of all three solutes in the stabilisation of solute clusters and subsequent nucleation and growth, leading to solute-rich embrittling defects under irradiation.

The observations made in this work show that radiation induced dislocation loops act as nucleation sites for Fe- free Mn-Ni-Si precipitates which, under proton-irradiation at around 350 °C, will form in Fe-Mn-Ni-Si alloys with solute content below solubility limits, and that Ni promotes solute segregation and clustering under irradiation.

8.1 Proposed future work

Although this work has made progress towards understanding the synergistic effects of Mn, Ni and Si on radiation hardening and embrittlement, it has not thoroughly investigated the full range of irradiated alloys using TEM techniques, and it has not provided the key link between microstructural evolution and the effects on mechanical properties. The first piece of further work would be to repeat the proton irradiation, employing the methods described in the discussion, to avoid nitrogen contamination. This would facilitate the identification of relationships between pairs of solutes in RPV steels and clarify the effect of removing Mn, Ni or Si from the situation. The results of this would assist with verifying cluster dynamics simulations of solute clustering around dislocation loops.

In order to validate the use of protons for accelerated defect evolution studies it would be valuable to investigate the effects of proton dose rate on defect structures forming in both A508-3 and model alloys. To see a clear effect of dose rate it would be necessary to reduce the dose rate by at least an order of magnitude. The comparison of microstructures at different dose rates in both the RPV steel and model alloys would be useful for the design of future accelerated radiation testing of ferritic steels for nuclear applications.

The nitrogen contamination in this work underscores one of the key issues with using super clean model alloys, as impurities introduced into the system behave in ways they would not in a real RPV steel. However, the effect of interstitial solutes and impurities are likely to affect radiation stability significantly in steels, particular where they stabilise dislocation loops, and

act as nucleation sites. An interesting piece of further work would be to use APT to investigate the effect of different levels of N, P and S in RPV steels on the dislocation loop and cluster morphology caused by radiation damage.

Many existing studies into radiation hardening assume the nature of clusters and precipitates, and apply this to the dispersed barrier hardening model. 4D-STEM could be used to validate these assumptions by investigating the coherency of precipitate interfaces with the Fe matrix, which can then be used to model the interaction of dislocations with radiation induced features.

Bibliography

[1] "Energy Statistics Data Browser – Data Tools - IEA- Topic:Energy Consumption, Indicator:Electricity Consumption ." Available at: https://www.iea.org/data-and-statistics/data-tools/energy-statistics-data-browser?country=WORLD&fuel=Energy%20consumption&indicator=TotElecCons, accessed 18/09/2024.

[2] "PRIS - Reactor status reports - In Operation & Suspended Operation - By Type." Available at: https://pris.iaea.org/PRIS/WorldStatistics/OperationalReactorsByType.aspx, accessed 12/08/2024.

[3] "PRIS - Miscellaneous reports - Operational by Age." Available at: https://pris.iaea.org/pris/worldstatistics/operationalbyage.aspx, accessed 18/09/2024.

[4] "Number of nuclear reactors worldwide 2023 | Statista." Available at: https://www.statista.com/statistics/263945/number-of-nuclear-power-plants-worldwide/, accessed 11/09/2024.

[5] "Nuclear Power in Germany - World Nuclear Association." Available at: https://world-nuclear.org/information-library/country-profiles/countries-g-n/germany, accessed 11/09/2024.

[6] "Press release Hinkley Point C Update," 2024. Available at: https://www.edf.fr/sites/groupe/files/epresspack/7023/Hinkley-Point-C-PR-23012024.pdf, accessed 28/08/2024.

[7] "Nuclear Plant Life Extensions Help Clean Energy Transition| IAEA." Available at: https://www.iaea.org/newscenter/news/

iaea-data-animation-nuclear-power-plant-life-extensions-enable-clean-energy-transition, accessed 05/07/2021.

[8] MIT Technology Review, "Why the lifetime of nuclear plants is getting longer | MIT Technology Review." Available at: https://www.technologyreview.com/2024/04/04/1090630/old-nuclear-plants/, accessed 11/09/2024.

[9] "France extends lifetime of its oldest nuclear reactors Lifetime reactors France Lifetime reactors | The Independent." Available at: https://www.independent.co.uk/news/france-extends-lifetime-of-its-oldest-nuclear-reactors-france-lifetime-lifetime-reactors.html, accessed 11/09/2024.

[10] World Nuclear Association, "World Nuclear Performance Report 2024," 2024.

[11] E. D. Eason, G. R. Odette, R. K. Nanstad, and T. Yamamoto, "A physically-based correlation of irradiation-induced transition temperature shifts for RPV steels," Journal of Nuclear Materials, vol. 433, pp. 240–254, 2 2013.

[12] J. Kocik, E. Keilov, and I. Proch, "TEM and PAS study of neutron irradiated VVER-type RPV steels," Journal of Nuclear Materials, vol. 303, pp. 52–64, 2002.

[13] B. M. Jenkins, J. O. Douglas, N. Almirall, N. Riddle, P. A. Bagot, J. M. Hyde, G. R. Odette, and M. P. Moody, "The effect of composition variations on the response of steels subjected to high fluence neutron irradiation," Materialia, vol. 11, 6 2020.

[14] Y. Lin, W. Yang, Z. Tong, C. Zhang, and G. Ning, "Charpy impact test on A508-3 steel after neutron irradiation," Engineering Failure Analysis, vol. 82, pp. 733–740, 12 2017.

[15] N. Almirall, P. B. Wells, S. Pal, P. D. Edmondson, T. Yamamoto, K. Murakami, and G. R. Odette, "The mechanistic implications of the high temperature, long time thermal stability of nanoscale Mn-Ni-Si precipitates in irradiated reactor pressure vessel steels," Scripta Materialia, vol. 181, pp. 134–139, 5 2020.

[16] E. A. Kuleshova, G. M. Zhuchkov, S. V. Fedotova, D. A. Maltsev, A. S. Frolov, and I. V. Fedotov, "Precipitation kinetics of radiation-induced Ni-Mn-Si phases in VVER-

1000 reactor pressure vessel steels under low and high flux irradiation," Journal of Nuclear Materials, vol. 553, p. 153091, 9 2021.

[17] G. R. Odette, T. Yamamoto, T. J. Williams, R. K. Nanstad, and C. A. English, "On the history and status of reactor pressure vessel steel ductile to brittle transition temperature shift prediction models," Journal of Nuclear Materials, vol. 526, p. 151863, 12 2019.

[18] T. Williams and R. Nanstad, "Low-alloy steels," in Structural Alloys for Nuclear Energy Applications, pp. 411–483, Elsevier, 1 2019.

[19] J. C. van Duysen and G. Meric de Bellefon, "60th Anniversary of electricity production from light water reactors: Historical review of the contribution of materials science to the safety of the pressure vessel," 2 2017.

[20] G. R. Odette and G. E. Lucas, "Recent progress in understanding reactor pressure vessel steel embrittlement," http://dx.doi.org/10.1080/10420159808229676, vol. 144, no. 1-4, pp. 189–231, 2006.

[21] F. Gillemot, "Review on steel enhancement for nuclear rpvs," Metals, vol. 11, 12 2021.

[22] F. A. Smidt and H. E. Watson, "Effect of residual elements on radiation strengthening in iron alloys, pressure vessel steels, and welds," Metallurgical Transactions 1972 3:8, vol. 3, pp. 2065–2073, 8 1972.

[23] M. K. Miller, P. Pareige, and M. G. Burke, "Understanding Pressure Vessel Steels: An Atom Probe Perspective," tech. rep., 2000.

[24] "Basic Principles Objectives IAEA Nuclear Energy Series Integrity of Reactor Pressure Vessels in Nuclear Power Plants: Assessment of Irradiation Embrittlement Effects in Reactor Pressure Vessel Steels,"

[25] P. A. Beaven, F. Frisius, R. Kampmann, R. Wagner, and J. R. Hawthorne, "SANS Investigation of Irradiated A533-B Steels Doped with Phosphorus," ASTM Special Technical Publication, vol. STP 1011, pp. 243–256, 1989.

[26] G. R. Odette, "On the dominant mechanism of irradiation embrittlement of reactor pressure vessel steels," Scripta Metallurgica, vol. 17, no. 10, pp. 1183–1188, 1983.

[27] S. Cui, M. Mamivand, and D. Morgan, "Simulation of Cu precipitation in Fe-Cu dilute alloys with cluster mobility," Materials & Design, vol. 191, p. 108574, 6 2020.

[28] V. T. Witusiewicz, F. Sommer, and E. J. Mittemeijer, "Reevaluation of the Fe-Mn phase diagram," Journal of Phase Equilibria and Diffusion, vol. 25, pp. 346–354, 10 2004.

[29] S. M. Murphy, "Instabilities in concentrated alloys under irradiation," Philosophical Magazine A, vol. 58, no. 2, pp. 417–433, 1988.

[30] L. M. Yu, J. S. Wrobel, N.-M. D. Dudarev, M. Y. Lavrentiev, J. S. Wró, D. Nguyen-Manh, and S. L. Dudarev, "Magnetic and thermodynamic properties of face-centred cubic Fe-Ni alloys," Phys. Chem. Chem. Phys, vol. 16, p. 16049, 2014.

[31] J. Yang, X. Xing, S. Liu, C. Zhao, Y. Zhao, and Q. Yang, "Structural and chemical contributions on solubility of silicon and carbon in ferrite studied by first-principles calculations," Journal of Alloys and Compounds, vol. 695, pp. 2717–2722, 2 2017.

[32] D. K. Vogt, "Nuclear Fission Reactors: Boiling Water and Pressurized Water Reactors," Encyclopedia of Energy, pp. 333–340, 1 2004.

[33] J. Way, "The World's Reactors, No. 83, Sizewell B," 1982.

[34] USNRC, Reactor Concepts Manual Pressurized Water Reactor Systems. 2007.

[35] W. L. Server and R. K. Nanstad, "International Atomic Energy Agency Coordinated Research Projects on Structural Integrity of Reactor Pressure Vessels," ASTM Special Technical Publication, vol. 1513 STP, pp. 1–25, 2010.

[36] M. Burke, R. Stofanak, J. Hyde, and C. English, "Microstructural aspects of irradiation damage in A508 Gr 4N forging steel: composition and flux effects," 2002.

[37] N. Almirall, P. B. Wells, T. Yamamoto, K. Wilford, T. Williams, N. Riddle, and G. R. Odette, "Precipitation and hardening in irradiated low alloy steels with a wide range of Ni and Mn compositions," Acta Materialia, vol. 179, pp. 119–128, 10 2019.

[38] H. Takamizawa, K. Hata, Y. Nishiyama, T. Toyama, and Y. Nagai, "The role of silicon on solute clustering and embrittlement in highly neutron-irradiated pressurized water reactor surveillance test specimens," Journal of Nuclear Materials, vol. 556, p. 153203, 12 2021.

[39] Nuclear Energy Agency Committee on the Safety of Nuclear Installations, "VVER-Specific Features Regarding Core Degradation Status Report 73719," tech. rep., 1999.

[40] C. Xie, Z. Liu, X. Wang, X. He, and S. Qiao, "Effect of two-step tempering treatment on microstructure and impact toughness of bainitic steel for heavy wall thickness reactor pressure vessels," Materials Characterization, vol. 160, p. 110070, 2 2020.

[41] B. Marini, X. Averty, P. Wident, P. Forget, and F. Barcelo, "Effect of the bainitic and martensitic microstructures on the hardening and embrittlement under neutron irradiation of a reactor pressure vessel steel," Journal of Nuclear Materials, vol. 465, pp. 20–27, 10 2015.

[42] Y. Liu, N. Qu, J. Ren, Y. Zhang, and J. Zhu, "Phase transition kinetics and microstructures of A508-3 steel under continuous cooling process," Heat Treatment and Surface Engineering, vol. 4, no. 1, pp. 13–19, 2022.

[43] E. J. Pickering and H. K. Bhadeshia, "Macrosegregation and microstructural evolution in a pressure-vessel steel," Metallurgical and Materials Transactions A: Physical Metallurgy and Materials Science, vol. 45, pp. 2983–2997, 3 2014.

[44] H. K. Bhadeshia and D. V. Edmonds, "The mechanism of bainite formation in steels," Acta Metallurgica, vol. 28, pp. 1265–1273, 9 1980.

[45] D. A. Porter, K. E. Easterling, and M. Y. Sherif, "Diffusional transformations in solids," in Phase Transformations in Metals and Alloys, vol. 1, pp. 334–341, third ed., 2009.

[46] T. Wang, J. Gao, S. Li, J. Li, J. Li, H. Bu, H. Qi, Z. Li, and M. Li, "Microstructure evolution and mechanical properties degradation behavior of nuclear power pressure vessel steel induced by prolonged thermal aging," Journal of Materials Research and Technology, vol. 34, pp. 2740–2753, 1 2025.

[47] G. Ning, W. Zhong, J. Li, T. Cong, J. Sun, H. Wang, G. Qian, and F. Berto, "Effect of environmental media on the fatigue property of Chinese A508-3 steel of AP1000," International Journal of Fracture, vol. 234, pp. 263–272, 4 2022.

[48] J. N. Emerson, E. H. Marrero-Jackson, G. A. Nemets, M. A. Okuniewski, and J. P. Wharry, "Nuclear Reactor Pressure Vessel Welds: A Critical and Historical Review of Microstructures, Mechanical Properties, Irradiation Effects, and Future Opportunities," Materials & Design, vol. 244, p. 113134, 8 2024.

[49] M. Yu, Y. J. Chao, and Z. Luo, "An Assessment of Mechanical Properties of A508-3 Steel Used in Chinese Nuclear Reactor Pressure Vessels," 2015.

[50] Z. Zhou, Z. Tong, G. Qian, W. Zhong, C. Wang, W. Yang, and F. Berto, "Irradiation effect on impact fracture behavior of A508-3 steel in ductile-to-brittle transition range," Engineering Failure Analysis, vol. 97, pp. 836–843, 3 2019.

[51] Was. G., "Fracture and Embrittlement," in Fundamentals of Radiation Materials Science, pp. 643–709, Springer, Berlin, Heidelberg, 7 2007.

[52] C. Bouchet, B. Tanguy, J. Besson, and S. Bugat, "Prediction of the effects of neutron irradiation on the Charpy ductile to brittle transition curve of an A508 pressure vessel steel," Computational Materials Science, vol. 32, pp. 294–300, 3 2005.

[53] E. E. Gdoutos, "Chapter 5: Critical stress intensity factor fracture criterion.," in Fracture mechanics : an introduction, pp. 131–147, Cham, Switzerland: Springer, 3rd ed., 2020.

[54] J. Chen and R. Cao, "Introduction," in Micromechanism of Cleavage Fracture of Metals, pp. 1–54, Elsevier, 2015.

[55] Y. A. Nikolaev, A. V. Nikolaeva, and Y. I. Shtrombakh, "Radiation embrittlement of low-alloy steels," International Journal of Pressure Vessels and Piping, vol. 79, pp. 619–636, 8 2002.

[56] E. A. Kuleshova, B. A. Gurovich, Z. V. Lavrukhina, D. A. Maltsev, S. V. Fedotova, A. S. Frolov, and G. M. Zhuchkov, "Study of the flux effect nature for vver-1000 RPV welds with high nickel content," Journal of Nuclear Materials, vol. 483, pp. 1–12, 1 2017.

[57] "ASTM E706 - 16 Standard Master Matrix for Light-Water Reactor Pressure Vessel Surveillance Standards."

[58] "ASTM E900 - 15e2 Standard Guide for Predicting Radiation-Induced Transition Temperature Shift in Reactor Vessel Materials."

[59] M. Sánchez, S. Cicero, B. Arroyo, G. Bonny, H. Swan, P. Lappalainen, E. Altstadt, T. Petit, and F. Obermeier, "FRACTESUS Project overview: objectives, organisation and initial findings," Procedia Structural Integrity, vol. 47, pp. 22–29, 1 2023.

[60] R. K. Nanstad and M. A. Sokolov, "The Assessment and Validation of Mini-Compact Tension Test Specimen Geometry and Progress in Establishing Technique for Fracture Toughness Master Curves for Reactor Pressure Vessel Steels," 2016.

[61] R. Chaouadi and J. Schuurmans, "Critical analysis of the mini-CT geometry for fracture toughness characterization of the 73W high-copper submerged-arc weld in the unirradiated and irradiated condition," Engineering Fracture Mechanics, vol. 298, p. 109929, 3 2024.

[62] M. Kolluri, P. ten Pierick, T. Bakker, B. Straathof, A. Magielsen, Z. Szaraz, E. D'Agata, C. Ohms, and O. Martin, "Influence of Ni-Mn contents on the embrittlement of PWR RPV model steels irradiated to high fluences relevant for LTO beyond 60 years," Journal of Nuclear Materials, vol. 553, p. 153036, 9 2021.

[63] G. Was, "The Damage Cascade," in Fundamentals of Radiation Materials Science, pp. 125–154, Springer, Berlin, Heidelberg, 7 2007.

[64] G. S. Was, "Point Defect Formation and Diffusion," in Fundamentals of Radiation Materials Science: Metals and Alloys, p. 155190, Springer Berlin Heidelberg, 2007.

[65] W. J. Phythian and C. A. English, "Microstructural evolution in reactor pressure vessel steels," Journal of Nuclear Materials, vol. 205, pp. 162–177, 10 1993.

[66] E. Meslin, M. Lambrecht, M. Hernández-Mayoral, F. Bergner, L. Malerba, P. Pareige, B. Radiguet, A. Barbu, D. Gómez-Briceño, A. Ulbricht, and A. Almazouzi, "Characterization of neutron-irradiated ferritic model alloys and a RPV steel from combined APT,

SANS, TEM and PAS analyses," Journal of Nuclear Materials, vol. 406, pp. 73–83, 11 2010.

[67] ASTM, "ASTM 185-82e2 Standard Practice for Conducting Surveillance Tests for Light-Water Cooled Nuclear Power Reactor Vessels, E 706 (IF)," tech. rep., 2017.

[68] N. Hashimoto, E. Wakai, and J. P. Robertson, "Relationship between hardening and damage structure in austenitic stainless steel 316LN irradiated at low temperature in the HFIR," Journal of Nuclear Materials, vol. 273, pp. 95–101, 6 1999.

[69] R. Chaouadi, R. Gérard, E. Stergar, and W. Van Renterghem, "Neutron irradiation hardening of chemically-tailored RPV steels with respect to Cu/P and Ni/Mn elements," Journal of Nuclear Materials, vol. 519, pp. 188–204, 6 2019.

[70] M. Laver, B. J. Connolly, C. Cooper, J. Kohlbrecher, S. Samothrakitis, and K. Wilford, "Characterizing accelerated precipitation in proton irradiated steel," Journal of Nuclear Materials, vol. 557, p. 153195, 12 2021.

[71] L. T. Belkacemi, E. Meslin, B. Décamps, J. P. Crocombette, O. Tissot, T. Vandenberghe, P. Desgardin, T. Sauvage, and C. Berthier, "Role of displacement cascades in Ni clustering in a ferritic Fe-3.3 at%Ni model alloy: Comparison of heavy and light particle irradiations," Scripta Materialia, vol. 188, pp. 169–173, 11 2020.

[72] N. H. Packan, K. Farrell, and J. O. Stiegler, "Correlation of neutron and heavy-ion damage: I. The influence of dose rate and injected helium on swelling in pure nickel," Journal of Nuclear Materials, vol. 78, pp. 143–155, 11 1978.

[73] L. Malerba, "Molecular dynamics simulation of displacement cascades in α-Fe: A critical review," Journal of Nuclear Materials, vol. 351, pp. 28–38, 6 2006.

[74] A. De Backer, A. E. Sand, K. Nordlund, L. Luneville, D. Simeone, and S. L. Dudarev, "Subcascade formation and defect cluster size scaling in high-energy collision events in metals," Europhysics Letters, vol. 115, p. 26001, 8 2016.

[75] G. S. Was and T. Allen, "Radiation-induced segregation in multicomponent alloys: Effect of particle type," Materials Characterization, vol. 32, pp. 239–255, 6 1994.

[76] F. Soisson, E. Meslin, and O. Tissot, "Atomistic modeling of α' precipitation in Fe-Cr alloys under charged particles and neutron irradiations: Effects of ballistic mixing and sink densities," Journal of Nuclear Materials, vol. 508, pp. 583–594, 9 2018.

[77] R. K. Nanstad, G. R. Odette, N. Almirall, J. P. Robertson, W. L. Server, T. Yamamoto, and P. Wells, "Effects of ATR-2 Irradiation to High Fluence on Nine RPV Surveillance Materials," 2017.

[78] J. C. Haley, S. de Moraes Shubeita, P. Wady, A. J. London, G. R. Odette, S. Lozano-Perez, and S. G. Roberts, "Microstructural examination of neutron, proton and self-ion irradiation damage in a model Fe9Cr alloy," Journal of Nuclear Materials, vol. 533, p. 152130, 5 2020.

[79] A. Kamboj, N. Almirall, T. Yamamoto, S. Tumey, E. A. Marquis, and G. R. Odette, "Dose and dose rate dependence of precipitation in a series of surveillance RPV steels under ion and neutron irradiation," Journal of Nuclear Materials, vol. 588, p. 154772, 1 2024.

[80] G. Was, B. Wirth, A. Motta, D. Morgan, D. Kaoumi, P. Hosemann, and R. Odette, "High Fidelity Ion Beam Simulation of High Dose Neutron Irradiation," 4 2018.

[81] S. Ortner, P. Styman, and E. Long, "The effects of flux on the radiation-induced embrittlement of reactor pressure vessel steels: review of current understanding and application to high fluences," Frontiers in Nuclear Engineering, vol. 3, 2 2024.

[82] G. F. Knoll, "Chapter 2: Radiation Interactions," in Radiation Detection and Measurement, pp. 29–64, John Wiley & Sons Inc., 3rd ed., 2000.

[83] L. T. Belkacemi, E. Meslin, J. P. Crocombette, B. Radiguet, F. Leprêtre, and B. Décamps, "Striking effect of solute elements (Mn, Ni) on radiation-induced segregation/precipitation in iron-based model alloys," Journal of Nuclear Materials, vol. 548, p. 152807, 5 2021.

[84] G. S. Was and R. S. Averback, "Radiation damage using ion beams," in Comprehensive Nuclear Materials, vol. 1, pp. 195–221, Elsevier Ltd, 1 2012.

[85] N. Soneda, S. Ishino, A. Takahashi, and K. Dohi, "Modeling the microstructural evolution in bcc-Fe during irradiation using kinetic Monte Carlo computer simulation," in Journal of Nuclear Materials, vol. 323, pp. 169–180, North-Holland, 12 2003.

[86] C. Courilleau, B. Radiguet, R. Chaouadi, E. Stergar, A. Duplessi, and P. Pareige, "Contributions of Ni-content and irradiation temperature to the kinetic of solute cluster formation and consequences on the hardening of VVER materials," Journal of Nuclear Materials, vol. 585, p. 154616, 11 2023.

[87] L. Messina, T. Schuler, M. Nastar, M. C. Marinica, and P. Olsson, "Solute diffusion by self-interstitial defects and radiation-induced segregation in ferritic Fe–X (X=Cr, Cu, Mn, Ni, P, Si) dilute alloys," Acta Materialia, vol. 191, pp. 166–185, 6 2020.

[88] D. Vizoso, C. Deo, and R. Dingreville, "The effects of dose, dose rate, and irradiation type and their equivalence on radiation-induced segregation in binary alloy systems via phase-field simulations," Journal of Nuclear Materials, vol. 569, p. 153924, 10 2022.

[89] T. Toyama, T. Yamamoto, N. Ebisawa, K. Inoue, Y. Nagai, and G. R. Odette, "Effects of neutron flux on irradiation-induced hardening and defects in RPV steels studied by positron annihilation spectroscopy," Journal of Nuclear Materials, vol. 532, p. 152041, 4 2020.

[90] R. Chaouadi and R. Gérard, "Neutron flux and annealing effects on irradiation hardening of RPV materials," Journal of Nuclear Materials, vol. 418, pp. 137–142, 11 2011.

[91] R. Chaouadi and R. Gérard, "Confirmatory investigations on the flux effect and associated unstable matrix damage in RPV materials exposed to high neutron fluence," Journal of Nuclear Materials, vol. 437, no. 1-3, pp. 267–274, 2013.

[92] I. I. Novoselov, D. I. Savin, and A. V. Yanilkin, "The effect of irradiation conditions on generation of defects and their clusters," Journal of Nuclear Materials, vol. 546, p. 152762, 4 2021.

[93] L. K. Mansur, "Correlation of neutron and heavy-ion damage: II. The predicted temper-

ature shift if swelling with changes in radiation dose rate," Journal of Nuclear Materials, vol. 78, pp. 156–160, 11 1978.

[94] S. B. Adisa and M. J. Swenson, "PROPERTIES AND EVOLUTION OF DEFECTS AND INTERFACES Temperature Shift for Nanocluster Evolution in Ion-Irradiated Ferritic-Martensitic Alloys," JOM, vol. 74.

[95] Z. Yao, M. L. Jenkins, M. Hernández-Mayoral, and M. A. Kirk, "The temperature dependence of heavy-ion damage in iron: A microstructural transition at elevated temperatures," Philosophical Magazine, vol. 90, pp. 4623–4634, 12 2010.

[96] E. A. Kuleshova, B. A. Gurovich, E. V. Krikun, A. S. Frolov, D. A. Maltsev, Z. V. Bukina, M. A. Saltykov, and A. G. Balikoev, "Specific features of structural-phase state and properties of reactor pressure vessel steel at elevated irradiation temperature," Science and Technology of Nuclear Installations, vol. 2017, 2017.

[97] Sarah Connolly, Jonathan Hyde, Philippe Pareige, David Parfitt, Paul Styman, and Keith Wilford, "The Effect of Irradiation Temperature on Precipitation in RPV Steels," in SMiRT-23, (Manchester), IASMiRT, 8 2015.

[98] M. Nastar and F. Soisson, "1.18 - Radiation-Induced Segregation," in Comprehensive Nuclear Materials: Volume 1-5, vol. 1-5, pp. 471–496, Elsevier, 1 2012.

[99] M. L. Jenkins, Z. Yao, M. Hernández-Mayoral, and M. A. Kirk, "Dynamic observations of heavy-ion damage in Fe and Fe–Cr alloys," Journal of Nuclear Materials, vol. 389, pp. 197–202, 5 2009.

[100] N. Gao, Z. W. Yao, G. H. Lu, H. Q. Deng, and F. Gao, "Mechanisms for <100> interstitial dislocation loops to diffuse in BCC iron," Nature Communications, vol. 12, 12 2021.

[101] M. Hernández-Mayoral and D. Gómez-Briceño, "Transmission electron microscopy study on neutron irradiated pure iron and RPV model alloys," Journal of Nuclear Materials, vol. 399, pp. 146–153, 4 2010.

[102] J. J. Shi, W. Z. Zhao, Y. C. Wu, X. B. Liu, and J. Jiang, "Characterization of proton-irradiated Chinese A508-3-type reactor pressure vessel steel by slow positron beam, TEM,

and nanoindentation," Nuclear Instruments and Methods in Physics Research, Section B: Beam Interactions with Materials and Atoms, vol. 443, pp. 62–69, 3 2019.

[103] T. Fujita, J. Hirabayashi, Y. Katayama, F. Kano, and H. Watanabe, "Contribution of dislocation loop to radiation-hardening of RPV steels studied by STEM/EDS with surveillance test pieces," Journal of Nuclear Materials, vol. 572, p. 154055, 12 2022.

[104] K. Shi, W. Zhang, Z. Ning, H. Wang, J. Liao, Y. Yang, N. Liu, and J. Yang, "Proton and Au-ion irradiation induced damage and hardening in ferritic/martensitic steel," Nuclear Materials and Energy, vol. 26, p. 100929, 3 2021.

[105] K. Nohara and K.-I. Hirano, Proc. Int. Conf. on Sci. and Tcchnol. Iron and Steel, 1267. 1970.

[106] K. Hirano, M. Cohen, and B. L. Averbach, "Diffusion of nickel into iron," Acta Metallurgica, vol. 9, pp. 440–445, 5 1961.

[107] R. J. Borg and D. Y. Lai, "Diffusion in α-Fe–Si Alloys," Journal of Applied Physics, vol. 41, pp. 5193–5200, 12 1970.

[108] C. D. Versteylen, N. H. Van Dijk, and M. H. Sluiter, "First-principles analysis of solute diffusion in dilute bcc Fe- X alloys," Physical Review B, vol. 96, p. 094105, 9 2017.

[109] Q. Chen, R. Hu, S. Jin, F. Xue, and G. Sha, "Irradiation-induced segregation/desegregation at grain boundaries of a ferritic Fe-Mn-Si steel," Acta Materialia, vol. 220, p. 117297, 11 2021.

[110] B. M. Jenkins, P. D. Styman, N. Riddle, P. A. Bagot, M. P. Moody, G. D. Smith, and J. M. Hyde, "Observation of Mn-Ni-Si-rich features in thermally-aged model reactor pressure vessel steels," Scripta Materialia, vol. 191, pp. 126–130, 1 2021.

[111] P. D. Edmondson, C. M. Parish, and R. K. Nanstad, "Using complimentary microscopy methods to examine Ni-Mn-Si-precipitates in highly-irradiated reactor pressure vessel steels," Acta Materialia, vol. 134, pp. 31–39, 8 2017.

[112] P. Prak Tom, K. Murakami, V. N. Luu, B. V. C. Nguyen, and L. Chen, "Effect of solute elements (Ni, Mn) in Fe-based alloys on dislocation loop evolution under Fe2+ ion irradiation," Journal of Nuclear Materials, vol. 559, p. 153489, 2 2022.

[113] P. H. Warren, C. D. Clement, C. Yang, A. Sen, W. Y. Chen, Y. Wu, L. Wang, and J. P. Wharry, "The role of Cr, P, and N solutes on the irradiated microstructure of bcc Fe," Journal of Nuclear Materials, vol. 583, p. 154531, 9 2023.

[114] Nguyen Ba Vu Chinh, K. Murakami, L. Chen, P. P. Tom, X. Chen, T. Hashimoto, T. Hwang, A. Furusawa, and T. Suzuki, "Interaction of solute manganese and nickel atoms with dislocation loops in iron-based alloys irradiated with 2.8 MeV Fe ions at 400 °C," Nuclear Materials and Energy, vol. 39, p. 101639, 6 2024.

[115] N. Castin, G. Bonny, A. Bakaev, F. Bergner, C. Domain, J. M. Hyde, L. Messina, B. Radiguet, and L. Malerba, "The dominant mechanisms for the formation of solute-rich clusters in low-Cu steels under irradiation," Materials Today Energy, vol. 17, p. 100472, 9 2020.

[116] M. Chiapetto, C. S. Becquart, C. Domain, and L. Malerba, "Nanostructure evolution under irradiation of Fe(C)MnNi model alloys for reactor pressure vessel steels," Nuclear Instruments and Methods in Physics Research Section B: Beam Interactions with Materials and Atoms, vol. 352, pp. 56–60, 6 2015.

[117] T. M. Whiting, P. A. Burr, D. J. M. King, and M. R. Wenman, "Understanding the importance of the energetics of Mn, Ni, Cu, Si and vacancy triplet clusters in bcc Fe," J. Appl. Phys, vol. 126, p. 115901, 2019.

[118] G. Bonny, C. Domain, N. Castin, P. Olsson, and L. Malerba, "The impact of alloying elements on the precipitation stability and kinetics in iron based alloys: An atomistic study," Computational Materials Science, vol. 161, pp. 309–320, 4 2019.

[119] G. R. Odette and B. D. Wirth, "A computational microscopy study of nanostructural evolution in irradiated pressure vessel steels," tech. rep., 1997.

[120] R. Ngayam-Happy, C. S. Becquart, C. Domain, and L. Malerba, "Formation and evolution of MnNi clusters in neutron irradiated dilute Fe alloys modelled by a first principle-based AKMC method," Journal of Nuclear Materials, vol. 426, pp. 198–207, 7 2012.

[121] M. Carter, C. Gasparrini, J. O. Douglas, N. Riddle, L. Edwards, P. A. Bagot, C. D. Hardie, M. R. Wenman, and M. P. Moody, "On the influence of microstructure on the neutron irradiation response of HIPed SA508 steel for nuclear applications," Journal of Nuclear Materials, vol. 559, p. 153435, 2 2022.

[122] S. Kotrechko, "Embrittlement of RPV metal under long-term irradiation: State-of-the-art and challenges," in Procedia Structural Integrity, vol. 13, pp. 11–21, Elsevier B.V., 1 2018.

[123] A. Ulbricht and J. Böhmert, "Small angle neutron scattering analysis of the radiation susceptibility of reactor pressure vessel steels," in Physica B: Condensed Matter, vol. 350, 7 2004.

[124] N. Almirall, P. B. Wells, T. Yamamoto, K. Yabuuchi, A. Kimura, and G. R. Odette, "On the use of charged particles to characterize precipitation in irradiated reactor pressure vessel steels with a wide range of compositions," Journal of Nuclear Materials, vol. 536, p. 152173, 8 2020.

[125] A. Wagner, F. Bergner, A. Ulbricht, and C. D. Dewhurst, "Small-angle neutron scattering of low-Cu RPV steels neutron-irradiated at 255 °c and post-irradiation annealed at 290 °c," Journal of Nuclear Materials, vol. 441, pp. 487–492, 10 2013.

[126] F. Bergner, A. Ulbricht, P. Lindner, U. Keiderling, and L. Malerba, "Post-irradiation annealing behavior of neutron-irradiated FeCu, FeMnNi and FeMnNiCu model alloys investigated by means of small-angle neutron scattering," Journal of Nuclear Materials, vol. 454, pp. 22–27, 11 2014.

[127] Q. Tencé, "Couplage entre microstructure et précipitation sous irradiation dans les alliages base fer," 4 2023.

[128] W. Xiong, H. Ke, R. Krishnamurthy, P. Wells, L. Barnard, G. R. Odette, and D. Morgan,

"Thermodynamic models of low-temperature Mn–Ni–Si precipitation in reactor pressure vessel steels," MRS Communications, vol. 4, pp. 101–105, 9 2014.

[129] D. J. Sprouster, J. Sinsheimer, E. Dooryhee, S. K. Ghose, P. Wells, T. Stan, N. Almirall, G. R. Odette, and L. E. Ecker, "Structural characterization of nanoscale intermetallic precipitates in highly neutron irradiated reactor pressure vessel steels," Scripta Materialia, vol. 113, pp. 18–22, 3 2016.

[130] D. J. King, S. C. Middleburgh, P. A. Burr, T. M. Whiting, P. C. Fossati, and M. R. Wenman, "Density functional theory study of the magnetic moment of solute Mn in bcc Fe," Physical Review B, vol. 98, p. 024418, 7 2018.

[131] D. J. King, M. Yang, T. M. Whiting, X. Liu, and M. R. Wenman, "G-phase strengthened iron alloys by design," Acta Materialia, vol. 183, pp. 350–361, 1 2020.

[132] T. M. Whiting, D. J. King, and M. R. Wenman, "On the formation and structure of Mn-Ni-Si Γ2 precipitates in steels," Journal of Nuclear Materials, vol. 542, p. 152429, 12 2020.

[133] J. Xue, S. Jin, R. Hu, F. Xue, and G. Sha, "Ion-irradiation-induced clustering in Fe-Mn-Ni-(Si) steels: Nucleation, growth and chemistry evolution," Journal of Nuclear Materials, vol. 560, p. 153477, 3 2022.

[134] M. Jenkins and M. Kirk, "The role of transmission electron microscopy in characterizing radiation damage," in Characterisation of Radiation Damage by Transmission Electron Microscopy, pp. 11–15, CRC Press, 12 2020.

[135] K. Yabuuchi, M. Saito, R. Kasada, and A. Kimura, "Neutron irradiation hardening and microstructure changes in Fe-Mn binary alloys," Journal of Nuclear Materials, vol. 414, pp. 498–502, 7 2011.

[136] N. Almirall, P. B. Wells, H. Ke, P. Edmondson, D. Morgan, T. Yamamoto, and G. R. Odette, "On the elevated temperature thermal stability of nanoscale Mn-Ni-Si precipitates formed at lower temperature in highly irradiated reactor pressure vessel steels," Scientific Reports, vol. 9, 2019.

[137] L. Chen, K. Nishida, K. Murakami, T. Kobayashi, Z. Li, and N. Sekimura, "Evaluation of Hardening under Ion Irradiation in Reactor Pressure Vessel Model Alloys by Nano-indentation Techniques," E-Journal of Advanced Maintenance, vol. 9, no. 2, pp. 72–77, 2017.

[138] K. Fujii, T. Ohkubo, and K. Fukuya, "Effects of solute elements on irradiation hardening and microstructural evolution in low alloy steels," Journal of Nuclear Materials, vol. 417, pp. 949–952, 10 2011.

[139] Y. Yang, C. Zhang, J. Li, J. Gou, and Z. Ding, "The influence of solute elements on grain size, hardness and irradiation-induced defect clusters in dilute Fe-based alloys," Journal of Nuclear Materials, vol. 588, p. 154818, 1 2024.

[140] A. Kamboj, M. N. Bachhav, M. Dubey, N. Almirall, T. Yamamoto, E. A. Marquis, and G. R. Odette, "The effect of phosphorus on precipitation in irradiated reactor pressure vessel (RPV) steels," Journal of Nuclear Materials, vol. 585, p. 154614, 11 2023.

[141] D. Sharma, A. Etienne, R. Henry, C. Kaden, M. Picot, B. Radiguet, and a. Un, "Understanding the effect of phosphorous on the ion-irradiation behaviour of RPV model steels using atom probe tomography and nanoindentation," Acta Materialia, vol. 270, p. 119859, 2024.

[142] A. Hosseinzadeh Delandar, O. I. Gorbatov, M. Selleby, Y. N. Gornostyrev, and P. A. Korzhavyi, "Ab-initio based search for late blooming phase compositions in iron alloys," Journal of Nuclear Materials, vol. 509, pp. 225–236, 10 2018.

[143] M. K. Miller, K. A. Powers, R. K. Nanstad, and P. Efsing, "Atom probe tomography characterizations of high nickel, low copper surveillance RPV welds irradiated to high fluences," Journal of Nuclear Materials, vol. 437, pp. 107–115, 6 2013.

[144] S. Shu, B. D. Wirth, P. B. Wells, D. D. Morgan, and G. R. Odette, "Multi-technique characterization of the precipitates in thermally aged and neutron irradiated Fe-Cu and Fe-Cu-Mn model alloys: Atom probe tomography reconstruction implications," 2017.

[145] L. Yu, H. Guan, J. Tian, Y. Jing, and S. Huang, "Formation and stability of the early stage solute and defect clusters in Cu-free ferritic steels during irradiation," Journal of Nuclear Materials, vol. 557, p. 153297, 12 2021.

[146] M. Nastar, L. T. Belkacemi, E. Meslin, and M. Loyer-Prost, "Thermodynamic model for lattice point defect-mediated semi-coherent precipitation in alloys," Communications Materials, vol. 2, 12 2021.

[147] H. Ke, P. Wells, P. D. Edmondson, N. Almirall, L. Barnard, G. R. Odette, and D. Morgan, "Thermodynamic and kinetic modeling of Mn-Ni-Si precipitates in low-Cu reactor pressure vessel steels," Acta Materialia, vol. 138, pp. 10–26, 10 2017.

[148] P. B. Wells, T. Yamamoto, B. Miller, T. Milot, J. Cole, Y. Wu, and G. R. Odette, "Evolution of manganese-nickel-silicon-dominated phases in highly irradiated reactor pressure vessel steels," Acta Materialia, vol. 80, pp. 205–219, 2014.

[149] P. D. Edmondson, M. K. Miller, K. A. Powers, and R. K. Nanstad, "Atom probe tomography characterization of neutron irradiated surveillance samples from the R. E. Ginna reactor pressure vessel," Journal of Nuclear Materials, vol. 470, pp. 147–154, 3 2016.

[150] F. Bergner, A. Ulbricht, and H.-W. Viehrig, "Acceleration of irradiation hardening of low-copper reactor pressure vessel steel observed by means of SANS and tensile testing," Philosophical Magazine Letters, vol. 89, pp. 795–805, 12 2009.

[151] A. Seeger, "On the theory of radiation damage and radiation hardening," 1959.

[152] Was. G.S., "Irradiation Hardening and Deformation," in Fundamentals of Radiation Materials Science, ch. 12, pp. 581–640, Springer Berlin / Heidelberg, 1 ed., 2007.

[153] "Final Report Summary - PERFORM 60 (Prediction of the Effects of Radiation FOr reactor pressure vessel and in-core Materials using multi-scale modelling - 60 years foreseen plant lifetime) | Report Summary | PERFORM 60 | FP7 | CORDIS | European Commission."

[154] J. P. Massoud, S. Bugat, B. Marini, D. Lidbury, and S. V. Dyck, "PERFECT – Prediction of Irradiation Damage Effects on Reactor Components: A summary," Journal of Nuclear Materials, vol. 406, pp. 2–6, 11 2010.

[155] E. Altstadt, E. Keim, H. Hein, M. Serrano, F. Bergner, H. W. Viehrig, A. Ballesteros, R. Chaouadi, and K. Wilford, "FP7 Project LONGLIFE: Overview of results and implications," Nuclear Engineering and Design, vol. 278, pp. 753–757, 10 2014.

[156] J. M. Hyde, M. G. Burke, G. D. Smith, P. Styman, H. Swan, and K. Wilford, "Uncertainties and assumptions associated with APT and SANS characterisation of irradiation damage in RPV steels," Journal of Nuclear Materials, vol. 449, pp. 308–314, 6 2014.

[157] M. K. Miller, B. D. Wirth, and G. R. Odette, "Precipitation in neutron-irradiated Fe–Cu and Fe–Cu–Mn model alloys: a comparison of APT and SANS data," Materials Science and Engineering: A, vol. 353, pp. 133–139, 7 2003.

[158] C. Abromeit, "Aspects of simulation of neutron damage by ion irradiation," Journal of Nuclear Materials, vol. 216, pp. 78–96, 10 1994.

[159] Q. Chen, R. Hu, D. Mu, S. Jin, F. Xue, and G. Sha, "Irradiation-induced clustering in a Fe-Mn-Si alloy at different doses and temperatures," Journal of Nuclear Materials, vol. 557, p. 153237, 12 2021.

[160] J. Jiang, Y. C. Wu, X. B. Liu, R. S. Wang, Y. Nagai, K. Inoue, Y. Shimizu, and T. Toyama, "Microstructural evolution of RPV steels under proton and ion irradiation studied by positron annihilation spectroscopy," Journal of Nuclear Materials, vol. 458, pp. 326–334, 2015.

[161] "James Ziegler - SRIM & TRIM." SRIM 2013, available at:http://srim.org/.

[162] S. J. Jepeal, L. Snead, and Z. S. Hartwig, "Intermediate energy proton irradiation: Rapid, high-fidelity materials testing for fusion and fission energy systems," Materials & Design, vol. 200, p. 109445, 2 2021.

[163] R. E. Stoller, "Evaluation of neutron energy spectrum effects and RPV thru-wall attenuation based on molecular dynamics cascade simulations," Nuclear Engineering and Design, vol. 195, pp. 129–136, 2 2000.

[164] ASTM, "E521-25 Standard Practice for Investigating the Effects of Neutron Radiation Damage Using Charged-Particle Irradiation 1,"

[165] R. E. Stoller, M. B. Toloczko, G. S. Was, A. G. Certain, S. Dwaraknath, and F. A. Garner, "On the use of SRIM for computing radiation damage exposure," Nuclear Instruments and Methods in Physics Research, Section B: Beam Interactions with Materials and Atoms, vol. 310, pp. 75–80, 2013.

[166] R. E. Stoller, M. B. Toloczko, G. S. Was, A. G. Certain, S. Dwaraknath, and F. A. Garner, "Erratum: (On the use of SRIM for computing radiation damage exposure (2013) 310 (75–80), (S0168583X13005053), (10.1016/j.nimb.2013.05.008))," Nuclear Instruments and Methods in Physics Research, Section B: Beam Interactions with Materials and Atoms, vol. 459, pp. 196–197, 11 2019.

[167] M. J. Norgett, M. T. Robinson, and I. M. Torrens, "A proposed method of calculating displacement dose rates," Nuclear Engineering and Design, vol. 33, pp. 50–54, 8 1975.

[168] "11.7 Applications of Magnetic Forces and Fields - University Physics Volume 2 | OpenStax." Available at : `https://openstax.org/books/university-physics-volume-2/pages/11-7-applications-of-magnetic-forces-and-fields`, accessed 05/08/2024.

[169] E. Young, "Advanced scattering techniques for the investigation of radiation-induced damage in nuclear materials," 2021.

[170] N. Soppera, M. Bossant, and E. Dupont, "JANIS 4: An improved version of the NEA Java-based nuclear data information system," Nuclear Data Sheets, vol. 120, pp. 294–296, 2014.

[171] R. F. Egerton and M. Watanabe, "Spatial resolution in transmission electron microscopy," Micron, vol. 160, p. 103304, 9 2022.

[172] D. B. Williams and C. B. Carter, "Lenses, Apertures and Resolution," in Transmission Electron Microscopy, vol. 1, ch. 6, pp. 91–114, 2nd ed., 2009.

[173] D. B. Williams and C. B. Carter, "The Instrument," in Transmission Electron Microscopy, pp. 141–171, Boston, MA: Springer, Boston, MA, 2009.

[174] T. Fisher Scientific Technical Publications Hillsboro, "Talos Basic General Information," tech. rep., 2002.

[175] J. Schindelin, I. Arganda-Carreras, E. Frise, V. Kaynig, M. Longair, T. Pietzsch, S. Preibisch, C. Rueden, S. Saalfeld, B. Schmid, J. Y. Tinevez, D. J. White, V. Hartenstein, K. Eliceiri, P. Tomancak, and A. Cardona, "Fiji: an open-source platform for biological-image analysis," Nature Methods 2012 9:7, vol. 9, pp. 676–682, 6 2012.

[176] J. K. Cockcroft and L. M. D. Cranswick, "Single Crystal 5," 2024.

[177] P. B. Hirsch, A. Howie, R. B. Nicholson, D. W. Pashley, M. J. Whelan, and L. Marton, "Electron Microscopy of Thin Crystals," Physics Today, vol. 19, pp. 93–95, 10 1966.

[178] D. B. Williams and C. B. Carter, "Obtaining CBED Patterns," in Transmission Electron Microscopy: A Textbook for Materials Science, pp. 301–318, Springer US, 2009.

[179] Y. U. Heo, "Comparative study on the specimen thickness measurement using EELS and CBED methods," Applied Microscopy, vol. 50, pp. 1–7, 12 2020.

[180] ThermoFisher Scientific, "Transmission Electron Microscopy | Velox Software - UK."

[181] D. B. Williams and C. B. Carter, "X-ray Spectrometry," in Transmission Electron Microscopy, vol. 4, ch. 32, pp. 581–603, Springer, 2nd ed., 2009.

[182] "Atom Probe Tomography - Introduction to the technique." Available at: `https://www.cameca.com/products/apt/technique`, accessed 02/05/2024.

[183] "Atom Probe Tomography sample prep using Plasma FIB technology Microstructural characterization for materials analysis APPLICATION NOTE,"

[184] Baptiste Gault, Michael P. Moody, Julie M. Cairney, and Simon P. Ringe, "Atom Probe Microscopy," p. 33.

[185] B. Gault, M. P. Moody, J. M. Cairney, and S. P. Ringer, "Atom Probe Microscopy," in Atom Probe Microscopy, vol. 160, ch. 7.2.1.1, p. 167, New York, NY: Springer New York, 2012.

[186] B. Gault, F. De Geuser, L. T. Stephenson, M. P. Moody, B. C. Muddle, and S. P. Ringer, "Estimation of the reconstruction parameters for atom probe tomography," Microscopy and Microanalysis, vol. 14, pp. 296–305, 8 2008.

[187] Andrew J. London, "AtomProbeLab," 2023.

[188] A. J. London, "Quantifying Uncertainty from Mass-Peak Overlaps in Atom Probe Microscopy," 2019.

[189] "Appendix H: Kingham Curves," in Atom Probe Microscopy, vol. 160, pp. 256–362, 2012.

[190] "Atomic Weights and Isotopic Compositions for All Elements."

[191] O. C. Hellman, J. A. Vandenbroucke, J. Rüsing, D. Isheim, and D. N. Seidman, "Analysis of Three-dimensional Atom-probe Data by the Proximity Histogram," Microscopy and Microanalysis, vol. 6, pp. 437–444, 9 2000.

[192] T. Philippe, F. De Geuser, S. Duguay, W. Lefebvre, O. Cojocaru-Mirédin, G. Da Costa, and D. Blavette, "Clustering and nearest neighbour distances in atom-probe tomography," Ultramicroscopy, vol. 109, pp. 1304–1309, 9 2009.

[193] A. Guinier, G. Fournet, C. B. Walker, and N. York, "SMALL-ANGLE SCATTERING OF X-RAYS," 1955.

[194] C. M. Jeffries, Z. Pietras, and D. I. Svergun, "The basics of small-angle neutron scattering (SANS for new users of structural biology)," EPJ Web of Conferences, vol. 236, 2020.

[195] G. J. Long, "2.6 Neutron Diffraction," in Comprehensive Coordination Chemistry II, pp. 83–90, 2003.

[196] G. KOSTORZ, "Small-Angle Scattering and Its Applications to Materials Science," vol. 15, pp. 227–289, Elsevier, 1 1979.

[197] P. Spätig, R. Schäublin, N. Baluc, J. Kohlbrecher, and M. Victoria, "SANS investigation of proton-irradiated EUROFER97," in Journal of Nuclear Materials, vol. 329-333, pp. 289–293, North-Holland, 8 2004.

[198] J. Van Den Bosch, O. Anderoglu, R. Dickerson, M. Hartl, P. Dickerson, J. A. Aguiar, P. Hosemann, M. B. Toloczko, and S. A. Maloy, "SANS and TEM of ferritic-martensitic steel T91 irradiated in FFTF up to 184 dpa at 413 °c," Journal of Nuclear Materials, vol. 440, no. 1-3, pp. 91–97, 2013.

[199] B. Hammouda, "PROBING NANOSCALE STRUCTURES-THE SANS TOOLBOX," tech. rep.

[200] "Neutron Scattering Lengths List | NIST." Available at: `https://www.nist.gov/ncnr/neutron-scattering-lengths-list`, accessed 17/05/2024.

[201] M. Fitzsimmons and C. Majkzak, "Application of polarized neutron reflectometry to studies of artificially structured magnetic materials," in Modern Techniques for Characterizing Magnetic Materials, pp. 107–155, Springer, Boston, MA, 10 2005.

[202] S. Muhlbauer, D. Honecker, E. A. Perigo, F. Bergner, S. Disch, A. Heinemann, S. Erokhin, D. Berkov, C. Leighton, M. R. Eskildsen, and A. Michels, "Magnetic small-angle neutron scattering," Reviews of Modern Physics, vol. 91, 3 2019.

[203] C. D. Dewhurst, I. Grillo, D. Honecker, M. Bonnaud, M. Jacques, C. Amrouni, A. Perillo-Marcone, G. Manzin, and R. Cubitt, "The small-angle neutron scattering instrument D33 at the Institut Laue–Langevin," urn:issn:1600-5767, vol. 49, pp. 1–14, 2 2016.

[204] "Instrument layout - ILL Neutrons for Society." Available at `{https://www.ill.eu/users/instruments/instruments-list/d33/description/instrument-layout}, accessed17/04/2024`.

[205] "Grasp - ILL Neutrons for Society." Available at : https://www.ill.eu/users/support-labs-infrastructure/software-scientific-tools/grasp, accessed 05/07/2021.

[206] "SasView - Small Angle Scattering Analysis." Available at : https://www.sasview.org/, accessed 30/05/2024.

[207] B. Hammouda, "A new Guinier–Porod model," urn:issn:0021-8898, vol. 43, pp. 716–719, 5 2010.

[208] J. Crangle and G. M. Goodman, "The magnetization of pure iron and nickel," Proceedings of the Royal Society of London. A. Mathematical and Physical Sciences, vol. 321, pp. 477–491, 3 1971.

[209] C. P. Harmer, S. Kamali, O. I. Lebedev, S. J. Lee, R. A. Ribeiro, P. C. Canfield, and K. Kovnir, "Pseudo-Polymorphism in Layered FeS Intercalates: A Competition between Charged and Neutral Guest Species," Chemistry of Materials, vol. 34, pp. 5397–5408, 6 2022.

[210] J. Ilavsky and P. R. Jemian, "Irena: tool suite for modelling and analysis of small-angle scattering," Journal of Applied Crystallography, vol. 42, pp. 347–353, 2009.

[211] NIST, "• SANS Model Function Documentation," tech. rep.

[212] J. A. Potton, G. J. Daniell, and B. D. Rainford, "Particle size distributions from SANS data using the maximum entropy method," Journal of Applied Crystallography, vol. 21, pp. 663–668, 12 1988.

[213] J. A. Potton, G. J. Daniell, and B. D. Rainford, "A New Method for the Determination of Particle Size Distributions from Small-Angle Neutron Scattering Measurements," J. Appl. Cryst, vol. 21, pp. 891–897, 1988.

[214] P. R. Jemian, J. R. Weertman, G. G. Long, and R. D. Spal, "Characterization of 9Cr-1MoVNb steel by anomalous small-angle X-ray scattering," Acta Metallurgica et Materialia, vol. 39, pp. 2477–2487, 11 1991.

[215] P. Sudharshan Phani and W. C. Oliver, "A critical assessment of the effect of indentation spacing on the measurement of hardness and modulus using instrumented indentation testing," Materials & Design, vol. 164, p. 107563, 2 2019.

[216] "TI 950 TriboIndenter User Manual," 2014.

[217] W. Oliver and G. Pharr, "An improved technique for determining hardness and elastic modulus using load and displacement sensing indentation experiments," Journal of Materials Research, vol. 7, pp. 1564–1583, 6 1992.

[218] A. C. Fischer-Cripps, "Other Techniques in Nanoindentation," in Nanoindentation, ch. 9, pp. 163–178, Springer, 3rd ed., 2011.

[219] A. Jacob, C. Domain, G. Adjanor, P. Todeschini, and E. Povoden-Karadeniz, "Thermodynamic modeling of G-phase and assessment of phase stabilities in reactor pressure vessel steels and cast duplex stainless steels," Journal of Nuclear Materials, vol. 533, p. 152091, 5 2020.

[220] X. Liu, C. Liu, J. Wu, X. Zhang, X. Zhu, and J. Wang, "Morphological instability of the G-phase induced a different contribution to hardening of ferrite phase in a duplex stainless steel," Materials Science and Engineering: A, vol. 832, p. 142421, 1 2022.

[221] G. Kurdjumov and G. Sachs, "Crystallographic orientation relationship between α-and γ-Fe," Annales de physique., vol. 64, p. 325, 1930.

[222] D. Zagorac, H. Müller, S. Ruehl, J. Zagorac, and S. Rehme, "Recent developments in the Inorganic Crystal Structure Database: theoretical crystal structure data and related features," J. Appl. Cryst, vol. 52, pp. 918–925, 2019.

[223] S. J. Ahmed, J. E. Greedan, C. Boyer, and M. Niewczas, "Magnetic and Structural Studies of G-Phase Compound Mn6Ni16Si7," Inorganic Chemistry, vol. 57, pp. 14144–14151, 11 2018.

[224] B. Pimentel, V. M. Andrade, V. G. Paula, K. R. Pirota, F. Béron, M. A. Cardoso, J. N. Gonçalves, J. S. Amaral, A. M. Santos, and M. S. Reis, "Cubic to hexagonal tuning in

Fe2Mn(Si1−xGex) Heusler alloys," Journal of Alloys and Compounds, vol. 893, p. 162236, 2 2022.

[225] Y. Babanova, P. Gel'd, F. Sidorenko, and N. Basov, "Ordering of solid solutions (fe1-x mnx)3 si.," Physics of Metals and Metallography 38, pp. 122–126, 1974.

[226] Y. Kuz'ma, E. Gladyshevskii, and E. Cherkashin, " The Mn-Ni-Si system," Russian Journal of Inorganic Chemistry, vol. 9, no. 8, pp. 1028–1031, 1964.

[227] J. Häusler, R. Niklaus, J. Minár, and W. Schnick, "Ammonothermal Synthesis and Optical Properties of Ternary Nitride Semiconductors Mg-IV-N2 , Mn-IV-N2 and Li-IV2 -N3 (IV=Si, Ge)," Chemistry (Weinheim an der Bergstrasse, Germany), vol. 24, pp. 1686–1693, 2 2018.

[228] N. C. Siersch, G. Criniti, A. Kurnosov, K. Glazyrin, and D. Antonangeli, "Thermal equation of state of Fe3O4 magnetite up to 16 GPa and 1100 K," American Mineralogist, vol. 108, pp. 1322–1329, 7 2023.

[229] X. Yan, A. Grytsiv, P. Rogl, V. Pomjakushin, and X. Xue, "On the crystal structure of the Mn–Ni–Si G-phase," Journal of Alloys and Compounds, vol. 469, pp. 152–155, 2 2009.

[230] F. J. G. Landgraf, J. R. F. Da Silveira, and D. Rodrigues-Jr., "Determining the effect of grain size and maximum induction upon coercive field of electrical steels," Journal of Magnetism and Magnetic Materials, vol. 323, pp. 2335–2339, 10 2011.

[231] J. F. Löffler, H. B. Braun, W. Wagner, G. Kostorz, and A. Wiedenmann, "Crossover in the magnetic properties of nanostructured metals," Materials Science and Engineering: A, vol. 304-306, pp. 1050–1054, 5 2001.

[232] M. Bischof, P. Staron, A. Michels, P. Granitzer, K. Rumpf, H. Leitner, C. Scheu, and H. Clemens, "The influence of spin-misalignment scattering on the SANS data evaluation of martensitic age-hardening steels," Acta Materialia, vol. 55, pp. 2637–2646, 5 2007.

[233] R. Heenan, "Introduction to SANS 1 ISIS Neutron Training Course Introduction to SANS,"

[234] Y. Ji, A. P. Radlinski, T. Blach, L. de Campo, P. Vu, H. Roshan, and K. Regenauer-Lieb, "How to avoid multiple scattering in strongly scattering SANS and USANS samples," Fuel, vol. 325, p. 124957, 10 2022.

[235] J. R. D. Copley, "Dynamics and Neutron Scattering,"

[236] E. Aydogan, J. G. Gigax, S. S. Parker, B. P. Eftink, M. Chancey, J. Poplawsky, and S. A. Maloy, "Nitrogen effects on radiation response in 12Cr ferritic/martensitic alloys," Scripta Materialia, vol. 189, pp. 145–150, 12 2020.

[237] B. M. Jenkins, A. Zakirov, F. Vurpillot, A. Etienne, C. Pareige, P. Pareige, and B. Radiguet, "On the Iron Content of Mn-Ni-Si-rich Clusters That Form in Reactor Pressure Vessel Steels During Exposure to Neutron Irradiation," Acta Materialia, p. 120384, 9 2024.

[238] D. J. King, P. A. Burr, S. C. Middleburgh, T. M. Whiting, M. G. Burke, and M. R. Wenman, "The formation and structure of Fe-Mn-Ni-Si solute clusters and G-phase precipitates in steels," Journal of Nuclear Materials, vol. 505, pp. 1–6, 7 2018.

[239] Y. Matsukawa, T. Takeuchi, Y. Kakubo, T. Suzudo, H. Watanabe, H. Abe, T. Toyama, and Y. Nagai, "The two-step nucleation of G-phase in ferrite," Acta Materialia, vol. 116, pp. 104–113, 9 2016.

[240] M. Yang, D. J. M. King, I. Povstugar, Y. Wen, J. Luan, B. Kuhn, Z. Jiao, C. Wang, M. R. Wenman, and X. Liu, "Precipitation behavior in G-phase strengthened ferritic stainless steels," Acta Materialia, vol. 205, p. 116542, 2021.

[241] B. Schwarz, S. R. Meka, R. E. Schacherl, E. Bischoff, and E. J. Mittemeijer, "Nitriding of iron-based ternary Fe–V–Si alloy: The precipitation process of separate nitrides," Acta Materialia, vol. 76, pp. 394–403, 9 2014.

[242] K. P. Gupta, "The Mn-Ni-Si (manganese-nickel-silicon) system," Journal of Phase Equilibria and Diffusion, vol. 27, pp. 529–534, 10 2006.

[243] M. Kolenda, A. Szytuła, J. Leciejewicz, and C. Maletka, "Magnetic properties of Mn6Ni16Si7 and Mn3Cr3Ni16Si7," Journal of Magnetism and Magnetic Materials, vol. 96, pp. 121–124, 6 1991.

[244] S. K. Adhikari, R. Roy, S. C. Das, J. Sannigrahi, S. Pramanick, S. Chattopadhyay, C. Ritter, D. T. Adroja, and S. Chatterjee, "Ni-doping assisted modification of the non-collinear antiferromagnetic ordering in Mn5Si3 alloy," Journal of Alloys and Compounds, vol. 967, p. 171752, 12 2023.

[245] C. B. Shoemaker, D. P. Shoemaker, T. E. Hopkins, and S. Yindepit, "Refinement of the Structure offl-Manganese and of a Related Phase in the Mn-Ni-Si System*," Aeta Cryst, vol. 34, pp. 3573–3576, 1978.

[246] M. Große, A. Gokhman, and J. Böhmert, "Dependence of the ratio between magnetic and nuclear small angle neutron scattering on the size of the heterogeneities," Nuclear Instruments and Methods in Physics Research Section B: Beam Interactions with Materials and Atoms, vol. 160, pp. 515–520, 4 2000.

[247] S. Esmaeilzadeh, U. Hålenius, and M. Valldor, "Crystal growth, magnetic, and optical properties of the ternary nitride MnSiN2," Chemistry of Materials, vol. 18, pp. 2713–2718, 5 2006.

[248] W. Roberts, P. Grieveson, and K. Jack, "Precipitation of silicon nitrides and manganese-silicon nitrides in steel," Journal of the Iron and Steel Institute, vol. 210, pp. 931–937, 12 1972.

[249] T. Shiraiwa, Y. Sakamoto, and N. Fujino, "Identification of New Manganese-Silicon-Nitride in Steel by Electron Probe Microanalyser," Japanese Journal of Applied Physics, Part 1: Regular Papers and Short Notes and Review Papers, vol. 6, no. 8, pp. 1025–1026, 1967.

[250] D. Shinoda and S. Asanabe, "Magnetic Properties of Silicides of Iron Group Transition Elements," Journal of the Physical Society of Japan, vol. 21, no. 3, p. 555, 1966.

[251] S. Wires, T. Baumgartner, M. Eisterer, and H. W. Weber, "Irradiation Induced Modifications in Magnetic Property of Mn/n-Si Structure You may also like Effects of neutron irradiation on pinning force scaling in state-of-the-art Nb," J. Phys.: Conf. Ser, vol. 266, p. 12126, 2011.

[252] N. Akdogan, A. Nefedov, H. Zabel, A. B. Drovosekov, N. M. Kreines, A. O. Savitsky, Q. Feng, W. Dizayee, X. Li, S. H. Song, M. H. Jung, S. H. Lim, and M. Opel, "High temperature magnetism and microstructure of ferromagnetic alloy Si 1−x Mn x Magnetic anisotropy peculiarities of high-temperature ferromagnetic MnxSi1x (x 0.5) alloy films Enhanced magnetic properties in ZnCoAlO caused by exchange-coupling to Co nanoparticles Magnetic phases in Ge-Fe thin films containing high Fe content Spintronic oxides grown by laser-MBE," 2016.

[253] K. Hammura, H. Udono, and T. Aono, "Solid evidence for magnetic moment enhancement in micro-particles of Mn11Si19," physica status solidi (c), vol. 10, pp. 1735–1738, 12 2013.

[254] Songlin, Dagula, O. Tegus, E. Brück, J. C. Klaasse, F. R. De Boer, and K. H. Buschow, "Magnetic phase transition and magnetocaloric effect in Mn5−xFexSi3," Journal of Alloys and Compounds, vol. 334, pp. 249–252, 2 2002.

[255] M. A. Haddouch, N. Abboushi, N. Sharma, A. Eich, A. Grzechnik, C. Li, M. Tolkiehn, H. Alsamamra, J. Voigt, and K. Friese, "Site dependence of the magnetocaloric effect in Mn5–xFexSi3," Journal of Applied Crystallography, vol. 55, pp. 1164–1172, 10 2022.

[256] B. Das, B. Balasubramanian, P. Manchanda, P. Mukherjee, R. Skomski, G. C. Hadjipanayis, and D. J. Sellmyer, "Mn5Si3 Nanoparticles: Synthesis and Size-Induced Ferromagnetism," Nano letters, vol. 16, pp. 1132–1137, 2 2016.

[257] S. Asano and S. Ishida, "Electronic and Magnetic Properties of X2Mn1-xVxSi (X=Fe and Co)," http://dx.doi.org/10.1143/JPSJ.63.1881, vol. 63, pp. 1881–1888, 11 2013.

[258] J. V. Leitão, Y. Xinmin, L. Caron, and E. Brück, "Magnetostructural study of the (Mn,Fe)3(P,Si) system," Journal of Alloys and Compounds, vol. 520, pp. 52–58, 4 2012.

[259] R. J. Caraballo Vivas, S. S. Pedro, C. Cruz, J. C. Tedesco, A. A. Coelho, A. M. G. Carvalho, D. L. Rocco, and M. S. Reis, "Experimental evidences of enhanced magnetocaloric properties at room temperature and half-metallicity on Fe2MnSi-based Heusler alloys," Materials Chemistry and Physics, vol. 174, pp. 23–27, 5 2016.

[260] M. Mamivand, P. Wells, H. Ke, S. Shu, G. R. Odette, and D. Morgan, "CuMnNiSi precipitate evolution in irradiated reactor pressure vessel steels: Integrated Cluster Dynamics and experiments," Acta Materialia, vol. 180, pp. 199–217, 11 2019.

[261] G. Bonny, D. Terentyev, A. Bakaev, E. E. Zhurkin, M. Hou, D. Van Neck, and L. Malerba, "On the thermal stability of late blooming phases in reactor pressure vessel steels: An atomistic study," Journal of Nuclear Materials, vol. 442, pp. 282–291, 11 2013.

[262] G. Bonny, A. Bakaev, P. Olsson, C. Domain, E. E. Zhurkin, and M. Posselt, "Interatomic potential to study the formation of NiCr clusters in high Cr ferritic steels," Journal of Nuclear Materials, vol. 484, pp. 42–50, 2 2017.

[263] J. Stein, R. E. Schacherl, M. Jung, S. Meka, B. Rheingans, and E. J. Mittemeijer, "Solubility of nitrogen in ferrite; The Fe-N phase diagram," International Journal of Materials Research, vol. 104, pp. 1053–1065, 11 2013.

[264] W. D. Callister and D. G. Reithwisch, "Chapter 7 Diffusion," in MaterialsScienceandEngineering, pp. 180–207, Wiley, 9th ed., 2015.

[265] K. Swift and J. Booker, "Surface Engineering Processes," in Manufacturing Process Selection Handbook, pp. 243–280, Elsevier, 2013.

[266] E. Wolowiec-Korecka, J. Michalski, and B. Kucharska, "Kinetic aspects of low-pressure nitriding process," Vacuum, vol. 155, pp. 292–299, 9 2018.

[267] P. M. Rice and R. E. Stoller, "The effect of solutes on defect distributions and hardening in ion-irradiated model ferritic alloys," Journal of Nuclear Materials, vol. 244, pp. 219–226, 4 1997.

[268] S. C. Yeo, S. S. Han, and H. M. Lee, "Adsorption, dissociation, penetration, and diffusion of N2 on and in bcc Fe: first-principles calculations," Physical Chemistry Chemical Physics, vol. 15, pp. 5186–5192, 3 2013.

[269] T. Steiner and E. J. Mittemeijer, "Alloying Element Nitride Development in Ferritic Fe-Based Materials Upon Nitriding: A Review," Journal of Materials Engineering and Performance, vol. 25, pp. 2091–2102, 2016.

[270] F. Weitzer and J. C. Schuster, "Phase diagrams of the ternary systems Mn, Fe, Co, Ni Si N," Journal of Solid State Chemistry, vol. 70, pp. 178–184, 10 1987.

[271] S. R. Meka, K. S. Jung, E. Bischoff, and E. J. Mittemeijer, "Unusual precipitation of amorphous silicon nitride upon nitriding Fe–2at.%Si alloy," Philosophical Magazine, vol. 92, pp. 1435–1455, 4 2012.

[272] H. P. Van Landeghem, M. Gouné, S. Bordère, F. Danoix, and A. Redjaïmia, "Competitive precipitation of amorphous and crystalline silicon nitride in ferrite: Interaction between structure, morphology, and stress relaxation," Acta Materialia, vol. 93, pp. 218–234, 7 2015.

[273] S. Gašparová, V. Kršjak, P. Noga, J. Šoltés, M. Mikloš, Y. Song, M. Petriska, S. Sojak, D. Vaňa, Z. Száraz, B. Stríbrnský, R. Hinca, T. Shen, and J. Degmová, "Positron annihilation spectroscopy evaluation of using proton irradiation as a surrogate for early neutron radiation damage," Journal of Nuclear Materials, vol. 596, p. 155111, 8 2024.

[274] J. Xue, R. Hu, G. Bai, J. Mei, F. Xue, and G. Sha, "Temperature-Dependent Irradiation-Induced Clustering in a Fe–Mn–Ni Alloy," Metallurgical and Materials Transactions A: Physical Metallurgy and Materials Science, vol. 52, pp. 4264–4274, 9 2021.

[275] H. J. Spies and A. Dalke, "Case Structure and Properties of Nitrided Steels," Comprehensive Materials Processing: Thirteen Volume Set, vol. 12, pp. 12–439, 1 2014.

[276] M. Vrellou, "Atom Probe Tomography and in-situ micro-compression coupling for understanding the mechanisms involved in hardening of neutron irradiated ferritic model alloys," 3 2023.

[277] R. E. Stoller and S. J. Zinkle, "On the relationship between uniaxial yield strength and resolved shear stress in polycrystalline materials," Journal of Nuclear Materials, vol. 283-287, no. PART I, pp. 349–352, 2000.

[278] F. Gao, R. L. Johnston, and J. N. Murrell, "Empirical many-body potential energy functions for iron," Journal of Physical Chemistry, vol. 97, no. 46, pp. 12073–12082, 1993.

[279] J. T. Busby, M. C. Hash, and G. S. Was, "The relationship between hardness and yield stress in irradiated austenitic and ferritic steels," Journal of Nuclear Materials, vol. 336, pp. 267–278, 2 2005.

[280] D. Terentyev, X. He, G. Bonny, A. Bakaev, E. Zhurkin, and L. Malerba, "Hardening due to dislocation loop damage in RPV model alloys: Role of Mn segregation," Journal of Nuclear Materials, vol. 457, pp. 173–181, 2 2015.

[281] L. Lai, J. E. Brandenburg, P. Chekhonin, A. Duplessi, F. Cuvilly, A. Etienne, B. Radiguet, D. Rafaja, and F. Bergner, "Microstructure-Informed Prediction of Hardening in Ion-Irradiated Reactor Pressure Vessel Steels," Metals 2024, Vol. 14, Page 257, vol. 14, p. 257, 2 2024.

[282] F. Bergner, F. Gillemot, M. Hernández-Mayoral, M. Serrano, G. Török, A. Ulbricht, and E. Altstadt, "Contributions of Cu-rich clusters, dislocation loops and nanovoids to the irradiation-induced hardening of Cu-bearing low-Ni reactor pressure vessel steels," Journal of Nuclear Materials, vol. 461, pp. 37–44, 6 2015.

[283] M. Fedorov, J. S. Wróbel, A. J. London, K. J. Kurzydłowski, C. C. Fu, T. Tadić, S. L. Dudarev, and D. Nguyen-Manh, "Precipitation of Cr-rich clusters in Fe-Cr alloys: Effects of irradiation from first principles modeling and experimental observations," Journal of Nuclear Materials, vol. 587, p. 154715, 12 2023.

[284] C. D. Hardie, C. A. Williams, S. Xu, and S. G. Roberts, "Effects of irradiation temperature and dose rate on the mechanical properties of self-ion implanted Fe and Fe–Cr alloys," Journal of Nuclear Materials, vol. 439, pp. 33–40, 8 2013.

[285] D. M. Hata, E. V. Brewer, and N. J. Louwagie, “CHAPTER 3: An Introduction to Vacuum Systems.”

[286] G. Was, O. Toader, T. Kubley, and R. Hensley, “Michigan Ion Beam Laboratory Annual Research Report,” tech. rep., University of Michigan, Ann Arbor, 2021.

Appendix A

Appendices

A.1 SANS Experimental Proposal- D33, ILL

Characterising Irradiation Induced Mn-Ni-Si Precipitates in Low Cu Steels for Generation III Reactor Pressure Vessel Steels

Background

With many Generation II light-water cooled nuclear reactors (Pressurised Water Reactors and Boiling Water Reactors) approaching the end of their design lives, there is an increasing need for accurate prediction models of Reactor Pressure Vessel (RPV) mechanical properties. Over the design lifetime of an RPV, ~40 years (for generation II reactors) the damage accumulated due to neutron irradiation is generally of the order of 0.1dpa (displacements per atom).[2] Displacements of atoms in the lattice by neutron bombardment increase the rate of diffusion in the steel enabling the formation of various microstructural defects. These have significant effects on the bulk mechanical properties of the steel, reduction in fracture toughness and strength and an increase in hardening and embrittlement. [1] (See Figure 1.) The ability to create accurate fracture toughness models based on understanding of defect formation mechanisms will enable safe lifetime extensions of existing RPVs, providing secure electricity production continuity and reducing the overall environmental impact of the plant.

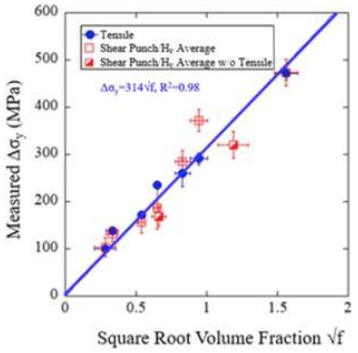


Figure 1-Graph showing the effect of irradiation induced precipitate volume fraction in RPV steels on the increase in hardness.[1](Figure 5)

Key defects induced by irradiation comprise matrix effects, such as vacancy and self-interstitial clusters, precipitates, and segregation of solute atoms to grain boundaries and dislocations.[3] As the wt.% of Copper has decreased in RPV steels the effect of Mn-Ni-Si rich precipitate evolution on mechanical properties has gained interest. Compared with copper rich precipitates, Mn-Ni-Si precipitates show smaller average sizes and narrower size distribution.[4] They also only reach measurable sizes (nm) in samples exposed to high radiation fluence which has resulted in them being referred to as “late-blooming”.[5]

Previous work in the field disagrees on whether Mn-Ni-Si precipitates are stable thermodynamic phases. Some studies claim they form stable G and Γ_2 Mn-Ni-Si phases after high fluence irradiation [6]. Others claim the precipitates nucleate at low fluence, are metastable and grow at high fluences. [7] Precipitates have been found in alloys where elements are present in lower wt.% content than the solid solubility limits at irradiation temperature; suggesting they are not thermodynamically stable. Determination of the structure and stability of these phases is essential to investigating the possibility of using annealing for irradiation damage recovery of RPVs as well as for prediction of properties.

Previous Related Work

Figure 2 shows the results of a preliminary test measurement performed on D22 on RPV low alloy steel during an unrelated experiment in 2019. A non-saturating magnetic field was applied at the sample position to separate magnetic and nuclear scattering components. The irradiated sample shows a larger difference in magnetic and nuclear scattering and tentative fits resolve precipitates of 3 nm radius with a magnetic to nuclear scattering ratio of 2.7. A similar method will be applied to measurements in the experiments proposed below.

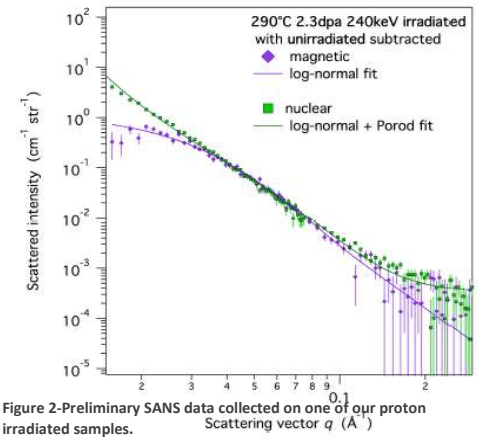


Figure 2-Preliminary SANS data collected on one of our proton irradiated samples.

Aims of the Study

This project aims to;

- Characterise the size distributions of Mn-Ni-Si precipitates in model alloys.
- Understand the formation and evolution of Mn-Ni-Si precipitates at different fluences.

Figure A.1: Proposal submitted for SANS beamtime p1.

- To quantify the effects of different solute concentrations on the acceleration of Mn-Ni-Si precipitate nucleation and growth.

After SANS, the samples will be analysed using complementary techniques (APT, TEM, nano-indentation) to investigate local characteristics of the microstructural effects of radiation. These data will provide insight into mechanisms of precipitate formation in Mn, Si and Ni containing steels. This will enhance understanding of the mechanisms of RPV embrittlement and provide crucial missing data for databases, used in thermodynamic modelling software such as CALPHAD. It will provide grounding for future studies of post-irradiation in-situ SANS annealing of irradiated samples at elevated temperatures to further investigate the stability of Mn-Ni-Si precipitates in RPV steels. The results from these experiments will indicate whether annealing can be used to provide irradiation damage recovery for low alloy RPVs without removing them from service.

Proposed experiment

We plan to measure 15 samples using the D33 instrument. The samples comprise 4 model alloy steels of varying Mn, Ni and Si content (Figure 3) and an A508-3 RPV steel (wt.%C-0.17, Cu-0.03, Ni-0.74, Mn-1.35, Si-0.19, Mo-0.48, P-0.005, S-0.002, Cr-0.09, V-0.007). Three each of these; an unirradiated, tempered sample and two samples of each irradiated with 2-3MeV to simulation different fluences at ~300 ̊C will be measured. Irradiation of samples will be carried out using a proton beam (MC40 Cyclotron, University of Birmingham) to simulate neutron damage. Proton damage has been shown to provide similar effects on the microstructure of alloys to neutron irradiation in much shorter irradiation times. Protons have a significantly smaller penetration depth than neutrons and as a result the proton flux and sample depth with be selected so that the expected Primary Knock-on Atom energy and damage cascade formation occurs in the appropriate sample volume. It is possible to induce damage expected to occur due to neutron irradiation over the lifetime of a light water reactor pressure vessel over the course of a few days using protons on a small sample. Fluences will be approximately 0.1dpa and 0.2dpa to simulate the radiation effects after approximately 40 years and 80 years.

Sample	Mn	Ni	Si
1	1.35	0.75	-
2	1.35	-	0.20
3	-	0.75	0.20
4	1.35	0.75	0.20

Figure 3- Table showing the compositions in wt.% of the Fe-Mn-Ni-Si model alloys to be measured in this project.

Samples will be mounted on a vertical sample changer and a horizontal saturating magnetic field (1 T) applied perpendicular to the neutron beam to separate magnetic and nuclear scattering components and provide information on the composition of the precipitates. Unirradiated samples will have been tempered at the same temperature as irradiation took place to provide a control for thermal effects on precipitation. Comparison of scattering data between different compositions and damage fluences will enable an assessment of the effects of different Mn-Ni-Si content in the steels in terms of precipitate size and distribution across the bulk of the samples. The A508-3 steel will give an indication of the effects of long-term irradiation damage on current RPV material. Comparing the results with the model alloys will enable the quantification of the effect of a small Cu wt.% on the acceleration of precipitation and growth of Mn-Ni-Si precipitates.

The preliminary data in Figure 2 were collected over 2hrs each for an unirradiated and irradiated sample on D33 over 2 detector distances. For similar samples, better statistics will be required in the high q range and the overall q range should be extended to lower q and higher q to probe the nuclear incoherent scattering. As such longer measurement times will be required; 3.5 to 5 hours per sample depending on the anticipated strength of the Mn-Ni-Si precipitates scattering signal. More time will be necessary to obtain sufficient scattering intensity from samples irradiated to lower fluence as precipitates will be smaller and have lower number density. The neutron flux and magnetic field provided by D33 will enable measurements with scattering statistics of sufficient quality to identify precipitation in the irradiated samples even where the number density of precipitates is low. Therefore, we ask for 3 days on the D33 instrument including time for background (air scattering and Cd) measurements.

This proposal forms an essential part of the PhD thesis of Alexandra Dickinson-Lomas.

1. N.Almirall et al., Acta Materialia, 119-128. (2019)
2. J.C.van Duysen and G. Meric de Bellefon, Journal of Nuclear Materials, 484, p. 209-227. (2017)
3. W.J.Phythian, C.A.English, Journal of Nuclear Materials, 205, p. 162-177. (1993)
4. M. Hernández-Mayoral and D. Gomez-Briceno, Journal of Nuclear Materials, 399, p. 146-153. (2010)
5. Yabuuchi et al., Journal of Nuclear Materials, 414, p. 498-502. (2011)
6. PB. Wells et al., Acta Materialia, 80, p. 205-219. (2014)
7. Ngayam-Happy, B., Domain, Malerba.,. Journal of Nuclear Materials, 426,: p. 198-207. (2012)

Figure A.2: Proposal submitted for SANS beamtime p2.

A.2 SANS D33 Supplementary Experimental Information

- 6AA settings summary
- Source aperture=30 mm x 30 mm square
- Sample aperture=9 mm diameter circle

Table A.1: Table of D33 instrument settings used for low, medium and high Q ranges and transmission measurements.

	HQTr	HQ	LQTr	LQ	MQTr	MQ
Att	2	0	2	0	2	0
Att factor	447	1	447	1	447	1
Det1 (m)	1.2	1.2	12.2	12.2	4.7	4.7
Det2 (m)	2	2	13	13	5.5	5.5
OyT (mm)	285	285	350	350	350	350
OyB (mm)	300	300	375	375	375	375
OxL (mm)	305	305	375	375	375	375
OxR (mm)	340	340	370	370	370	370
Coll (m)	2.8	2.8	12.8	12.8	5.3	5.3
Bx (mm)	1	1	5	5	3.5	3.5
By (mm)	-320	6.5	-320	-2.5	-320	2

Table A.2: Table showing sample position, thickness and transmission values.

Sample Position	Sample	Thickness(µm)	LQ Transmission 1	LQ Transmission 2	Mean	Error on Mean
1	Fe-Mn-Ni-Si PI	142.67	0.9883	0.9980	0.9932	0.0049
2	Fe-Mn-Ni-Si HT	240.33	0.9807	0.9785	0.9796	0.0011
3	Fe-Mn-Si PI	144.33	0.9896	0.9915	0.9905	0.0010
4	Fe-Mn-Si HT	267.33	0.9796	0.9795	0.97953	2.5E-05
5	Fe-Ni-Si PI	147.33	0.98767	0.99299	0.9903	0.0027
6	Fe-Ni-Si HT	237.67	0.9829	0.9853	0.9841	0.0012
7	Fe-Mn-Ni PI	305.67	0.9745	0.9772	0.9759	0.0014
8	Fe-Mn-Ni HT	264.00	0.9794	0.9806	0.9800	0.0006
2	A508-3 PI		0.9928			
6	A508-3 HT		0.9819			

A.3 Consideration of Sector Angle in Calculation of Magnetic and Nuclear Scattering

When measuring the scattering at 0 degrees (to obtain nuclear component) and 90 degrees (to obtain the total magnetic and nuclear component of scattering) the value extracted using GRASP is an average over a sector angle ϕ for a strip of the sector corresponding to $q+\Delta q$.

If the expression for the expected, or average, value of a function over a given interval is taken to be:

$$\langle f(x)\rangle = \frac{1}{b-a}\int_a^b f(x)\,\mathrm{d}x.$$

and the measured scattering intensity at a fixed value of q is expressed as:

$$I(\alpha) = N + Msin^2(\alpha)$$

where it is assumed that N and M for a given q value are constant values of nuclear scattering intensity and magnetic scattering intensity.

Then the measured value, averaged over the section of a sector with radius from q to $q+\Delta q$ and ϕ can be expressed as

$$\langle I(\alpha)\rangle = \frac{1}{\phi}\int_{\alpha-\frac{\phi}{2}}^{\alpha+\frac{\phi}{2}} N + Msin^2(\alpha)\,\mathrm{d}\alpha.$$

Integrating over the range of $\alpha-\frac{\phi}{2}$ and $\alpha+\frac{\phi}{2}$ which corresponds to the area being averaged using GRASP.

$$\langle I(\alpha)\rangle = \tfrac{1}{\phi}[N\alpha]_{\alpha-\frac{\phi}{2}}^{\alpha+\frac{\phi}{2}} + \tfrac{M}{\phi}[\tfrac{1}{2}(\alpha - \tfrac{1}{2}sin(2\alpha))]_{\alpha-\frac{\phi}{2}}^{\alpha+\frac{\phi}{2}}$$

$$\langle I(\alpha)\rangle = N + \tfrac{M}{2\phi}[\alpha+\tfrac{\phi}{2} - \tfrac{1}{2}sin(2\alpha+\phi) - \alpha + \tfrac{\phi}{2} + \tfrac{1}{2}sin(2\alpha-\phi)]$$

$$\langle I(\alpha)\rangle = N + \tfrac{M}{2\phi}\phi - \tfrac{1}{2}sin(2\alpha+\phi) + \tfrac{\phi}{2}sin(2\alpha-\phi)]$$

As theta is measured only at $\alpha = 0$ = nuclear scattering, and $\alpha = \frac{\pi}{2}$ = total scattering this result can be simplified into two equations:

$$\langle I(\alpha = 0)\rangle = N + \frac{M}{2}[1 - \frac{sin(\phi)}{\phi}] = N_m$$

$$\langle I(\alpha = \frac{\pi}{2})\rangle = N + \frac{M}{2}[1 + \frac{sin(\phi)}{\phi}] = T_m$$

This therefore suggests that the measured average value of intensity deviates from the theoretical values as a function of sector opening angle, ϕ. The values of N and M can be expressed in terms of the measured values and ϕ:

$$N = N_m - \frac{M}{2}(1 - \frac{sin\phi}{\phi})$$

$$\langle I(\alpha = \frac{\pi}{2})\rangle = N + M - \frac{M}{2}[1 - \frac{sin(\phi)}{\phi}] = T - \frac{M}{2}[1 - \frac{sin(\phi)}{\phi}]$$

$$M = T - N = T_m + \frac{M}{2}[1 - \frac{sin(\phi)}{\phi}] - N_m + \frac{M}{2}(1 - \frac{sin\phi}{\phi})$$

$$M = T_m - N_m + M((1 - \frac{sin\phi}{\phi})$$

$$M(1 - 1 + \frac{sin\phi}{\phi}) = T_m - N_m$$

$$M = (T_m - N_m)\frac{\phi}{sin\phi}$$

Therefore, the absolute nuclear and magnetic scattering values can be corrected from the measured values, using the corrections above.